

AFRPL-TR-65-153

470462

INVESTIGATION OF LEAKAGE AND SEALING PARAMETERS

CATALOGED BY: DDG

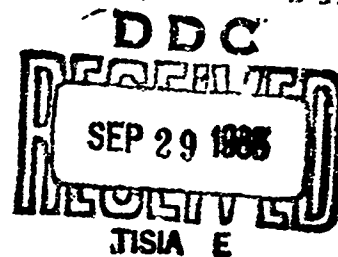
AS AD NO. _____

Paul Bauer
IIT Research Institute

Technical Report AFRPL -TR-65-153

August 1965

Air Force Rocket Propulsion Laboratory
Research and Technology Division
Air Force Systems Command
Edwards, California



**Best
Available
Copy**

NOTICES

Qualified users may obtain copies of this report from the Defense Documentation Center.

Defense Documentation Center release to the Office of Technical Services is not authorized (see Foreward).

When U. S. Government drawings, specifications, or other data are used for any purpose other than a definitely related Government procurement operation, the Government thereby incurs no responsibility or any obligation whatsoever, and the fact that the Government may have formulated, furnished, or in any way supplied the said drawings, specifications, or other data, is not to be regarded by implication or otherwise, or in any manner licensing the holder or any other person or corporation, or conveying any rights or permission to manufacture, use, or sell any patented invention that may in any way be related thereto. If this copy is not needed, return to AFRPL (RPRPD), Edwards, Calif.

INVESTIGATION OF LEAKAGE AND SEALING PARAMETERS

**Paul Bauer
IIT Research Institute**

FOREWORD

This final report on Project 6753 Investigation of Leakage and Sealing Parameters was prepared in compliance with Contract AF04(611)-9704 covering the performance from February 1964 through February 1965. The research was conducted by the IIT Research Institute for the Air Force Rocket Propulsion Laboratory and designated as IITRI Project K6062. Mr. James Lawrence (RPRP) was AFRL Project Engineer.

The IITRI project team comprised P. Bauer (Project Engineer), M. Glickman, and F. Iwatsuki (Program Manager) as principal investigators; J. Ash, S. Bhattacharyya, R. Cuenca, T. Eichler, C. Gustafson, A. Hehn, and L. Smith.

Publication of this report does not constitute Air Force approval of the report's findings or conclusions. It is published only for the exchange and stimulation of ideas.

James R. Lawrence
Project Engineer

ABSTRACT

This report documents investigations conducted to expand and refine analytical techniques for static and dynamic seals. A systematic investigation was made on those aspects of a seal pertaining to the sealing interface, structure, cavity, and related parts. Since the sealing interface was the problem area most lacking in reliable and concise information, major effort was directed toward its study. The problem was approached both analytically and experimentally by independently studying sealing interfaces with and without gross relative motion. The parameters influencing static interfaces were identified as surface finish, applied load, contact area and material hardness. These parameters were correlated to form design criteria suitable for use by systems designers to predict seal leakage performance. Additionally, these parameters were studied for rubber contact interfaces with wear added as the most significant parameter. The importance of wear on seal leakage was identified not as surface damage but as the effect of wear debris fragments and frictional heating. To the extent of experimentally supported information, all parameters were correlated in the form of design criteria. The output from these and other investigations produced applicable criteria and provided an insight into the relationship between parameters that can be used to optimize sealing and serve as guidelines for attaining minimum leakage. Commercial and other seals were utilized to show, by example, the design and analysis techniques leading to leakage performance predictions. The degree of success achieved was established by demonstration of experimental performance.

CONTENTS

1. INTRODUCTION	1
2. INTERFACE DEFORMATION AND LEAKAGE FLOW	5
2.1 Load Deformation, and Material Properties	5
2.2.1 Surface Interaction	6
2.1.2 Formation of the Leak Path	20
2.2 Macroscopic Interface Geometry	22
2.2.1 Experimental Studies	25
2.2.2 Load, Deformation and Area of Contact Characteristics	29
2.2.3 Leakage and Width of Interface Contact	34
2.3 Surface Topography	39
2.3.1 Surface Construction	39
2.3.2 Surface Topography and the Leakage Path	40
2.3.3 Surface Measurement and Identification	45
2.3.4 Surface Fabrication	46
2.4 Effect of Contaminants on the Deformation of an Interface	50
2.4.1 Experimental Studies	53
2.4.2 Observations	56
2.5 Conductance Parameter	62
2.6 Empirical Correlation of Parameters for Metallic and Plastic Interfaces	66
2.6.1 General Procedures	66
2.6.2 Ground Rules	67
2.6.3 Correlation Details	72
2.7 Observations	86
2.7.1 Lapped and Polished Surfaces	91
2.7.2 Turned Surfaces	95
2.7.3 Ground Surfaces	95
2.7.4 General Surface Effects	96

2.8	Supplementary Metallic and Plastic Interface Criteria	99
2.8.1	Load, Deformation, and Material Properties	99
2.8.2	Surface Topography	99
2.8.3	Interface Geometry	100
2.8.4	Calculation of Leakage	102
2.8.5	Hysteresis	102
2.8.6	Reusability of Sealing Interfaces	104
2.9	References	106
2.10	Symbols	107
3.	INTERFACE WEAR AND LEAKAGE FLOW	109
3.1	Fundamental Concepts of Wear and Friction	110
3.1.1	Characterization of Wear	114
3.1.2	Adhesive Wear	115
3.1.3	Abrasive Wear	125
3.1.4	Corrosive Wear	128
3.1.5	Friction	131
3.2	Wear, Surface Topography, and the Leakage Path	136
3.3	Criteria for Dynamic Sealing Interfaces, Contacting Type	143
3.3.1	Materials Selection	145
3.3.2	Bulk Wear Rates	146
3.3.3	Heat Generation	146
3.3.4	Surface Roughness	159
3.3.5	Leakage Flow and Its Prediction	159
3.4	References	173
3.5	Symbols	175
4.	BOUNDARY LUBRICATION - LUBRICANT FILMS	177
4.1	Boundary Lubricants	178
4.1.1	Solid Organic Base Materials	179
4.1.2	Inorganic Base Materials	180
4.1.3	Composite Base Materials	180
4.2	Solid Film Materials	183
4.2.1	Chemically Reacted Films	183
4.2.2	Self Adhering Films	187
4.2.3	Bonded Solid Films	187
4.3	References	188

5.	INTERSTITIAL ROTATING SHAFT SEALS	191
5.1	Seal Description	193
5.1.1	Hydrostatic Seals	193
5.1.2	Hydrodynamic Seals	195
5.2	Plane Slider Interstice	195
5.3	The Plane Slider Applied to a Simply Rotating Shaft Seal	199
5.4	Observations	205
5.4.1	Seal Geometry	205
5.4.2	Seal Performance	207
5.5	Design Classification of Rotating Shaft Seals	210
5.6	References	211
6.	SEAL INSPECTION AND FABRICATION TECHNIQUES	213
6.1	Measurement Techniques	213
6.2	Metalworking Processes	222
6.3	Dimensional Criteria	228
6.4	Summary	229
6.5	References	241
7.	ANALYTICAL CRITERIA FOR TYPICAL METALLIC SEAL STRUCTURES	243
7.1	Case I, Constant Thickness Seal Leg, Plastically Deformed at the Interface	244
7.1.1	General Analysis	244
7.1.2	Design Example	253
7.2	Case II, Constant-Thickness Seal Leg, Elastically Deformed	264
7.3	Case III, Linearly Varying Thickness Seal Leg, Elastically Deformed	272
7.4	References	275
7.5	Symbols	279
8.	ANALYTICAL CRITERIA FOR SEAL HOUSINGS	281
8.1	Structural Load Effects	282
8.2	Thermal Considerations	292
8.3	Dynamic Seal Housing	307
8.4	Observations	308
8.5	References	310

9.	INTERACTION OF SEALING PARAMETERS	311
9.1	General Considerations, Input Data	311
9.2	Mode of Interface Deformation and Leakage	311
9.2.1	Material Selection	312
9.2.2	Determination of the Interface Geometry	313
9.2.3	Preliminary Estimate of Leakage	314
9.3	Seal Housing Deformation	316
9.4	Structure Criteria	320
9.5	Experimental Evaluation	332
9.5.1	Structural Deformation Experiments	335
9.5.2	Leakage Experiments	335
9.6	References	343
10.	ANALYTICAL PREDICTION AND EXPERIMENTAL VERIFICATION OF LEAKAGE PERFORMANCE ON ADDITIONAL SEALS	345
10.1	Navan Naflex Seal	346
10.1.1	Description	346
10.1.2	Structural Analysis	347
10.1.3	Experimental Verification of the Structural Analysis	348
10.1.4	Interface Contact Area	348
10.1.5	Leakage Prediction	352
10.1.6	Experimental Performance	354
10.1.7	Observations	361
10.2	Cook Airtomic Seal	361
10.3	Evaluation of Additional Commercially Available Seals	363
10.3.1	Description	363
10.3.2	Structural Analysis	370
10.3.3	Leakage Prediction	374
10.3.4	Observations	376
10.4	IITRI Lip-Type Sliding Seal	386
10.4.1	Description	386
10.4.2	Experimental Evaluation	387
11.	CRITERIA FOR THE USE OF ADHESIVES AND SEALANT MATERIALS IN SEAL APPLICATIONS	405
11.1	Adhesives	405
11.2	Sealants	405
11.3	References	408

12. EMPIRICAL CORRELATION OF PARAMETERS FOR RUBBER INTERFACES	413
12.1 Material Properties and Interface Deformation	413
12.2 Surface Topography and Interface Deformation	414
12.3 Conductance Parameter and Interface Deformation	418
12.4 Correlation of Parameters	419
12.4.1 Leakage Experiments	421
12.4.2 Empirical Correlation	422
12.5 Observations	427
12.6 References	431
13. APPLICATION OF RUBBER INTERFACE CRITERIA	435
13.1 Rectangular Seal Ring	437
13.2 O-Ring Analysis	441
13.3 References	447
14. CONCLUSION	449
14.1 Design Criteria	449
14.1.1 Static Seals	449
14.1.2 Dynamic Seals	450
14.2 Minimum Leakage Sealing	451
14.2.1 Static Seals	451
14.2.2 Dynamic Seals	454
14.3 Recommendations	455
14.3.1 Static Seals	455
14.3.2 Dynamic Sealing	456
14.4 References	457
APPENDIX	
I EXPERIMENTAL RESULTS OF STATIC GASKET EXPERIMENTS	460
I-1 Experimental Apparatus and Procedures	460
I-2 Experimental Results	462
I-3 References	462
II EXPERIMENTAL INVESTIGATION OF SLIDING CONTACT AND LEAKAGE OF A SEALING INTERFACE	509
II-1 Experimental Apparatus	509
II-2 Leakage Flow and Measurement	510

II-3	Interface Loading	510
II-4	Initial Installation and Wear Compensation	515
II-5	Driving Mechanism	517
II-6	Experimental Parts	517
II-7	Experimental Results and Observations	518
II-8	Summary	530
II-9	Comments on the Fabrication and Inspection of Cylindrical Surfaces	531
II-10	References	538
III	EFFECTS OF PHASE CHANGES ON LEAKAGE RATES THROUGH ROTARY FACE SEALS	539
III-1	Introduction	539
III-2	Surface Tension	540
III-2.1	Static Equilibrium Surface Tension	540
III-2.2	Surface Tension in a Moving Fluid	546
III-2.3	The Role of Surface Tension under Nonequilibrium Conditions Instability of the Interface	549
III-3	Two-Phase Leakage Flows	563
III-3.1	The Liquid and Vapor Phases Treated Separately	563
III-3.2	Concurrent Liquid and Vapor Flow	571
III-4	The Energy Equation	579
III-5	References	582
IV	EXPERIMENTAL LOAD-DEFLECTION CURVES	583
V	CRITERIA FOR COMPONENT COVERS	602
V-1	Classification of Covers	602
V-2	Theoretical Analysis	604
V-3	Solutions to the Cover Equations	618
V-4	Sample Cover Problem Solution	619
V-5	General Comments and Conclusions	623
V-6	Symbols	623
VI	STRUCTURAL ANALYSIS OF SEALS AND DERIVATION OF FACTOR K	625
VII	DESCRIPTION OF STATIC AND SLIDING SEAL EXPERIMENTAL APPARATUS	657
VII-1	Static Seal Apparatus	657
VII-2	Sliding Seal Apparatus	657

VIII DEVELOPMENT OF A COMPUTER CODE FOR ESTABLISHING EMPIRICAL DATA FROM EXPERIMENTAL DATA	662
VIII-1 Mathematical Curve-Smoothing Technique	663
VIII-2 Iterative Smoothing Process	669
VIII-3 Curve Fitting of an Analytic Function Having Undetermined Parameters	670

ILLUSTRATIONS

	<u>Page</u>
1-1 Factors involved in the analysis of seals	3
2-1 Typical stress-strain diagram	7
2-2 Hypothetical model of an interface	8
2-3 Hypothetical interface deformation	14
2-4 Photomicrographs of surfaces in contact	21
2-5 Typical representation of interface geometries	24
2-6 Initial wedge profiles	25
2-7 Apparent area load characteristics for an 1141 steel wedge on an 1100-0 aluminum flat surface, (elastic-wedge case)	27
2-8 Apparent area load characteristics for an 1100-0 aluminum wedge on an 1141 flat steel surface (plastic-wedge case)	28
2-9 Plastic deformation of wedge	29
2-10 Plastic deformation of the flat surface in the elastic wedge case	29
2-11 Load deflection characteristics of an 1141 steel wedge on an 1100-0 flat aluminum surface (elastic-wedge case)	30
2-12 Load deflection characteristics of an 1100-0 aluminum wedge on an 1141 flat steel surface (plastic-wedge case)	31
2-13 Leakage load characteristics for the elastic wedge case	32
2-14 Leakage load characteristics for the plastic wedge case	33
2-15 Projected contact area load characteristics for an 1141 steel wedge on an 1100-0 aluminum flat surface (elastic wedge case)	35
2-16 Relationship between apparent and projected contact area for the elastic wedge case	36
2-17 Leakage flow versus projected contact area for the elastic wedge case	37
2-18 Leakage flow versus apparent contact area for the plastic wedge case	38
2-19 Schematic representation of waviness and deformation	41
2-20 Relative effects of stress on leakage	44

	<u>Page</u>
2-21 Location of topographical measurements on a circular gasket surface	46
2-22 Photomicrograph of a 321 stainless steel surface polished with diamond dust	48
2-23 Interferometer photomicrograph of a 321 stainless steel surface as shown in figure 2-22	48
2-24 Photomicrograph of a 321 stainless steel surface with fine turned and polished grooves	49
2-25 Interference photomicrograph of a 321 stainless steel surface as shown in figure 2-24	49
2-26 Photomicrograph of a 321 stainless steel lapped surface	51
2-27 Interference photomicrograph of the 321 stainless steel surface shown in figure 2-26	51
2-28 Photomicrograph of a 6061 T6 aluminum lapped surface	52
2-29 Interference photomicrograph of a 6061 T6 aluminum surface shown in figure 2-28	52
2-30 Effect of contaminant particle	53
2-31 Photomicrograph of a contaminated and clean lapped 6061 T6 aluminum surface	54
2-32 Photomicrograph of a contaminated and clean turned 6061 T6 aluminum surface	54
2-33 Interference photomicrograph of an uncontaminated lapped 6061 T6 aluminum surface	55
2-34 Interference photomicrograph of an uncontaminated turned 6061 T6 aluminum surface	55
2-35 Conductance parameter characteristics of contaminated and noncontaminated lapped surfaces	57
2-36 Conductance parameter characteristics of contaminated and noncontaminated turned aluminum surfaces	58
2-37 Photomicrograph of the lapped aluminum surface with embedded boron carbide particles resulting from an apparent contact stress of 40,000 psi	59
2-38 Photomicrograph of the turned aluminum surface with embedded boron carbide particles resulting from an apparent contact stress of 50,000 psi	59
2-39 Effect of contamination on the conductance parameter contact load characteristics of various surfaces	61
2-40 Flow chart of the correlation process	63

2-41	Approximate range of waviness with roughness for various fabrication processes	70
2-42	Comparison of surface roughness groups for turned surfaces	73
2-43	Comparison of surface roughness groups for ground surfaces	74
2-44	Comparison of surface roughness groups for lapped and polished surfaces	75
2-45	Design criteria for turned surfaces	87
2-46	Design criteria for ground surfaces	88
2-47	Design criteria for lapped and polished surfaces	89
2-48	Comparison of ranges of variation in data for lapped and polished surface groups at a modified stress ratio of 10^{-2}	92
2-49	Comparison of ranges of variation in data for turned surface groups at a modified stress ratio of 10^{-2}	93
2-50	Comparison of ranges of variation in data for ground surface groups at a modified stress ratio of 10^{-2}	94
2-51	Nondimensionalized relationship between parameters	97
2-52	Effects of installation on the orientation of seal interface	101
2-53	Hysteresis effects for an aluminum on steel interface	103
2-54	Leakage - normal stress response for Yatabe 347 stainless steel specimens (first set)	105
3-1	Sliding wear with leakage flow in the direction of wear damage	111
3-2	Sliding wear with leakage flow normal to the direction of wear damage	111
3-3	Pin-end-on-ring method	112
3-4	Pin-side-on method	112
3-5	Pin-on-disk method	112
3-6	Wear characteristics of a 60:40 brass pin on a hard steel disk	114
3-7	Effect of total load on wear of carbon against chromium plate	117
3-8	Wear coefficient of two steels as a function of contact stress	119

	<u>Page</u>
3-9 Transferred metal at critical point	120
3-10 Pyramidal point showing a groove in a hard surface	127
3-11 Abrasion resistance as a function of yield stress for metals abraded under a load of 1 kg on dry grade-3 emery paper	129
3-12 Wear of unlubricated metals as a function of load	130
3-13 Friction as a function of surface roughness for unlubricated copper on copper with a 1000-gm load at a velocity of 0.01 cm/sec	133
3-14 Schematic of a cone forming a groove in a flat surface	134
3-15 Face seal description	149
3-16 End view of face seal apparatus showing the carbon-glass interface	154
3-17 Side view of the face seal apparatus showing the carbon seal and adjustable loading mechanism	154
3-18 Dispersion of air bubble in the static interface	155
3-19 All static interface completely filled with a liquid film	155
3-20 Cavitation trails forming after one minute of running at 2000 rpm	155
3-21 View of interface shown in figure 3-19 magnified three times	155
3-22 Reduction in number of cavitation trails just before rotation ceased	155
3-23 Condensation of vapor one minute after rotation ceased	155
3-24 Interference photomicrograph of glass surface	157
3-25 Wear and friction of organic-impregnated carbons in liquid nitrogen	158
3-26 Effect of particle size on interface clearance	160
3-27 Distribution of copper fragments	161
3-28 Effect of particle generation on a linear sliding interface	171
3-29 Effect of particle generation on a rotational sliding interface	172
5-1 Hydrostatic seals	194
5-2 Plane slider	195

	<u>Page</u>
5-3 Pressure profile	197
5-4 Load capacity as a function of the clearance ratio for a plane slider	198
5-5 Face seal configuration	199
5-6 Separating force as a function of assumed minimum interstitial clearance with the slider geometry shown as a parameter	201
5-7 Face seal configuration	202
5-8 Leakage characteristics of a hydrodynamic seal	206
5-9 Pressure and flow distribution in a flat face seal with small undulations	210
7-1 Initial state of a seal leg with constant thickness	244
7-2 The geometric relationships between the leg length and deflection for a seal of uniform thickness	246
7-3 Deflection of a seal	249
7-4 Geometric relations for the portion of the leg flattened by fluid pressure	250
7-5 Cross section of prototype sliding seal	254
7-6 Effects of pressure on a flexible leg	257
7-7 Modified Goodman diagram for AISI 414 stainless steel	260
7-8 Effect of fluid pressure on lip deflection	263
7-9 Seal with cantilever leg of constant thickness	264
7-10 Nomograph, straight cantilever seal design	266
7-11 Nomograph, straight cantilever seal design	267
7-12 Nomograph, straight cantilever seal design	269
7-13 Nomograph, straight cantilever seal design	270
7-14 Inclined cantilever seal-leg	271
7-15 Tapered cantilever seals	273
7-16 Nomograph, straight cantilever seal design	274
7-17 Nomograph, cantilever seal design, varying thickness	276
7-18 Nomograph, cantilever seal design, varying thickness	277
7-19 Nomograph, cantilever seal design, varying thickness	278

	<u>Page</u>
7-20 Nomograph, cantilever seal design, varying thickness	279
8-1 General cover geometry	283
8-2 Flat cover plate geometry	284
8-3 Deflection parameter versus radius ratio for a flat cover	288
8-4 Slope parameter versus radius ratio for a flat cover	288
8-5 Linear thermal expansion for 17-7PH and similar metals	294
8-6 Linear thermal expansion for plain carbon steel	295
8-7 Linear thermal expansion for 304 stainless and similar metals	296
9-1 Typical geometry of the seal interface	313
9-2 Flat cover geometry	316
9-3 Housing dimensions	322
9-4 Functional aspects of the seal structure and support ring	326
9-5 Support ring	333
9-6 IITRI wedge seal	334
9-7 Contact width as a function of load IITRI wedge seal 2	336
9-8 Load deformation data, IITRI wedge seal 3	336
9-9 Helium leakage at 80°F for IITRI wedge seal 5	339
9-10 Helium leakage versus gas temperature at 200 psi IITRI wedge seal 5	340
9-11 Helium leakage as a function of pressure at various temperatures IITRI wedge seal 1	341
9-12 Helium leakage as a function of gas temperature at 200 psi IITRI wedge seal 1	342
9-13 Helium leakage as a function of gas temperature at 200 psi IITRI wedge seal 1	344
10-1 Two-inch diameter seal	346
10-2 Load deflection characteristics of a Naflex seal	349
10-3 Structural performance data from the Naflex seal catalog	350
10-4 Experimentally observed contact area of a Naflex seal	352

	<u>Page</u>
10-5 Leakage of a two-inch Naflex seal at 80°F	355
10-6 Leakage of a Naflex seal at low temperature	356
10-7 Leakage of a Naflex seal as a function of temperature for a fluid pressure of 1000 psig	357
10-8 Leakage of a Naflex seal at elevated temperature	358
10-9 Pressure cycling apparatus	359
10-10 Experimental apparatus disassembled after 73500 pressure pulsation cycles	359
10-11 Pressure cycling housing completely disassembled	360
10-12 Contact interface of Teflon-coated seal after 73,500 pressure pulsation cycles	361
10-13 Cook static seal, type FW	362
10-14 X-shaped seals	364
10-15 K-shaped seals	365
10-16 W-shaped seals	366
10-17 E-shaped seals	367
10-18 O-shaped seals	368
10-19 C-shaped seals	369
10-20 Beam with axial and transverse loading	371
10-21 Nonparallel interface contact	375
10-22 Helium leakage as a function of pressure for K-1 seal	377
10-23 Helium leakage as a function of pressure for K-2 seal	378
10-24 Helium leakage as a function of pressure for W-1 seal	379
10-25 Helium leakage as a function of pressure for W-2 seal	380
10-26 Helium leakage as a function of pressure for E-1 and E-2 seals	381
10-27 Helium leakage as a function of pressure for O-1 seal	382
10-28 Helium leakage as a function of pressure for O-2 seal	383
10-29 Dimensions of a lip-type sliding seal	386
10-30 Leakage as a function of gas pressure for metallic lip seals	388

	<u>Page</u>
10-31 Gas leakage as a function of shaft position in seal 1 at 300-psi gas pressure	389
10-32 Gas leakage as a function of shaft position for seal 2 at 300-psi gas pressure	390
10-33 Leakage variation during sliding for seal 2 at 300-psi gas pressure	391
10-34 Leakage variation during sliding for seal 1 at 300-psi gas pressure	392
10-35 Oil leakage for various pressures for metallic lip seals	395
10-36 Oil leakage at 1000-psi pressure differential as a function of total stroke-inches for metallic lip seal	397
10-37 Oil leakage at 1000 psi for varying sliding velocities for metallic lip seals	399
12-1 Leakage characteristics of butyl materials mated against 30 and 300 μ in. PTV turned steel surfaces	417
12-2 Pressure and contact forces acting at the interface	418
12-3 Flow chart of the correlation process for rubber interface parameters	420
12-4 Rubber gasket evaluation apparatus	421
12-5 Leakage characteristics of butyl materials mated against a 100-PTV turned steel surface	423
12-6 Leakage characteristics of Viton materials mated against a 100-PTV turned steel surface	424
12-7 Leakage characteristics of silastic materials mated against a 100-PTV turned steel surface	425
12-8 Leakage characteristics of Buna N materials mated against a 100-PTV turned steel surface	426
12-9 Mean relationship between the conductance clear- ance and apparent contact stress for 70 Shore A rubber materials	428
12-10 Variation of contact stress with hardness for geometrically identical Buna-N rubber gaskets at an arbitrarily selected leakage rate of 10^{-4} cc/sec (STP)	429
12-11 Relationship between the constant in equation (12-9) and hardness	430
12-12 Air permeabilities of elastomers at elevated temperatures	435

	<u>Page</u>
13-1 Experimental apparatus for evaluating rubber materials	438
13-2 Approximate geometrical representation of the seal interface	438
13-3 Theoretical and experimental leakage characteristics of a Butyl rubber ring	440
13-4 Cross section of an O-ring installed in a groove	441
13-5 Dimensions of the 70 Shore A seal and cavity	443
13-6 Deformation data for a 2-3/4 x 3 x 1/8 70 Duro O-ring	444
13-7 Experimental and approximate deformation characteristics of an 70 Shore A O-ring	445
I-1 Seal evaluation fixture	461
I-2 Conductance parameter-modified stress ratio for 1-μin. PTV seal surfaces	463
I-3 Conductance parameter-modified stress ratio for 1-μin. PTV seal surfaces	464
I-4 Conductance parameter-modified stress ratio for 1-2-μin. PTV seal surfaces	465
I-5 Conductance parameter-modified stress ratio for 2-2-3-μin. PTV seal surfaces	466
I-6 Conductance parameter-modified stress ratio for 3-μin. PTV seal surfaces	467
I-7 Conductance parameter-modified stress ratio for 5.6-7-μin. seal surfaces	468
I-8 Conductance parameter-modified stress ratio for 7.4-7 9-μin. PTV seal surfaces	469
I-9 Conductance parameter-modified stress ratio for 10.5-11-μin PTV seal surfaces	470
I-10 Conductance parameter-modified stress ratio for 11-11.2-μin. PTV seal surfaces	471
I-11 Conductance parameter-modified stress ratio for 11.2-μin. PTV seal surfaces	472
I-12 Conductance parameter-modified stress ratio for 13-14-μin. PTV seal surfaces	473
I-13 Conductance parameter-modified stress ratio for 19-20-μin. PTV seal surfaces	474
I-14 Conductance parameter-modified stress ratio for 23-30-μin. PTV seal surfaces	475

	<u>Page</u>
I-15 Conductance parameter-modified stress ratio for 34-35- μ in. PTV seal surfaces	476
I-16 Conductance parameter-modified stress ratio for 35- μ in. PTV seal surfaces	477
I-17 Conductance parameter-modified stress ratio for 42-45- μ in. PTV seal surfaces	478
I-18 Conductance parameter-modified stress ratio for 45-46- μ in. PTV seal surfaces	479
I-19 Conductance parameter-modified stress ratio for 55- μ in. PTV seal surfaces	480
I-20 Conductance parameter-modified stress ratio for 56-57- μ in. PTV seal surfaces	481
I-21 Conductance parameter-modified stress ratio for 65-75- μ in. PTV seal surfaces	482
I-22 Conductance parameter-modified stress ratio for 88-99- μ in. PTV seal surfaces	483
I-23 Conductance parameter modified stress ratio for 120-155- μ in. PTV seal surfaces	484
I-24 Conductance parameter-modified stress ratio for 155-156- μ in. PTV seal surfaces	485
I-25 Conductance parameter-modified stress ratio for 163- μ in. PTV seal surfaces	486
I-26 Conductance parameter-modified stress ratio for 175-188- μ in. PTV seal surfaces	487
I-27 Conductance parameter-modified stress ratio for 225-280- μ in. PTV seal surfaces	488
I-28 Conductance parameter-modified stress ratio for 300-350- μ in. PTV seal surfaces	489
I-29 Conductance parameter-modified stress ratio for 450- μ in. PTV seal surfaces	490
I-30 Conductance parameter-modified stress ratio for 600-840- μ in. PTV seal surfaces	491
I-31 Conductance parameter-modified stress ratio for lapped and polished seals having a 0-2- μ in. PTV roughness	492
I-32 Conductance parameter-modified stress ratio for lapped and polished seals having a 2-5- μ in. PTV roughness	493

	<u>Page</u>
I-33 Conductance parameter-modified stress ratio for lapped and polished seals having a 5-10- μ in. PTV roughness	494
I-34 Conductance parameter-modified stress ratio for lapped and polished seals having a 10-30- μ in. PTV roughness	495
I-35 Conductance parameter-modified stress ratio for lapped and polished seals having a 0-10.5- μ in. PTV roughness	496
I-36 Conductance parameter-modified stress ratio for turned seals having a 11-30- μ in. PTV roughness	497
I-37 Conductance parameter-modified stress ratio for turned seals having a 20-30- μ in. PTV roughness	498
I-38 Conductance parameter-modified stress ratio for turned seals having a 30-50- μ in. PTV roughness	499
I-39 Conductance parameter-modified stress ratio for turned seals having a 50-75- μ in. PTV roughness	500
I-40 Conductance parameter-modified stress ratio for turned seals having a 75-100- μ in. PTV roughness	501
I-41 Conductance parameter-modified stress ratio for turned seals having a 100-200- μ in. PTV roughness	502
I-42 Conductance parameter-modified stress ratio for turned seals having a 200-400- μ in. PTV roughness	503
I-43 Conductance parameter-modified stress ratio for turned seals having over 400- μ in. PTV roughness	504
I-44 Conductance parameter-modified stress ratio for ground seals having a 0-10.5- μ in. PTV roughness	505
I-45 Conductance parameter-modified stress ratio for ground seals having 11-50- μ in. PTV roughness	506
I-46 Conductance parameter-modified stress ratio for ground seals having 50-100- μ in. PTV roughness	507
I-47 Conductance parameter-modified stress ratio for ground seals having 100-200- μ in. PTV roughness	508
II-1 Sliding wear experimental apparatus	511
II-2 Experimental sliding wear and leakage evaluation apparatus	512
II-3 Seal and loading ring for sliding wear and leakage apparatus	512
II-4 Sliding piston for sliding wear and leakage apparatus	512

	<u>Page</u>
II-5 Deformation of concentric rings	514
II-6 Seal ring	519
II-7 Experimental sliding shaft	520
II-8 Leakage rate and friction characteristics of Nitralloy sliding on Nitralloy as a function of total sliding distance	523
II-9 Exaggerated view of piston and ring geometry	524
II-10 Leakage rate of Nitralloy sliding on Nitralloy as a function of total sliding distance	526
II-11 Friction characteristics of Nitralloy sliding on Nitralloy as a function of total sliding distance	527
II-12 Photomicrograph of wear particles collected after 178,483 stroke-inches at 200-psi contact stress	527
II-13 Taper dimensions of the ring	529
II-14 Total wear of a Nitralloy-135 ring sliding in an air environment	532
II-15 Schematic view of a circular tracing instrument	534
II-16 Nonalignment of planar centers	534
II-17 Form letter requesting information on fabricating cylindrical surfaces to very precise tolerances	537
III-1 Liquid attachment to a vertical plate	541
III-2 Liquid attachment between two plates	542
III-3 Geometrical relation between clearance, contact angle, and film radius of curvature for a narrow clearance	545
III-4 Creation of contact angle by the three distinct surface tension forces	546
III-5 Vapor generation at points of minimum clearance	547
III-6 The dynamic contact angle for vaporization	547
III-7 The dynamic contact angle for condensation	548
III-8 Perturbation of interface	549
III-9 Vapor penetration of the liquid	553
III-10 Stresses in the liquid at the interface	554

	<u>Page</u>
III-11 Liquid-vapor flow configuration	557
III-12 Pressure distribution ahead of the vapor cavity	561
III-13 Alternate regions of vapor penetration through the liquid phase	562
III-14 Increased pressure gradients caused by vaporization	563
III-15 Velocity profiles in lubricating film	564
III-16 Radial pressure distribution for liquid leakage	566
III-17 Radial pressure and temperature distributions with a phase change at r''	568
III-18 Two-phase velocity distribution, vaporization on rotor face	571
III-19 Tangential velocity distribution, vaporization on stator face	574
III-20 Temperature distribution across liquid film	577
IV-1 Cross section of load-deflection piston assembly	583
VII-1 Seal test apparatus	658
VII-2 Over-all view of the assembled static seal apparatus	659
VII-3 Lower base and cover assembly	659
VII-4 View of the heating coil	659
VII-5 Schematic of static seal evaluator facility	660
VII-6 Sliding seal experimental fixture	661
VIII-1 Experimental data scatter	667
VIII-2 1st smoothing at Y's	668
VIII-3 Y's then X's	671
VIII-4 15th iteration	672
VIII-5 Relative standard error	673
VIII-6 Analytic functions at original points	676
VIII-7 Analytic functions based on smooth points iterated 15 times	678

TABLES

<u>Table</u>		<u>Page</u>
2-1	Meyer hardness and index for various materials	13
2-2	Modes of interface deformation	43
2-3	Experimental data index	76
3-1	Typical values of coefficient of wear	117
3-2	Wear particle size and surface roughness for sliding metal systems	122
3-3	Wear particle size for copper sliding on copper in various fluids	124
3-4	Ratio of hardness to modulus of elasticity for various materials	126
3-5	Coefficient of friction for various metal combinations	126
3-6	Wear rates for various materials in air obtained from a pin and ring test with a 400-gram load at a velocity of 180 cm/sec	137
3-7	Wear rates from pin on disk experiments in selected propellants	138
3-8	Estimated number of wear particles generated in one inch of sliding contact	144
3-9	Wear of seal faces in liquid nitrogen	147
4-1	Techniques for supplying films at interfaces	179
4-2	Properties of organic materials	181
4-3	Friction performance of ceramics and cermets	182
4-4	Performance characteristics of composite materials	184
4-5	Solid film lubrication techniques	186
5-1	Minimum separation clearances	204
5-2	Classes of rotating shaft seals	212
6-1	Dimensional criteria	230
6-2	Tolerance variations on shaft	232
6-3	Tolerance variations on housing	234
6-4	Tolerance variations on flange	236
6-5	Tolerance variations on ring	238
7-1	Effect of pressure loading on flexible leg of uniform thickness	256
7-2	Hoop stress distribution for a lip seal of uniform thickness ($p = 100$ psi)	259

7-3	Deflection of leg seal with pressure loading	262
8-1	Mean coefficient of thermal expansion of high-strength, high-temperature fastener alloys at various temperatures	293
8-2	Linear thermal expansion for 17-7PH and similar metals	297
8-3	Linear thermal expansion for plain carbon steel	298
8-4	Linear thermal expansion for 304 stainless and similar metals	299
8-5	Modulus of elasticity of high-strength, high-temperature fastener alloys at various temperatures	304
8-6	Yield strength of high-strength, high-temperature fastener alloys at various temperatures	305
8-7	Creep strength of metals	306
9-1	Bending stress as a function of leg length to thickness ratio	325
9-2	Bending stress due to fluid pressures as a function of leg length to thickness ratio	328
9-3	Bending stress due to a deflection of 0.0015 in. as a function of leg length to thickness ratio	329
9-4	Actual and predicted leakage rates of helium for the IITRI wedge seal	337
10-1	Leakage prediction of a Naflex seal	353
10-2	Loading properties of seal configurations	373
10-3	Summary of theoretical and experimental leakage rates for various seal configurations	384
10-4	Variations in oil leakage for varying applied pressures	394
10-5	Oil leakage as a function of time at 1000-pounds-per-square-inch pressure	396
10-6	Sealing characteristics of metallic lip seals	401
10-7	Results of continued cycling of lip seal at 300 psi gas pressure	402
10-8	Results of pressure shock test on metallic lip seals	407
11-1	Mechanical properties of elastomeric sealants	409
11-2	Environmental and electrical properties of elastomeric sealants	410
11-3	Processing characteristics of elastomeric sealants	411

12-1	Shore hardness measuring instruments	415
12-2	Relative effect of parameters on leakage	416
12-3	Permeation comparison for rubber materials	431
12-4	Air permeabilities at various temperatures, various elastomers	432
II-1	Effects of wear on ring and shaft dimensions and surface finish	521
II-2	Variation of leakage with cumulative sliding of the parts under load	524
II-3	Variation of leakage with angular position of parts	525
II-4	Variation of leakage with cumulative sliding of the parts under load for contact stress of 200 psi	528
II-5	Effects of wear on ring and shaft dimensions and surface finish	528
II-6	Leakage variation with position for new ring and shaft	530
VI-1	Calculated results of pressure-energization factor C	655

1. INTRODUCTION

The principal objective of a study initiated by the Air Force Rocket Propulsion Laboratory* in February 1962 was the development of analytical techniques for the design of static and dynamic seals for use in rocket fuel systems. The results of this study showed that the state-of-the-art of sealing was undeveloped from the standpoint of analytical criteria and that the attainment of the objective required substantial investigation in many diverse areas. In the case of static seals, the parameters influencing sealing were identified and promising guidelines developed whereby the parameters could be interrelated to form handbook criteria. Dynamic seals, on the other hand, posed additional problems in that not all of the parameters were identified and for those known parameters no satisfactory interrelationship was apparent.

To further advance this work, the Air Force Rocket Propulsion Laboratory initiated this follow-on program with the following objectives:

- (1) To expand and refine the analytical procedures in a format suitable for use by systems designers.
- (2) To develop concise interrelationships between parameters leading to the optimization of seal designs.
- (3) To continue the development of analytical techniques in those areas where little progress has been attained.
- (4) To demonstrate the application and reliability of the design criteria by comparison with the experimental performance of seals under simulated operating conditions.

The approach employed in this program was based on the philosophy that a seal is composed of at least three principal parts that can be studied independently: an interface barrier to leakage flow formed by surfaces in contact; an interface substructure composed of the surface substrate and extending to a structural configuration as may be found in most demountable seals; and a housing or seal cavity which contains the seal and includes all seal related parts.

The initial topics considered were interface deformation and leakage (Section 2) and interface wear and leakage (Section 3).

*Contract AF04(611)-8020 Analytical Techniques for the Design of Seals for Use in Rocket Propulsion Systems Volumes I and II. AFRPL-TR-65-61 May 1965.

These topics, pertinent to static and dynamic seals respectively, are considered in a general manner, whereby each of the influencing parameters is viewed independently. Following the general considerations, unique relationships between parameters were developed, forming design criteria. The criteria for static seal interfaces are developed in Section 2 for metal and plastic materials and in Section 12 for rubber materials. The parameters include interface loading, material properties, surface geometry and topography, and surface fabrication. Dynamic seal interface criteria are developed in Section 3 for rubbing surfaces where the primary consideration is wear and the formation of leakage paths. These criteria are also unique in that this is the first known attempt to apply the work of friction and wear investigators to the dynamic sealing problem. The usual approach has been solely from a fluid mechanics viewpoint. The case where surfaces are separated hydrostatically or hydrodynamically is considered in Section 5. Another mechanism of lubrication considered independently is boundary lubrication. While some consideration is given to lubricated rubbing contact in Section 3, the topic is sufficiently broad, covering solid film and other lubrication techniques, to require individual consideration in Section 4.

Seal structures were then considered in Section 7 from the standpoint of the loading induced by the structure on the interface. Since structural shapes are only limited by the designers imagination, those most promising and typical were chosen for analysis, using simple beam theory applied to elastically deformed structures. Since the process of fabricating sealing surfaces, seal structures, and seal-related parts imposes limitations on leakage performance, the effects are considered as a supplementary study in Section 6. Following the general methods of structural analysis, criteria for seal housings are developed in Section 8. Finally, the criteria from each independent study are superimposed in the analysis of over-all seal performance. This topic is covered in Section 9 for plastic and metallic seals and in Section 13 for rubber seals. Performance of dynamic seals is contained in Sections 3, 5 and 10. Charts showing the interrelationship between topics are shown on figure 1-1.

Following the general analysis of seals, specific seals were selected for fabrication and experimental evaluation. These results, contained in Section 10 establish the reliability of the criteria and method of analysis. These demonstration experiments were conducted on commercial and IITRI design seals. Experiments on sixteen seals showed that the correlation of parameters and other criteria produce leakage predictions within one order of magnitude of the actual leak rate.

To complete the topic of sealing, adhesives and sealants are briefly discussed in Section 11.

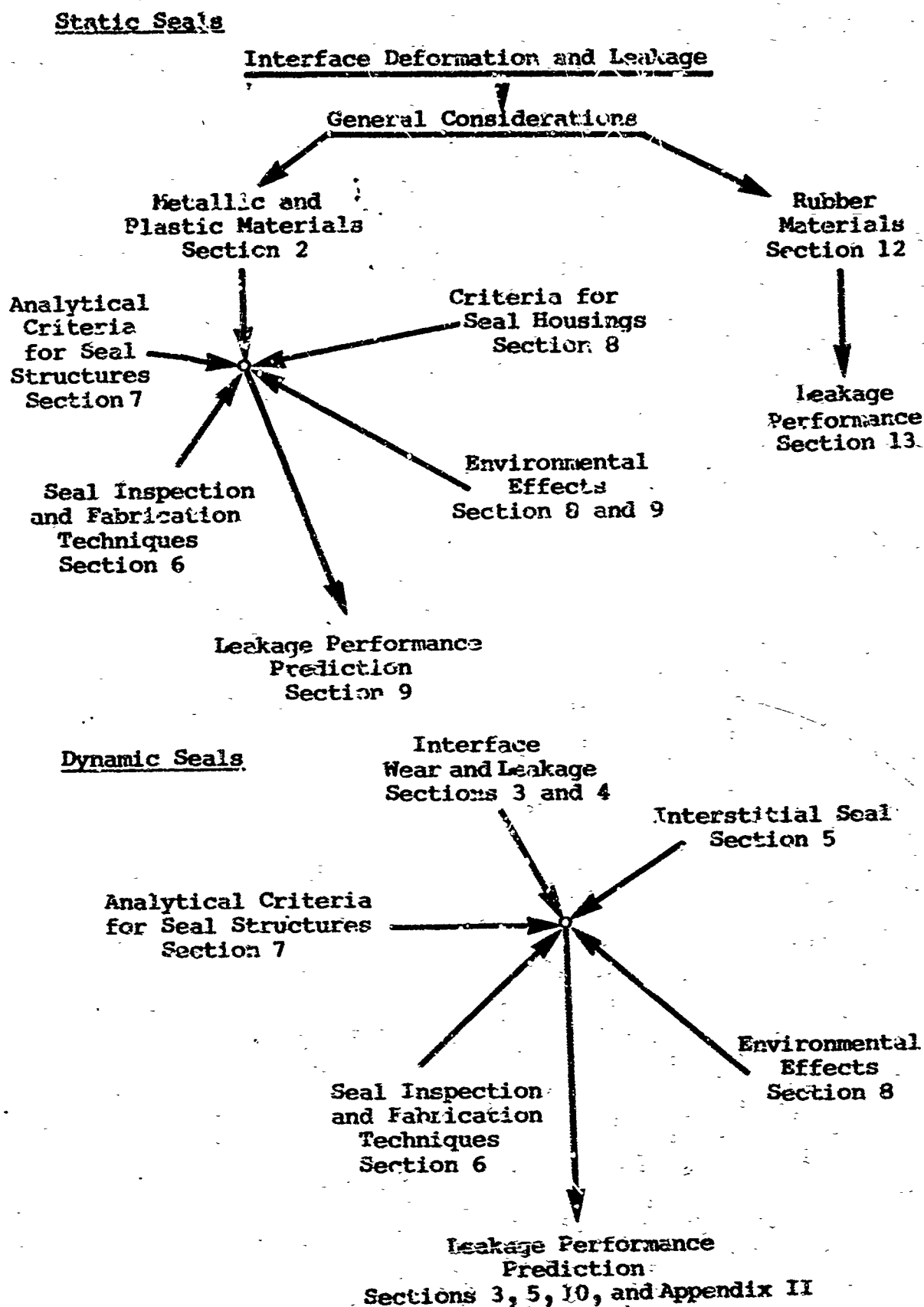


Figure 1-1 Factors involved in the analysis of seals

2. INTERFACE DEFORMATION AND LEAKAGE FLOW

One of the greatest difficulties in developing seal criteria is the generation of quantitative relationships among performance parameters that can be used in the prediction of leakage. This task is further complicated by the fact that the parameters are complex, interrelated, and not easily defined. The resulting criteria cannot be presented simply unless a philosophy, details of development, and substantiation of results are first discussed. This section, therefore, begins with a detailed definition of the following parameters:

- Load, deformation and material properties
- Interface geometry
- Surface topography
- Contaminants

Each parameter is then correlated with the others using the conductance concept developed in Reference 2-1. The criteria are presented along with a summary of the important rules used in the correlation process. The form of the criteria is such that the leakage performance of a sealing interface can be closely approximated when the following known input information is available:

- Fluid pressure and properties
- Interface forces determined from a structural analysis of the seal structure and related parts
- Interface material properties
- Surface fabrication methods and resulting interface surface topography and geometry

Although each of these criteria is usually known, all can be determined from a specified leak rate.

2.1 Load, Deformation, and Material Properties

When roughened surfaces are pressed together, void spaces and contact junctions are formed. The interconnection of certain randomly located void spaces forms an interface consisting of one or more paths through which a fluid can flow. In the process of pressing the surfaces together, however, deformation of the materials occurs, disrupting the chance interconnection of void spaces. Thus, the problems associated with leakage flow through an interface fall into two categories, which can be considered separately:

Surface interaction, the macroscopic and microscopic deformation of the materials forming the interface.

Formation of leak paths, the probabilistic interconnection of void spaces.

2.1.1 Surface Interaction

Surface interaction behavior cannot be quantitatively described by any of the pertinent scientific disciplines. This is attributed to the complex nature of the phenomenon. Some inroads have been made through an understanding of the fundamental properties but the results are not sufficiently encompassing nor have they been completely verified. While a complete understanding cannot be realized, the important properties have, at least, been identified. The parameters that govern surface interaction include bulk or volume properties of the material and the surface properties. The volume properties of importance are the plastic deformation parameters described by the yield strength and penetration hardness. Of lesser importance are the elastic modulus, shear modulus, fracture stress, thermal properties and stored elastic energy. The surface properties of interest are the chemical reactivity, molecular diffusion and, possibly, the surface energy. Each of the volume and surface properties is dependent on the others but the extent of this dependence has not been defined.

2.1.1.1 Volume Properties

Elastic Properties. The elastic nature of a material is determined by measured properties given in terms of strain, the reversible or nonpermanent deformation of a material compared with its original shape. Engineering strain ϵ_e in a conventional tensile test is

$$\epsilon_e = \frac{l_f - l_o}{l_o}$$

and real strain,

$$\epsilon = \log l_f / l_o$$

where

l_f = final length of a specimen subjected to a load typified by a tensile test

l_o = original length

A typical stress-strain curve for a material is shown as figure 2-1. The slope of the curve in the elastic region is almost constant and defines Young's modulus E or $E = \sigma/\epsilon$. The maximum stress within the almost constant slope range is

described as the proportional limit. Actually, the slope varies over the entire range of stress, consequently, the proportional limit is not well defined. The point on the curve at which a substantial change in strain occurs is described as the elastic limit and, like the proportional limit, is subject to interpretation. To overcome the problem of interpretation, a 0.2 per cent yield stress σ_y is commonly used to describe a relative value of the elastic limit and, simultaneously, the yield stress. The 0.2 per cent yield stress corresponds to a plastic strain of 0.2 per cent. Each of the preceding properties is measured and, consequently, varies with the instrumentation employed, the shape of the specimen, and such other effects as strain-rate sensitivity. Additionally, the elastic properties are observed effects and do not describe the cause of the effects.

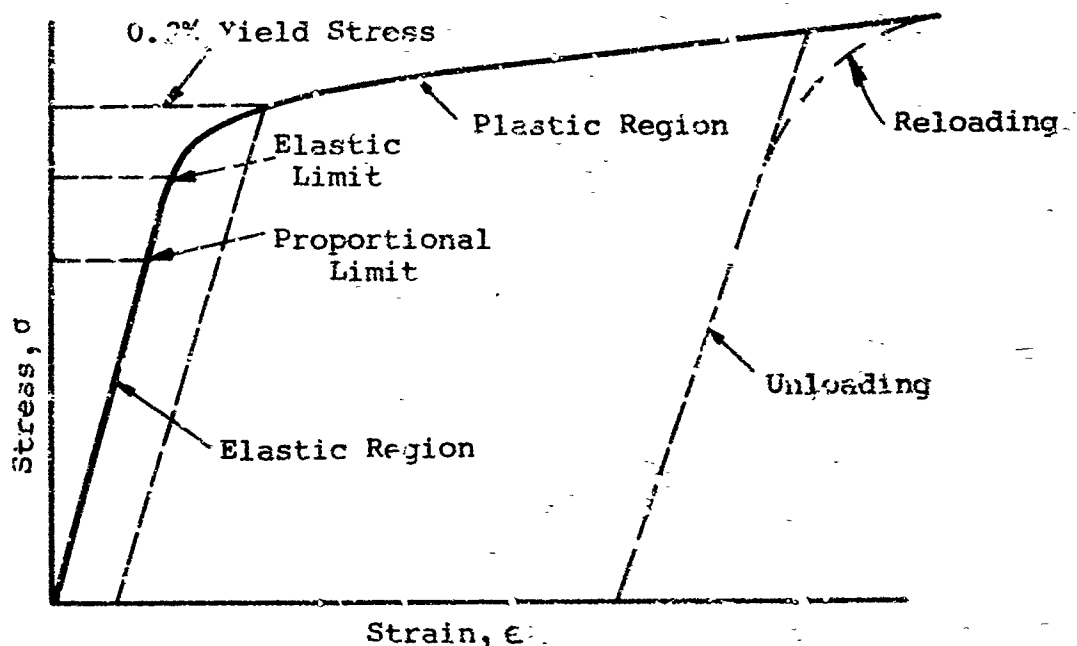


Figure 2-1 Typical stress-strain diagram

A close relationship exists between the yield strength and Young's modulus of many metals and their alloys. A comparison of data in References 2-2 and 2-3 shows that $\sigma_y \approx 0.003E$. Carrying this approximation further and applying the definition

$$\epsilon_y = \sigma_y / E,$$

we can see that the strain at which yielding occurs is 0.003. The yield strain of plastic ranges between 0.008 and 0.03, while rubber approaches 1.0. The interdependence of properties is attributed to the molecular bond strength. It can also be shown that the amount of elastic energy stored in metallic materials is very small. The elastic energy per unit volume is $0.5 \sigma_y$ or $0.5 (\epsilon_y)^2 E$. If ϵ is 0.003 and E is 30×10^6 psi, the energy is ~50 in.-lb per cu in.

The influence of elastic deformation on a seal interface is twofold. First, the loading of the bulk seal material produces deformation of the entire material. The magnitude of the deformation and the energy required is a function of shape and composition of the material. Secondly, the surface asperities are deformed during the loading process, thereby influencing the geometrical nature of the leakage path. The influence of both effects can be described by considering a hypothetical model of two sets of surfaces pressed together, as shown on figure 2-2. In the first case, the application of a load to the bulk material produces a significant change in the leak path dimension h , as compared with the second case. The elastic deformities of the asperities, however, will be the same in each case for the same load and contact area. To show the magnitude of effect the following calculations are shown for the deformation of the hypothetical surface shown in figure 2-2(b).

The relative deformation can be defined as

$$\% \frac{h_o - h_f}{h_o} = \frac{\sigma}{E} \times 100\% = \epsilon \times 100\% \quad (2-1)$$

where

h_f = final leak path dimension

h_o = initial leak path dimension

$\sigma = P/A_R$ = applied load/real contact area

Consider steel with a modulus of 30×10^6 and a yield stress of 100,000 psi. The relative deformation is 0.3 per cent and is negligible. On the other hand, a rubber material with an apparent modulus of 1000 psi deforms 100 per cent at a stress of 1000 psi. It should be noted, however, that rubber does not completely obey the stress-strain relationship that applies to metals and many nonmetals. In the case considered the results are a close approximation.

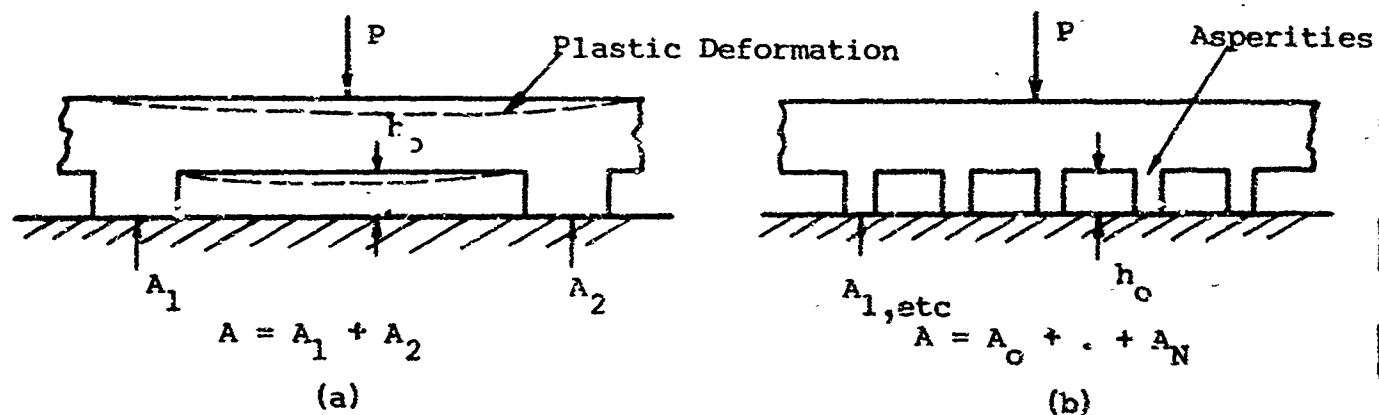


Figure 2-2 Hypothetical model of an interface

It may be concluded that the leak path geometry of interfaces formed by materials of high elastic modulus will be influenced by the size distribution of asperities and the shape and composition of the bulk material. Leak paths formed between low elastic modulus materials will be influenced primarily by the applied load or stress.

Plastic Properties. Plastic deformation is characterized by the relatively flat portion of the stress-strain curve shown on figure 2-1, where large changes in strain occur with little change in stress. The parameters available to describe plasticity are the yield strength and penetration hardness. The importance of hardness as a seal parameter will be demonstrated in the following discussion. Before proceeding, we should compare the two parameters.

Yield stress and hardness are closely related. Tabor (Ref. 2-4) demonstrated, theoretically and experimentally, that the hardness H of many metals and nonmetals is $\sim 3\sigma_y$. At first glance it would appear that either property could be used to describe the plastic flow of materials, particularly in respect to the filling of leak path void spaces in a seal interface. However, the relationship between hardness and yield stress is not sufficiently unique and is dependent upon other factors. These factors plus other seal-related advantages qualify hardness as a more important parameter. The argument may be stated as follows.

- Hardness can be measured more easily than yield stress.
- The hardness measuring process is geometrically close to the pressing of an asperity into a surface.
- Hardness measurement instrumentation is more consistent with respect to the reproducibility of results. Yield strength instrumentation is also consistent, but the shape of the material specimens varies as do the results.

Hardness is measured by pressing a hard indenter into a flat surface of the material to be evaluated, and measuring the area of indentation produced by a given load. The ratio of load to area is defined as the indentation hardness.

Hardness measurements can be relatively insensitive to the material shape. Tabor (Ref. 2-4) points out that most hardness instrumentation produce data representative of an 8 per cent strain, thereby qualifying the technique as consistent.

The most common measurement method is the Brinell test. This test consists of indenting a surface using a 10-mm steel ball with standardized loads between 500 and 3000 kg, depending on the softness of the material. The load is applied for a standard time,

usually 30 sec, and the diameter of the indentation measured with a low power microscope. The Brinell hardness number (BHN) is expressed as the load P divided by the surface area of the indentation:

$$\text{BHN} = \frac{P}{(\pi D/2) (D - \sqrt{D^2 - d^2})} \quad (2-2)$$

where

P = applied load (kg)

D = diameter of ball (mm)

d = diameter of indentation (mm)

Other indenter shapes and materials are also used in measuring hardness. The indenter may be a diamond pyramid as in the Vickers or Knoop test or a ball of hardened steel or tungsten carbide as is used in the Rockwell tests. The Rockwell test departs from the Brinell area measurement procedure in that the normal deformation is measured. The results can be correlated since the difference between area and normal deformation is simply one of ball geometry.

The Vickers hardness test employs a pyramidal indenter whose angle between opposite forces is 136 deg. This angle was chosen because it approximates the most desirable ratio of indentation-to-ball diameter in the Brinell hardness test. The Vickers hardness number (VHN) is defined as the load divided by the surface area of the indentation, i.e.,

$$\text{VHN} = \frac{2P \sin (\theta/2)}{L^2} = \frac{1.854 P}{L^2}$$

where

L = average length of the impression (mm)

P = applied load (kg)

θ = 136 deg

Several deficiencies exist that limit the interpretation of hardness measurements:

- 1) The human error in measuring the impression diameter that is caused by ill-defined edges of the indentation.
- 2) The elastic recovery of the indentation induces an error that is a function of the indenting load.

- 3) the interpretation of the contact area and its relationship to the deformation phenomena.
- 4) the variation in results that is due to the magnitude of applied load and the geometry of the indenter. Unless geometrical similarity is maintained, strain-hardening effects can predominate and prevent the correlation of test results.

The definition of Brinell hardness is an example of improperly defined surface area. The applied load is assumed to be distributed over the apparent or surface area of the dent. It can be shown that the Brinell hardness number of a material is constant only for one applied load and diameter of ball. To obtain consistency of results at nonstandard loads, geometrical similarity must be maintained. This problem was investigated by Meyer (discussed by Dieter, Ref. 2-5), who suggested that the projected area of contact is an improved parameter. The mean contact stress between the surface of the indenter and indentation is defined as projected area of the indentation.

$$\text{Meyer Hardness} = \sigma_m = \frac{4P}{\pi d^2} \quad (2-3)$$

Meyer hardness is reportedly less sensitive to applied load than Brinell hardness. For a cold-worked material, the Meyer hardness is essentially constant and independent of load while the Brinell hardness decreases as the load increases (Ref. 2-5). For an annealed material, the Meyer hardness increases continuously with increasing load, whereas the Brinell hardness first increases and then decreases.

An experimental comparison of the variation between hardness determined by apparent and projected areas is shown on figures 2-7 and 2-15. These data were obtained for various shaped hard indenters pressed against a softer surface. The slope of the curves represents the hardness of the material. Figure 2-7 shows hardness based on the apparent contact area, as varying between 14,000 and 38,000 psi, depending on the shape of the indenter. On the other hand, the hardness based on projected contact area (figure 2-15) results in a hardness range between 48,000 and 52,000 psi.* Thus, it can be concluded that hardness, based on projected area contact, is independent of the indenter shape and is a consistent parameter to describe material properties. For this reason, the Meyer hardness was selected as an important seal-related parameter.

*The 10-deg shallow wedge shape is neglected because of elastic deformation effects.

Meyer (Ref. 2-5) also proposed an empirical relation between load and the diameter of the indentation considering the effects of strain hardening. This relation, usually called Meyers law, is

$$P = kd^{n'} \quad (2-4)$$

where

n' = material constant related to strain hardening
(Meyer index)

k = a material constant representing the resistance
of a metal to deformation

The material constant in the exponential equation for the true law is approximately equal to the strain-hardening coefficient n plus 2; i.e.,

$$n' = n + 2$$

The strain-hardening coefficient can be readily determined from the slope of a log-log plot of a plastic portion of the stress-strain curve, as shown typically on figure 2-1.

When indentations are made with different diameter indenters, different values of k and n' are obtained.

$$P = k_1 D_1^{n'_1} = k_2 D_2^{n'_2} = k_j D_j^{n'_j}$$

Meyer also found that n' was almost independent of the indenter D but that k decreased with increasing D . The general expression of Meyers' law becomes

$$P = \frac{C d_1^{n'}}{D_1^{n'-2}} = \frac{C d_2^{n'}}{D_2^{n'-2}} = \dots \frac{C d_j^{n'}}{D_j^{n'-2}}$$

where

$$C = k_1 D_1^{n'-2} = k_2 D_2^{n'-2} = \dots k_j D_j^{n'-2}$$

An easy method for determining the Meyer index n' is through a hardness test. By pressing an indenter against a surface under varied load conditions, the dent diameter can be measured. The Meyer index can be determined from a log plot of the data if we consider Meyer's law in the form

$$\log P = \log k + n' \log d. \quad (2-5)$$

The slope of the curve is n' . For hard materials, the various loadings available in a Brinell testing machine may be used and for softer metals a standard testing machine may be used to provide the load, and a precision steel ball used for an indenter. In making these measurements care should be exercised to maintain geometrical

similarity in the ratio of the impression diameter to the ball diameter (d/D) for all of the metals tested. The range of validity for Meyer's law is $0.1 < d/D < 1.0$ (Ref. 2-5). A series of experiments was conducted on a number of metals and nonmetals. These results, shown on Table 2-1, were obtained for d/D approximately 0.5.

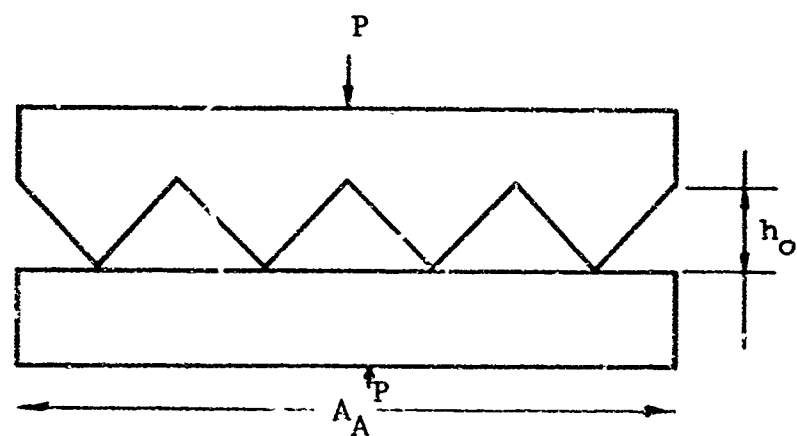
Table 2-1

MEYER HARDNESS AND INDEX FOR VARIOUS MATERIALS

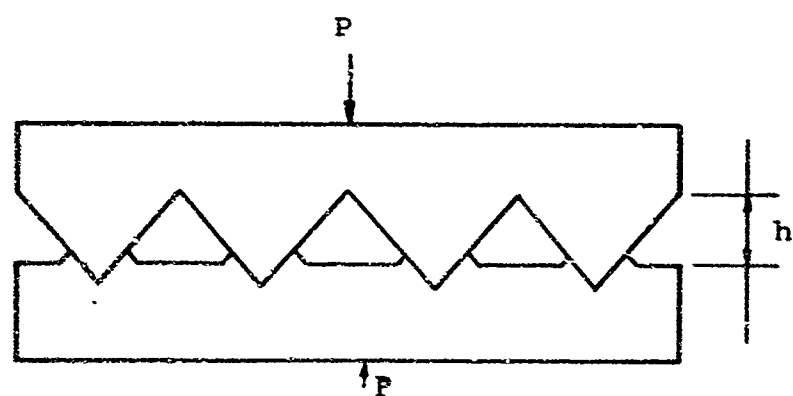
Material	Meyer Hardness (psi)	Meyer Index
102 Copper	109,000	2.09
1100 - 0 Al	48,700	2.19
2024 - 0 Al	89,600	2.44
5086 - H32 Al	139,000	2.14
6061 - T6 Al	159,000	2.00
2024 - T351 Al	202,000	2.00
7075 - T6 Al	262,000	2.00
Teflon	3,870	2.80
Lead	4,390	2.33
321 CRS	202,000	2.35
C1141 Steel	308,500	2.22

Creep may have an important effect on the magnitude of Meyer hardness and index, particularly for Teflon and lead. The results shown on Table 2-1 were obtained for a load application of one minute. While it is recognized that the results may not be completely accurate, they are sufficient for use in the development of interface deformation correlations.

From the preceding discussion of plastic deformation from a volume viewpoint, we can attempt to describe the deformation of a sealing interface. As a start, the interface can be viewed as being composed of one surface having uniform asperities mated against a flat surface, as shown in figures 2-3(a) and (b). The deformation under each asperity is assumed identical to that under an indenter pressing against a soft surface as described by hardness measurement techniques. Application of a load, figure 2-3(b), reduces the characteristic size, h , of the leakage path. It is assumed that the area under each asperity contains no void spaces and, therefore, does not contribute to the leakage path. Thus, we see that, when $P/A_A = \sigma_m$, the leakage path is nonexistent. Also, if the initial leakage path characteristic is h_0 , we might expect that h will vary inversely with P/A_A since the projected area of contact varies with P/A_A , as demonstrated by the hardness measurements. The deformation can be written as



(a) Initial Condition



(b) Under Load

Figure 2-3 Hypothetical interface deformation

$$\sigma = P/A_A$$

and, for terminal conditions $\sigma = \sigma_m$, $h = 0$,

$$\sigma/\sigma_m = \frac{K(h_o - h)}{Kh_o}$$

or

$$h = h_o (1 - \sigma/\sigma_m) \quad (2-6)$$

where

σ = applied stress

K = constant

A = apparent contact area

Actually, the preceding analysis is a gross oversimplification of the seal interface. The following factors were not considered:

- The asperities are not uniformly distributed nor is the real surface flat with the asperities superimposed on it. Therefore, the deformation across an interface will not be uniform.
- The shape of the asperities depends upon the fabrication process, as does the possibility of interconnecting void spaces. Since the interconnection of void spaces constitutes the leakage path, the degree of plastic deformation does not solely determine the occurrence of leakage.
- The real interface is composed of two roughened surfaces. Therefore, hard asperities deform the softer surface and simultaneous soft asperities are deformed by the hard surface. An equivalent hardness for a soft indenter on a hard surface is approximately one-half the hard indenter hardness. An experimental comparison of the deformation is shown on figures 2-8 and 2-15. In view of this phenomenon, it may be expected that the preponderance of deformation will be attributed to the soft asperities deforming against a harder surface. Equation (2-6) can be rewritten:

$$h = h_o \left(1 - \frac{2\sigma}{\sigma_m}\right) \quad (2-7)$$

where σ_m represents the Meyer hardness as defined for the softer material.

- The apparent contact area A_A in figure 2-3(a) will increase with increasing stress above the yield stress. Thus, it may be exceedingly difficult to achieve a maximum stress of $P/A_A = \sigma_m$. In any event, the geometry of the substrate will have an important effect on substrate deformation and maximum stress.
- The influence of material displaced between asperities must be considered. Unfortunately, a clear description of the deformation is not available. The initial characteristic leak-path dimension, however, should be the sum of the initial roughness of both surfaces. If the void space is assumed to equal the volume of asperity material, the total plastic deformation Δh should be

$$\Delta h = (h_0 - h) = (h_0(1) + h_0(2) - h) \quad (2-8)$$

where

$h_0 = h_0(1) + h_0(2)$, the initial roughness of surfaces 1 and 2.

- Strain hardening of the asperities and substrate were not included but can be approximated by implementing Meyer's law. The relationship between load and indentation diameter is

$$P = k d^{n'}$$

or, rearranging,

$$P^{2/n'} = k^{2/n'} d^2$$

and the stress applied to the asperities in figure 2-3 is

$$\sigma' \sim \frac{P^{2/n'}}{Nd^2}$$

where

N = number of asperities

d = dimension of the projected area of asperity indentation

Therefore,

$$\sigma = \frac{P^{2/n'}}{A_A}$$

Combining equations (2-7), (2-8) and (2-9),

$$h = (h_0(1) + h_0(2)) \left(1 - \frac{2P^{2/n'}/A_A}{\sigma_m}\right) \quad (2-10)$$

It will be shown in subsequent sections that equation (2-10) is not representative of experimentally observed interface deformation. However, it does form the basis for a rational approach to

the correlation of parameters by experimental methods. It will be assumed that the characteristic leakage path dimension varies with the initial surface topography, load, and hardness. From these assumptions, it may be expected that zero leakage can be achieved when

$$\frac{2P/A_A}{\sigma_m} = 1$$

(n' equals 2 for a fully cold-worked material).

Experimental correlations will subsequently verify this observation (Subsection 2.7).

2.1.1.2 Surface Properties

To know more about the flow of asperities under applied stress, an insight into the surface properties, contaminants and environments and their interaction with dislocation movement in the material is necessary. From a sealing viewpoint, additional knowledge of the influence of sealed fluids in terms of oxides, contaminants, and absorbed materials should be obtained. Unfortunately, very little quantitative data are available on most of these topics. Volume properties of materials often cannot be used to describe the phenomena. For example, thin oxide coatings (20-50A) (Ref. 2-6) formed on surfaces at room temperature are quite likely to have different mechanical and chemical properties from the bulk properties (Ref. 2-7, 2-8).

For complete mating at an interface, the metal along with its oxides and other contaminants must be capable of flowing under a given load. In other words, if we assume a dislocation mechanism for deformation and flow in solids, it becomes necessary that the dislocations already existing in the material be able to multiply and move out of the surface of the material to produce flow. For elastic deformation, the dislocations must be able to bow and stretch between their pinning points and multiplication of dislocations is not necessary. The pinning effect and the mobility of the dislocations are related to the diverse internal defects, both natural and artificially created, and are also dependent on the lattice structure of the material crystal and its properties. Contaminants and absorbed materials on the surface will also affect the elastic constants and lattice parameters.

To realize total contact between surfaces, it may be necessary that the asperities flow in the direction normal to the interface. In other words, with increased applied stress, dislocations generated in the crystal should have adequate chance to escape through the surface. A dislocation pileup at clean surfaces is possible under one theory, i.e., the image force acting on the dislocation is less than the surface restraint of a clean surface. The converse has also been suggested, indicating that the common

metals, except lead, have image forces 1.5 to 2.5 times larger than the surface restraint. This situation is strongly modified, however, when we consider that the ratio of image force to surface restraint is equal to

$$Gb/C\gamma$$

where

- G = shear modulus
- b = Burger's sector
- C = numerical factor
- γ = surface energy

Even on clean surfaces, environment might vary the modulus by 2 to 5 per cent and simultaneously change surface energy by 100 per cent within the elastic strain range. Thus, the surface restraint will increase and dislocation pileup will take place, preventing further flow of asperity material.

When a metal is covered with another material, e.g., oxide, the boundary between the metal and the oxide acts as a barrier to dislocation movement. In addition, the dislocation sources at the metal - metal oxide interface are tied down and are not readily available for generation of further dislocations. This dual behavior has very pronounced effects on the material properties. For example, the elastic moduli of aluminum and aluminum oxides are approximately 10,000 and 40,000 ksi, respectively. A thin layer of aluminum oxide will create a pileup of dislocations near the aluminum - aluminum oxide interface, stopping approach of all dislocations at a certain distance below the surface, the distance being proportional to the ratio of the elastic moduli of aluminum oxide to aluminum. In this case, the distance at which the dislocation pileup occurs will be approximately equal to the thickness of the aluminum oxide layer. Thus, a 20Å thick oxide layer will cause dislocation pileup in the substrate at a depth of ~20Å. The only way this hardening effect can be removed is to remove the aluminum oxide layer, or in other words, to produce a "clean" surface. In addition to hardening due to the oxide layer, the usual deformation hardening of the aluminum surface will contribute adversely to the flow properties of the metal. Again, we must not overlook the fact that the elastic moduli of bulk aluminum oxide has been considered in this analysis. It is quite possible that an aluminum oxide layer of 20Å thickness might have considerably higher elastic modulus and will create dislocation pileup at a greater depth than that predicted.

Aluminum oxide is very hard and brittle, and when the substrate plastically deforms under load, the coating ruptures. Unless the material is tested under high vacuum, the surface immediately heals, i.e., a coating is again formed. The force required to move a

dislocation out of a material through its coated surface is strongly influenced by the specific surface free energy and elastic modulus of the coating. In aluminum oxide, the specific surface free energy depends on its crystal structure and varies widely ranging from 1000 to 5000 ergs per sq cm. The high specific surface free energy and elastic modulus of 40,000 ksi indicate the relative immobility of dislocations inside and through the body of the oxide layer. A low modulus in the coating will be essential for rapid movement of dislocations inside the coating oxide crystal and, along with a low specific surface free energy, will give better deformation and flow properties. This possibility does not exist in the case of aluminum and its alloys.

Rabinowitz (Ref. 2-9), developed a relationship between surface energy and hardness after deducing that high strength characteristics are associated with bond strength. The relationship obtained for some metals and nonmetals was of the form

$$\gamma \sim H^{1/3}$$

where γ is surface energy

The Rabinowitz work was directed primarily toward an understanding of friction and wear. It does have significance in that it relates an observed property to a parameter of atomic stature. Section 3 contains an additional discussion of surface energy concepts.

Efforts to obtain a clearer understanding of the cause of surface deformation should be continued, possibly leading to the achievement of "ideal" materials or at least obtain definite relationships between all deformation parameters. Parameters suggested for investigation include:

- Surface oxides and other contaminants and their mechanical properties, crystal structure, and degree of coherence with substrate.
- Absorbed gases and their effect on surface elastic properties.
- Effect of oxides and other contaminants on dislocation movement.
- Variation of surface energy with strain.
- Dislocation pileup at clean surfaces derivable from shear modulus, Burger's sector, dislocation width, and applied stress based on sound approximations.
- Dislocation pinning effect due to dislocation environment interaction.

2.1.2 Formation of the Leak Path

It can be stated confidently that leak paths are formed by the interconnection of void spaces in an interface, while little can be said about the actual nature of the leak path except that it is generally small in size. The void spaces are formed by fabrication marks, damage, and foreign contaminants. Thus, the general size and number of the leakage paths will vary considerably with at least the fabrication process because of the widely divergent surface characteristics that can be generated. Gitzendanner (Ref. 2-10) described a series of experiments using photomicrographic techniques involving the reflectivity of light from a surface pressed against a glass plate. The surfaces investigated were lathe-turned aluminum, Teflon and rubber. The lathe-turned surfaces showed breaks in the turned crest lines in addition to the spiral grooves generated in the turning process. Good contact was observed with rubber while Teflon showed substantially less contact. Unfortunately, no firm conclusions could be made for the following reasons:

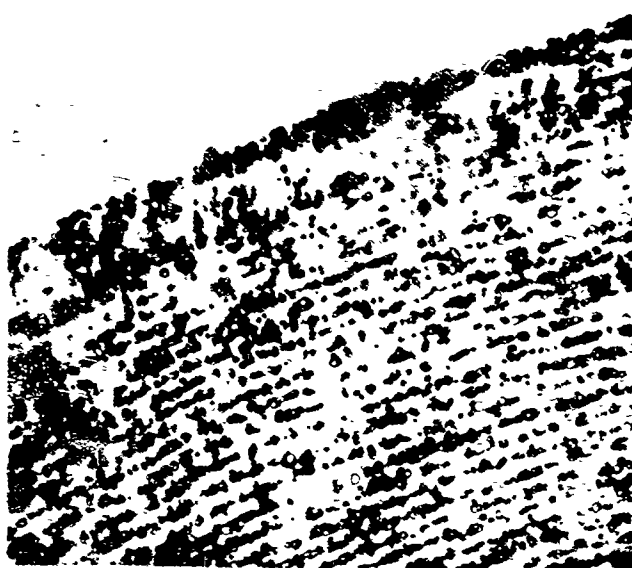
- The diffusion of light in the glass can cause some areas in contact to appear not in contact.
- A very smooth glass surface was mated against a rough surface whereas the real case is typified by two rough surfaces mated together.
- The proximity of the surface area not in contact to the glass surface (i.e., the depth of the void spaces) could not be determined.

These experiments were helpful, however, in providing qualitative understanding of the leakage path. For this purpose, two of the photomicrographs are reproduced as figure 3-4.

Another factor that must be considered is the interconnection of void spaces from the standpoint of how many voids form an interconnecting link between the inside and outside of the seal interface. Even if Gitzendanner's apparatus (Ref. 2-10) produced conclusive evidence of the area of contact, it would be a difficult task to establish which void spaces provide the interconnecting link. General Electric (Ref. 2-11) is presently engaged in a mathematical analysis of leakage probability developed for model surfaces. Their results are not yet available.



Contact Pattern for Aluminum Seal
at 6450 psi Sealing Stress



Contact Pattern for Aluminum Seal
at 17,500 psi Sealing Stress

Figure 2-4 Photomicrographs of surfaces in contact (Ref. 2-6)

Two other methods for contact evaluation have been considered. The first employed a chemically reactive gas, which was passed through the sealing interface. The reaction produced a discoloration in the leak channels and color contrast which could indicate the size of the leak path. Unfortunately, the chemical reaction caused clogging of the leak paths and affected the validity of results. Another method considered employs an autoradiographic technique. A tracer gas of argon 41 or carbon dioxide with carbon 14 was considered as a sealed fluid which, when passed through the sealing interface, would produce β -ray absorption on the surface. The leak path and contrast depth could be obtained by placing a ray-sensitive film over the surface. This technique was not fully investigated because of funding problems and the likelihood of success. The major problem envisioned is the resolution of the sensitized film with respect to the leak path size.

2.2 Macroscopic Interface Geometry

In the preceding subsection, two of the parameters influencing the leakage path were identified as the initial surface topography and contact load. The application of a load to contacting surfaces produces modes of deformation, which can be viewed as microscopic surface deformation and macroscopic substrate deformation. Most engineering surfaces are composed of a fabrication roughness superimposed on an average surface contour. Roughness can be defined as a microscopic property while the average contour is a macroscopic property. This, then, forms a distinction between the two factors, specifically:

- (1) Macroscopic interface geometries, which are produced deliberately from design concepts. A typical deliberate macroscopic geometry is shown in figure 2-8(b).
- (2) Microscopic surface topography, which includes roughness and waviness when waviness is described as a surface variation resulting from the fabrication process.

Both of these factors are additional load-dependent parameters influencing the leak path. They are somewhat independent of each other and, thus, can be studied separately. The first parameter is considered in this subsection while the second is considered in Subsection 2.3.

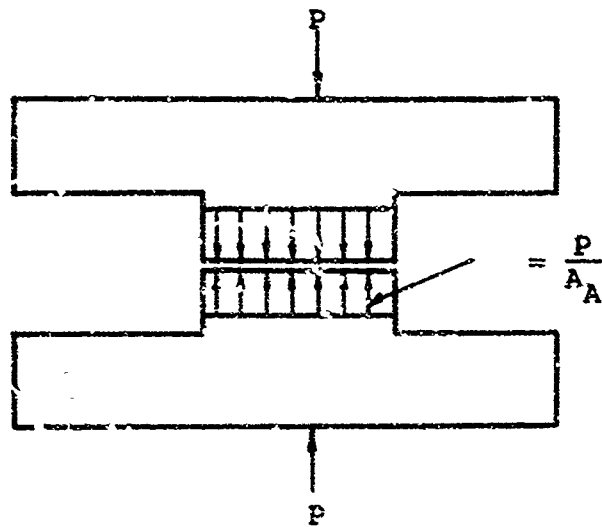
Before proceeding further, we should develop a qualitative feeling for the importance of interface geometry. The most common interface encountered is the mating of flat surface as shown in figure 2-5(a). An external load applied to the bulk material is transmitted throughout the material. The distribution of load, however, is not necessarily uniform and depends upon the bulk geometry and deformation. For simplicity, we may assume that the normal interface load distribution is uniform. This assumption is a sufficiently close approximation at least for the purpose of developing design criteria. Further support of this assumption is contained in subsequent discussions.

When the normal load distribution or stress is uniformly distributed across an interface, it seems logical to assume that the deformation and the resulting leakage path must be uniform at least from a statistical average viewpoint. We can now consider the effect of a substantial departure from the flat surface case by assuming a surface geometry as shown in figure 2-5(b). The application of a load to the bulk materials produces plastic deformation of the wedge (figure 2-5(c)). Again, we may assume that the normal stress distribution at the interface is uniform. This will be shown to be a simplifying assumption, but by itself, is not sufficient. The only real parameters we know are the applied load and the material properties. To know the uniform stress, we must develop a means of describing the apparent area of contact. This, then is one of the objectives in the present study. Unlike the flat surface case, the apparent area of contact is determined by the material properties, load, and geometry of the surfaces. Another important benefit to be derived is a description of the over-all dimensions of an interface for use in calculating the conductance parameter of an interface.* The important fact to be considered at this time is that the conductance parameter (h^3) is proportional to the interface geometry.

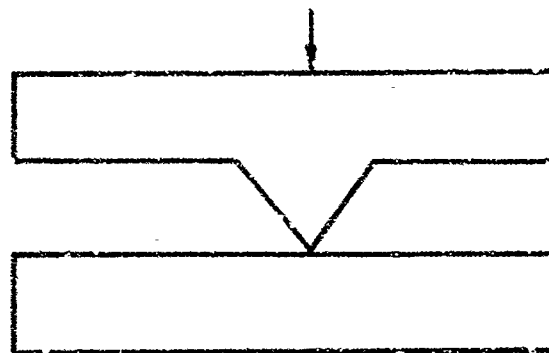
$$(h^3) \sim \frac{\text{Over-all length of the interface in the direction of leakage flow.}}{\text{Width of the interface normal to the direction of leakage flow.}}$$

A final benefit to be derived from this study is the establishment of a minimum width of interface for minimum leakage. This can be best described by considering the wedge shown in figure 2-5(c) with leakage flow as shown. Plastic deformation under the wedge tends to fill most of the interconnecting void spaces forming the leakage path. When the contact width is very small, surface imperfections and other factors can form large leakage paths. As the deformation and width increase, the

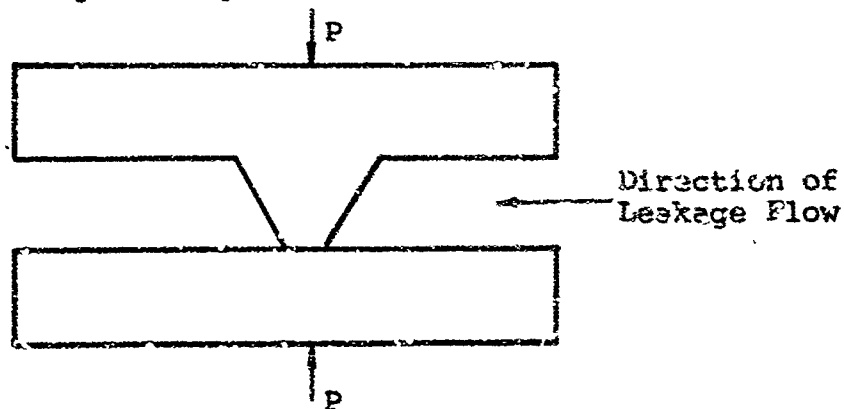
*See Subsection 2.5 for details.



(a) Flat Mating Surfaces



(b) Wedge Mating with a Flat Surface



(c) Wedge Deformed

Figure 2-5 Typical representation of interface geometrie

statistical probability of a large leak path diminishes, finally reaching the same statistical probability of a leak as demonstrated by large flat mating surfaces. Following this argument, another objective of this study is to determine the factors influencing the minimum width of contact and obtain quantitative criteria for its description.

Each of the three preceding problems was studied concurrently through a series of experiments on various shaped surfaces and mated against flat surfaces.

2.2.1 Experimental Studies

An experimental program was conducted in two phases. The first phase was an investigation of the relationship between applied normal load and apparent contact area. Punch sets, composed of irregular and flat surfaces, were fabricated for this purpose. The second phase was an experimental leakage evaluation of wedge surfaces. The leakage rate and deformation was measured under conditions of variable load. Thus, the results of the first phase can be correlated to the second phase and, in addition, provide information not readily obtainable during the leakage experiments.

Two cases of deformation were considered. The first case involved a soft metallic wedge surface pressed against a hard flat surface. In the second case, a hard wedge was pressed against a soft surface. In the following discussion, the two modes of deformation are termed the plastic and elastic wedge cases. The materials used were:

<u>Material</u>	<u>Hardness</u>	<u>Meyer Hardness</u>
1100-0 Aluminum	30 BHN*	48,000 psi
1141 Steel	175 BHN*	308,000 psi

Four configurations, typical of those found in common seal applications, were chosen for evaluation. The profiles, shown on figure 2-6, are identified as a 10-deg straight wedge, 30-deg straight wedge, 60-deg straight wedge, and a 0.093-in.-radius hemispherical wedge.

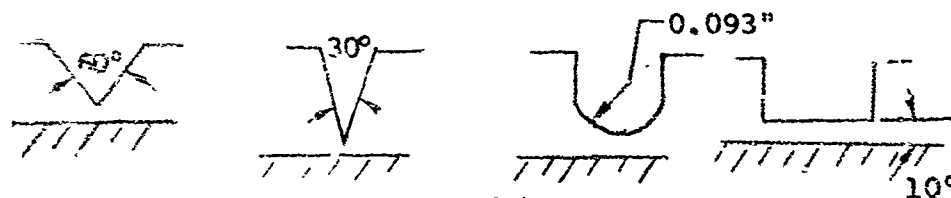


Figure 2-6 Initial wedge profiles

*500-kg load, 10mm ball

Phase I Deformation of Punch Sets

An objective of this experiment was to obtain the deformation characteristics of various-shaped wedge surfaces pressed against a flat surface. The deformation was visually observed and measured after a known load was applied to the punch sets. Figures 2-7 and 2-8 show the apparent contact area relationship with load for the elastic and plastic wedges. Considerable differences in deformation characteristics may be observed in both cases. Generally, a linear relationship exists between load and apparent contact load.

In the plastic wedge case, the load per unit area is the largest for the hemispherical wedge followed in order by the 60-deg wedge, 30-deg wedge, and 10-deg shallow wedge. The general characteristics can at least be intuitively explained on the basis of observation. Figure 2-9 shows a schematic view of the deformed wedges. The explanation which seems most logical is based on the displacement of material during deformation. Considering each of the shapes shown in figure 2-9, the hemispherical wedge contains the largest volume of material that must be displaced laterally along the surface. The least resistance should be offered by the 30-deg wedge. The shallow wedge, however, appeared to be even lower in resistance. Most of this discrepancy is attributed to elastic deformation of the wedge producing a larger apparent contact area than would result from pure plastic deformation. No significant deformation of the harder steel surface was observed.

In the case of the elastic wedge, virtually all of the deformation occurred in the flat soft surface. It is difficult to arrive at any conclusions concerning deformation since the material displaced differs with the geometrical shape involved. The effects of local deformation are transmitted throughout the deformed material. Figure 2-10 shows schematically the deformation in a typical wedge case.

Phase II Leakage Experiments

Flange sets having combinations of a plastically and elastically deformed members were pressed together under varied load conditions. Helium gas was introduced into the center of the flanges and the leakage was measured. The apparatus used is described in Appendix I. A 39-psi pressure difference was maintained across the interface during each experiment. Simultaneously with the leakage measurements, the deflection of the plastically deformed member was measured. Figure 2-11 and 2-12 show the deflection characteristics of the plastic and the elastic wedge shapes. The leakage-load characteristics for the two modes of deformation are shown on figures 2-13 and 2-14.

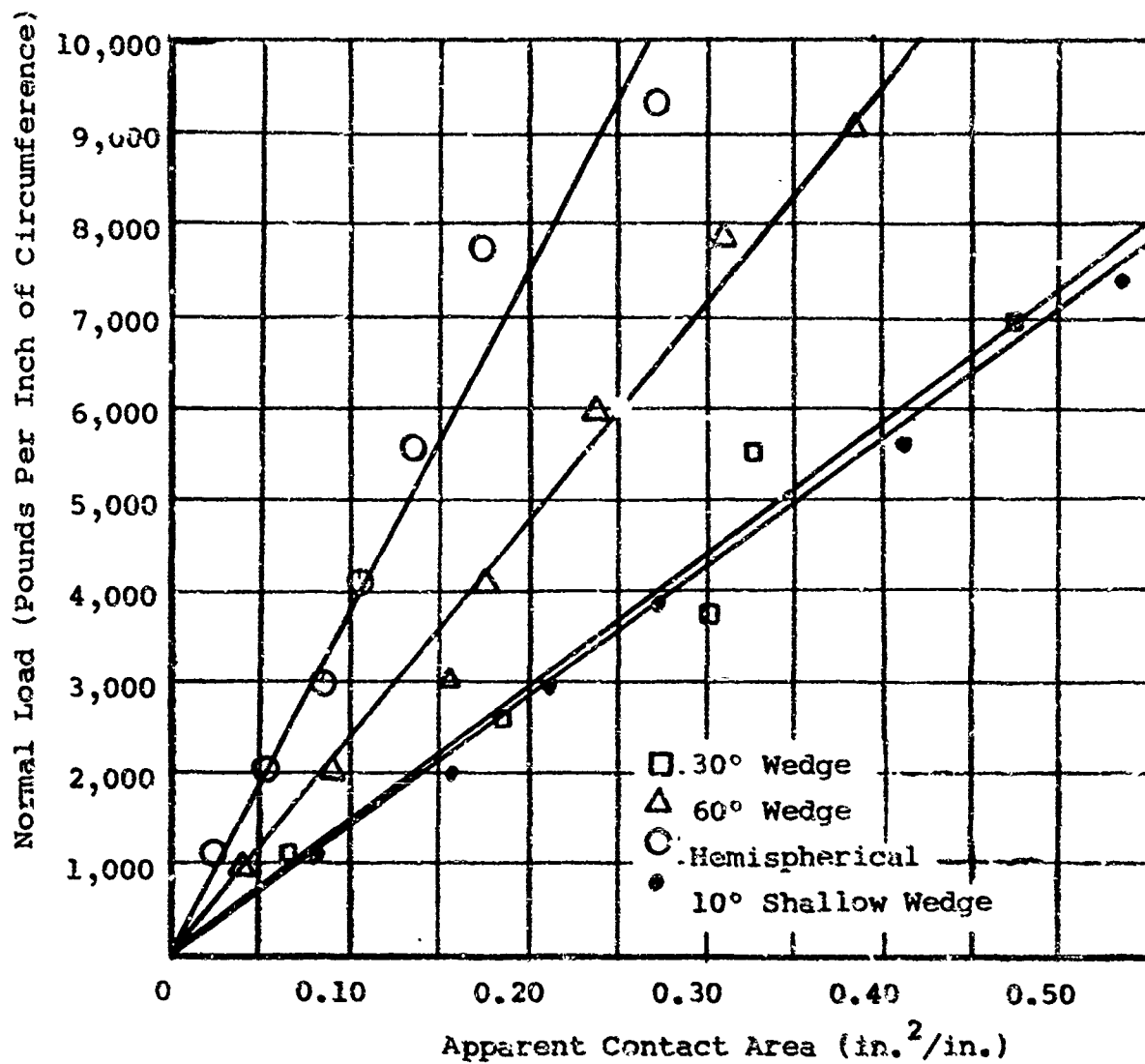


Figure 2-7 Apparent area load characteristics for an 1141 steel wedge on an 1100-0 aluminum flat surface, (elastic-wedge case)

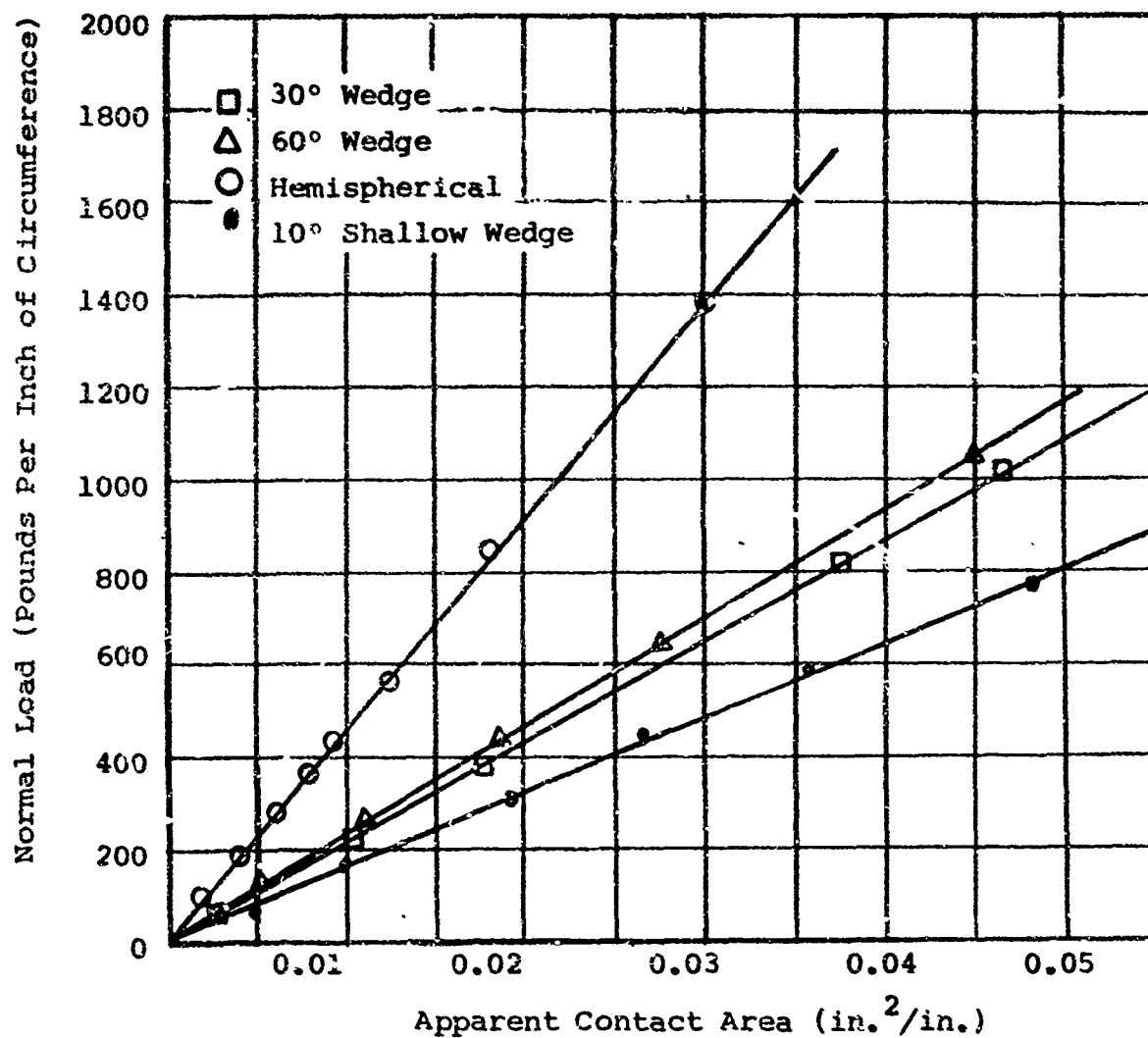


Figure 2-8 Apparent area load characteristics for an 1100-0 aluminum wedge on an 1141 flat steel surface (plastic-wedge case)

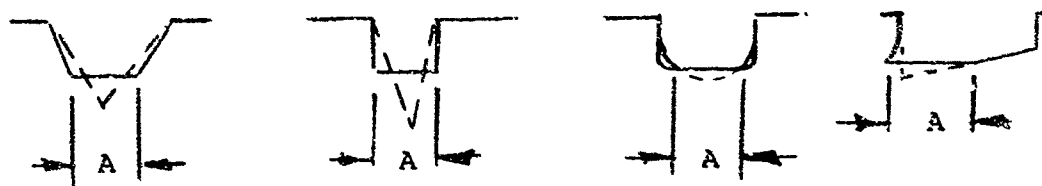


Figure 2-9 Plastic deformation of wedge

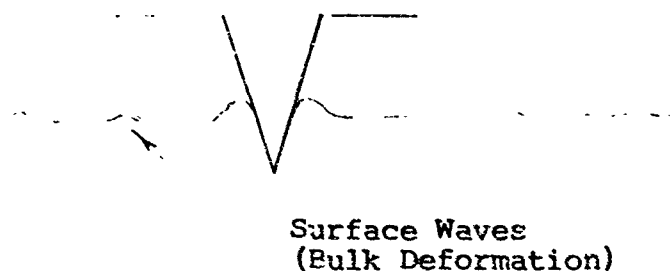


Figure 2-10 Plastic deformation of the flat surface in the elastic wedge case

2.2.2 Load, Deformation and Area of Contact Characteristics

The load-contact area relationships for the materials and profiles studied are linear. This implies that strain-hardening effects are a minimum or at least not measurable within the sensitivity of the instrumentation.

The apparent contact area-load relationship for the elastic profile varies considerably with the profile. Average stresses range between 15,000 and 38,000 psi with the minimum and maximum represented by the shallow wedge and hemisphere as shown on figure 2-7. The elastic indenter, however, suggests that the deformation process is very similar to the hardness measurements described in Subsection 2.1. It was shown that the hardness should

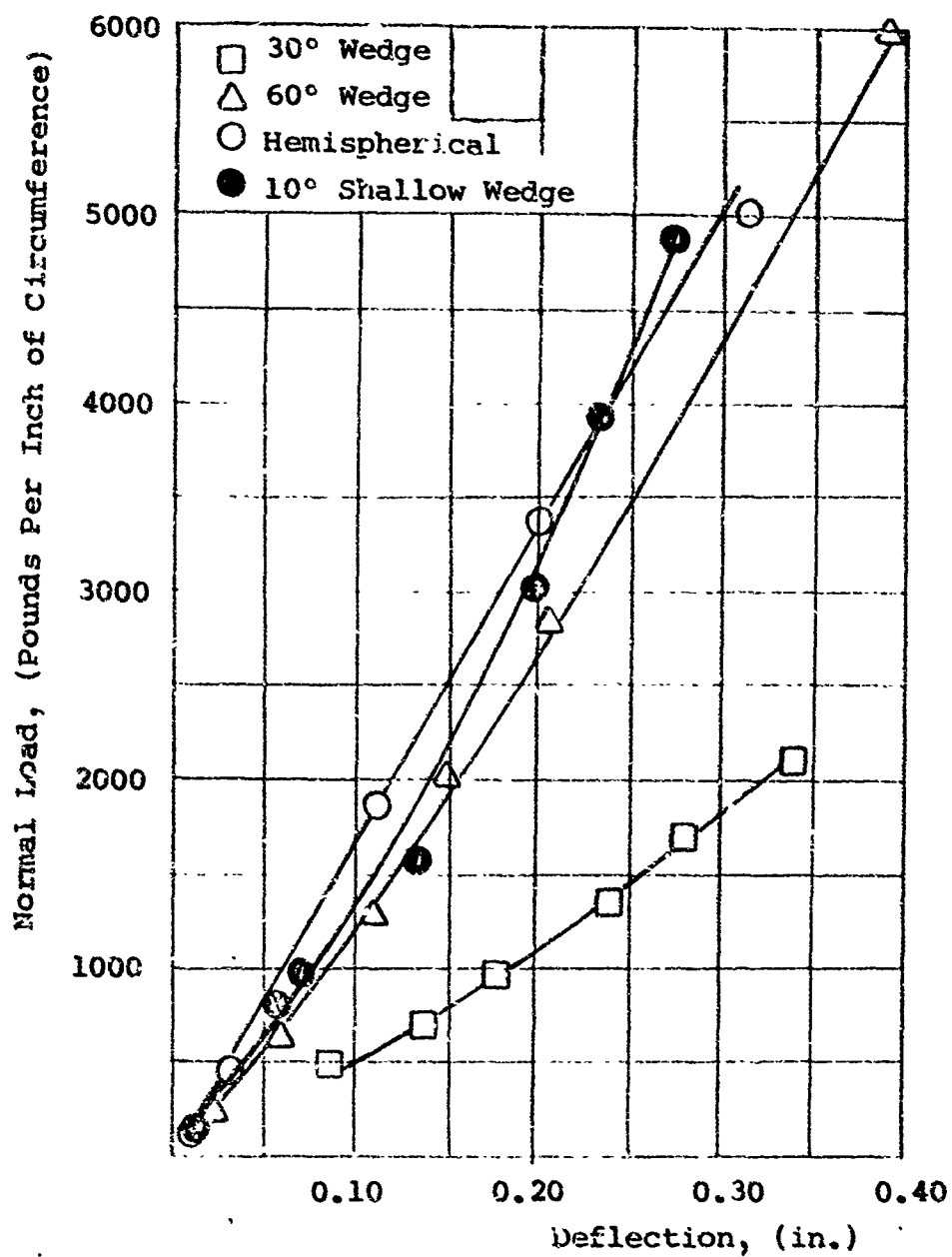


Figure 2-11 Load deflection characteristics of an 1141 steel wedge on an 1100-0 flat aluminum surface (elastic-wedge case)

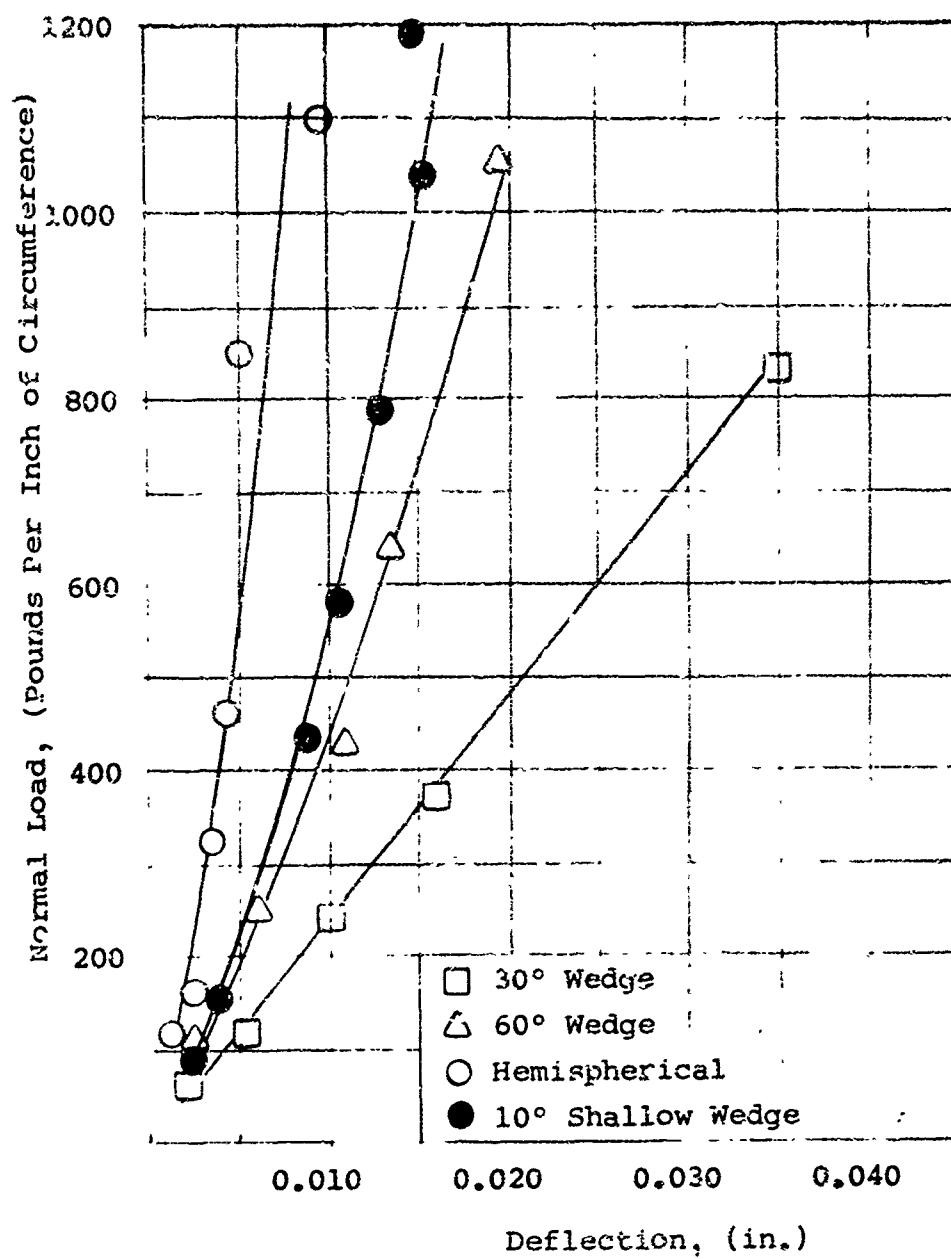


Figure 2-12 Load deflection characteristics of an 1100-0 aluminum wedge on an 1141 flat steel surface (plastic-wedge case)

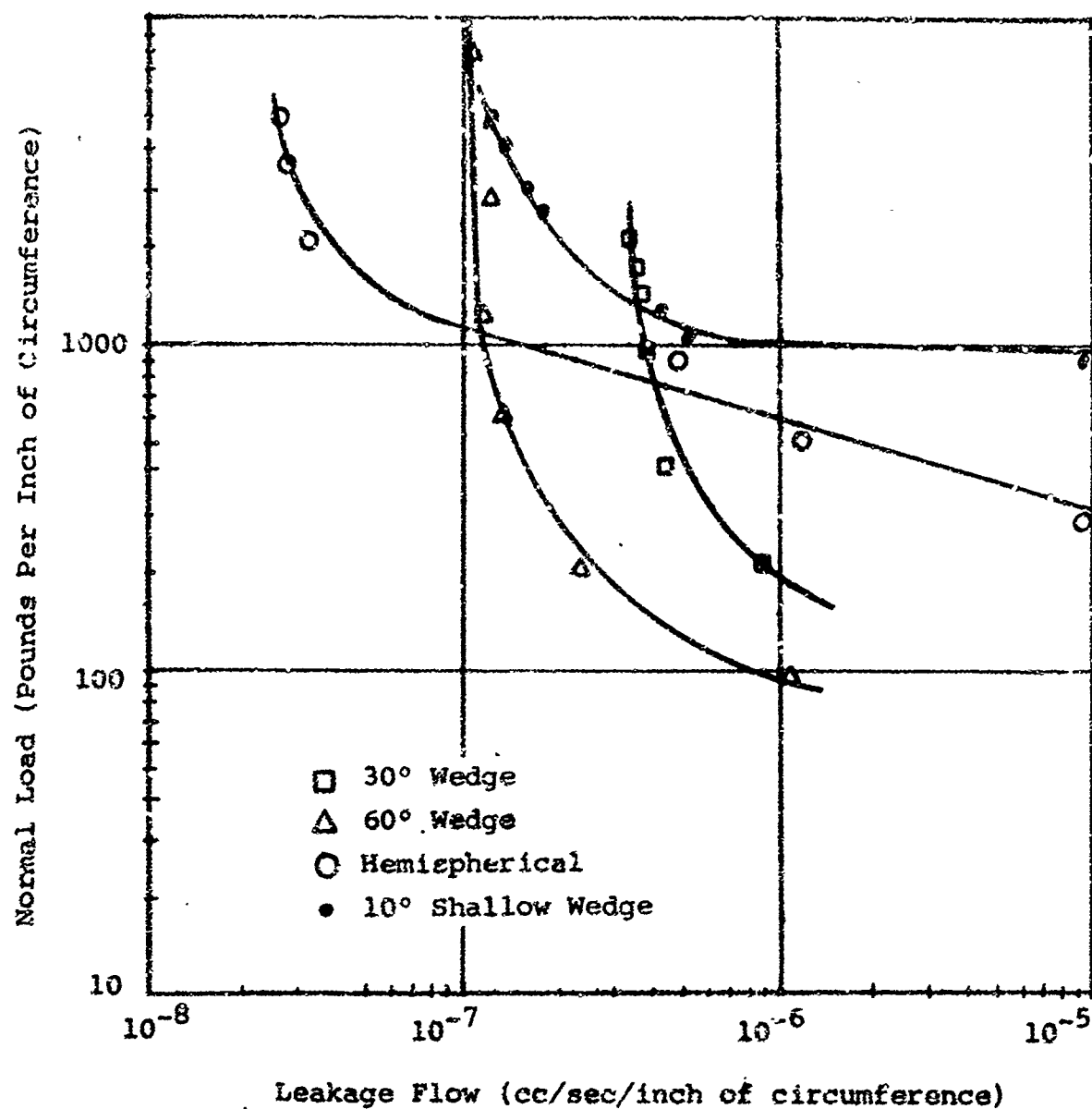


Figure 2-13 Leakage load characteristics for the elastic wedge case

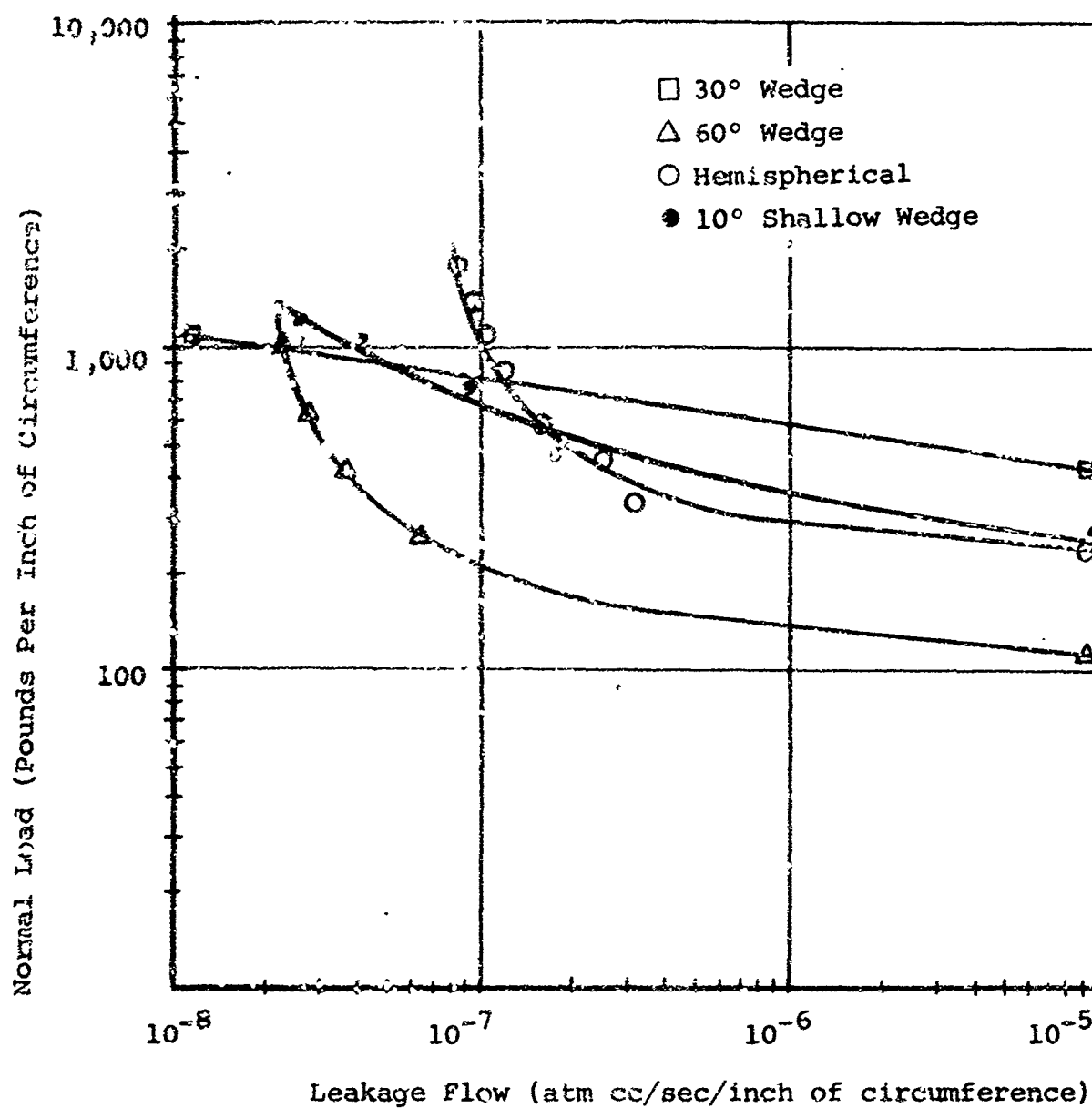


Figure 2-14 Leakage load characteristics for the plastic wedge case

be based on the projected area of contact. This new relationship, shown on figure 2-15, demonstrates that, indeed, the contact stress is almost independent of indenter shape. The range of average stress is 40,000 to 52,000 psi. The average stress is 48,000 psi and is equal to the Meyer hardness of the material as determined by conventional hardness measurements. The contact area for an elastic indenter is:

$$A_A = \frac{P}{\sigma_m}$$

A comparison of the apparent and projected area of contact is shown on figure 2-16.

Plastic deformation of the indenter is substantially more uniform in all cases except the hemispherical wedge, as shown on figure 2-8. The average stress is 21,000 psi and is approximately one-half of the elastic wedge case. The lower stress value is attributed to the relative ease of lateral deformation. On this basis, it may be expected that the hemispherical shape would offer greater resistance to deformation.

2.2.3 Leakage and Width of Interface Contact

The relationships between load and leakage are important since they produce an insight into the minimum interface width required for plastically deformed interfaces. Minimum leakage rates of 10^{-7} cc per sec were obtained for all interface geometries and combinations of materials evaluated when a contact width of 0.030 in. had been achieved. In the case of the plastically deformed spherical and 60 deg wedge interfaces, a contact area less than 0.010 will produce leakage rate in the 10^{-7} cc per sec region. Leakage rates in the order of magnitude of 10^{-7} cc per sec can also be achieved with elastic shapes having a 30 deg, 60 deg, and possibly a spherical profile and 0.010-in. projected contact width. The leakage - area of contact characteristics are shown on figures 2-17 and 2-18.

The factors influencing the minimum width of contact are primarily attributed to the surface finish and tearing of the material due to plastic deformation. The surfaces employed in the experiments were lathe-turned, having a spiral ridge disturbance wavelength of 0.003 in. For complete contact across any one ridge to occur, at least several ridges must be involved in the deformation process. Also, it is a difficult task to fabricate wedge surfaces with crests that form a plane. A typical variation in the crest from a straight-line plane was 0.002 in.

Assuming that a 0.010-in. width interface will produce a minimum leakage rate, the next step is to correlate the results with load per inch of contact. The load per inch of

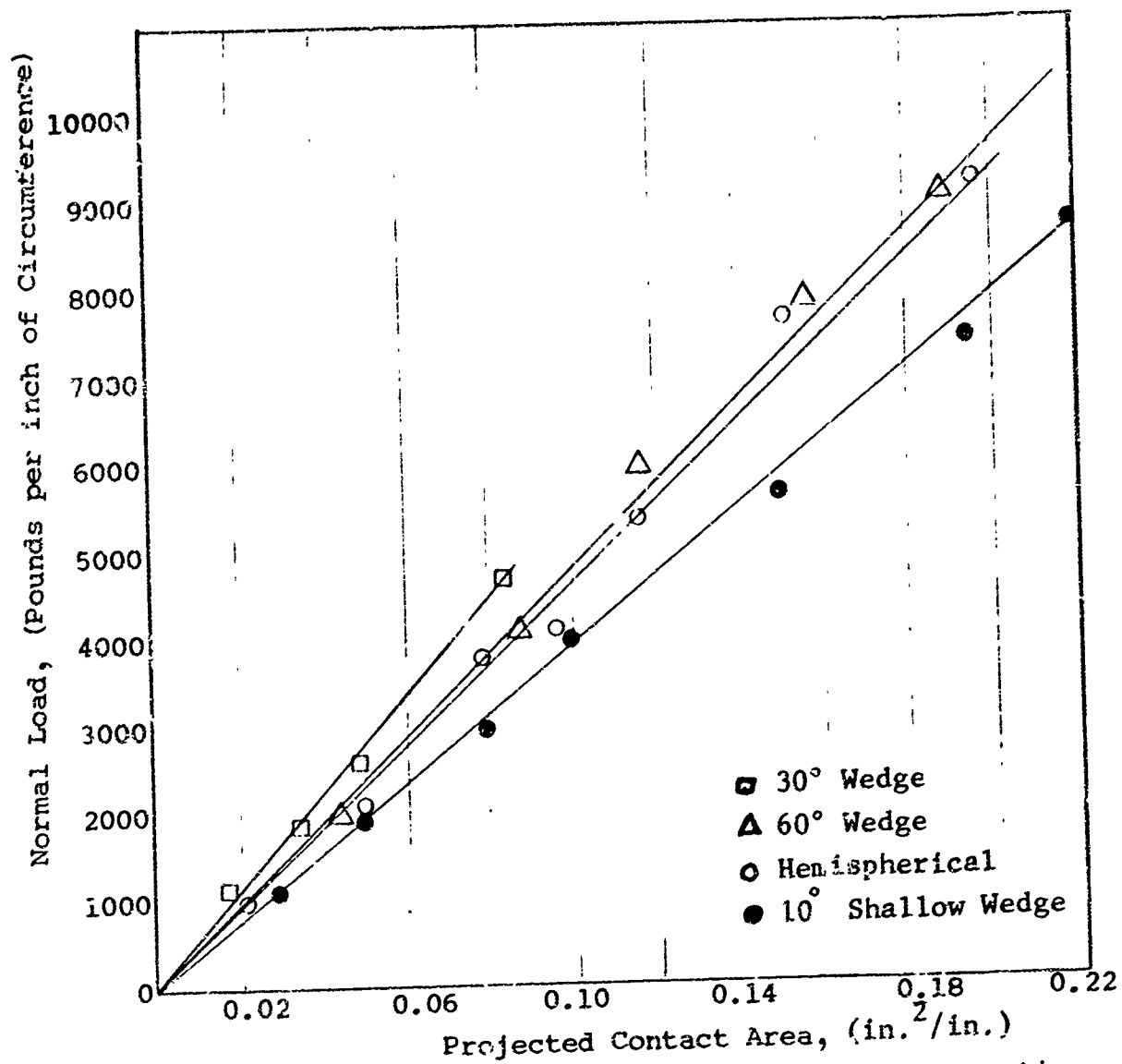


Figure 2-15 Projected contact area load characteristics for a 1141 steel wedge on a 1100-0 aluminum flat surface (elastic wedge case)

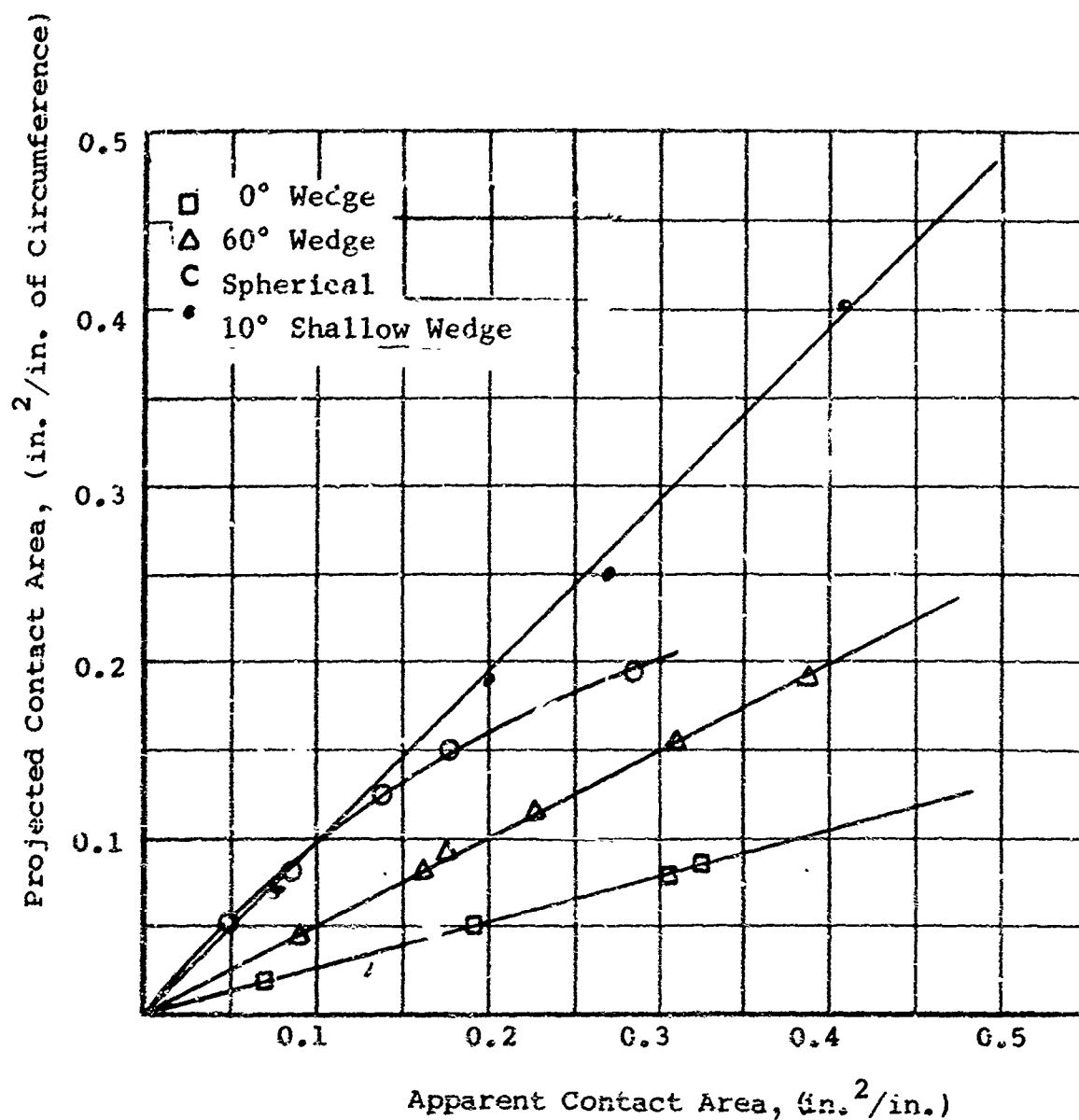


Figure 2-16 Relationship between apparent and projected contact area for the elastic wedge case

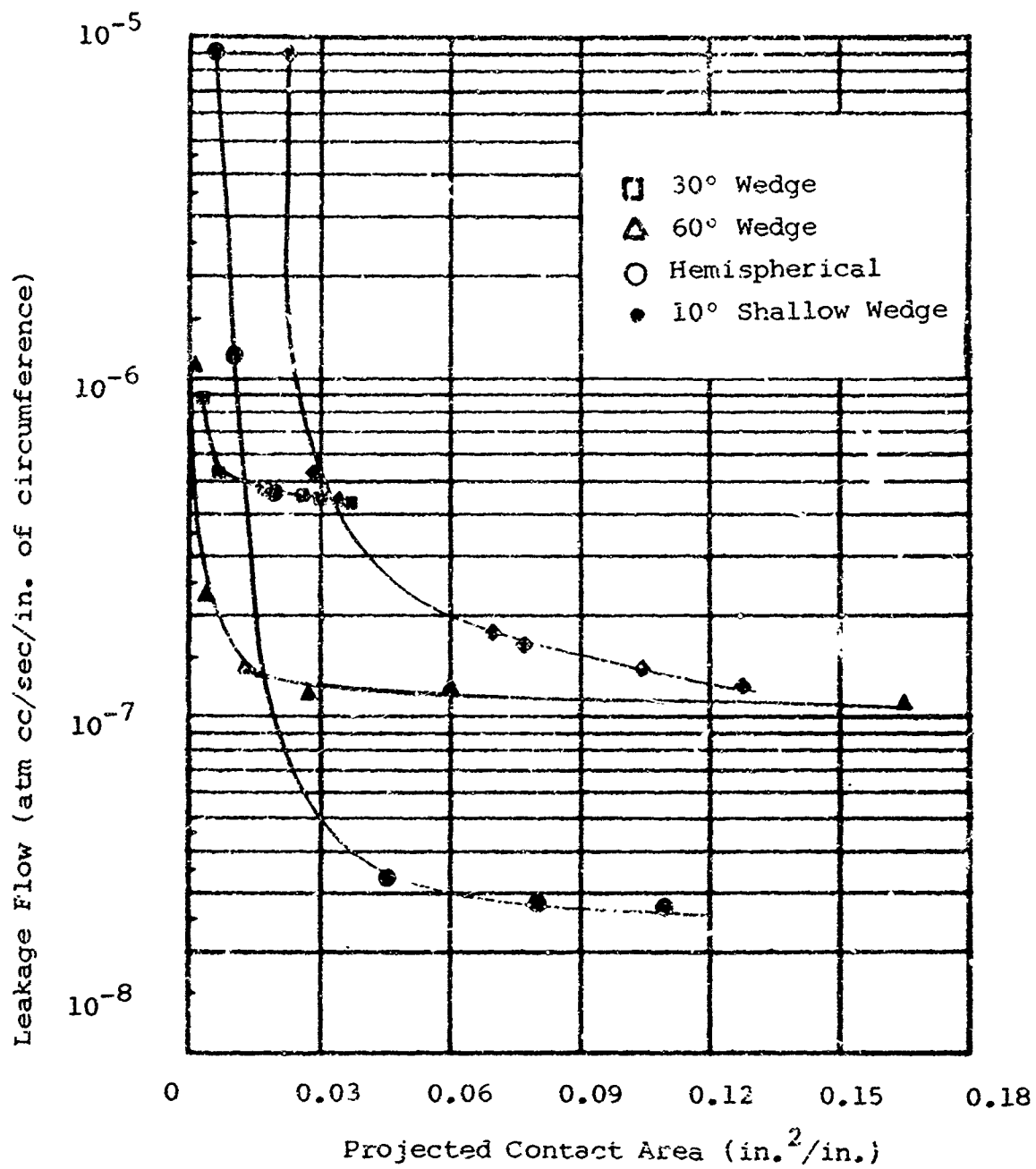


Figure 2-17 Leakage flow versus projected contact area for the elastic wedge case

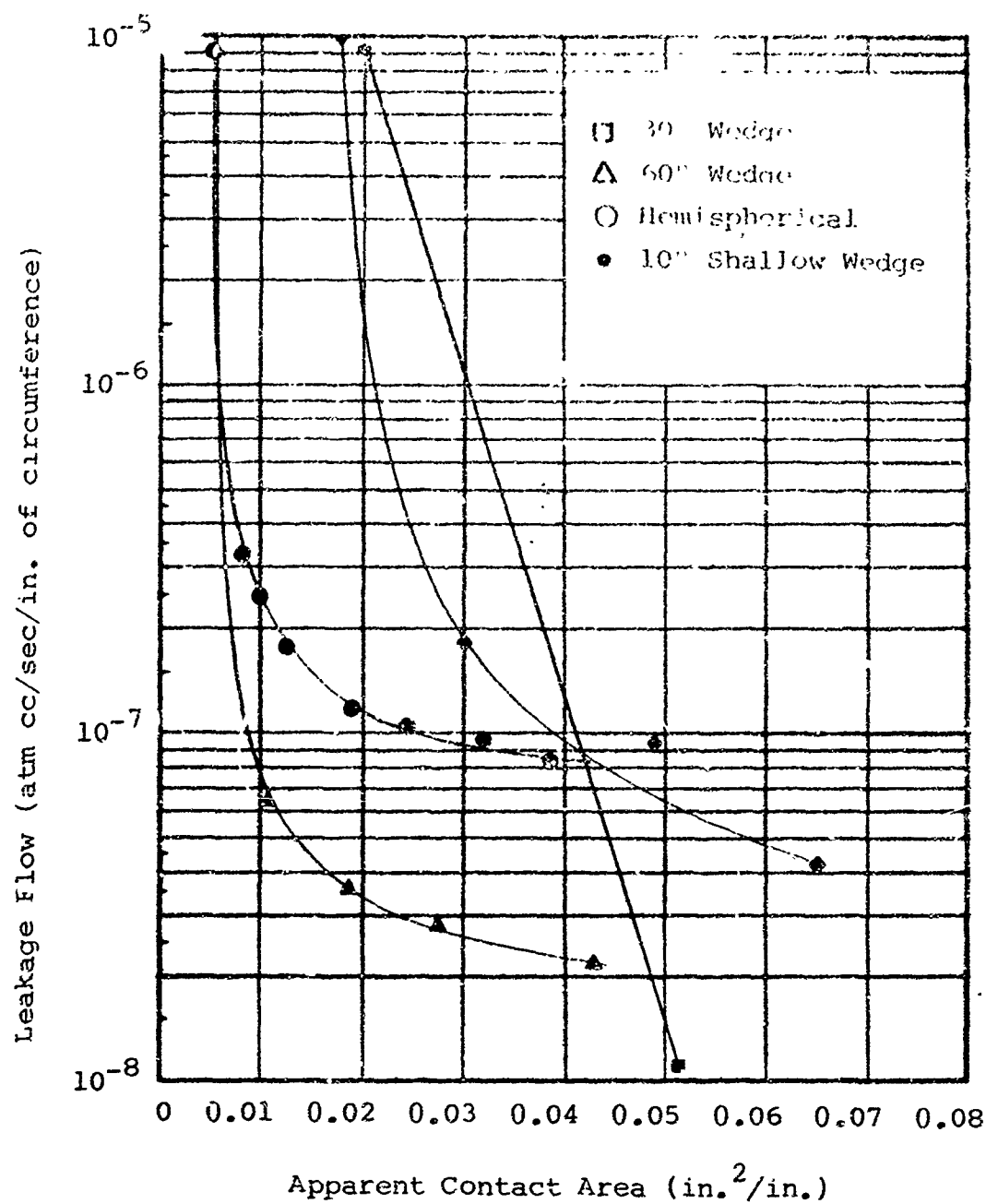


Figure 2-18 Leakage flow versus apparent contact area for the plastic wedge case

contact for the elastic hemispherical and 60-deg wedge is 480 lb. The corresponding load for a 60-deg plastic wedge width of 0.010 in. is 220 lb. When the maximum of two loads is taken it can be summarized that minimum leakage can be obtained if the interface is at least 0.010 in. wide and the load per in. of contact is equal to 1 per cent of the Meyer Hardness of the material. The requirements are that plastic deformation occur and the shape be initially one of the more promising performance-wise, as demonstrated by the 60-deg included-angle surface.

2.3 Surface Topography

Of all the parameters influencing sealing, surface topography is the most important and also the most nebulous. It is a complex parameter that is difficult to measure, impossible to describe simply, and that varies with material properties, substrate geometry, and fabrication processes. To present a comprehensive survey of each of these aspects would require the repetitions presentation of very adequate discussions available in the literature. To maintain continuity, however, each will be briefly considered with the suggestion that the reader refer to References 2-1, 2-11, and 2-17 for additional details.

An appreciation of the problem can be best developed by considering the cause and effect of surface topography with emphasis on the formation of the leakage path when two surfaces are mated together. Following this preliminary discussion, typical surfaces used in leakage experiments are described. Data developed from these experiments are ultimately developed into interface criteria in Subsection 2.5.

2.3.1 Surface Construction

Although a majority of surfaces appear to have random topographies and consist of many irregular, jagged protrusions, there are definite patterns that characterize a surface. These patterns can generally be classified according to the number of occurrences or, if viewed as a periodic disturbance, the wavelength. The irregularities of longest wavelength are caused by flexure of the part being formed of deflections of shafts and slideways in the machine tool. Superimposed upon this waveform are other vibrational effects. The next shorter wavelength is that contributed by the method of fabrication such as the formation of spiral crests formed in a lathe-turning process. This pre-ominant orientation of a surface pattern is defined as lay of a surface. The controlling factor is in the fabrication process producing variations described as spiral, parallel, circular, multidirectional, and circular, relative to some reference.

The smallest disturbance is produced by localized tearing and shearing between the cutting element and the surface. In addition to these surface characteristics, there is a class of

random irregularities called flaws. These occur at one place or at infrequent intervals on a surface. Scratches, ridges, holes, cracks or checks are examples of flaws.

The preceding characteristics are often broadly classified by the terms surface roughness or waviness. Roughness takes into account the finer irregularities caused by the cutting tool and the machine tool feed, while waviness is the wider spaced irregularity, resulting from machine or work deflections, vibrations, heat treatments, etc. To distinguish between these two forms, a roughness-width cutoff is often defined to specify the maximum width of surface over which roughness is measured.

2.3.2 Surface Topography and the Leakage Path

Having considered the general effects of the surface fabrication process, we can now hypothesize a relationship between surface topography and the leakage path. Consider two surfaces pressed together under very light load, as shown in figure 2-19(a). The leakage path can be characterized by the maximum surface variations defined as gross waviness. An increase in load, however, produces deformation of two forms: elastic, as described in Subsection 2.1, and plastic at localized points of contact. The predominance of one form depends largely on the geometry of the substrate material. For example, the material substrate may be very slender, providing large elastic deformation when small loads are applied. On the other hand, massive substrate may not deform significantly even under very large loads. Consequently, the characteristic size of the leakage path would change little with increasing load.

Considering the bulk geometry surrounding most sealing interfaces, it is felt that the elastic deformation will be small when compared with the initial waviness. The deformation that does occur is most likely that shown on figure 19(b). The implications of this effect in the present study are:

- Minimum leakage can be obtained when waviness is a minimum, preferably equal to the surface roughness.
- Realizing that waviness is a function of at least the fabrication process, there are restrictions on the minimum waviness which can be attained. Other factors, such as bulk geometry and material properties, also influence the minimum waviness. Therefore, waviness can be considered as a variable which cannot be controlled but only minimized for specific circumstances. Additional discussion of minimum waviness is contained in Section 6.

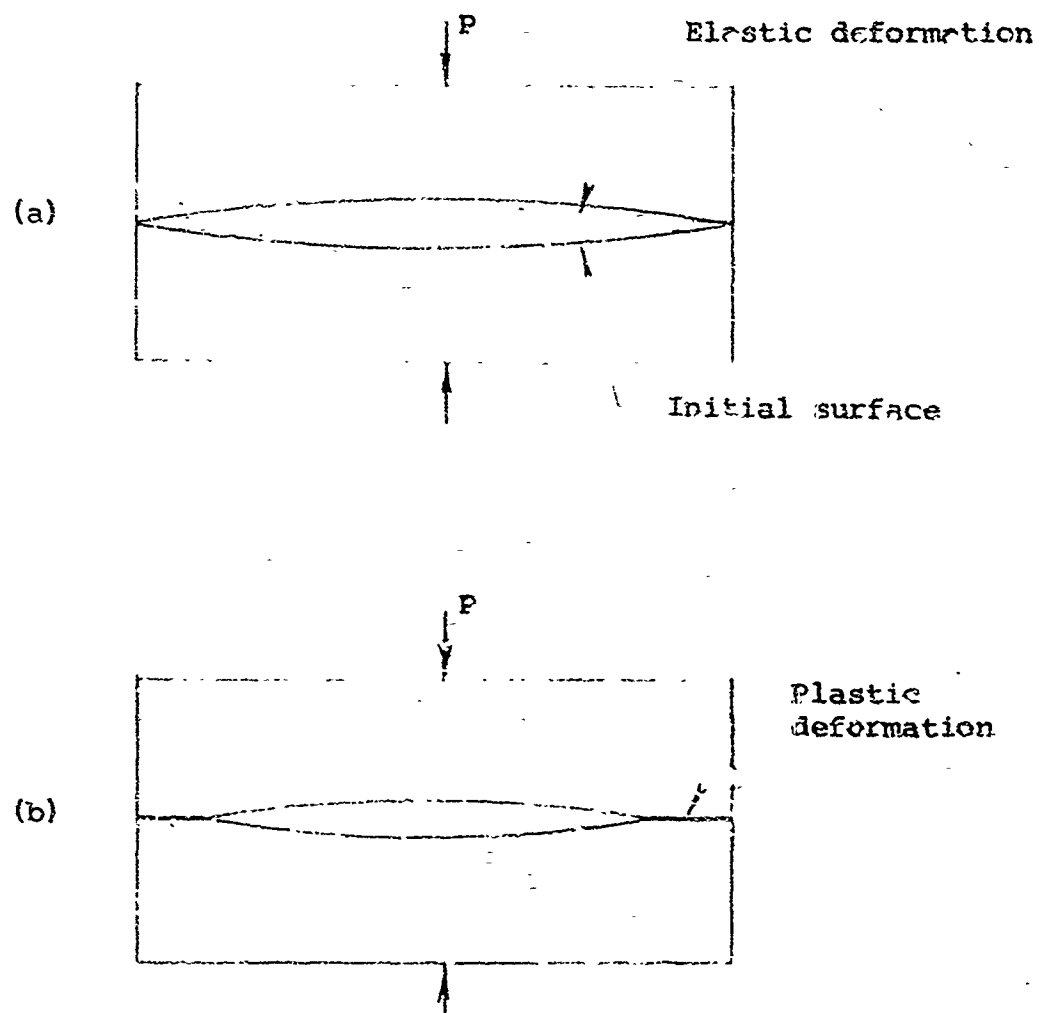


Figure 2-19 Schematic representation of waviness and deformation. Leakage is assumed to flow normal to the interface.

The influence of surface lay can be hypothesized almost intuitively. When surfaces are rough $>15\mu\text{in. PTV}$, the orientation of lay should be normal to the average direction of leakage flow for minimum leakage (Ref. 2-1). This observation is reasonable if we consider that a surface possessing lay has uniform crests and valleys. Thus, a leak is easily formed by the valleys when their orientation is in the same direction of leakage flow. Surface variations less than $15\mu\text{in. PTV}$ do not require preferential orientation because the valleys usually have the same depth as the irregularity in the crests. It should be noted that multidirectionally formed surfaces do not have preferentially formed crests and valleys. These surfaces often have variations less than $15\mu\text{in. PTV}$ and, consequently, can be expected to produce leaks similar to fine-finish, preferentially oriented surfaces.

The last hypothesis to be made concerns roughness, which includes lay as well as shear-induced variations. Three alternatives appear feasible from the standpoint of minimizing the leak path. They are:

- the mating of surfaces possessing no crests or high points. The definition of a surface with no variation must, of course, be qualified by the device used in evaluating the surface. The limits of the interference microscope can be used for this purpose.
- the mating of surfaces having an undisrupted lay which when pressed together produces uniform plastic deformation of the crests oriented normal to the direction of leakage flow. The inference of plastic deformation suggests that no leak path can be formed.
- the mating of general engineering surfaces forming almost random void spaces. To ensure that a minimum of void spaces interconnect; a substantial amount of gross plastic deformation is necessary.

The preceding hypothesis of a minimum leak path with respect to both waviness and roughness can be combined as follows: Elastic deformation of the material substrate waviness can produce a minimum leak path if the surface roughness is commensurate with the deformation. The smaller the roughness, the lower the load required.

When the modes of substrate and roughness variations and deformation are combined, four possible combinations of contacting surfaces can be postulated. These modes are identified on Table 2-2. A relative prediction of contact load effects on leakage for a given material is shown on figure 2-20.

Table 2-2
MODES OF INTERFACE DEFORMATION

Class	Size of Surface Variations	Types of Surface Variation	Substrate		Surface	
			Plastic	Elastic	Plastic	Elastic
I	None	None		X		
II	1 μ in.	Random and few		X	X	X
III	> 1 μ in.	Undisrupted lay		X	X	
IV	> 1 μ in.	Engineering surfaces with large number of disturbances		X	X	

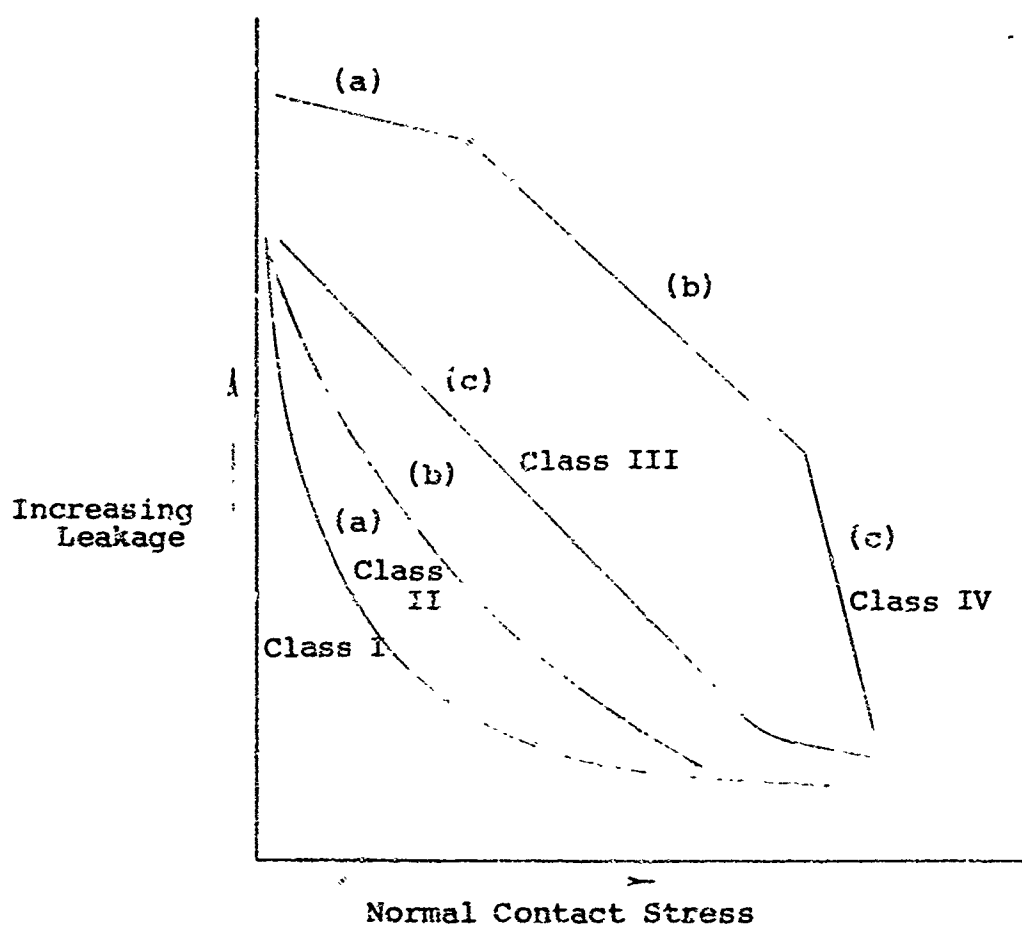


Figure 2-20 Relative effects of stress on leakage
 Modes of deformation
 (a) elastic substrate
 (b) elastic substrate and plastic surface
 (c) plastic substrate and surface

2.3.3 Surface Measurement and Identification

One of the most significant deficiencies in the advancement of the state-of-the-art of sealing is the inability to develop a language by which a surface can be described. The development of a language implies a universal method of surface description that is not only quantitatively adequate but also serves as a means of communication between the researcher, designer, and fabricator. At the present time, the available methods are neither universal nor adequate. To a large extent, this state of affairs is attributed to the lack of suitable instrumentation, lack of concepts for improvement, and insufficient interest on the part of those who stand to benefit most. The purpose of this discussion is to reiterate the deficiencies and to describe the not-too-satisfactory methods employed in the development of criteria for sealing interfaces. Specific details of the instrumentation and techniques for microscopic surface evaluation are not included since these topics have been adequately covered in references 2-1, 2-11, and 2-12. On the other hand, instrumentation and techniques for macroscopic surface evaluation have not received sufficient attention. This topic is considered in detail in Section 6.

The measurement and identification of surfaces employed in the present study are based on a human interpretation of information obtained from stylus, optical flat and interferometer instruments. The real surface, being complex, introduces substantial variations in interpretation of data. To completely describe a surface, the following information must be known as a minimum:

- the waviness of the over-all surface assuming a definition of waviness based upon the 2nd, 3rd, or n^{th} order wavelength characteristics of the topographical disturbances.
- the average roughness
- the maximum average roughness (peak-to-valley variations)
- the statistical distribution of asperities by height wavelength, and location over the entire surface
- the directional pattern of the surface lay

Each of these factors can be described, but not in simple terms. Unless the language is simple, the factors cannot be interrelated. In view of the limitations on surface interpretation, waviness and average peak-to-valley roughness were chosen as the factors for data correlations. The selection was based solely on the ability to define the factors easily.

Waviness is interpreted as a maximum surface variation having a wavelength greater than 0.030 in. and conforms with MIL-STD-10A. The surface waviness of importance to sealing is that normal to the direction of leakage flow, as shown typically on figure 2-21. Roughness, on the other hand, is measured either in the direction of or normal to the leakage flow. When surface lay predominates, the roughness in the direction of flow is used while surfaces possessing no lay effect are measured normal to leakage flow. Roughness is interpreted as an average peak-to-valley variation since it has some similarity to the seal leak path and is more reliable than rms or AA descriptors (Ref. 2-1). Following this procedure, two numerical descriptions are developed, one to describe waviness and the other roughness. Other directions of waviness, for example, could be described but this would induce another descriptor and it is not known how this additional number could be gainfully employed.

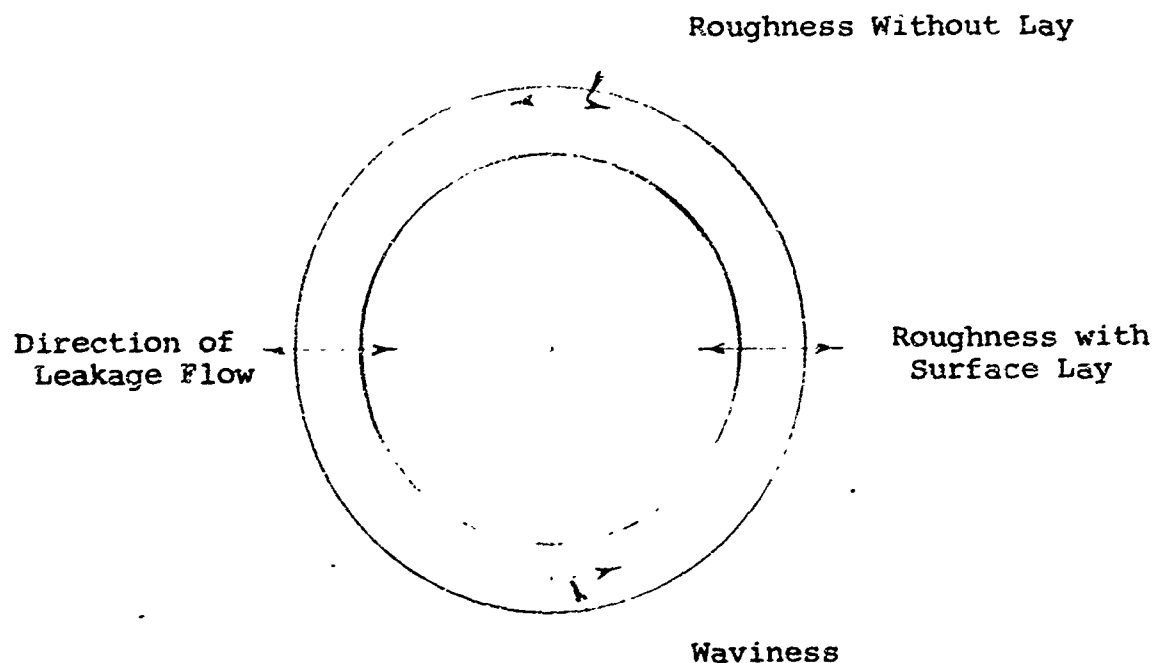


Figure 2-21 Location of topographical measurements on a circular gasket surface

2.3.4 Surface Fabrication

The surfaces of particular interest in this study are those that produce minimum leakage when mated together. These surfaces were classed into four categories in the preceding discussion. An attempt will now be made to show representative surfaces and the factors involved in their generation.

The first two classes of surfaces are very similar in that an attempt is made to achieve surfaces having minimum surface variations. Actually, it is difficult to achieve Class-I surfaces because of contaminants, imperfections in the fabrication process, and damage due to handling. General Electric (Ref. 2-13 and 2-14) obtained surfaces which came close to having no surface variations. These surfaces were generated by Jones Optical Company, Cambridge, Massachusetts and the Up-Hi Company, Ltd., Tokyo, Japan. These references give photomicrographic evidence of the degree of surface perfection that can be achieved. The distinction between Classes I and II is not well defined except that the Class-II surface has slightly more topographical protrusions. Figure 2-22 shows a photomicrograph of a Class-II surface prepared on 321 stainless steel. A corresponding interferometer photo is shown on figure 2-23. The minor surface disturbances are indeed small and beyond the range of interferometer measurement. A small scratch having a depth of $\sim 2\mu\text{in.}$ is shown in the center of the photo.

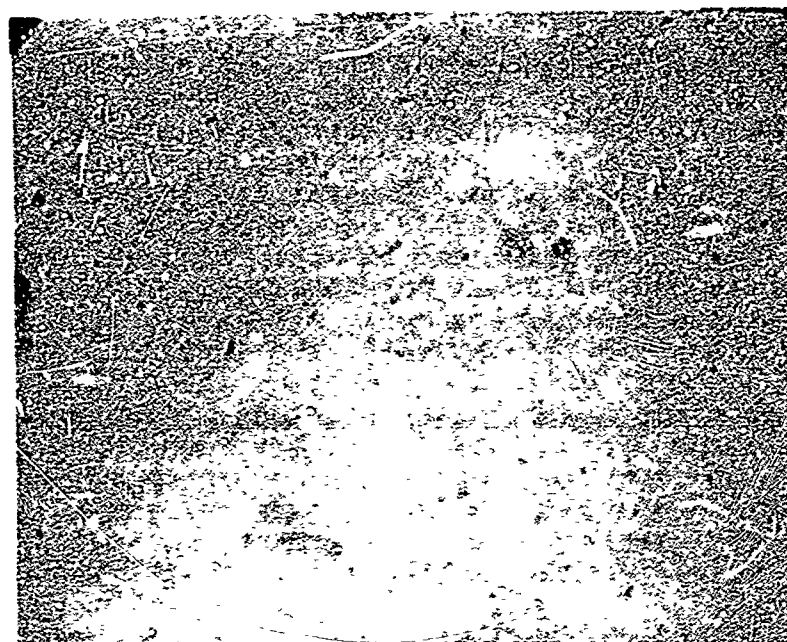
The generation of Class-II surfaces is one of polishing lapped surfaces using fine diamond or oxide dust. Class-I surfaces are probably obtained in a similar manner, but using special techniques. The process used by the two firms cited is considered proprietary information.

Class-III surfaces are typically those that have a preferentially oriented and undisrupted lay. Methods of producing these surfaces were investigated without success. The methods were:

- photoengraving
- electrodischarge machining
- electrochemical machining
- laser machining
- ultrasonic machining

In particular, the photoengraving and electrochemical methods appeared promising. The disadvantage that excluded their development was the inability to achieve uniform crest height. This crest height variation can be described as waviness on a macroscopic scale.

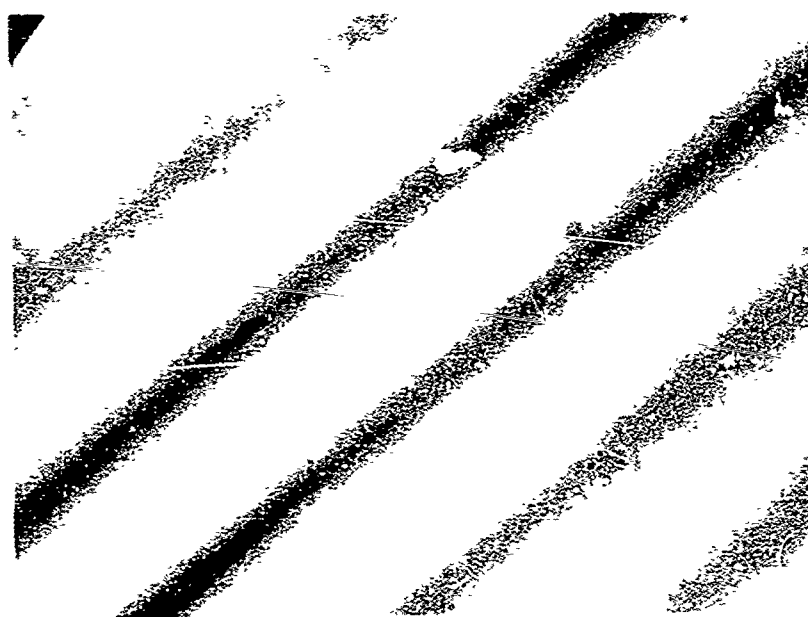
A close approximation to the Class-III surface was obtained by lathe-turning very small spiral grooves on a surface, followed by a diamond-polishing operation to remove the last vestiges of gross waviness variations. Figure 2-24 shows the resulting surface on 321 stainless steel while figure 2-25 shows a corresponding interferometer photomicrograph. The depth of the valleys was approximately $15\mu\text{in.}$



X960

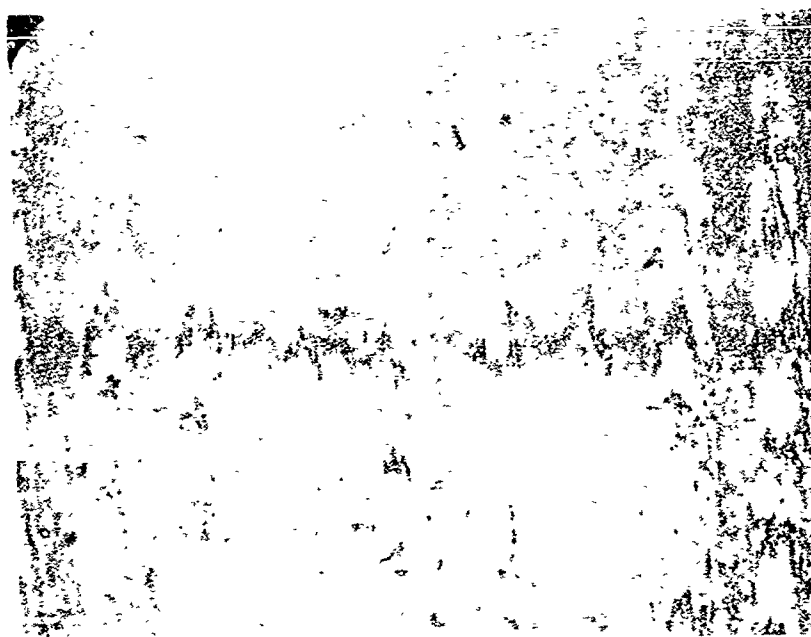
→ | ← 0.0005 in.

Figure 2-22 Photomicrograph of a 321 stainless steel surface polished with diamond dust



→ | ← 0.0005 in.

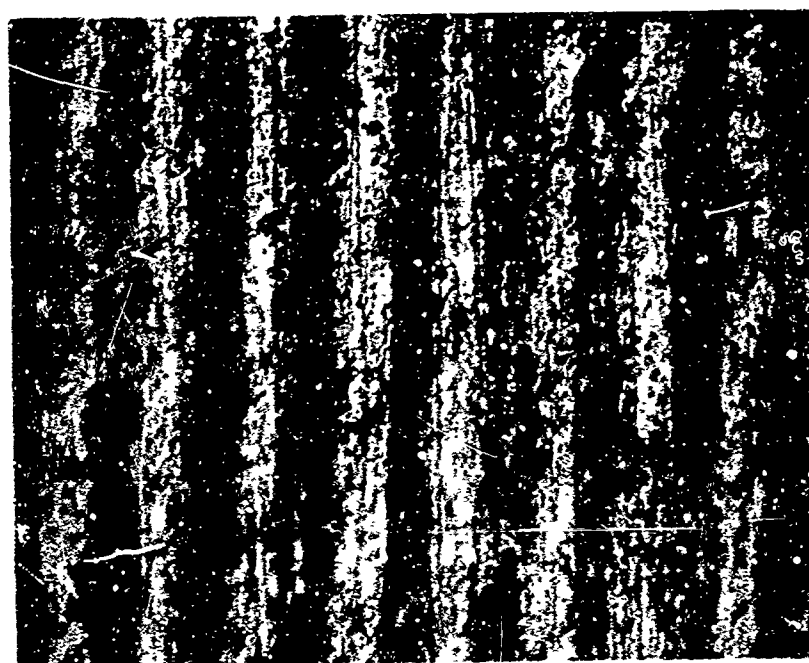
Figure 2-23 Interferometer photomicrograph of a 321 stainless steel surface as shown in figure 2-22.



X960

→ | | ← 0.0005 in.

Figure 2-24 Photomicrograph of a 321 stainless steel surface with fine turned and polished grooves



→ | | ← 0.0005 in.

Figure 2-25 Interference photomicrograph of a 321 stainless steel surface as shown in figure 2-24. Roughness is approximately $15\mu\text{in. PTV}$

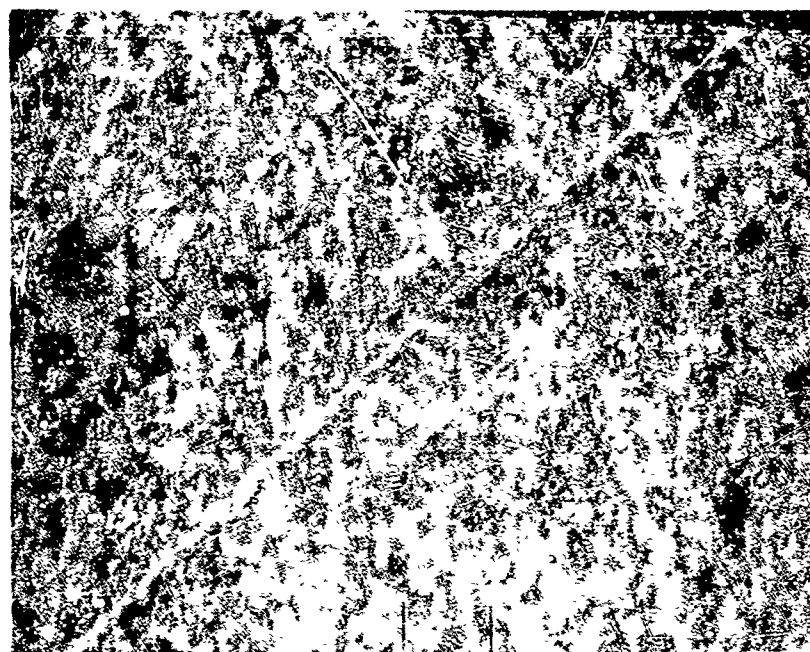
Class-IV surfaces encompass the vast majority of surfaces encountered in most engineering practice. Two typical 321 stainless steel and 6061T6 aluminum surfaces are shown on figures 2-26 and 2-27. These surfaces may be considered good lapped surfaces and yet, when compared with figure 2-22, are extremely rough. The topographical variations shown on the interferometer photographs (figures 2-28 and 2-29) are in the range of 2 to 5 μ in. The aluminum surface is slightly rougher than the steel. This rougher surface on soft materials is common in lapping and polishing processes.

A comparison of rougher Class-IV surfaces is contained in reference 2-1. These include ground and lathe-turned surfaces.

2.4 Effect of Contaminants on the Deformation of an Interface

Contamination of an interface can be described as beneficial or detrimental depending on the circumstances surrounding the deposition of the particle in the interface. Beneficial contamination includes the clogging of the leakage paths after the surfaces forming the interface have been pressed together. If the contact forces at the interface are not reduced sufficiently to permit elastic relaxation of the surfaces, the contaminants will at least remain ineffective. On the other hand, contaminants deposited on the surfaces before they are pressed together can produce detrimental effects. Consider two perfectly flat surfaces pressed together with one small contaminant wedged in between, as shown in figure 2-30.

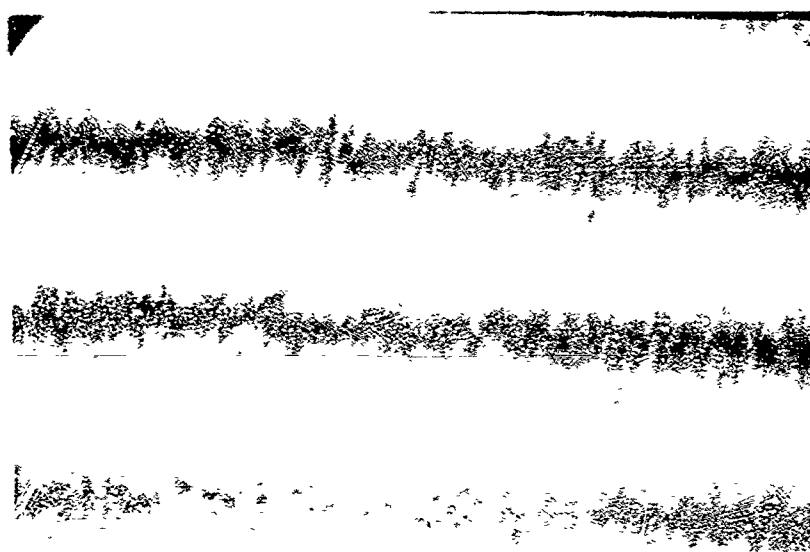
The influence of the particle on the mating of the surfaces is twofold. First, the particle can be elastically absorbed into one or both surfaces. In the immediate vicinity of the particle some plastic deformation may occur. The volume subtended by the particle is displaced through the substrate of the interface, ultimately resulting in elastic deformation of parts of the substrate. The second effect is purely one of plastically enveloping the contaminant. In both cases translation of a volume equivalent to the particle size must occur. One of the objectives of this study is to determine the influence of material translation on the leakage path. As a secondary objective, an investigation is made to determine if a turned surface possessing relatively deep valleys can absorb particles more readily than fine lapped surfaces. The philosophy behind this is that the contaminants can fill the valleys of the turned surface, thus requiring less surface loading for leakage.



X960

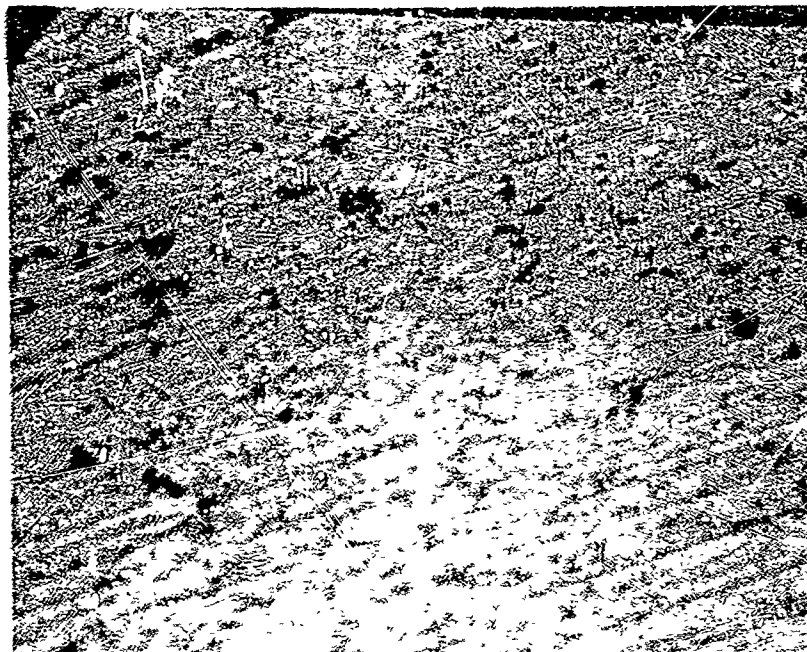
→ | ← 0.0005 in.

Figure 2-26 Photomicrograph of a 321 stainless steel lapped surface



→ | ← 0.0005 in.

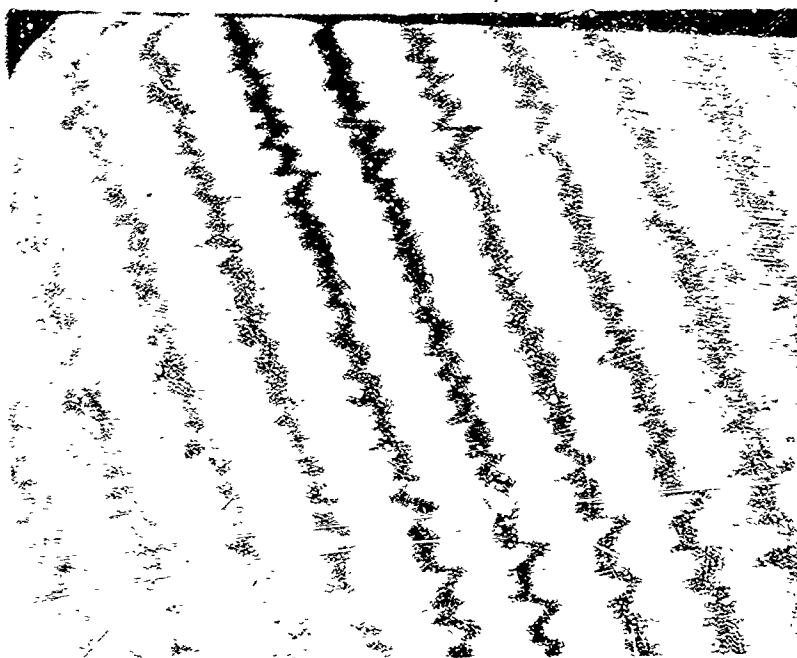
Figure 2-27 Interference photomicrograph of the 321 stainless steel surface shown in figure 2-26. Roughness is approximately $2\mu\text{in. PTV}$



X960

→ | ← 0.0005 in.

Figure 2-28 Photomicrograph of a 6061T6 aluminum lapped surface



→ | ← 0.0005 in.

Figure 2-29 Interference photomicrograph of a 6061T6 aluminum surface shown in figure 2-28. Roughness is approximately 5μ in. PTV

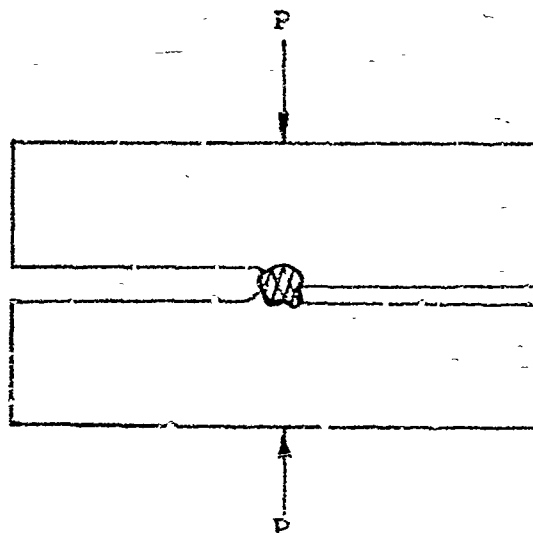


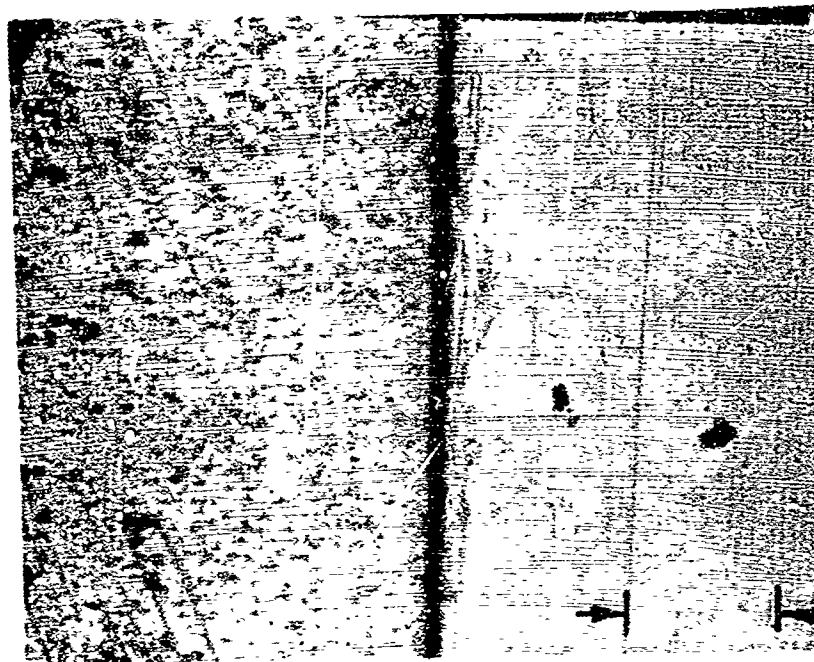
Figure 2-30 Effect of contaminant particle

2.4.1 Experimental Studies

Leakage experiments were conducted on four sets of 6061T6 aluminum flanges. Two flanges, composing each set, were pressed directly together without an intermediate gasket. Helium gas was introduced into the center of the flange assembly producing a 38-psi pressure difference across the sealing interface. Experiments were conducted on two sets of lapped and two sets of turned flanges. One set of each surface finish was evaluated in the clean and contaminated state. Pertinent data on the surfaces follow:

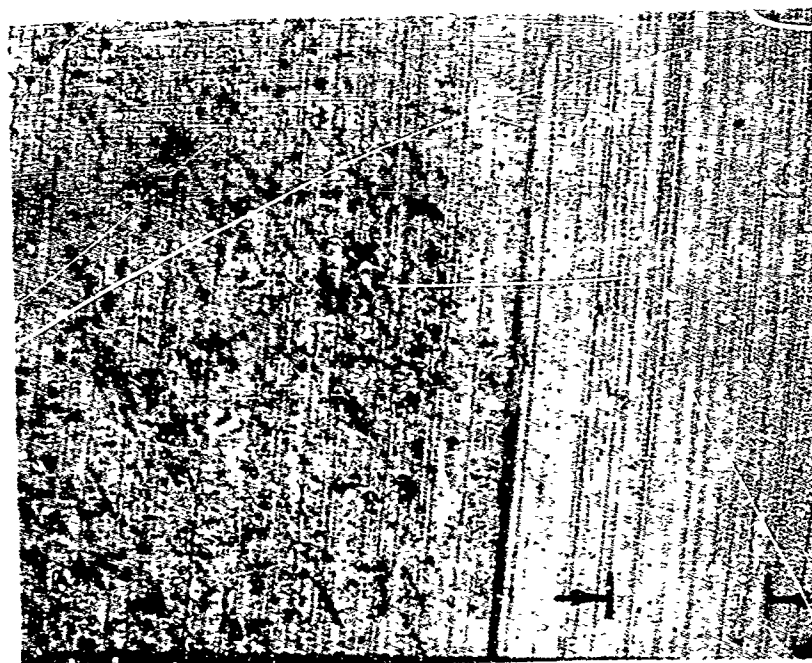
<u>Characteristic</u>	<u>Lapped Surface</u>	<u>Turned Surface</u>
Inside diameter	1.882 in.	2.232 in.
Outside diameter	2.263 in.	2.500 in.
Hardness	104 - 110 BHN	104 - 110 BHN
Roughness (PTV average)	3 - 4 in.	7 - 8 in.
Waviness	10 in.	50 in.

The contaminant, boron carbide, was selected on the basis of its high hardness compared with the aluminum flange material. The nominal particle size was 140 μ in. or 5 microns. The particles were dusted on the interface surface until a uniform haze was visually observed. Figures 2-31 and 2-32 show a comparison of the particle distribution of both surface finishes along with the surface in the noncontaminated condition. Figures 2-33 and 2-34 show the same surfaces, noncontaminated and at a higher magnification with interference light bands showing the topographical profile of the surface.



0.0005 in.

Figure 2-31 Photomicrograph of a contaminated and clean lapped 6061T6 aluminum surface



0.0005 in.

Figure 2-32 Photomicrograph of a contaminated and clean turned 6061T6 aluminum surface

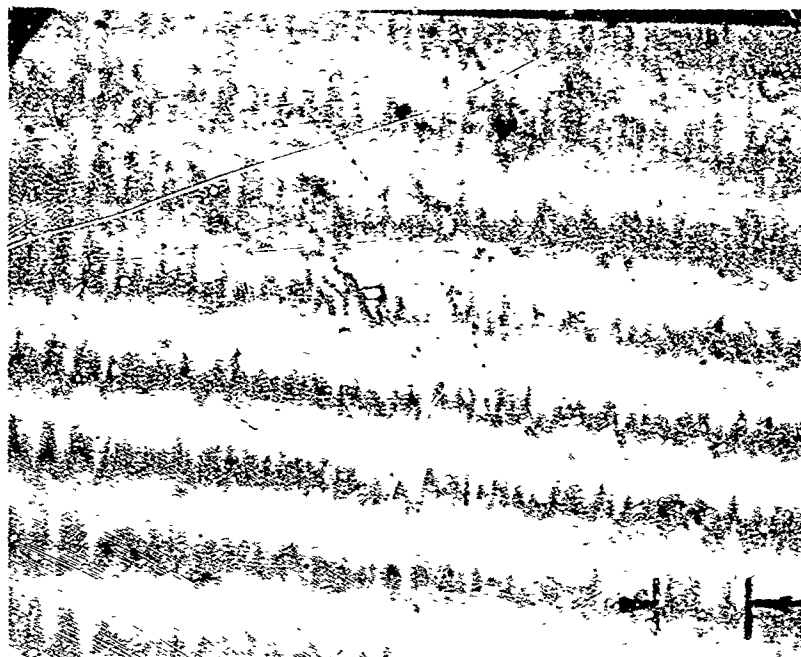


Figure 2-33 Interference photomicrograph of an uncontaminated lapped 6061T6 aluminum surface

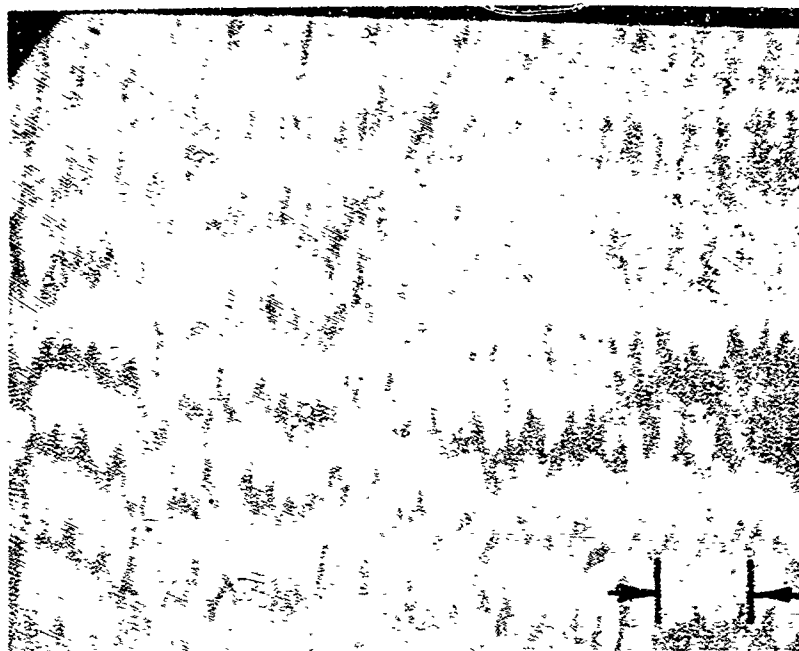


Figure 2-34 Interference photomicrograph of an uncontaminated turned 6061T6 aluminum surface

Flange load was progressively increased and the flow rate measured. Using the experimental leakage rate, the conductance parameter was calculated and related to apparent contact stress. The results of the four experiments are shown in figures 2-35 and 2-36. An inspection of the contaminated surfaces after being pressed together showed the particles embedded into the mating surfaces to an extent that the particles appeared to be an integral part of the flange material. Figures 2-37 and 2-38 show photomicrographs of the contaminated surfaces after the experiment.

2.4.2 Observations

The well established conclusion that contaminants should be prohibited from depositing on the interface surfaces of static seals was reached. Since this condition is difficult to achieve, a level of tolerable contaminant particle size and number must be determined. Unfortunately, the present investigation was too brief to establish tolerable contamination levels. However, some general conclusions may be made.

When metallic interface contact stresses are less than 1/20 of yield strength the leakage rate of fluid will be affected by:

- the average size of the contaminant if the size is greater than the surface roughness and waviness.
- the surface roughness or waviness if the contaminant size is smaller than the topography.

These conclusions are based on the results of experiments conducted by ITTRI and Rocketdyne (Ref. 2-12). If the leakage measurements obtained from sealing interfaces are used to calculate an equivalent leakage channel clearance, a correlation between contaminant size can be made for conditions of low contact stress. A correlation of these results follows:

<u>Contaminant</u>	<u>Particle Size (μin.)</u>	<u>Equivalent Channel Clearance (μin.)</u>	<u>Type of Surface</u>	<u>Contact Stress (psi)</u>	<u>Source</u>
Boron Carbide	140	70	Lapped Aluminum	500	Figure 2-35
Boron Carbide	140	80	Turned Aluminum	260	Figure 2-36
Diamond Particles	400	100	Lapped 440% CRES	380	Rocketdyne

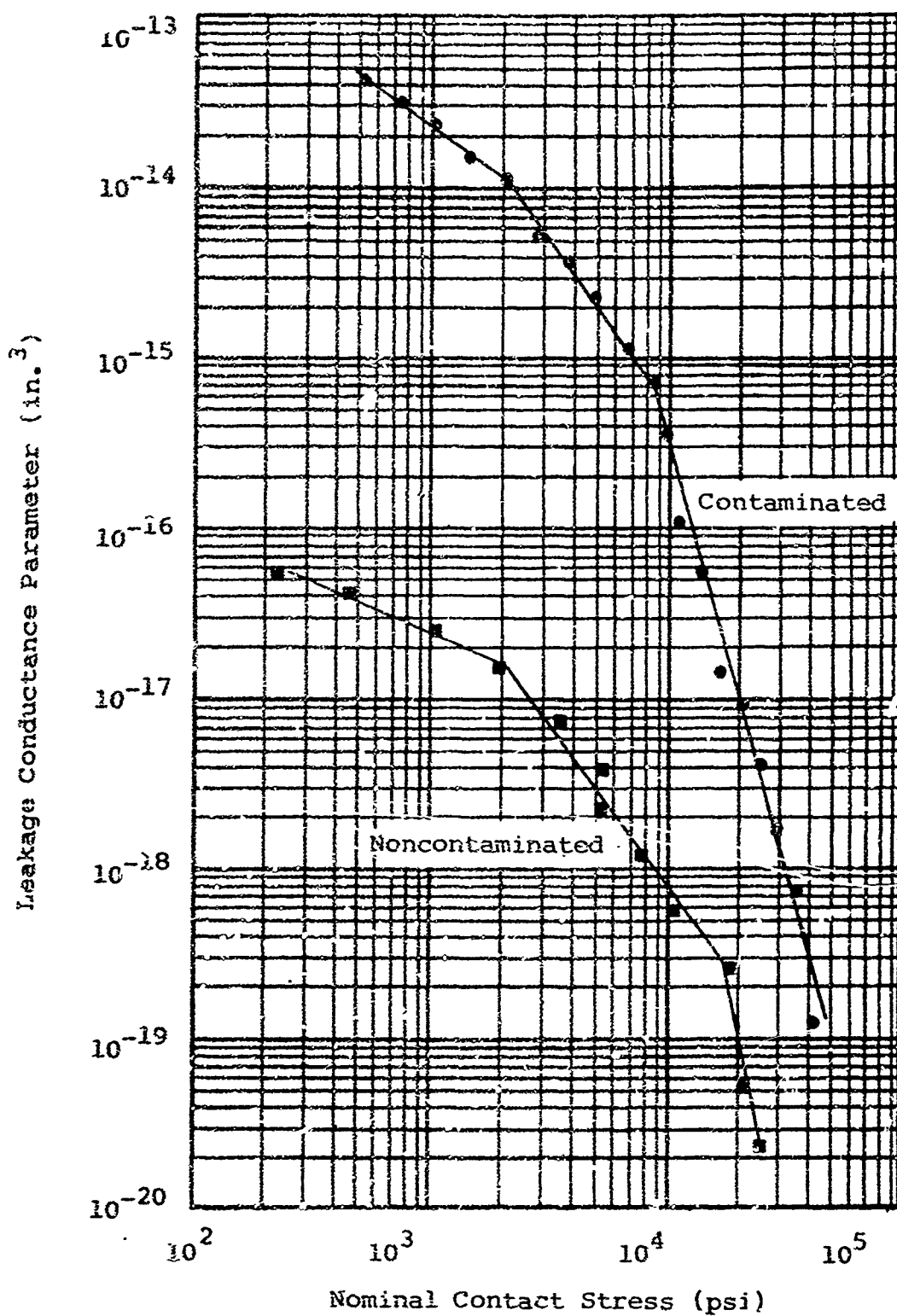


Figure 2-35 Conductance parameter characteristics of contaminated and noncontaminated lapped surfaces

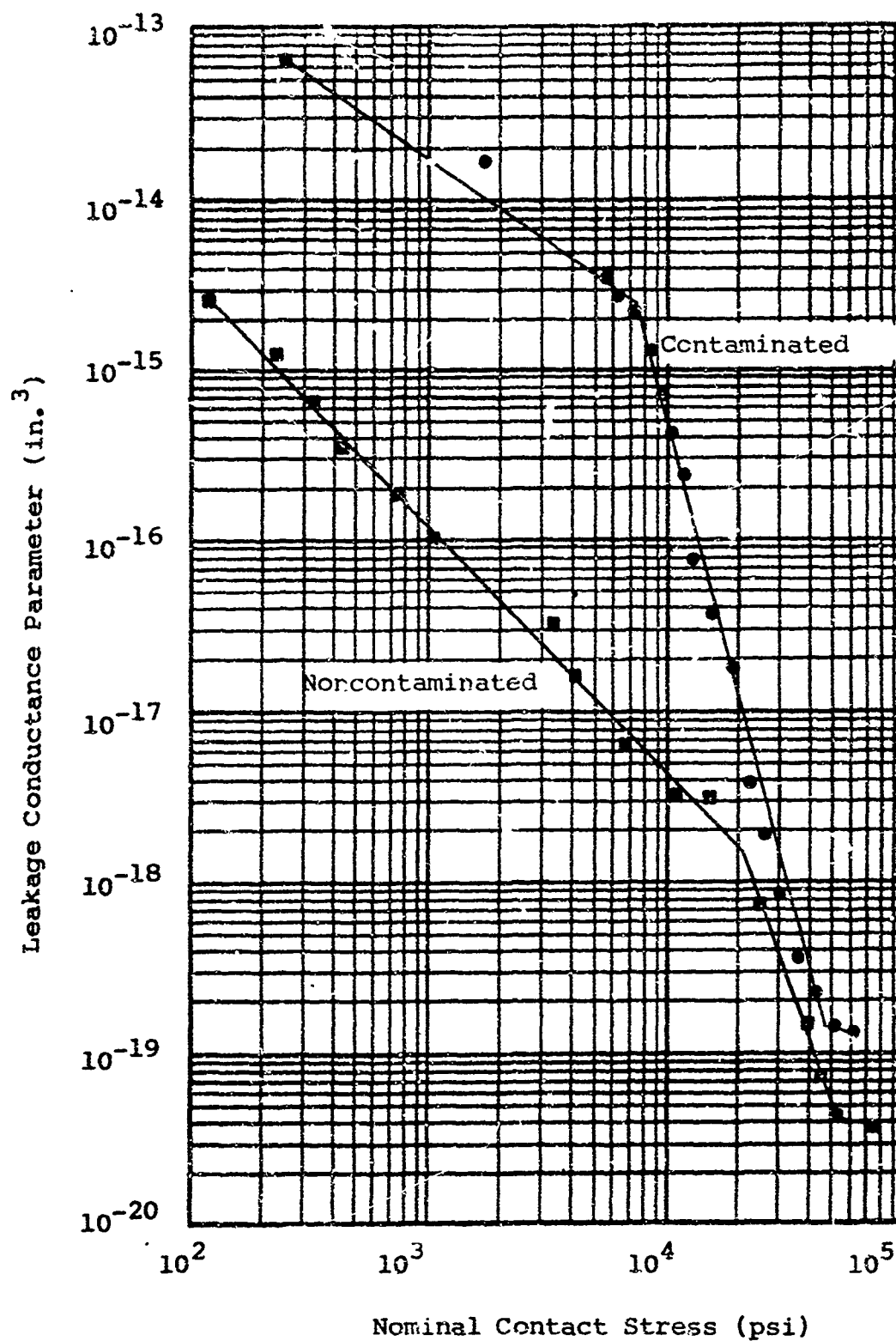
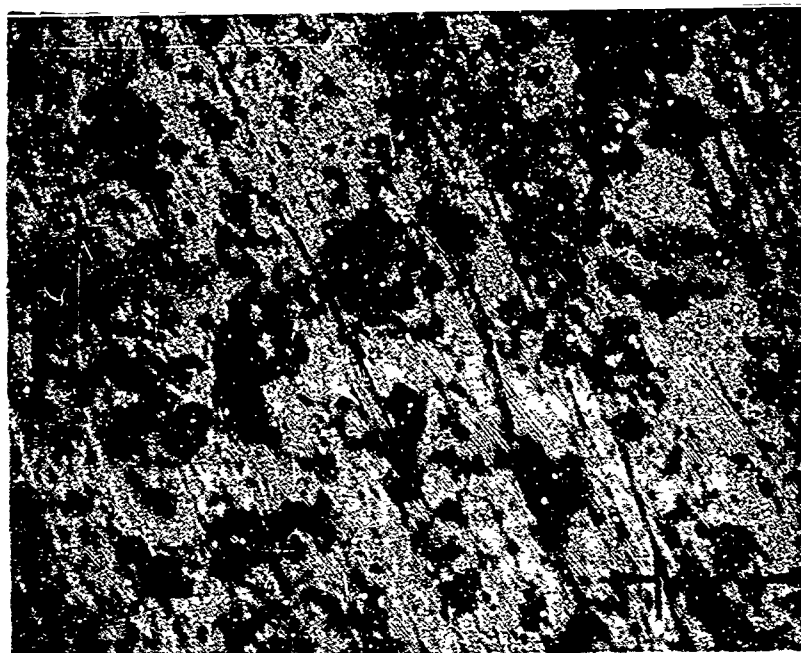


Figure 2-36 Conductance parameter characteristics of contaminated and noncontaminated turned aluminum surfaces



0.0005 in.

Figure 2-37 Photomicrograph of the lapped aluminum surface with embedded boron carbide particles resulting from an apparent contact stress of 40,000 psi.



0.0005 in.

Figure 2-38 Photomicrograph of the turned aluminum surface with embedded boron carbide particles resulting from an apparent contact stress of 50,000 psi.

The equivalent channel clearance is at least one order of magnitude smaller than the initial particle size, indicating that some deformation has occurred at the interface. In the Rocketdyne experiment, three diamond contaminant particles were employed while the IITRI experiments were made with a vast number of contaminant particles, as shown of figures 2-31 and 2-32. In both cases, the load deformation effects were small compared with the performance of similar surfaces in the noncontaminated state. A correlation of surface roughness with the equivalent channel clearance in the noncontaminated state follows:

<u>Type of Surface</u>	<u>Surface Finish (μin.)</u>	<u>Contact Stress (psi)</u>	<u>Equivalent Conductance Clearance (μin.)</u>	<u>Source</u>
Lapped Aluminum	4 PTV	230	8	Figure 2-35
Turned Aluminum	8 PTV	105	14	Figure 2-35
Lapped 440V	≈ 1 AA	150	1	Rocketdyne

Thus, it may be concluded that the number of contaminant particles is not as important as the size of the contaminants in the low contact stress condition.

An additional correlation of IITRI and Rocketdyne results was made by relating the conductance parameter (h^3) obtained from leakage measurements, with the nondimensional stress ratio. The nondimensional stress ratio is defined as the apparent contact stress to the Meyer hardness of the interface materials. Figure 2-39 shows the results of the Rocketdyne three-diamond particle experiment with the IITRI boron carbide experiment. The results show a larger conductance parameter in the IITRI experiments, which is attributed to the number of particles used. A close correlation of results was obtained for the noncontaminated experiments.

Contact stress greater than the yield strength of the materials produces sufficient deformation of the interface to minimize the effect of the contaminants. The results, figures 2-35 and 2-36, show that when substantial plastic deformation of the interface occurs, the effect on the conductance parameter (hence leakage) is relatively small. It is felt that a very small number of particles would have no influence on the leakage characteristics for the condition of substantial plastic deformation.

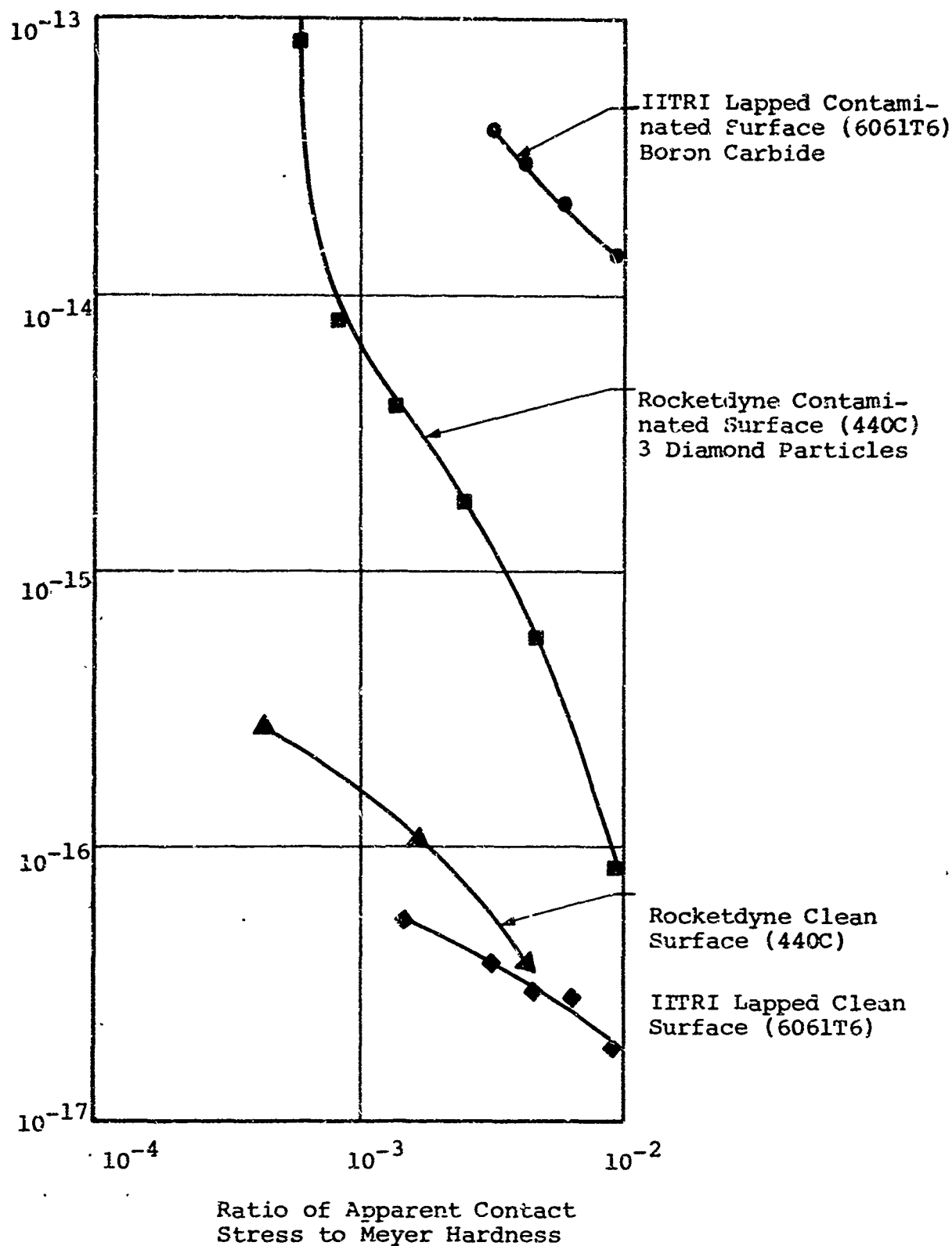


Figure 2-39 Effect of contamination on the conductance parameter contact load characteristics of various surfaces

The relative influence of a turned surface and a lapped surface was not explicitly determined. In view of the requirement that the contaminant size be less than the roughness, it is felt that the performance of either surface, when contaminated, will be substantially the same. This observation is based on the fact that contaminants, including airborne and other foreign particles, are usually larger than 1/4 micron. The experimental results, shown in figures 2-35 and 2-36, show identical leakage results for both surface finishes when contaminated. Another factor that must be considered is the minimum waviness that can be achieved with turned surfaces. Generally, the minimum waviness is approximately 10 times greater than the roughness. Hence, contaminants in turned interfaces will have lesser effect than the waviness.

2.5 Conductance Parameter

Although the factors influencing the deformation process have been identified, theoretical or experimental results that satisfy the requirements for a description of the interface leakage path have not been found. At this point the interface problem can be more clearly stated. The problem is to determine parameters describing the leakage path and, subsequently, establish the effect of such influencing factors as load and roughness. Preferably, the end result should be in a form suitable for use by component designers.

The interface leakage paths are probably very complicated judging from the studies of contact area. There may be a few large paths or many very small paths, depending on the initial surface topography and load. In any event, it is almost impossible to obtain dimensional descriptors of something which appears to be a random phenomenon. About the only conclusive fact that can be stated is that the interface of two materials provides resistance to the interchange of fluid. The term resistance takes on significant meaning when the interface-leakage problem is viewed from the analogous resistance, current, and potential in electricity. Suppose the undefinable leakage path could be represented by a lumped parameter conductance factor Z . The leakage flow rate Q is analogous to current and the pressure difference Δp across the interface is analogous and potential. On the basis of this hypothesis, the relationship between factors is

$$Q = Z \Delta p$$

Since the conductance Z is unknown and must be determined, the values of Q and Δp must be known. If a series of experiments is designed to vary factors such as load and roughness and accurate leakage measurements are obtained, the conductance value can be

calculated for any interface condition. Thus, a single parameter may be experimentally obtained to describe the interface leakage passageway. This approach to the problem is simple and straightforward. Marginal assumptions were made, however, which required substantiation. Briefly, the argument may be stated as follows.

- What is the relationship between leakage rate, geometry, fluid properties, and pressure difference across the interface?
- If a relationship does exist, can it be applied and is it consistent for any seal interface?
- How can the effects of load, material properties, and surface topography be introduced as variables?

The concept of interface conductance has greater significance in the field of fluid mechanics than the simple electrical concept would suggest. The concept is similar to the treatment of the turbulent flow of fluid in a roughened pipe. Since turbulence must be viewed statistically, no completely theoretical analysis is possible. Most of the energy losses occur at the wall and an empirical roughness factor is used to help describe the energy loss. The analysis of flow through an interface is treated in the same general manner but not necessarily assuming turbulent flow conditions.

A modeling analysis of a seal interface is initiated by assuming a theoretical relationship for flow through a channel. Upon completion of the analysis, experimental results are used to verify the assumption. The first equation considered is for laminar, viscous, compressible flow between two circular plates uniformly separated. The equation relating the fluid properties, flow path geometry, and flow rate is

$$Q_o = \frac{\pi(p_2^2 - p_1^2) \bar{h}^3}{12\mu p_o \ln r_o/r_i}$$

where

- \bar{h} = uniform channel clearance
- p_o = pressure at standard conditions
- p_1 = exit fluid pressure
- p_2 = inlet fluid pressure
- Q_o = volume rate of flow at standard conditions
- r_o, r_i = outside and inside radii of plates
- μ = absolute viscosity
- ρ_o = fluid density at standard conditions

When the terms are rearranged, the uniform channel clearance

$$\bar{h} = \sqrt[3]{\frac{12p_o \mu \ln r_o/r_i Q_o}{\pi(p_2^2 - p_1^2)}}$$

The terms in the righthand side of the equation contain the descriptors of the apparent channel geometry, pressure conditions, and fluid properties. If the assumption is made that the apparent length and width dimension of the channel sufficiently describe the average of seal interface leakage paths, then the uniform clearance h may be sufficiently descriptive of the remaining dimensional factor. Since h may not be geometrically significant for real surfaces in contact, a new term, the conductance parameter (h^3), is introduced. The concept of a conductance parameter is difficult to support in view of the random nature expected of the seal leakage path. However, the seal leakage paths could conceivably be statistically averaged in nature. Thus, the behavior of geometrically similar interfaces is the same. Experimental verification sufficient to support the arguments is presented in Reference 2-1. The experimental results substantiated the hypothesis of the conductance by:

- the almost complete independence of conductance with respect to pressure variation.
- the almost complete independence of conductance with respect to viscosity variations.

Additionally, the mechanics of leakage flow were verified as laminar flow at least in the range of leakage flow encountered. The importance of the conductance parameter is threefold. First, the conductance provides a means of relating the factors influencing fluid flow and the geometry of the interface together. Secondly, the conductance parameter is assumed to be a function of the interface load, surface topography, and material properties. Thus, it can serve as a common factor in correlating these factors. Substantiation of this assumption and a correlation of results are presented in Reference 2-1, Volume I. The third benefit to be attained is the development of empirical criteria that can be used in the analysis of a seal. Consider that for given interface load, material properties, and surface topography; a conductance parameter can be predicted. In turn, the conductance parameter could be substituted into the equation along with the fluid properties, sealed pressure and interface geometry. A solution of the equation would yield the leakage rate. This is the final objective of the present work.

In this study, experimental gas leakage rates range from laminar to molecular flow with an intermediate range described as transition flow. Equations describing each mode of flow were presented in Reference 2-1, Volume II. The major problem in the present study is to determine when to apply the appropriate flow equation. A test for the appropriate flow regime is the Knudsen number defined as

Molecular mean free path, λ
Leakage Channel Clearance, h

The application of this test to a seal interface is difficult and requires substantiation. The problems involved are:

- Is the leakage path composed of many small or few large void space interconnections? If the leak path is small, molecular flow will predominate the flow process much earlier than if the leak path is large.
- The molecular mean free path is a function of pressure. Thus, the molecular free path could be very small in the region of the sealed fluid, and laminar flow would occur. As the flow progresses downstream through the interface, the molecular free path increases as a result of the flow pressure gradient. At some point downstream the free path could become sufficiently large and molecular flow could prevail. Since the resistance to flow is greater for laminar flow, it may be expected that it would be the controlling factor even if mixed flow occurred.

Each of these problems is suggested for further study. In lieu of not being able to select a mode of interface leakage flow, an arbitrary assumption was made that the flow is described by the transition equation which can be written for flow between circular plates as

$$Q_o = \frac{\pi h^3 (r_o + r_i) (p_2^2 - p_1^2)}{12\mu (r_o - r_i) p_o} \left(1 + \frac{12.76 \epsilon p_o \lambda_o}{(p_2 + p_1) h} \right)$$

where h^3 = conductance parameter or uniform clearance

λ_o = molecular mean free path at standard conditions

ϵ = correction factor ~0.9 for a single gas and 0.65 for a mixture.

While it is recognized that errors can be introduced by applying the wrong equation in deriving the conductance parameter from experimental leakage measurements and this equation; it must be remembered that the resulting correlations are destined for use as design criteria and the implementation of these criteria requires a flow assumption. If the same flow assumption is made, the errors may cancel each other. This equation includes a geometrical approximation for circular plate geometry as described in Reference 2-1, Volume II.

2.6 Empirical Correlation of Parameters for Metallic and Elastic Interfaces

In this subsection we are concerned with the correlation of parameters influencing the flow of leakage through flat sealing interfaces. These parameters, discussed individually in preceding subsections, are tabulated again on figure 2-40. To provide the reader with an insight into the detailed development, an over-all view of the procedure first must be outlined. This is followed by a statement of the ground rules and, subsequently, the detailed correlation.

2.6.1 General Procedures

The results of leakage experiments form the input data used in the correlation process. These experiments can be described as follows.

Two or more circular surfaces were pressed together under varied loads. The circular surfaces formed sealing interfaces, which impeded the transposition of a gas sealed within the circular interface. Leakage flow under known conditions of sealed gas pressure was measured at each load. The material properties and topography of the surfaces were varied. An experimental apparatus similar to that shown in Appendix I was used in obtaining the data.

Next, the input data were used to form two correlation factors:

- 1) a modified stress ratio described in Subsection 2.1 and given as

$$\frac{P^{2/n'}}{A_A} / \sigma_m$$

where

P = applied load

n' = Meyer index, a property of the interface material

A_A = apparent area of interface

σ_m = Meyer hardness, a property of the interface materials

- 2) the conductance parameter described in Subsection 2.5 and given as

$$(h^3) + \frac{12.76 \epsilon p_o \lambda_o (h^2)}{p_2 - p_1} = \frac{12 \mu (r_o - r_i) p_o Q_o}{\pi (r_o + r_i) (p_2^2 - p_1^2)}$$

where

- (h^3) = Conductance parameter
- p_2, p_1 = Inlet and outlet fluid pressures
- λ_o = Molecular mean free path of the gas at STP
- μ = Viscosity of the gas
- r_i, r_o = Dimensions of the circular interface
- p_o = Standard pressure
- Q_o = Leakage at STP

An inspection of the preceding factors shows that each of the influencing parameters is represented except surface topography.

At this point, the data obtained in each experiment were graphically correlated using the conductance parameter and modified stress ratio factors as variables. In turn, the graphical data were grouped on the basis of similar surface topography.

Finally, mean relationships between conductance and modified stress ratio were formed. These results are presented graphically with surface topography shown as a parameter. A flow chart of the preceding procedures is shown on figure 2-40.

2.6.2 Ground Rules

The purpose of the ground rules is to provide a clarification of all factors involved in the correlation. Each parameter is considered individually.

Load. The load of interest in the present work can be defined as the net load acting on a sealing interface. This load is the total load pressing the surfaces together minus the effects of fluid pressure acting on any part of the surfaces including the flow pressure gradient. Volume I of Reference 2-1 contains a discussion of the net load.

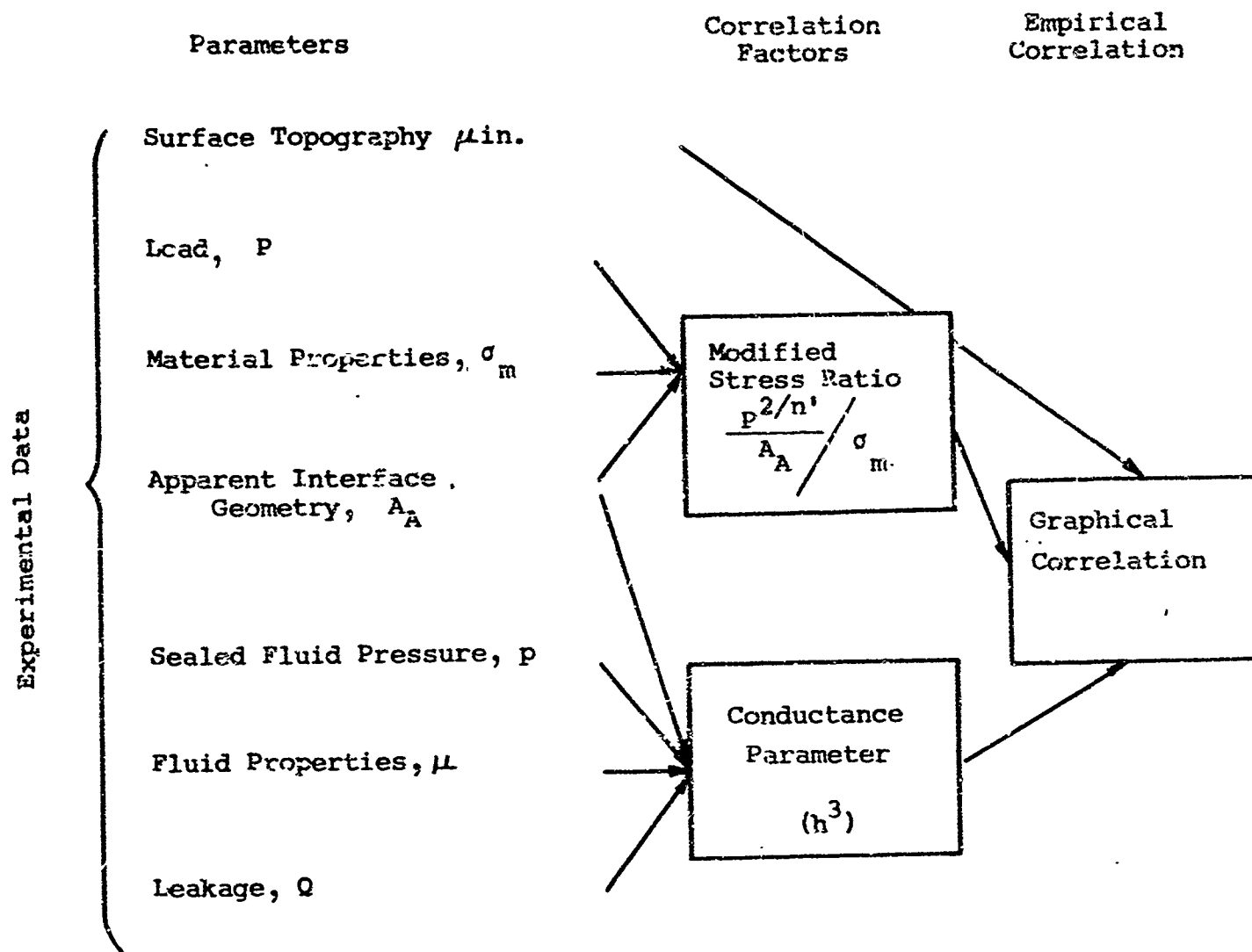


Figure 2-40 Flow chart of the correlation process

Apparent Interface Geometry. The apparent interface geometry is essentially that of two flat, circular surfaces having the known dimensions r_0 and r_1 , the outside and inside diameters of the surface. The application of a substantial load may cause plastic deformation thereby changing the geometry. This effect is recognized and compensated for in the calculation of the modified stress ratio.

Material Properties. Hardness of the interface material is the most important measure of the ability of a material to deform under load. The hardness of interest, defined as the Meyer hardness of the softer material forming the interface, was obtained using a Brinell test apparatus. The Meyer strain-hardening index was also obtained through hardness tests described in Subsection 2.1. In the ensuing work, experimental data from other sources were used that did not include all material information. Where this information was lacking, handbook values of hardness were employed and the Meyer index n' was assumed to be 2.

Surface Topography. In view of the deficiency in adequately describing surfaces, we have little choice but to accept the best available method of identification. Topography descriptions were obtained through profilometer or microscopic surface in the average direction of leakage flow. An average peak-to-valley (PTV) roughness was derived by visual interpretation of the instrumentation output. Roughness of the harder surface forming the interface was ultimately used as a parameter.

Because of other important surface factors not described by a single measurement, it was necessary to introduce additional descriptors for waviness and fabrication process. Waviness is primarily determined by the surface fabrication process. Even with the same process, substantial variations occur. Thus, it is not possible to associate a specific waviness with any fabrication process or other factor. It is possible, however, to assign ranges of waviness variations which can be associated with the fabrication process. Since the eventual correlation is based on considerable data; it is felt that the waviness influence becomes an averaged effect. Figure 2-41 shows approximate range of waviness obtained from experimental surfaces. It should be noted that this information is restricted to interface size geometries less than 3 in. in diameter.

In addition to the grouping of experimental data according to similar surface roughness, the data were grouped by fabrication processes. Where different surface finishing processes produce very similar leakage results; their data were grouped together. The topographical groupings used in the correlation process can be summarized:

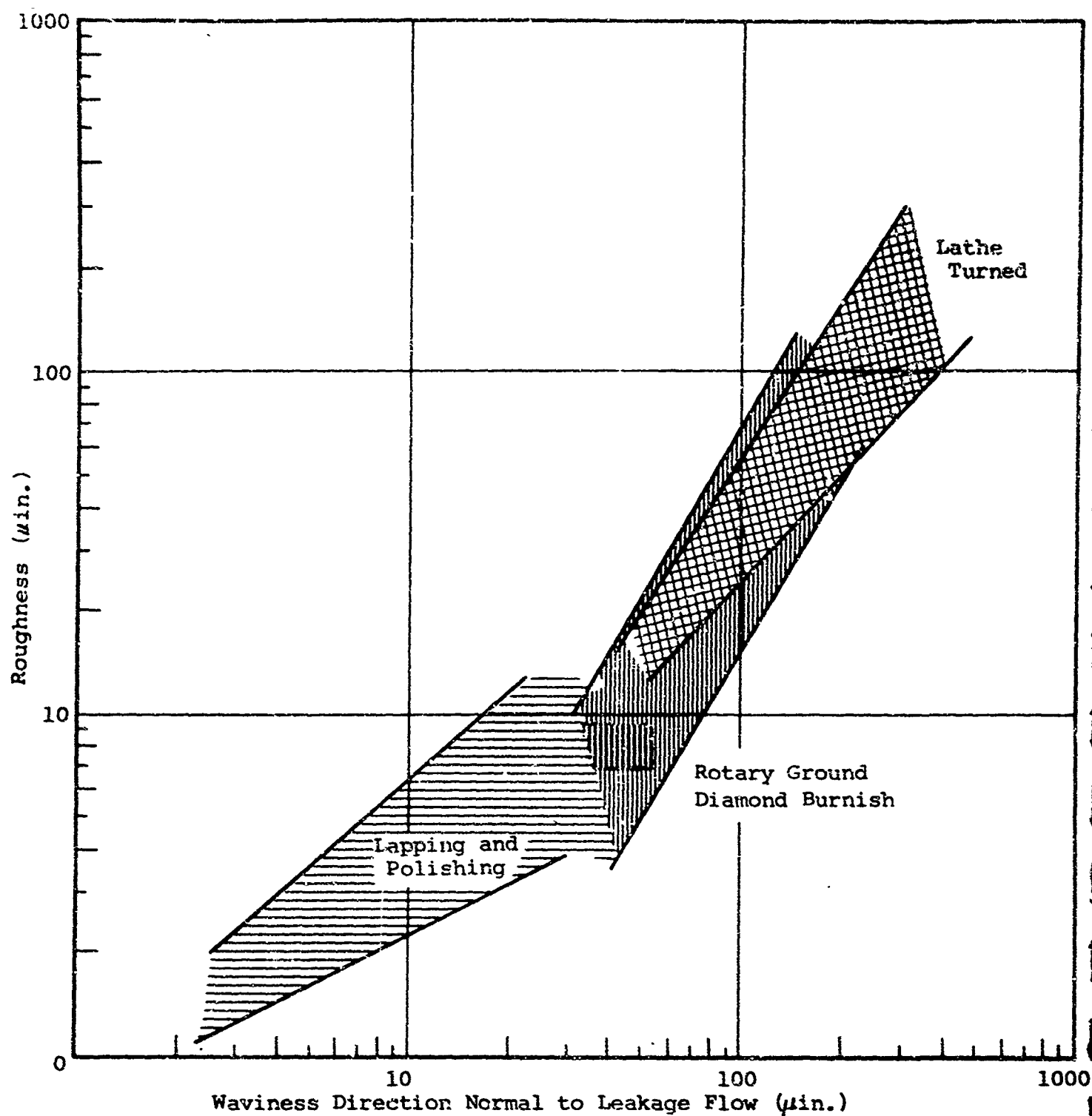


Figure 2-41 Approximate range of waviness with roughness for various fabrication processes

<u>Basic Fabrication Group</u>	<u>Similar Process</u>	<u>Roughness Groups of the Harder Interface Surface (μin.)</u>
Lathe-Turned	Diamond Burnish	0 - 10
		10 - 20
		20 - 30
		30 - 50
		50 - 75
		75 - 100
		100 - 200
		200 - 400
Rotary-Ground		0 - 10
		10 - 50
		100 - 200
Lapped	Polished; Multi- directional Grinding	0 - 2
		2 - 5
		5 - 10
		10 - 20

Leakage. Measurement deviations account for most of the variations encountered in the correlation process. These are due to calibration errors in the leakage measuring devices and techniques. Since data were obtained from three sources, the over-all deviation can be expected to vary widely. An estimated leakage error reflected in terms of the conductance parameter follows:

<u>(h^3)</u>	<u>Deviation</u>
$< 10^{-18}$	$\pm 700\%$
10^{-14} to 10^{-18}	$\pm 300\%$
$> 10^{-14}$	$\pm 100\%$

Conductance Parameter. While the conductance parameter is derived from the equations of laminar flow through uniform channels, generally, the equations have been found to apply for compressible and incompressible flow. In the present correlations, however, the range of flow varies from laminar compressible to molecular flow with a range in between described as transition flow. There is no easy way to identify the transition region. Rather than attempt a distinction, the transition flow equation is assumed. This possibly introduces an erroneous conductance parameter. However, it must be remembered that the final correlations are destined for use as design criteria and the implementation of these criteria requires a flow assumption. If the same flow assumption is made, the errors, if any, should cancel each other.

2.6.3 Correlation Details

The first step in the correlation process was to convert data from ninety-nine experiments into relationships between the modified stress ratio and conductance parameter. These data, obtained from experiments conducted at IITRI, Rocketdyne, and General Electric Co. (Ref. 2-1, 2-15 thru 2-20) were catalogued into surface topography and fabrication process groups. The results are shown graphically on figures I-2 through I-30 in Appendix I. An index table containing a code designation of the experiments and a description of the materials is shown on Table 2-3.

It should be noted that the calculations for the conductance parameter and modified stress ratio were obtained using a computer. The conductance parameter is a cubic equation which is difficult to solve solved manually.

The second step was to derive an average relationship for each range of surface topography and finishing process. The average relationship was actually based on the mean difference between individual experimental results. For example, the conductance parameters from four experiments at the same stress ratio are

$$(h^3, h_2^3, h_3^3, h_4^3)$$

with the order of presentation indicating increasing magnitude. The average value of conductance for the four points is

$$h_{avg}^3 = h_1^3 + \left[\frac{(h_2^3 - h_1^3) + (h_3^3 - h_1^3) + (h_4^3 - h_1^3)}{3} \right]$$

This procedure was also applied to stress ratio values for a constant conductance. This method of averaging yields the same results as the preceding method. The choice of averaging was determined by the data characteristics.

The average relationship for each topographical group is shown on figures I-31 through I-47. In addition, the maximum deviations are shown as curves somewhat parallel and adjacent to the average curve.

The third step in the correlation process was the superimposition of roughness groups for each basic fabrication process. This step is shown graphically on figures 2-42, 2-43 and 2-44.

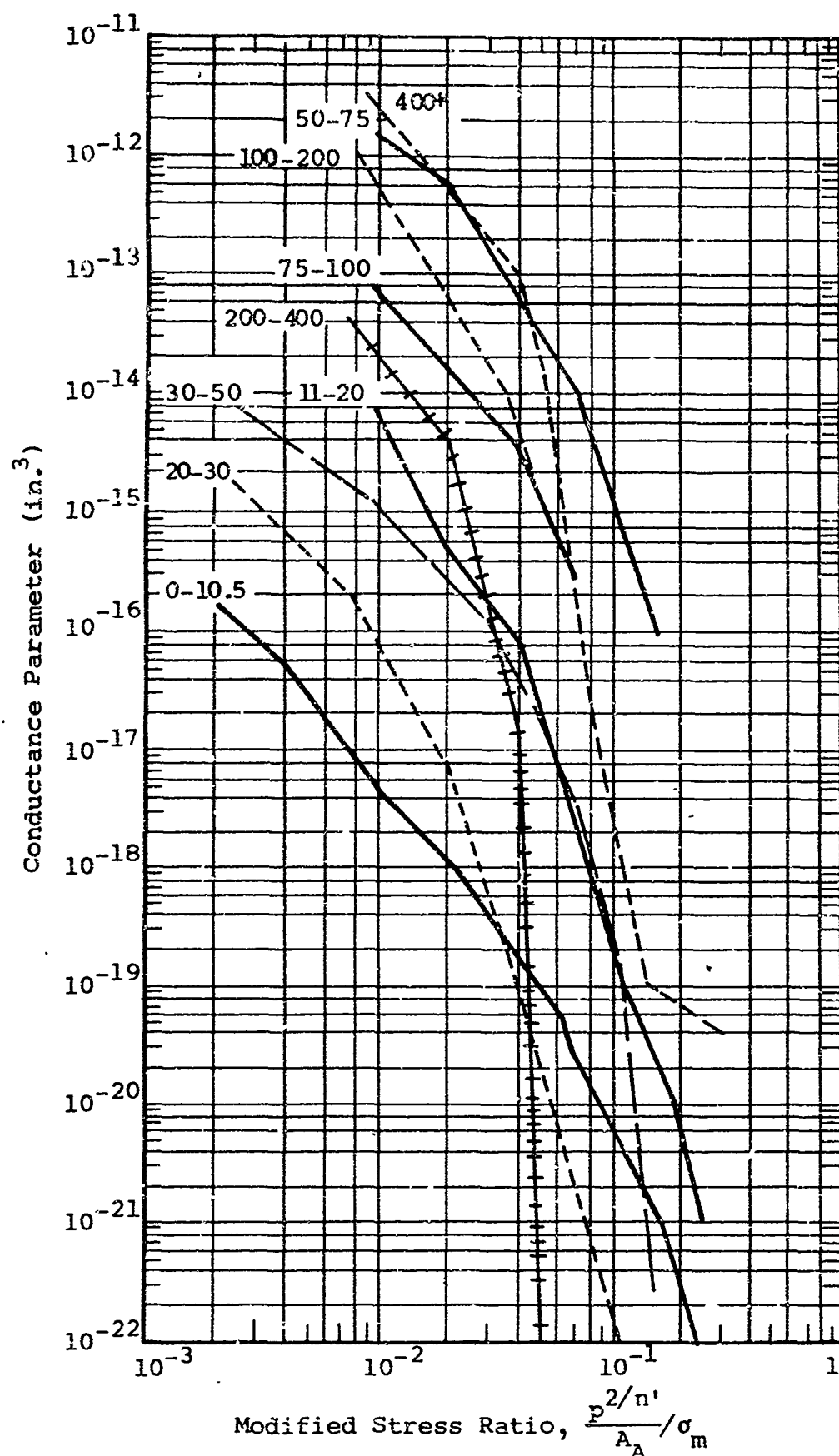


Figure 2-42 Comparison of surface roughness groups for turned surfaces. Surface roughness (PTV) is shown as a parameter.

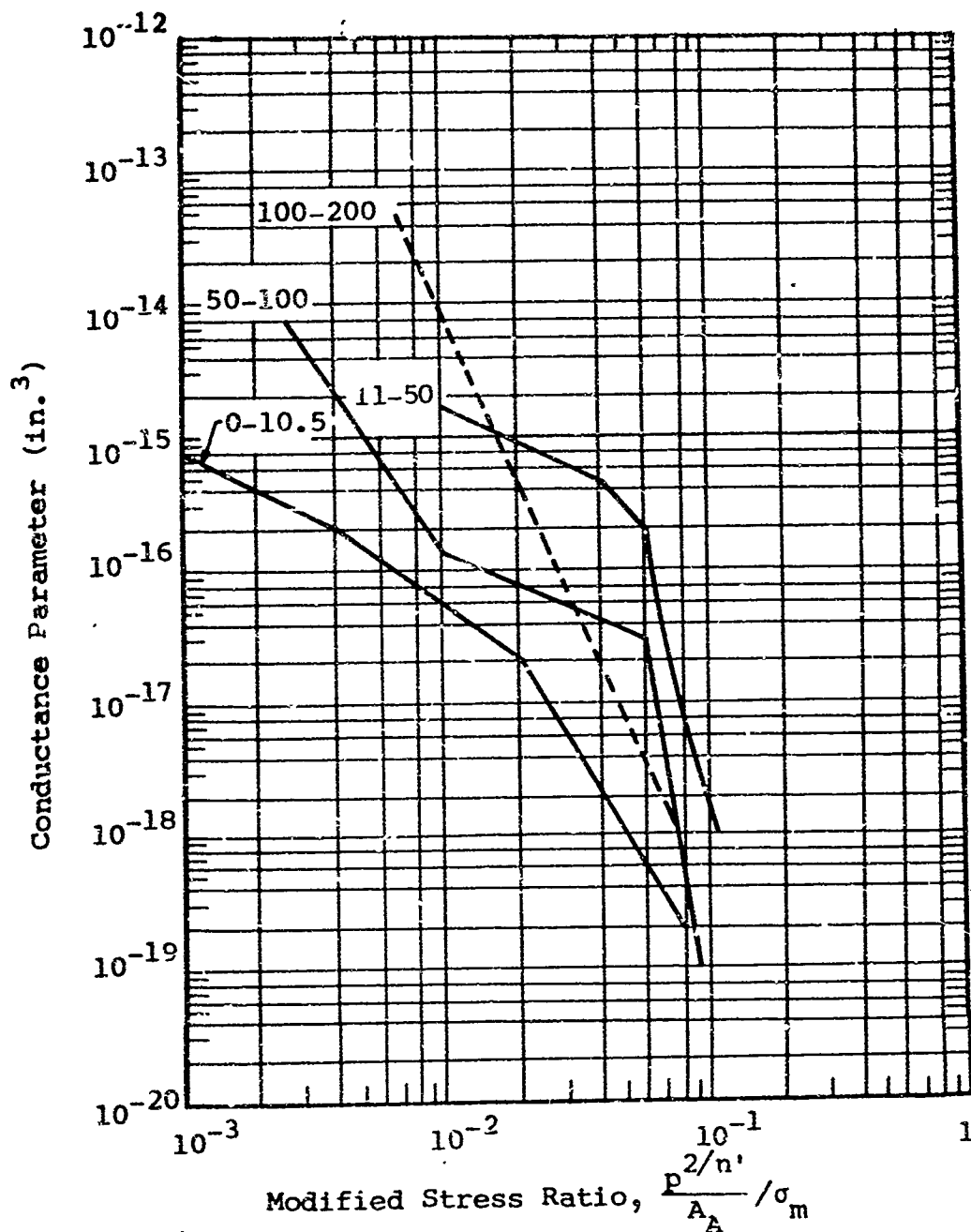


Figure 2-43 Comparison of surface roughness groups for ground surfaces. Surface roughness (PTV) is shown as a parameter.

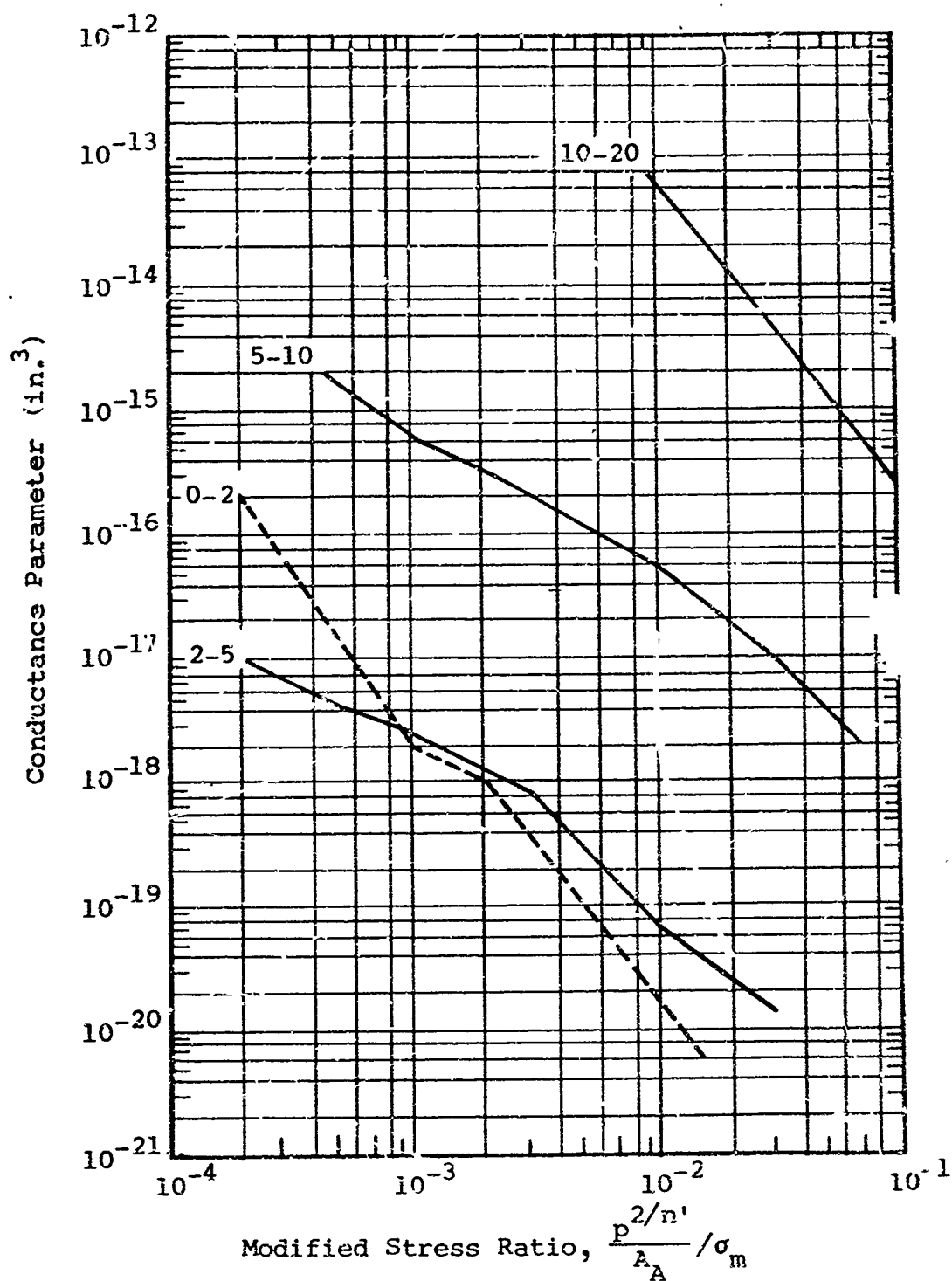


Figure 2-44 Comparison of surface roughness groups for lapped and polished surfaces. Surface roughness (PTV) is shown as a parameter.

Table 2-3

EXPERIMENTAL DATA INDEX

Experiment Identification				Materials	Hardness	
Investigator	Code	Reference	Reference Figure		BHN	Meyer (kpsi)
Rocketdyne	R ₁	2-15	I-2	6061T651 Al poppet	110	117.8
				WC seat	880	---
	CC ₁	2-15	I-2	440 C poppet	772	1,040
				WC seat	880	---
	BE ₁	2-16	I-2	440 C poppet	772	1,040
				WC seat	880	---
	L ₁	2-16	I-2	440 C	722	1,040
General Electric	RH ₁	2-15	I-3	440 C	722	1,040
	RH ₂	2-16	I-3	440 C	722	1,040
	GE-1	2-14	I-3	347SS	162-185	232
	GE-12	2-14	I-3	347SS	162-185	232
	GE-24	2-14	I-4	347SS	162-185	232
Rocketdyne	RE ₀	2-17	I-4	440 C	722	1,040
IITRI	62-7		I-4	321SS	162-185	202
	62-8		I-4	321SS	162-185	202
Rocketdyne	RF ₀	2-17	I-5	440 C	722	1,040
	RG ₀	2-17	I-5	440 C	722	1,040
	RA ₀	2-17	I-5	440 C seat	722	1,040
IITRI	62-6		I-5	WC poppet	880	---
				6061T6 Al	104-119	159
Rocketdyne	RG ₁	2-15	I-6	440 C	722	1,040
	RB ₁	2-15	I-6	440 C	722	1,040
	RB ₂	2-16	I-6	440 C	722	1,040
	RB ₀	2-17	I-7	440 C	722	1,040
	RK ₀	2-17	I-7	6061T651 Al	110	177.3
	RJ ₀	2-17	I-7	17-4PH	---	579.5
IITRI	62-5		I-7	6061T6 Al	104-110	150

Fabrication Method	Surface Roughness (μ in., PTV)	Meyer Index	Comments
turned	---	2.00	10 μ in. 10.03 in. concave taper on aluminum surface
diamond lapped	1	---	texture of carbide surface composed primarily of oils in carbide
circular diamond lapped			
circular diamond lapped	1	---	
	---	2.00	
circular diamond lapped	1	---	
unidirectional diamond lapped	1	2.00	
diamond lapped	1	2.00	circular lay
diamond lapped	1	2.00	circular lay
polished	1	2.35	Yatabe Fine Finish, random scratches
polished	1	2.35	Yatabe Fine Finish, random scratches
polished	1	2.35	Jones Optical Polished Surface, randomly located small pits
diamond lapped	1.8	2.00	unidirectional lay, significant number of scratches
polished and circular scratched	2	2.35	polished surface scratched circumferentially with Al_2O_3
polished	2	2.35	unidirectional lay
diamond lapped	2.2	2.00	unidirectional lay
diamond lapped (scratched)	2.3	2.00	
diamond lapped		2.00	~20% of poppet covered with 4 μ in. scratches
diamond lapped	3	---	multidirectional lay
polished	3	2.00	unidirectional lay
unidirectional diamond lapped	3	2.00	
circular diamond lapped	3	2.00	
diamond lapped	3	2.00	
	5.6	2.00	multidirectional lay
diamond lapped	6.0	2.00	multidirectional lay
	6.0	2.00	multidirectional lay
turned	7	2.00	finest turned surface produced, turned on Harding's precision lathe

Experiment Identification				Hardness		
Investigator	Code	Reference	Reference Figure	Materials	BHN	Meyer (kpsi)
	RF _O	2-17	I-8	440C	722	1,040
	RI _O	2-17	I-8	440 C	722	1,040
Rocketdyne	RD ₁	2-18	I-8	440 C	722	1,040
	RA ₁	2-18	I-9	440 C	722	1,040
	RN ₁	2-18	I-9	17-4PH	---	579.5
IITRI	A ₁ DL		I-9	2024-O gasket	40	89.6
				1141 steel flanges	192	308.5
	O ₄ DT		I-9	1100-O gasket	20	48.7
				1141 steel flanges	192	308.5
	A ₂ DL		I-10	2024 O gasket	40	89.6
				1141 flanges	192	308.5
	S ₆ DL		I-10	1141 steel	192	308.5
General Electric	VI	2-19	I-10	lead gasket	4	12.2
				2024T4 flanges	115	170
	IX	2-19	I-11	lead gasket	4	12.2
				2024T4 flanges	115	170
	XIII	2-19	I-11	1060-O gasket	19	33.4
				2024T flanges	115	170
	XV	2-19	I-11	copper gasket	40	59.2
				2024T flanges	115	170
	X	2-19	I-11	nickel gasket	89	129
				347SS flanges	162-185	232
IITRI	S ₂ DL		I-12	1141	192	308.5
Rocketdyne	R ² C _O	I-17	I-12	440 C	722	1,040
IITRI	62-1		I-13	6061T6	104-110	159
Rocketdyne	D _O	I-17	I-13	440 C	722	1,040
IITRI	62-4		I-13	321	162-185	202
	62-NP2		I-13	nickel plated gasket	285-300	427
				321 flanges	162-185	202
	62-NP6		I-14	nickel plated gasket	285-300	427
				321 flanges	162-185	202
	50-10A		I-14	2024-O gasket	40	89.6
				6061T6 flanges	104-110	159

Fabrication Method	Surface Roughness (μ in., PTV)	Meyer Index	Comments
diamond lapped	7.4	2.00	multidirectional lay
diamond lapped	7.9	2.00	24 μ in. out-of-flatness; multidirectional lay
unidirectionally ground	7.5	2.00	significant long and short period waviness
circular ground	10.5	2.00	significant long and short period circumferential waviness
turned	10.5	2.00	5 μ in. 10.03 concave taper
lapped	---	2.44	multidirectional lay
lapped	11	---	
turned	---	2.19	multidirectional lay
lapped	11	---	
lapped	---	2.44	multidirectional lay
lapped	11	---	
lapped	11	2.22	multidirectional lay
---	---	2.25	
diamond burnished	11.2	---	
---	---	---	
diamond burnished	11.2	---	
turned	---	2.30	
diamond burnished	11.2	---	
turned	---	2.29	
diamond burnished	11.2	---	
turned	---	2.18	
diamond burnished	11.2	---	
lapped	13	2.22	multidirectional lay
diamond burnished	14	2.00	surface pitted, multidirectional lay
turned	19	2.00	
diamond lapped	19	2.00	multidirectional lay
turned	20	2.35	unable to produce a fined turned surface on 321 stainless
turned and plated	20	---	plating thickness 0.0014-0.0021, flatness deviation across surface 190 μ in.
turned	---	2.35	
turned and plated	23	---	plating thickness 0.0026-0.0038 in. flatness deviation across surface 250 in.
turned	---	2.35	
turned	---	2.44	
turned	30	---	

Experiment Identification				Hardness		
Investigator	Code	Reference	Reference Figure	Materials	BHN	Meyer (kpsi)
IITRI	60-10B	I-14	5086H32 gasket		81	139
				6061T6 flanges	104-110	159
	62-10E	I-15	7075T6 gasket		151-155	262
				321 flanges	162-185	202
	62-NP4	I-15	nickel plated gasket		285-300	427
				321 flanges	162-185	202
	62-TC ₁	I-15	Teflon coated gasket		---	3.8
				321 glanges	162-185	202
	62-TC5	I-15	Teflon coated gasket		---	3.8
				321 flanges	162-185	202
IITRI	62-10C	I-16	6061T6 gasket		104-110	159
				321 flanges	162-185	202
	620TC ₆	I-16	Teflon coated gasket		---	3.8
				321 flanges	162-185	202
	62-10D	I-16	2024T351 gasket		115	202
				321 flanges	162-185	202
Rocketdyne	62- ₁	I-18	321SS		162-185	202
				17-4 PH	---	579.5
	O ₁ CT	I-17	1100-O gasket		20	48.7
				1141 flanges	192	308.5
IITRI	C ₆ CT	I-17	1100-O gasket		20	48.7
				1141 flanges	192	308.5
IITRI	O ₉ CT	I-18	1100-O gasket		20	48.7
				1141 flanges	192	308.5
	62-2	I-18	6061T6		104-110	159
				1141	192	308.5
	S ₈ CR	I-19	1100-O gasket		20	48.7
				1141 flanges	192	308.5
	O ₅ BT	I-19	1100-O gasket		20	48.7
				1141 flanges	192	308.5
	O ₆ BT	I-19	1100-O gasket		20	48.7
				1141 flanges	192	308.5
T ₆ AT9	I-19	Teflon gasket		---	3.9	
			1141 flanges	192	308.5	
IITRI	S ₁ BT	I-20	1141 steel		192	308.5
				1141 steel	192	308.5
	S ₁ CR	I-20	1141 steel		192	308.5
				1141 steel	40	109
	C ₆ BT-6	I-21	Cu gasket		192	308.5
				1141 flanges	20	48.7
	O ₂ CT	I-21	1100-O gasket		192	308.5
				1141 flanges	20	48.7
	O ₈ CT	I-21	1100-O gasket		192	308.5
				1141 flanges	20	48.7
O ₉ BT	I-21	1100-O gasket		192	308.5	
			1141 flanges	20	48.7	

Fabrication Method	Surface Roughness (μ in., PTV)	Meyer Index	Comments
turned	---	2.14	
turned	30	---	
turned	---	2.00	
turned	34	---	
turned and plated	35	---	plating thickness 0.009-0.0015 in., flatness deviation across surface 135 μ in.
turned	---	2.35	
spray coated	---	2.80	coating thickness 0.0041-0.0044
turned	35	---	
spray coated	---	2.80	coating thickness 0.001 in.
turned	35	---	
turned	---	2.00	
turned	35	---	
spray coated	---	2.80	coating thickness 0.0017-0.0027 in.
turned	35	---	
turned	---	2.00	
turned	36	2.35	
turned	42	2.35	
turned	43.5	2.00	50 μ in./0.03 in. concave taper
turned	---	2.19	
rotary ground	45	---	
turned	---	2.19	
rotary ground	45	---	
turned	---	2.19	
rotary ground	45	---	
turned	46	2.00	
rotary ground	46	2.22	
turned	---	2.19	
turned	55	---	
turned	---	2.19	
turned	55	---	
---	---	2.80	confined seal
turned	55	---	
turned	56	2.22	
rotary ground	57	2.22	
rotary ground	57	2.22	
turned	---	2.09	confined seal
turned	65	---	
turned	---	2.19	
rotary ground	70	---	
turned	---	2.19	
rotary ground	70	---	
turned	---	2.19	
rotary ground	75	---	

Experiment Identification				Hardness		
Investigator	Code	Reference	Reference Figure	Materials	BHN	Meyer (kpsi)
IITRI	O ₂ BT		I-22	1100-O gasket	20	48.7
				1141 flanges	192	308.5
	S ₅ BT		I-22	1141 steel	192	308.5
	S ₈ BT		I-22	1141 steel	192	308.5
General Electric	7	2-19	I-23	347SS	162-185	232
	VII	2-19	I-23	bb gasket	4	12.2
				2024T4 flanges	115	170
	VIII	2-19	I-23	bb gasket	4	12.2
				2024T4 flanges	115	170
	XVI	2-19	I-23	1060-O al gasket	19	33.4
				347SS flanges	162-185	232
	XIV	2-19	I-24	cu gasket	40	59.2
				347SS flanges	162-185	232
	XII	2-19	I-24	nickel gasket	89	129
IITRI				347SS flanges	162-185	232
	A ₁ AT		I-24	2024-O gasket	40	89.6
				1141 flanges	192	308.5
	O ₈ AT		I-24	1100-O gasket	20	48.7
				1141 flanges	192	308.5
	A ₆ AT		I-25	2024-O gasket	40	89.6
				1141 flanges	192	308.5
	O ₂ AT		I-25	1100-O gasket	20	48.7
				1141 flanges	192	308.5
	O ₉ AT		I-25	1100-O gasket	20.7	48.7
IITRI				1141 flanges	192	308.5
	S ₁ AT		I-26	1141 steel	192	308.5
	S ₈ AT		I-26	1141 steel	192	308.5
	S ₅ AT		I-26	1141 steel	192	308.5
General Electric	8	I-20	I-27	1060-O al	19	33.4
	XX	I-19	I-27	1060-O gasket	19	33.4
				2024T4 flanges	115	
	XXI	I-19	I-27	cu gasket	40	59.2
				2024T4 flanges	115	
	XXII	I-19	I-27	nickel gasket	89	129
IITRI				2024T4 flanges	115	177.8
	A ₆ BT-1		I-28	2024-O gasket	40	89.6
				1141 flanges	192	308.5
	A ₆ BT-3		I-28	2024-O gasket	40	89.6
				1141 flanges	192	308.5
	A ₆ BT-5		I-29	2024-O gasket	40	89.6
				1141 flanges	192	308.5

Fabrication Method	Surface Roughness (μ in., PTV)	Meyer Index	Comments
turned	---	2.19	
turned	88	---	
turned	93	2.22	
turned	93	2.22	
radially ground	120	2.35	
unfinished	---	2.25	
radially ground	155	---	
unfinished	---	2.25	
radially ground	155	---	
turned	---	2.30	
radially ground	155	---	
turned	---	2.29	
radially ground	155	---	
turned	---	2.18	
radially ground	155	---	
turned	---	2.44	
turned	156	---	
turned	---	2.19	
turned	156	---	
turned	---	2.44	
turned	163	---	
turned	---	2.19	
turned	163	---	
turned	---	2.19	
turned	163	---	
turned	175	2.22	
turned	175	2.22	
turned	188	2.22	
turned	225	2.30	
turned	---	2.30	
turned	280	---	
turned	---	2.29	
turned	280	---	
turned	---	2.18	
turned	280	---	
turned	---	2.44	confined seal
turned	300	---	
turned	---	2.44	confined seal
turned	350	---	
turned	---	2.44	confined seal
turned	450	---	

Experiment Identification				Hardness		
Investi- gator	Code	Refer- ence	Refer- ence Figure	Materials	BHN	Meyer (kpsi)
IITRI	T ₆ AT-5	I-29		Teflon gasket	---	3.9
				1141 flanges	192	308.5
	L ₆ AT-3	I-29		bb gasket	4	4.3
				1141 flanges	192	308.5
	L ₆ AT-4	I-29		bb gasket	4	4.3
				1141 flanges	192	308.5
	C ₆ BT-3	I-30		cu gasket	40	109
				1141 flanges	192	308.5
General Electric	XVII	I-19	I-30	1060 gasket	19	33.4
				2024T4 flanges	115	170
	XIX	I-19	I-30	nickel gasket	89	129
				347SS flanges	162-185	232
	XVIII	I-19	I-30	cu gasket	40	59.2
				347SS flanges	162-185	232

Fabrication Method	Surface Roughness (μ in., PTV)	Meyer Index	Comments
unfinished	---	2.80	confined seal
turned	450	---	
unfinished	---	2.33	confined seal
turned	450	---	
unfinished	---	2.33	confined seal
turned	450	---	
turned	---	2.09	confined seal
turned	600	---	
turned	---	2.30	
turned	840	---	
turned	---	2.18	
turned	840	---	
	---	2.29	
turned	840	---	

The final step was a subsequent averaging process of the data shown on figures 2-42, 2-43 and 2-44. The averaging was accomplished by curve smoothing techniques. In addition to the omission of data not following the over-all trend, the curve-smoothing process develops a series of easily interpreted curves primarily for use as design criteria. These curves, the culmination of all previous efforts, are shown on figures 2-45, 2-46 and 2-47.

2.7 Observations

The correlations of the conductance parameter with the modified stress ratio are difficult to assess solely on a scientific basis. From a practical standpoint, however, the correlations are an advance in the state-of-the-art of sealing. This observation is based on the following views:

- It is the first attempt on a large scale to interrelate all of the parameters.
- The correlations provide an insight into the relative effects of each parameter on the others leading to conclusions concerning the optimization of seals and sealing interfaces. Probably most important, they show the limits of sealing and the parameters that are most influential, thereby pointing out areas of further investigation.
- Finally, the correlations are reduced into the form of design charts, figures 2-45, 2-46 and 2-47, which relate the parameters on the basis of easily measured properties. As will be demonstrated in subsequent sections, the charts can be readily employed by systems or seal designers.

It must be recognized that the correlations of parameters may not be the ultimate from the standpoint of theory and/or procedures used in the development process. The important point is that it does provide a practical design tool which the designer can employ in predicting leakage with some degree of reliability. This is important when one considers that no information of this type was previously available.

The theoretical basis for the correlations is vulnerable. For example, a conductance parameter was derived from the laminar or molecular flow equations for flow between two plates where the parameter appears as the cube of a hypothetical clearance and is obtained from experimental leakage measurements. Certain relationships suggesting this flow were observed (Ref. 2-1), for example, leakage varying inversely with the viscosity,

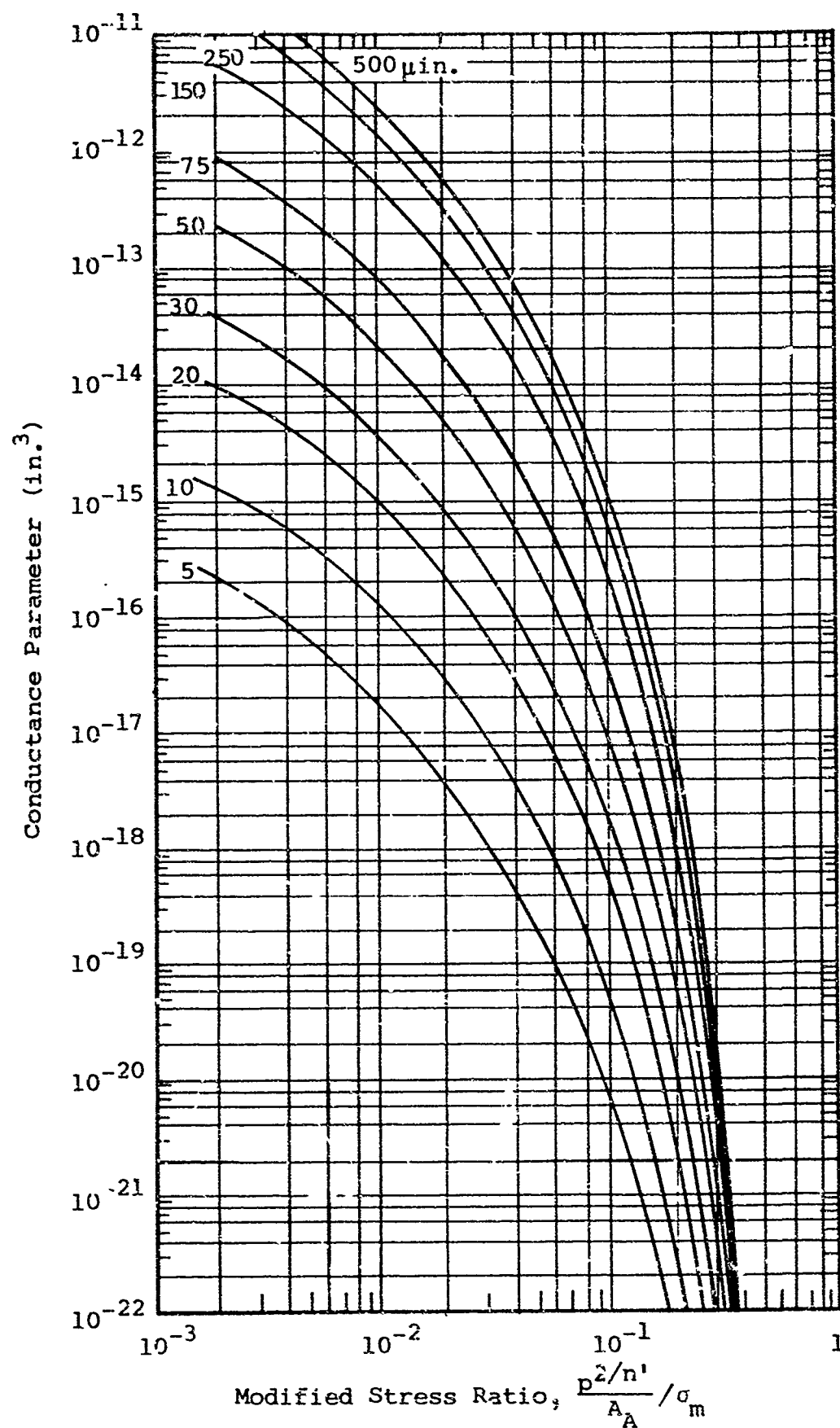


Figure 2-45 Design criteria for turned surfaces. Surface roughness is shown as a parameter.

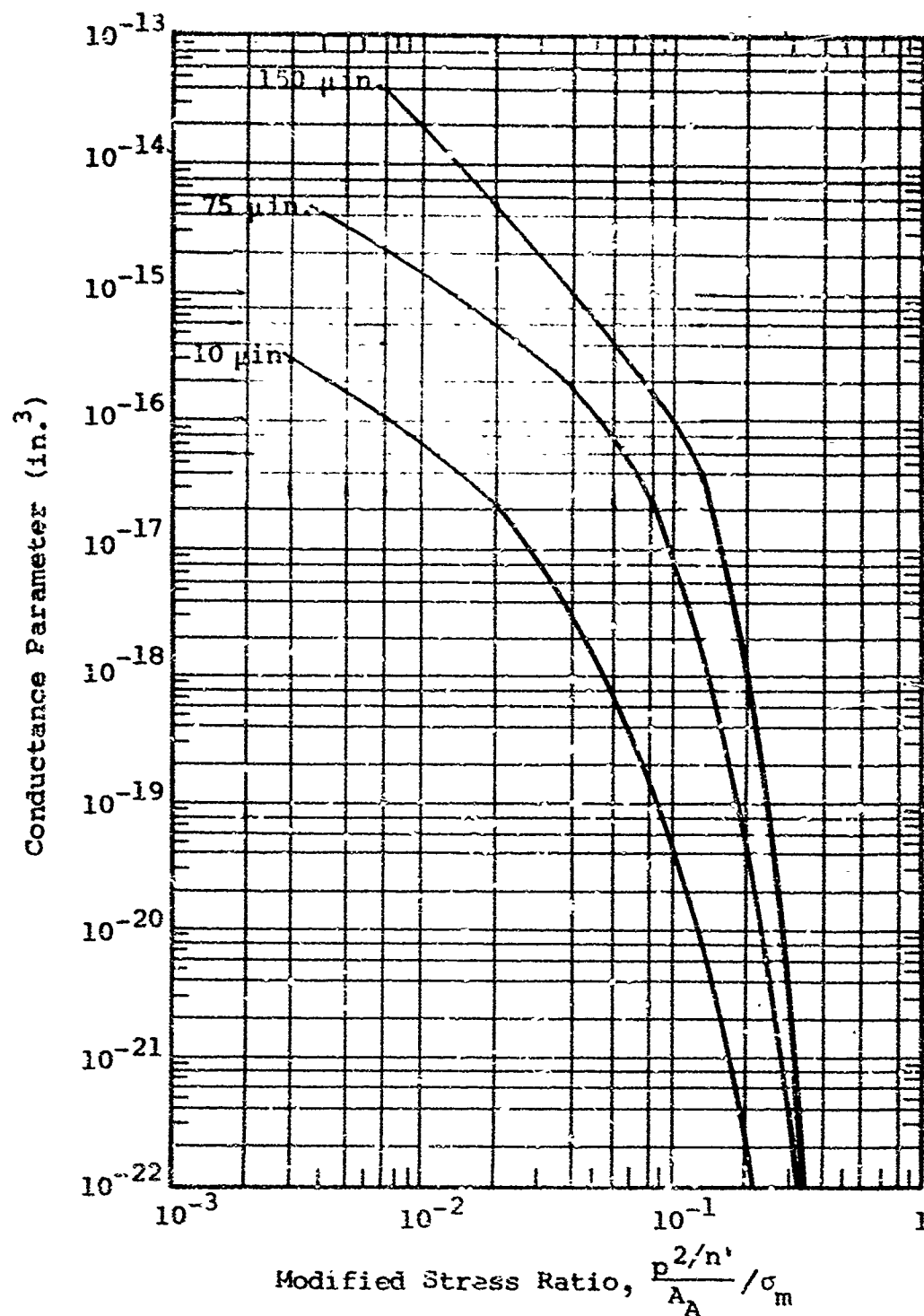


Figure 2-46 Design criteria for ground surfaces. Surface roughness is shown as a parameter.

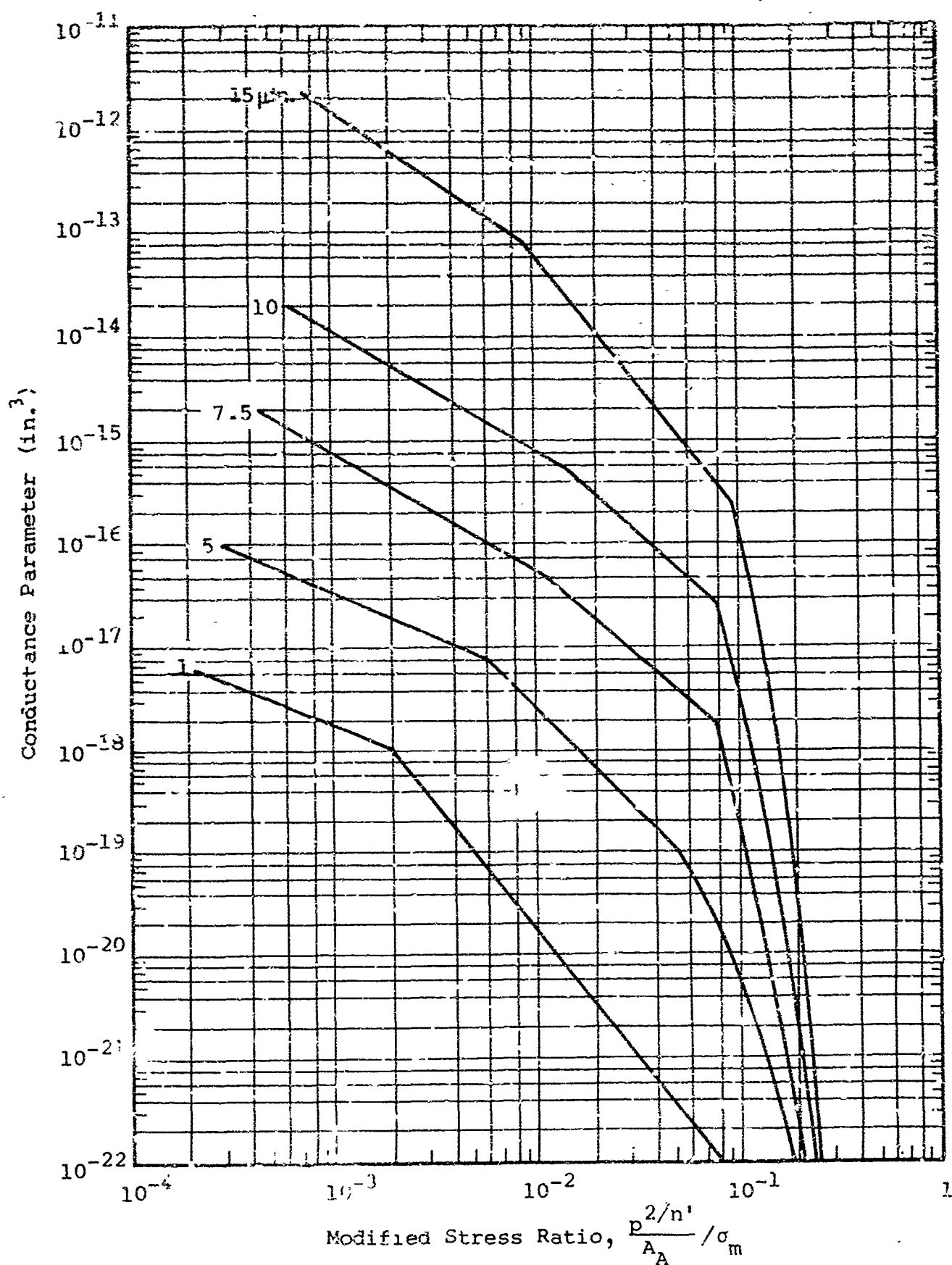


Figure 2-47 Design criteria for lapped and polished surfaces. Surface roughness is shown as a parameter.

proportional to the pressure, and somewhat functionally with the length and width of the over-all interface. There is, however, no certainty that leakage varies with the cube of a calculated number. It could vary with the fourth power of a number if it were assumed that the leakage path is really composed of small circular channels. Similarly, other relationships could exist in view of the fact that little is known about the structure of the microscopic interface.

The modified stress ratio was also developed on marginal assumptions, particularly, the assumption that microscopic and macroscopic deformation are identical and can be described by volume properties. Another assumption not having a firm theoretical basis is the effect of strain hardening and its relationship to the apparent contact area, load, and size and distribution of asperities.

From the preceding negative arguments it might be concluded that a more scientific approach should have been chosen. This may be a logical observation but such a method was not forthcoming. Too many of the parameters are not sufficiently defined, i.e., surface topography, microscopic deformation, and the inter-connection of void spaces.

At this point, overlooking the theoretical implications and settling for practical merits is justifiable. The question which we can ask is "Do the correlations offer consistency in describing the interaction of parameters?" If this question can be answered 'yes', then the correlations have practical merit even if the foundations are theoretically vulnerable. The affirmative arguments which can be offered are:

- The conductance and modified stress ratio parameters correlate for materials possessing like surface topography with widely varying properties from plastics to hard metallics and loads from virtually nothing to loads producing complete plasticity.
- The conductance and modified stress ratio parameters show a consistent trend in terms of the effect of initial surface finish of the mating surfaces. This trend is exemplified by substantial sensitivity on leakage at light loads and low sensitivity at very high loads.

In fairness to the preceding arguments, it may be observed from the data presented in Appendix I that all of the correlations were not close and, in some cases, wide divergence occurred. The experimental results may be classed according to a rough interpretation of the deviation as follows:

Surface Roughness Group (μ in.)	Method of Fabrication	Degree of Correlation *
0-2	Lapped, Polish	Poor
2-5		Poor
5-10		Good
10-20	Turned	Poor
0-10		Good
11-20		Good
20-30		Good
30-50		Good
50-75		Fair
75-100		Good
100-200	Ground, Burnished	Good
200-400		Good
0-10		Good
11-50		Fair
50-100		Fair
100-200		Good

The preceding interpretation of data correlations is intended to show an over-all interpretive view of the results. To give a feel for the reliability of the results, a quantitative evaluation can be made. This is accomplished by plotting the mean values of conductance and the extremes in deviation for an arbitrary modified stress ratio. The experimental data, shown on figures I-31 through I-47, are replotted on figures 2-48, 2-49 and 2-50 for a modified stress ratio of 10-2. Each figure shows a fabrication group with roughness and conductance as variables. An interpretation of these results follow.

2.7.1 Lapped and Polished Surfaces

The deviation of rougher surfaces ($> 5\mu$ in. PTV) is approximately two orders of magnitude while the finer finishes vary three orders of magnitude.

The lack of closer correlation is attributed to the influence of elastic deformation principally affected by the waviness and substrate geometry of the materials. It must be noted, however, that the experimental data were correlated by grouping surface finishes. If an average line through the mean value points, shown on figure 2-48 is drawn, the average line shows that a range of conductance variation compatible with the variation of the surface finish group. For example, experimental data were grouped for finishes between 5 and 10μ in. as identified by points A and B on figure 2-48. The average line comes close to minimum point A and maximum point B. This observation shows

* It is difficult to assign values to the degree of correlation, hence, an interpretation is necessary. It is suggested that the reader review the results and form his own interpretation.

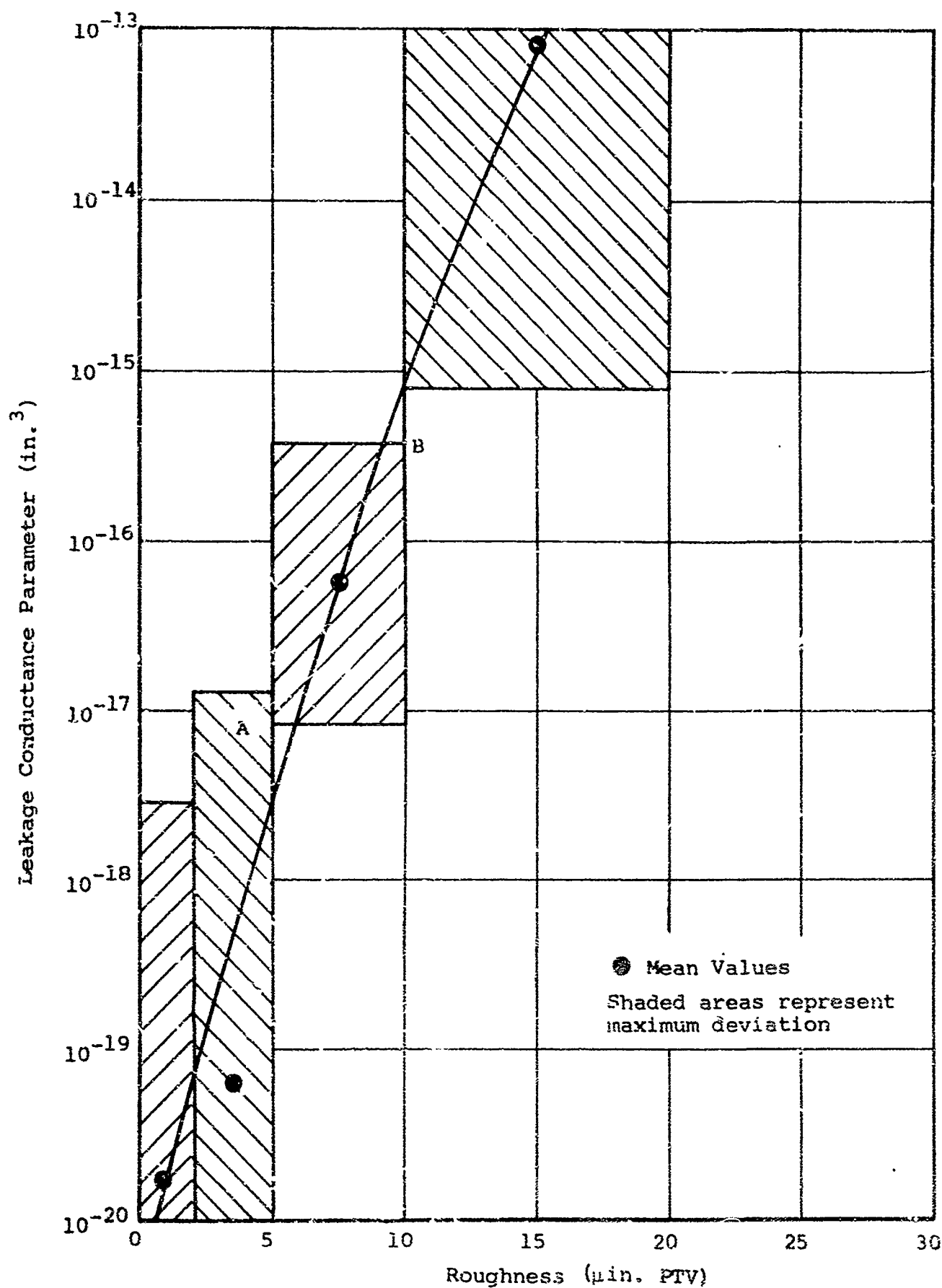


Figure 2-48 Comparison of ranges of variation in data for lapped and polished surface groups at a modified stress ratio of 10⁻²

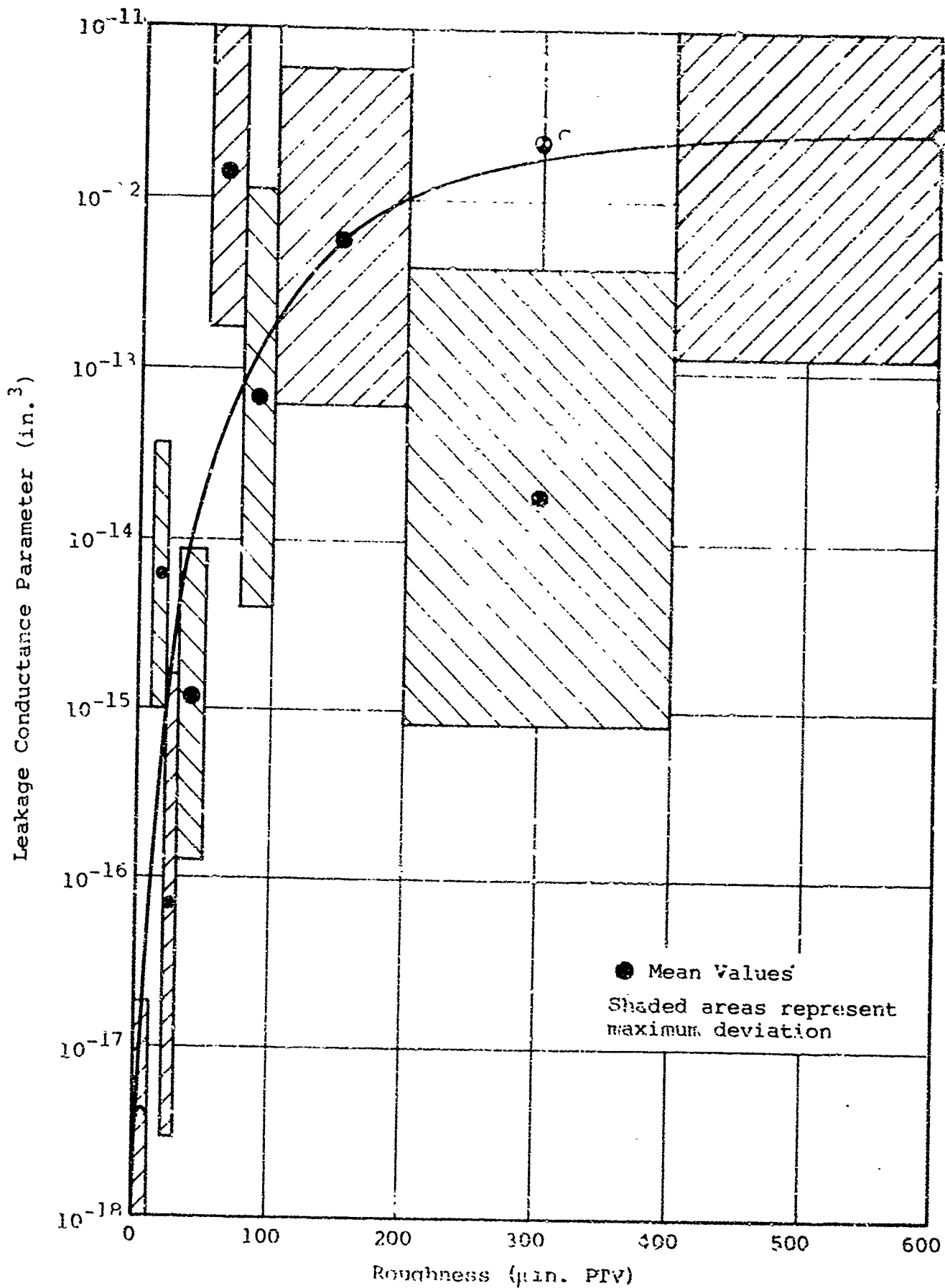


Figure 2-49 Comparison of ranges of variation in data for turned surface groups at a modified stress ratio of 10⁻²

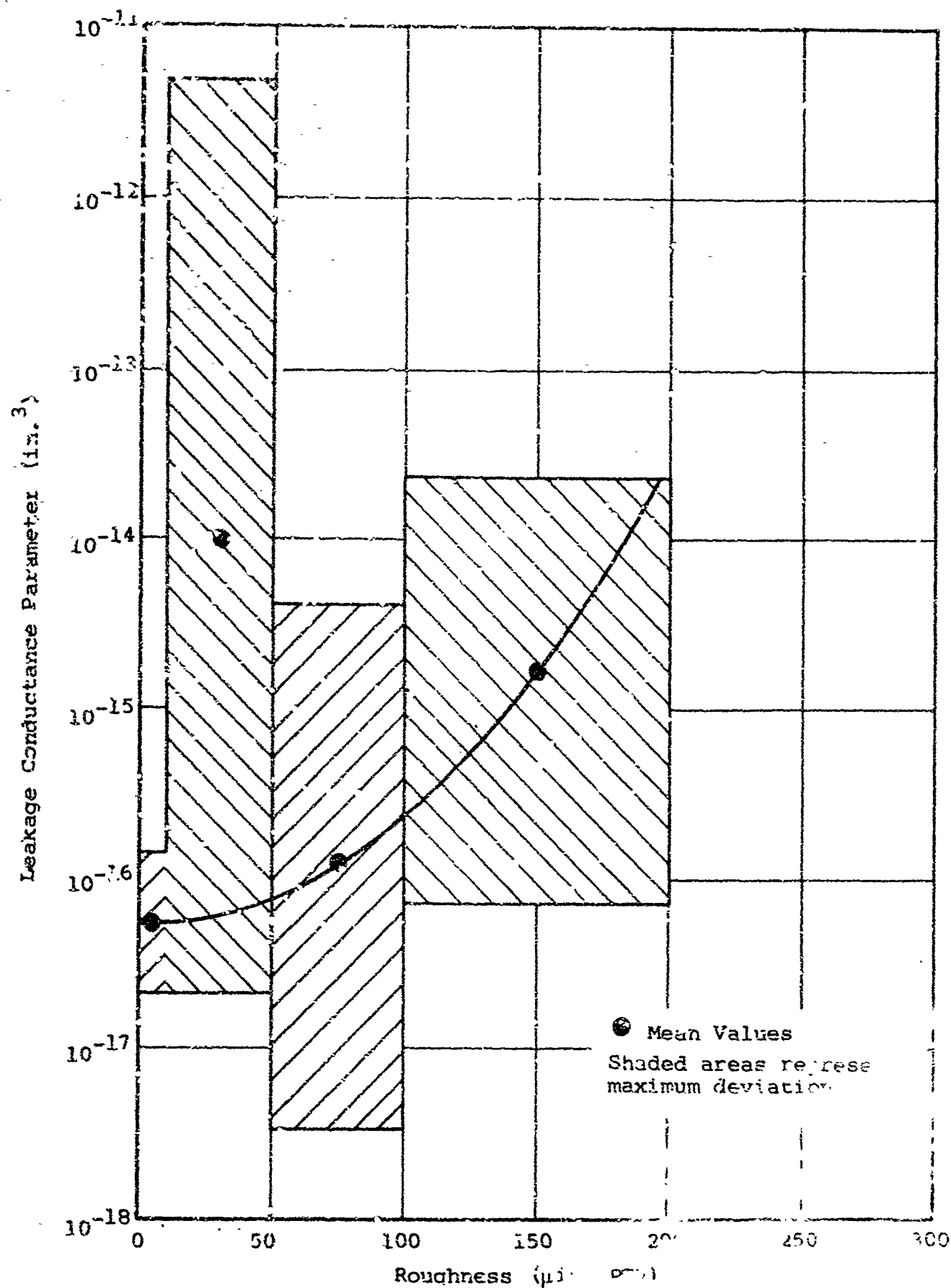


Figure 2-50 Comparison of ranges of variation in data for ground surface and σ_r at a modified stress ratio of 10-2

that the order of magnitude deviation is really not objectionable and also shows the relative influence of initial surface finish. A closer correlation could possibly be achieved if the surface finish groups were smaller. Considering waviness effects and the fact that the present correlations are already based on a large number of experiments, it is felt that no significant improvement can be attained.

2.7.2 Turned Surfaces

The influence of waviness variations of turned surfaces is considered the major cause of variations in conductance, as shown on figure 2-49. A review of figure 2-41 shows that waviness of turned surfaces varies widely with respect to surface finish. An average curve through the mean values does, however, show the sensitivity of surface finish on conductance and explains the reason for the deviation. The total deviation from the average is approximately two orders of magnitude.

One group of turned surfaces did not correlate with the other data. This was the 200 to 400 μ in. PTV group shown on figure 2-49. The data comprising this group were obtained from IITRI experiments on confined gaskets (Ref. 2-1). In these experiments, aluminum gasket material was prevented from flowing laterally by semi-rigid walls. While the calculated modified stress ratio for these data included strain-hardening effects, it is felt that strain hardening should not have been considered in view of the lateral restraints. This would imply that the influence of strain hardening is related to the substrate deformation and not the microscopic surface deformation. A recalculation of this data, neglecting strain hardening, yields a mean value identified as point C on figure 2-49. Thus, it is concluded that strain hardening is solely a property of the substrate deformation.

2.7.3 Ground Surfaces

The deviation of the conductance parameter for ground surfaces, shown on figure 2-50 was substantially greater than the preceding surfaces. Again, the variation is attributed to waviness. It shows up most significantly in the range of 10 to 50 μ in. PTV. Surfaces of lower roughness usually are produced by precision tooling and, consequently, the roughness and waviness are approximately the same. Surfaces with roughness greater than 50 μ in. also have a waviness close to the roughness. In both of these cases, waviness is expected to have a lesser effect. In the range of 10 to 50 μ in., however, the ratio of waviness to roughness can be greater than 10 or as low as one, depending upon the specific method of fabrication. Since all similar finishes were grouped together without distinction, it may be expected that the variation would be significant. This observation does point out the importance of waviness and the need for improvements in surface evaluation.

2.7.4 General Surface Effects

The design charts, shown on figures 2-45, 2-46, and 2-47, can be combined in almost nondimensionalized form by introducing the parameter

$$\frac{(h^3)}{(PTV)^3} = \frac{\text{conductance parameter}}{\text{average initial surface roughness cubed}}$$

The resulting chart is shown on figure 2-51. The relationship departs from a nondimensionalized form because of the Meyer index in the modified stress ratio.

It can be observed from figure 2-51 that turned and polished surfaces possess very similar deformation characteristics. The ratio of $(h^3)/(PTV)^3$ is greater than unity at low stress ratios. This is to be expected from surfaces where the waviness is greater than the roughness. When the waviness variation is close to the roughness, as in the case of ground surfaces, it is expected that closer conformability of the surface is possible at low stress ratios. This is borne out on figure 2-51 by the ground surfaces which have a lower $(h^3)/(PTV)^3$ ratio at low stress ratios ($<10^{-1}$).

The significance of figure 2-51 becomes clear when we consider that (h^3) is proportional to the leakage rate. Minimum leakage corresponds to a low value of $(h^3)/(PTV)^3$ and, consequently, the smoother a surface is initially, the lower the leakage rate is under any load condition. It should be noted that figure 2-51 does not imply that any surface finish process can produce low leakage nor does the ground surface necessarily offer optimum characteristics. Each fabrication method has self-imposed limitations on minimum roughness. This can be described as follows by assuming an interface stress ratio of 10^{-2} and comparing the relative magnitude of conductance, hence, leakage.

<u>Process</u>	<u>Minimum Roughness (μin.PTV)</u>	<u>Ratio $\frac{(h^3)}{(PTV)^3}$</u>	<u>Conductance (h^3) at a Stress Ratio of 10^{-2}</u>
Turned	10	1.6×10^{-1}	$1.6 (10^{-16})$
Ground	5	1×10^{-2}	$1.3 (10^{-18})$
Polished	0.5	1.6×10^{-1}	$2 (10^{-20})$

It can be seen that a four-order-of-magnitude variation in leakage can occur between the turned and polished surfaces.

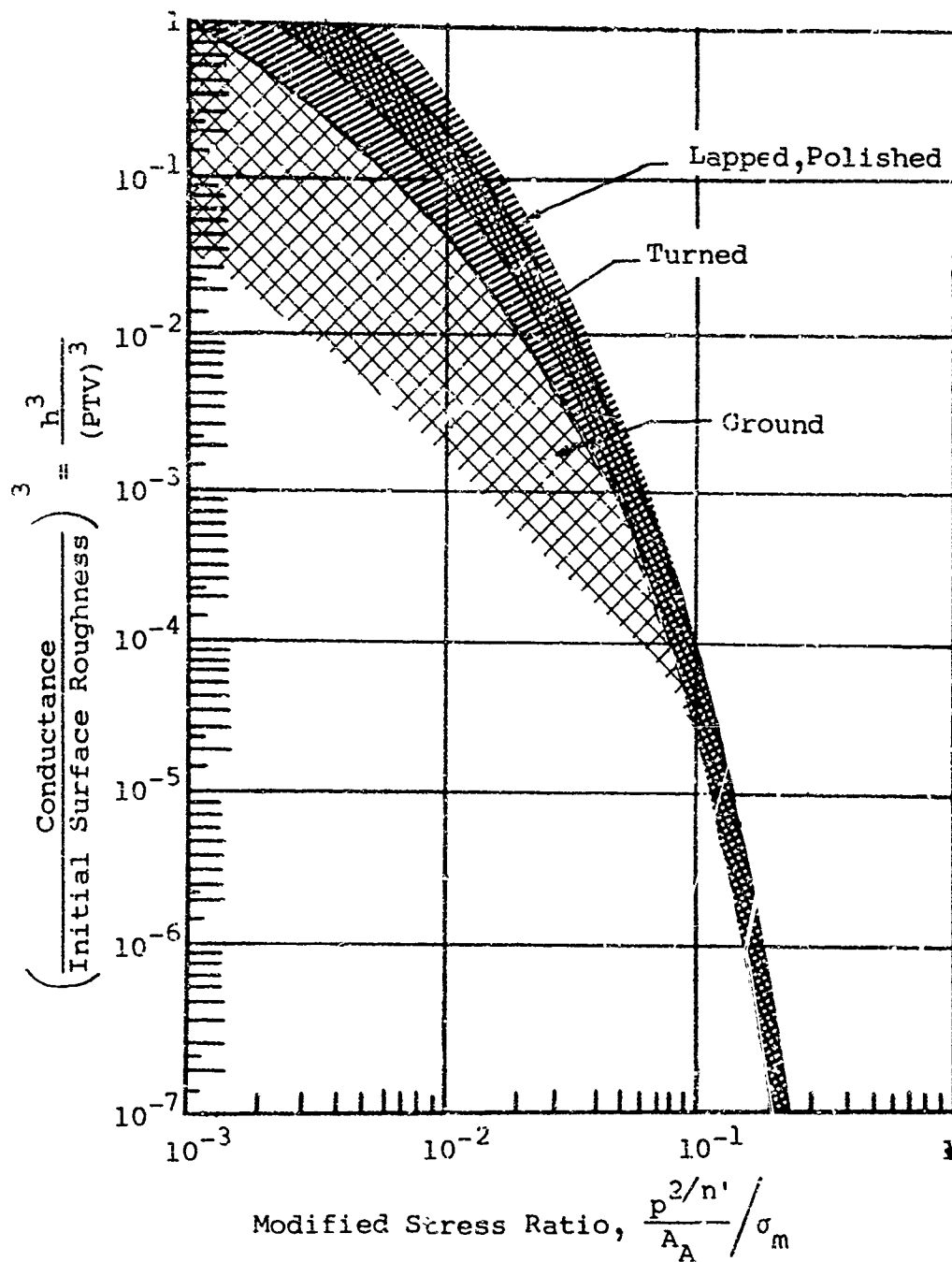


Figure 2-51 Nondimensionalized relationship between parameters

Other observations that can be made are:

- The conductances of fine turned, lapped, and ground surfaces in the range of 5 to $10\mu\text{in.}$ are very similar. Therefore, no preference in finishing process can be stated except with respect to cost of fabrication. This, in turn, depends upon the geometry of the seal parts.
- Rotary grinding and diamond burnishing are preferable fabrication processes for rougher surfaces ($>10\mu\text{in. PTV}$), compared with turning.
- Preferential orientation of surface lay is preferable for surface roughness greater than $10\mu\text{in.}$ Roughnesses of less than $10\mu\text{in.}$ show no significant conductance dependence upon lay.
- The deformation and the resulting leakage path as characterized by the conductance parameter are dependent upon the material forming the immediate interface. The performance of platings and other coatings is expected to be the same as if the surface and substrate were composed solely of the plating or coating material. This statement must be interpreted on the basis of plating thicknesses not less than 0.0005 in. No information was obtained on platings or coatings less than 0.0005 in. Since platings and coatings are usually soft materials covering hard materials, it may be expected that very thin coatings would approach the performance of the harder material.
- The empirical correlations were, for the most part, derived from experimental data of similar finish surfaces pressed together. When different finishes were involved, the finish of the harder surface had the predominant effect.

The preceding observations are by no means complete. Other observations are included in the following sub-section, which summarizes the criteria for sealing interfaces. Before proceeding, however, a final comment regarding the method of correlation must be made. The development of the design charts was based on an interpretation of average values. An excellent possibility exists that the formulation could be based on sound statistical methods. For this reason, the detailed results are presented in Appendix I so that data are available for correlation improvements. In any event, the correlations presented thus far indicate an approximate deviation of one order of magnitude from the mean.

2.8 Supplementary Metallic and Plastic Interface Criteria

The previously stated criteria are reviewed and supplementary information for use in applying these criteria to the analysis of seal performance is presented in this subsection. The actual application of the criteria is presented in subsequent sections. Each of the parameters influencing the interface is considered independently, when possible.

2.8.1 Load, Deformation, and Material Properties

Four modes of deformation can be utilized in achieving minimum leakage. Preferably, the mode requiring the least load can be considered as an optimum. In order of increasing loads for a given interface, the surface requirements are:

Class I No surface disturbances on either mating surface observable with common microscopes (1000X).

Class II Few random disturbances not exceeding $2\mu\text{in.}$, PTV.

Class III Preferential orientation of one surface so that a uniform interface is formed to contain a fluid. The interface is deformed by full plastic deformation.

Class IV Rough surfaces having many variations and greater than $2\mu\text{in.}$ PTV.

Each of the preceding classes is dependent upon the topography, and, as such, is considered under that topic. The materials for Class I and II surfaces should be very hard, making them less susceptible to handling damage. An alternative arrangement is to utilize a very smooth surface mated against a soft surface. This arrangement is preferable if contaminants are present.

The materials for Class III and IV surfaces should be composed of a soft material mated against a hard surface. Thus, plastics are preferable over metals and soft metals preferable over hard metals. In Section 12, it will be shown that rubber is preferable over either plastics or metallics. These requirements are stated for minimum leakage performance. If higher leakage rates can be tolerated, the choice of materials and hardness can be varied extensively.

2.8.2 Surface Topography

The lowest leakage rates at lowest loads can be obtained with metallic seal surfaces that approach the Class I and II category. The requirements for such a seal are that the mating surfaces be

extremely smooth and extremely flat so that the deformation which occurs can be described as elastic. Next in line of preference is the Class III interface. A wedge having a 60-deg included-angle profile mated against a flat surface appears to offer the greatest efficiency in sealing from a standpoint of lowest load and minimum leakage. The Class III and IV interfaces are also sensitive to surface finish. Therefore, in all cases, surface finish and waviness must be a minimum. Class IV surfaces are recommended only in cases where higher leakage rates and lower loads are tolerable.

If possible, both surfaces should have the same surface finish. In the event this is not feasible, the harder surface should possess the finer finish.

2.8.3 Interface Geometry

The mating of surfaces together can be classed in two basic categories. The first consists of flat mating surfaces. An application of a load to these surfaces produces some elastic substrate deformation and localized plastic deformation of asperities. As the load is increased, the deformation becomes predominantly plastic, ultimately resulting in plastic deformation of the entire substrate. The second category contains various irregular surfaces, such as wedges. When pressed together even under the lightest load, plastic deformation of the substrate occurs.

The conductance parameter for flat mating surfaces can be obtained from the design charts, figures 2-45, 2-46 or 2-47, when the load and material properties are known. Leakage can then be calculated using the apparent contact geometry and the appropriate flow equation.

Leakage calculations for the second category of surfaces are not too obvious. First, the apparent contact geometry may not be known. An approximation for the apparent contact area can be obtained from the relation

$$A_A = \frac{P}{\sigma_m}$$

where P is the applied load.

The second problem is the determination of the modified stress ratio. The stress ratio should be constant with load and varying between 0.15 and 0.4, depending upon the surface finish. A review of figures 2-45, 2-46, and 2-47, shows the lowest measured values of conductance to be $(h^3) = 10^{-22}$ cu in. Since a distinction cannot be made for values lower than this, it can only be assumed at this time that 10^{-22} cu in. is a conductance for surfaces having

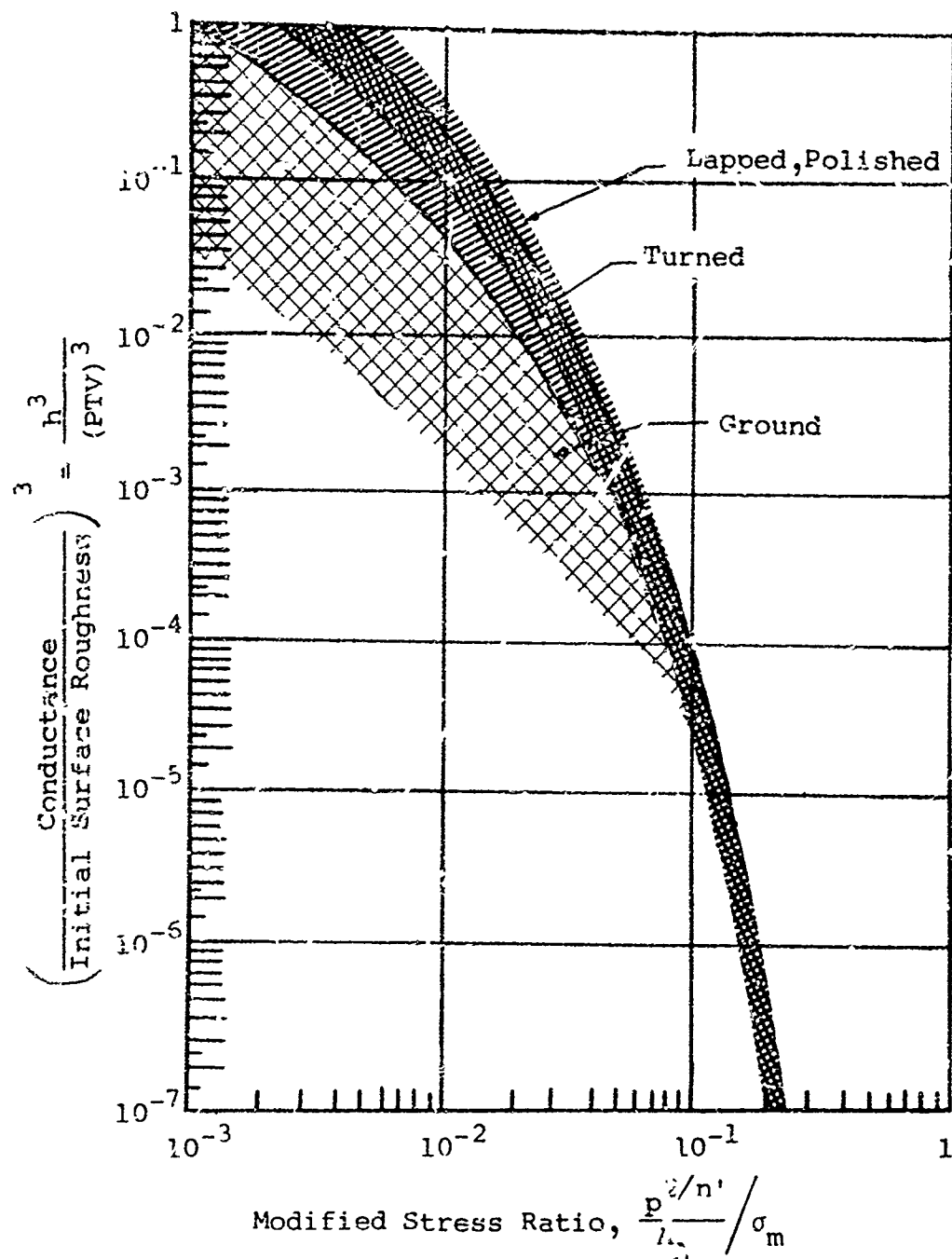


Figure 2-51 Nondimensionalized relationship between parameters

Other observations that can be made are:

- The conductances of fine turned, lapped, and ground surfaces in the range of 5 to $10\mu\text{in.}$ are very similar. Therefore, no preference in finishing process can be stated except with respect to cost of fabrication. This, in turn, depends upon the geometry of the seal parts.
- Rotary grinding and diamond burnishing are preferable fabrication processes for rougher surfaces ($>10\mu\text{in.PTV}$), compared with turning.
- Preferential orientation of surface lay is preferable for surface roughness greater than $10\mu\text{in.}$ Roughnesses of less than $10\mu\text{in.}$ show no significant conductance dependence upon lay.
- The deformation and the resulting leakage path as characterized by the conductance parameter are dependent upon the material forming the immediate interface. The performance of platings and other coatings is expected to be the same as if the surface and substrate were composed solely of the plating or coating material. This statement must be interpreted on the basis of plating thicknesses not less than 0.0005 in. No information was obtained on platings or coatings less than 0.0005 in. Since platings and coatings are usually soft materials covering hard materials, it may be expected that very thin coatings would approach the performance of the harder material.
- The empirical correlations were, for the most part, derived from experimental data of similar finish surfaces pressed together. When different finishes were involved, the finish of the harder surface had the predominant effect.

The preceding observations are by no means complete. Other observations are included in the following sub-section, which summarizes the criteria for sealing interfaces. Before proceeding, however, a final comment regarding the method of correlation must be made. The development of the design charts was based on an interpretation of average values. An excellent possibility exists that the formulation could be based on sound statistical methods. For this reason, the detailed results are presented in Appendix I so that data are available for correlation improvements. In any event, the correlations presented thus far indicate an approximate deviation of one order of magnitude from the mean.

2.8 Supplementary Metallic and Plastic Interface Criteria

The previously stated criteria are reviewed and supplementary information for use in applying these criteria to the analysis of seal performance is presented in this subsection. The actual application of the criteria is presented in subsequent sections. Each of the parameters influencing the interface is considered independently, when possible.

2.8.1 Load, Deformation, and Material Properties

Four modes of deformation can be utilized in achieving minimum leakage. Preferably, the mode requiring the least load can be considered as an optimum. In order of increasing loads for a given interface, the surface requirements are:

Class I No surface disturbances on either mating surface observable with common microscopes (1000X).

Class II Few random disturbances not exceeding $2\mu\text{in.}$ PTV.

Class III Preferential orientation of one surface so that a uniform interface is formed to contain a fluid. The interface is deformed by full plastic deformation.

Class IV Rough surfaces having many variations and greater than $2\mu\text{in.}$ PTV.

Each of the preceding classes is dependent upon the topography, and, as such, is considered under that topic. The materials for Class I and II surfaces should be very hard, making them less susceptible to handling damage. An alternative arrangement is to utilize a very smooth surface mated against a soft surface. This arrangement is preferable if contaminants are present.

The materials for Class III and IV surfaces should be composed of a soft material mated against a hard surface. Thus, plastics are preferable over metals and soft metals preferable over hard metals. In Section 12, it will be shown that rubber is preferable over either plastics or metallics. These requirements are stated for minimum leakage performance. If higher leakage rates can be tolerated, the choice of materials and hardness can be varied extensively.

2.8.2 Surface Topography

The lowest leakage rates at lowest loads can be obtained with metallic seal surfaces that approach the Class I and II category. The requirements for such a seal are that the mating surfaces be

extremely smooth and extremely flat so that the deformation which occurs can be described as elastic. Next in line of preference is the Class III interface. A wedge having a 60-deg included-angle profile mated against a flat surface appears to offer the greatest efficiency in sealing from a standpoint of lowest load and minimum leakage. The Class III and IV interfaces are also sensitive to surface finish. Therefore, in all cases, surface finish and waviness must be a minimum. Class IV surfaces are recommended only in cases where higher leakage rates and lower loads are tolerable.

If possible, both surfaces should have the same surface finish. In the event this is not feasible, the harder surface should possess the finer finish.

2.8.3 Interface Geometry

The mating of surfaces together can be classed in two basic categories. The first consists of flat mating surfaces. An application of a load to these surfaces produces some elastic substrate deformation and localized plastic deformation of asperities. As the load is increased, the deformation becomes predominantly plastic, ultimately resulting in plastic deformation of the entire substrate. The second category contains various irregular surfaces, such as wedges. When pressed together even under the lightest load, plastic deformation of the substrate occurs.

The conductance parameter for flat mating surfaces can be obtained from the design charts, figures 2-45, 2-46 or 2-47, when the load and material properties are known. Leakage can then be calculated using the apparent contact geometry and the appropriate flow equation.

Leakage calculations for the second category of surfaces are not too obvious. First, the apparent contact geometry may not be known. An approximation for the apparent contact area can be obtained from the relation

$$A_A = \frac{P}{\sigma_m}$$

where P is the applied load.

The second problem is the determination of the modified stress ratio. The stress ratio should be constant with load and varying between 0.15 and 0.4, depending upon the surface finish. A review of figures 2-45, 2-46, and 2-47 shows the lowest measured values of conductance to be $(h^3) = 10^{-22}$ cu in. Since a distinction cannot be made for values lower than this, it can only be assumed at this time that 10^{-22} cu in. is a conductance for surfaces having

full plasticity conditions. Leakage rates for an interface can therefore be calculated using the approximate contact area.

In some cases, it may be difficult to decide the geometry of an interface. For example, a seal having an initially flat surface as shown in figure 2-52 may assume a nonparallel orientation when installed in a housing. This case can be analyzed in two ways. First, it may be assumed that the surface remains flat. Performance can, therefore, be determined using the flat surface procedures. The second approach is to assume that a wedge exists with full plasticity at the point of contact. The area of contact, conductance, and leakage can then be calculated for the case of full plasticity. It is suggested that when the mating geometry is in doubt, both calculations be made and the higher value of leakage assumed to be representative of the seal. It should be noted that, in the first case, the contact area is large while a very small contact area is typical of the second case. Also, the conductance is large in the first case and very small in the second case. Since leakage varies with the ratio of conductance to contact geometry (contact width), the predicted leakage should not be significantly different in either case.

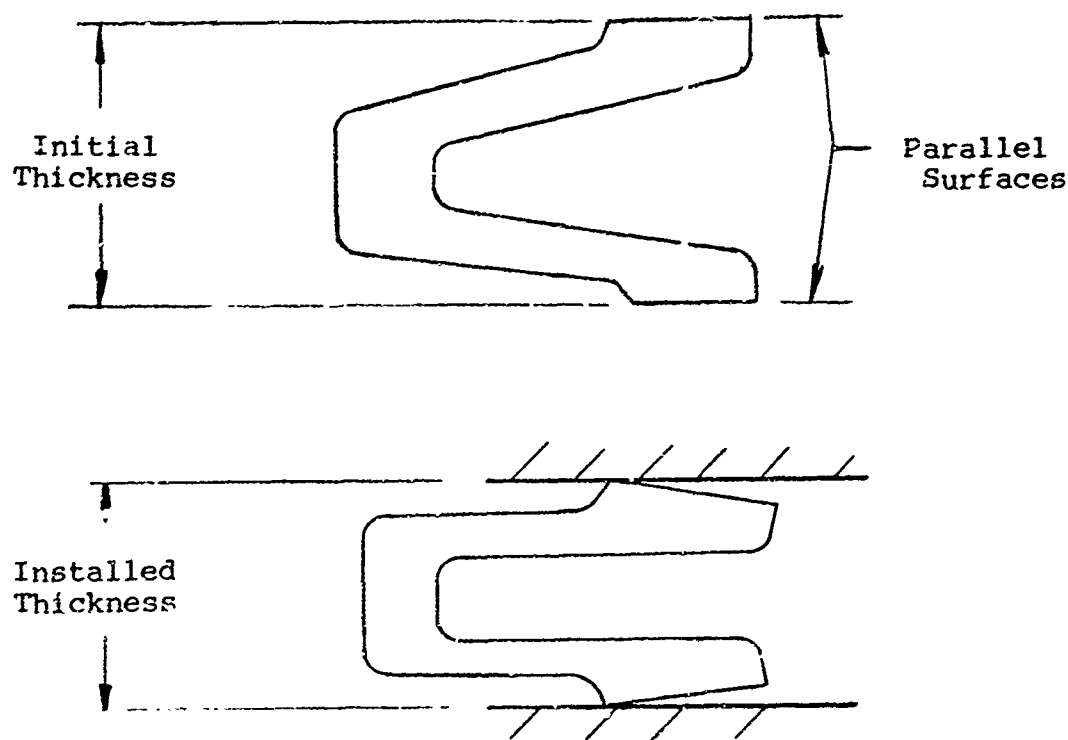


Figure 2-52 Effects of installation on the orientation of seal interface

In addition to the preceding analytical procedures, another requirement is imposed with respect to the minimum width of contact. From the limited number of experiments conducted, minimum leakage (10^{-5} cc/sec of a gas) can be achieved if the interface width normal to the direction of leakage flow is greater than 0.012 in. This deduction is made by the superposition of data shown on figures 2-7, 2-8, 2-13, and 2-14.

2.8.4 Calculation of Leakage

Once the conductance parameter is known, leakage can be calculated by applying the fluid properties and over-all interface geometry in the equations for laminar or molecular flow in uniform channels. These equations are described in Volume II of Reference 2-1. This can be accomplished without difficulty for liquids or gases. It must be noted that the conductance parameter was developed for the case of gas transition flow. Experiments, however, have shown that the conductance is independent of the state of the fluid (Ref. 2-1). Caution must be exercised when calculating liquid leakage. Surface tension effects may predominate the flow process when the conductance is small. An estimate of the effects of surface tension can be obtained by assuming surface tension in a hypothetical channel of a dimension equal to the cube root of the conductance. Unfortunately, the influence of surface tension is unknown because the variables of wetting angle, surface contamination, and leak path geometry cannot be precisely defined.

2.8.5 Hysteresis

The hysteresis phenomenon is described as the relative effects of permanent interface deformation compared with the elastic deformation. This phenomenon (Volume I, Ref. 2-1) can be described as follows: Two surfaces pressed together under load produce a given leakage rate. When the load is relaxed, little change in leakage occurs until the load is sufficiently relaxed, whereupon a significant increase in leakage occurs. A further increase in load produces a lower leakage rate and if the load is again relaxed, the same phenomenon occurs. The magnitude of load relaxation permissible depends upon the maximum applied stress. Typical results from Reference 2-1 are shown on figure 2-53.

The exact nature of the hysteresis phenomenon is tied in very closely with the elastic deformation of the interface substructure. This would include the seal structure and other seal-related parts. Hence, it is impossible to define rigid guidelines for its effect. Another problem is to define the limits of acceptance in terms of increase in leakage. For example, in Reference 2-1, it was found that the stress on flat mating surfaces could be relaxed as much as 50 per cent without a 100 per cent increase in leakage. A corresponding one-order-of-magnitude change in leakage for stresses between the yield and σ_m . When the stresses are below yield, the effects of hysteresis are variable and should not be depended upon for sealing. When the

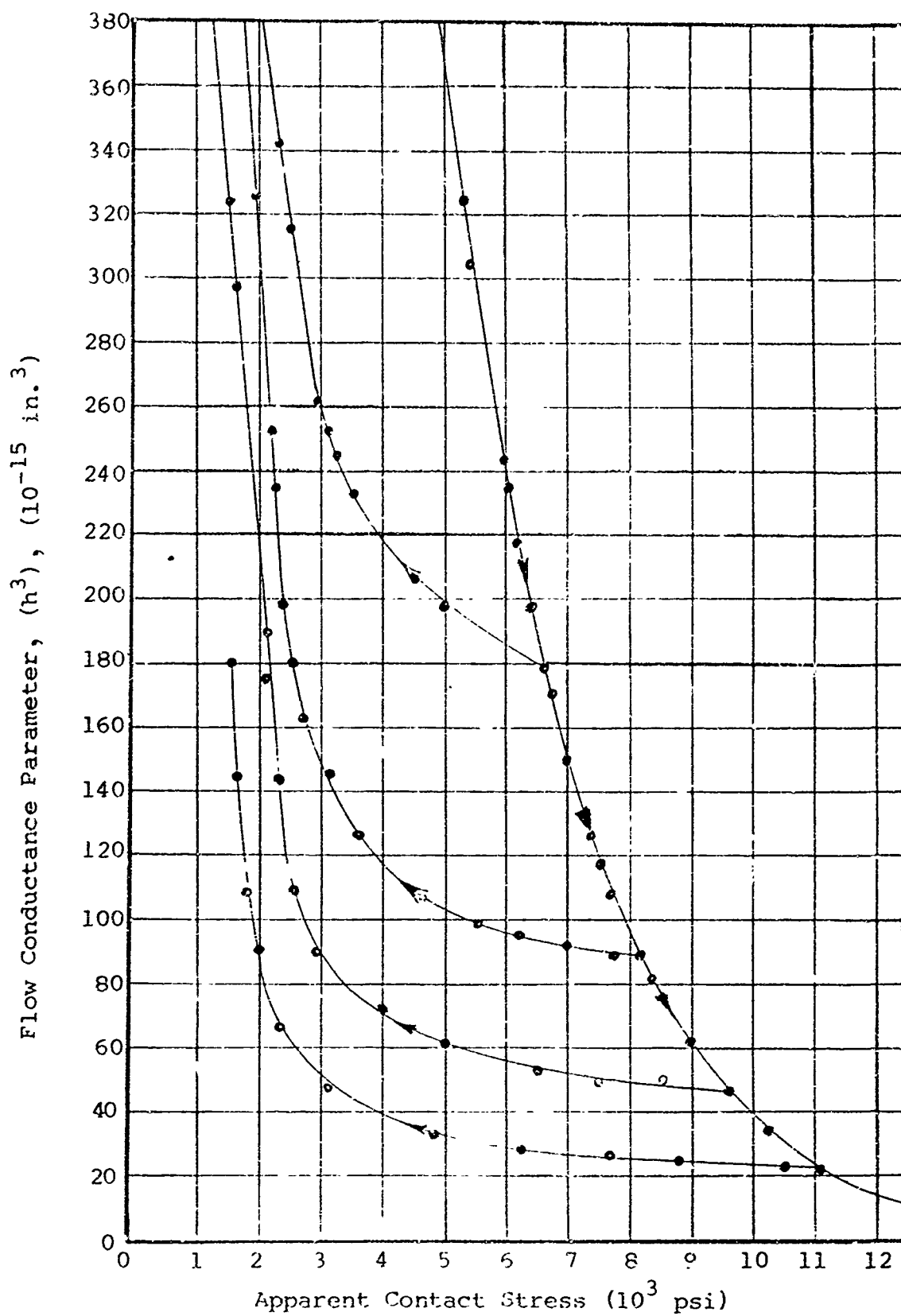


Figure 2-53 Hysteresis effects for an aluminum on steel interface (aluminum gasket 2A; helium; 95 psi pressure; 80°F)

maximum stress is equivalent to σ_m , the load on the surface can be relaxed until the load is approximately equal to 1/10 the load necessary for minimum interface contact width. An increase in leakage less than one order of magnitude can be expected.

2.8.6 Reusability of Sealing Interfaces

The reusability of static sealing interfaces is not permissible unless an increase in interface load accompanies each reuse. The increased load is required to produce additional deformation of the bulk surface or localized disturbances. The most promising surface classes for reuse are as follows.

Class I or II. The deformation of these surfaces, being mostly elastic, should require no increase in load prior to each reuse. However, solid and liquid contaminants are often present when the surfaces are disjoined. To achieve elastic contact when rejoined, all contaminants must be removed. This implies that particles less than 1/40 micron must be cleaned from the surface. This is indeed a difficult task employing the best cleaning techniques. Another source of contamination is to the sealed fluid. When the surface substrate relaxes due to a decrease in load, leakage increases corresponding with a small separation of the surfaces. The separation permits small particles of fluid-borne contaminants to enter the sealing interface and, when the load is reapplied, the surfaces no longer contact each other. To improve the contact, a higher load must be applied causing localized elastic and plastic deformation around the contaminants. This effect was shown by General Electric (Ref. 2-14). Typical leakage results of a Yatabe polished surface are shown on figure 2-54. Two polished surfaces were pressed together and a one atmosphere differential was impressed across the system. Leakage was measured with increases in normal stress until a leakage rate of 10^{-6} cc per sec (helium) was reached. At this time the internal pressure was increased and the load adjusted so that the normal stress remained constant although leakage increased as a result of the higher pressure. Again, the normal stress was increased and leakage was observed. The results following this procedure are shown on figure 2-54. It can be observed that after each successive increase in leakage, a higher stress was required for minimum leakage. This is attributed to the gas contaminants entering the interface. After the fourth repetition of this process, it required 31,000 psi contact stress to achieve a minimum leak rate of 5×10^{-7} cc per sec. This stress is approximately equal to $0.13\sigma_m$. At this stress, a leakage of the same range could have been obtained by plastically deforming rougher surfaces.

Class III. These surfaces depend entirely on plastic deformation for sealing. When the surfaces are disjoined and rejoined, a load increase of 5 per cent is sufficient to produce full plasticity.

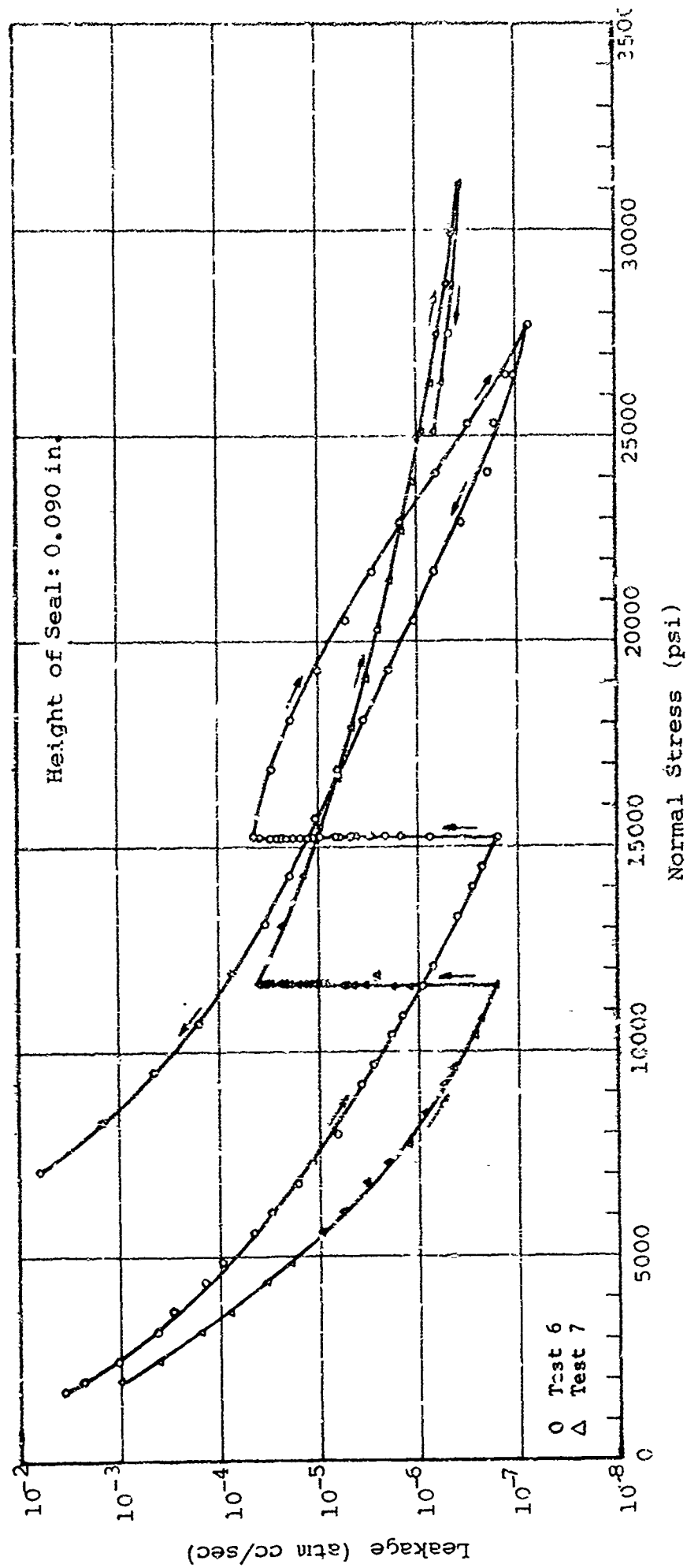


Figure 2-54 Leakage - normal stress response for Yatabe 347 stainless steel specimens (first set)

In summary, neither surface or deformation mode is entirely satisfactory from a reusability standpoint. The Class III surface offers greatest reliability since the magnitude of load increase is not dependent on very small contaminants. However, the load required for initial deformation is substantially higher than the Class I or II surface. The Class I or II surfaces are susceptible to handling as well as to contaminants and the load increase is not readily predictable. Hence, a compromise must be made on the choice of surface when reusability is a requirement.

2.9 References

- 2-1 Paul A. Bauer, Myron Glickman and Frank Iwatsuki, Analytical Techniques for the Design of Seals for use in Rocket Propulsion Systems, Volumes I and II, AFRPL-TR-65-61, IIT Research Institute, Chicago (May 1965).
- 2-2 AMS Metals Handbook, Volume I, (1961)
- 2-3 Materials Selector Issue "Materials in Design Engineering" 60 No. 5, mid-Oct. 1964.
- 2-4 R. Tabor, The Hardness of Metals, Oxford University Press, Oxford (1951).
- 2-5 George E. Dieter, Jr., Mechanical Metallurgy, McGraw-Hill, N.Y. (1961)
- 2-6 O. Kubachewski and B.E. Hopkins, Oxidation of Metals and Alloys, Academic Press, London (1953).
- 2-7 G.A. Tomlinson, Phil. Mag. (Ser. 7) 7, 905, Suppl. (1929).
- 2-8 G.A. Tomlinson, P.L. Thorpe, and H.J. Gough, Proc. Inst. Mech. Engrs. (London) 141, 223, (1939).
- 2-9 E. Rabinowitz, Friction and Wear of Materials
- 2-10 L.G. Gitzendanner, "Optical Observations of Sealing Phenomenon" Proc. Conference and Design of Leak-Tight Separable Fluid Connectors, NASA, 24 March 1964.
- 2-11 General Electric, Design Criteria for Zero-Leakage Connectors for Launch Vehicles, Final Report, Contract NAS8-4012, NASA, George C. Marshall Space Flight Center. 15 Mar 1963.
- 2-12 Rocketdyne Division, North American Aviation, Test Results, Deformation Characteristics of Contaminants Between Flat Metal to Metal Seals, Report CEM 4137-8020, 14 Apr 1964

- 2-13 General Electric, "Design Criteria for Zero-Leakage Connectors for Launch Vehicles" Quarterly Report 7, Contract NAS8-4012, NASA - George C. Marshall Space Flight Center, July 1964.
- 2-14 General Electric, "Design Criteria for Zero-Leakage Connectors for Launch Vehicles", Quarterly Report 8, Contract NAS8-4012, NASA - George C. Marshall Space Flight Center, Oct. 1964.
- 2-15 Rocketdyne Division, North American Aviation, Contract Status Report, Analytical Design Data on Rocket Propulsion System Seats and Poppets, Report 64RC15455, Contract AF04(611)-9712 18 Sep 1964.
- 2-16 Rocketdyne Division, North American Aviation, Contract Status Report, Analytical Design Data on Rocket Propulsion System Seats and Poppets, Report 64RC17154, Contract AF04(611)-9712 18 Sep 1964.
- 2-17 Rocketdyne Division, North American Aviation, Rocket Engine Valve Poppet and Seat Design Data, Report RPL-TDR-64-68, May 1964.
- 2-18 Rocketdyne Division, North American Aviation, Contract Status Report, Analytical Design Data on Rocket Propulsion System Seats and Poppets, Report 64RC13616, Contract AF04(611)-9712 17 Aug 1964.
- 2-19 General Electric, "Design Criteria for Zero-Leakage Connectors for Launch Vehicles" Quarterly Report 3, Contract NAS8-4012 NASA - George C. Marshall Space Flight Center, Jan 1963
- 2-20 General Electric, "Design Criteria for Zero-Leakage Connectors for Launch Vehicles" Quarterly Report 4, Contract NAS8-4012 NASA - George C. Marshall Space Flight Center 15 June 1963

2.10 Symbols

A	= area, (sq in.)
A_A	= apparent contact area, (in. ²)
BHN	= Brinell hardness number
d	= diameter of hardness measurement indentation
H	= hardness, (kg/mm ²)
h	= hypothetical leak path dimension, (in.)
h_f	= final hypothetical leak path dimension, (in.)
h_o	= initial hypothetical leak path dimension, (in.)
\bar{h}	= uniform channel clearance, (in.)
(h^3)	= conductance parameter, (cu in.)
n	= strain hardening coefficient
n'	= Meyer index
P	= load, (lb)
\bar{P}	= load per inch of contact, (lb/in.)
p_o	= standard atmospheric pressure, (psi)
p_i	= downstream fluid pressure, (psi)
p_2	= upstream fluid pressure, (psi)
Q_o	= leakage rate at standard conditions, (in. ³ /sec)
r_i	= inner radius of a circular interface
r_o	= outer radius of a circular interface
λ_o	= molecular mean free path at standard conditions, (in.)
μ	= absolute viscosity, reyns, (lb-sec/in. ²)
σ	= applied normal stress, (psi)
σ_m	= Meyer hardness, (psi)
σ_y	= 0.2 per cent offset yield strength, (psi)

3. INTERFACE WEAR AND LEAKAGE FLOW

As shown in Section 2, leakage flow occurs through the interconnection of void spaces formed by the topographical variations of static mating surfaces. Deformation of the surfaces by applied loads produced a change in the interconnection of void spaces. Leakage, therefore, was shown to be dependent upon the degree of deformation. When gross relative motion occurs between surfaces, the magnitude of applied loading must intentionally be small to minimize energy dissipation. Hence, the deformation exhibited by rubbing surfaces is not expected to be the same as that by static surfaces. Another form of deformation caused by wear predominates in rubbing contact. A disruption in the chance orientation of void spaces is accompanied by changes in surface topography through the various mechanisms of wear.

The factors influencing the magnitude of fluid interchange or leakage through a static interface have been identified as material properties, applied load, and the initial topography of the surfaces. Similarly, these factors may be expected to be of significance for interface surfaces having relative motion. The imposed motion, however, introduces two additional factors, wear and friction. Each of these factors, while somewhat related, has different effects from the viewpoint of sealing. Friction is of interest because of detrimental energy dissipation, in the form of low system efficiency, heat generation, thermal deformation of seal parts, and heat generation producing physical or chemical changes in the fluid between the interface surfaces. Wear, on the other hand, is of interest because of the loss of material from the rubbing surfaces and, more importantly, the topographical changes of the surfaces associated with the wear process. The latter aspect is considered significant solely from experimental observations of leakage through static interfaces (Ref. 3-1, 3-2, and 3-3) and the resulting roughness observed when surfaces rub together. For example, two mild steel surfaces of $10\mu\text{in.}$ finish, when statically pressed together, produce an equivalent leakage channel gap* of approximately $10\mu\text{in.}$ Observations by Finken (Ref. 3-4), however, showed that the rubbing of similar surfaces in air produced a surface roughness of $200\mu\text{in.}$ Hence, rubbing may be expected to produce a larger equivalent leakage channel with a corresponding three-order-of-magnitude increase in leakage through the interface. Unfortunately, little information that ties wear, surface topographical changes, and leakage together is available.

As a starting point in developing design criteria for rubbing seal interfaces, wear was selected for study because of its

* The concept of an equivalent leakage channel gap is based on the results of experimental leakage measurements and theoretical flow equations. The equivalent channel represents a model of the interconnection void spaces in the interface. Further definition may be found in Section 2.5.

greater influence on leakage and seal performance. The objectives of the study are twofold:

- (1) To determine quantitatively the effects of the factors influencing wear and ultimately define these factors in terms of known engineering input data relatable to the topography of the interface and, hence, leakage. The input data consist of applied load, materials, contact area, rubbing velocity and duration of rubbing. An additional factor to be considered is the relationship of the surface damage due to rubbing with respect to the average direction of leakage flow. Figures 3-1 and 3-2 show the two simplest combinations of contact where leakage flow can be in the same direction or normal to the direction of motion and wear damage.
- (2) To identify the magnitude of bulk wear rate with respect to known engineering input data and seal durability. Since bulk wear is not necessarily related to leakage performance, it is considered separately.

To develop criteria for rubbing interfaces, it is necessary first to consider the fundamental concepts of wear, and then appraise the information on the basis of its applicability to rubbing seal interfaces.

3.1 Fundamental Concepts of Wear and Friction

The investigation of wear phenomena has been very extensive, some investigators devoting their lifetime to this study. The success realized has been encouraging but no complete answers have been obtained. Thus, it must be realized at the start that the development of criteria for dynamic seals from a wear viewpoint will not be complete. In addition, few of the investigators were interested in the sealing problem. Most investigators have been involved in studies applicable to bearings and metal cutting with emphasis on bulk wear rather than surface topography.

Theories have been developed and, to a certain extent, substantiated. Even the generation of theories, however, has been developed through extensive experimental investigations and interpretation of results. In addition, wide variations in experimental apparatus have been employed. Thus, interpretation of results must be viewed with respect to the methods of gathering data. The methods employed are too numerous to describe but include semistandardized equipment such as the Shell four-ball wear machine to a wide range of nonstandard equipment. Typical common methods of wear evaluation are shown on figures 3-3, 3-4, and 3-5. Variations within these methods are also prevalent. For example, the pins used in figure 3-5

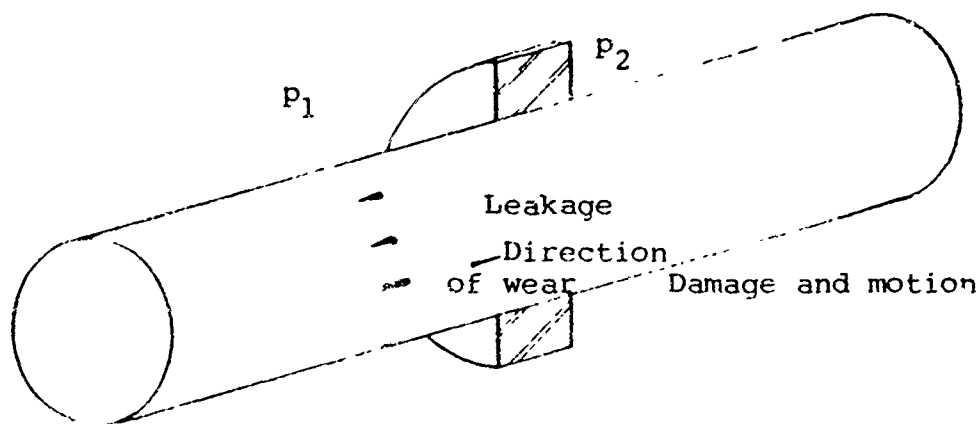


Figure 3-1 Sliding wear with leakage flow in the direction of wear damage

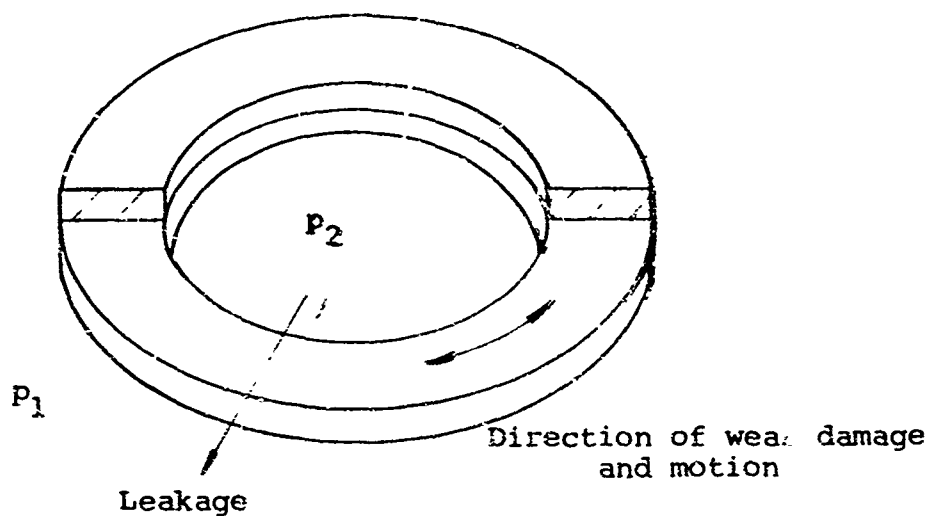


Figure 3-2 Sliding wear with leakage flow normal to the direction of wear damage

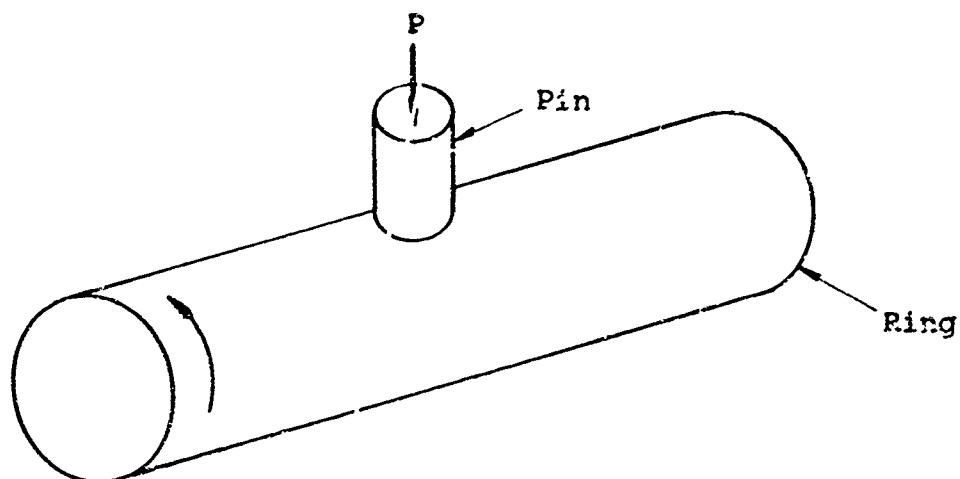


Figure 3-3 Pin-end-on-ring method

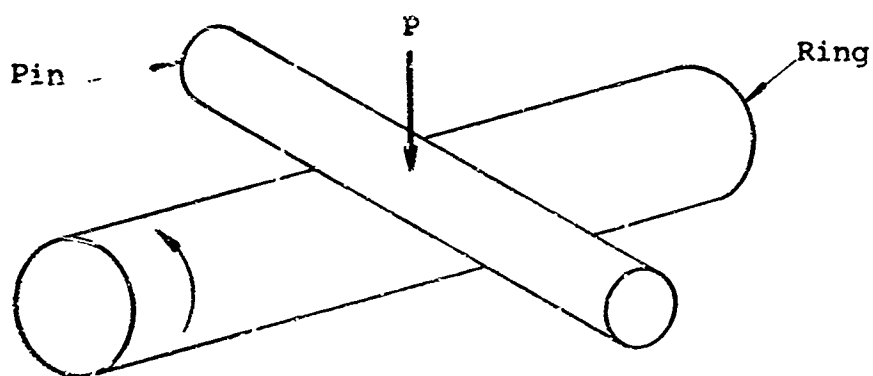


Figure 3-4 Pin-side-on method

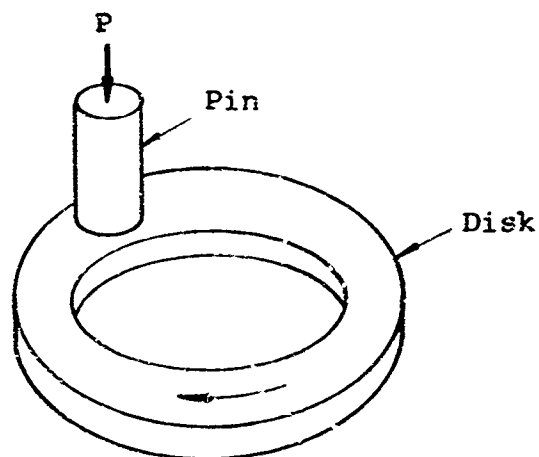


Figure 3-5 Pin-on-disk method

may have a flat or almost arbitrarily rounded rubbing surface, each producing different wear effects.

The present state of knowledge of wear, while pertinent to bearings, is not necessarily suitable for developing an understanding of wear or leakage flow in an interface. Even the experimental equipment, from which most of the knowledge is obtained, is not representative of the conditions of a seal.

The wear of surfaces under conditions of rubbing contact is a complex process influenced by many factors including physical contact and chemical changes. While considerable effort has been made to define the wear process and influencing factors, no satisfactory quantitative laws of wear have been generated. Certain generalizations, such as that hard surfaces wear less than soft surfaces, can be made but many important factors such as load, velocity of rubbing, material properties, and lubrication have not been defined or correlated with each other. The difficulties involved may be exemplified by the effect of small variations in rubbing conditions which change the entire wear process. Controlled experiments seldom give reproducible or conclusive results and great care must be exercised in interpreting results. Because of the many factors involved, a change in conditions may completely alter their mode and magnitude of interaction. Since the advances in wear theory have been predicated on experimental data, it is not surprising that no quantitative laws have been developed.

Burwell (Ref. 3-5) classified wear into at least four mechanisms which are often viewed as distinct and independent phenomena:

- Adhesive or shear wear
- Abrasive and cutting wear
- Corrosive wear
- Surface fatigue

While it is convenient to describe the wear process by easily comprehended definitions, the wear process is often the result of all factors, each interdependent. For example, wear fragments from one surface can be transposed to the other and back to the original surface. The effects of this back-transfer could very easily be interpreted as adhesive, abrasive or surface fatigue and, possibly, all three mechanisms are involved.

3.1.1 Characterization of Wear

Bulk wear characteristics have been described very adequately by Bowden (Ref. 3-6), who considered a 60:40 brass pin rubbing against a hard steel ring (figure 3-6). Loads below 0.5 kg produced low wear rates and loads above 1 kg resulted in high wear rates. Loads between 0.5 and 1.0 kg produced wear rates ranging between the extremes. In the low load region, wear was described as mild and characterized by the formation of dark powder debris. The surfaces become polished with little subsurface damage. At a 0.5-kg load, the surface roughness was $\sim 20\mu\text{in.}$ * Higher loads produced severe wear characterized by debris consisting of metallic flakes with considerable subsurface damage. The surface roughness at a 1.0-kg load was $1000\mu\text{in.}$ While the magnitude of wear is additionally determined by other factors, such as velocity and lubricant films, the same general characteristics may be observed with respect to the significant observable differences between mild and severe wear.

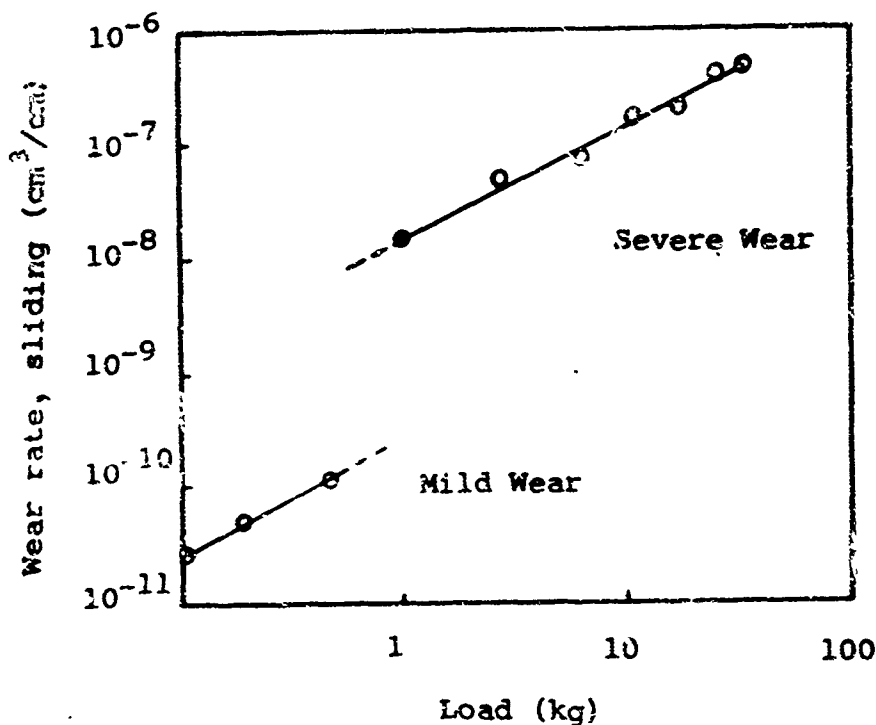


Figure 3-6 Wear characteristics of a 60:40 brass pin on a hard steel disk (Ref. 3-6)

*Method of measurement not defined in Reference 3-6.

3.1.2 Adhesive Wear

Severe wear and the corresponding high wear rate are attributed primarily to the shearing of intermetallic junctions under high specific loading where strong adhesion occurs at the points of real contact. Bowden (Ref. 3-6) uses the following four cases to illustrate the interaction of two surfaces where wear is expected to vary considerably depending on the properties of the materials.

- (1) The interface is slightly weaker than the substrate of the surfaces. Shear occurs only at interface and the wear is small. An example is tin sliding on steel.
- (2) The interface is stronger than one of the materials and weaker than the other. Shear occurs in the soft material and debris is left adhering to the hard surface as in the case of lead sliding on steel.
- (3) The interface is stronger than one metal and occasionally stronger than the other. A transfer from the softer surface occurs and occasionally fragments are removed from the harder surface.
- (4) The interface is stronger than both metals resulting in substrate shearing and severe wear. This is exhibited by the rubbing of similar metals particularly where work hardening or oxide effects are predominant on the surface.

Archard (Ref. 3-7) described the wear properties of surfaces by a factor k representing the fraction of the friction junctions producing wear. A simple model for the shearing of metallic junctions may be generated by assuming each junction has a radius, a , and a contact area πa^2 . The normal load supported at each junction is $P = \sigma_m \pi a^2$, where σ_m is the flow pressure of the metal. When the junction shears, the wear fragment generated is assumed to be hemispherical shape with a volume of $\frac{2}{3}\pi a^3$. The wear fragment is formed in a sliding distance equal to the fragment diameter or $2a$. The wear volume per unit sliding distance is defined as z ;

$$z = \frac{\pi a^2}{3}$$

Since $P/\sigma_m = \pi a^2$, the wear volume per unit sliding distance can be redefined by

$$z = \frac{P}{3\sigma_m}$$

Because every junction in contact does not necessarily produce a wear fragment, a coefficient k representing the fraction of active junctions is included in the preceding relationship:

$$Z = \frac{kP}{3\sigma_m} \quad (3-1)$$

Burwell (Ref. 3-5) attacked the problem of shear wear in a similar manner arriving at the result

$$\frac{V}{L} = k' \frac{P}{H} \quad (3-2)$$

where: $\frac{V}{L} \approx Z$ and $k' \approx \frac{k}{3}$

V = Volume of wear material

L = Distance of travel

H = Hardness*

If both sides of equation (3-2) are divided by the apparent contact area, A_o , the equation becomes

$$h = \frac{k' \sigma L}{H} \quad (3-3)$$

where: h = Average depth of wear

σ = Average apparent stress

An inspection of equations (3-1) and (3-2) shows that wear is proportional to the normal load, distance of sliding contact, and material properties. Equally important, the results show that wear is independent of contact area and roughness.

The following experimental evidence substantiates these observations. Figure 3-7 shows that wear is a linear function of load and independent of apparent contact area. While all results are not as convincing, the general characteristics can be observed. For fairly clean surfaces Bowden (Ref. 3-6) indicates that the wear coefficient, k , may vary between 0.1 and 0.01 and for lubricated surfaces may range to 10^{-7} . Additional values of the coefficient obtained from Reference 3-8 are shown on Table 3-1.

*Hardness is synonymous with the flow pressure of the material. By definition, it is equivalent to the Meyer hardness of the material and is identified as σ_m throughout this report.

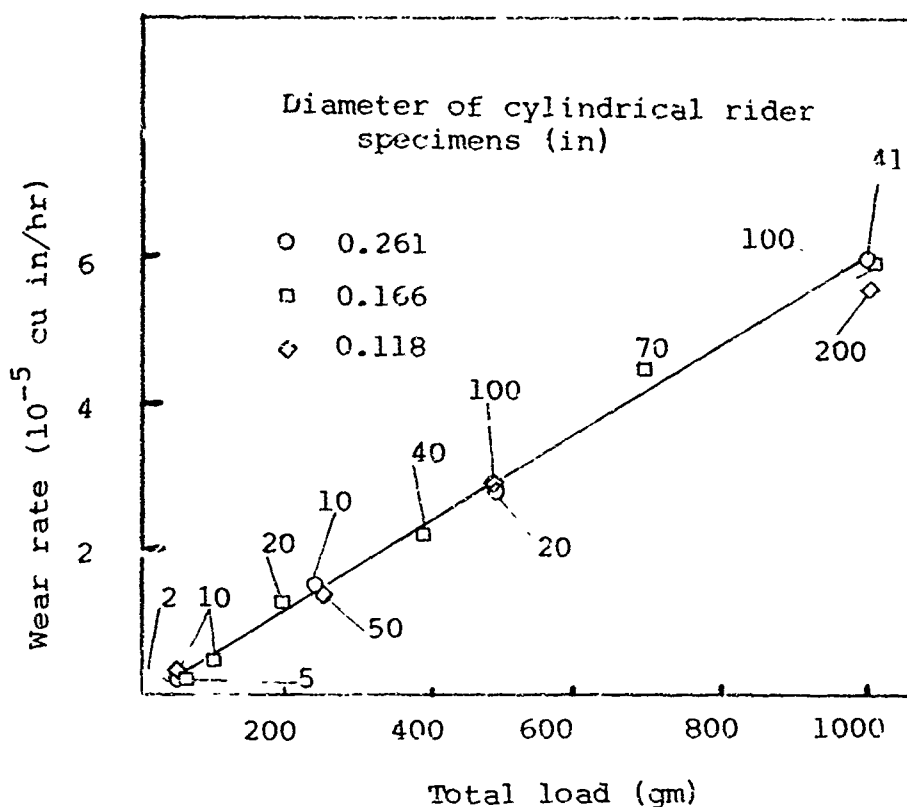


Figure 3-7 Effect of total load on wear of carbon against chromium plate. Sliding velocity 10,000 fpm, temp 360°F, dry air. Numbers adjacent to points show apparent contact stress in psi. (Ref. 3-9)

Table 3-1

TYPICAL VALUES OF COEFFICIENT OF WEAR k
FROM REFERENCE 3-8

Condition	Metal on Metal		Nonmetal on Metal
	Like	Unlike	
Clean	5×10^{-3}	2×10^{-4}	5×10^{-6}
Poorly lubricated	2×10^{-4}	2×10^{-4}	5×10^{-6}
Average lubrication	2×10^{-5}	2×10^{-5}	5×10^{-6}
Excellent lubrication	2×10^{-6} to 2×10^{-7}	2×10^{-6} to 2×10^{-7}	2×10^{-6}

Additional experiments by Burwell (Ref. 3-5) show that, for high loads, the wear coefficient is not constant. Figure 3-8 shows the variation of wear coefficient with average contact stress for two steels having different hardness. The wear coefficient in this case is defined as $k'' = k'/H$. The wear coefficient is constant up to one-third of the indentation hardness and whereupon a sharp increase was observed. The increase resulted in large-scale welding and seizure. The increase is attributed to plastic deformation of the surface asperities.

Another interesting observation can be made from equation (3-3). If the depth of wear is proportional to the rubbing distance, then the resulting surface roughness must be constant for a given load and material. It would appear that the leakage path in a rubbing interface would be a function of the applied load.

These theories of adhesive wear consider the transfer of material from one surface to the other without distinguishing the process of wear. Recent theories (Ref. 3-10, 3-11, 3-12, and 3-13) establish the process of wear as transfer from one rubbing surface to the other with material being lost as debris or transferred back and forth across the interface (Ref. 3-12 and 3-13). The irregularities built up by the transferred material, plus the grooving effects of dragging loose wear particles through the base material, constitute surface roughness.

Metal transfer takes place by welding at contacting asperities which are deformed under the normal and tangential (friction) forces. Since the number of contacting asperities is a function of surface roughness, an equilibrium might be expected in a given sliding system, in which the metal transfer, the wear particle size and rate of generation, and the surface roughness remain constant. This has been proved by experiment (Ref. 3-10, 3-11, 3-4, 3-14). In a system starting with nonequilibrium surface conditions (such as wrong surface finish), the time to achieve equilibrium is greatly dependent on the presence of surface contaminants (Ref. 3-4). If we consider that metal transfer will continue until a critical size of metal accumulates, at which time a loose wear particle is generated, then a correlation should exist between the diameter of the junction which forms the critical size mass, the diameter of the wear particle, and the surface roughness. This relation is shown schematically in figure 3-9. The peak-to-peak surface roughness should be between $0.5d$ and $1d$, where d is the wear particle diameter. The relation between critical junction diameter and wear particle size is less obvious, but should also lie somewhere between $0.5d$ and $1d$. Rabinowicz (Ref. 3-8, 3-15 and 3-16) has shown that the average wear particle size can be accurately predicted on the basis of known conditions in the sliding system,

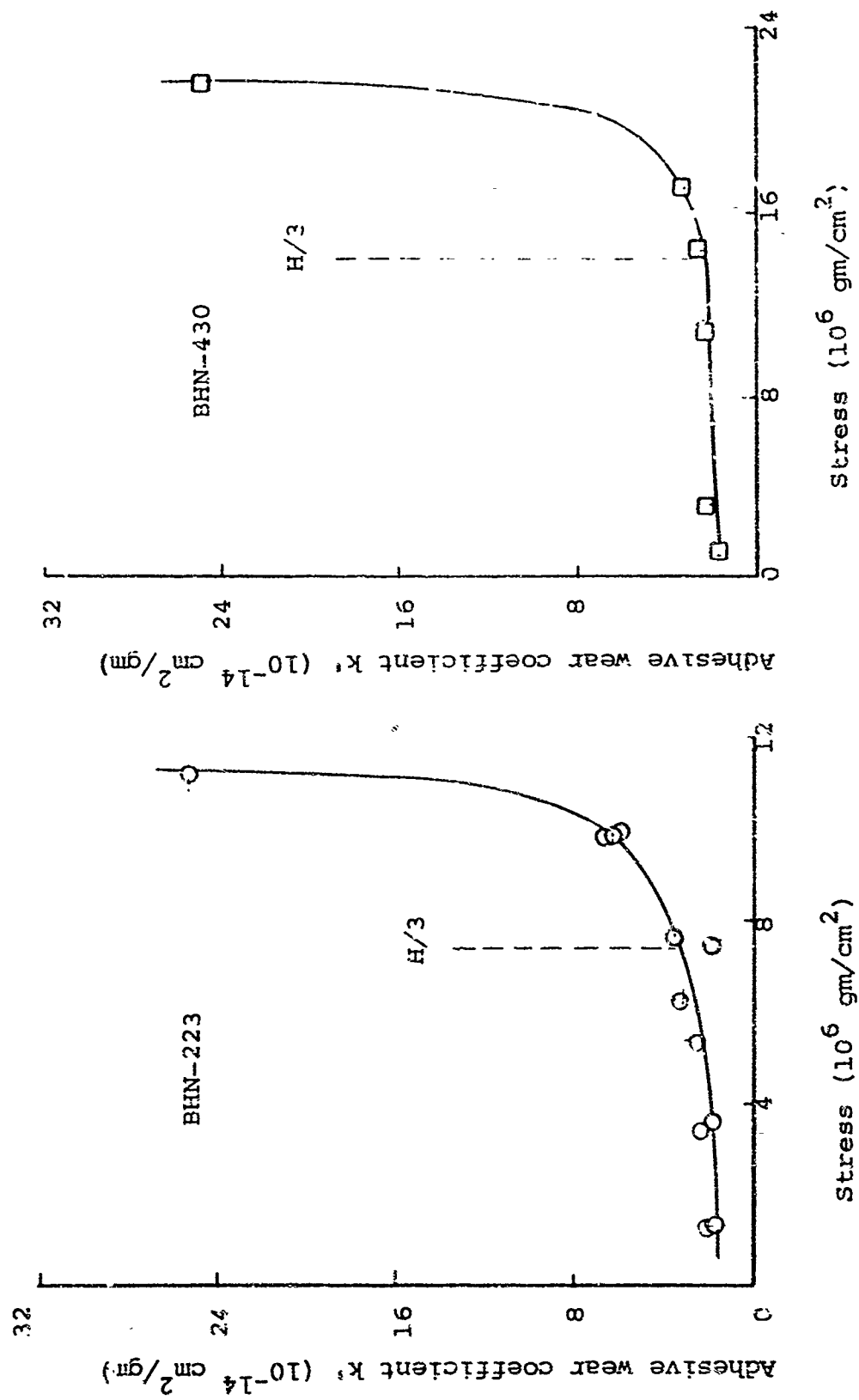


Figure 3-8 Wear coefficient of two steels as a function of contact stress (Ref. 3-5)

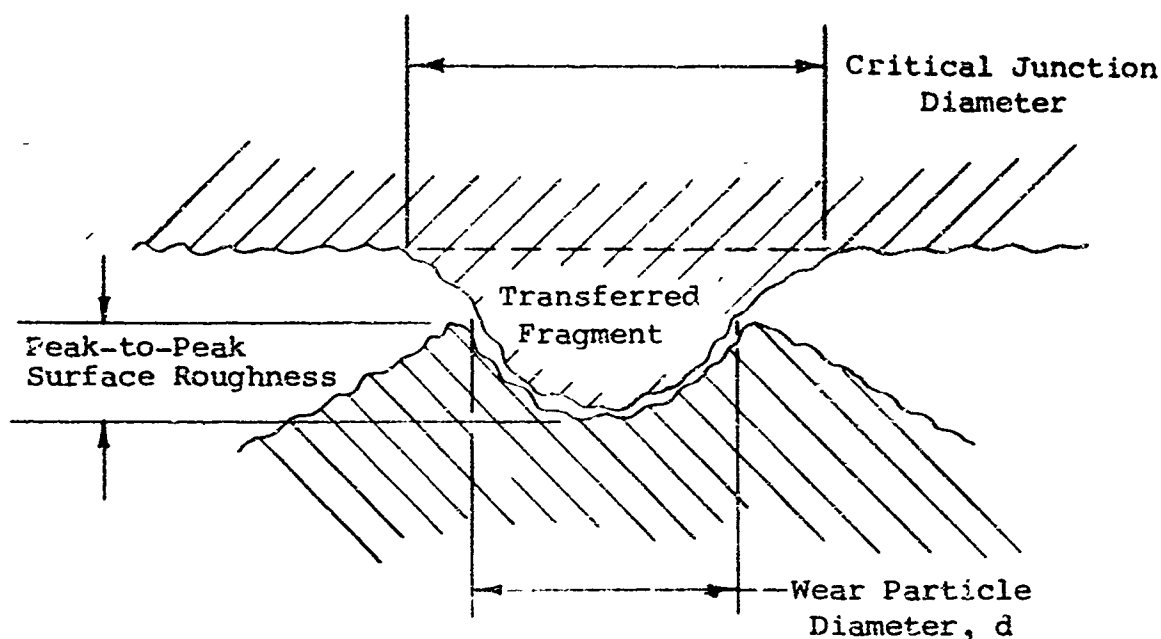


Figure 3-9 Transferred metal at critical point

thereby permitting us to estimate the surface roughness to within a factor of three. The average particle diameter here is defined as the size of that particle for which the weight of all larger particles equals the weight of all smaller particles. The measurement of surface finish by profilometer traces involves an averaging process also. Since it is the larger particles that produce the surface damage, direct comparison of averages is not exactly correct. However, these figures will be used to examine existing data.

In predicting the average wear particle diameter, Rabinowicz (Ref. 3-15) postulates that for a particle to come off loose, the elastic energy stored in the particle must equal or exceed the energy which binds it to the substrate. When it is assumed that the critical mass exists in hemispherical shape, the relation is

$$d = 60,000 \frac{W_{ab}}{H_m} \text{ (cm)} \quad (3-4)$$

where: W_{ab} = the work of adhesion of the contacting materials in ergs/cm²

H_m = the hardness of the material in dynes/cm²

Little data exist on the work of adhesion for engineering materials. However, W_{ab} , the work of adhesion between materials a and b, can be expressed as

$$W_{ab} = Y_a + Y_b - Y_{ab} \quad (3-5)$$

where

Y_a, Y_b = the surface free energies per unit area

Y_{ab} = the interfacial free energy, per unit area

Surface energies are highest for clean metals in vacuum and in inert atmospheres. The values diminish markedly in chemically reactive environments or in the presence of strongly adsorbing vapors. The properties of some metallic elements are shown in Table 3.2.

The interfacial free energy is negligibly small when both surfaces are of the same material. Little data exist for dissimilar materials, but studies by Coffin (Ref. 3-17) and Goodzeit (Ref. 3-18) indicate that interfacial free energy decreases with increasing solid solubility or alloying tendencies. Use of free energies of the metals in predicting surface roughness leads to errors if chemical reactions (such as oxidation) are occurring at the interface. If the loose wear particles are oxides, such things as the relative hardness of the oxide and the metals will be important in determining surface roughness. In two-component systems with greatly differing hardnesses, the softer metal will contribute larger wear particles, but their effect on roughening the surface of the harder material will be diminished.

The average wear particle diameters for various sliding systems have been calculated using Rabinowicz's surface energy formula, which becomes:

$$d = 2.3 \times 10^{-4} \frac{W_{ab}}{H} \text{ (in)} \quad (3-6)$$

when W_{ab} is expressed in ergs/cm², H in kg/mm² and d in inches (the units in which most data are given). Where values of W_{ab} could not be found in the literature, the surface energy was calculated from hardness data using the equation

$$Y = 300 + 38H^{0.75} \text{ (ergs/cm}^2\text{)} \quad (3-7)$$

where H is the hardness in kg/mm².

This formula was derived from a plot of Y as a function of H for a number of metals in Reference 3-8. The value of Y_{ab}

Table 3-2

WEAR PARTICLE SIZE AND SURFACE ROUGHNESS
FOR SLIDING METAL SYSTEMS

Couple	Fluid Environment	γ_a (ergs/cm ²)	Source	γ_b (ergs/cm ²)	Source
Copper/Copper	Vacuum	1400	3-20	1400	3-20
Copper/Copper	Inert	750	3-20	750	3-20
Copper/Copper	Air	1380	*	1380	*
Copper/Copper	Cetane				
Copper/Copper	DC200 (10 cs)				
Copper/Copper	DC200 (10 cs)				
Silver/Silver	Inert	1140	3-20	1140	3-20
Silver/Silver	Air	400	3-20	400	3-20
Mild Steel/Mild Steel	Air	2100	*	2100	*
Mild Steel/Mild Steel	DC200 (100 cs)				
Gold/Gold	Vacuum	1360	3-20	1360	3-20
Gold/Gold	Air	1780	3-20	1780	3-20
Gold/Gold	HCl	670	3-20	670	3-20
Gold/Gold	Oleic Acid				
Gold/Gold	DC200 (100 cs)				
60/40 Brass/60/40 Brass	Air	1460	*	1460	*
Hard Tool / Hard Tool Steel / Steel	Air	6230	*	6230	*
Stellite 1/Stellite 1	Air	5430	*	5430	*
Sintered WC/Sintered WC	Air	8480	*	8480	*
60/40 Brass/Stellite	Air	1460	*	5430	*
Silver/Copper	Air				
Mild Steel/Copper	Air				
Mild Steel/Silver	Air				

W_{ab} (ergs/cm ²)	H Ref. 19 (kg/mm ²)	d (Calc) (in.)	d (Meas) (in.)	Source	Peak to Peak Surface Roughness (in.)	Source
2800	87	7.4×10^{-3}				
1500	87	4.0×10^{-3}				
2760	87	7.3×10^{-3}	7.0×10^{-3} 9.5×10^{-3} 4.7×10^{-4} 4.7×10^{-4} 3.2×10^{-4} 9.5×10^{-4} 3.7×10^{-4}		3.3×10^{-3} 4.5×10^{-4} 1.4×10^{-4} 3.6×10^{-4}	3-4 3-4 3-4 3-4
2280	75	7.0×10^{-3}				
800	75	2.5×10^{-3}	2.4×10^{-3}			
4200	186	5.2×10^{-3}	2.4×10^{-3}		2.8×10^{-4} 1.5×10^{-3}	3-4 3-4
2720	79	8.0×10^{-3}				
3560	79	1.1×10^{-2}				
1340	79	4.0×10^{-3}			3.0×10^{-4} 1.9×10^{-4}	3-21 3-21
2920	95	7.1×10^{-3}				
12,460	850	3.4×10^{-3}				
10,960	690	3.6×10^{-3}				
16,960	1300	3.0×10^{-3}				
6890	95 690	1.7×10^{-2} 2.3×10^{-3}	5.9×10^{-4}		6.7×10^{-4}	3-11
2330	75 87	7.2×10^{-3} 6.2×10^{-3}				
2675	186 87	3.3×10^{-3} 7.1×10^{-3}				
712	186 75	8.8×10^{-4} 2.2×10^{-3}				

was taken to be zero for like metals. These data are given in Table 3-2. Also shown in Table 3-2 are data from the literature on measured wear particle size and measured surface roughness. The correlation between measured particle size and roughness is excellent. The correlation between calculated and measured particle sizes is good for like metal systems, considering the inaccuracies involved in calculation W_{ab} and the unknown effects of work hardening at the interface.

The predicted particle sizes for most systems in air fall between 10^{-2} and 10^{-3} in. The effects of operation in other environments can be judged from Table 3-3 (from Ref. 3-8), which shows measured particle sizes for copper sliding on copper in various fluids. The particle size in less active environments than air will be approximately double that in air. In more active fluids, such as lubricants, the particle size will be ten or twenty times smaller as a result of decrease in free surface energy by the lubricant.

Table 3-3
WEAR PARTICLE SIZE FOR COPPER SLIDING
ON COPPER IN VARIOUS FLUIDS
FROM REFERENCE 3-8

Fluid	Average Particle Size (μ in.)
Nitrogen	18900
Helium	15000
Carbon Dioxide	11800
Dry Air	8830
Oxygen	7920
Air (50% Humidity)	6980
Air (100% Humidity)	5750
Cetane	470
Silicone DC 200	380
Ucon LB-70X	380
Palmitic Acid in Cetane	320

3.1.3 Abrasive Wear

Abrasive wear may be described as surface damage resulting from the collision of surface disturbances. The plowing of a soft surface by a hard surface or the interaction of contaminants with either surface are representative of abrasive wear. The contaminant can be a foreign object such as a deliberately used abrasive in a lapping operation or an object induced by the surrounding atmosphere. In addition, the contaminant may be formed by chemical reaction of the particles generated in the wear process with the atmosphere. The formation of ferric oxide particles is an example of a self-induced abrasive when iron materials are involved in the rubbing process.

The factors influencing abrasive wear have not been conclusively determined. Through experiments, Kruschov (Ref. 3-22) concluded that hardness of the surfaces is of importance while Oberle (Ref. 3-23) points out that elastic deformation of the surface may be important. Similarly, Spurr and Newcomb (Ref. 3-24) correlated wear with elastic modulus and hardness. Intuitively, it appears that both properties would be significant by the nature of the abrasive process. If a collision of surface disturbances occurs, a low elastic modulus would permit greater deformation, thus permitting the surface disturbances to avoid each other readily without plowing or gouging. A high hardness, on the other hand, implies high strength capabilities and greater resistance to plastic deformation. Hence, for minimum abrasive wear the materials of contact should have a high hardness and low modulus of elasticity. Table 3-4 shows the relative hardness-to-modulus ratio of various materials (3-25).

Preferential orientation of the crystalline structure of chrome produces a material having a high hardness and low elastic modulus and seen on Table 3-4. Plating at a specific current density and temperature results in a bright chromium plate with its crystals almost all oriented with their planes parallel to the base material (Ref. 3-26). The grain orientation persists even after recrystallization (Ref. 3-27). The oriented plating has an elastic modulus of 12×10^6 psi as compared with 36×10^6 psi for nonoriented plating. Thus, bright chrome plating appears to have the necessary requirements for abrasion resistance. This is substantiated by a low coefficient of static and sliding friction as shown on Table 3-5.

Table 3-4

RATIO OF HARDNESS TO MODULUS OF ELASTICITY
FOR VARIOUS MATERIALS (Ref. 3-25)

Material	Condition	Modulus of Elasticity (Mpsi)	Brinell Hardness	Hardness Modulus Ratio $\times 10^6$
Alundum (Al_2O_3)	bonded	14	2000	143
Chromium plate	bright	12	1000	83
Gray iron	hard	15	500	33
Tungsten carbide	9% cobalt	81	1800	22
Steel	hard	29	600	21
Titanium	hard	17.5	300	17
Aluminum alloy	hard	10.5	120	11
Gray iron	as-cast	15	150	10
Structural steel	soft	30	150	5
Malleable iron	soft	25	125	5
Wrought iron	soft	29	100	3.5
Chromium metal	as-cast	36	125	3.5
Copper	soft	16	40	2.5
Silver	pure	11	25	2.3
Aluminum	pure	10	20	2.0
Lead	pure	2	4	2.0
Tin	pure	6	4	0.7

Table 3-5

COEFFICIENT OF FRICTION FOR VARIOUS METAL COMBINATIONS

Metal Combination	Static Coefficient	Sliding Coefficient
Chromium-plated steel/ chromium-plated steel	0.14	0.12
Chromium-plated steel/babbitt	0.15	0.13
Chromium-plated steel/steel	0.17	0.16
Steel/babbitt	0.25	0.20
Babbitt/babbitt	0.54	0.19
Steel/babbitt	0.30	0.20
Bright chromium plate/cast iron		0.06
Bright chromium plate/bronze		0.05
Bright chromium plate/babbitt		0.08
Hardened steel/cast iron		0.22
Hardened steel/bronze		0.11
Hardened steel/babbitt		0.19

Bowden (Ref. 3-6) developed a simple model of the abrasive wear process by assuming a hard pyramidal point sliding over a metal surface as shown in figure 3-10.

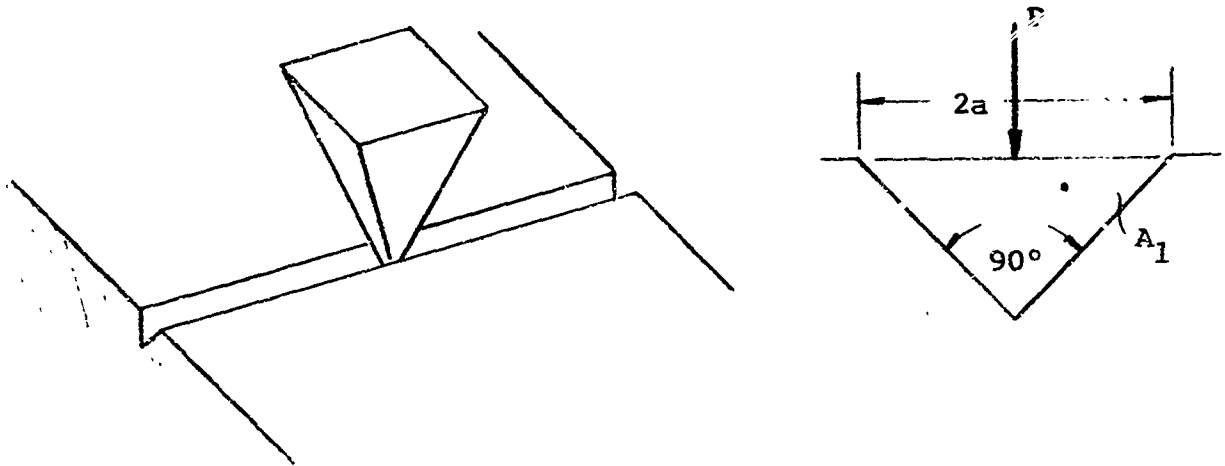


Figure 3-10 Pyramidal point showing a groove in a hard surface

The cross-sectional area of the groove A_1 is a^2 if a load P produces a groove width of $2a$. Allowing for build-up and for the fact that part of the trailing edge of the pyramid also supports load, the projected area A_2 supporting the load P is approximately $2a^2$. The flow pressure of the material is $\sigma_m = A_2 P$,

therefore $A_1 \approx P/\sigma_m$

and $A_2 \approx P/2\sigma_m$.

The volume of the groove per length of sliding contact is $P/2\sigma_m$. If the pyramidal abrasive particles vary in size, however, only a portion of the maximum wear volume will occur. If 10 per cent of the particles are effective, the wear rate Z is

$$Z = P/20\sigma_m,$$

or, rearranging into the format of equation (3-3),

$$Z = k''' \frac{P}{\sigma_m}$$

where k''' = abrasive wear constant.

Another method of expressing abrasive wear is in reciprocal form defined as abrasion resistance R where

$$R = 20\sigma_m/P \quad (3-8)$$

Experimental results obtained by Avient, Goddard, and Wilman (Ref. 3-28) correlate closely with equation (3-8). These results for various metals sliding on abrasive paper containing 150-particles are shown on figure 3-11. Two conditions of sliding were evaluated -- the initial and equilibrium states. An observation may be made that the wear resistance of metals increases with increasing hardness as determined from Table 3-2. Kruschov (Ref. 3-32) obtained similar correlations with 80 abrasive particles.

Typical values of the wear constant, k'' , have been found to range between 0.2 and 0.002 (Ref. 3-8) depending upon the abrasive wear process. If the process is identified as a hard rough surface gouging a soft surface, the abrasive wear constant will be closer to 0.2.

On the other hand, if the process is one of lapping two hard surfaces by a third material, the constant is closer to 0.002.

3.1.4 Corrosive Wear

Corrosive wear is a complicated interaction of chemical, physical, and mechanical processes often resulting from initial adhesive and abrasive wear. A fragment plucked from a surface by adhesion can end up in several forms:

- It can be transferred to the mating surface by the normal adhesion transfer process.
- It can be oxidized (chemical reaction) forming one or more compounds, each having different properties. The oxides can be expelled from the interface, producing abrasive wear in the process.
- It can be oxidized and embedded into the same or mating surfaces producing an increase in abrasive wear and a decrease in adhesive wear.

Similarly, fragments produced by abrasion can be expelled or retained in the interface. Bowden (Ref. 3-29) discusses experiments conducted by Dies (Ref. 3-27) with mild steel on mild steel and mild steel on hard chromium steel. These experiments led to a comparison of severe wear (mild steel/mild steel) and abrasive wear (hard chrome/mild steel). The results are shown on figure 3-12. For loads up to 10 kg per sq cm, the wear

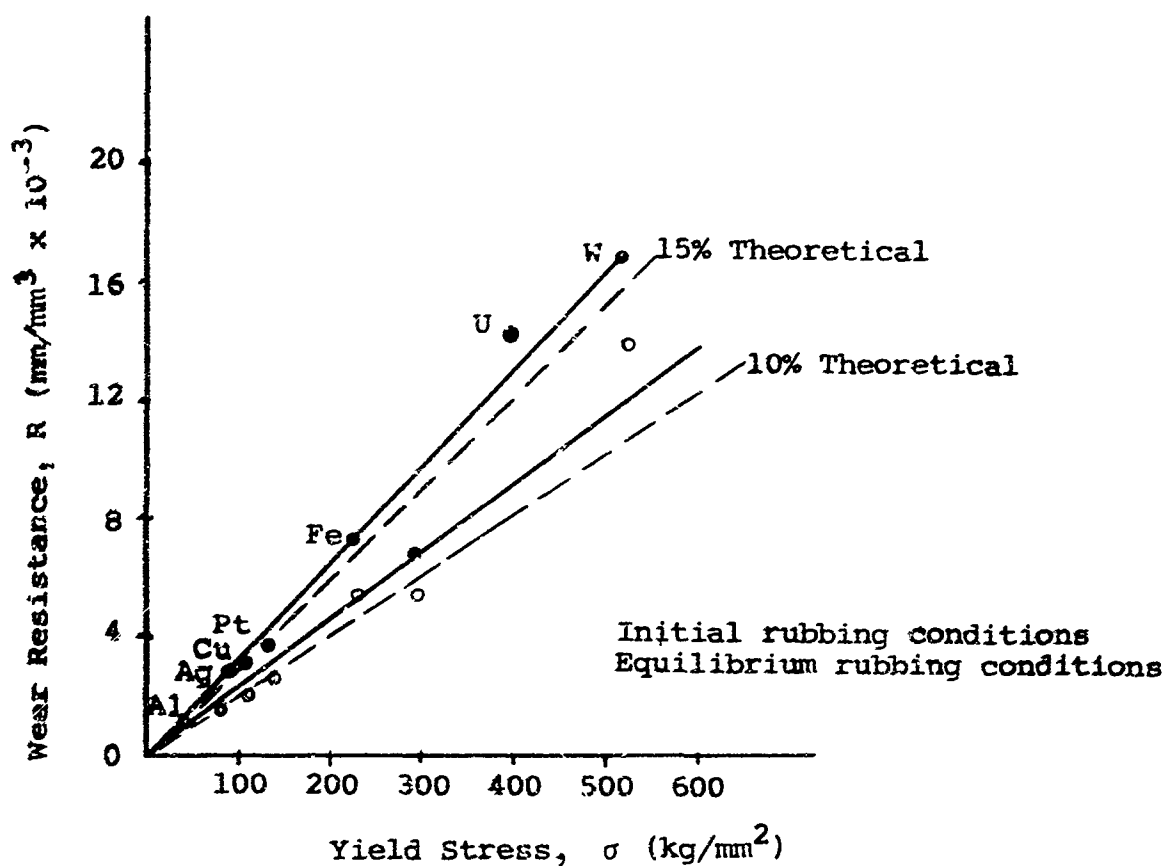


Figure 3-11 Abrasion resistance R as a function of yield stress σ for metals abraded under a load of 1 kg on dry grade-3 emery paper

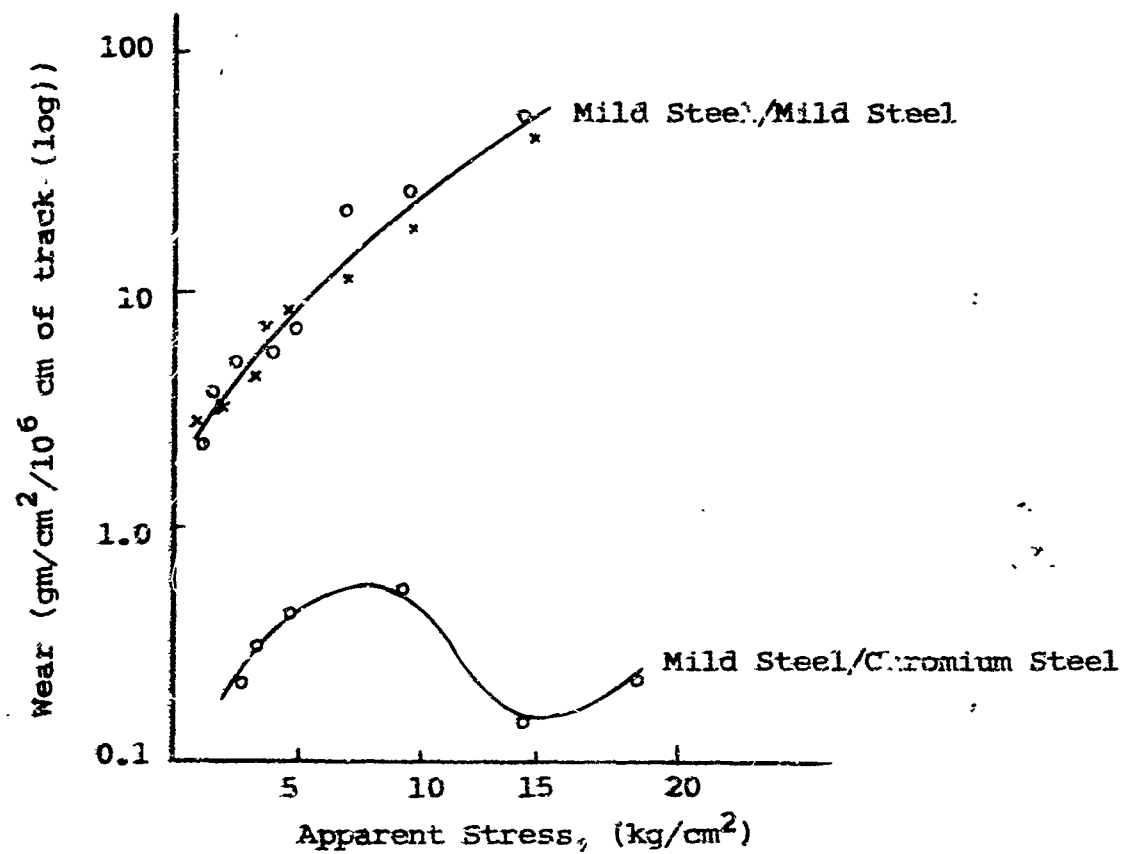


Figure 3-12 Wear of unlubricated metals as a function of load

products were ferrous oxide and iron. At higher loads the wear products were ferric oxide and ferrous oxide. A significant decrease in wear occurred which was attributed to the ferric oxide. The development of the harder oxide produced a greater proportion of abrasive wear compared with adhesive wear, thus reducing the wear rate. Simultaneously, an increase in surface temperature occurred, causing a change in hardness of the mild steel. The hardening was attributed to the formation of nitrided layers, with the nitrogen furnished by the surrounding atmosphere. Other than the preceding oxidation effects, little can be said about the general nature of corrosive wear. Some of the influencing factors, however, can be identified as:

- the ambient atmosphere including temperature, lubricant degradation and gaseous environment
- the nature of the materials rubbing
- the presence of a lubricant film which may reduce the magnitude of wear or protect the surfaces from the atmosphere.

3.1.5 Friction

Friction is expressed as the force exerted by either of two contacting bodies tending to oppose relative tangential displacement of the other. When the displacement is microscopic, the friction is identified as static, as opposed to sliding friction, in the case of gross tangential motion. The theory of friction as advanced by Bowden (Ref. 3-6) is based on the effects of strong adhesive forces between contacting asperities. As a load is applied to two surfaces, the asperities contact resulting in high local stresses at the points of contact. The high stress produces plastic flow of the asperities, thus exposing the clean substrate by removal of lubricants and other surface contaminants. Consequently, cold welding can occur at the junctions and, in the presence of relative motion, shear must occur before the motion can proceed. Reference 3-1, Volume 1, Section 2 should be reviewed for a complete description of a real surface. In addition, ploughing of asperities into the mating surface produces a force that resists tangential displacement. The resultant of the forces, called the friction force,

$$F = \text{shear (adhesion), } F_s + \text{ploughing forces, } F_p$$

and the coefficient of friction defined as

$$f = \frac{F}{P} \quad (3-9)$$

where P is the applied normal load.

The following statements can be made regarding friction:

- 1) The friction force is proportional to the normal force as given by equation (3-9).
- 2) The friction force is independent of the apparent area of contact.
- 3) The friction force is independent of the sliding velocity.
- 4) The friction force is independent of surface roughness.

In general, the first two statements are well obeyed with few exceptions. For example, frictional changes with load for very soft (Teflon) and very hard (diamond) materials may be observed (Ref. 3-8). Statement 3 requires further qualification. A distinction must be made between static and sliding friction based on the degree of tangential displacement. Static friction can vary as a result of material creep and other time-dependent effects. Sliding friction can increase with increasing velocity, decrease with increasing velocity, or both. For most purposes in which only limited velocity ranges are of interest, the sliding friction coefficients may be taken to be constant, independent of the velocity.

Statement 4 regarding surface roughness must also be qualified. With very smooth surfaces, friction tends to be high because the real area of contact grows excessively; similarly, very rough surfaces produce high friction because of the need to lift one surface over the asperities on the other. In between the two roughness extremes, however, the friction coefficient is fairly independent of roughness. Figure 3-13 shows the variation of friction coefficients for copper sliding on copper as a function of surface finish. An exception to this rule is often exhibited by surfaces lubricated with liquids. At certain velocities, the smooth surface may be functioning in a state of hydrodynamic lubrication while rough surfaces may be boundary lubricated.

With the characteristics of friction identified, it is possible to identify the factors of influence. The effects of friction were attributed to shear, F_s , and ploughing, F_p , forces at the interface. Assuming that each junction can be sheared by a force proportional to an average shear stress, τ_{avg} acting over the real area of contact, the friction force can be given

$$F_s = (\tau_{avg}) (A_R)$$

and

$$f = \frac{\tau_{avg}}{\sigma_m}$$

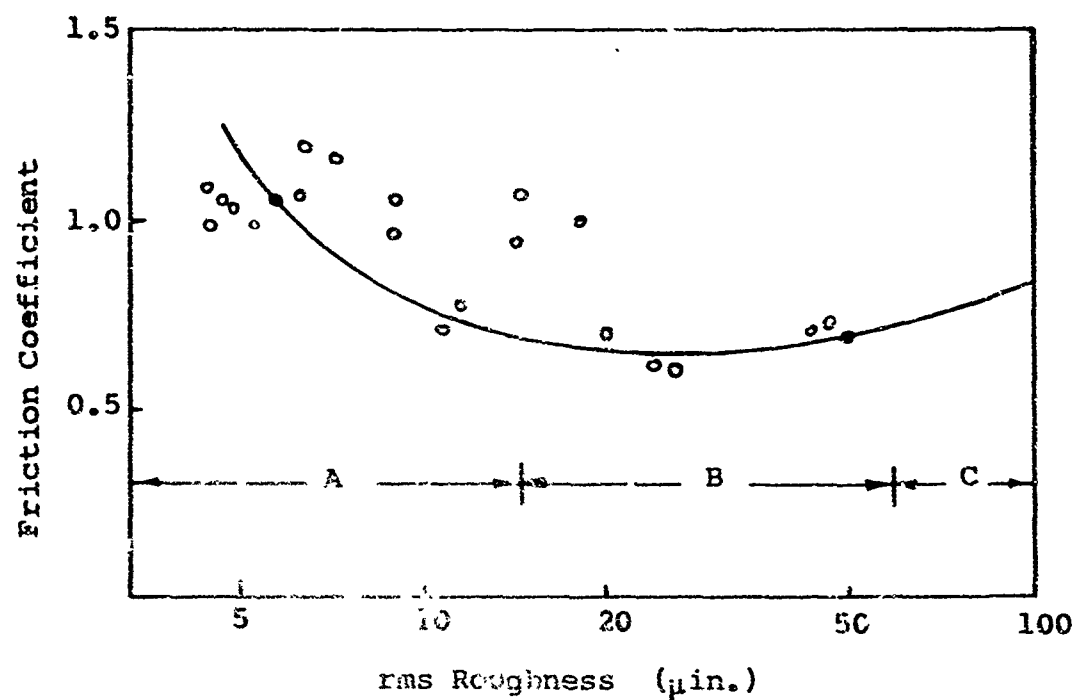


Figure 3-13 Friction as a function of surface roughness for unlubricated copper on copper with a 1000-gm load at a velocity of 0.01 cm/sec (Ref. 3-8) The regions of influence may be identified as:

- A: Friction affected by growth of real contact area
- B: Friction constant
- C: Friction affected by interlocking asperities

Hard, sharp asperities ploughing a soft surface produce scratches. If the asperities are assumed conical, the area swept out during sliding, as shown in figure 3-14, is

$$A_p = a^2 \tan \theta$$

In addition to the sliding resistance, the conical asperities must displace material with a force F_s . Hence, the frictional force,

$$F = a^2 \tau_{avg} + a^2 \tan \theta \cdot \sigma_m$$

where $F_p = a^2 \tan \theta \cdot \sigma_m$

$$\text{and } f = \frac{\tau_{avg}}{\sigma_m} + \frac{\tan \theta}{\pi} \quad (3-10)$$

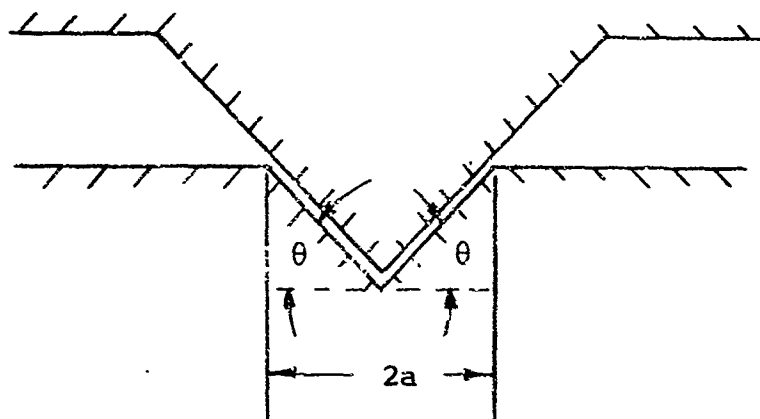


Figure 3-14 Schematic of a cone forming a groove in a flat surface

In most surfaces, the angle θ is less than 5 deg and governed to a large extent by the fabrication process and material properties. Consequently, the $\tan \theta/\pi$ term is often negligible. If the mechanical shear and hardness properties of materials are made analogous to the junction shear and plasticity stress in equation (3-10), the ratio of shear to hardness is very nearly the same for all metals and numerically equal to 0.2. This may be expected if the friction coefficient is not expected to vary widely. In practice, most unlubricated metals give a value of f of the order of unity. Hence, the simple model used in developing equation (3-10) has serious discrepancies primarily because the normal and tangential forces (stresses) are assumed independent. Plasticity theory, however, shows yielding at a juncture to be the result of the combined stresses.

The frictional properties of unlubricated metals are greatly affected by the presence of surface films or lack of films. The films may be identified as oxide layers, adsorbed layers of water vapor and oxygen, and finally an outermost layer of greasy films. Metal surfaces of this type found in most industrial environments have initial coefficients of friction in the range 0.1 to 0.3 when slid together. Higher values are reached when the grease film is degraded or worn away. Typical frictional properties are shown on Table 3-5. Other values may be obtained from various engineering handbooks.

When two grease-free metal surfaces slide together, the resulting frictional behavior can range from severe to mild. Severe conditions produce coefficients of friction in the range of 0.9 to 2.0, accompanied by the generation of large wear particles exceeding 0.002 in. in diameter. Mild conditions produce coefficients of friction between 0.3 and .7 under steady or "stick-slip" conditions with wear particles less than 0.001 in. in diameter.

A system of two clean metals does not obey the normal laws of friction. Tests have shown that two clean metal surfaces* sliding together in high vacuum produce friction coefficients from 5 to 200 (Ref. 3-8).

The frictional properties of nonmetals, including diamond, rubber, and wood are fairly uniform. Unlubricated sliding coefficients of friction range between 0.3 and 0.4 for velocities

*Prepared under conditions of high vacuum 10^{-7} torr or less by mechanically or chemically removing surface contaminants.

between 0.4 and 40 ips. Most lubricated nonmetals range between 0.1 and 0.3 as compared with lubricated metals which range between 0.04 and 0.10. In general, nonmetals sliding on metals or nonmetals produce frictional properties similar to that of the softer materials sliding on itself. This is attributed to the coating of the harder surface by the softer material producing a situation where the soft material slides on itself. Table 3-6 and 3-7 show the frictional properties of materials sliding under lubricated conditions where the lubricant is a rocket engine fuel or oxidizer liquid.

3.2 Wear, Surface Topography, and the Leakage Path

Leakage flow of fluid through a sealing interface is influenced substantially by the resistance to flow afforded by the physical condition of the interface. When the surface topographical variations are rough ($>1 \times 10^{-6}$ in.) and light loads are applied to the surfaces, the physical condition of the interface can be described by average topographical measurements of the surfaces. In turn, the average topographical variation can be assumed equal to a uniform clearance gap formed by two hypothetically flat surfaces. The uniform clearance is synonymous with the conductance parameter, described in Section 2.5, and, consequently can be used in the calculation of leakage rates using the appropriate flow equations presented in Volume II, Section 10 of Reference 3.2. If we can establish the physical condition of a dynamic seal interface, leakage flow can be predicted.

The factors influencing the physical condition of rubbing surfaces have been discussed in the preceding sections. The resulting physical condition, however, was not explicitly considered. The purpose of this discussion, therefore, is to elaborate on the effects of wear with respect to the leakage path.

To fully describe the effects of wear, consider the following example. Two surfaces possessing an initial roughness are rubbed together. The various mechanisms of wear produce an increase or decrease in roughness depending upon load, material properties, and initial finish. Simultaneously, wear debris and transfer particles are generated. If the debris and transfer particles are larger than the roughness, the surfaces will be separated by a distance determined by the debris size. If the debris and transfer particle size are smaller than the roughness, the surfaces will be in contact. Thus, the following statement logically follows:

Table 3-6

WEAR RATES FOR VARIOUS MATERIALS IN AIR OBTAINED
FROM A PIN AND RING TEST WITH A 400-GRAM LOAD
AT A VELOCITY OF 150 CM/SEC (Ref. 3-30)

Material	Wear Rate (10^{-10} cm ³ /cm)	Coefficient of Friction
Mild Steel on Mild Steel	1570	0.62
PTFE on Hardened Tool Steel	20	0.18
Stellite on Hardened Tool Steel	3.2	0.60
Ferritic Stainless on Hardened Tool Steel	2.7	0.53
Tungsten Carbide on Tungsten Carbide	0.02	0.35

Table 3-7

WEAR RATES FROM PIN ON DISK EXPERIMENTS
IN SELECTED PROPELLANTS (Ref. 3-31)

Specimens			Load (lb)	Total Distance Traveled (10 ⁻⁶ in.)	Button Wear by Volume (10 ⁶ cu in.)	Button Wear Rate (cu in./10 ¹² in.)	Friction Coefficient	
Plate	Button						Initial	Stabilized
Material	Material	Velocity						
440-C	440-C	1570	0.65	RP-1 0.565	3.30	7.26	0.185	0.185
	135M	2100	0.65	0.764	2.50	2.79	0.15	0.15
	B-25	2620	0.65	0.942	7.00	7.43	0.05	0.05
	440-C	3140	0.65	1.13	1.00	1.86	0.15	0.15
B-25	B-25	1570	0.6984	0.54	7.70	13.5	0.41	0.06
	135M	2100	0.698	0.72	0.30	0.331	0.36	0.017
	440-C	2620	0.698	0.9	0.52	0.530	0.31	0.04
	B-25	3140	0.581	1.08	100.0	97.4	0.51	0.03
9310	135M	1570	0.698	0.54	0.93	1.71	0.42	0.05
	440-C	2100	0.698	0.72	3.80	5.56	0.365	0.04
	B-25	2620	0.698	0.90	28.00	31.1	0.56	0.035
	52100	3140	0.698	1.08	6.10	5.56	0.38	0.04
135M	Al	1570	0.77	0.54	120.00	220.0	0.16	0.05
	Al ₂ O ₃	2100	0.77	0.72	0.28	0.389	0.30	0.08
	52100	2620	0.77	0.90	8.00	8.9	0.52	0.07
	135M	3140	0.77	1.08	5.20	4.82	0.26	0.05
440-C	B-25	4750	0.77	1.71	---	---	1.0	0.54
	Bakelite	6330	0.77	2.28	---	---	0.53	0.44
	Carbon	7910	0.77	2.85	---	---	0.73	0.52
	GST*	9500	0.77	3.42	---	---	0.69	0.59
440-C	B-25	1570	0.77	---	---	---	0.11	0.04
	Bakelite	2100	0.77	---	---	---	0.12	0.07
	Carbon	2620	0.77	---	---	---	0.165	0.12
	GST	3140	0.77	---	---	---	0.185	0.085
440-C	B-25	1570	0.77	1.832	140.0	76.3	0.09	0.09
	Bakelite	2100	0.77	2.443	6.5	2.65	0.04	0.04
	Carbon	2620	0.77	3.054	8.0	2.62	0.06	0.06
	GST	3140	0.77	3.664	8.5	2.32	0.06	0.06

* Glass-supported Teflon:

Table 3-7 (Cont.)

Specimens			Load (lb)	Hertz Stress (psi)	Total Distance Traveled (10 ⁻⁶ in.)	Button Wear by Volume (10 ⁶ cu in.)	Button Wear Rate (cu in./10 ¹² in.)	Friction Coefficient	
Plate	Button							Initial	Stabilized
Material	Material	Velocity (fpm)							
Ethylene Diamine									
440-C	440-C	1570	0.77	105,000	0.622	9.0	14.45	0.52	0.05
	B-25	2100	0.77	90,000	0.829	88.0	106.0	0.38	0.03
	B-25	2620	0.77	90,000	1.040	70.0	67.3	0.53	0.48
	440-C	3140	0.77	105,000	1.242	10.0	8.05	0.43	0.20
440-C	Carbon	4720	0.77	---	1.855	72.0	38.8	0.17	0.17
	GST	6290	0.77	---	2.475	80.0	32.3	0.082	0.082
	Carbon	7860	0.77	---	3.090	80.0	25.9	0.082	0.082
	GST	9440	0.77	---	3.71	105.0	28.3	0.11	0.11
UDMH									
440-C	Carbon	4870	0.77	---	1.96	11.1	5.66	0.10	0.10
	GST	6500	0.77	---	2.61	10.7	4.1	0.075	0.075
	Carbon	8120	0.77	---	3.26	48.0	14.71	0.10	0.10
	GST	9740	0.77	---	3.92	10.8	2.76	0.051	0.051
440-C	Al	1610	0.77	72,600	0.628	420.0	669.0	0.41	0.14
	52100	2150	0.77	105,000	0.84	70.0	83.0	0.29	0.08
	B-25	2680	0.77	90,000	1.05	280.0	266.0	0.35	0.12
	440-C	3220	0.77	105,000	1.26	9.5	7.54	0.20	0.15
Hydrazine									
440-C	Al	1635	0.77	72,600	0.648	1059.0	1620.0	0.20	0.20
	440-C	2180	0.77	105,000	0.864	25.0	28.9	0.30	0.06
	B-25	2725	0.77	90,000	1.08	2.9	2.68	0.03	0.04
	440-C	3270	0.77	105,000	1.295	2.0	1.54	0.15	0.075
440-C	Carbon	4875	0.77	---	1.755	61.0	28.8	0.155	0.155
	GST	6500	0.77	---	2.34	511.0*	218.0	0.18	0.18
	GST	8125	0.77	---	2.925	125.0*	42.5	0.18	0.18
	GST	9750	0.77	---	3.55	125.0*	36.2	0.29	0.29
Liquid Oxygen									
440-C	Carbon	5190	0.77	---	1.87	80.0	42.7	0.34	0.16
	GST	6920	0.77	---	2.49	22.0	8.8	0.036	0.036
	Carbon	8650	0.77	---	3.115	220.0	70.7	0.35	0.17
	GST	10,380	0.77	---	3.72	52.0	14.0	0.065	0.065

Table 3.7 (Cont.)

Specimens			Load (lb)	Hertz Stress (psi)	Total Distance Traveled (10 ⁻⁶ in.)	Button Wear by Volume (10 ⁶ cu in.)	Button Wear Rate (cu in./10 ¹² in.)	Friction Coefficient	
Plate	Button							Initial	Stabilized
Material	Material	Velocity (fpm)							
Liquid Oxygen									
440-C	440-C	1572	0.77	105,000	0.566	6.0	10.6	0.20	0.11
	440-C	2095	0.77	105,000	0.755	4.5	5.95	0.21	0.08
	B-25	2620	0.77	90,000	0.925	40.0	43.2	0.42	0.30
	440-C	3140	0.77	105,000	1.132	16.0	14.12	0.33	0.15
Liquid Hydrogen									
440-C	440-C	1572	0.77	105,000	0.566	2.3	4.06	0.09	0.09
	B-25	2095	0.77	90,000	0.755	30.0	39.7	0.075	0.45
	440-C	2620	0.77	105,000	0.925	8.4	9.09	0.14	0.14
	440-C	3140	0.77	105,000	1.132	8.8	7.76	0.13	0.13
440-C	B-25	5190	0.77	90,000	1.742	22.0	12.6	0.15	0.15
	Bakelite	6920	0.77	---	2.32	90.0	38.8	0.13	0.13
	Carbon	8650	0.77	---	2.90	24.0	8.3	0.10	0.10
	GST	10,380	0.77	---	3.49	10.0	2.87	0.11	0.11
Nitrogen Tetroxide									
440-C	Carbon	4875	0.77	---	1.755	1.5	0.854	0.02	0.03
	GST	6500	0.77	---	2.34	8.4	3.59	0.025	0.025
	Carbon	8125	0.77	---	2.92	5.0	1.71	0.03	0.04
	GST	9750	0.77	---	3.51	23.0	6.55	6.55	0.120
440-C	440-C	1572	0.77	105,000	0.566	0.69	1.22	0.3	0.011
	440-C	2345	0.77	105,000	0.756	0.75	0.991	0.27	0.015
	440-C	2940	0.77	105,000	0.443	0.9	0.995	0.29	1.01
	440-C	3520	0.77	105,000	1.132	1.7	1.50	0.18	0.01
Inhibited Red Fuming Nitric Acid									
440-C	440-C	1760	0.77	105,000	0.633	1.4	2.21	0.23	0.03
	440-C	2345	0.77	105,000	0.844	1.9	2.25	0.18	0.025
	440-C	2940	0.77	105,000	1.055	3.8	3.60	0.11	0.03
	440-C	3520	0.77	105,000	1.267	4.0	3.16	0.075	0.045
440-C	Carbon	5100	0.77	---	1.835	740.0*	403.0	0.05	0.05
	GST	6800	0.77	---	2.450	23.0	9.35	0.025	0.025
	Carbon	8500	0.77	---	3.060	1350.0*	441.0	0.09	0.09
	GST	10,200	0.77	---	3.672	30.0	8.18	0.07	0.07
* In part by rider erosion									

* In part by rider erosion

The physical condition (leakage path) of an interface is determined by the magnitude of surface roughness or the size of wear debris and transfer particles depending upon which is larger.

At first glance it would appear that debris and transfer particle size are directly related to surface finish. As the particles are plucked from the surfaces, a void space is left behind equal to the volume of the particle. Hence, the resulting surface roughness should be equal to the particle size. This observation is not readily accepted as the basis of experimental evidence.

There has been little systematic work in determining the sizes and shape of transferred or debris particles. Even less has been accomplished with respect to surface finish. Rabinowicz (Ref. 3-8) describes an experimental investigation of copper mated against a low-carbon steel. The materials were chosen because of color differences and the ability to radio-activate the materials. A flat steel surface was rubbed over a hemispherically ended rider leaving a number of wear fragments. Through various mass and length measurements, it was concluded that the adhesive fragments were semiellipsoids having relative dimensions approximately 1.7 by 1 by 0.5. The largest dimension being in the direction of sliding and the smallest normal to the surface. The shape of the particles was fairly independent of the particle size. The average breadth dimension obtained from a histogram distribution was between 0.001 and 0.002 in., although the observed variation was between 0.000 and 0.004 in. The average size of particle measured substantiates the calculated adhesive particle size based on junction theory discussed previously and shown on Table 3-2. Other experimental evidence (Ref. 3-8) substantiates the theory. A conclusion reached from these investigations is that transferred particles are large, ranging from 0.0002 to 0.002 in. for a wide variety of materials in rubbing contact.

To substantiate these results, an experimental program was conducted on a Nitralloy shaft sliding within a Nitralloy ring. These experiments are described in detail in Appendix II. It was observed that wear debris in the form of oxide particles ranged between very small (less than $10\mu\text{in.}$) to particles of $150\mu\text{in.}$ with an average size of $100\mu\text{in.}$ This is not consistent with the adhesive fragment and the ultimate debris size need not be identical. A considerable size reduction could occur before the particle was expelled from the interface. Also, the work of adhesion W_{ab} is not known for nitrided steels. If the work of adhesion is low and combined with the high material hardness (870 kg/mm^2); it is possible that the theory could predict transferred particles closer to the debris size. In any event, the debris particle is substantially large.

It should be noted, however, that all investigators do not concede that debris particles are singular in nature. References 3-33, 3-34 and 3-35, suggest that the large particles are the resulting coalescence of smaller particles.

The effect of wear on surface topography was also investigated experimentally using Nitralloy rubbing elements. Surfaces having an initial finish of 2 in. PTV increased to 5 μ in. PTV when equilibrium wear was reached. The same results were obtained for lubricated and unlubricated interfaces. The details of these experiments are contained in Appendix II. It was concluded that large debris particles can be formed without drastically affecting the surface roughness. This is attributed to:

- the relative size of the particle compared to the entire surface area and the inability to observe the origin of the particle. Thus, the surface disturbance due to a particle may be rough in one very small spot, and hence, undetectable.
- continued rubbing producing a smear and/or back transfer of particles, thus obliterating the origin of the debris.

The possibility of a surface becoming smoother as a result of rubbing is remote. In the absence of a third material, such as very small abrasive particles, it is expected that roughness will increase. The frictional characteristics of surfaces (e.g., figure 3-13) show an increase in friction when the surface finish is decreased. It may be expected that the increased friction produces an increase in wear rate.

A final consideration of the effects of wear can be directed to the number of particles generated in the rubbing process. An estimate of the number of particles, N , generated per unit of sliding distance can be derived from equation (3-1) along with an assumed geometry of the wear particle. For simplicity, consider the particle to be cubic of characteristic dimension, b . The number of particles generated per distance of sliding is:

$$N = \frac{kP}{3\sigma_m b^3} \quad (3-11)$$

To illustrate the number of particles involved, mild steel, Nitralloy, and phenolic-impregnated carbon were assumed to rub against unlike materials under a 125-lb load. The surfaces were in a clean and well lubricated condition. The coefficient of wear was obtained from Table 3-1. The hardness for mild steel was 330,000 psi, and for Nitralloy 984,000 psi. In the case of

carbon, an unlubricated wear rate of 2.5×10^{-9} cu in. per in. was obtained from the literature. The wear rates for the steel materials were

	<u>Unlubricated</u>	<u>Lubricated</u>
Mild Steel	3×10^{-8} in. ³ /in.	2×10^{-11} in. ³ /in.
Nitralloy	8×10^{-9} in. ³ /in.	8×10^{-12} in. ³ /in.

The results shown on Table 3-8 indicate that even if large debris particles are assumed (0.001 in.), the number of particles generated per inch of sliding is substantial. Only in the case of lubricated Nitralloy and mild steel was the number of particles relatively insignificant.

It should be noted that the preceding calculations of Nitralloy wear rates were substantiated by the experimental results contained in Appendix II.

In summary, the effect of wear on the leakage path is characterized by the size of the debris and transfer particles generated within the interface. The sizes of the particles have been experimentally measured in the range of 10^{-4} to 10^{-2} in., depending upon the degree of lubrication. This evidence supports the surface energy-adhesive wear theory presented in Subsection 3.1.2. Thus, it is assumed that equation (3-6) produces a description of the average particle size. In turn, the average particle size describes the conductance clearance or leakage path of any rubbing interface. Lubrication can reduce the particle size by at least a factor of 20, compared with the unlubricated condition and based on the experimental results shown on Table 3-3. The number of particles generated is substantial and would appear to cause continuous particle separation of surfaces in most seal applications.

3.3 Criteria for Dynamic Sealing Interfaces, Contacting Type

This subsection summarizes the design criteria developed in previous sections for uniform contact sealing interfaces. The criteria are applicable to interfaces of arbitrary geometry but limited to those cases where the surfaces are always in contact or separated by wear transfer or debris particles. The effect of hydrodynamic surface separation is considered separately in Section 4. Essentially, the criteria developed consist of delineating the factors influencing friction and wear and, subsequently, the effects of friction and wear on leakage. The criteria are cataloged as follow:

Table 3-8

ESTIMATED NUMBER OF WEAR PARTICLES GENERATED
IN ONE INCH OF SLIDING CONTACT
(load equivalent to 100 psi)

Material	Assumed Cubic Particle of Side, b (in.)					
	1×10^{-6}	5×10^{-5}	1×10^{-4}	5×10^{-4}	1×10^{-3}	
Mild Steel						
	Unlubricated	3×10^{10}	2.4×10^5	3×10^4	2.4×10^2	30
Nitralloy	Lubricated	3×10^7	2.4×10^2	30	0.24	0.03
	Unlubricated	8×10^9	6.4×10^4	8×10^3	64	8
Phenolic Impregnated Carbon	Lubricated	8×10^6	64	8	0.06	0.008
	Unlubricated	2.5×10^9	2×10^4	2.5×10^3	20	2.5
	Lubricated	1×10^9	8×10^3	1×10^3	8	1

- Materials Selection
- Bulk Wear Rates
- Heat Generation on
 - the flow of leakage
 - the surfaces of contact
- Surface Finish
- Leakage Flow and its Predictions

3.3.1 Materials Selection

The choice of rubbing materials must be based on:

- materials with low wear rates and minimum quantity of debris particles generated
- fluid compatibility
- fluid lubricity
- size of transfer and debris particles generated
- applied loads

Minimization of adhesive wear can be achieved by mating hard materials with low surface interaction. This suggests that the material surfaces should have low values of energy of adhesion, W_{ab} . An alternative is to employ materials with high values of W_{ab} and use a boundary lubricant to reduce the effective W_{ab} . Simply hardening a material to its limit does not improve the wear rate significantly as can be seen from a comparison of mild steel Rockwell C 20 (200 kg/mm²) to hardened steel Rockwell C 60 (800 kg/mm²). Since the wear rate varies inversely with hardness; it will be reduced by only a factor of four. Ideally, an improvement of one or two orders of magnitude should be achieved. For example, the ratio of W_{ab}/σ_m for hardened steel is

$$\frac{6200 \text{ ergs/cm}^2}{800 \text{ kg/mm}^2} \approx 8.$$

If aluminum oxide were considered, the ratio is

$$\frac{740 \text{ ergs/cm}^2}{2150 \text{ kg/mm}^2} \approx 0.3.$$

Since wear is proportional to the ratio W_{ab}/σ_m , the wear rate for aluminum oxide is twenty-seven times lower than for hardened steel. Other metalloids such as tungsten carbide, iron carbide, and boron carbide offer similar low energy of adhesion and high hardness. In any event it is important to utilize the maximum obtainable hardness for any material. This also will reduce or eliminate abrasive wear which might result from contaminants or oxide debris.

Like lubricated hard metals can be mated against each other safely. When unlubricated like metals are mated, the wear will be similar to unlike combinations except in the case of clean surfaces. It is frequent practice, however, to use unlike combinations, preferably one a nonmetal. A classification of materials in order of decreasing preference is: diamond, boron carbide, silicon carbide, aluminum oxide, tungsten carbide, titanium carbide, nitrided steel, and carburized steel.

Abrasive wear can become a predominant factor in the wear process if the particles plucked from one rubbing surface oxidize before transfer can take place. The wear debris can be substantially harder than the base material resulting in abrasive wear. For minimum wear, current theory suggests materials with a high hardness to elastic modulus ratio as shown typically on Table 3-4. Again, a hard surface is preferred over a softer surface.

3.3.2 Bulk Wear Rates

Wear rate data of common materials are shown on Tables 3-6, 3-7, and 3-9. The data is particularly useful since they were obtained from wear experiments using many rocket engine fuel and oxidizer fluids as lubricants. The data can be extrapolated with a reasonable degree of success to other conditions of sliding by applying the laws of wear presented in subsection 3.1.2.

3.3.3 Heat Generation

When surfaces rub together, virtually all of the energy dissipated in friction appears in the form of heat at the interface. This frictional heat is, in turn, dissipated through the surface substrate and, eventually, to the surrounding environment. The resulting mean temperature of the surface is, therefore, determined by the geometry, thermal conductivity, and other factors.

The contact of rubbing surfaces occurs at few isolated junctions. Consequently, the heat generated is initially transferred from the junctions to the surface substrate. Since the thermal energy generated per junction is very high,

Table 3-9

WEAR OF SEAL FACES IN LIQUID NITROGEN (Ref. 3-35)

Contact pressure: 200 psi. Peripheral velocity: 8000 fpm

Material		Wear (in.)		Test Time (min)	Comments
Nose	Mating Ring	Nose	Ring		
Carbon	Nitralloy	0.006	0.0002	5	Low leakage
Carbon	Chrome plate	0.005	0.0001	5	Low leakage
Bronze	Nitralloy	0.001	0.0005	3	Severe scoring
Polytrifluoro-chloroethylene	Nitralloy	0.042	Nil	1	Failure
Polytetrafluoro-ethylene	Nitralloy	0.018	Nil	1/2	Failure
Carbon	Titanium carbide	Nil	Nil	5	Low leakage
Aluminum hard anodized	Chrome plate	-	-	1/6	Failure, anodizing case worn through

the temperature at the junction is substantially greater than the mean temperature of the surface. The local junction temperature is often described as the flash temperature. The mean temperature of the surface is directly related to maximum temperature, thus the maximum temperature can be defined as the sum of the two components.

$$T_{\max} = T_{\text{mean}} + T_{\text{flash}} \quad (3-12)$$

Rabinowicz (Ref. 3-8) found experimentally that the flash temperature can be approximated by

$$T_{\text{flash}}(^{\circ}\text{F}) = \frac{V}{2} (\pm \text{a factor of } 3) \quad (3-13)$$

where V is the velocity of rubbing in ft per min.

The prediction of the maximum temperature is important from the following sealing viewpoints:

- At high temperatures, the material properties can become sufficiently relaxed to result in increased wear and possibly localized melting of the surface.
- If the fluid sealed is a lubricant, decomposition can occur at the higher temperature, producing, in turn, adverse wear conditions by the introduction of solid contaminants into the interface.
- The generation of heat can produce changes in the state of the fluid sealed. If the fluid is a liquid, vaporization will influence the mechanics of flow and decrease the degree of lubrication afforded by the liquid. If the fluid is a gas, an increase in temperature can produce a beneficial increase in viscosity.

The amount of heat generated at the rubbing surface can be closely approximated if the friction coefficient is known. Typical values of dynamic friction coefficients can be obtained from many handbooks in addition to the sources identified in Subsection 3.3.2. The heat generated is equivalent to the product of the friction coefficient, normal load, and sliding velocity. As an example, consider two circular surfaces representative of a rotating shaft face seal as shown in figure 3-15.

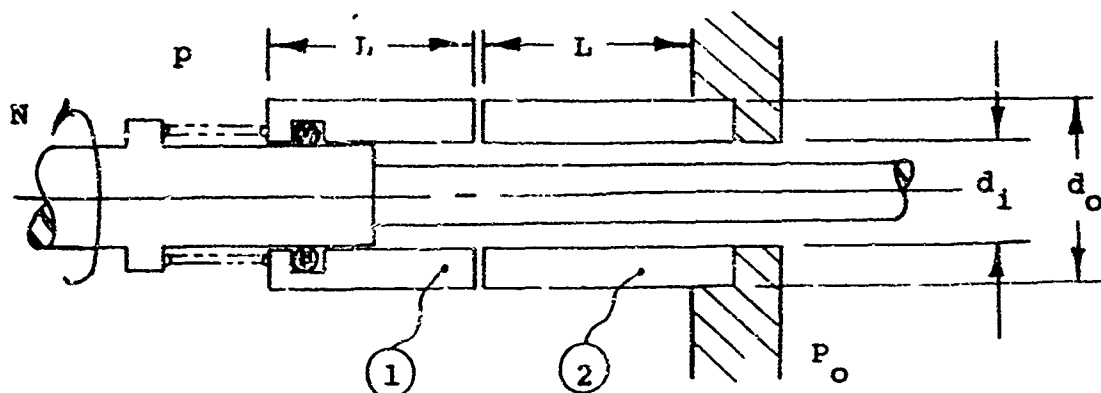


Figure 3-15 Face Seal Description

Unbalanced Face Seal

$$d_i = 1.9 \text{ in.}$$

$$d_o = 2.1 \text{ in.}$$

$$d_m = 2.0 \text{ in. (mean diameter)}$$

$$p = 100 \text{ psi sealed fluid pressure}$$

Fluid sealed: dry air

$$N = 2000 \text{ rpm rotational speed}$$

Material: Surface 1 - carbon graphite
Surface 2 - tungsten carbide (LW-1)

$$\text{Coefficient of friction, } f = 0.2$$

The heat generated;

$$q = 6.42(10^{-3}) f p \pi d_m N \text{ Btu/hr} \quad (3-14)$$

where P = normal interface load obtaining from a summation of forces acting at the interface

$$= \left(\frac{P - P_o}{2} \right) \pi d_m (d_o - d_i), (\text{lb}) \text{ (spring load neglected)}$$

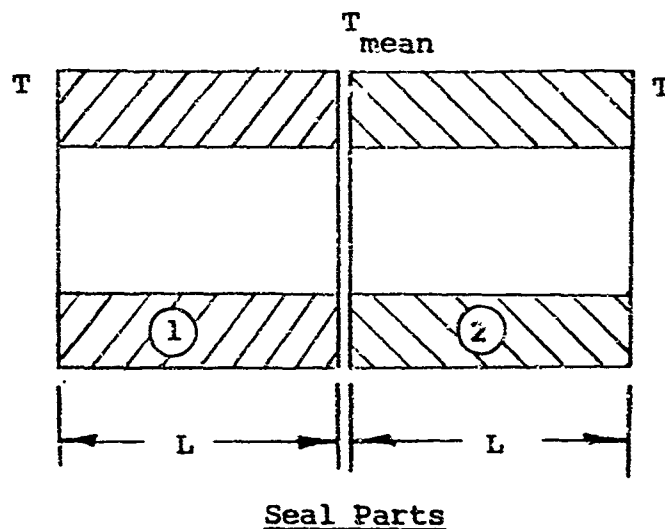
$$N = \text{rpm}$$

$$d_m, d_o, d_i = \text{in.}$$

$$p = \text{psi}$$

$$q = 5.05 \times 10^2 \text{ Btu/hr}$$

The next step in the seal analysis is to determine the maximum and mean temperature at the interface. A comprehensive solution to the problem is indeed difficult because of convective heat losses to the surrounding environment and conductive heat losses to the surrounding hardware. To obtain a solution considerably more must be known about the physical characteristics of the seal. The resulting solution would predict a nonuniform temperature gradient at the interface. To show order of magnitude of effects, however, the geometry and boundary conditions can be simplified for the case of heat transfer solely by conduction. The geometry, boundary conditions, and thermal properties for the seal shown on figure 3-15 can be reduced to two simple parts rubbing together.



where

T = ambient or sealed fluid temperature

k_1 = thermal conductivity of tungsten carbide
 $= 4 \frac{\text{Btu-ft}}{\text{hr-}^\circ\text{F-ft}^2}$

k_2 = thermal conductivity of carbon graphite
 $= 12 \frac{\text{Btu-ft}}{\text{hr-}^\circ\text{F-ft}^2}$

L = length of seal = 1 in.

The heat lost by conduction through both materials must be equal to the heat generated. A heat energy balance may be written

$$q_1 = \frac{k_1 A_1}{L_1} (T_{\text{mean}} - T)$$

$$q_2 = \frac{k_2 A_2}{L_2} (T_{\text{mean}} - T)$$

since $A_1 = A_2 = A$, $L_1 = L_2 = L$, and $q_1 + q_2 = q$

$$q = (k_1 + k_2) \frac{A}{L} (T_{\text{mean}} - T)$$

where $q = \text{Btu/hr}$

$$A = \frac{\pi d_o (d_o - d_i)}{2}, \text{ ft}$$

$$L = \text{ft}$$

Substituting the values given, the mean interface temperature is

$$T_{\text{mean}} = 600 + T_{\text{ambient}} (^\circ\text{F}) \quad (3-15)$$

The flash temperature obtained from equation (3-13) is

$$T_{\text{flash}} = \begin{matrix} 175^\circ\text{F} & (\text{minimum}) \\ 523^\circ\text{F} & (\text{average}) \\ 1570^\circ\text{F} & (\text{maximum}) \end{matrix}$$

Hence, the maximum interface temperature in an ambient environment of 100°F can be obtained using equation (3-12)

$$T_{\text{max}} = \begin{cases} 770^\circ\text{F} & (\text{minimum}) \\ 1200^\circ\text{F} & (\text{average}) \\ 2300^\circ\text{F} & (\text{maximum}) \end{cases}$$

The preceding calculations show the mean interface temperature to be within the recommended maximum for many carbon graphite materials. In addition, the maximum junction temperature of 1200°F is within the maximum temperature limitations of some high temperature carbons. While the preceding analysis can only yield approximate results; it does provide some guide lines for design evaluations. The method of analysis should provide a conservative performance estimate provided that

judicious choice of heat flow paths is made. Minimum interface temperatures can be achieved through improved thermal conductivity or by the use of external coolant fluids circulated near the sealing interface. If the sealed fluid leakage rate is very small (10^{-3} cc/sec for liquids) as is the case in small passage ways, very little heat transfer can be expected via the leakage flow. Other observations which can be made from the previous discussion follow.

The amount of heat generated and maximum temperature is proportional to the normal load and velocity. Thus, for a given set of materials under given conditions of rubbing contact a maximum temperature will be reached at which severe wear occurs. This lends some credence to the use of the pV factor used by some investigators to describe the limitations of material combinations. The term p refers to the load per unit contact area and V refers to the velocity of sliding. From the preceding analysis the following quantities are proportional

$$T_{\max} \sim \frac{f W L V}{A k} + V \quad (3-16)$$

or

$$T_{\max} \sim (ab)pV$$

where $a = \frac{f}{k}$ is a property of the materials

b is a property of the seal structure $\sim L$

If a critical* surface temperature does exist when severe wear occurs, then pV might be considered a constant. However, the geometry of the structure is a variable and when coupled with other heat loss effects, it is doubtful that the factor has all-encompassing significance. It is an interesting approach and further work is suggested to incorporate the additional factors into an evaluation of experimental pV wear-rate data.

The effect of heat generation on the fluid in the interface can be adverse if the fluid is a liquid and the lubrication properties are depended upon for minimum friction and wear. The high temperatures at the contacting junctions produce vaporization of the liquid. The form of the vaporization can be discrete bubbles or elongated bubbles formed in the direction of motion. The following discussion describes visual observations of the state of a liquid in a rotating seal interface.

*Degradation temperature at which welding occurs.

A fixture that permitted viewing of an interface having relative motion was constructed. The seal is carbon rubbing on a glass plate. Figure 3-16 shows the carbon face as seen through the glass plate. The sealed fluid is introduced to the center of the seal assembly by an external connection through the glass plate. The pertinent data on the sealing interface follow.

Rotating Face	Morganite CY10 Carbon Graphite
Stationary Face	Tempered Glass
Waviness of Carbon	10 μ in.
Waviness of Glass	1 μ in.
Outside Diameter	2.25 in.
Inside Diameter	1.87 in.
Sealed Fluid	SAE 10 Oil

The average contact stress at the interface was variable by means of the spring preloading arrangement shown on figure 3-17. The experiments were made with a 5-psi pressure difference across the seal interface. Based on the assumption of linearly varying pressure gradient, the average contact stress was 7 psi.

The observed phenomena showed that cavitation occurs in face seals. Figure 3-18 shows the scattering of an air bubble trapped at the static interface. The elongated bubbles formed are attributed to the effects of surface tension and the pressure gradient acting across the interface. This evidence leads to the supposition that vapor bubbles may form in an elongated shape concentric with the seal interface. Figure 3-19 shows the same static interface area after the entrapped air was eliminated. The evidence shows that all of the surface voids are filled with liquid.

Figure 3-20 shows the formation of the vapor trails as a result of rubbing contact. The vapor is assumed to be mostly water that was in solution with the oil. However, some vapor may also be attributed to volatile hydrocarbons. The trails are almost concentric rings around the interface. This characteristic is somewhat different than the photographic results obtained by General Electric (Ref. 3-). This reference shows a photograph of a large cavitation trail extending one-third the circumference of the seal interface and formed by many small bubbles. To obtain a true photograph of the almost instantaneous occurrence, the photo image must be formed in a very small time interval, otherwise superposition of an image occurs. The variation is attributed to the camera shutter speed and possible differences in the distribution of contact junctions. Figure 3-21 is a magnification of the interface shown in figure 3-20. Approximately 880 line trails per inch are visible. The experiment was conducted at rotational speeds between 600 and 3000 rpm. No significant change in phenomenon was observed. The trails are not fixed at the

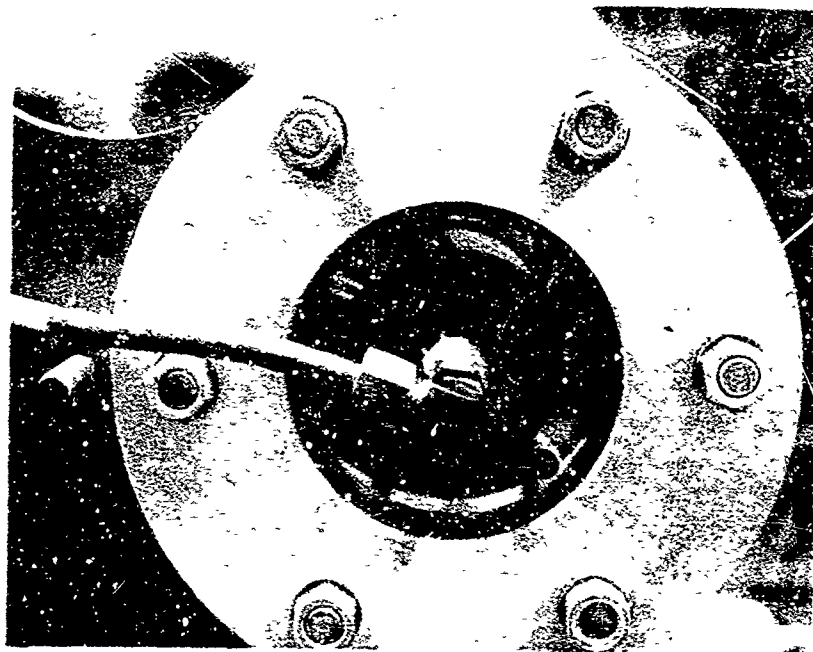


Figure 3-16 End view of face seal apparatus showing the carbon-glass interface

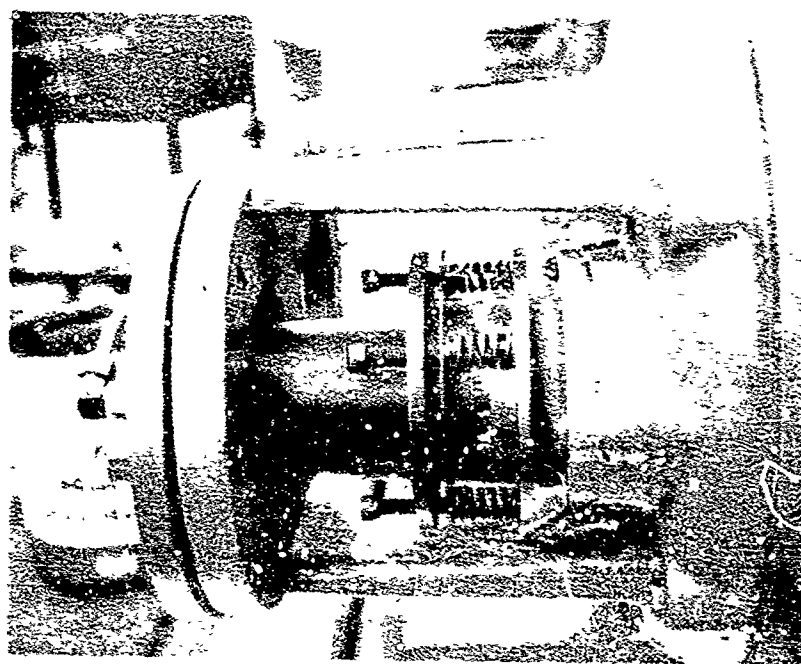


Figure 3-17 Side view of the face seal apparatus showing the carbon seal and adjustable loading mechanism

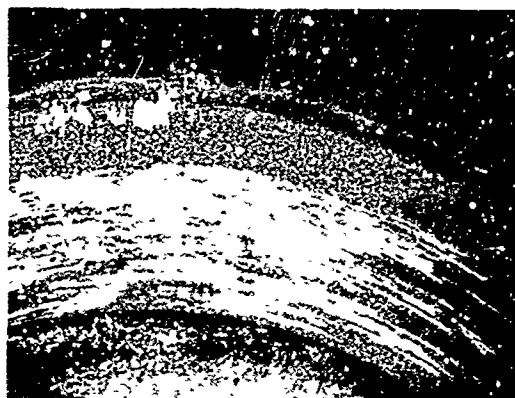


Figure 3-18

Dispersion of air bubble in the static interface

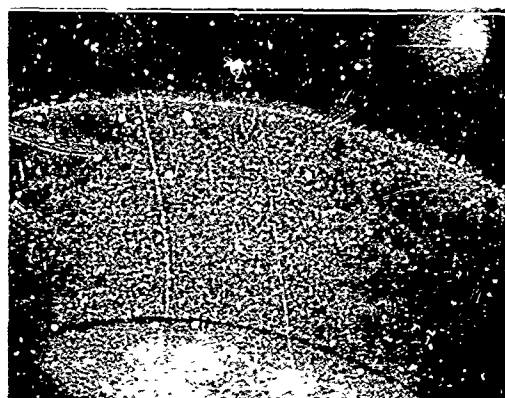


Figure 3-19

All static interface completely filled with a liquid film

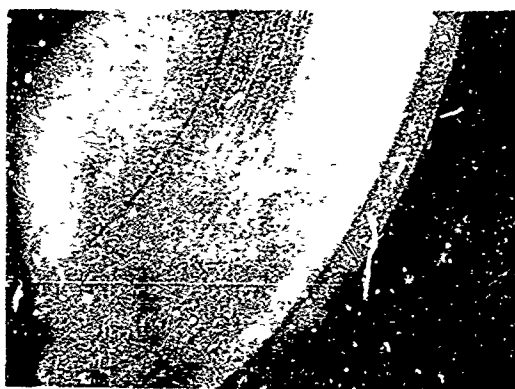


Figure 3-20

Cavitation trails forming after one minute of running at 2000 rpm

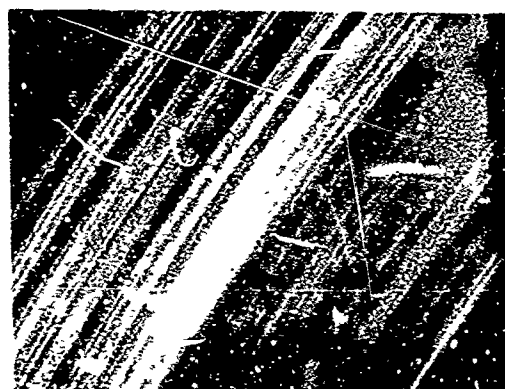


Figure 3-21

View of interface shown in figure 3-19 magnified three times

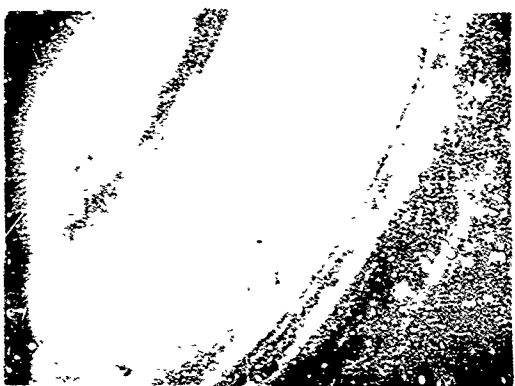


Figure 3-22

Reduction in number of cavitation trails just before rotation ceased

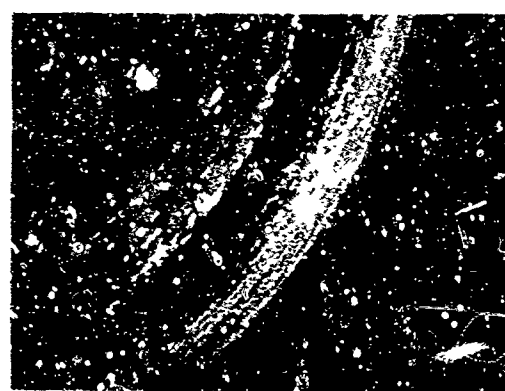


Figure 3-23

Condensation of vapor one minute after rotation ceased

interface but expand outward radially with new vapor trails continuously being formed. Again it must be emphasized that the trails may not really be a continuous bubble but may be composed of many small bubbles.

When the rotation had almost ceased, the vapor began condensing. Figure 3-22 shows the reduction in number of cavitation trails at 50 rpm. When motion ceases, the vapor trails continue to condense. Figure 3-23 shows the interface one minute after motion ceased. Complete condensation occurs in 10 min, thereby restoring the viewed surface to the condition shown in figure 3-19.

An inspection of the glass surface after running for two hours showed small pitmarks of 30 in. depth had formed on the surface. Figure 3-24 shows the interface before and after the experiment. The pitting was attributed to wear and cavitation erosion.

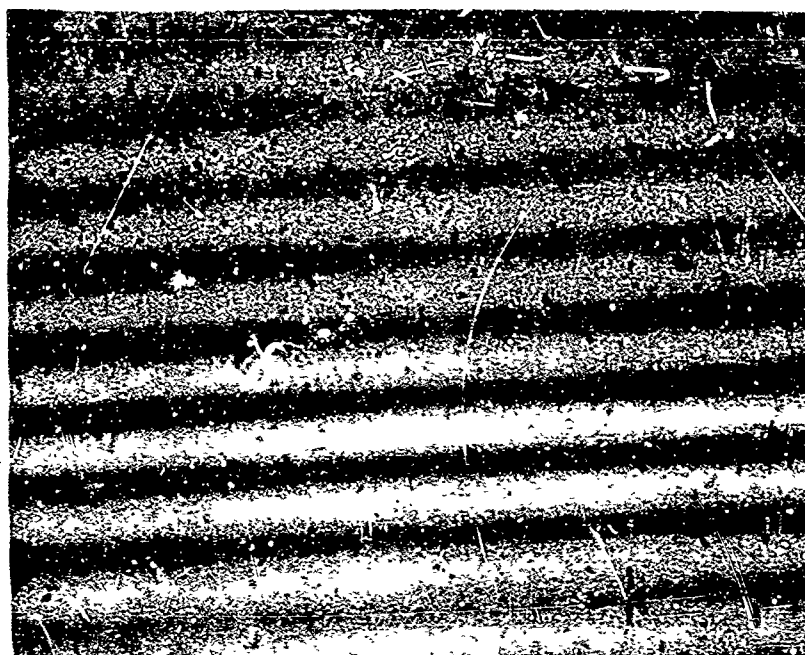
The calculated heat generated at the interface was 42 Btu per hr, assuming a friction coefficient of 0.1 for lubricated carbon-graphite on glass. Temperature measurements made on the glass surface very close to the interface showed an average equilibrium temperature of 160°F. Assuming that the measured temperature is close to the mean interface temperature, the maximum junction temperature from equations (3-8 and (3-9) is

$$T_{\max} = 160^{\circ} + 525 \left(\pm \text{a factor of } 3 \right)$$

$$\begin{aligned} T_{\max} &= 335^{\circ}\text{F (minimum)} \\ &685^{\circ}\text{F (average)} \\ &1730^{\circ}\text{F (maximum)} \end{aligned}$$

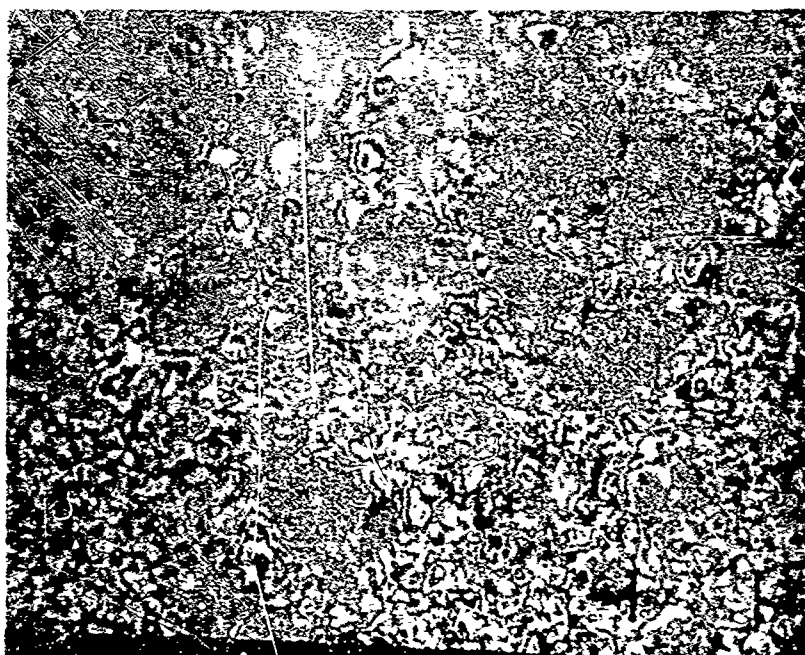
The preceding results show junction temperatures in excess of the vaporization temperature of water entrained in the oil. Hence, it is not surprising that vaporization occurred. Similar experiments using water instead of oil show identical interface characteristics. This leads to the conclusion that even small quantities of easily vaporized liquids (less than 1 per cent of the oil was water) will produce the same effects as a 100 per cent liquid easily vaporized.

In summary, the junction temperature of the interface can be predicted with some degree of reliability. In all cases, the maximum temperature should be less than the melting (or degradation) temperature of the material. For metals rubbing with an oxidizing fluid media, the maximum temperature should be that temperature at which substantial oxide formation occurs. For a mild steel in air this temperature is probably



0.0005 in.

(a) Initially



0.0005 in.

(b) After 1 hr of operation

Figure 3-24 Interference photomicrograph of glass surface

close to 1000°F. At higher temperatures the flakes of oxides are substantially large in size and may promulgate abrasive wear. When lubricants are involved, the maximum junction temperature should at least be less than the degradation temperature of the lubricant. However, interface temperatures lower than the maximum can produce corrosive wear. Because of the wide range of their behavior, no conclusive statements can be made concerning lubricants.

If the interface loads and relative velocity are sufficiently high to produce vaporization of a liquid in the interface, it is reasonable to expect an increase in friction and wear. The ultimate equilibrium conditions would approach the rubbing characteristics of the surfaces solely in the presence of the vapor. This conclusion is somewhat substantiated by the friction results of various carbon materials in air and liquid nitrogen shown on figure 3-25. If the mean interface temperature is assumed to be -320°F, the maximum average junction temperature based on equation (3-12) would be 770°F, resulting in interface boiling of the liquid nitrogen. In both cases, therefore, the rubbing contact could be described as unlubricated and the friction characteristics expected to be similar.

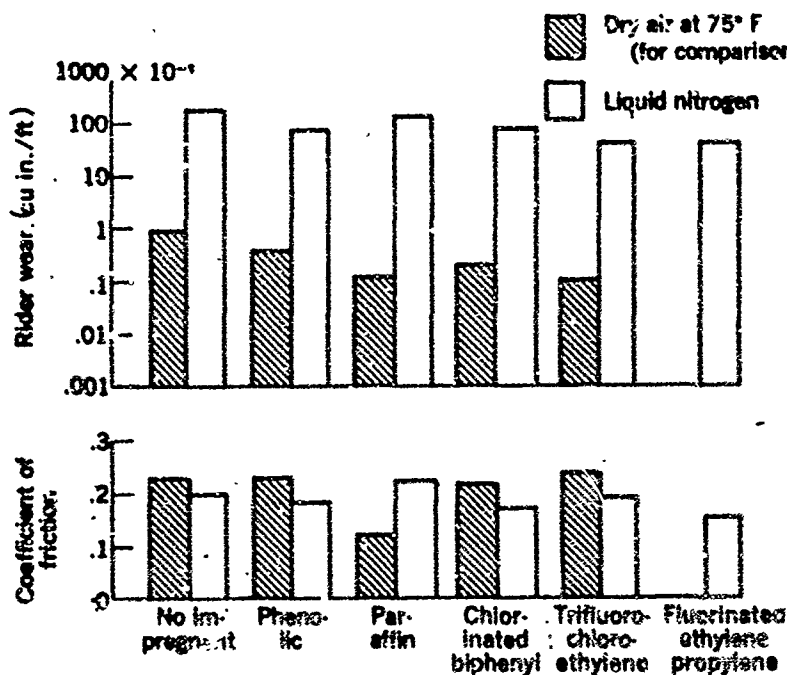


Figure 3-25 Wear and friction of organic impregnated carbons in liquid nitrogen. Sliding velocity, 2300 fpm; load, 1000 gm; disk, 304 stainless steel. (Ref. 3-36)

3.3.4 Surface Roughness

The size of debris particles generated in rubbing contact were described as being larger than 100 μ in. for most materials. Consequently, the size of the particle influences the leakage path of a seal, depending upon the relative influence of surface roughness and waviness. The resulting extremes of interface contact can be described schematically (figure 3-26).

To achieve minimum fluid leakage through an interface, the total roughness of the mating must be less than the average size of the wear debris particles. This suggests that the maximum roughness of one surface be 50 μ in. PTV or the approximate equivalent of 18 μ in. rms. This value is consistent with minimum friction-roughness characteristics of materials and shown typically on figure 3-13. It also produces an additional explanation for the frictional behavior demonstrated on this figure. When the surfaces are rough, wear will be mostly adhesion because mating surfaces can come into contact. When the surfaces are smoother, the debris fragments separate the surfaces and can produce abrasive wear. If the average particle is the same as the total roughness, both wear effects occur but abrasion is minimized due to minimum effective forces on the particles and the presence of abrasive particles, similarly, minimizes adhesion.

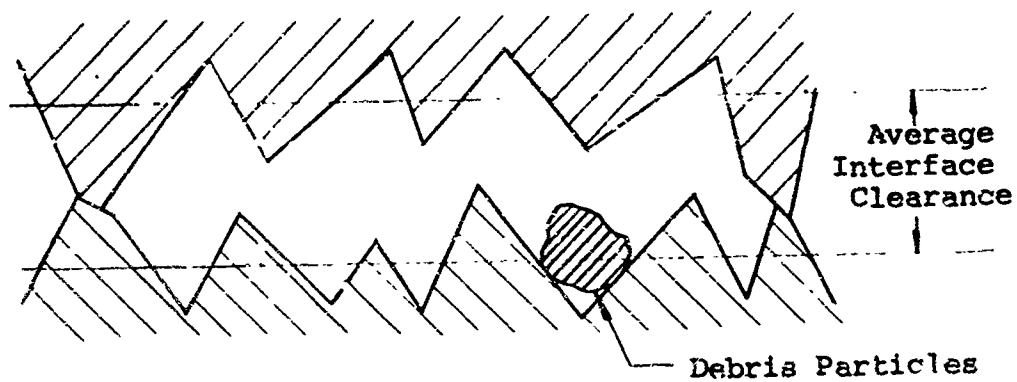
In summary, the roughness of surfaces in rubbing contact should not exceed 50 μ in. PTV. An optimum or minimum roughness should, therefore, be based on the economy of surface fabrication. Generally, flat surfaces of 20 μ in. PTV roughness and 15 μ in. in waviness are easily obtainable. Curved surfaces of contact, however, pose mating problems identified as out-of-roundness. Further discussion of this problem is contained in Appendix II.

3.3.5 Leakage Flow and Its Prediction

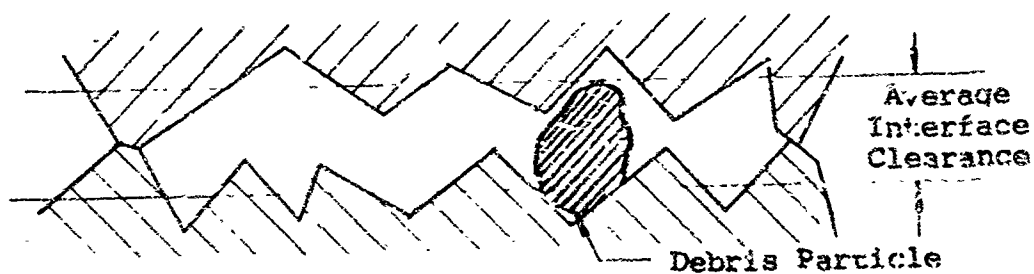
The conclusion concerning the relative influence of debris and transferred particle size may be restated:

The physical condition (leakage path) of an interface is determined by the magnitude of surface roughness or the size of wear debris and transfer particles depending upon which is larger.

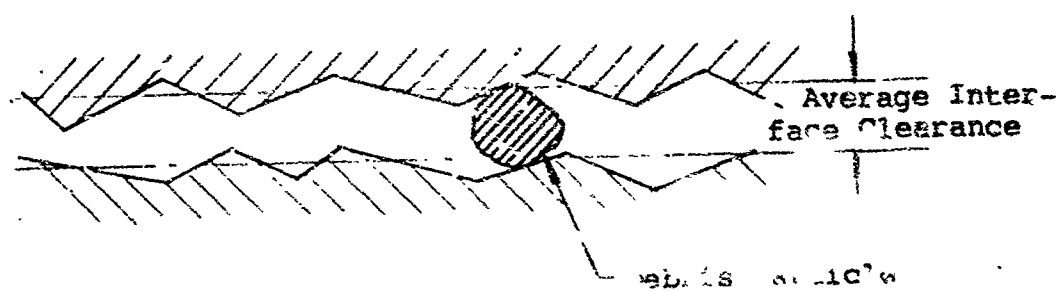
If the roughness is always less than the particle size, the particles generated will separate the surfaces. The separation distance can be defined as an equivalent uniform leakage channel height h , and should be numerically equal to the average particle size generated. It must be realized that particles



Debris particle smaller than
surface roughness



Debris particle equal to the
surface roughness



Debris particle greater
than the surface roughness

Figure 3-26 Effect of particle size on interface clearance

larger than the average will occur. An experimental investigation by Rabinowicz (Ref. 3-8) showed that the majority of particles generated for copper sliding on copper were smaller than the average. Figure 3-27 shows a distribution diagram of the particles generated. Only 20 per cent of the total particles were greater than the average.

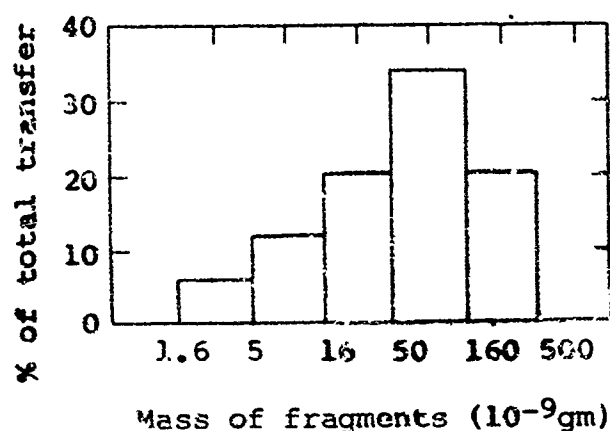


Figure 3-27 Distribution of copper fragments (Ref. 3-8)

On the basis of these limited data, the effect of larger particles is neglected and the average is assumed to be sufficiently representative of the channel height.

Leakage of a gas through an interface can be calculated by assuming an equivalent channel having a characteristic height h . In turn, the channel height when cubed, becomes the conductance parameter (h^3). A definition and use of the conductance parameter in calculating leakage is described in Subsection 2-5. As an example of its application, assume that laminar compressible flow occurs in direction L , between two flat surfaces having width w and length L . The weight rate of flow,

$$W_g = \frac{\gamma_o w (P_2^2 - P_1^2)}{24 \mu P_o L} \cdot (h^3) \quad (3-17)$$

where (h^3) is the conductance parameter.

For surfaces in rubbing contact, the equivalent channel height should be greater than $100\ \mu\text{ in.}$ The conductance parameter, therefore, is $(h^3) = 10^{-12}\ \text{cu in.}$ The maximum channel height, determined by maximum particle size, is $1000\ \mu\text{ in.}$ The conductance parameter for most materials in rubbing contact can be expected to vary

$$10^{-9}\ \text{in.}^3 < (h^3) < 10^{-12}\ \text{in.}^3$$

To determine particle sizes resulting from specific material combinations in sliding contact, review subsection 3.1.2.

Leakage of a liquid through an interface can be calculated following similar procedures. For example, laminar incompressible leakage between two flat surfaces is

$$W_L = \frac{\gamma W (P_2 - P_1)}{12\mu L} (h^3) \quad (3-18)$$

If the heat generated at the interface as the result of friction produces vaporization, the leakage will be either full vapor or two phase flow. The case of vapor flow can be treated the same as gas flow. Two-phase flow presents additional effects which were studied and discussed in Appendix III. The principal conclusion of the study was that vaporization will reduce leakage. The question of how much probably cannot be answered on a purely analytical basis.

A number of points of view that can be adopted for analysis, no one of which can be expected to be conclusive. In Appendix III, several approaches are pursued, and methods of analysis are developed but are not carried out to a quantitative numerical conclusion.

In particular, three aspects are considered, each leading to a reduction in leakage due to vaporization:

- (1) surface tension directly
- (2) surface tension indirectly through instability of the interfacial film, and
- (3) concurrent two-phase flow

Further effort can be directed either toward completion of the analyses presented or toward consideration of other aspects (e.g., local heating due to dry friction, or effects of larger surface asperities).

The preceding criteria regarding interface conditions are not consistent with the criteria set forth in Reference 3-1, Volume II, which contained the results of initial investigations leading to the present conclusions. The most serious discrepancy may be found in Section 4.4 where the liquid state of a sealed liquid was assumed to exist in the interface of a face seal. Further work, however, showed that vaporization does occur.

The study described in Reference 3-1 was an experimental investigation whereby actual seal leakage rates of liquids were obtained and employed in the laminar incompressible flow equation for the calculation of (h^3) . As an example, equation (3-18) could be used if the leakage rate, sealed fluid pressure, and fluid properties were known. The calculated clearances, h , ranged between 30 and 150 μ in. with an average of 90 μ in. for all experimental data.

In view of the possibility of vaporization, the results must be re-evaluated. Assume for simplicity that equations (3-17) and (3-18) represent the leakage through the seal. The relationship between the liquid and gas leakage is

$$(W)_{\text{Liquid}} = \left[\frac{\gamma_{OG}}{\gamma_L} \right] \left[\frac{\mu_L}{\mu_G} \right] \left[\frac{P_2 + P_1}{2P_0} \right] (W)_{\text{Gas}}$$

and, if $P_1 = P_0$,

$$(W)_{\text{Liquid}} = \left[\frac{\gamma_{OG}}{\gamma_L} \right] \left[\frac{\mu_L}{\mu_G} \right] \left[\frac{P_2 + 1}{2P_0} \right] (W)_{\text{Gas}}$$

The next step is to assume values for the properties of the liquid and gas. In this case, the gas is assumed to be saturated steam and the liquid JP-4 and light oil.

$$P_{2(\text{min})} = 100 \text{ psi}$$

$$P_{2(\text{max})} = 400 \text{ psi}$$

$$P_0 = 14.7 \text{ psi}$$

	Density (lb ^Y /in ³)	Viscosity μ
<u>Gas</u>		
Saturated Steam	2.2×10^{-5} @ 14.7 psi	2.8×10^{-9} @ 400°F
<u>Liquid</u>		
Light Oil	3.1×10^{-2}	
JP-4	9×10^{-6}	

The extreme variations that can be expected are:

$$\begin{aligned} \text{to } (W)_{\text{Liquid}} &= 0.9 (W)_{\text{Gas}} \\ (W)_{\text{Liquid}} &= 34 (W)_{\text{Gas}} \end{aligned}$$

with an average

$$(W)_{\text{Liquid}} = 17 (W)_{\text{Gas}}$$

These results show that leakage for full vapor flow is not substantially different than for full liquid flow. If we consider that liquid and vapor flow are simultaneous, it is reasonable to expect that full liquid flow will predominate since it offers a greater resistance to flow. Hence, the results presented in Reference 3-1 may be considered a close representation of actual conditions. Since the calculated clearance averaged $90 \mu\text{in.}$ and was independent of the surface roughness*, waviness, pressure and viscosity, it is concluded that the results of the previous experimental study do substantiate the present concept of wear particle separation of interface surfaces.

Another factor influencing leakage is the orientation of relative motion between surfaces to the direction of leakage. The two modes of motion shown on figures 3-1 and 3-2 describe linear and rotational sliding effects. The debris generated in linear sliding can be expelled readily from the interface because a fresh surface is continually entering into contact with the smaller surface. This condition is beneficial because

- (1) the heat transfer rate from the interface is improved, consequently interface temperatures are lower, and

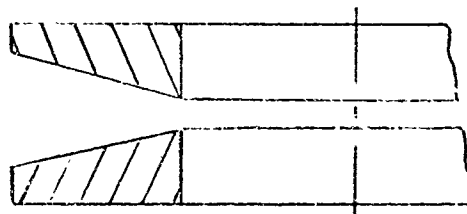
*It should be noted that the roughness and waviness of the experimental seals described in Reference 3-1, Volume II, were in all cases less than the estimated particle size. Therefore, roughness and waviness would have little effect.

- (2) the debris has less chance to collect in the interface because the leakage flow is generally unidirectional and, therefore, can be transported with the leakage.

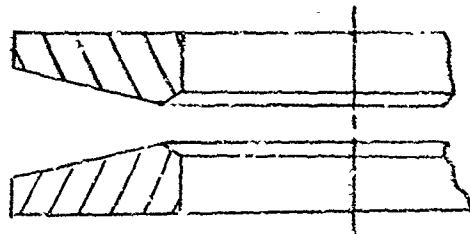
Thus uniform interface wear rates could be expected in the direction normal to the motion. In the direction of motion, however, the wear rate can vary. Consider a plate sliding under a fixed plate as shown on figure 3-28(a). Assuming that the wear rate at each point on the surface is initially uniform, the debris will be uniformly distributed. However, relative motion will cause the debris to congregate at the trailing edge figure 3-28(b). Thus, the trailing edge may have greater abrasion damage than the leading edge. However, the motion is reciprocating and the wear may tend to be uniformly distributed. If the leakage flow velocity is substantial, the particle may be swept downstream as shown in figure 3-28(c). Thus, in spite of the reciprocating motion gross wear occurs at the downstream edge producing a surface as shown in figure 3-28(d).

Rotational sliding, on the other hand, is composed of two surfaces in continuous contact. Thus, the mean interface temperature will be higher and debris will not be expelled readily. Consider two circular plates rubbing together as shown in figure 3-29(a) with a uniform rate of particle generation across the interface. The effects of relative rotational motion will tend to congregate more particles at the outer edge (figure 3-29(b)) producing an interface as shown on figure 29(c). The effects of flow velocity will depend on the direction of flow. If the flow is outward radially, the particles will produce the same bulk abrasive wear at the outer edge (figure 29(c)). If the flow is inward, the larger particles may still be expelled outward but the smaller particles will congregate inwardly (figure 29(d)). Thus, more uniform abrasive wear may occur and the surfaces may remain flat. At very high flow velocities, wear may occur at the inner edge, (figure 29(e)).

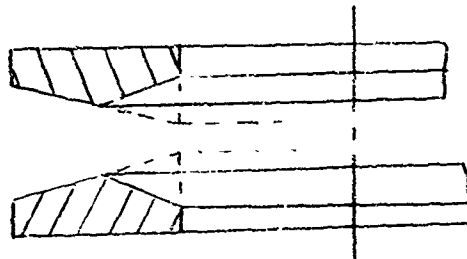
These effects can be expected to be time-dependent. For example, the surface at one interval may have the form



with the majority of wear taking place at the inner edge. Continued rubbing may produce a new surface shape

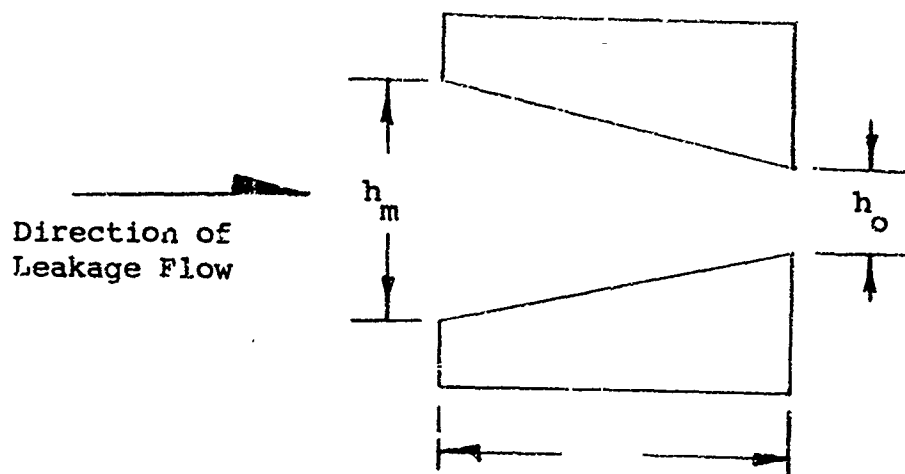


with a high point moving outward radially

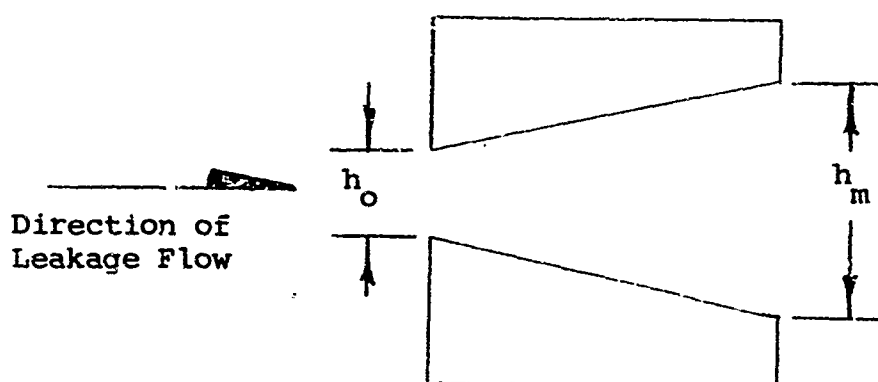


If the interface surfaces are separated by debris and transfer particles having an average dimension h_0 ; it is reasonable to assume that the maximum variation in interface substrate geometry will be $2 h_0$. In other words, the effect of adhesive and abrasive wear at the interface will probably be no greater than twice the average particle size. A clearance larger than $2 h_0$ would imply the intercollision of three particles. The third particle, however, would be relatively free of the interface surfaces, and could be moved about the interface without producing wedging action. Thus, the third particle would not contribute substantially to the wear process and surface deformation.

From the preceding arguments, two hypothetical interface extremes can be postulated and the leakage calculated. The leakage passageways are described in the following illustrations:

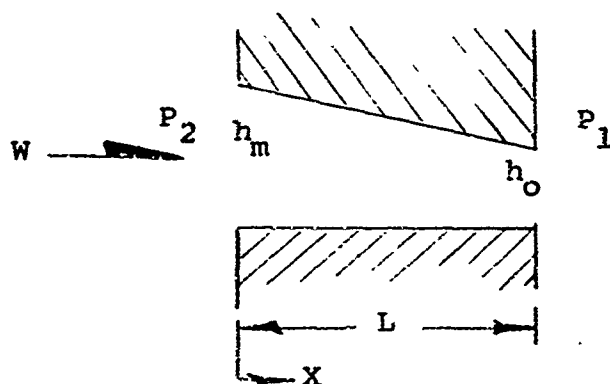


Converging



Diverging

Leakage flow through these interface configurations can be calculated by solving the general Reynolds equation with suitable boundary conditions for the following simplified surface geometry without relative motion:



Linearly Varying Channel

For incompressible laminar flow through a linearly varying channel of width w , the weight rate of flow is

$$W_{\text{Liquid}} = \frac{\gamma_L w (P_2 - P_1)}{6 \mu L} \cdot \frac{h_o^2 h_m^2}{h_m + h_o} \quad (3-19)$$

For compressible laminar flow

$$W_{\text{Gas}} = \frac{\gamma_o w (P_2^2 - P_1^2)}{12 \mu L P_o} \cdot \frac{h_o^2 h_m^2}{h_m + h_o} \quad (3-20)$$

Equations (3-19) and (3-20) are equally valid for a diverging channel. The flow rate is determined by the dimensions of the leakage path and is not dependent on the direction of convergence.

A comparison of uniform channel flow with a linearly varying channel when $h_{\text{uniform}} = h_o$ is

$$\frac{W_{\text{uniform}}}{(h_o^3)} = W_{\text{linearly varying}} \frac{(h_m + h_o)}{2 h_o^2 h_m^2}$$

Assuming $h_m = 2h_o$ for maximum influence of wear,

$$W_{\text{linearly varying}} = 2.7 W_{\text{uniform}}$$

It can be concluded that the effects of small channel variations will have little effect on the weight rate of flow.

When one surface moves at velocity V with respect to the other, the weight rate of flow is:

For a uniform channel;

$$W_{\text{Liquid}} = \frac{\gamma_L w (P_2 - P_1) h^3}{12 \mu L} + \frac{V \gamma_L w h}{2} \quad (\text{incompressible})$$

$$W_{\text{Gas}} = \frac{\gamma_o w (P_2^2 - P_1^2) h^3}{24 \mu L P_o} + \frac{V (P_2 + P_1) \gamma_o w h}{4 P_o} \quad (\text{compressible})$$

For a linearly varying channel;

$$W_{\text{Liquid}} = \frac{Y_L W (P_2 - P_1) (h_o^2 h_m^2)}{6 \mu L (h_m + h_o)} + \frac{V Y_L W h_o h_m}{(h_m + h_o)} \quad (\text{incompressible})$$

$$W_{\text{Gas}} = \frac{Y_o W (P_2^2 - P_1^2) (h_o^2 h_m^2)}{12 \mu L P_o (h_m + h_o)} + \frac{V (P_2 + P_1) Y_o W h_o h_m}{2 (h_m + h_o) P_o} \quad (\text{compressible})$$

If, again, wear is assumed to effect the geometry in the order of $h_m = 2 h_o$, the difference in flow rate between a uniform and linearly varying channel is:

$$W_{\text{linearly varying}} = 2.7 W_{\text{uniform without motion}} + \frac{2V C}{3}$$

$$W_{\text{uniform}} = W_{\text{uniform without motion}} + \frac{V C}{2}$$

where $C = \text{constant}$.

If the magnitude of relative motion is small, the effects can be neglected. At higher velocities, the effects will also be small and may be expected to reach a maximum difference of

$$W_{LV} = \frac{4}{3} W_{UN}$$

Leakage through nonlinear interface surfaces is more difficult to analyze. If h_m and h_o are known, however, the leakage rate of flow can be closely approximated by assuming an average conductance parameter,

$$(h^3)_{\text{avg}} = \frac{(h_m^3 + h_o^3)}{2}$$

and using the equation for uniform channel flow.

It should be noted that variations in the interface surface geometry will influence the pressure distribution across the interface*. In turn, the characteristics of the pressure distribution affect the normal interface loading, and consequently, the wear rate. Minimum interface separation h_0 , however, is determined by transfer and debris particle size. Therefore, the leakage rate through an interface is virtually independent of the surface forces, at least in the region of mild wear conditions.

In summary, the following procedures are suggested for the prediction of leakage through a dynamic sealing interface.

- Obtain the maximum normal load on the sealing interface and material hardness.
- Calculate the estimated transfer particle size from equation (3-6), Subsection 3.1.2.
- Use the particle size dimension as an equivalent channel clearance and calculate leakage using the appropriate laminar flow equation. (In some instances turbulent flow can prevail. Refer to Reference 3-1, Volume II, Section II for details).
- If the fluid is a liquid, apply equation (3-8) to determine the state of the liquid. If the mean interface temperature is above the vaporization temperature (at maximum pressure); apply the flow equation for gases. If below the critical, the incompressible flow equation may provide a close approximation.

*Refer to Section 6.2, Volume II, Reference 3-1 for further discussion of the effect of surface geometry on the pressure distribution.

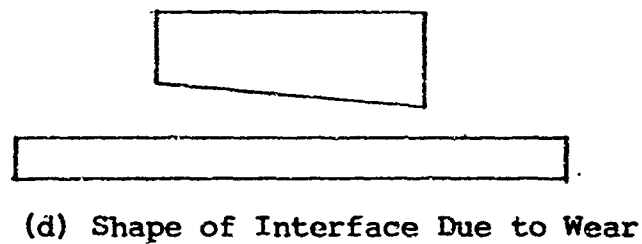
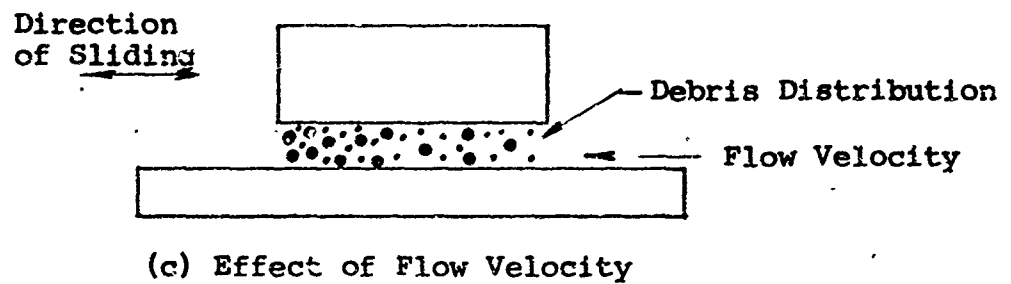
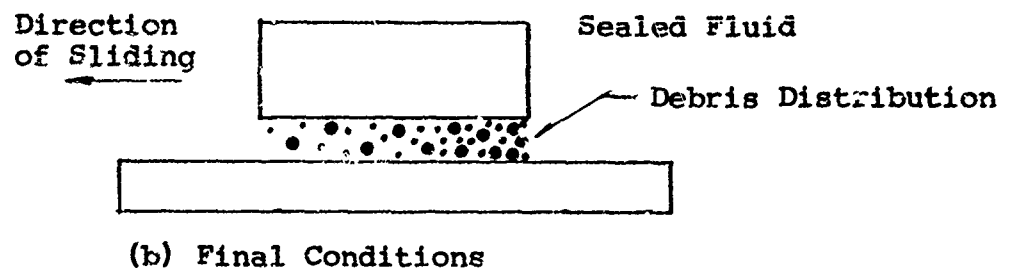
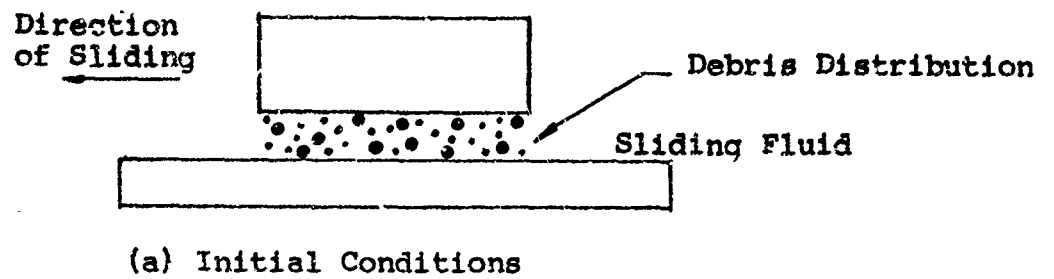
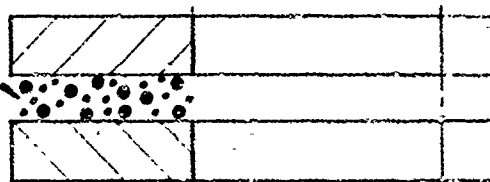


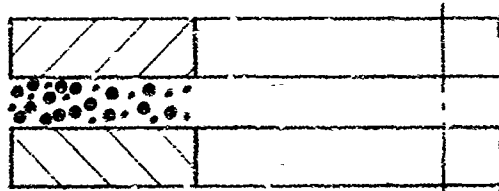
Figure 3-28 Effect of particle generation on a linear sliding interface. Assuming initial uniform wear particle generation on the interface surfaces

Motion normal to the cross section

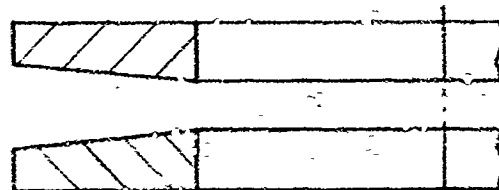
Debris
Distribution



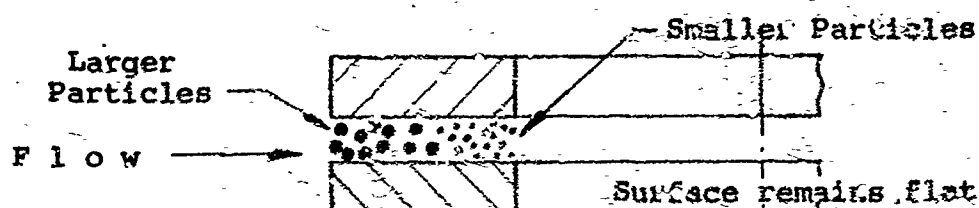
(a) Initial Conditions



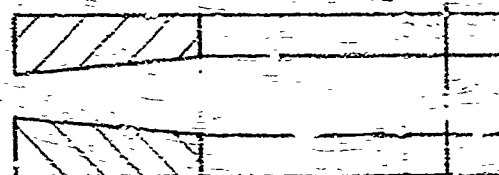
(b) Effect of Rotation



(c) Wear of the Surface Substrate



(d) Nonuniform Distribution
of Particles Result
from Flow Velocity



(e) Effect of High Flow Velocity
on the Surface Substrate

Figure 3-29 Effect of particle generation on
a rotational sliding interface

3.4 References

- 3-1 Paul A. Bauer, Myron Glickman and Frank Iwatsuki, Analytical Techniques for the Design of Seals for Use in Rocket Propulsion Systems, Volumes I and II, AFRPL-TR-65-61, IIT Research Institute, Chicago May 1965
- 3-2 Rocketdyne Division, North American Aviation, Rocket Engine Valve Poppet and Seat Design Data, Report RPL-TDR-64-68, May 1964
- 3-3 General Electric, Design Criteria for Zero-Leakage Connectors for Launch Vehicles, Final Report, Contract NAS8-4012, NASA, George C. Marshal Space Flight Center, 15 Mar 1963
- 3-4 E. Finken "Surface Roughness in Wear," Wear 6, 293-302 (1963)
- 3-5 John T. Burwell, "Survey of Possible Wear Mechanism" Wear 1 No. 2 (1957)
- 3-6 F. P. Bowden and D. Tabor, The Friction and Lubrication of Solids Part II, Clarendon Press, Oxford (1964)
- 3-7 J. F. Archard, "Contact and Rubbing of Flat Surfaces" J. Appl. Phys. 24, 981-988 (1953)
- 3-8 E. Rabinowicz, Friction and Wear of Materials, John Wiley (1965)
- 3-9 R. L. Johnson, M. A. Swikert and J. M. Bailey, Wear of Typical Carbon-Base Sliding Materials at Temperatures to 700°F NACA TN 3595 (1956)
- 3-10 J. F. Archard and W. Hirst, "The Wear of Metals under Unlubricated Conditions" Proc. Roy. Soc. (London) 236A, 397-410 (1956)
- 3-11 M. Kerridge and J. K. Lancaster, "The Stages in a Process of Severe Metallic Wear: Proc. Roy. Soc. (London) 236A, 250-264 (1956)
- 3-12 E. Rabinowicz and D. Tabor, "Metallic Transfer between Sliding Metals: An Autoradiographic Study" Proc. Roy. Soc. (London) 208A, 455-75 (1951)
- 3-13 I-Ming Feng, "Analysis of the Effect of Various Factors on Metal Transfer and Wear between Specimen Pairs of Same Metal and Same Shape I. The Basic Scheme of Formulation of Metal Transfer and Wear" J. Appl. Phys. 26, 24-27 (1955)
- 3-14 E. Rabinowicz "Autocorrelation Analysis of the Sliding Process" J. Appl. Phys. 27 No. 2 131-135 (1956)

- 3-15 E. Rabinowicz "Influence of Surface Energy on Friction and Wear Phenomena" J. Appl. Phys. 32 No. 8 1440-1444 (1961)
- 3-16 E. Rabinowicz, "Effect of Surface Energy on the Wear Process" Paper 63 Lub S-1 American Society of Mechanical Engineers (1963)
- 3-17 L. F. Coffin, "Some Metallurgical Aspects of Friction and Wear" p. 36-66, Proceedings of the Symposium on Friction and Wear Elsevier (1959)
- 3-18 C. L. Goodzeit, "The Seizure of Metal Pairs during Boundary Lubrication" p. 67-83 Proceedings of the Symposium on Friction and Wear Elsevier (1959)
- 3-19 C. I. Smithells, Metals Reference Book Butterworth, London (1955)
- 3-20 D. McLean, Grain Boundaries in Metals Oxford University Press, New York (1957)
- 3-21 M. Antler, "The Lubrication of Gold" Wear 6 44-65 (1963)
- 3-22 M. M. Kruschov, "Resistance of Metals to Wear by Abrasion, as Related to Hardness" Institute of Mechanical Engineers Proceedings, Conference on Lubrication and Wear London (1957)
- 3-23 T. L. Oberle, "Properties Influencing Wear of Metals" J. Metals 3 No. 6 1951
- 3-24 R. T. Spurr and T. P. Newcomb, "The Friction and Wear of Various Materials Sliding against Unlubricated Surfaces of Different Types and Degrees of Roughness" Institute of Mechanical Engineers Proceedings, Conference on Lubrication and Wear London (1957)
- 3-25 E. Bisson and W. S. Anderson, Advanced Bearing Technology NASA SP-38 (1964)
- 3-26 W. Hume-Rothery and R. J. Wyllie, Proc. Roy. Soc. (London) 181A 332 (1943)
- 3-27 C. A. Snavely and C. L. Faust, J. Electrochem. Soc. 97, No. 3, 99 (1950)
- 3-28 B. Avient, J. Goddard and H. Wilman, Proc. Roy. Soc. (London) 258A, 159 (1960)
- 3-29 F. P. Bowden and D. Tabor, The Friction and Lubrication of Solids, Clarendon Press, Oxford (1954)

- 3-30 J. F. Archard, "Single Contacts and Multiple Encounters" J. Appl. Phys., 32, No. 8, 1420-1425, 1961
- 3-31 M. F. Butner, "Propellant Lubrication Properties Investigation" WADD-TR-61-77, Rocketdyne, Division of North American Aviation, Jun 1961
- 3-32 M. Kerridge "Metal Transfer and the Wear Process" Proc. Phys. Soc. (London) 68B (1955)
- 3-33 M. Kerridge and J. K. Lancaster, Proc. Roy. Soc. (London) 236A, 250 (1956)
- 3-34 M. Cocks, J. Appl. Phys. 29 (1958)
- 3-35 J. E. Wolfe and R. E. Connelley, "Development of Seals for Rocket Engine Turbopumps" Am. Soc. Lub. Engr. Preprint No. 58LC-5, Oct 1958
- 3-36 D. W. Wisander and R. L. Johnson "Wear and Friction of Impregnated Carbon Seal Materials in Liquid Nitrogen and Hydrogen" p. 210-218 Vol 6 Advances in Cryogenic Engineering (K. D. Timmerhaus, editor) Plenum Press (1960)

3.5 Symbols

A	= area of contact
d	= wear fragment diameter
F	= friction force, (lb)
F_p	= friction force contribution due to ploughing, (lb)
F_s	= friction force contribution due to shear, (lb)
f	= friction coefficient
H	= hardness, (kg/mm^2 or dynes/cm^2)
h	= leakage path dimension
(h^3)	= conductance parameter
k	= adhesive wear coefficient
k'	$k' = k/3$
k''	$k'' = k'/H$
k'''	$k''' = \text{abrasive wear coefficient}$
k_1, k_2	= thermal conductivity, ($\text{Btu-ft/hr-}^\circ\text{F-ft}^2$)
L	= length
N	= number of wear particles generated per distance of sliding
P	= load
P_1	= downstream fluid pressure, (psi)
P_2	= upstream fluid pressure, (psi)
q	= heat flow, (Btu/hr)
T	= temperature, ($^\circ\text{F}$)
W_{ab}	= work of adhesion, (ergs/cm^2)
W_g	= weight rate of gaseous flow, (lb/sec)
W_l	= weight rate of liquid flow, (lb/sec)
w	= width
z	= wear rate, ($\text{in.}^3/\text{in.}$)
γ	= free surface energy per unit area, (ergs/cm^2)
γ	= specific weight, (lb/in.^3)
γ_0	= specific weight standard conditions, (lb/in.^3)
μ	= viscosity
σ	= normal stress
σ_m	= Meyer hardness, flow pressure, (psi or kg/mm^2)
τ	= shear stress, (psi)

4. BOUNDARY LUBRICATION - LUBRICANT FILMS

A lubricant can be described as a substance, generated within or artificially induced between two rubbing surfaces, that reduces friction and wear. The effect of a lubricant as described in Section 3 is to drastically reduce the interaction between contacting surfaces. This condition is achieved by the partial or complete separation of the surfaces through the action of the lubricant.

Complete separation of surfaces is developed by thick films of a third material. When the third material is a solid, the mode of lubrication is generally referred to as solid film lubrication. If the third material is a gas or liquid, the process is referred to as fluid lubrication, identified as hydrodynamic or hydrostatic lubrication. In the latter case, the mechanical properties of the fluid and the mechanics of surface motion are the factors governing surface separation. This form of lubrication is considered separately in Section 5.

Partial separation of surfaces is produced by thin films of lubricants where the film is of the order of magnitude of one monolayer. This form of lubrication is called boundary lubrication. The interaction between surfaces is achieved by changing the surface properties through chemical or surface energy effects or simply by improving the heat transfer and reducing the interfacial temperature.

The forms of lubrication considered in this section can be summarized as boundary and solid film lubrication. Since each is theoretically complex with respect to surface interactions only a general description can be presented within the scope of this study. Because of this limitation, liquid lubricants are not considered except on an effect basis (Section 3). Each of the following classes of lubricant materials, unless otherwise noted, is considered in this section.

Boundary Lubricants

- Materials generated within the interface by sliding, e.g., oxides and nitrides formed by chemical reaction and heat (Refer to Section 3)
- Abrasion-resistant films such as chromium and rhodium (Refer to Section 3)
- Materials used in the construction of seals that have low friction characteristics. These materials are identified as base materials and are further subclassed as

- Solid organic bases
- Inorganic bases
- Composite bases

Solid film materials

- Chemically reacted films
- Self-adhering films
- Bonded solid films

Liquid lubricants (Refer to Section 3)

4.1 Boundary Lubricants

It is generally recognized that the surface layers of solids exist in a chemical and physical state considerably different from the bulk material. A description of the constitution of seal surfaces is contained in Reference 4-1, and should be reviewed for an understanding of seal surfaces. In the absence of bulk material influences, the wear properties would be determined solely by the surface state. However, in the application of pressure and motion to irregular contacting bodies, considerable bulk deformation occurs. If the deformation is small and the surface state remains essentially unchanged, little effect will be noted on the adhesive component of wear. If, on the other hand, the surface state is modified by bulk processes, wear may be altered considerably.

Examples of this may be seen in the sliding of two metals separated by a thin film of chemically different species (oxides or other). If the metals are hard and the film is soft and pliable, deformation may occur without damage to the film. Sliding usually occurs within the film or at the film/metal interface. Friction remains unchanged as long as the film is not worn away. If the film is hard and friable, contact will occur between the two metals. Friction will then be determined by the bonding between the metals as well as by the film. Covalent bonds thus formed are usually weak and friction and surface damage are low. If the bond is metallic, the friction will be high and separation may occur within the bulk metal. Thus, surface damage occurs and the potential for further film penetration increases. If the metals are soft, the deformation will be increased, thus, the total number of atoms in contact will increase. Not only will this increase the total friction of the film, but metal displacement may take place within the bulk, thereby destroying the geometry required for low friction sliding.

In practice, the differences between the requirements of the interface and those of the substrate are usually irreconcilable. Thus, current design practice is to use a two-component system. The structural material fulfills the substrate requirements, and an artificial or natural surface film provides the necessary interfacial conditions. This imposes an additional requirement to

describe the necessary film-substrate relationship; maintenance of a continuous film in the area of contact at all times. The methods currently used for supplying and maintaining surface films are listed in Table 4-1. The ranges of usefulness and design considerations of one-component (without film) and two-component systems (with film) are considered in the following sections.

Table 4-1

TECHNIQUES FOR SUPPLYING FILMS AT INTERFACES

Type of Film	Film Materials	Supply Technique
1. Chemically reacted	Oxides, sulfides, nitrides, chlorides	Initially applied, supplied from reservoir as gas or liquid
2. Chemisorbed	Fatty acids, extreme pressure lubricants	Initially applied, supplied from reservoir as liquid
3. Physically applied solids	MoS ₂ , graphite, polytetrafluorethylene	Initially applied, supplied from reservoir as solid (must physically contact wear track), supplied from composite structural element
4. Physically applied	Oil lubricants	Initially applied, supplied from reservoir as liquid or vapor
5. Bonded solids	MoS ₂ + binder graphite + binder metal films	Initially applied only

4.1.1 Solid Organic Base Materials

Many organic materials have been used in unlubricated sliding, both as structural materials and as thin films applied to metal substrates. The advantages of their use are:

- low interent friction
- good performance under marginal lubrication
- good damping characteristics

The major disadvantages are:

- poor thermal conductivity
- poor dimensional stability
- large differences in thermal expansion coefficients from metals.

The disadvantages have led to blending the substances with inorganic materials to improve performance characteristics. A complete listing of the properties and performance characteristics is beyond the scope of this report. Summary data on materials for space applications are listed in Table 4-2. These data are representative values and should not be used for design purposes. More comprehensive design data can be obtained from References 4-2 through 4-5, and from manufacturers' literature.

The lowest friction of any plastic is provided by Teflon. The major limitations in its use are thermal degradation from frictional heating and its poor dimensional stability under load (cold flow). Addition of metal fillers improves its mechanical properties and increases the thermal conductivity (thereby decreasing interfacial temperatures), but also increases friction. Optimum performance is provided by a thin film of Teflon on a metal substrate. The recent development of polyimides represents an improvement in mechanical properties. New fluorocarbons are under development (Ref. 4-6), although no design data are currently available.

4.1.2 Inorganic Base Materials

Ceramics and cermets offer advantages due to their high hardness, high temperature stability and minimum cold welding tendencies. Disadvantages arise from their high friction and brittleness. Best use is made of these materials as high temperature rubbing elements in face seals, although their fatigue life is low and failure is almost always catastrophic. Typical performance characteristics are listed in Table 4-3.

4.1.3 Composite Base Materials

The more desirable properties of two or more materials may be obtained by combining the materials in a composite structure. The structures may have the following forms:

- Metals incorporating microinclusions
- Sintered powdered metals impregnated with:
 - oils
 - solid organic lubricants
 - solid inorganic lubricants
- Porous ceramics impregnated with:
 - solid organic lubricants
 - solid inorganic lubricants
- Inorganic fiber structures incorporating:
 - solid organic lubricants
 - solid inorganic lubricants

Table 4-2

PROPERTIES OF ORGANIC MATERIALS

	Maximum Load Capacity		Dry Friction Coefficient	Relative Wear in Sliding	Maximum Usable Temp. (°K)	Vacuum Evaporation (gm/cm ² sec) Room Temp.	Radiation Resistance	Thermal Expansion (per °F)	Thermal Conductivity (Btu/°F/hr/ft ² /in.)
	(kg/cm ²)	(ksi)							
Fluorocarbon (TFE + Filled Teflon)	4.2	6	0.05 - 0.4	High	530	10 ⁻⁹	Good	10 ⁻⁹	1.7
TFE with Glass Filler	8.4	12	0.05 - 0.4	Low	530	---	Good	9 x 10 ⁻⁵	2.1
TFE with Metal Filler	8.4	12	0.05 - 0.4	Low	500	---	Good	---	---
Polyamide (Nylon)	8.4	12	0.15 - 0.7	High	425	10 ⁻⁷	Good	6 x 10 ⁻⁵	1.7
Acetal (Delrin)	7.0	10	0.15 - 0.35	Moderate	350	10 ⁻⁷	---	5 x 10 ⁻⁵	1.6
Polyamide	9.2	13	0.15 - 0.55	Very low to moderate	775	---	Excellent	3 x 10 ⁻⁵	2.2
Polyamide with Graphite Filler	6.3	9	0.25	High	775	---	Excellent	2 x 10 ⁻⁵	---

References 4-2, 4-3, 4-4, 4-5, 4-6, 4-7, 4-8, 4-9, 4-10, 4-12.

Table 4-3

FRICTION PERFORMANCE OF CERAMICS AND CERMETS

Material	LT-2	LT-1B	LT-2	LT-2	Rene 41	Boron Nitride
Composition	W-25-Cr-15 Al ₂ O ₃	Cr-19Al ₂ O ₃ 20Mo-2TiO ₂			Ni-19Cr-11Ca-10Mo-3Ti-1.5Al-0.09Cr-0.005B	
Sliding Against	LT-1B	LT-1B	LT-1B	LT-2	LT-1B	Boron Nitride
Atmosphere	Air	Air	Air	Vacuum	Vacuum	Vacuum
Friction Coefficient at °F	-140	---	---	0.51	---	---
	90	0.48	0.6	0.48	0.95	0.61
	500	---	---	---	---	0.67
	1200	---	---	---	---	0.35
	1300	0.033	0.035	0.035	---	---
	1500	0.30	0.38	0.35	3.93	0.75
	1700	0.30	0.45	0.39	---	---
	1900	0.31	0.50	0.31	0.83	---
Wear (in. ³ /ft)	3000 psi	1.2 x 10 ⁻⁷	1 x 10 ⁻⁷	---	---	---
	7500 psi	2 x 10 ⁻⁷	1.8 x 10 ⁻⁷	2 x 10 ⁻⁷	---	---
	12000 psi	---	---	---	1 x 10 ⁻⁶	1 x 10 ⁻⁶
	15000 psi	---	---	5 x 10 ⁻⁷	---	---
Source	4-13	4-13	4-13	4-14	4-14	4-15

- Sintered organic powders impregnated with:

- oils
- solid organic lubricants
- solid inorganic lubricants

- Compressed powder mixtures of:

- metals
- solid organic lubricants
- solid inorganic lubricants

The performances of typical composites are summarized in Table 4-4. The basic scheme is to take a satisfactory structural material and to combine with it a sufficient amount of material with low friction properties to assure satisfactory performance. In general, it is desirable to incorporate a substance which will form a continuous film over the interface under the action of sliding, so that the structural materials do not contact. The number of possible combinations is infinite and the designer is referred to References 4-2, 4-3, 4-4, 4-5, 4-7, 4-8, 4-9, 4-10, and 4-11 for specific applications.

Performance characteristics of composite structures are usually a compromise between those of the structural material and those of the filler material. Thermal tolerance limits are usually established by the weaker of the two.

4.2 Solid Film Materials

A film of solid material with low friction properties on a substrate of high hardness can produce acceptable friction performance and minimum wear. This technique has received considerable attention for space devices and countless numbers of materials and application methods have been investigated. The major problems have been short wear lives and lack of performance reproducibility.

The various techniques for lubricating with solid films are listed in Table 4-5. The materials that show the best performance characteristics for each technique are also listed. The principles underlying each technique and their limitations are discussed below.

4.2.1 Chemically Reacted Films

In this technique, lubricant films are formed by chemical reaction of the surface layer of the bearing material with a vapor or liquid. Such films are thin and easily worn away, thus requiring continuous or periodic replenishment for severe duty.

Table 4-4

PERFORMANCE CHARACTERISTICS OF COMPOSITE MATERIALS

	Sliding Against	Atmosphere	Temperature		Load	
			(°K)	(°F)	(kg)	(lb)
Sintered Cu/Teflon	Steel	Air	288-523	59-482	---	---
Sintered Nylon/Oil	---	---	---	---	13.7 kg/cm ²	195 psi
Sintered Nylon/Oil	---	---	---	---	9.5 Kg/cm ²	135 psi
Sintered Cu/MoS ₂	Steel	Air	---	---	4.0	8.8
85% Ag, 5% Cu 10% MoS ₂ (Hot Pressed)	Steel	Air	---	---	1.0	2.2
Nylon/40% MoS ₂	M-10 Steel	N ₂	303-344	86-160	1.36	3.0
Nylon/20% C	M-10 Steel	N ₂	303-344	86-160	1.36	3.0
Glass Fiber/ Teflon-MoS ₂	M-10 Steel	N ₂	303-344	86-100	1.36	3.0
Glass Fiber/ Teflon	M-10 Steel	N ₂	303-344	86-100	1.36	3.0
Carbon/Teflon	M-10 Steel	N ₂	303-344	86-100	1.36	3.0
20% Ni, 80% C (Pressed)	M-10 Steel	N ₂	---	---	1.36	3.0
70% Ag, 20% Teflon, 10% WSe ₂ (Pressed)	440 Stain- less Steel	Vacuum		Room	1-4	2.2-8.8
Teflon/7% WSe ₂ (Pressed)	440 C Stain- less Steel	Vacuum		Room	1-4	2.2-8.8
Teflon/3% WSe ₂ (Pressed)	440 C Stain- less Steel	Vacuum		Room	1-4	2.2-8.8
20% Ni, 80% C (Pressed)	M-10 Steel	N ₂	1360	1000	1.36	3.0
Co/Sb ₂ S ₃	M-10 Steel	N ₂	1360	1000	1.36	3.0
40% Fe, 60% C (Heat-Treated)	M-10 Steel	N ₂	1360	1000	1.36	3.0
Ni, 2% NiO	---	10 ⁻⁸ -10 ⁻⁹	291	75	1.0	2.2
Ni, 20% Sn	---	10 ⁻⁹ torr	291	75	1.0	2.2
Fe, 0.825% FeS	---	10 ⁻⁹ torr	291	75	1.0	2.2

Table 4-4 (Cont.)

Sliding Speed (m/min)	Speed (fpm)	Friction Coefficient	Wear Rate (cm ³ /cm ² hr)	Source
---	---	0.05	---	4-11
73 m/sec	240 fps	0.10	0.11	4-11
73 m/sec	240 fps	0.12	0.08	4-11
---	---	0.13-0.2	---	4-11
2440	8000	0.21	---	4-11
70-140	230-460	0.17-0.20	0.09	4-16
70-140	230-460	0.08-0.09	0.09	4-16
70-140	230-460	0.02-0.03	0.19	4-16
70-140	230-460	0.39-0.50	0.36-0.44	4-16
70-140	230-460	0.02-0.03	0.09-0.16	4-16
70-140	230-460	0.05-0.09	0.75	4-16
0.265	0.87	0.09-0.12	0.90	4-16
0.265	0.87	0.20	0.70	4-16
0.265	0.87	0.04-0.06	0.013	4-16
140	460	0.05	0.65	4-16
70	230	0.15	0.25	4-16
140	460	0.1	0.44	4-16
20 m/sec	65 fps	0.76	0.020 (cm ³ /hr)	4-17
20 m/sec	65 fps	0.17	0.0066 (cm ³ /hr)	4-17
20 m/sec	65 fps	0.25	0.041 (cm ³ /hr)	4-17

Table 4-5
SOLID FILM LUBRICATION TECHNIQUES

Type of Film	Application Technique	Most Suitable Materials	Performance	Limitations	Source
1. Chemically Reacted	Reaction with Vapors	Sulfides	Poor to Fair	Requires Continuous Supply	Ref. 4-24
		Chlorides	Fair	Requires Continuous Supply	Ref. 4-18, 19
	Reaction with Liquids	Carbamates	Good	Requires Continuous Supply	Ref. 4-25
		Amines	Fair	Requires Continuous Supply	Ref. 4-26
		Halogenated Hydrocarbons	Fair	Requires Continuous Supply	Ref. 4-27, 28, 29
2. Self Adhering	Burnishing	Phosphates	Good	Short Wear Life	Ref. 4-27, 28, 29
		Sulfides	Fair	Short Wear Life	Ref. 4-30
	Metal Plating	MoS ₂ -Yielding Compounds	Good	High Friction	Ref. 4-20, 31
		MoS ₂	Fair	Highly Reactive	Ref. 4-22, 23
		WS ₂	Good	Requires Continuous Supply	Ref. 4-21
3. Bonded Solid	Gas Entrained Powder	Gold	Fair to Good	Requires Continuous Supply	Ref. 4-32, 32
		Silver	Good	Reservoir Sometimes Structurally Unstable	Ref. 4-25, 34, 35, 36, 37
	Transfer Film	Indium	Good	Excellent	Ref. 4-38, 39, 40, 41, 42, 43
		Gallium	Good	Excellent	Ref. 4-45
	Vacuum Deposition	Barium	Good	Good	

Materials such as vapors of carbamates and amines show good potential with low flow rates (Ref. 4-18, 4-19). Lightweight reservoir systems can probably be developed which will make this technique useable, but the state of development is low. Inclusion of MoS_2 -yielding compounds in oils offers a method of improving the reliability of oil lubricated devices, but does not solve the problems of volatility and radiation damage associated with oil lubrication.

4.2.2 Self-Adhering Film

Of the various techniques for using self-adhering films, only soft metal platings and transfer film techniques have any real application to space mechanisms. Thin films (1 micron thickness) of low shear strength metal, applied to hard bearing materials can effect good friction performance in rolling bearings for many thousands of hours. The use of gold (Ref. 4-20) probably compromises low friction (low shear strength) for good wear life (high hardness) and chemical inertness. In many applications, superior friction performance could be effected by using metals (lead, bismuth (Ref. 4-21), barium (Ref. 4-22), or gallium (Ref. 4-23)).

Films of solid lubricant applied by transfer during sliding provide excellent long-term operation of bearings and gears. The films are transferred to load bearing elements by rubbing against a lightly loaded secondary member (bearing retainer, idler gear) made from the solid lubricant material. Generally, two classes of material are used together; a layer lamellar powder (MoS_2 , graphite, etc.) and a film former (Teflon, nylon) to hold the powder in place. Such materials are available commercially (Ref. 4-46) and from research labs operating under government contract (Ref. 4-34, 4-35). Members made from these materials are generally weaker than other parts and may suffer structural damage if loading is high.

4.2.3 Bonded Solid Films

A widely used and generally satisfactory technique for applying solid lubricant films is to bond them to the load bearing surfaces with an organic or inorganic binder. Excellent results have been achieved with a mixture of MoS_2 , graphite and gold flakes bound with a sodium silicate binder (Ref. 4-40, 4-42, 4-47). Other bonded coatings are available commercially (Ref. 4-43, 4-45). Special surface preparation is required for optimum performance with bonded coatings (Ref. 4-40, 4-41, 4-43).

4.3 References

- 4-1 Paul A. Bauer, Myron Glickman, and Frank Iwatsuki, Analytical Techniques for the Design of Seals for Use in Rocket Propulsion Systems, Volume I and II, AFRPL-TR-65-61, IIT Research Institute, Chicago (May 1965)
- 4-2 Plastics Book Issue, Machine Design, 34, 22, 20 Sep 1962
- 4-3 Bearings Book Issue, Machine Design, 35, 14, 13 Jun 1963
- 4-4 Materials Selector Issue "Materials in Design Engineering" 58, No. 5, Mid-Oct. 1963
- 4-5 M. J. Devine and A. E. Kroll, "Aromatic Polyimide Compositions for Solid Lubrication," Lubrication Eng., 20, No. 6, Jun 1964
- 4-6 I. B. Johns, Monsanto Research Corp., Private communication, Jun 1964
- 4-7 R. P. Bringer, "Fluorocarbon Plastics Under the Influence of Unusual Environmental Conditions," National Symposium on the Effects of Space Environment on Materials, St. Louis, Soc. of Aerospace Materials and Process Engineers, May 1962
- 4-8 D. H. Buckley and R. L. Johnson, Friction, Wear and Decomposition Mechanisms for Various Polymer Compositions in Vacuum to 10^{-9} Millimeter of Mercury, NASA TN D-2073, Dec 1963
- 4-9 W. D. Craig, Jr., "Friction Variation of PTFE and MoS₂ During Thermal Vacuum Exposure," Lubrication Eng., 20 No. 7, 274-7, (1964)
- 4-10 D. H. Buckley, R. L. Johnson, and M. Swikert, "Friction, Wear and Evaporation Rates of Various Materials in Vacuum to 10^{-7} mm Hg," ASLE/ASME Lubrication Conference Preprint No. 61 LC-2, Oct 1961
- 4-11 E. R. Parker (Editor), Materials for Missiles and Spacecraft, McGraw-Hill, (1963)
- 4-12 M. M. Faulk and K. S. Horr, Sublimation of Some Polymeric Materials in Vacuum, TN 62-118, Ball Brothers Research Corp., Sep 1962
- 4-13 R. D. Brown, R. A. Burton, and P. M. Ku, Friction and Wear Characteristics of Cermets at High Temperature and High Vacuum, ASD-TR-61-301, Sep 1961
- 4-14 R. D. Brown, R. A. Burton, and P. M. Ku, Research on High Temperature Bearings, ASD-TDR-61-705, Aug 1962, AD-288-892
- 4-15 G. W. Rowe, "Some Observations of the Frictional Behavior of Boron Nitride and of Graphite," Wear, 3, 274-85. (1960)
- 4-16 P. H. Bowen, Lubrication of Bearings and Gears in Aerospace Environmental Facilities, AEDC-TRD-63-166, Jul 1963, AD-411-430

- 4-17 D. H. Buckley and R. L. Johnson, Influence of Microstructural Inclusions on Friction and Wear of Nickel and Iron in Vacuum to 10^{-9} Millimeters of Mercury, NASA TN-D-1708, May 1963
- 4-18 L. Stallings, Vapor Lubrication of High Speed Bearings, NAEC-AML-1758, 12 Sep 1963
- 4-19 L. Stallings, Volatile Organic Solids for High Speed Ball Bearing Lubrication, NAEC-AML-1532, 29 Sep 1962
- 4-20 H. Evans and T. W. Flatley, "Bearings for Vacuum Operation - Retainer Material and Design," J. Eng. for Industry, 129-34, May 1963
- 4-21 H. Esten, P. Lewis, S. F. Murray, and M. B. Peterson, Lubricant Evaluation for Bearing Systems Operating in Spatial Environments, ASLE Trans., 6, No. 1, 67-79
- 4-22 Z. J. Atlee, J. C. Filmer, and J. T. Wilson, "Lubrication in Vacuum by Vaporized Thin Metallic Films," J. Appl. Phys., 11, No. 9, 611-15, Sep 1940
- 4-23 D. H. Buckley and R. L. Johnson, Gallium-Rich Films as Boundary Lubricants in Air and in Vacuum to 10^{-9} mm Hg, ASLE Trans., 1, No. 6, 1-11, Jan 1963
- 4-24 E. E. Bisson, D. Godfrey, R. L. Johnson, and M. A. Swikert, Friction, Wear, and Surface Damage of Metals as Affected by Solid Surface Films, NACA Report 1254, (1956)
- 4-25 W. J. Anderson and E. E. Bisson, Advanced Bearing Technology, NASA SP-38, (1964)
- 4-26 R. C. Gunderson and A. W. Hart (Editors), Synthetic Lubricants, Reinhold, N.Y. (1962).
- 4-27 W. L. Perilstein, Fundamental Studies of New Boundary Lubrication Mechanisms, WADD-TR-61-87, Apr 1961, AD-268-087
- 4-28 C. E. Vest, Adaptation of an MoS₂ "In Situ" Process for Lubrication Spacecraft Mechanical Components, NASA TN D-2288, (1964)
- 4-29 M. R. Adams, I-Ming Feng, and W. L. Perilstein, Solid Film Deposition and Non-Sacrificial Boundary Lubrication, ASLE Trans., 6, No. 1, 60-6, (1963)
- 4-30 D. H. Buckley and R. L. Johnson, Lubricants and Mechanical Components of Lubrication Systems for a Space Environment, NASA TMX-52031, (1964)
- 4-31 F. P. Bowden and D. Tabor, "The Lubrication by Thin Metallic Films and the Action of Bearing Metals," J. Appl. Phys., 14, 141-51, (1963)
- 4-32 A. Schlosser, "Development of Gas-Entrained Power Lubricants for High Speed and High Temperature Operation of Spur Gears," Progress Report No. 2, Contract AF 33(657)-8625, Fairchild Stratos, Jan 1963

- 4-33 The Development of Lubricants for High Speed Rolling Contact Bearings Operating over the Range of Room Temperature to 1200 Degrees F, WADD TR 60-732, Jan 1961, AD-257-339
- 4-34 P. H. Bowen, Lubrication of Bearings and Gears in Aerospace Environmental Facilities, AEDC-TDR-63-166, Jul 1963, AD 411-430
- 4-35 D. J. Boes, "Self-Lubricated Bearings," Lubrication Eng., 19, No. 4, 137-42, (1963)
- 4-36 R. D. Brown, R. A. Burton, and P. M. Ku, Research on High Temperature Bearings, ASD-TR-61-705, Aug 1962, AD 288-892
- 4-37 T. L. Ridings and A. G. Williams, Operational Evaluation of Dry-Lubricant Composites in a High Vacuum Chamber, AEDC-TDR-63-67, May 1963, AD 406-127
- 4-38 J. R. Jones, "Finishes Which Lubricate," Metal Finishing, 44-99, Nov 1962
- 4-39 B. C. Stupp and J. W. Wright, "Investigation of Binders for Solid Lubricants at Elevated Temperatures," Lubrication Eng., 463-9, (1963)
- 4-40 J. H. Brown, M. J. Devine, and E. R. Lamson, "Inorganic Solid Film Lubricants," J. Chem. and Eng. Data, 6, No. 1, Jan 1961
- 4-41 E. B. Palmer, "Solid Film Molybdenum Disulfide Lubricants," Mater. in Des. Eng., 122-6, (1961)
- 4-42 K. E. Demorest and E. C. McKannan, "Dry Film Lubrication of Highly Loaded Bearings in Vacuum," Lubrication Eng., 20, No. 4, 134-41, (1964).
- 4-43 A. DiSapio, "Borated-Lubricant Coatings," Machine Des., 35, No. 12, 167-72, (1963).
- 4-44 Electrofilm Inc., North Hollywood Calif., Solid Film Lubricants in Vacuum and Space, Technical Bulletin No. 2068
- 4-45 CBS Laboratories, Stanford, Conn., Vacuum Bearings and Dry Film Lubricants, Technical Bulletin 463-6-A
- 4-46 Bearings Book Issue, Section 5, Bearing Materials and Parts, Machine Design, 14, 246-55, (1963).
- 4-47 D. H. Gaddis, V. Hopkins, and R. D. Hubbell, "Development of Inorganic Solid Lubricant Films," USAF-SWRI Aerospace Research Conference, San Antonio, Texas, Mar 1964

5. INTERSTITIAL ROTATING SHAFT SEALS

The seals considered in this section supplement those considered in Reference 5-1, Volume II, Section 5. The interstitial seals previously considered were fixed clearance seals, i.e., seals in which the leakage path is constant and determined solely by the seal geometry. The additional seals can be classed broadly as variable clearance-interstitial seals. Specifically, the seals can be identified as hydrostatic and hydrodynamic seals.

Variable clearance seals offer several advantages over fixed clearance seals.

- (1) Theoretically, they can provide lower leakage characteristics.
- (2) They can be less complicated, therefore, less expensive.
- (3) They are not as susceptible to thermal deformation, consequently, can operate in extremes of environment.
- (4) They are suitable for sealing gases as well as liquids, whereas most of the minimum leakage fixed clearance seals are suitable only for liquids.

While the relative merits of fixed as opposed to variable clearance seals are worthy considerations, these are less important than the relative merits of interfacial as opposed to interstitial seals. This concern is generated by the commonly accepted concept that interfacial seals leak less than interstitial seals. One of the principal objectives in this discussion is to point out that this may not be the case and, indeed, may offer substantial improvement from the standpoint of:

- lower leakage
- virtually no wear
- reduced power losses due to friction.

In Section 3, interfacial seals were described as contacting-type seals where one face rubs against the other. A conclusion reached was that fragments resulting from wear are of such a size that substantial separation of the sealing surfaces occurs. Rubbing under well lubricated conditions with low surface loading will produce wear fragments with an average size generally not less than 0.0001 in. and ranging to 0.01 in. On the basis of these conclusions, interfacial seals could be more appropriately classed as fixed clearance seals where the wear fragment size determines

the size characteristics of the leakage path. This leads to the conclusion that if a seal concept were available in which no wear occurs and yet small clearances ($<100 \mu\text{in.}$) can be maintained under any environmental condition*, this seal would offer optimum performance. Hydrostatic and hydrodynamic seal concepts can theoretically produce this performance.

Much investigative work remains before actual judgement can be made in favor of the variable clearance seal. These seals have been used (Ref. 5-2, 5-3) successfully in custom applications. In most cases, the acceptable leakage rate was substantially high, therefore, little effort was made to design the seals for an absolute minimum leakage.

The theory of hydrostatic and hydrodynamic seals is complex and has not reached an adequate state of development. The foundation, however, has been built by persons engaged in the theoretical development of hydrostatic and hydrodynamic lubrication applied to bearings. While the present theories are substantial advances in bearing technology, they are not readily applicable to seals. This is understandable because load-supporting ability is the important factor in a bearing, whereas leakage is the important factor in a seal.

Because of the complexity of the seal theory and uncertainty of the actual results, no attempt was made to present design criteria for these seals. While Subsection 5.2 does contain an elementary analysis of a hydrodynamic seal, this analysis is presented only to show the principle of operation and the possible benefits over a contacting seal. If one were to embark on a comprehensive analysis, Reference 5-4 is suggested as a means of obtaining the preliminary theory as well as a discussion of the problems involved.

A brief introduction to variable clearance seals is presented in Subsections 5.1, 5.2 and 5.3 to show the general mechanism of operation. In addition the design classification of seals presented in Reference 5-1 was revised to reflect the hydrostatic and hydrodynamic seal. The revisions are presented in Subsection 5.4.

*The environmental effects can be identified more concisely as thermal and pressure deformation. In fixed clearance seals, the minimum clearance is determined by the deformation effects.. Small clearances, such as $100 \mu\text{in.}$, are difficult to manufacture, much less provide design compensations for deformations of this magnitude.

5.1 Seal Description

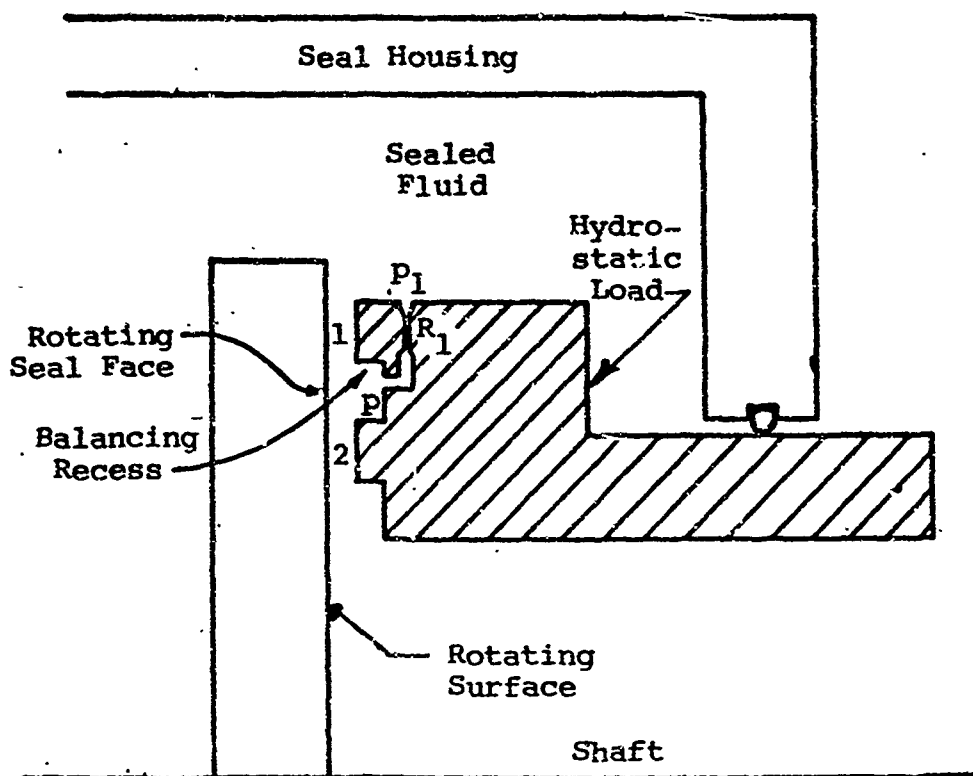
5.1.1 Hydrostatic Seals

A hydrostatic seal is formed when two surfaces are placed in close proximity, forming an interstice. The loads imposed on the sealing surfaces by fluid pressure are balanced to an extent that the surfaces will not come into contact. Figure 5-1 shows schematic representations of hydrostatic seals. The operation of the seal shown in figure 5-1(a) is as follows. Assume that the surfaces at 1 and 2 are in contact with the fixed surface. The balancing recess is then at sealed fluid pressure p_1 providing that the resistance to flow R_1 is less than the resistance to fluid flow across surface 2. Pressure p_1 then acts across surface 1 and the balancing recess. Pressure p_1 acting over this area is greater than the hydrostatic load. Therefore, the movable surface separates. Separation increases the flow of leakage across surfaces 1 and 2. In turn, the flow of leakage produces a gradient across both surfaces. Whereas the gradient across surface 1 and the recess cavity were uniform when the surfaces were in contact, separation alters the gradient and reduces the separating force. The degree of separation is determined by:

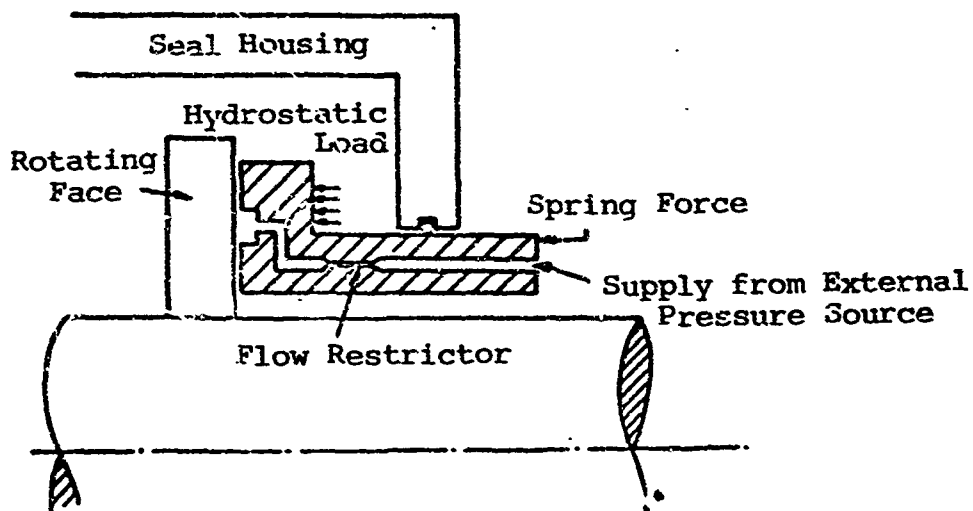
- The resistances to flow, which are composed of the clearances at 1 and 2 and the orifice resistance R_1
- The magnitude of hydrostatic load unbalancing
- The properties of the fluid sealed
- The over-all geometry of the seal
- Sealed fluid pressure
- Spring-like devices usually used to urge the movable surface against the fixed surface in overcoming static seal friction.

The principles of operation of both seals shown on figure 5-1 are the same. In figure 5-1(a), the balancing fluid is the sealed fluid and in figure 5-1(b), the balancing fluid is provided by an external supply.

As in the case of hydrostatic bearings, a number of individual balancing recesses are usually employed around the face of the seal. Other bearing design innovations are also used, principally to overcome self and externally induced vibrations. Reference 5-4 is suggested for a review of these techniques.



(a) Internally Pressurized



(b) Externally Pressurized

Figure 5-1 Hydrostatic seals (Ref. 5-2)

5.1.2 Hydrodynamic Seals

The separation of surfaces in hydrodynamic seals is accomplished by the generation of pressure between surfaces due to shear of the fluid. The rate of shear is determined by the relative velocity of the surfaces, fluid properties and seal geometry. This seal differs from the hydrostatic seal in that it is velocity sensitive. A further description of hydrodynamic seals is presented in Subsection 5.3.

5.2 Plane Slider Interstice

This section presents a one-dimensional analysis of the factors influencing the separation of two surfaces forming an interstice. The interstice geometry considered is formed by one flat surface moving relatively and inclined to the other flat surface as shown schematically in figure 5-2. The analysis, being one-dimensional, neglects side effects and consequently represents an interstice infinitely wide or a finite interface with closed and non-influencing boundaries. While the boundary assumptions are not representative of real sealing interstices, the simplifications in the analysis do produce a solution in terms of surface separation. More importantly, the analysis shows the relative influence of surface load, velocity, geometry, and fluid properties on the separation clearance.

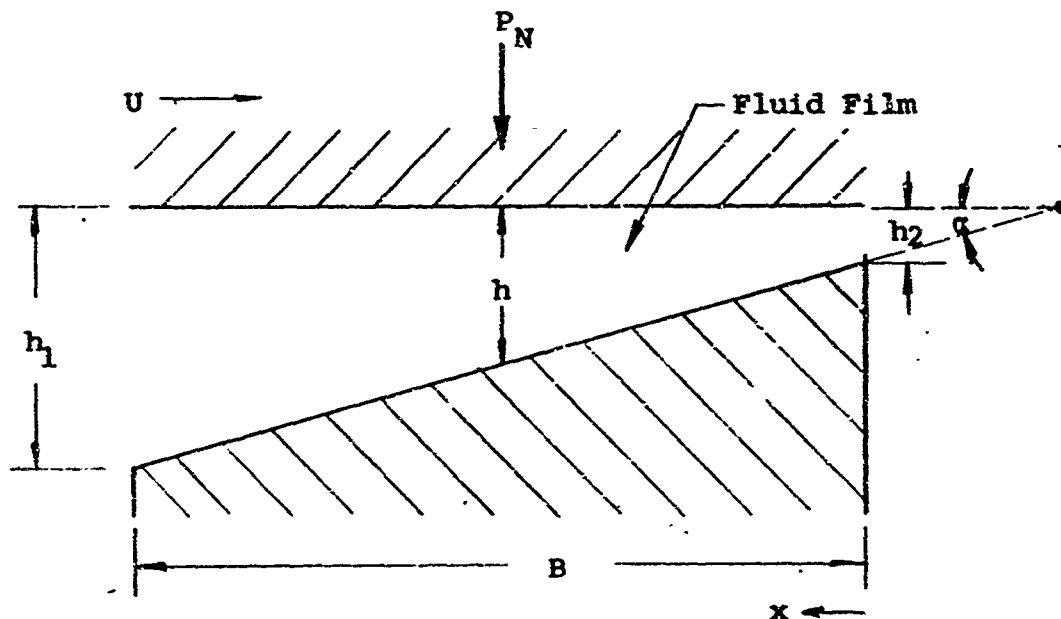


Figure 5-2 Plane slider

The development of an analysis for the plane slider, shown in figure 5-2, starts with the statement of the Navier-Stokes equations and through several assumptions reduces to a form of the Reynolds equation:

$$\frac{d}{dx} \left(\frac{h^3}{\mu} \frac{dp}{dx} \right) = 6U \frac{dh}{dx} \quad (5-1)$$

Some of the important assumptions may be stated:

- Constant density throughout the fluid film, therefore, fluid must be liquid
- No pressure variation in the width w or height h directions
- Laminar fluid flow
- Fluid inertia neglected
- No slip at the surfaces.

Integration of equation (5-1) yields results that can be manipulated into the form:

Pressure at any x
between $\frac{h_1}{a} \geq x \geq \frac{h_2}{a}$

$$P = \frac{6\mu U}{a^3} \frac{(h_1 - ax)(ax - h_2)}{(h_1 + h_2)x^2} \quad (5-2)$$

Load on the surface
(equivalent to the
separating force)

$$\begin{aligned} P &= \frac{6\mu U w B^2}{h_2^2} \left(\frac{1}{a-1} \right)^2 \left[\ln a - \frac{2(a-1)}{a+1} \right] \\ &= \frac{\mu U w B^2}{h_2^2} C_p \end{aligned} \quad (5-3)$$

Frictional force

$$\begin{aligned} P_f &= \frac{w h_2}{B} \frac{2(a^2-1) \ln a - 3(a-1)^2}{3(a+1) \ln a - 6(a-1)} \\ &= \frac{\mu U w B}{h_2} C_f \end{aligned} \quad (5-4)$$

Maximum pressure

$$p_m = \left(\frac{3\mu UB}{h_2^3} \right) \left(\frac{(a-1)}{(a+1)a} \right) \quad (5-5)$$

Location of
maximum pressure

$$x_m = \frac{2aB}{(a-1)(a+1)} \quad (5-6)$$

The following substitutions, other than those self-evident, are defined:

$$h = ax = \frac{h_2(a-1)}{B} x$$

$$a = h_1/h_2$$

The pressure profile given by equation (5-2) will have a shape as exemplified by figure 5-3. The separating force generated between the surfaces is equal to the surface load and is obtained by an integration of the pressure function over the surface area. The load capacity and friction coefficients C_p and C_f can be evaluated for assumed values of h_1/h_2 . These results, shown on figure 5-4, are included to facilitate an evaluation of the order of magnitude of influence each variable possesses.

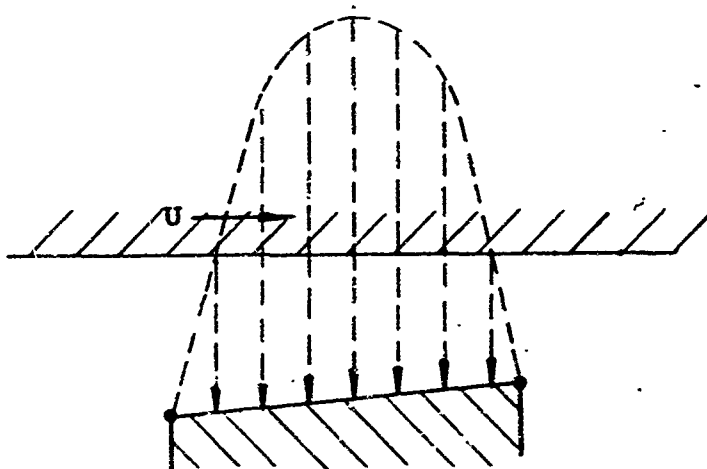


Figure 5-3 Pressure profile

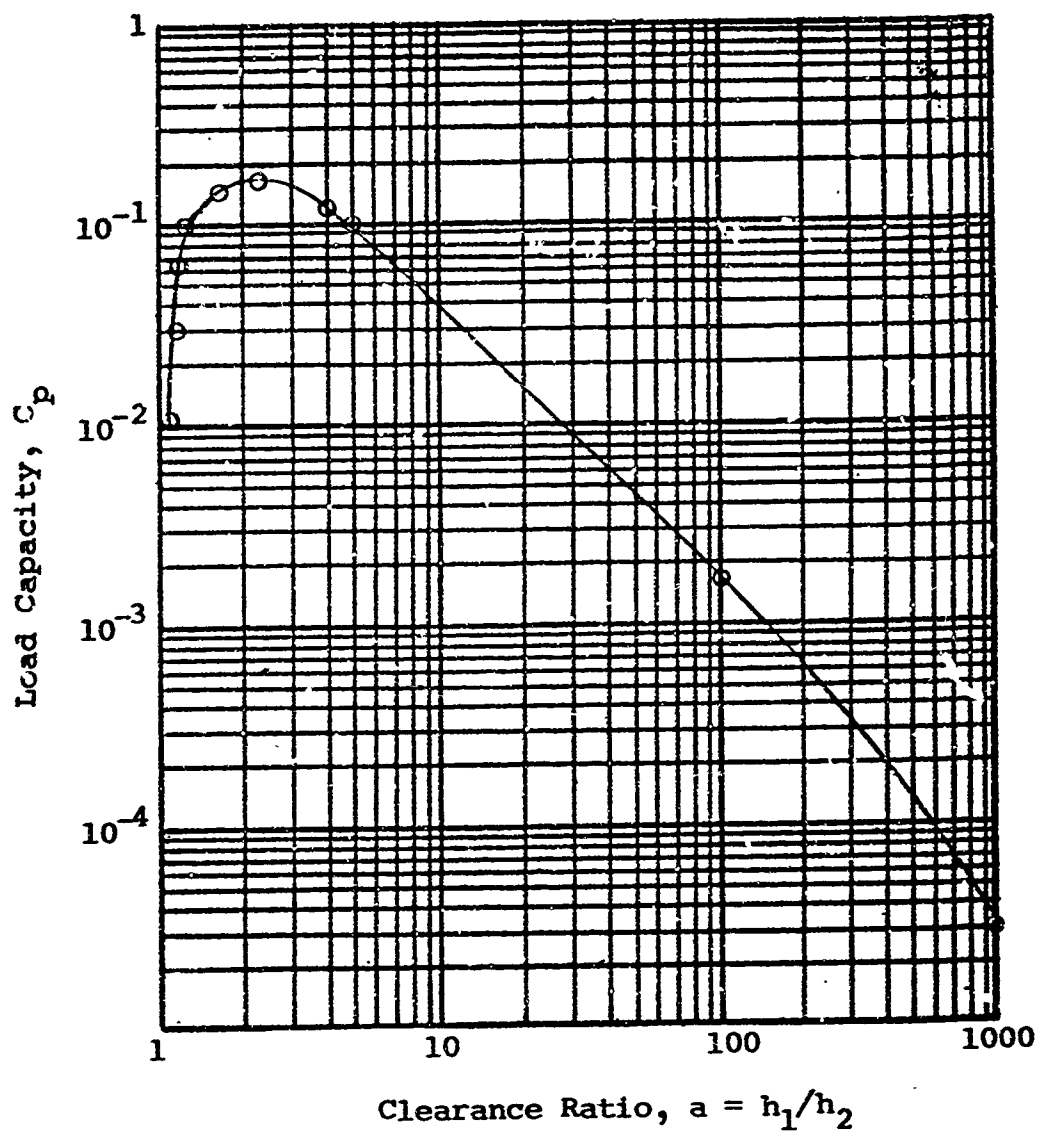


Figure 5-4 Load capacity as a function of the clearance ratio for a plane slider

5.3 The Plane Slider Applied to a Simple Rotating Shaft Seal

An unbalanced rotating shaft face seal having the equivalent of two plane sliders on one face is assumed for illustrative purposes. The seal, shown in figure 5-5, is analyzed using the theory set forth in the preceding subsection. The seal is assumed to be sealing water, hence, the fluid in the interface is water. At this stage in the analysis, the forces due to sealed fluid pressure are neglected. The forces of primary interest are the separating forces generated by the plane sliders. The total separating force P_T at the interstice is composed of nP , where n is the number of sliders. As a further aid in showing the magnitude of effects, a specific seal face geometry was selected as shown in figure 5-5.

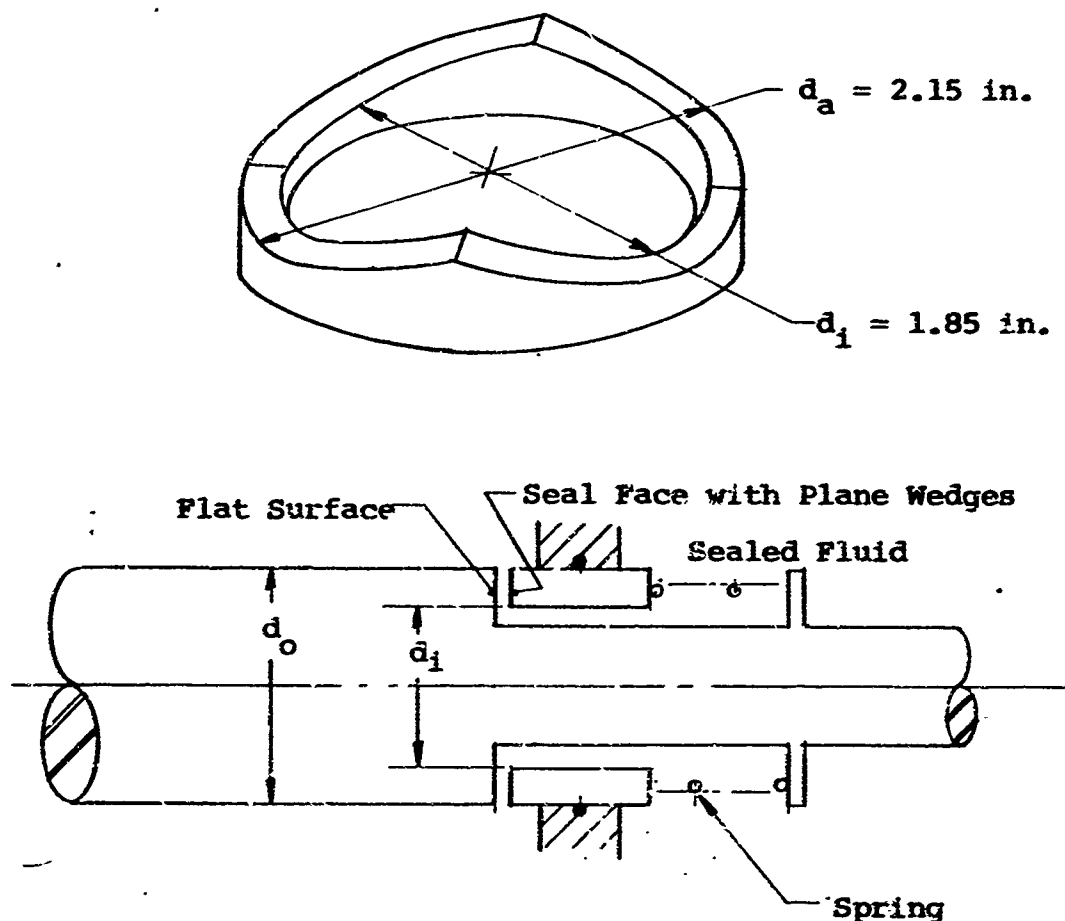


Figure 5-5 Face seal configuration

To obtain the separating force P_T , equation (5-3) can be rewritten in terms of equivalent variables:

$$\frac{P_T}{N} = \frac{6.74(10^{-7})}{h_2^2} C_p, \text{ lb/rps} \quad (5-7)$$

where $\mu = 1.45 \times 10^{-7} \frac{\text{lb-sec}}{\text{in.}^2}$, viscosity of water

$$w = \frac{d_a - d_i}{2}$$

$$B = \frac{\pi(d_a + d_i)}{8}$$

$$U = \pi N \frac{(d_a + d_i)}{2}$$

$$P_T = 2P$$

The next step in the analysis is to select a geometry (or film shape) for the slider face. With reference to figure 5-2, the geometry can be identified as $(h_1 - h_2)$ equal to a constant. Three surface shapes were selected for study:

$$\begin{array}{ll} \text{Case I} & (h_1 - h_2) = 8 \text{ } \mu\text{in.} \\ \text{Case II} & (h_1 - h_2) = 100 \text{ } \mu\text{in.} \\ \text{Case III} & (h_1 - h_2) = 1000 \text{ } \mu\text{in.} \end{array} \quad (5-8)$$

The total separating force can be calculated by substituting each of the preceding conditions into equation (5-7) and arbitrarily assuming a minimum interstice clearance. The results of these calculations are shown graphically on figure 5.6. It may be observed that the separating force varies substantially with minimum clearance and increases sharply with decreasing wedge angle.

The final step in a seal analysis is to consider refinements in the seal configuration and introduce the effects of sealed fluid pressure. Once this point is reached, the leakage characteristics of the seal can be estimated. The general geometry of the seal is the same as shown on figure 5-5, except that modifications are made to the wedge-shaped face. The modifications, shown on figure 5-7, include:

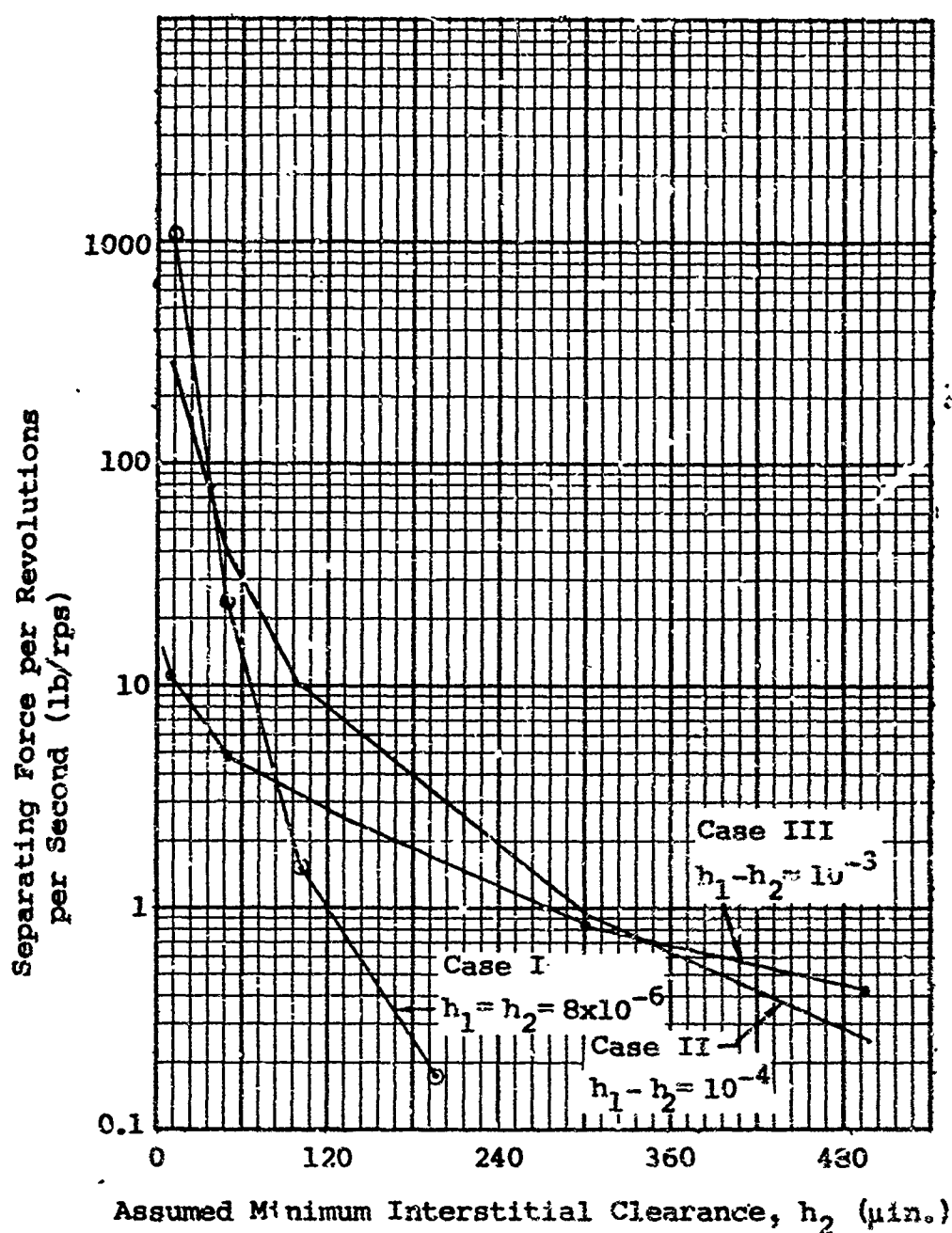


Figure 5-6 Separating force as a function of assumed minimum interstitial clearance with the slider geometry shown as a parameter

- an outer contacting surface, which provides support when the seal is at rest and also serves as an apron to minimize interfacial leakage when static and side leakage when rotating.
- an inner apron adjacent to the pressure generating wedge for minimizing side leakage. The influence of the inner and outer aprons is dependent upon the wedge geometry. For example, the apron for Case I is not essential because the maximum wedge clearance is in the order of magnitude of surface roughness.
- a relatively large inlet cavity of height dimension h_a . This cavity should be sufficiently large that fluid can readily enter the wedge and compensate for side leakage at the pressure generating wedge. Thus, cavitation problems are minimized.

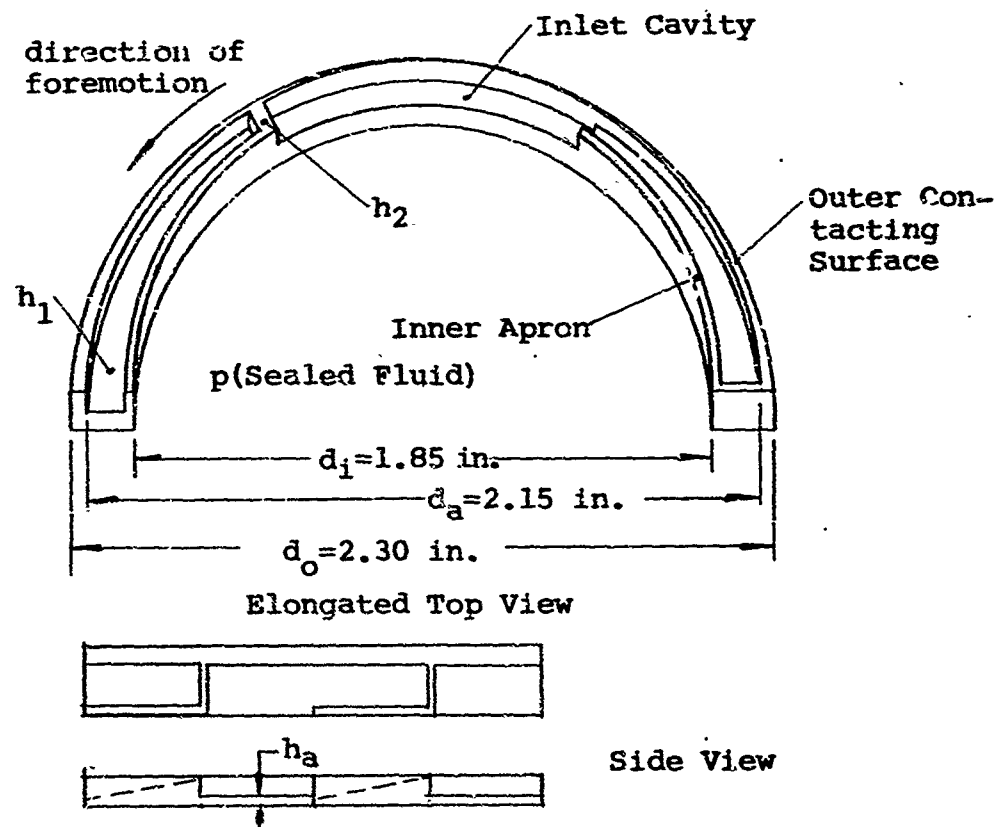


Figure 5-7 Face seal configuration

The forces resulting from sealed fluid pressure can be described as:

- Pressure acting on the rear side of the movable seal element given by

$$p\pi \frac{(d_o^2 - d_i^2)}{4} = 1.46 p$$

- Pressure gradient* effect on the outer contacting surface that is due to leakage flow from the inlet cavity. This inlet cavity pressure is assumed to be p

$$p\pi \frac{(d_o^2 - d_a^2)}{16} = 0.127 p$$

- Pressure gradient* effect on the outer contacting surface that is due to leakage flow from the wedge. The mean pressure under the wedge is assumed to be uniform over the circumferential length of the wedge. The mean pressure is defined as the sealed fluid pressure plus the separating force divided by the projected area of the wedge.

$$\left[p + \frac{8W_T}{\pi(d_a^2 - d_i^2)} \right] \left[\frac{\pi(d_o^2 - d_a^2)}{16} \right] = 0.127p + 0.268W_T$$

- Pressure acting over the projected area of the inlet cavities and wedge

$$p\pi \frac{(d_a^2 - d_i^2)}{4} = 0.948p$$

- The separating force P_T .

Summing the forces on the movable seal element yields

$$1.46p = 0.127p + 0.127p + 0.268W_T + 0.948p + W_T$$

and

$$P_T = 0.2055p. \quad (5-9)$$

The net static contacting stress is $p/2$ and the load,

$$P_c = 0.255p$$

*A linear pressure gradient is assumed, based on laminar flow conditions.

It should be noted that the force contributed by the spring, shown in figure 5-5, was neglected. The force can be defined as:

$$P_S = P_{SO} + kh_2$$

where P_{SO} is the initial preload.

The minimum separation distance h_2 can be obtained using equation (5-9) and figure 5-6 for a specific wedge shape, seal rotational speed, and sealed fluid pressure. The slider shapes selected are Cases I and II in equation (5-8). The rotational speeds were arbitrarily selected as 1, 10, and 100 rps, equivalent to 60, 600, and 6000 rpm. Sealed fluid pressures were also arbitrarily chosen as 10, 100, and 1000 psi. The procedures used in the calculation of minimum clearance, as shown on Table 5-1, were as follows:

- Assume an arbitrary pressure of 100 psi, a rotational speed of 10 rps, and a geometry given as $h_1 - h_2 = 0.0001$ in.
- Calculate the separating force from equation (5-9): $P_T = 0.2055(100) = 20.5$ lb
- Divide the separating force P_T by the rotational speed N to obtain

$$\frac{P_T}{N} = \frac{20.5}{10} = 2.05 \text{ lb/rps}$$

- Use figure 5-6, Case I to obtain the separation distance, h_2 : $h_2 = 95 \mu\text{in.}$

Table 5-1

MINIMUM SEPARATION CLEARANCES, h_2 , ($\mu\text{in.}$)

Case I, $h_1 - h_2 = 8 \mu\text{in.}$				Case II, $h_1 - h_2 = 100 \mu\text{in.}$		
Speed (rps) →	1	10	100	1	10	100
Pressure (psi) ↓						
1000	28	50	95	15	75	230
100	50	95	190	75	230	540
10	95	190		230	540	—

Leakage flow can be calculated using the equation for laminar, incompressible flow between two uniformly spaced circular surfaces, as discussed in Reference 5-1, Volume II. In the present analysis, the circular surfaces are the contacting surfaces of the seal and the spacing is h_2 . The assumptions made in applying this equation are:

- Leakage is not greatly influenced by the pressure gradient under the separating wedge. The error induced by this effect could be minimized by using the total mean wedge pressure as the sealed fluid pressure acting over the interstice.
- Centrifugal forces acting on the fluid are neglected. This effect could also be included by employing the complete flow equation given in Section 6.4, Volume II of Reference 5-1. Preliminary calculations showed the influence to be negligible in the range of operation considered.

The results of the calculations are shown graphically on figure 5-8.

5.4 Observations

5.4.1 Seal Geometry

The location of the slider surfaces with respect to the sealed fluid is important from the standpoint of maintaining a continuous film under the slider. If the slider surfaces are located on the upstream side of a liquid seal, sufficient liquid will most likely be available for a continuous film. On the other hand, the film supply flow for downstream sliders is the leakage flow. When leakage flow is not sufficient, a two-phase film with reduced separation or no separation can result. Gas seals may function satisfactorily with the slider upstream or downstream but further investigations are necessary before a definite statement can be made.

The location of the sealed fluid can be on the inner or outer diameter of the seal. The configuration selected for study, as shown on figure 5-7, is an "outward sealing" seal. The analysis of this seal is equally pertinent to an "inward sealing" seal. The theoretical results obtained would be the same for seals with the same relative geometry, neglecting the rotationally induced flow forces.

The difference in the load capacities of curved sliders and plane sliders is insignificant. Once h_1 and h_2 are fixed, the

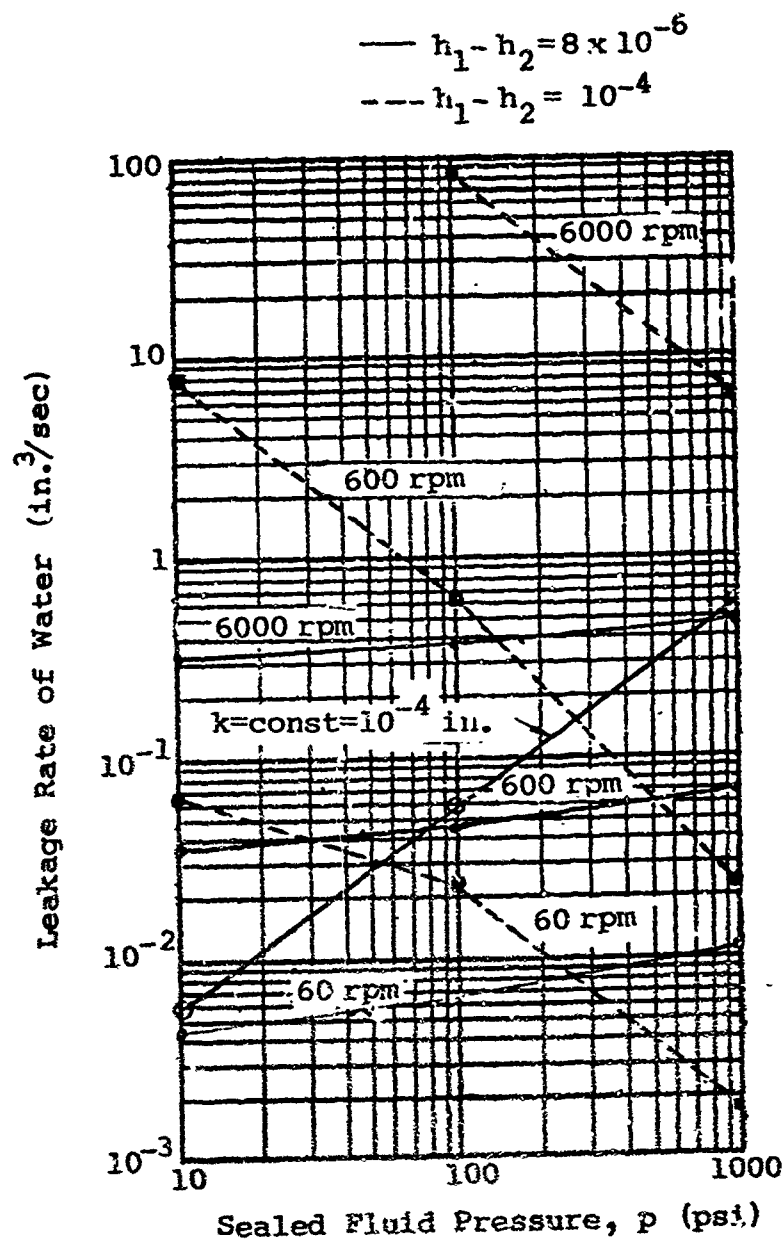


Figure 5-8 Leakage characteristics of a hydrodynamic seal

exact shape of the fluid film is no longer important. For example, the maximum load capacity of a plane slider is

$$P_{MAX} = 0.1602 \frac{\mu U W B^2}{h_2^2} \text{ when } a = 2.2 \text{ (from figure 5-4),}$$

while the maximum load capacity for a parabolically shaped slider is

$$P_{MAX} = 0.163 \frac{\mu U W B^2}{h_2^2} \text{ when } a = 2.3 .$$

An optimum film shape is a stepped configuration having a load capacity

$$P_{MAX} = 0.205 \frac{\mu U W B^2}{h_2^2} .$$

Another factor not considered in the seal analysis was the influence of a spring, usually required to urge the surfaces together initially. The preload of the spring should be a minimum so that the static surface loading is low. The scale of the spring, however, will influence the separation of the surfaces, particularly when the separating force is low and the separation large. The effects of the spring scale cannot be generalized completely without assuming a definite mode of operation.

It is beneficial to have low static contact loads because of the wear problem during the start and stop of motion. The initial contact loads on the interface surface can be reduced by employing pressure balancing techniques to the seal geometry.

5.4.2 Seal Performance

It should be realized that the theoretical performance of a hydrodynamic seal may differ substantially from the actual case. Thus, the following observations must be accepted with this in mind.

The leakage characteristics of hydrodynamic seals can vary considerably depending on the shape of the slider, speed, and pressure. Leakage calculations, presented graphically on figure 5-8, show a small increase in leakage with pressure for a shallow slider ($h_1 - h_2 = 8 \mu\text{in.}$) while the steeper slider ($h_1 - h_2 = 100 \mu\text{in.}$) possesses inverse characteristics.

A comparison between a flat face seal and a seal possessing a wedge capable of producing a separating force can be made as follows:

If the conclusion that contacting surfaces are separated by wear fragments having a minimum average size of 100 μ in. is valid, then the surfaces form a leakage channel having a separation of the same magnitude. The leakage rate of water through a flat seal equivalent of the seal can be calculated using the incompressible, laminar flow equation. This result is also shown on figure 5-8. It may be observed that lower leakage rates can be achieved by a hydrodynamic seal, as compared with a flat face seal. It is highly possible that a hydrodynamic seal can be tailor-designed through judicious choice of seal geometry to produce lower leakage over an entire range of operation than an equivalent flat face seal. In addition, the frictional characteristics of the hydrodynamic seal will be substantially lower than a contacting face seal. As an example, the power loss of the seal in figure 5-7, Case II, operating at 100 psi and 600 rpm is theoretically 321 times lower than a contacting seal having a friction coefficient of 0.1 under the same operating conditions.

The final observation that can be made is mostly pertinent to flat face seals. Fabrication techniques, wear and other deformation factors produce small undulations on the faces of flat face seals. A typical minimum representation of the undulations is about $h_1 - h_2 = 8 \mu$ in. Thus, the possibility of hydrodynamic surface separation exists even in the flat face seal. Since these seals are usually designed for low net contact loads (approximately 10 lb or less), the degree of surface separation can be substantial. As an example, consider a Case I seal having separating force characteristics as shown on figure 5-6. Assuming rotational speeds of 10 and 100 rps and a contact load of 10 lb, the effective separation of the surface would vary between 10 and 40 μ in. Thus, the degree of separation may be small compared with the average wear fragment size depending upon the actual geometry.

The effectiveness of small undulations on flat seal faces in producing separation is not completely defined. Intuitively, it would seem that hydrodynamic separation effects in liquid seals can be neglected for the following reasons:

- If the seal surfaces are initially in contact either through direct contact or through fragment separation, vaporization of the liquid can occur as a result of frictional heating. Thus, the fluid film will not be continuous and the separating force (load capacity) at the interface will be greatly reduced.

- Cavitation within the interface can occur because of side leakage effects. The side leakage effects produce a net loss of fluid in the interface and, consequently, a discontinuous fluid film. Consider the effects of pressure generation under a slider (figure 5-9) coupled with the effects of sealed fluid pressure. If the localized flow rates are given as:

$$Q_{p2} \sim K(p_2 - p_s) \quad \text{Flow into the leading slider}$$

$$Q_{p1} \sim K(p_s - p_o) \quad \text{Flow out of the leading slider}$$

$$Q_{w2} \sim K(p_m - p_2) \quad \text{Flow inward from the load-generating slider}$$

$$Q_{w1} \sim K(p_m - p_o) \quad \text{Flow outward from the load-generating slider;}$$

where p_2 = sealed fluid pressure

p_m = mean slider pressure

p_s = upstream slider pressure

p_o = outside pressure = 0

K = flow conductance;

the net flow into the seal must be equal to the net flow out of the seal.

$$\Sigma Q_{in} = \Sigma Q_{out}$$

$$\Sigma Q_{p2} - \Sigma Q_{w2} = \Sigma Q_{p1} + \Sigma Q_{w1}$$

and

$$p_2 - p_s - p_m + p_2 = p_s + p_m$$

$$p_2 = p_s + p_m$$

For the case $p_m > p_2$,

$$Q_{in} < Q_{out}$$

and

$$p_m = p_2$$

$$Q_{in} \approx Q_{out} \quad \text{when } p_s \rightarrow 0$$

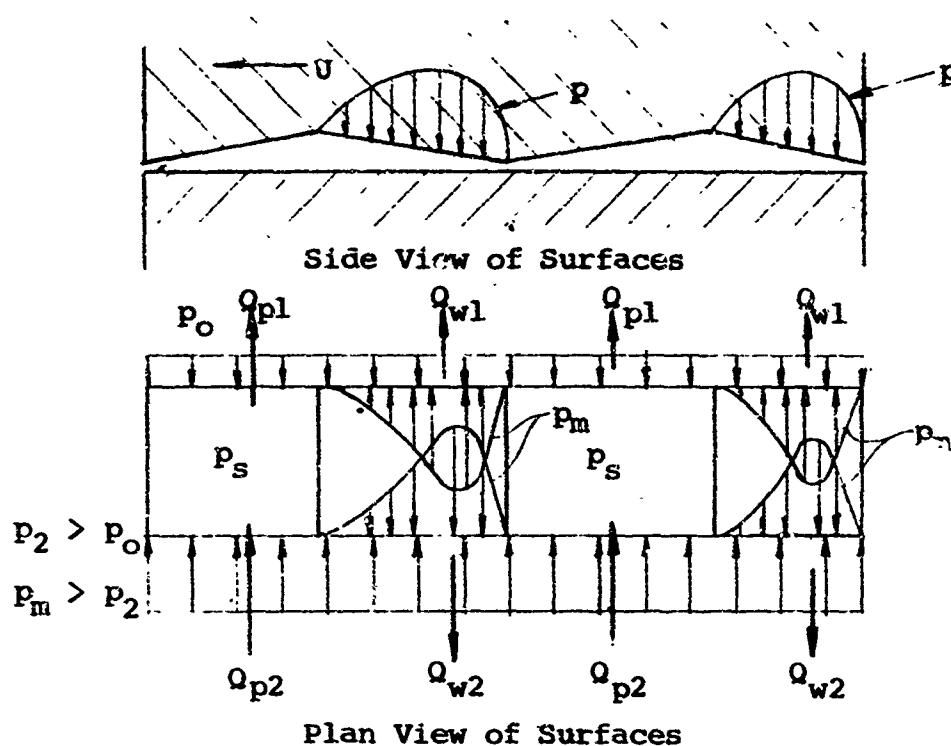


Figure 5-9 Pressure and flow distribution in a flat face seal with small undulations

For a separation force to exist, p_m must be greater than p_2 . Consequently, a net loss of flow occurs between the sealing surfaces resulting in cavitation. The preceding argument is grossly simplified and must be accepted on this basis. A comprehensive analysis of fluid flow requires a complex mathematical solution for a specific seal geometry. The argument as presented, however, shows the need for minimum flow resistance into the upstream side of the slider. For example, if $Q_{p2} = K_1(p_2 - p_s)$ and $K_1 \gg K$, then

$$K_1(p_2 - p_s) = K[2p_m - (p_2 - p_s)]$$

and Q_{in} can at least equal Q_{out} for a sufficiently large value of K .

A large inlet flow conductance into the upstream side of the slider can be achieved by having a large inlet cavity as typified on figure 5-7.

5.5 Design Classification of Rotating Shaft Seals

The classification method employed in Section 9, Volume II of Reference 5-1 was founded upon the construction features and

principles of operation of the seals. This procedure is again used to classify additional seals. The information presented herein is supplementary to that contained in the previous study (Ref. 5-1).

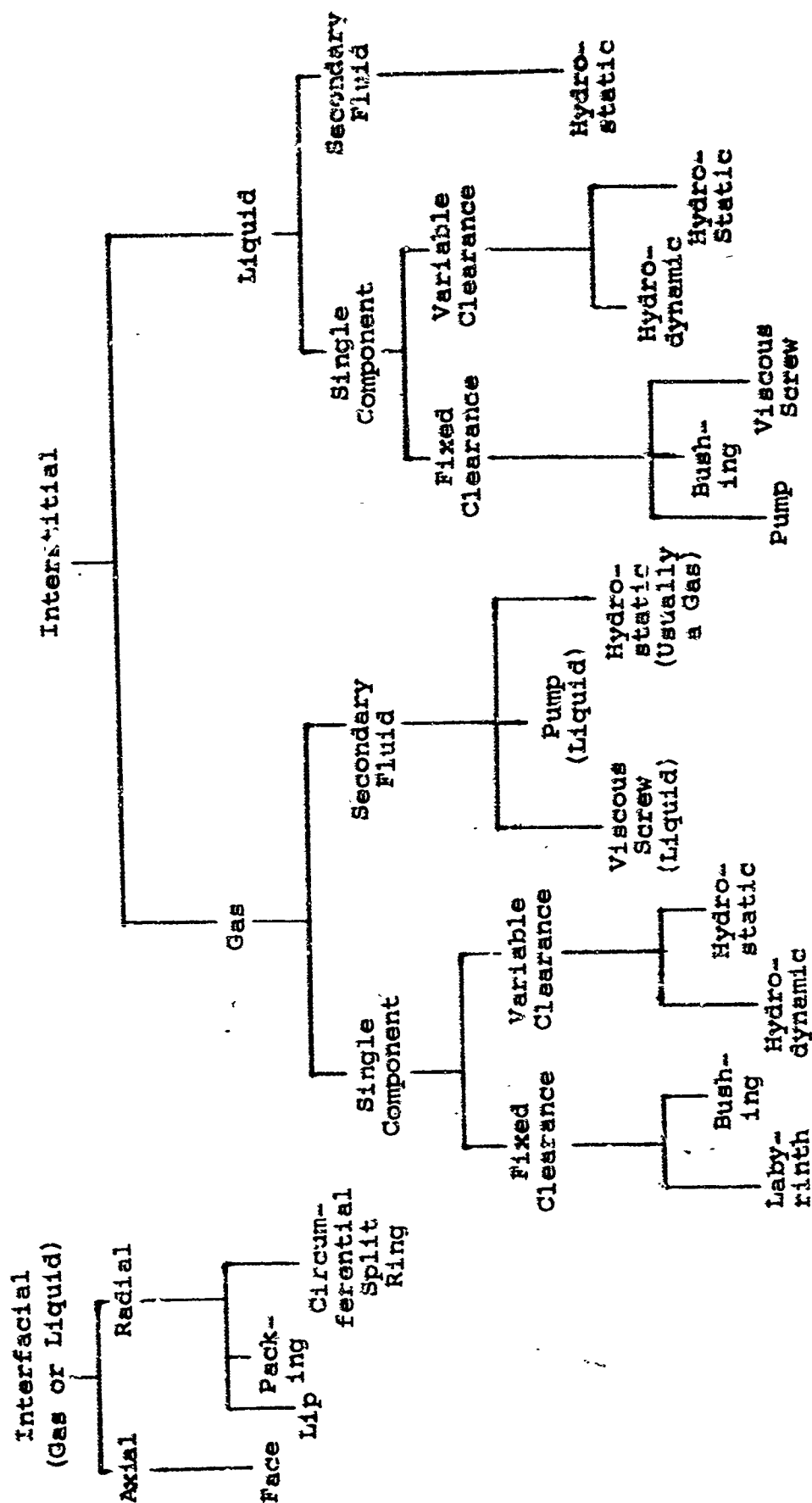
The changes in the classification system are twofold. First, a distinction is made between whether the seal is generally used in gas or liquid applications. Secondly, a new subclassification is introduced based on whether a secondary fluid is used as a sealing fluid. The additional seals classified are hydrostatic and hydrodynamic seals. A revised classification chart reflecting these changes is presented in Table 5-2.

5.6 References

- 5-1 Paul A. Bauer, Myron Glickman and Frank Iwatsuki, Analytical Techniques for the Design of Seals for Use in Rocket Propulsion Systems, Volume I and II, AFRPL-TDR-65-61, IIT Research Institute, Chicago (May 1965)
- 5-2 R. M. Austin and M. J. Fisher, "A Hydrostatic Seal for Boiler Feed Pumps," Second Intl. Conf. on Fluid Sealing, BHRA, Cranfield, England (April 1964)
- 5-3 E. Goldwag and R. S. Bounds, "Hydrostatic Seals for Water Turbine Shafts," Second Intl. Conf. on Fluid Sealing, BHRA, Cranfield, England (April 1964)
- 5-4 O. Pinkus and B. Sternlicht, Theory of Hydrodynamic Lubrication, McGraw-Hill (1961)

Table 5-2.

CLASSES OF ROTATING SHAFT SEALS



6. SEAL INSPECTION AND FABRICATION TECHNIQUES

To attain adequate theoretical and actual correlation for leakage prediction methods it is imperative to know the dimensional accuracies of the seal and sealed bodies as well as the surface characteristics of the interface. The machining process utilized in manufacturing the components governs the dimensional and surface conditions obtained. Thus, by determining the state-of-the-art of machining techniques, realizable tolerances as to flatness, roundness, concentricity, parallelism, squareness, and taper can be specified and leakage predictions confidently based on these dimensional variations.

Knowing the accuracy capabilities of metalworking processes is not sufficient, however. Inspection techniques to determine whether the component is made to the allowable tolerance variation, and, perhaps more important, where the component lies in the tolerance band necessitates the use of very accurate inspection and measuring methods. Thus, the state-of-the-art of inspection and measuring equipment must also be known.

The importance of knowing the absolute dimensions of the seal and seal component can best be shown by the sealing parameters directly affected by dimensional inaccuracies. For example, in a cantiliver leg seal,

- The cube of the seal leg thickness varies inversely with deflection for a given load
- Out-of-roundness or flatness determines necessary deflection for conformability
- Taper of seal leg varies the deflection for a given applied load
- Diametral variations necessitate higher- or lower-than-predicted applied load and deflection for desired contact stress.

The limitations of the various manufacturing techniques and inspection methods were determined by searching and reviewing the metalworking and metrology literature and by discussions with machine tool builders, inspection instrument manufacturers, and users of this equipment and with Government agencies directly connected with the field.

6.1 Measurement Techniques

Fundamentally, measurement is the act, or the result, of a quantitative comparison between a predefined standard

and an unknown magnitude (Ref. 6-1). If a measurement is to be meaningful, two requirements must be met:

- (1) the standard must be accurately known and commonly accepted, and
- (2) the validity procedure and apparatus employed for obtaining the comparison must be provable.

Two basic methods of measurement exist:

- direct comparison with a standard,
- an indirect comparison with a standard through the use of a calibrated system.

Both measurement systems fall within the framework of a generalized arrangement consisting of three stages.

Stage 1, The Detector-Transducer Stage detects or senses the input signal. The device must be sensitive to the input quantity, but, ideally, should be insensitive to other possible inputs. For example, a displacement transducer should be insensitive to temperature.

Stage 2, The Intermediate Stage modifies the transducer signal so that it is acceptable to the third stage. In addition, it may perform one or more basic operations, such as selective filtering, integration, or differentiation, as required.

Stage 3, The Terminating Stage provides the information sought in a meaningful form. The output is presented in the form of a relative displacement such as an indicating hand or displacement of oscillograph beam, or in digital form such as by a mechanical counter.

The following measurement techniques and systems are applicable to metalworking accuracy variations.

Micrometer Calipers

Type: Direct comparison

Tolerance: ± 0.0001 to ± 0.0005 in. (Readable)

Source: Reference 6-2.

Screw Micrometers with Optical Indicators

Type: Direct comparison
Tolerance: ± 0.0001 in.
Repeatability
of Reading: 0.00001 in.
Source: Reference 6-2

Electronic Micrometers

Type: Direct comparison employing displacement transducer
Tolerance: 0.00002 in.
Source: Reference 6-3

Dial Indicators

Type: Direct comparison
Tolerance: Very high magnification through gearing, makes possible readings to 0.000001 in.
Source: Reference 6-2

Special Dial Indicators

Type: Direct comparison
Tolerance: Taylor-Hobson; ± 0.002 in.
Hirth micrometer; ± 0.00002 in. (mechanical magnification)
Zeiss passometer; ± 0.0001 in. (over entire measuring range)

More gearing is necessary for high magnification; therefore, the indicator becomes less sensitive and responsive. Usually a 0.0005 - or 0.0010 -in. unit is suitable because of lighter contact pressure and greater sensitivity.

Source: Reference 6-2

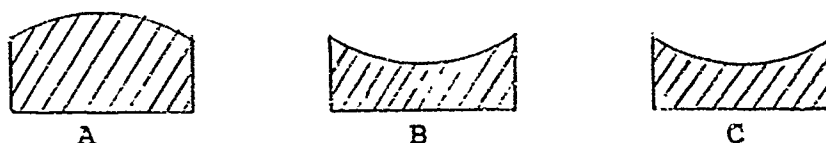
Ship Gages (Johannson Blocks)

Type: Reference devices, flat to within 10 μ in., used to measure flatness by the Whitworth or three-surface method*

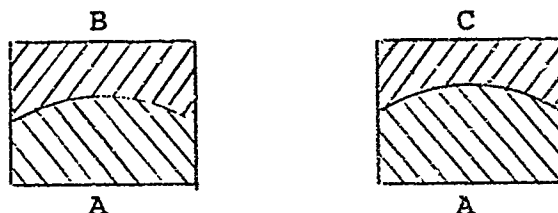
Tolerance: Reference Grade: 2 μ in. below 1 in.
2 μ in. above 1 in.
Inspection Grade: 5 μ in. below 1 in.
5 μ in. above 1 in.
Workshop Grade: 10 μ in. below 1 in.
10 μ in. above 1 in.

Source: Reference 6-3

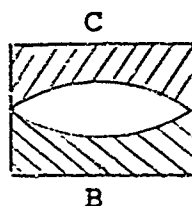
*The Whitworth Method: If two plates (one reference, one to be tested) are scraped or machined and tested against each other until contact is obtained between them over the whole surface in all relative positions, they may both be truly flat or one may be spherically convex, the other concave. In the absence of other means of testing, it is impossible to determine the contour of each surface. If, however, a third plate is machined to mate with one of the surfaces, it can then be tested against the second surface. For example, consider plates, A, B and C.



First A and B are mated: then C and A are mated.



If A is convex and B concave, C is concave. When C is tested against B, the fact that both are concave is apparent.



The only possible condition under which all three surfaces will mate is true flatness of each plate.

Standard Squares

Type: Indirect comparison to verify perpendicularity or squareness

Tolerance: ± 0.004 in.

Precision

Square Accuracy: ± 0.002 in.

Source: Reference 6-4

Straightedges

Type: Direct comparison used to measure linear distances and flatness or straightness of parts

Tolerance: ± 0.002 in. for 1- to 2-ft lengths
 ± 0.006 in. for 3- to 6-ft lengths

Source: Reference 5-4

Surface Plates

Type: Reference table. Plate material generally is chosen to minimize temperature effects, e.g., a 4-in. length of iron or steel expands 26 to 30 μ in. per $^{\circ}$ F

Tolerance: Grade A: ± 0.003 in. between 6 and 12 in.
increasing by 0.0002 in. for each ft of length

Grade B: twice tolerance of Grade A allowable

Grade C: twice tolerance of Grade B allowable

Source: Reference 6-3

Sine Bars

Type: Reference plate

Factors controlling accuracy:

Flatness of upper surface
Equality of size and roundness of rollers
Exact distance between roller axes and mutual parallelism
Parallelism of rollers to upper surface and equality of axis distances from surface

Tolerance: To attain accuracies to within ± 5 sec or 0.003 in.
 ≤ 0.00004 to 0.001 in.

Angles greater than 45° to the reference surface should not be measured: The optical level protractor (accuracy: 2-1/2 min of arc) and the precision protractor with dial-type gage readout (accuracy: 1 min of arc) are also used to measure angles.

Sources: Reference 6-2

Microscopes

Type: Measuring microscope with calibrated graticules, digital or scalar (Vernier type) readout used extensively for very precise measurements

Tolerance: ± 0.00004 in. (limitation: measurable length from 1-1/2 to 2 in.)

Type: Toolmaker's microscope, with a 6-in. by 2-in. movement range utilizing a large drum-type micrometer for table motion (ship gages may be used to extend range of travel)

Tolerance: ± 0.00001 in.

Type: Centerscope, a low-power magnification (X43) microscope used on jigs and fixtures to line up center of holes, etc., with spindle

Tolerance: ± 0.0001 in.

Type: Watts microscope, an optical centering device utilized in drilling, milling, jig-boring and lathe machines. By use of an inclined optical axis (insertion of prism) spindle runout can be compensated for. Setting of locator is adjusted to view a point in line with the axis of rotation of the machine spindle.

Tolerance: 0.0001 in.

Sources: Reference 6-5

Projectors

Type: Operate on same principles as ordinary lantern slide projectors. Project profiles of such objects as screw threads, profile gages and gear teeth onto a screen to a definite magnification, e.g., 25 or 50 times. Comparison with a similarly enlarged outline of the required or standard profile allows detection of errors of deviation. Projectors that are equipped with micrometer measuring stages can measure the image: the result is divided by the magnification power. The Vickers contour projector, Hilger inspection enlarger, Franklin Carter contour projector, the Venwick, Bausch and Lomb projectors generally have X25 to X50 magnification with 18 or 20 in. screens.

Tolerance: ± 0.0002 in. @ X50 magnification

Source: Reference 6-2

Autocollimator

Type: Checks alignment or straightness of nominally flat surfaces. Normally used to measure the straightness of long and relatively narrow surfaces such as the beds of long lathes and planing machines. Shows flatness or deviation from flatness of surface along a line representing the extrusion of the optical axis.

Tolerance: ± 0.001 in over 50-ft length 6-sec arc angle of tilt

Source: Reference 6-6

Optical Flat

Type: Commercially available direct observation technique used to check flat areas of gages, measuring surfaces, micrometer and other flat contacts. Accuracy of reference flats such that, in any area of ~ 1 sq in., departure of flatness ≤ 2 μ in.

Tolerance: ± 0.00001 in.: by estimation: ± 0.000005 in.

Source: Reference 6-5

Interferometers

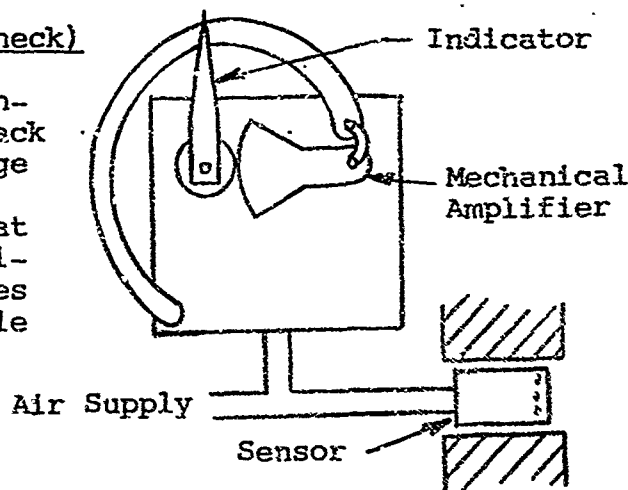
Type: Based on interference principle employed with optical flat. Extremely accurate device using light wavelengths as measuring units: red radiation of cadmium, 10^{-10} meter, official units

Tolerance: ± 0.000001 to 0.000005 in.; depending on care in observations and gage length.

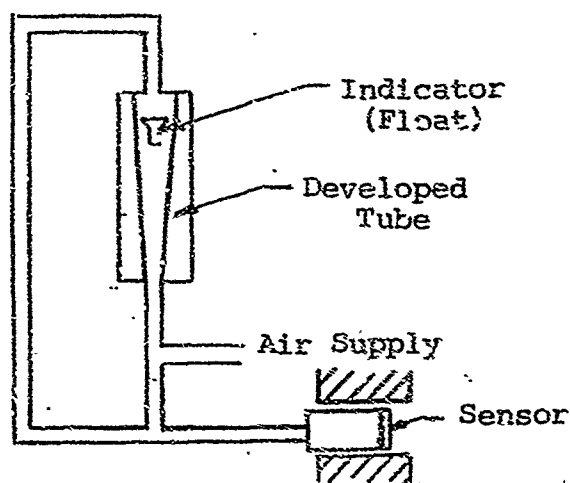
Limitations: measurable area extremely small, on order of $1/2$ in.

Pneumatic Gages (Electrocheck)

Type: Comparator device indicating change in back pressure, i.e., change in pressure due to change in clearance at sensor (variable orifice) as sensor moves through measured hole



Type: Comparator indicating device consisting of an internally-developed tapered glass tube in which a precision float is suspended in a stream of air. The relative position of this float indicates by comparison the dimension being checked. Float position determined by amount of air flowing through tube, past sensor and sensed surface.



Tolerance: ± 0.000005 in. (because of great amplifications possible)

Limitations: Working ranges for specific amplifications very limited. For example, for 5 μ in. accuracy, an amplification of 20,000:1 is used with a working range of ± 0.0001 in. deviation from reference

Source: Reference 6-7

Electrical and Electrolimit Gages

Type: Balanced ac bridge of four induction coils: two built into the electric head with a steel armature member, connected to the contact plunger or gaging spindle, between them. The bridge circuit is balanced to give a zero reading when the armature lies midway between the coils in the electric head. When the contact member moves, it causes the armature to move also, thus, upsetting the bridge circuit balance. This causes current to flow through the micrometer in proportion to the armature displacement. Sensitivity is governed by separation at coils from armature. Thus, when coils are close, magnification is high, when separated, low. Average magnification range: 1,000 to 18,000.

Tolerance: ± 0.000005 in. at high magnification

Source: Reference: 6-2

Roundness-Measuring Instruments (Talyrond, Proficorder)

Type: Used to measure external and internal diameters of such limited height parts as rollers, balls, pistons and cylinders. An electric displacement transducer or indicator carried on an optically worked precision spindle of extreme accuracy (runout $\leq 1 \mu\text{in.}$) is rotated round the inside or outside of the part to be examined. The part remains stationary on the work table. The signal from the transducer, i.e., is the deviation between reference spindle and part, is amplified and then fed into a polar or rectilinear chart recorder. The rotation of the polar chart is synchronized with that of the transducer spindle. When utilizing rectilinear charts, whereby increased chart speed and decreased transducer rotational speed provide surface roughness indication, synchronization is not attainable. The work table is movable to provide for initial centering of the part. Readout depends on the magnification utilized. Three lengths of stylus arms permit measurements to depths below the top surface of the work piece and magnification as follows:

Stylus	Depth below top of part (in.)	Magnification (X)
A	0 to 2	200, 400, 1,000, 2,000, 4,000, 10,000
B	0 to 4-1/2	100, 200, 500, 1,000, 2,000, 5,000
C	0 to 9-1/2	50, 100, 250, 500, 1,000, 2,500

Tolerance: ± 0.000005 in.

Source: Reference 6-8

This list of inspection equipment, while by no means complete, is a good indication of the commonly available and utilized equipment. The instrument manufacturers contacted as well as some of the users indicated a lack of very precise measuring equipment, which eliminates human transfer and interpolation error and which has a built-in reference. Attempts to achieve these objectives have resulted in the Newall measuring machine (Ref. 6-2), a length or end measuring machine with an accuracy of 5 μ in. The Societe Genevoise measuring machine (Ref. 6-2) designed for checking ring, snap, flat end bar, or screw thread gages, is capable of similar accuracies. Internal and external measurements can be made with $\pm 5 \mu$ in. attained accuracy. The Pitter universal measuring machine (Ref. 6-9) is another example of an ultraprecision measuring unit. This machine is used to determine the distance between holes in jigs or gages, and to measure profiles of plate gages, tapers and diameters of taper-plug gages. Accuracies of $\pm 5 \mu$ in. and ± 15 sec of arc are achieved.

6.2 Metalworking Processes

The manufacture of seals and related components requires the precisely controlled removal of material from an arbitrarily shaped piece of stock material. A list of the standard processes available for performing this follows. Accompanying this list are the maximum deviations from a true plane or circle the machines are allowed according to the Machine Tool Testing Code (Ref. 6-9, 6-10). Processes and equipment capable of machining parts to much lower deviations are available. However, they are specially designed or modified machines. Thus, limitations as to their general accuracies or maximum deviations are difficult to obtain.

Milling

One of the most versatile processes, milling, readily produces flat or contoured surfaces. Milling machines are of three basic types; knee-type horizontal milling machine, surface milling machine, and vertical milling machine. The machining accuracies based on the testing code to which machine tool builders must comply (Ref. 6-9, 6-10) are as follow.

- Work table flat or level in longitudinal and transverse direction: $\pm 0.0015/40$ in.
- Rise and fall of table during lengthwise movement: $\pm 0.0008/20$ in.
- Table parallel with cutter spindle: $\pm 0.0008/15$ in.

- Table inclination toward front or rear $\pm 0.0008/15$ in.
- Table inclination toward sides: $\pm 0.0008/15$ in.
- Overarm parallel and perpendicular to tables in horizontal and vertical plane: $\pm 0.0008/15$ in.

Machine tool manufacturers appear to agree that a milling machine with bearing ways and spindle runout held to one-half, even one-third, the limits shown can be produced.

Turning

The lathe, turret lathe, and multiple spindle lathe are the general categories of equipment utilized for turning operations. The operations which can be performed on these machines and the surface texture producible are the same for each category of equipment. The maximum deviation limits from a true plane or circle as specified by the Machine Tool Testing Code (Ref. 6-9, 6-10) and are as follow.

(1) Toolroom lathe, up to 8-in.-diam capacity

- Straightness of bed: $\pm 0.0008/40$ in.
- Bed level (no twist): $\pm 0.0008/40$ in.
- Work spindle trueness:
 - taper: ± 0.0004 in.
 - parallel to bed: $\pm 0.004/15$ in.
- Carriage slide parallel with work spindle in vertical plane: $\pm 0.0012/4$ in.
- Tailstock, parallel with bed:
 - in vertical plane; $\pm 0.0008/6$ in.
 - in horizontal plane; $\pm 0.0004/6$ in.
- Accuracy of lead screw pitch: $\pm 0.0008/15$ in.

(2) Toolroom lathe up to 15-3/4-in.-diam capacity

- Straightness of bed: $\pm 0.0008/40$ in.
- Bed level (from side to side): $\pm 0.0008/40$ in.
- Straightness of slideway up to 10 ft of cutting length: $\pm 0.0008/40$ in.

- Work spindle trueness:

Taper: ± 0.0004 in.
parallel to bed: $\pm 0.0008/15$ in. of travel

- Carriage slide parallel with work spindle in vertical plane; $\pm 0.0012/4$ in.

- Tailstock, parallel with bed:

in vertical plane; $\pm 0.0008/6$ in.
in horizontal plane; $\pm 0.0004/6$ in.

- Accuracy of lead screw pitch: $\pm 0.0012/15$ in.

(3) Toolroom lathe up to 32-in.-diam capacity

- Straightness of bed: $\pm 0.0012/40$ in.

- All other specifications the as for 15-3/4-in. unit

(4) Facing Lathe

- Faceplate level: $\pm 0.0016/40$ in. diam

- Faceplate trueness: $\pm 0.0024/40$ in. diam

- Straightness of carriage movement: $\pm 0.0012/40$ in.

- Working accuracy:

up to 10 ft turning diam round to 0.0012 in.
over 10 ft turning diam round to 0.0020 in.

- Lathe face (concave): $\pm 0.0020/40$ in. diam

(5) Turret Lathe

- Lathe turns round with turret head: ± 0.004 in.

- Lathe turns round with cutting off slide; ± 0.0004 in.

- Lathe turns cylindrically: $\pm 0.0012/15$ in.

- Lathe faces with turret head slide and cutting off slide; 0.0008/15 in.

(6) Multiple spindle automatic lathe

- After indexing, work spindle is in same position relative to tool clamping surfaces:
 - up to 2-in. diam; ± 0.0016 in.
 - over 2-in. diam; $\pm 0.0024/4$ in.
- Machine turns round:
 - up to 2-in. diam; ± 0.0006 in.
 - over 2-in. diam; $\pm 0.0008/4$ in.
- Machine turns cylindrically:
 - up to 2-in. diam; ± 0.0006 in.
 - over 2-in. diam; $\pm 0.0012/4$ in.
- Machine turns square:
 - up to 2-in. diam; ± 0.0004 in.
 - over 2-in. diam; $\pm 0.0006/4$ in.
- Work pieces taken from machine may vary one from another to the following extent:
 - to 45/64-in. bar diam; 0.0010 in.
 - 47/64 in. to 1-3/16 bar diam; 0.0013 in.
 - 1-3/16 in. to 2-in. bar diam; 0.0016 in.
 - 2-in. to 3-3/16-in. bar diam; 0.0019 in.
 - over 3-3/16-in. bar diam; 0.0022 in.

The data for prescribing tolerances for lathes are the most complete and concise available. Manufacturers are conforming to the specifications rather stringently and attribute this to the fact that the majority of lathes sold are not special; i.e., built per customer request to meet specific requirements either in accuracies desired or machine tool capacity. This allows standardization and generation of specifications.

Grinding

Equipment for grinding is of two types: that for cylindrical grinding and that for surface grinding. Cylindrical grinding is subdivided into centerless and between-center grinding. Surface grinding is accomplished either by moving the table to which the work piece is clamped or magnetically held, or by moving the grinding wheel head over the workpiece. The specifications listed in the Machine Tool Testing Code (Ref. 6-9, 6-10) to which the machine accuracies are compared are as follow.

(1) Cylindrical Grinding

- Grinds round:
 - up to 3-1/4-in. diam; ± 0.0013 in.
 - from 3-1/4- to 8-in. diam; ± 0.0020 in.
 - over 8-in. diam; ± 0.0040 in.
- Grinds cylindrically:
 - 40-in. long up to 3-1/4-in. diam;
0 to 0.0008 in.
 - 20-in. long up to 2-in. diam; 0 to 0.0004 in.
- Wheel spindle runout: not to exceed 0.001 in.
- Work spindle end play and runout: not to exceed 0.0006 in.

(2) Surface Grinding

- Ground work plane parallel; $\pm 0.0004/40$ in.
- Wheel square with table; $\pm 0.0004/15$ in.
- Wheel spindle parallel to table; $\pm 0.0004/15$ in.
- Bed and table flat and level; $\pm 0.0008/40$ in.
- Rise and fall of table in its lengthwise movement; 0.0004/40 in.
- Straightness of table movement; 0.0004/40 in.

Processes and equipment for more precise dimensional control and better surface texture generation are available. Jig borers and jig grinders are examples of such equipment. These machines are ultraprecise grinders or milling machines (named jig borers because they are primarily used for accurate location of holes, such as gear-center mounting holed). The precision attained is due to extra precautions taken in manufacturing. The bearing ways are hand-scraped for straightness and flatness, the spindles are designed for minimal axial and radial play. Accuracies of 0.0001 in. up to 24-in. measured linear or circular dimension are thus attainable. However, the calibration or measuring technique utilized for positioning the workpiece, table, or spindle limit the accuracy capabilities, as is the case with normal grinding, milling, and turning equipment.

Lapping and Honing

The purpose of lapping and honing is to produce fine surface finishes. Dimensional accuracies, such as soundness, squareness, straightness and flatness are generally not affected by these processes. Each of these gross variations is mainly predetermined by the preceding finishing process, such as grinding. Generation of a flat, smooth surface with an average roughness of 4 μ in. is possible by lapping or honing. However, flatnesses of from 0.5 to 20 μ in. up to 7 in. and 20 to 50 μ in. up to 20 in. are attainable by lapping as well as by spot grinding. Spot grinding consists of a stationary table on which the workpiece, placed on a surface plate, is moved under the grinding wheel by hand. The plane of the grinding wheel is mounted out-of-square with the spindle, thereby getting a wobbly wheel motion. Thus, the high spots are removed in a manner similar to lapping. Out-of-roundness of 1 to 20 μ in. can be generated by superfinish methods. These are lapping processes and the surfaces are essentially polished. The size of removed particles is microscopic. These methods are, however, very costly and, thus, utilized for generating measuring reference surfaces.

These processes, which may be termed standard processes, are attainable with equipment available in most machine shops. However, high-precision machining processes, developed primarily by bearing manufacturers, exist. These processes utilize the same general equipment -- grinders, lathes, milling machines, honing machines, lapping machines -- but the positioning system as well as position readout system is modified. For example, research carried out to improve the accuracy of workpieces produced on a center lathe enabled the achievement of diametral tolerances of ± 0.0001 in. The sequence enabling parts to be turned to this tolerance was first to replace the normal hand micrometer with a pneumatic micrometer caliper capable of measuring to an accuracy of 20 μ in. without relying on operator feel. The workpiece was turned to within approximately 0.002 in. of size. Without altering cutting tool or cross-slide setting, the workpiece was measured using the previously set pneumatic caliper. The tool slide was adjusted until the pneumatic gage reading showed zero. The final cut was then taken.

Another example of ultraprecision machining is the finishing of cylindrical parts for liquid springs. This process calls for machining inside diameters to 0.3 μ in. surface finish. The process begins with a "perfect" bore achieved by single point turning; next, 0.005 in. of stock is removed by rough honing; the third step is a finish hone to remove 0.002 in. of stock. The surface is then polished with two grades of metallurgical paper, using a cross-hatching principle (peaks created in the first rubbing are removed in the next as the tool moves

in the counterdirection). Finally, a two-stage lapping operation, using a Teflon lap covered with diamond particles is performed. The lap is moved in a linear direction because the desired finish pattern is parallel to the length of the bore. Thus, a surface finish of 5 μ in. is achieved.

Gas lasers are being applied to machine tools as workpiece positioning, gage setting and calibration, and other positioning devices. Operation of over 100 linear inches with accuracies of 0.00003 in. per ft up to 3 ft, or 0.00001 in. per ft from 3 ft to maximum distance are obtained. The laser output light can further be utilized in polarization studies, such as stress analysis of machined parts.

A honing process developed by Micro-Matic Hone results in improved geometric accuracy, roundness, concentricity, and surface finish of workpiece. The honing machine is capable of simultaneously honing the inside and outside diameters of a ring through use of expanding abrasive stones that also hold the workpiece. Out-of-roundness and concentricity tolerances of 25 μ in. are thus obtainable with surface finish of 1 rms.

Electrodischarge machining equipment that enables tolerances of ± 0.0005 in. on workpieces previously hardened has been obtained. Furthermore, this process permits triangular, square or round holes to be finish-machined or repaired to moderately accurate tolerances.

6.3 Dimensional Criteria

The information obtained from the measurement system and metalworking process limitations was used to establish limiting dimensional criteria. Thus, the reliability of the part being machined to the tolerance specified on the drawing and the reliability of the measuring process employed to inspect the part were established. The machining process used in finishing the part must be considered in conjunction with the inspecting system to be employed, however, to realize the true tolerance variation. For example, a Talyrond or Proficorder roundness-measuring instrument when applied to a turned shaft cannot produce a true roundness reading because of the plane in which the reading is taken cuts the involute machining marks thus generating a high and low point.

To realize correlative information pertaining to the sealing phenomena, Table 6-1 shows tolerance variables attainable for specific conditions, such as flatness and squareness. The dimensional criteria can be further summarized by hypothetical part geometries encountered during seal design. Tables 6-2, 6-3, 6-4 and 6-5 depict the hypothetical parts on the minimum tolerance variations attainable with state-of-the-art manufacturing and inspection equipment adaptable to the

specific surface-to-surface relationship. These tables can be utilized as design criteria in determining attainable manufacturing tolerances, specifying these tolerances on part detail drawings, and ensuring the machined tolerance with the inspection method capable of verifying it.

6.4 Summary

The lack of existing standards covering fabrication methods and equipment as well as inspection methods and techniques has made the objectives difficult to attain. The versatility of the lathe and milling machine allowed has made the standardization of this equipment. Thus, the most reliable data obtained have been concerned with turning and milling. Grinding equipment is not as standardized because of the many variations possible. Generally, the spindle-bearing structure and table ways govern the attainable grinding accuracies. The application of optical and/or electronic position control or readout systems has alleviated the previous error-producing area of dial reading and dial backlash. Such superfinishing processes of lapping, honing, and superfine grit grinding, cannot be qualitatively appraised because equipment and metal-removal methods vary.

The machine tool manufacturers surveyed were in accord with the instrument manufacturers in stating that a very precise absolute measuring process and accurate machine tools are lacking. The American Standard Society in conjunction with these manufacturers, has formed Committee B-59 in an attempt to rectify this problem. The goal of this committee is to establish machine tool accuracy requirements of:

- Flatness within 20 μ in.
- Roundness within 20 μ in.
- Concentricity within 10 μ in.
- Squareness within 50 μ in.
- Surface texture to 4 μ in. peak-to-valley.

To achieve these machining accuracies inspection devices must be developed capable of measuring:

- Flatness within 0.5 μ in. up to 12 in. and 2 μ in. to 20 in.
- Roundness with 2 μ in.
- Concentricity within 2 μ in.
- Squareness within 5 μ in.
- Taper within 2 seconds of arc to 30 deg angles and 3 to 5 seconds of arc for larger angles
- Surface texture of 1 to 2 μ in., peak-to-valley.

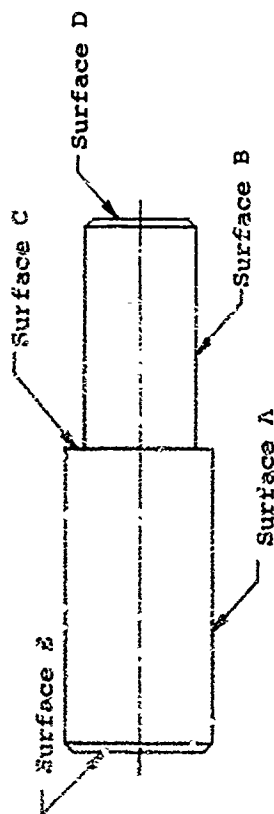
The Wright-Patterson Field Advanced Fabrication Techniques Section currently has contracted research dealing with development of metalworking and inspection equipment approaching these goals.

Table 6-1
D I M E N S I O N A L C R I T E R I A

To machine:	Process	Tolerance (10-3 in.)	Dimensional Limit (in.)	Comments
Flatness	Milling	+0.25	36	Tolerance limitation due to spindle runout, fluctuations in work table travel as cutting spindle travels. Large range machines do not exhibit accuracies applicable to low-leakage seal manufacture
	Lapping	+0.05	12	
	Grinding	+0.25	12	
Roundness	Turning	+0.2	15-3/4	Finish pattern, such as spiral for turning and cross hatch or X for lapping, is important parameter, along with tolerance in selecting methods
	Lapping	+0.05	32	
	Grinding	+0.10	12	
	Honing	+0.10	6	
Concentricity	Turning	+0.2	15-3/4	Runout of spindle governs the concentricity between two or more diameters. Part should be made in one clamping or chucking because removal and subsequent setup increase the concentricity duration
	Lapping	+0.05	32	
	Grinding	+0.10	12	
	Honing	+0.10	12	
Perpendicularity or squareness	Milling	+0.25	36	
	Turning	+0.5	32	
	Grinding	+0.25	12	
	Honing	+0.10	10	
Parallelism	Milling	+0.8	36	
	Turning	+1.0	15-3/4	
	Grinding	+0.25	12	
	Lapping	+0.05	12	
Taper	Honing	+0.10	10	
	Turning	+0.2 per 10-in. length	15-3/4	
	Grinding	+0.3 per 10-in. length	32	
	Honing	+0.1 per 10-in. length	12	
	Milling	+0.10	6	
	Grinding	+0.25	36	

Measurement	Instrument	Tolerance (10-3 in.)	Dimensional Range	Comments
Flatness	Optical flat	+0.002 to +0.004	under 1 in. to 12 in.	---
	Surface finish (Talyrod, Profil- ometer, brush)	+0.005	to 6 in.	---
	Pneumatic gage	+0.01		Indirect comparison system not a factor
	Electrical and electromagnetic gage	+0.005		Part signal not a factor. Deviation con- trols applied to magnification range
Roundness	Surface finish (Talyrod, Profil- ometer, brush)	+0.005	to 14 in.	Direct comparison with chart output
	Dial indicator	+0.10		Range not limited -- deviation from true round to 0.100 in.
	Electronic pneumatic gage	+0.01	to 12 in.	Direct comparison displacement device
	Surface finish (Talyrod, Profil- ometer, brush)	+0.00	to 14 in.	One of the diameters must act as the ref- erence with the others being compared to it. Thus, the actual reading obtained is a combination of out-of-roundness of reference diameter and diameter varia- tions
Concentricity	Dial indicator	+0.10	to 12 in.	Deviation range controls magnification
	Electronic pneumatic gage	+0.01		Deviation from square cannot exceed magnification
	Dial indicator	+0.10		One surface must act as reference surface with which the other is compared
	Comparator projector Standard square	+0.2 to ±	to 6 in. ---	
Perpendicularity or squareness	Flatness measuring equipment (4 employed. The part is placed on a surface of known flatness such as a surface plate (flat to within 0.003 in. in 12 in.). Thus, one surface of the part is used as a reference, the others compared to it.			
	Comparator projector	+0.2	to 6 in.	
	Sine bar	±3 or 5 sec of arc	Angles no greater than 45°	
	Optical level protractor	2-1/2 min of arc		
Taper	Precision protractor	1 min of arc		Use dial-type gage readout
	For taper of surfaces, parallelism measuring instruments are usable.			

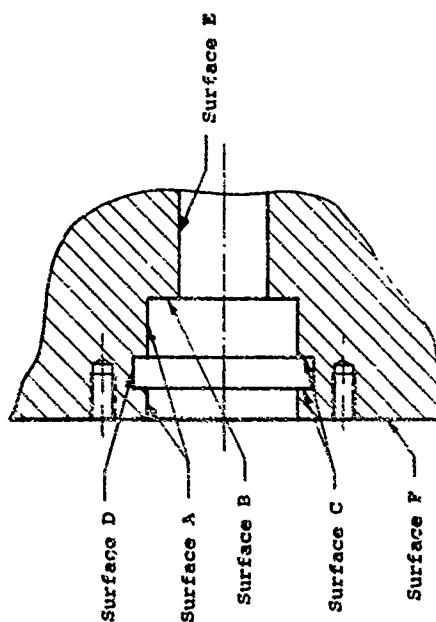
Table 6-2
TOLERANCE VARIATIONS ON SHAFT



Machining Process	Maximum diam (in.)	Description	General Tolerances (10-3 in.)					Surface Finish (μin.)
			Concentricity (A to B)	Out-of-Roundness (A or B)	Flatness (C)	Squareness (C to B C to A)	Taper (A or B) per 10 in.	
Turning	15-3/4	General machining, low to medium production	0.4	0.2	1.0	0.5	0.2	32
Turning	32	General machining, low to medium production	0.4	0.3	2.0	0.5	0.3	32
Diamond turning	15-3/4	Finish machining low to medium production	0.4	0.2	1.0	0.5	0.2	16
Honing	6	Super finish	---	0.1	0.1	---	0.10	2 - 4
Lapping	12	Super finish	---	0.05	0.05	---	---	2 - 4
Grinding	12	Cylindrical or centerless						

Measuring Device	Description	Maximum diam (in.)	Tolerance Limits (10 ⁻³ in.)			
			Concentricity (A to B)	Out-of-Roundness (A or B)	Flatness (C)	Squareness (A to C, B to C)
Limit gage	Go/no-go device	8	± 0.50	± 0.25	---	---
Air gage	Comparator	12	± 0.05	± 0.25	± 0.01	± 0.01
Micrometer	Absolute measurement	6	---	± 0.5	---	± 0.5
Electrocheck gage	Comparator	12	± 0.01 (high magnification)	---	± 0.01 (high magnification)	± 0.01
Talyrond/Proficorder	Comparator	14	---	± 0.005	± 0.005	---
Dial indicator	Absolute measurement	0.100 (deflection)	± 0.10	± 0.10	---	± 0.10

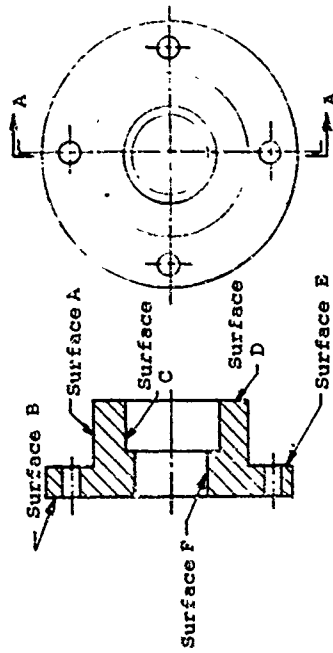
Table 6-3
TOLERANCE VARIATIONS ON HOUSING



Machining Process	Maximum Size (in.)	Description	General Tolerances (10 ⁻³ in.)					Surface Finish (μin.)	
			Concentricity (A to E, A to D)	Out-of-Round (A, E, D)	Flatness (B, F)	Squareness (C to D, A to B)	Parallelism (B to C, C to F)		
Turning	15-3/4	General machining low - medium production	0.4	0.2	1.0	0.5	0.2	1.0	32
Turning	32	General machining low - medium production	0.4	0.3	2.0	0.5	0.3	2.0	32
Grinding	12	Finish machining low - medium production	0.25	0.10	0.25	0.25	0.1	0.25	4 - 6
Milling	36	General machining	---	---	0.25	0.25	---	0.8	8
Honing	6	Super finish	---	0.10	---	---	0.10	0.1	2 - 4
Lapping	12	Super finish	---	0.05	0.05	---	---	---	2 - 4

Measuring Device	Description	Maximum Size (in.)	Tolerance Limits (10^{-3} in.)			
			Concentricity (A to E)	Out-of-Roundness (A, D, E)	Flatness (B, F)	Depth (F to B)
Limit gage	Go/no-go device	8	± 0.25	---	---	± 0.25
Air gage	Comparator	12	± 0.05	± 0.05	± 0.01	± 0.05
Micrometer	Absolute measurement	6	---	± 0.50	---	± 0.50
Electrocheck gage	Comparator	12	± 0.05	± 0.01	± 0.01	± 0.05
Talyrond/Proficorder	Comparator	14	± 0.005	± 0.005	± 0.005	---
Dial indicator	Absolute measurement	0.100 (deflection)	± 1.0	± 1.0	---	---
Caliper	Absolute measurement	12	± 1.0	± 1.0	---	± 1.0
Optical flat	Flatness measuring device	---	---	---	± 0.001	---
Depth gage		10	---	---	---	± 0.50

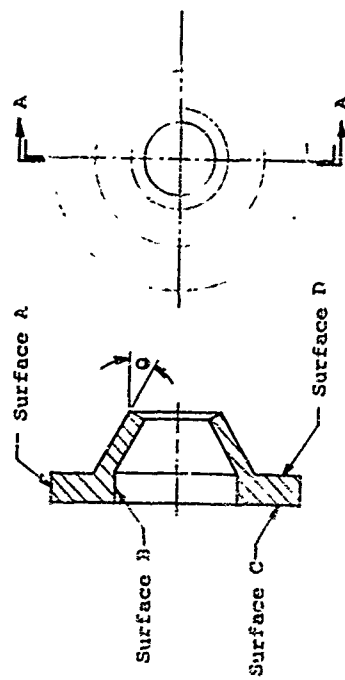
Table 6-4
TOLERANCE VARIATIONS ON FLANGE



Machining Process	Maximum Size (in.)	Description	General Tolerances (10^{-3} in.)						Surface Finish (μ in.)
			Concentricity (A to C) (C to F)	Out-of-Roundness (A, C, F)	Flatness (B, D, E)	Squareness (A to E) (C to D)	Taper (A, C, F) per 10 in.	Parallel (E to B)	
Turning	15	General machining low - medium production	0.4	0.2	1.0	0.5	0.2	1.0	32
Turning	32	General machining low - medium production	0.4	0.3	2.0	0.5	0.3	2.0	32
Grinding	12	Finish machining low - medium production	0.25	0.10	0.25	0.25	0.10	0.25	4 - 6
Milling	36	General machining	---	---	0.25	0.25	---	0.80	8
Honing	6	Super finish	---	0.10	---	---	0.10	0.10	2 - 4
Lapping	12	Super finish	000	0.05	0.05	---	---	---	2 - 4

Measuring Device	Description	Maximum Size (in.)	Tolerance Limits (10^{-3} in.)			
			Concentricity (A to C C to A)	Out-of-Roundness (A, C, F)	Flatness (B, D, E)	Parallelism (E to B)
Limit gage	Go/no-go device	8	± 0.25	± 0.25	---	---
Air gage	Comparator	12	± 0.05	± 0.05	± 0.01	± 0.01
Micrometer	Absolute measurement	6	---	± 0.50	---	± 0.50
Electrocheck gage	Comparator	12	± 0.05	± 0.01	± 0.01	± 0.01
Talysrond Proficorder	Comparator	14	± 0.005	± 0.005	± 0.005	± 0.005
Dial indicator	Absolute measurement	0.100 (deflection)	± 1.0	± 1.0	---	± 1.0
Caliper	Absolute measurement	12	± 1.0	± 1.0	---	± 1.0
Optical flat	Flatness measuring device	---	---	---	0.001	---
Depth gage	Absolute measurement	10	---	---	---	± 1.0

Table 6-5
TOLERANCE VARIATIONS ON RING



Machining Process	Maximum Size (in.)	Description	General Tolerances (10-3 in.)					Taper (0 to B or A) (sec. arc)	Surface Finish (μin.)
			Concentricity (B to A) (A, B)	Out-of-Roundness (C, D) (B to C)	Flatness (C, D) (B to C)	Squareness (C to D)	Parallelism (C to D)		
Turning	15-3/4	General machining low - medium production	0.4	0.2	1.0	0.5	1.0	±15	32
Turning	32	General machining low - medium production	0.4	0.3	2.0	0.5	2.0	±15	32
Grinding	12	Finish machining low - medium production	0.25	0.10	0.25	0.25	0.25	±5	4 - 6
Hulling	36	General machining	---	---	0.25	0.25	0.8	---	4 - 6
Honing	6	Super finish	---	0.10	---	---	0.1	±3	8
Lapping	12	Super finish	---	0.05	0.03	---	---	---	2 - 4

Measuring Device	Description	Maximum Size (in.)	Tolerance Limits (10-3 in.)			
			Concen- tricity (B to A)	Out-of- Roundness (A, B)	Flatness (C, D)	Taper (E)
Limit gage	Go/no-go device	8	± 0.25	± 0.25	---	± 0.25
Air gage	Comparator	12	± 0.05	± 0.05	± 0.01	---
Micrometer	Absolute measurement	6	---	± 0.50	---	± 0.50
Electrocheck gage	Comparator	12	± 0.05	± 0.01	± 0.01	---
Talyrond Proficorder	Comparator	14	± 0.005	± 0.005	± 0.005	---
Dial indicator	Absolute measurement	0.100 (deflection)	± 1.0	± 1.00	---	---
Caliper	Absolute measurement	12	± 1.0	± 1.0	---	± 1.0
Depth gage	Absolute measurement	10	---	---	---	± 0.50
Sine bar	Absolute measurement	45°	---	---	---	5 sec. of arc

The data and opinions gathered pertaining to the contributing factors to equipment inaccuracies point out that the reference means (surface plate, slip gage, plug gage, taper plug) and the operation readings that require interpretation and are susceptible operating errors are prime contributors to metrology instrument limitations. Machine tools are limited by the bearings and ways which determine their deviations. If, however, instrumentation that eliminates operator error becomes available, thus permitting reliable and repeatable measurement, machine-tool builders will be permitted to readily predict the inaccuracies of the bearings and ways they are employing and greater accuracy in machine tools and machined work pieces will be attained.

6.5 References

- 6-1 T. G. Beckwith and N. L. Buck, Mechanical Measurements, Addison-Wesley Publishing Co., Reading, Pa. (1961)
- 6-2 A. W. Judge, Engineering Precision Measurement, Chapman and Hall, Ltd. London (1942)
- 6-3 K. J. Hume, Engineering Metrology, MacDonald and Co., London (1953)
- 6-4 International Business Machines, Precision Measurement in the Metalworking Industry, Syracuse University Press, (1961)
- 6-5 K. J. Habell and A. Cox, Engineering Optics, Pitman Publishing Co. (1959)
- 6-6 H. C. Towre and R. Coleburne, Engineering Inspection Measurement and Testing, Odhams Press, London (1957)
- 6-7 Precision Gaging, The Sheffield Co., Dayton, Ohio (1960)
- 6-8 R. E. Reason, Basic Principles at Surface Metrology, Taylor, Taylor and Holison Paper 11, Taylor, Taylor and Holison, Inc., Leicester, England (1957)
- 6-9 G. Schlesinger, Testing Machine Tools, The Machinery Publishing Co. (1938)
- 6-10 Machine Tool Testing, The Tumpene Company, Inc. Macon, Ga. (1961)

BIBLIOGRAPHY

- W. H. Armstrong, Machine Tools for Metal Cutting, McGraw Hill (1957)
- Henry Frick, "Design Guide to Value - II," Product Engineering 35 No. 5, 45-53 (1964)
- R. Jenkins, Fundamentals of Mechanical Inspection, McGraw Hill (1955)
- J. Johnson, Precision Measurements, Pitman Publishing Co. (1957)
- R. F. Moore and F. C. Victory, Holes, Contours, and Surfaces, The Moore Special Tool Co., Bridgeport, Conn. (1961)

National Bureau of Standards, Precision Measurement and Calibration, Handbook 77 Volume 3 (1961)

Pratt and Whitney Co., Air Gages, Bulletin D 51, West Hartford Conn. (1963)

M. J. Puttock, "Precision Measurement of Circularity, Concentricity and Straightness of Plain and Taper Rings and Plugs" Machine Shop Magazine 9, 72, (1948)

F. H. Roit, Gauges and Fine Measurement Volumes 1 and 2, Macmillan (1929)

Sheffield Standards Laboratory Instruments, The Sheffield Company, Dayton, Ohio (1963)

Precision Measuring Tools, Van Keuren Company, Catalog and Handbook 36, Watertown, Mass. (1955)

INDIVIDUAL CONTACTS

Advances Fabrication Branch, Manufacturing Technology Division, Air Force Material Laboratory, Wright-Patterson Air Force Base Ohio

Mr. Robert T. Jameson
Mr. Lloyd Smith
Mr. John Snyder
Mr. William Webster
Mr. Floyd F. Whitney

U. S. Bureau of Standards, Washington D. C.

Mr. J. H. Tullmer, Chief of Metrology
Mr. W. Sandenburg

Air Force Quality Control Department, Midwest Region, O'Hare International Airport, Chicago, Ill.

Mr. R. Donner
Mr. J. Tiffani

U. S. Army Rock Island Arsenal, Production Planning Department, Rock Island, Ill.

Mr. F. Ahlberg

Inspection of Materials Office, Department of Army and Navy, Chicago, Ill.

Resident Inspector

Material Inspection Dept. U. S. Air Force Machine Tool Storage Site, Terre Haute, Ind.

7. ANALYTICAL CRITERIA FOR TYPICAL METALLIC SEAL STRUCTURES

An objective in the analysis of any interfacial seal is to relate the deformation of the seal structure to the load acting at the sealing interface. Among the factors governing deformation, the structural shape is the most significant variable. Aside from strength requirements, the shape of a seal is most often determined by the designers' conception of a seal. It is usually an individualistic design approach since there is often little agreement on the criteria for effective sealing. This is demonstrated by the vast array of commercially available seals, many of which are intended for the same functions.

A philosophy developed in the course of this seal research is that the shape of a seal structure is relatively unimportant compared to the requirements at the sealing interface. Assuming that certain interface load requirements can be attained, the remaining seal requirements are structurally related but not intrinsically related to the shape. This implies that many seal shapes can have the same structural function and behavior. The philosophy departs from the commercial viewpoint that the shape is of primary importance. While it is recognized that the shape is important, it must be placed in proper perspective with other seal requirements.

Considering the variety and importance of the structural shape, it is felt that development of comprehensive shape criteria is not beneficial. An alternative approach is to select several common seal shapes and demonstrate methods of structural analysis. This approach should provide the systems designer with sufficient insight into the over-all seal problem so that he can apply similar techniques to any seal shape.

To demonstrate rational analytical procedures, three lip seal configurations, that are similar in general appearance but contain slight structural differences were chosen:

- Case I A functionally elastic lip seal having a constant leg thickness with initial plastic deformation at the sealing interface.
- Case II An elastically deformed lip seal having constant leg thickness.
- Case III An elastically deformed lip seal having varying leg thickness.

Each of the preceding seals could be used in static, sliding or rotating seal applications. However, sample calculations are presented whereby a Case I seal is analyzed as a sliding seal and a Case II seal represented by a static seal. In each case, an

interface contact load is assumed followed by step-by-step procedure to determine the deformation and principal stresses.

In addition to the influence of structural shape, the other deformation factors considered are

- fluid pressure
- material properties
- seal housing or cavity geometry.

Other factors, such as pressure fluctuations and thermal deformation, are considered separately in Section 8, along with organized procedures for predicting over-all seal performance, including interfacial requirements.

7.1 Case I, Constant Thickness Seal Leg, Plastically Deformed at the Interface

7.1.1 General Analysis

The analysis of a constant thickness flexible leg seal, as shown on figure 7-1, is based on one-dimensional beam theory. While a three-dimensional stress field solution may be more encompassing, experiments have shown that the one-dimensional solution is a very close engineering approximation for the structure deformation.

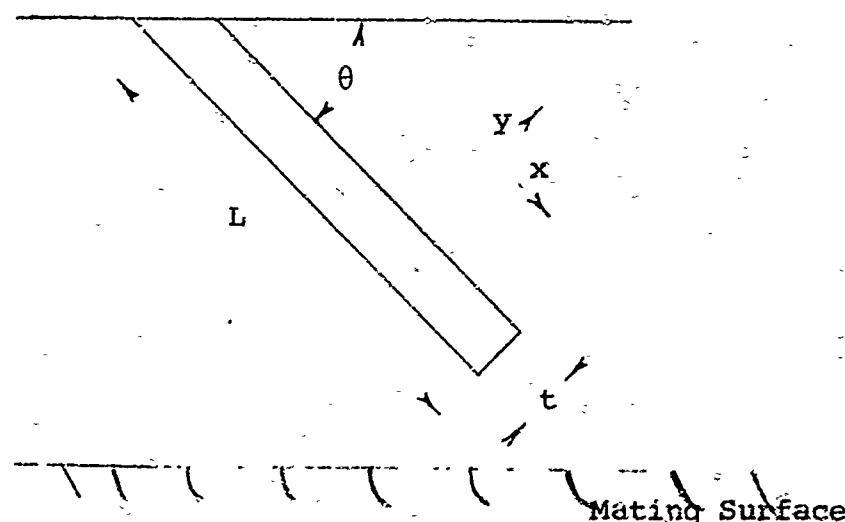


Figure 7-1 Initial state of a seal leg with constant thickness

One of the design objectives is to permit plastic deformation of a part of the seal leg in contact with the mating surface while the remainder of the leg deforms elastically. Since the most critical part of the seal function is the elastic deformation, comprehensive consideration is given to the maximum bending stress, hoop stress, and working stress.

Bending Stress. The initial configuration of the seal and the principal axis are shown on figure 7-1 and the geometric relationships between the leg length and deflection are defined on figure 7-2. When the seal is installed, the leg flexes and contacts the mating surface at the tip. The application of fluid pressure flattens the end of the leg a distance L_p . An active length, L_a , remains and constitutes that portion of the leg that deforms elastically.

The requirements for the initial radial deflection at the leg tip can be stated:

- It must be large enough to permit conformity with the mating surface.
- It cannot produce excessive bending stresses in the the leg length, L_a .
- It cannot produce excessive hoop stresses.
- It cannot create excessive friction force in sliding applications. Therefore, the radial load distributed across leg L_p must intentionally be low (i.e., 100 psi or less).

To satisfy these requirements, the lip thickness t must be such that:

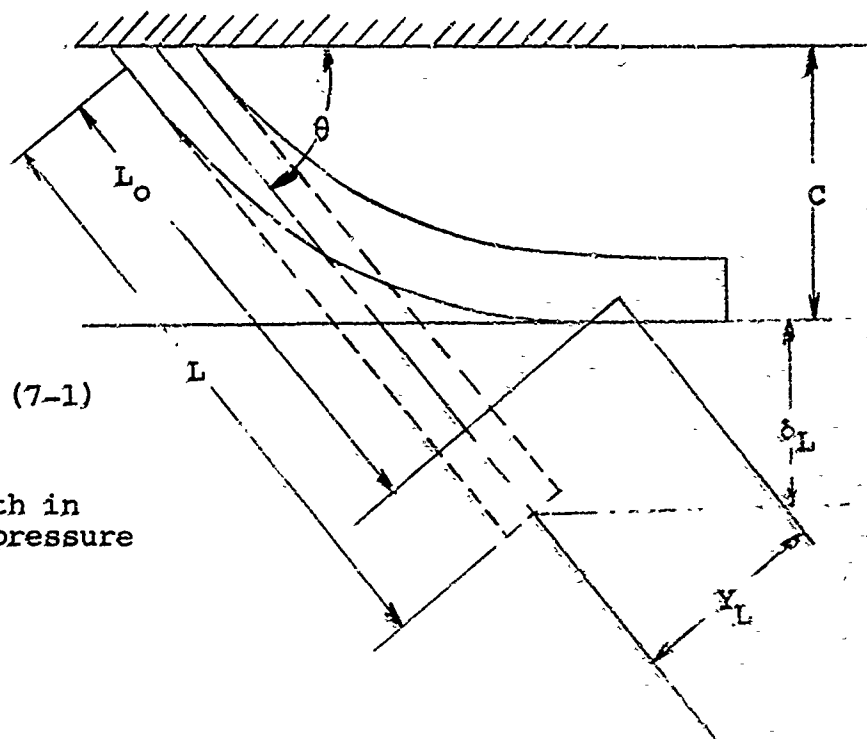
- Pressure loading can be elastically supported.
- Excessive axial force in assembly is not required.
- The lip has sufficient elasticity to compensate for radial movement of parts and initial installation.

Before the analysis can proceed, the following assumptions must be made.

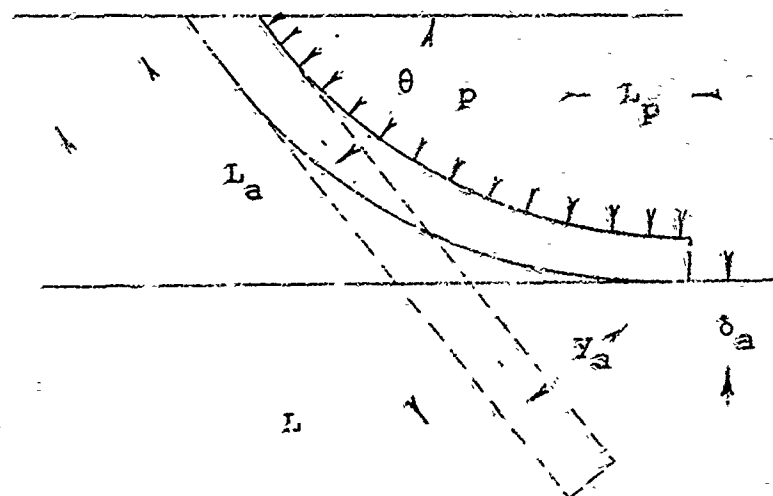
- The deflections are small enough to be able to apply simple beam theory.
- The hoop stresses are neglected.
- The tip of the lip can slide unconstrained along the contact surface under the influence of fluid pressure as shown in figure 7-2. The frictional restraint at the tip is neglected.

$$-y_L = \frac{C - L_o \sin \theta}{\cos \theta} \quad (7-1)$$

L_o = active leg length in the absence of pressure



(a) Installed State



$$-y_a = \frac{C - L_a \sin \theta}{\cos \theta} \quad (7-2)$$

(b) Pressurized State

Figure 7-2 The geometric relationships between the leg length and deflection for a seal of uniform thickness.

The restriction on the deflections imposed by the first assumption can usually be satisfied. The effect of the hoop stresses will be to create a two-dimensional stress field on the seal. This effect is considered later in this section. The effect of the frictional restraint at the tip is the imposition of an additional tensile stress in the lip in the same direction as the bending stress. By assuming negligible frictional restraint, this tensile stress is neglected.

From beam theory, the relationship between the deflection and the pressure loading p acting over the elastic length, L_a is

$$\frac{d^4 y}{dx^4} = -\frac{p}{EI} \quad (7-3)$$

The negative sign on the load p is a sign convention so that deflections y above the free-state neutral axis are positive.

Integration of equation (7-3) and application of the known boundary conditions yields a relationship for stress, deflection, and reaction load. The boundary conditions at the fixed end of the leg are

$$x = 0 \quad y = 0$$

$$x = 0 \quad \frac{dy}{dx} = 0$$

at the elastic extremity of the leg

$$x = L_a \quad y = y_a$$

$$x = L_a \quad \frac{dy}{dx} = \tan \theta$$

The following relationships are derived by integration of equation (7-3) and substitution of the boundary conditions.

After substituting $I = \frac{t^3}{12}$, the deflection of the leg:

$$y = \left[\frac{p}{2Et^3} \right] x^4 - \left[\frac{pL_a}{Et^3} + \frac{2C}{L_a^3 \cos \theta} - \frac{\tan \theta}{L_a^2} \right] x^3 + \left[\frac{pL_a^2}{2Et^3} + \frac{3C}{L_a^2 \cos \theta} - \frac{2 \tan \theta}{L_a} \right] x^2 \quad (7-4)$$

The bending stress given as $M = \frac{Et^3}{12} \frac{d^2 y}{dx^2}$ can be derived from equation (7-4). Following this step and imposing the boundary conditions $M = 0$ at $x = L_a$ yields

$$L_a^4 + \frac{2Et^3 \tan \theta}{p} L_a - \frac{6Et^3 C}{p \cos \theta} = 0 \quad (7-5)$$

Letting $p = 0$ in equation (7-5) and substituting the geometrical identities yields the following restriction on the dimensions

$$\frac{2C}{y_L} = \cos \theta \leq 1 \quad \text{and} \quad L_o = 3 C / \sin \theta \quad (7-6)$$

The maximum bending stress at the built in end is:

$$\sigma_a = \frac{pL_a^2}{2t^2} + \frac{3Et C}{L_a^2 \cos \theta} - \frac{2Et \tan \theta}{L_a} \quad (7-7)$$

Substituting equation (7-5) in (7-7)

$$\sigma_a = - \frac{3Et \tan \theta}{L_a} + \frac{6Et C}{L_a^2 \cos \theta} \quad (7-8)$$

and employing the trigometric properties of figure (7-1), equation (7-8) can be rewritten

$$\sigma_a = - \frac{3Et \sqrt{y_L^2 - 4C^2}}{2L_a C} - \frac{3Et y_L}{L_a^2} \quad (7-9)$$

Recombining equations (7-5) and (7-7) yields a quadratic equation having one positive root given in terms of the active length

$$L_a = t \sqrt{\frac{\sigma_a}{3p}} \sqrt{1 + \sqrt{1 + \frac{18 p E C}{t \sigma_a^2 \cos \theta}}} \quad (7-10)$$

The reaction force, \bar{P} , at length L_a is

$$\bar{P} = \frac{pL_a}{2 \cos \theta} - \frac{Et^3 C}{L_a^3 \cos^2 \theta} + \frac{Et^3 \tan \theta}{2L_a^2 \cos \theta} \quad (7-11)$$

Solving equation (7-5) for p and substituting the trigometric relationships for θ yields

$$\bar{p} = \frac{Et^3 y_L \left[4y_L c + L_a \sqrt{y_L^2 - 4c^2} \right]}{8L_a^3 c^2} \quad (7-12)$$

and when $p = 0$, the reaction force is

$$\bar{p}_0 = - \frac{Et^3 \left[y_L^2 - 4c^2 \right]^{3/2}}{216 y_L c^4} \quad (7-13)$$

where \bar{p}_0 is the sealing force due to initial installation.

Because of the complexity of the equations, the simplest approach is to assume several of the dimensions and use the equations to solve for the others. The initial choice of dimensions will be influenced by the application. For example, material strength determines the allowable stress. Movement of the mating surface because of shaft wobble, eccentricity, or side loading may determine the required deflection normal to the mating surface δ_L . In the case of secondary movement of the mating surface, the initial deflection δ_L must be greater than any motion of the mating surface to prevent loss of contact between the seal lip and the mating surface.

Hoop Stress. As the seal deflects against the mating surface, a circumferential elongation of the seal leg occurs as shown schematically in figure 7-3.

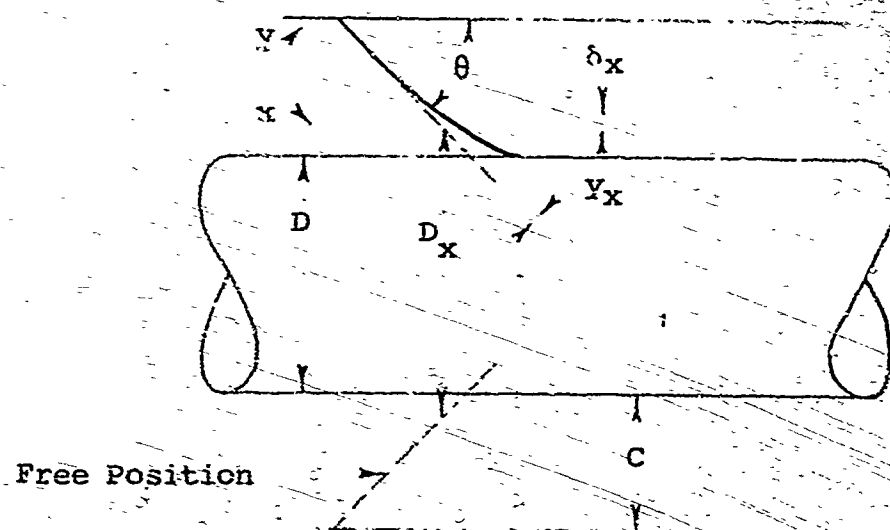


Figure 7-3. Deflection of a seal

The circumferential deflection of the seal at any position x along the length of the leg is given by

$$\delta_{cx} = \pi (Dx + 2\delta_x) - \pi DX \quad (7-14)$$

where

δ_{cx} = circumferential deflection at x (in.)

δ_x = deflection normal to the mating surfaces at x (in.)

Dx = free seal diameter at x (in.)

Then,

$$\delta_{cx} = 2\pi\delta_x \quad (7-15)$$

The circumferential strain will be given by

$$\epsilon = \frac{\delta_{cx}}{\pi Dx} \quad (7-16)$$

Additional consideration must be given to the portion of the lip that is deflected flat against the mating surface by the action of the fluid pressure. These geometric relations are shown in figure 7-4.

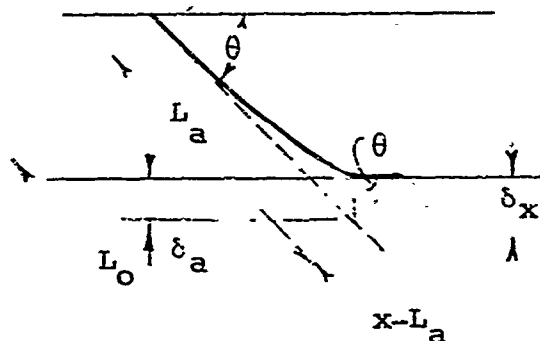


Figure 7-4 Geometric relations for the portion of the leg flattened by fluid pressure

In this case -

$$\delta_x = \delta_a + (x - L_a) \tan \theta \quad (7-17)$$

The values of δ_a and L_a can be found for any value of pressure loading P from equations (7-2) and (7-10).

The values of δx can now be found from equation (7-4) and $\delta x = y_x \cos \theta$ for the active portion of the lip and from equation (7-17) for the flattened portion of the lip. The values of δx can be used in equation (7-15) to find the circumferential elongation. The hoop stress is given by

$$\sigma_R = \epsilon E \quad (7-18)$$

The hoop stress distribution along the entire length of the seal lip can now be determined.

Maximum Working Stress. Variations in load produce variations in deflection of the seal lip, causing varying stresses in the lip. These varying deflections can be caused by:

- Secondary motion of the mating surface
- Pressure fluctuation

The probable presence of stress variations superimposed on a steady stress makes the consideration of the fatigue resistance of the seal design necessary.

Variations in the bending stress are likely to be the largest stress variations. This is because flexing of the lip not in contact with the mating surface will occur as the result of mating surface movement or pressure fluctuation. The hoop stresses in this portion of the lip are much smaller than the bending stresses. Thus, fatigue in bending becomes the dominant factor.

The amount of stress variation due to radial motion can be approximated by calculating the bending stress variation at the built-in end of the lip. This is due to changes in the tip deflection δ_L . The change in stress is calculated for the case of zero fluid pressure for simplicity, since changes in the bending stress due to changes in tip deflection are not influenced to a large extent by the pressure loading unless the pressure is fluctuating. The pressure loading will, however, have a very important influence on the steady or average stress.

The procedure followed is to calculate the bending stress at the built-in end of the leg for deflections δ_{L1} and δ_{L2} which are above and below the designed initial lip tip deflection δ_L . The values of δ_{L1} and δ_{L2} must be based on an estimation of the amplitude of the secondary motion expected in the mating surface. The maximum stress, σ_m , at p_m is given by equation (7-9).

In this manner a range of varying stress and an average stress are determined. The allowable combination of varying and average stresses that can be tolerated depends on the endurance limit S_e and the yield strength of the material. There is an infinite number of acceptable combinations. The acceptability of any particular combination of average and varying stress levels determined by the procedures previously discussed is determined graphically by the use of a Goodman diagram (Ref. 7-1).

At this point, the entire design analysis can be summarized in a step-by-step procedure. To determine a leg tip deflection δ_L

- (1) Select values of E , L_0 , t , and δ_L
- (2) Use equation (7-6) to find clearance C
- (3) From δ_L and C use the geometric relations shown in figure 7-2 and calculate angle θ
- (4) Let $p = 0$ in equation (7-7) and calculate the initial bending stress, due to installation, at the fixed end of the leg (in equation (7-7), when $p = 0$, $L_a = L_0$)
- (5) If the stress calculated in step 4 is acceptable, find L_a as a function of p by the use of equation (7-10). To employ equation (7-10), it must first be established that

$$\frac{18 p E C}{t \sigma_a^2 \cos \theta} > 1 \quad \text{and} \quad \left[\frac{18 p E C}{t \sigma_a^2 \cos \theta} \right]^{\frac{1}{2}} > 1.$$

Equation (7-10) then reduces to

$$L_a = t \left[\frac{2 E C}{t p \cos \theta} \right]^{\frac{1}{2}} \quad (7-19)$$

- (6) Find the bending stress at the fixed end of the leg from equation (7-9)
- (7) Find the reaction force at $x = L_a$ from equation (7-12)

If the bending stress calculated in step 4 is excessive, the initial geometry must be changed to bring the stress to an acceptable level. This may be accomplished by increasing the thickness or decreasing the initial leg tip deflection δ_L .

If step 4 gives an acceptable stress level but step 6 shows an excessive stress as a result of the pressure loading, then the thickness may be increased or the clearance C may be reduced, thus decreasing θ

- (8) After acceptable bending stresses have been attained, use the geometric relations shown in figure 7-2 and equations (7-14), (7-15), (7-16), and (7-17) to determine the hoop stress distribution in the seal lip.

For most cases the hoop stress will be large only at and near the leg tip. The hoop stress decreases at points approaching the fixed end. Thus, the hoop stress is large where the bending stress is small and vice versa. In most cases the effects of bending and hoop stresses can be considered separately. In many cases, the hoop stresses in the region near the leg tip, which is flattened by the action of the fluid pressure, may be large enough to cause some plastic deformation. However, since there is no bending in this region some plastic circumferential deformation is tolerable.

- (9) Assume extreme values of tip deflection δ_L and calculate maximum, minimum and average bending stresses at the fixed end using equation (7-19). Use a Goodman diagram drawn with the values of endurance limit σ_e , yield strength and ultimate strength of the material chosen. Determine if the operating stresses fall within the acceptable ranges for the material chosen.

7.1.2 Design Example

A sliding application is chosen to demonstrate the step-by-step procedures. The advantages of this seal in a sliding application are:

- The flexibility of the sealing leg will allow the seal to remain in contact even when a degree of motion of the mating surface takes place normal to the interface.
- A thin leg may deflect with a relatively small force. Thus, the contact stress will be limited.
- The pressure forces acting on the relatively thin leg increase the conformity of the lip to the mating surface.

The first two characteristics of this configuration make it suitable for use as a dynamic seal. This configuration can be used as a sliding seal for reciprocating motion or a face-type seal for rotary motion. The flexibility of the lip will allow it to tolerate a certain amount of mating surface motion as a result of eccentricity, shaft wobble, and side loading effects. By maintaining a fairly low contact stress, the wear rate is minimized. Since the problem of wear severely limits the allowable contact stress, the flexibility of the seal lip must provide the conformity.

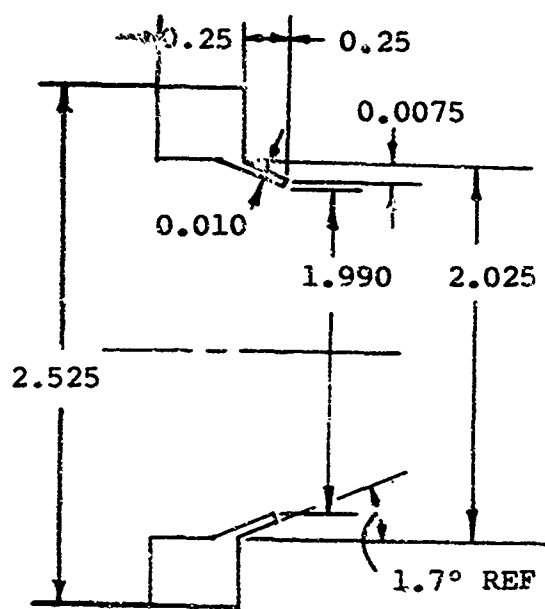


Figure 7-5 Cross section of prototype sliding seal

The seal is a single leg mating with a 2-in. shaft. The assumed properties are shown in step 1 and figure 7-5.

Step 1

Assume $E = 30,000 \text{ ksi}$
 $L = 0.25 \text{ in.}$
 $t = 0.010 \text{ in.}$
 $\delta_L = 0.005 \text{ in.}$
 Rod diameter $D = 2 \text{ in.}$

Step 2

Assume $\delta_L \approx y_L$

From equation (7-6), $\delta_L \approx y_L \geq 2C$

The clearance C is given

$$C = 2.5 \times 10^{-3} \text{ in.}$$

Step 3

From the geometry shown on figure 7-5

$$\theta = 1.7^\circ$$

Step 4

If p in equation (7-5) equals zero, $L_o = L_a$, and the bending stress at the fixed end is given by equations (7-6) and (7-7). The $\sigma_b = 37,100 \text{ psi}$.

Step 5

This bending stress is within the limits of most steel materials. The active length L_a is now found as a function of pressure by the use of equation (7-19). To apply this equation, the following must apply

$$\frac{18 p E C}{t \sigma_a^2 \cos \theta} \gg 1.$$

Substituting value (assuming σ_a at $p = 0$) yields $0.101 p \gg 1$. A minimum assumed pressure chosen is, therefore, 100 psi.

Solutions to equation (7-19) are shown on Table 7-1 and graphically on figure 7-6.

Table 7-1

EFFECT OF PRESSURE LOADING ON FLEXIBLE LEG
OF UNIFORM THICKNESS

Pressure (psi)	Active Length L_a (in.)	Bending Stress at Built-in End σ_a (psi)	Reaction Load per Unit Length of Mean Leg Circumference \bar{P} (lb/in.)
0	0.246	3.71×10^4	10
100	0.197	2.3	20
300	0.150	1.8	44
500	0.131	-5.4	66
700	0.121	-8.2	85
1000	0.111	-11.8	110
1200	0.106	-14.4	125

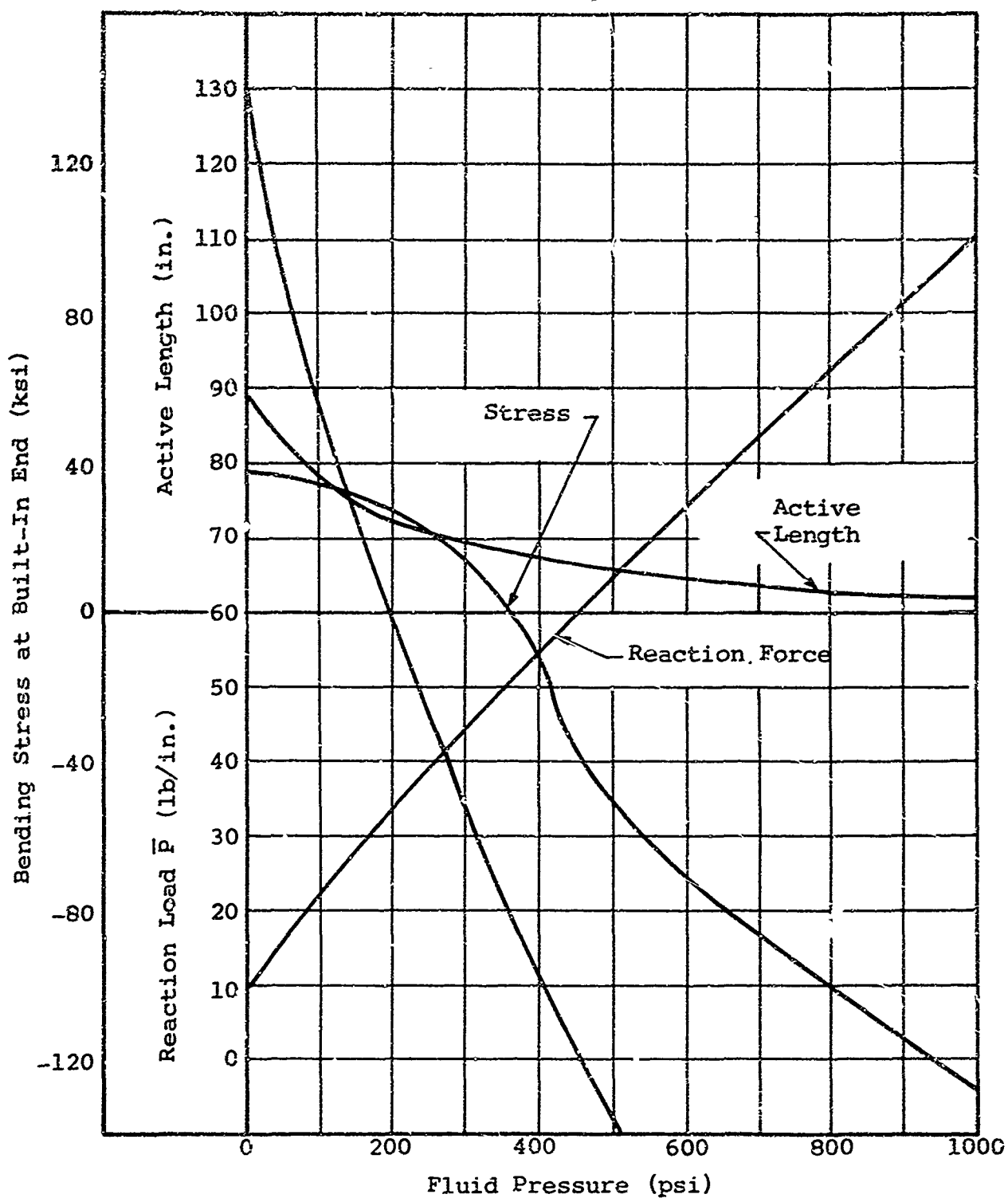


Figure 7-6 Effects of pressure on a flexible leg

Step 6

From the properties given and L_a , the bending stress at the fixed end is determined as a function of p .

Step 7

The reaction load is now found from equation (7-12).

The results of Steps 5, 6, and 7 are given in Table 7-1 and shown graphically on figure 7-6.

Step 8

The hoop stress distribution is found using the geometric relation of figure 7-2, values of L_a , δ_a and P from Table 7-1 and equations (7-15), (7-16), (7-17), and (7-18). The hoop stress distribution at 100 psi fluid pressure is given in Table 7-2.

Step 9

The design deflection δ_L was 0.005 in. The bending stress at the fixed end is calculated for $\delta_L = 0.006$ and $\delta_L = 0.004$ from equation (7-8) and assuming the maximum working pressure = 500 psi. This condition simulates the radial displacement of the shaft or seal housing deformation.

Where

$$y_L \approx \delta_L$$

The stress range is found as

$$\sigma_a = 90,000 \text{ psi when } \delta_L = 0.006 \text{ in.}$$

$$\sigma_a = 34,000 \text{ psi when } \delta_L = 0.004 \text{ in.}$$

Thus

$$\sigma_{av} = 62,000$$

These values are plotted on a modified Goodman diagram (figure 7-7) for AISI 414 steel. The operating range does not fall within the allowable range and hence, a lower working pressure must be selected. If the pressure fluctuates, a stress reversal occurs further reducing the maximum working pressure.

Table 7-2

HOOP STRESS DISTRIBUTION FOR A LIP SEAL
OF UNIFORM THICKNESS ($p = 100$ psi)

Position x (in.)	δ_y (in.)	Hoop Stress (ksi)
0.05	6.7×10^{-5}	2
0.10	8.2×10^{-4}	24.6
0.15	9.7×10^{-4}	29
$0.197 = L_a$	3.3×10^{-3}	99
0.25	4.9×10^{-3}	147

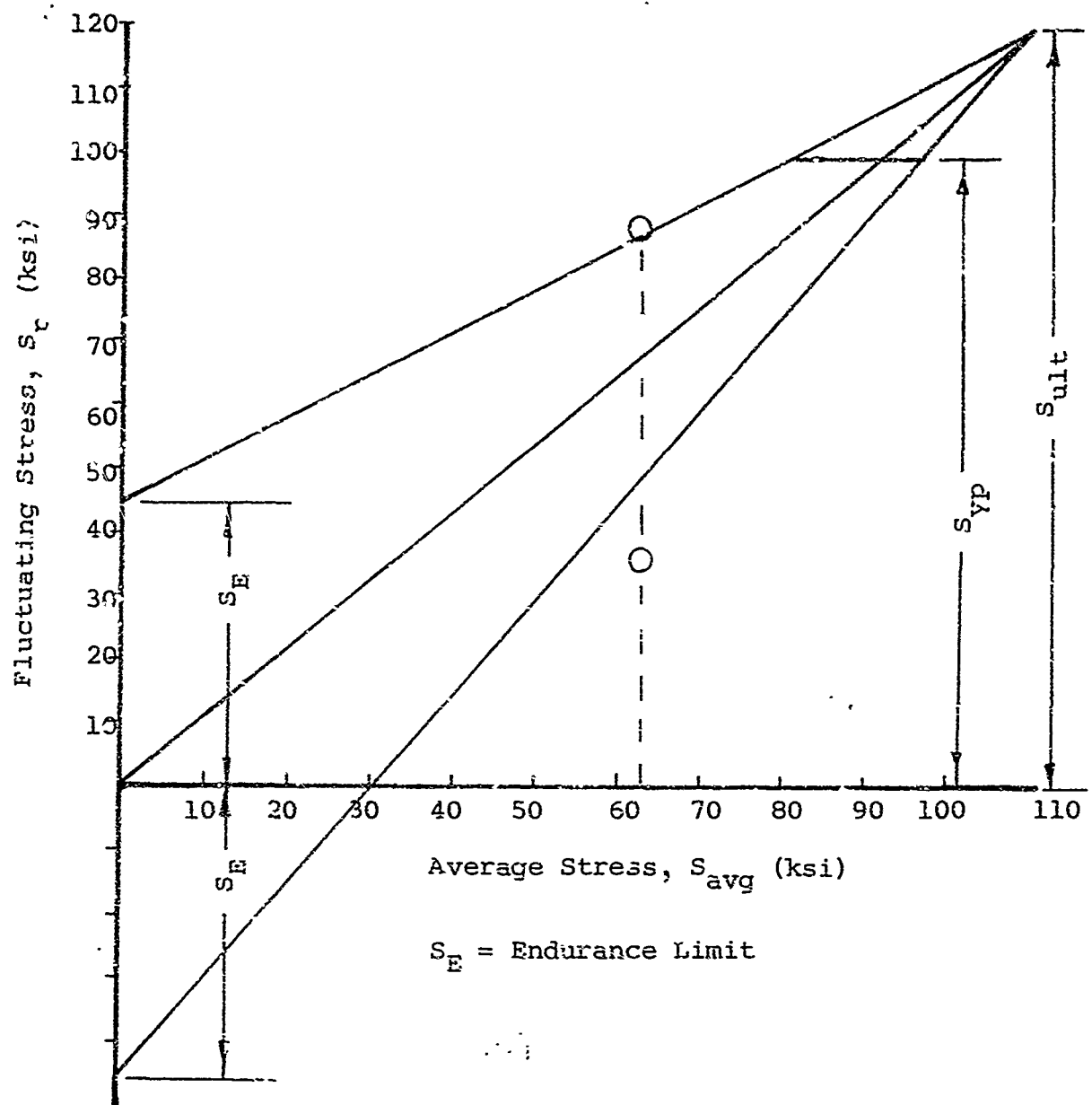


Figure 7-7 Modified Goodman diagram for AISI 414 stainless steel

As the curve of figure 7-6 and the data of Table 7-2 show, the effect of fluid pressure acting on the leg first reduces the bending stress at the built-in end. As the pressure increases, the bending stress reverses, then increases in the opposite direction. This is due to buckling of the leg near the built-in end, causing a stress reversal. As the pressure increases, the leg will tend to straighten in the vicinity of the built-in end. This action will cause the bending stress at the built-in end to decrease before the reversal of bending stress actually occurs. This effect is shown schematically in figure 7-8.

The values of deflection, calculated from the deflection equations given in Table 7-3, verify the deflection shapes shown in figure 7-8. The deflections near the built-in end are negative for a pressure of 518.8 psi, as seen in Table 7-3. This indicates that a double curvature, as shown in figure 7-8, occurs from increased fluid pressure. This effect has important implications in the design of a seal.

The bending stress at the built-in end of the leg is a function of the deflection of the leg tip. Thus, to keep the bending stress within acceptable limits, the vertical deflection δ_L must be kept small.

However, the ability of the seal to withstand the effects of pressure is dependent on the angle θ once an initial deflection δ_L and a length L_0 are chosen. Thus, the value of C , the clearance, is restricted. As the angle θ gets smaller, the reversal of stress occurs at higher fluid pressures. Thus, with an initial deflection δ_L small enough to keep the bending stress within an acceptable limit, a small angle θ will allow the seal to function at higher pressures. The restriction of equation (7-14) $y_L \geq 2C$ can serve as a criterion for establishing the angle θ . In an additional calculation, all values of the dimensional parameters of the leg used in the numerical example were kept constant except the angle θ , which was changed from 1.7° to 5° . With this configuration, a bending stress of 110 ksi in the reverse direction was calculated for a fluid pressure of 440 psi. This indicates the importance of the angle θ on the ability of the seal to function under the influence of fluid pressure.

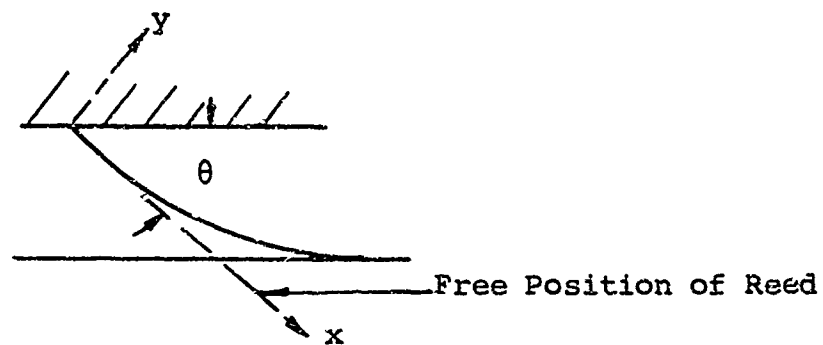
The previous discussion indicates that the deflection and the angle θ must be kept as small as possible in order for the seal to be able to function throughout a fairly wide range of pressures. Improvements in the ability of the seal to withstand the effects of fluid pressure can be attained by increasing the leg thickness t . This will most likely result in an increase in the reaction force at the constant point.

Table 7-3

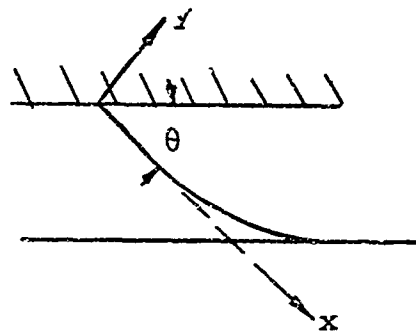
DEFLECTION OF LEG SEAL WITH PRESSURE LOADING

$L_0 = 0.25$ in., $t = 0.10$ in., $\theta = 1.7^\circ$

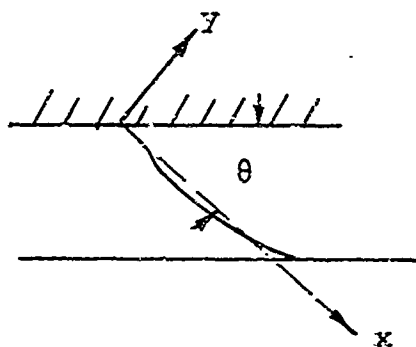
Distance Along Neutral Axis $x(\text{in.})$	Deflection for Pres- sure of 38 psi and L_a of 0.21 in. $y(\text{in.})$	Deflection for Pres- sure of 515.8 psi and L_a of 0.14 in. $y(\text{in.})$
0.01	0.0085×10^{-3}	-0.00096×10^{-3}
0.02	0.0348×10^{-3}	-0.0393×10^{-3}
0.04	0.1458×10^{-3}	-0.0430×10^{-3}
0.06	0.331×10^{-3}	0.0332×10^{-3}
0.08	0.594×10^{-3}	0.231×10^{-3}
0.10	0.932×10^{-3}	0.503×10^{-3}
0.12	1.339×10^{-3}	1.113×10^{-3}
0.14	1.808×10^{-3}	1.689×10^{-3}
0.16	1.977×10^{-3}	
0.18	2.932×10^{-3}	
0.20	3.479×10^{-3}	
0.21	3.784×10^{-3}	



(a) Deflection of reed with no fluid pressure



(b) Deflection of reed with low fluid pressure



(c) Deflection of reed with increased fluid pressure

Figure 7-8 Effect of fluid pressure on lip deflection

In a sliding seal, there are certain practical limitations on the geometry that are not present in static sealing applications. For example, the vertical deflection, δ_L , the angle θ , and the clearance C must be large enough to account for the radial motion, due to bearing play and shaft misalignment, that is always present in a sliding seal application.

7.2 Case II, Constant-Thickness Seal Leg, Elastically Deformed

The subsequent analytical criteria for the seal shown in figure 7-9 were originally developed by General Electric Company (Ref. 7-2). The general configuration of the seal is typical of many commercial seals. By maintaining a small contact area, fairly high contact stresses may be achieved without resorting to high total contact loads. This type of seal is usually designed so that the bending stresses in the seal legs remain elastic and the legs thus retain their resilience. A configuration of this type is particularly useful when the sealing contact area can be coated or plated with a soft material. If the seal is not coated or plated, it may be difficult to achieve the proper contact stress at the sealing contact area.

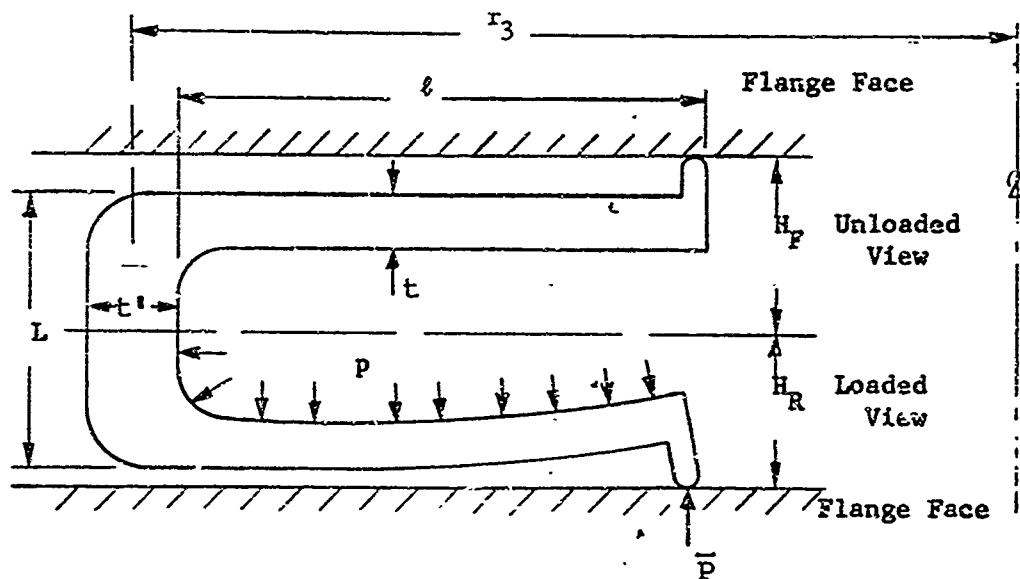


Figure 7-9 Seal with cantilever leg of constant thickness

As discussed in Subsection 7.1, the contact stress required to achieve adequate sealing with most structural metallic materials such as steel and aluminum is quite high. To attain a sufficient initial interface contact stress and stay within the elastic limits on the bending stress, σ_b , of the seal legs, the stiffness of the seal leg must be large. Large stiffness of the seal legs however, reduces their ability to deflect under the pressure loading, thereby reducing the effectiveness of the

pressure actuation. In any event the procedures developed by General Electric (Ref. 7-2) simplify the design calculation for these particular seal configurations and should prove useful in cases where the required sealing contact stress is relatively low, i.e., plated or coated contact surfaces. Because the contact load is usually high, these seals are seldom used in dynamic applications. Thus, this type of seal configuration is more suitable for static seal applications.

The following design procedures are based on simple beam theory, and are intended to yield shape dimensions that will allow the bending stresses in the flexible member to remain below a specified maximum stress. The major input data required for the analysis are the maximum stress for the seal material and the required sealing load which is assumed to be known from other considerations and the fluid pressure. The nomenclature used in this analysis is shown in figure 7-9.

The relationships for this configuration are:

Leg Tip Deflection:

$$y_l = \frac{4\bar{P}_0}{E} (1 - \nu^2) \left(\frac{l}{t}\right)^3 \quad (7-20)$$

where

\bar{P}_0 = initial sealing load (lb/in. of mean interface circumference)

ν = Poisson's ratio

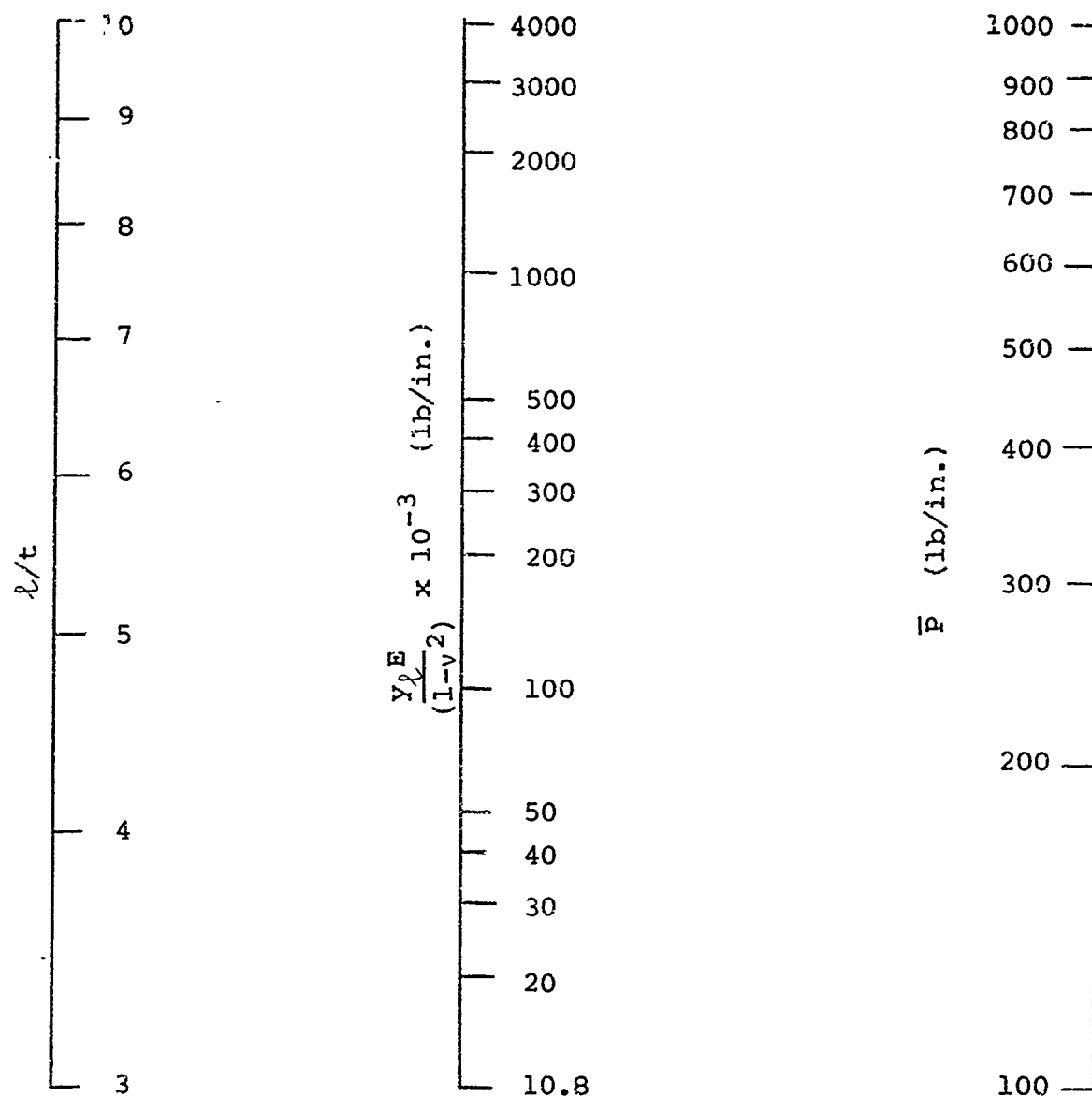
$y_l = H_F - H_R$ = initial leg deflection

Leg Length:

$$l = \frac{6y_l E}{(1-\nu^2) (l/t) [4\sigma_b - 3p (l/t)^2]} \quad (7-21)$$

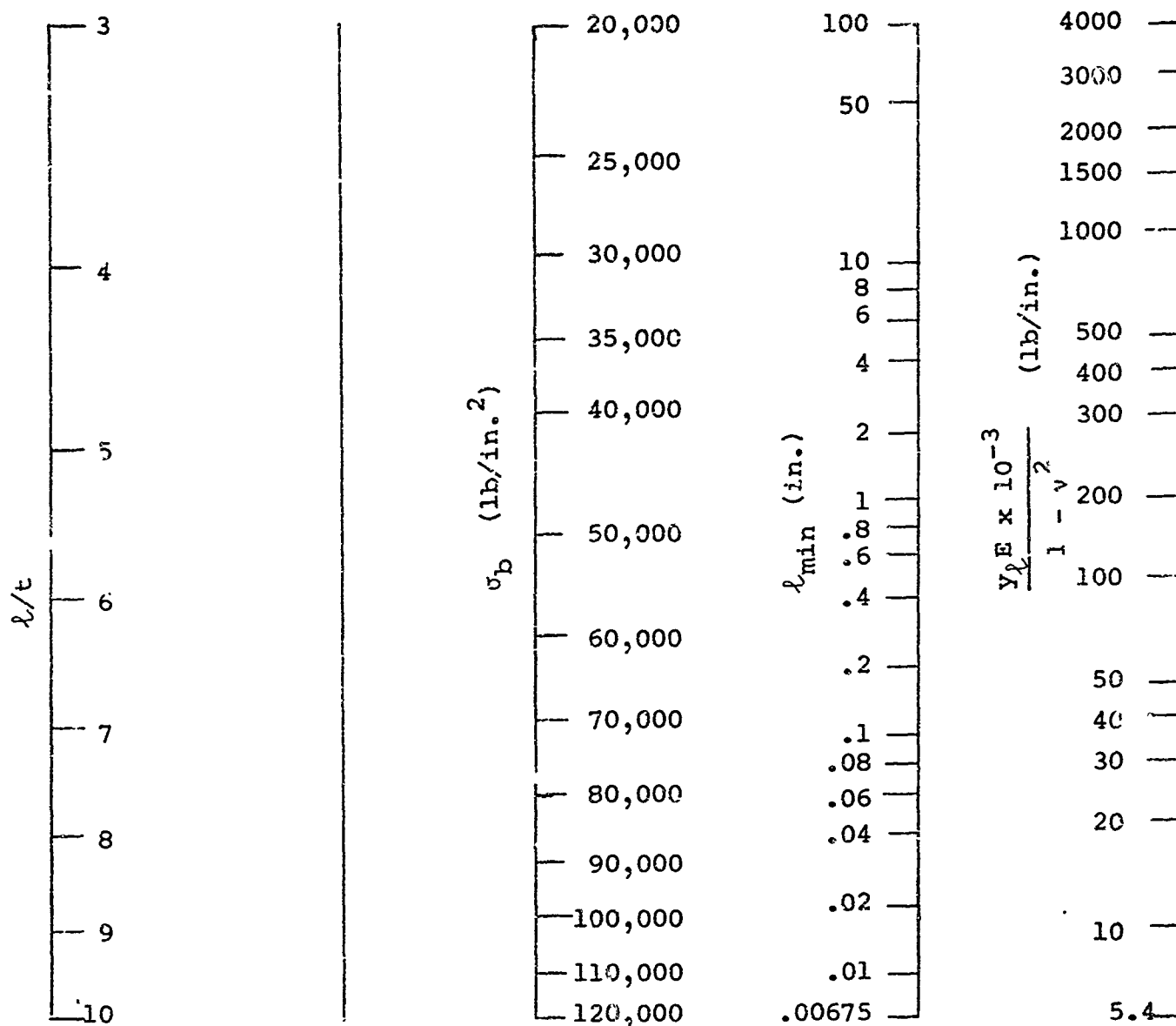
Equations (7-19) and (7-20) are represented in nomograph form on figures 7-10 and 7-11. The recommended procedure in using figure 7-10 follows.

- (1) Assume a value of the leg length-to-thickness ratio, l/t . This parameter defines the proportions of the seal leg.
- (2) From the required sealing force \bar{P} , determine the initial deflection parameter $\frac{y_l E}{1-\nu^2}$ at the tip of the seal from figure 7-10.



$$y_l = \frac{4P}{E} (1 - \nu^2) (l/t)$$

Figure 7-10 Nomograph, straight cantilever seal design, $\theta = 0$



$$l_{min} = \frac{3/2 y_l E}{(1 - \nu^2) (l/t) \sigma_b}$$

Figure 7-11 Nomograph, straight cantilever seal design, $\theta = \theta$

- (3) Determine the minimum seal leg length l_{min} from figure 7-11. l_{min} is the minimum length the seal can be and have the stress within the maximum allowable stress σ_b at $p = 0$.
- (4) Determine the critical seal leg length l_{crit} from figure 7-12 (l_{crit} is the length of seal leg required for the stress to be zero at $p = p$).
- (5) If $l_{crit} \geq l_{min}$: choose a length l equal to l_{min} , omit steps (6), (7), and (8) and proceed with step (9).
- (6) If $l_{crit} < l_{min}$: determine the maximum length l_{max} from figure 7-13. l_{max} is the maximum length the seal can be and have the stress within the maximum allowable stress at $p = p$.
- (7) If $l_{max} \geq l_{min}$: choose a length l equal to l_{min} , omit step (8) and proceed with step (9).
- (8) If $l_{max} < l_{min}$ choose a new, lower value of l/h and return to step (2).
- (9) Based on the length l and the value of l/h selected, calculate h .
- (10) Choose a web length L as short as possible consistent with the over-all structural requirement and deflection of the seal.
- (11) Calculate the depth of the flange recess, $2H_r$, from

$$2H_r = 2H_f - 2Y_L$$

In the design of the web, several requirements must be satisfied:

- The web must be rigid enough to support the bending moment of the seal leg.
- The hoop stress in the web that is due to the fluid pressure must not be excessive.
- The radial deformation due to the hoop stress must be minimized.

Because of the first requirement, the web thickness must be greater than the leg thickness. The hoop stress in the web can be calculated by the relation

$$\sigma_h = \frac{pt_1}{r}$$

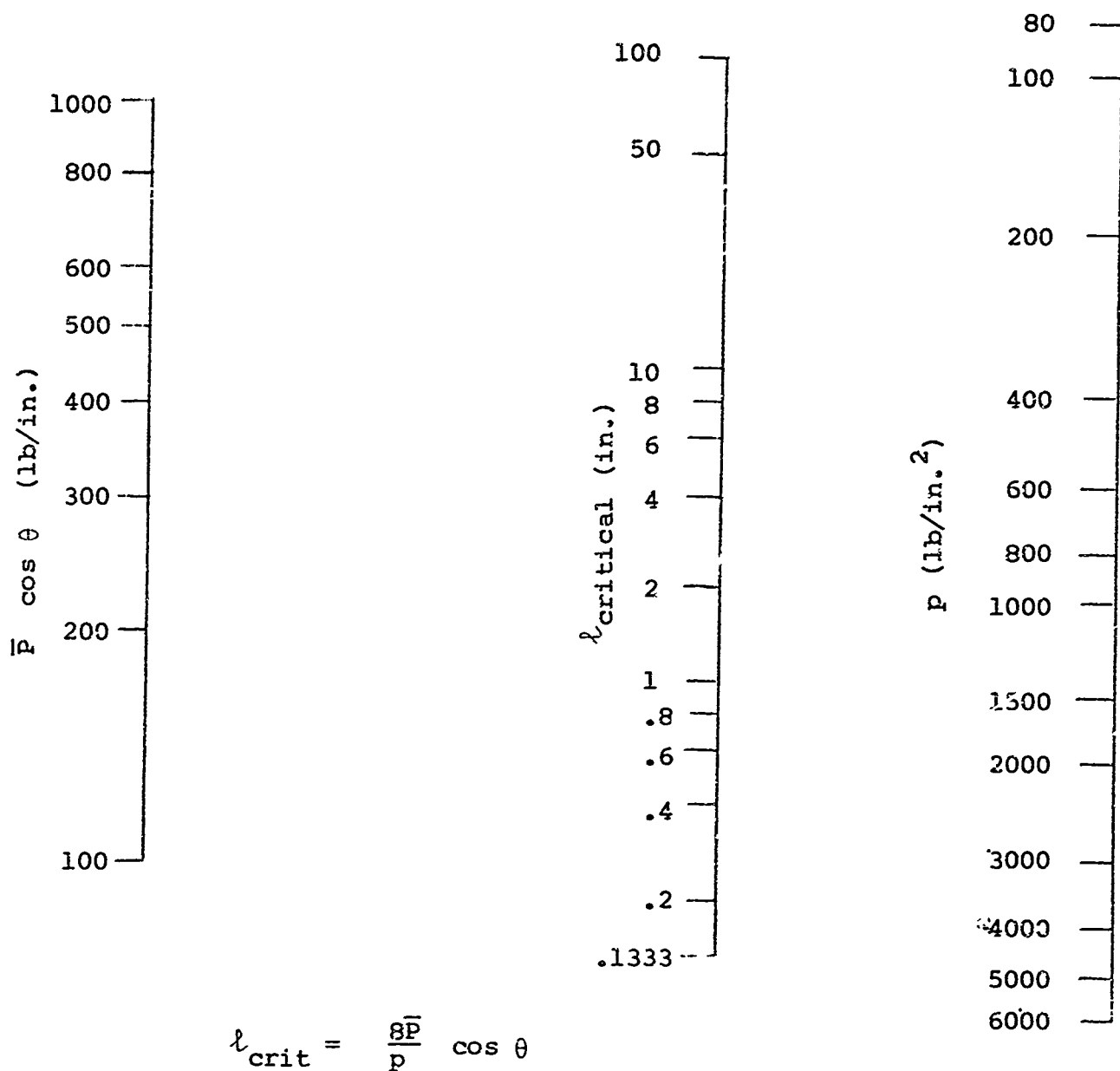
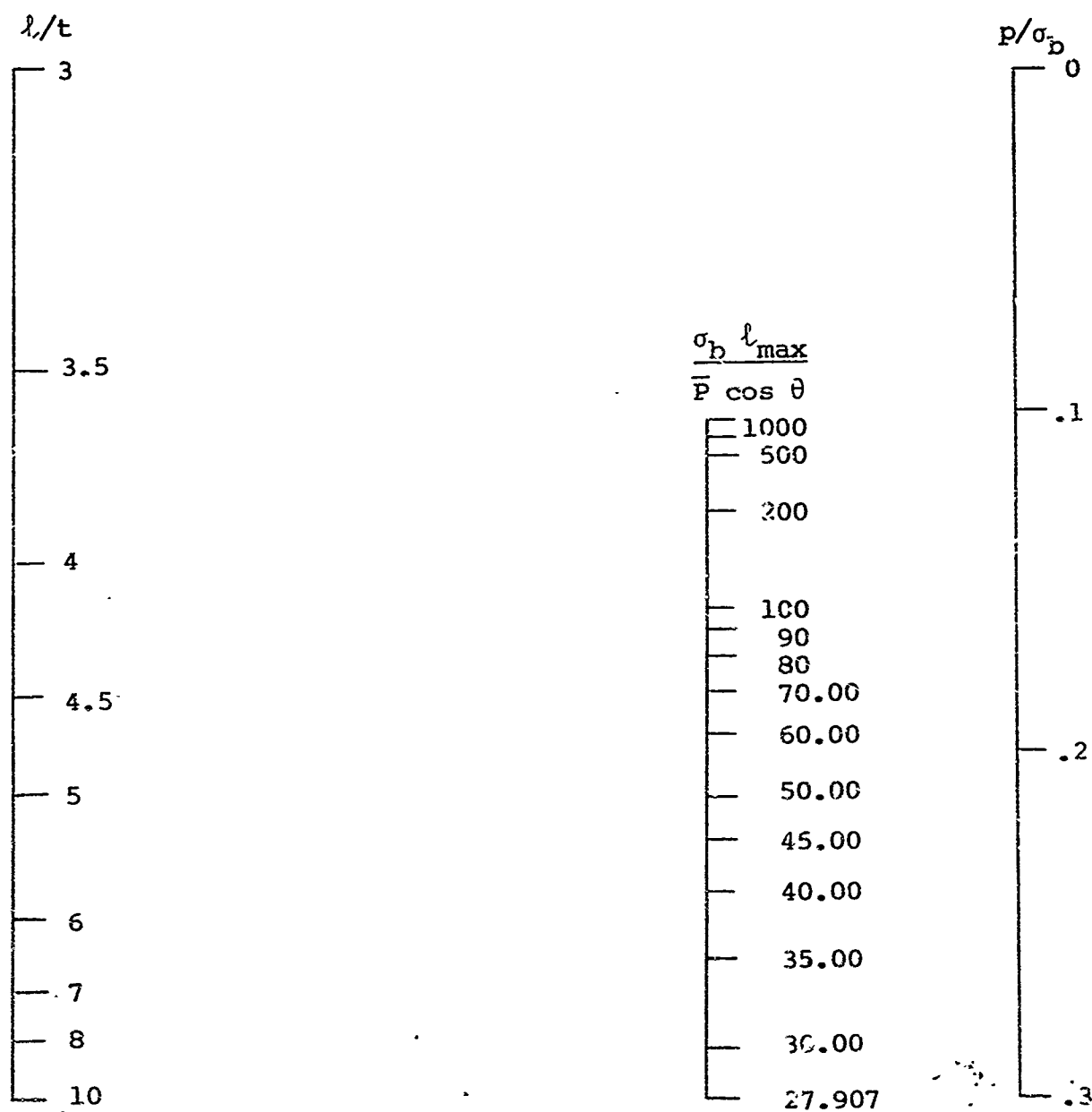


Figure 7-12 Nomograph, straight cantilever seal design, $\theta=0$



$$\frac{\frac{1}{\sigma_b l_{\max}}}{\bar{P}} = \frac{1}{8} p/\sigma_b - \frac{1}{6} (l/t)^2$$

Figure 7-13 Nomograph, straight cantilever seal design, $\theta = 0$

where

σ_h = hoop stress

The radial deformation can be estimated from the relation

$$\delta_r = \frac{\sigma_h t_3}{E}$$

The preceding analysis can be modified for the case of a seal leg that is initially at an angle θ to the mating surface. This configuration is shown in figure 7-16.

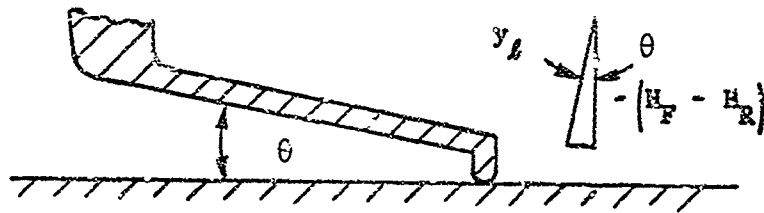


Figure 7-14 Inclined cantilever seal-leg

The design procedure for this case is as follows:

- (1) Assume a value of the leg length to thickness ratio l/t . This parameter defines the proportions of the seal leg.
- (2) From the required sealing force \bar{P} and the angle θ determine the initial deflection parameter $y_l E/l-v^2$ at the tip of the seal from figure 7-15.
- (3) Determine the minimum seal leg length l_{min} from figure 7-11. l_{min} is the minimum length the seal leg can be and have the stress within the maximum allowable stress σ_b at $p = 0$.
- (4) Determine the critical seal leg length l_{crit} from figure 7-12. l_{crit} is the length of seal leg required for the stress to be zero at $p = p$.
- (5) If $l_{crit} \geq l_{min}$: choose a length l equal to l_{min} , omit steps (6), (7), and (8) and proceed with step (9).
- (6) If $l_{crit} < l_{min}$, determine the maximum length l_{max} from figure 7-13. l_{max} is the maximum length the seal leg can be and have the stress within the maximum allowable stress at $p = p$.

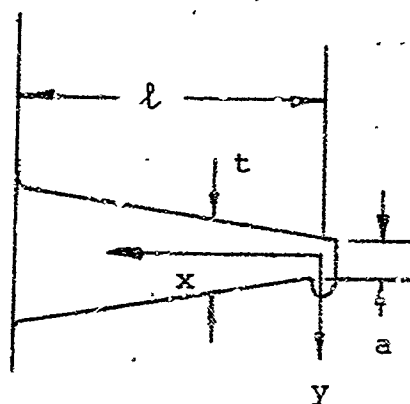
- (7) If $l_{\max} \geq l_{\min}$: choose a length l equal to l_{\min} , omit step (8) and proceed with step (9).
- (8) If $l_{\max} < l_{\min}$: choose a new lower value of l/t and return to step (2).
- (9) Based on the length l and the value of l/t selected, calculate h .
- (10) Choose a web length L as short as possible consistent with the over-all structural requirement and deflection of the seal.
- (11) Calculate the depth of the flange recess, $2H_r$, from

$$2H_r = 2H_f - 2Y_L \cos \theta$$

7.3 Case III, Linearly Varying Thickness Seal Leg, Elastically Deformed

It may be advantageous to use a seal leg of varying thickness. In this way, the flexibility at the leg tip can be improved without weakening the base or fixed end of the leg. The derivation of the design equations for this configuration is given in Reference 7-2. The equations for the configuration are considerably more complicated than for the case of a leg of constant thickness. The linear taper of the seal leg is given by the relation

$$t = a + bx$$



The constants a and b describe the taper. The equations for the various design parameters follow.

Initial deflection required for minimum sealing force at $p = 0$ is

$$y_{l_0} = \frac{12(1-\nu^2)\bar{P}}{2Eb^3} \left[\frac{bl(2a+3bl)}{(a+bl)^2} - 2 \log \left(1 + \frac{bl}{a} \right) \right]$$

The maximum bending stress as a function of fluid pressure is

$$\sigma_b = \frac{3l}{(a+bl)^2} \left\{ Pl - 2R_s + \frac{p \left[\frac{bl}{(a+bl)^2} (6a^2 + 9abl + 2b^2l^2 - 6a \log(1 + \frac{bl}{a})) \right]}{b \left[\frac{bl}{(a+bl)^2} (2a + 3bl) - 2 \log(1 + \frac{bl}{a}) \right]} \right\}$$

A design procedure for the leg shown on figure 7-15 also has been established using monograph charts. As before, it is assured that the required seal load R_s is known.

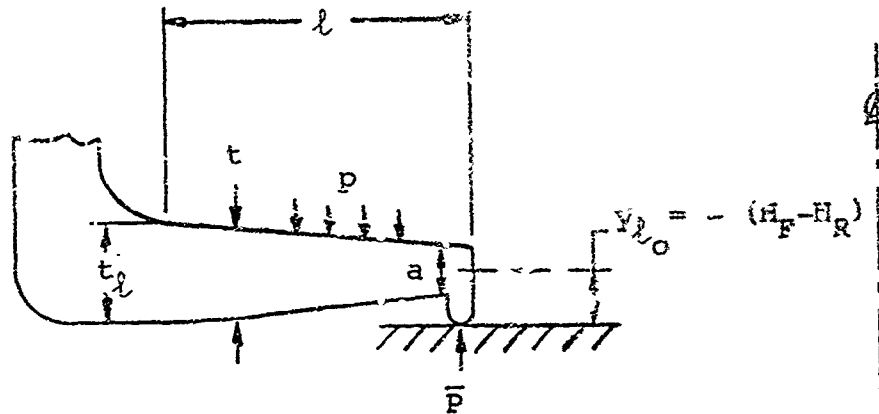


Figure 7-15 Tapered cantilever seals

- (1) Assume values for the ratios l/t_l and l/a , which specify the ratio $t_l/a = \frac{1}{l/t_l} \times l/a$.
- (2) From the required sealing force R_s determine the minimum seal leg length l_{min} from figure 7-17. l_{min} is the minimum length the seal leg can be and have the stress within the maximum allowable stress σ_b at $p = 0$.
- (3) Determine the critical seal leg length l_{crit} from figure 7-18. l_{crit} is the length of seal leg required for the stress to be zero at $p = p$.
- (4) If $l_{crit} \geq l_{min}$: choose a length l equal to l_{min} , omit steps (5), (6), and (7) and proceed with step (8).

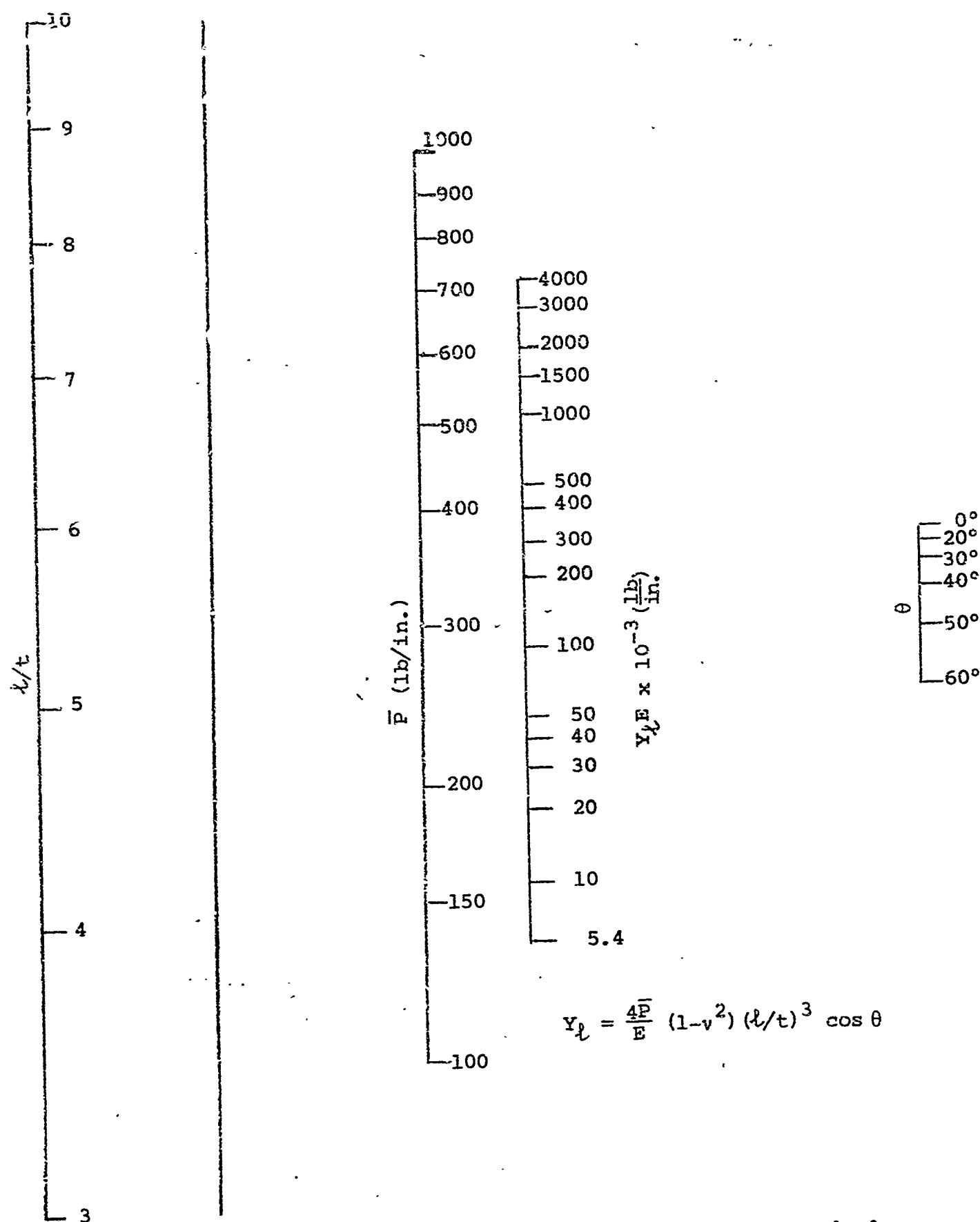
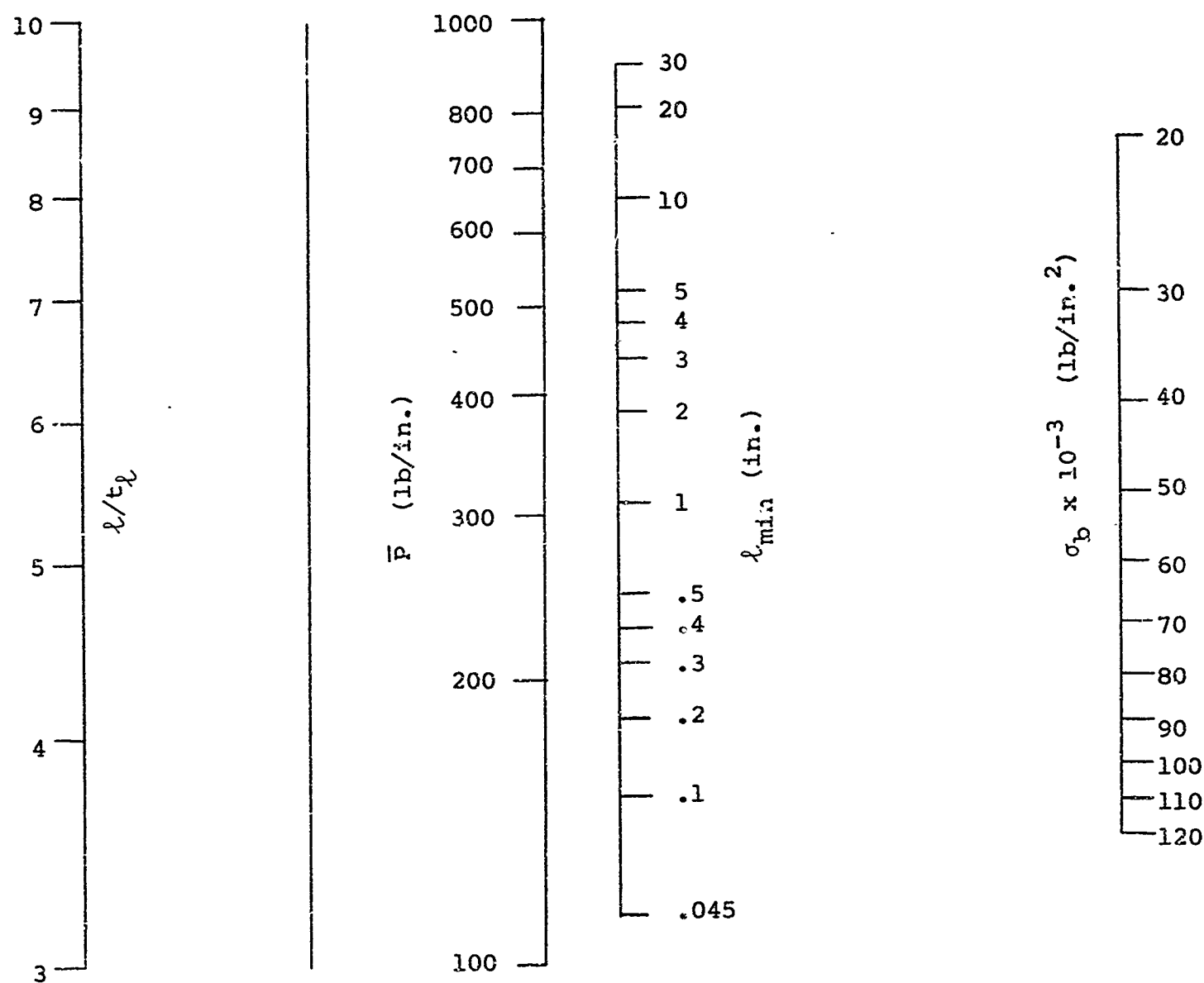


Figure 7-16 Nomograph, straight cantilever seal design, $\theta = 0$

- (5) If $l_{crit} < l_{min}$, determine the maximum length l_{max} from figure 7-19. l_{max} is the maximum length the seal can be and have the stress within the maximum allowable stress at $p = p$.
- (6) If $l_{max} \geq l_{min}$: choose a length l equal to l_{min} , omit step (7) and proceed with step (8).
- (7) If $l_{max} < l_{min}$: choose a new, lower value of l/t and return to step (1).
- (8) Determine the initial deflection Y_{0l} at the sealing end from figure 7-20.
- (9) Calculate t_l and a from the assumed ratios of l/t and l/a , based on the length l .
- (10) If the values Y_0 , t_l , a and l are not a reasonable design, return to step (1) and assume new ratios l/h and a/l .
- (11) Choose a web length L as short as possible consistent with the over-all structural requirement and deflection of the seal.

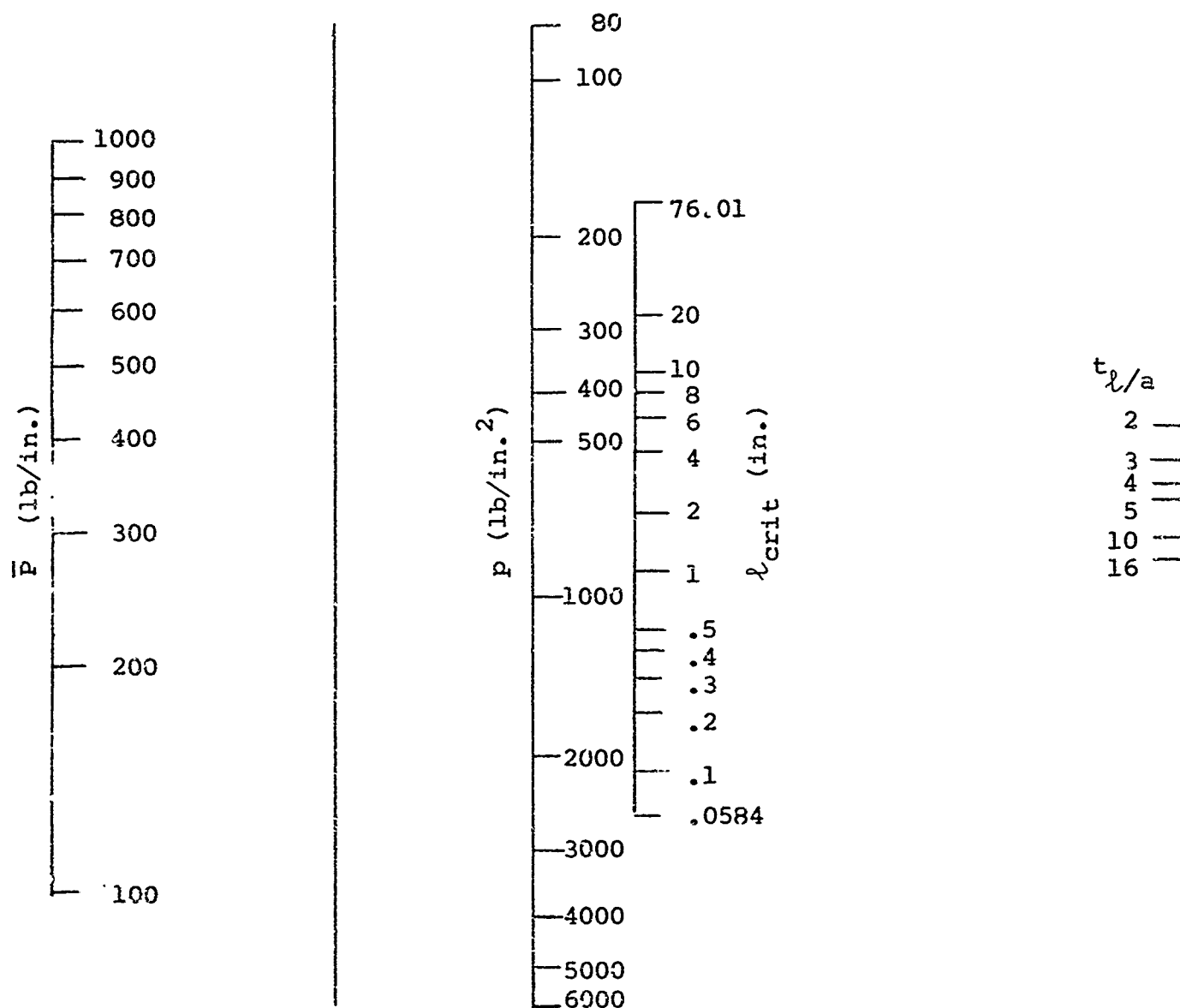
7.4 References

- 7-1 M.F. Spotts, Design of Machine Elements, Prentice-Hall, Englewood Cliffs, N.J., (1957)
- 7-2 B.T. Fang (editor), Design Criteria for Zero-Leakage Connectors for Launch Vehicles, Volume 5, "Pressure-Energized Seals," General Electric Trial Report on Contract NAS8-4012, 15 Mar 1963
- 7-3 Roark, Formulas for Stress and Strain, 3rd ed., McGraw Hill, (1954)



$$l_{min} = \frac{6(l/t)^2 \bar{P}}{\sigma_b}$$

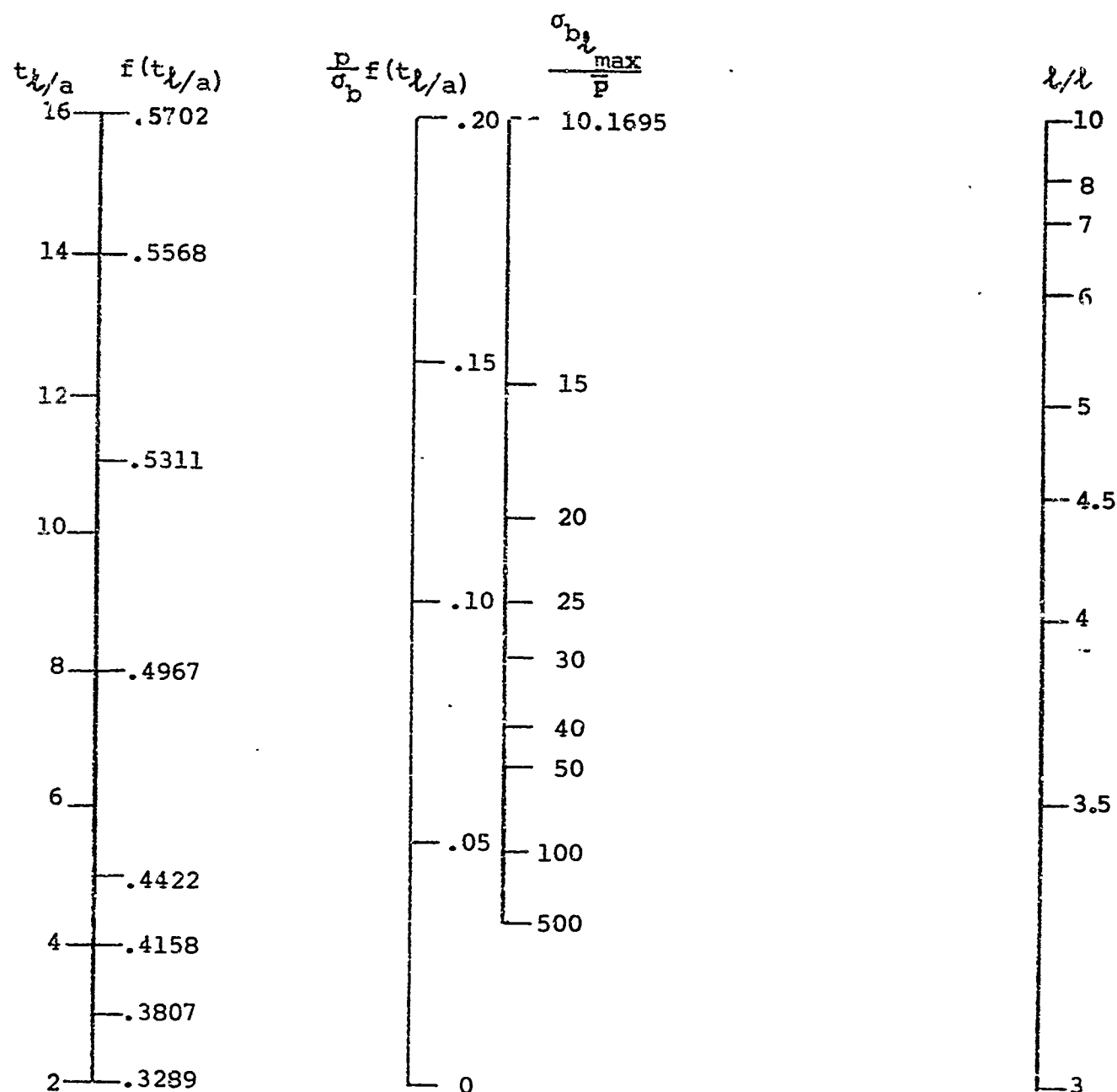
Figure 7-17 Nomograph, cantilever seal design, varying thickness



$$l_{crit} = \frac{2\bar{P}}{pf(t_{l/a})} =$$

$$p \left\{ 1 + \frac{2\bar{P}}{(t_{l/a}-1) \left[(t_{l/a}-1)(3t_{l/a}-1) - 2(t_{l/a})^2 \log t_{l/a} \right]} \right\}$$

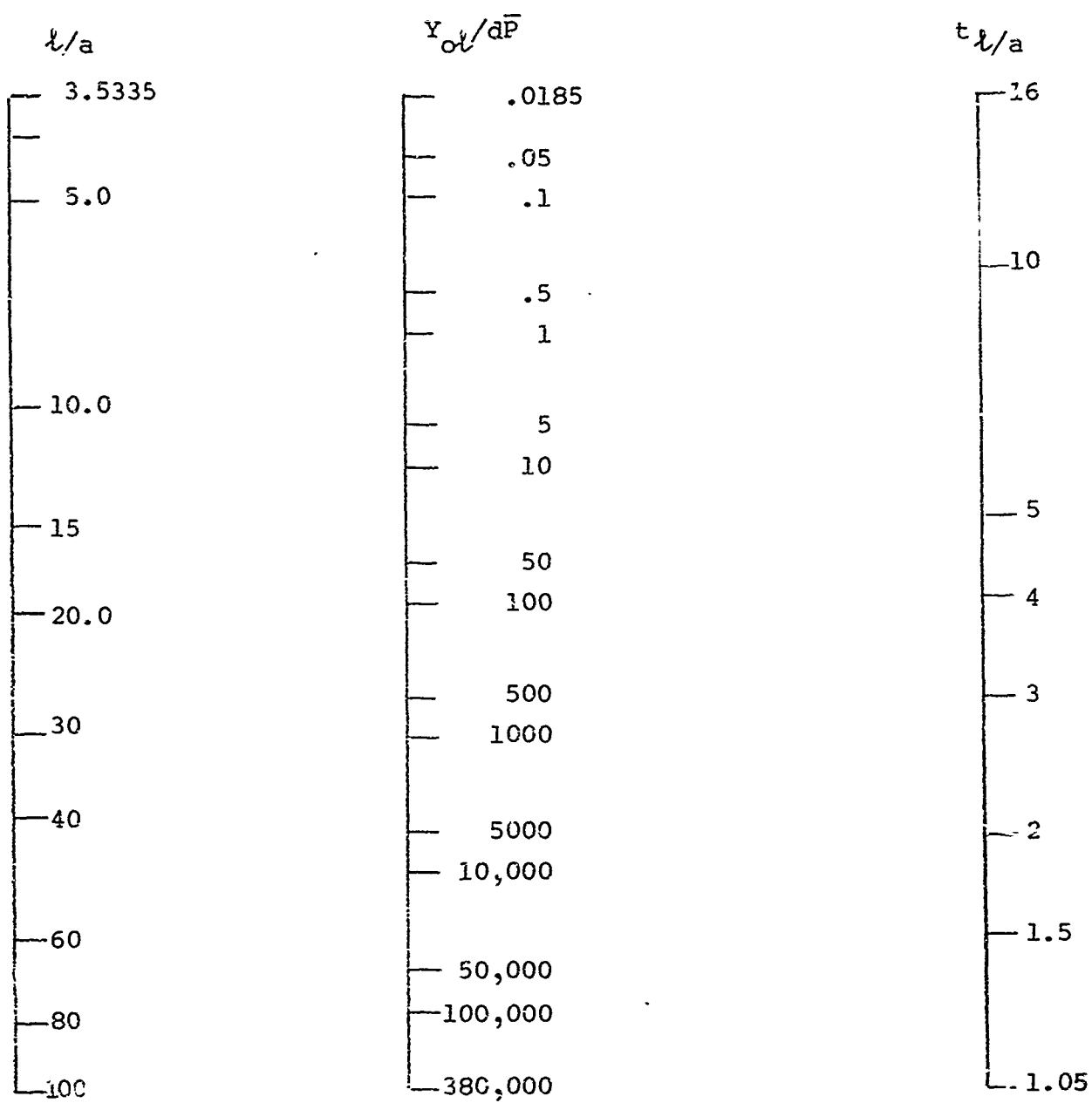
Figure 7-18 Nomograph, cantilever seal design, varying thickness



$$\frac{6\bar{p}}{\sigma_b l_{\max}} = \frac{3p}{\sigma_b} f(t_l/a) - (t_l/l)^2$$

$$= \frac{3p}{\sigma_b} \left\{ 1 + \frac{[6(t_l/a - 1) + 9(t_l/a - 1)^2 - 6(t_l/a)^2 \log t_l/a + 2(t_l/a - 1)^3]}{(t_l/a - 1) [(t_l/a - 1)(3t_l/a - 1) - 2(t_l/a)^2 \log t_l/a]} \right\} - (t_l/l)^2$$

Figure 7-19 Nomograph, cantilever seal design, varying thickness



$$(a/t)^3 \frac{Y_{ol}}{d\bar{P}} = \frac{1}{2} (a/t_l)^2 \frac{(3t_l/a - 1)}{(t_l/a - 1)^2} - \frac{\log t_l/a}{(t_l/a - 1)^3}$$

Figure 7-20 Nomograph, cantilever seal design, varying thickness

7.5 Symbols

C	= radial clearance between shaft and built-in point, (in.)
E	= modulus of elasticity, (psi)
L	= length of seal leg, (in.)
L_a	= active leg length, (in.)
L_0	= active leg length $p = 0$, (in.)
l	= length of seal leg, (in.)
P	= total load, (lb)
\bar{P}	= load per inch of contact, (lb/in.)
\bar{P}_0	= initial load per inch of contact, (lb/in.)
p	= fluid pressure, (psi)
t	= thickness of seal leg, (in.)
x, y	= coordinates along initial profile of seal leg
y_a	= deflection normal to seal leg, (in.)
y_l	= deflection normal to seal leg, $p = 0$, (in.)
δ_a	= deflection normal to sealing surface, (in.)
δ_l	= deflection normal to sealing surface, $p = 0$, (in.)
θ	= angle, (radians)
ν	= Poissons ratio
σ_a	= bending stress, (psi)
σ_b	= bending stress

2

8. ANALYTICAL CRITERIA FOR SEAL HOUSINGS

In the preceding section, consideration was given to the deformation of seal structures resulting from applied loads. These loads were composed of initial installation and fluid pressure effects. The loads were assumed to be acting solely on the seal structure. However, these loads also act on the seal housing producing deformation which is translated back to the seal structure. In addition, the seal housing and structure are deformed by thermal effects. Since both the structure and housing are interrelated, any overall seal must contain both aspects.

The seal housing must contain the seal such that a known interface load for sealing is maintained under all operating conditions. Thus, the seal interface requirements must serve as input data for the housing design. Following this premise, various types of housing are considered, and, in some cases, procedures are developed for their analysis.

In general, seal housings can be divided into at least the following functional groups: fluid conduit connecting, pressure vessel covers, dynamic seals, and general bulk head applications. The aspects of each seal housing must be considered separately because of differences in configuration and manner in which structural loads are applied.

A large number of the seals in rocket propulsion systems are duct and tube connector seals. The structural loads applied to this type of housing include:

- (1) Separation forces due to fluid pressure changes in flow momentum, and dynamic loading.
- (2) Torsion and bending due to tubing misalignment and thermal expansion.
- (3) Hoop stresses due to the fluid pressure.

In addition to the structural forces applied to the connector assembly the effects of variable thermal environment must be considered. The major effects on a connector assembly are:

- (1) Reduction in contact stress at the seal as a result of creep or relaxation in the support housing.
- (2) Reduction in strength and modulus of the materials as a result of elevated temperatures.
- (3) Increased brittleness of some materials at cryogenic temperatures.

- (4) Differential thermal expansion resulting from differences in the thermal expansion properties of the materials in the seal and housing assembly, and from temperature gradients in the seal and housing assembly.

Considering each of the preceding factors, the problem of connector housing design is indeed complex. The final design may often be a compromise between the opposing limitations of strength and weight. Extensive connector design criteria have already been developed and no attempt is made to duplicate this effort. This information is contained in References 8-1 and 8-2.

A second category of seal housings is pressure vessel covers. This general category includes such items as end caps of control valves, flange-type covers on fluid storage tanks, and hatches on space vehicles. In general, a pressure vessel cover can be considered to be any removable part that closes an opening in a vessel containing fluid, and whose primary purpose is not in the conduction of fluid from one region to another.

Since the cover is usually not a part of the fluid conduit system, it is not subjected to the torques, bending moments, and forces usually associated with the fluid conduit. The main structural loading on a cover comes from the pressure force due to the sealed fluid, the reaction loads due to contact with the seal, the loads imposed during installation, and gravitational effects.

The main function of the cover, and its fastening mechanism, is to provide the proper seal interface contact load. The interface load is intimately related to the deflections and distortions that take place in the cover and the seal. These distortions are mainly functions of:

- the fluid pressure force
- the seal reaction loads
- installation loads
- thermal phenomena such as differential thermal expansion and changes in material properties resulting from changes in environmental temperature.

The treatment of the problem including simultaneous consideration of thermal and structural loads is complex. Consequently, these effects are treated separately and the effects of each are subsequently superimposed.

8.1 Structural Load Effects

General Approach. A generalized approach to the structural analysis of a component cover was initiated but not completed. This approach, described in Appendix VII, has considerable merit

in that criteria could be developed for any cover geometry. The approach employed used existing plate and shell theory and established relationships for the elastic displacement of the housing in the vicinity of the seal interface. A general cover geometry was chosen, with the restriction that the geometry must have cylindrical symmetry. The cover geometry chosen is shown in figure 8-1.

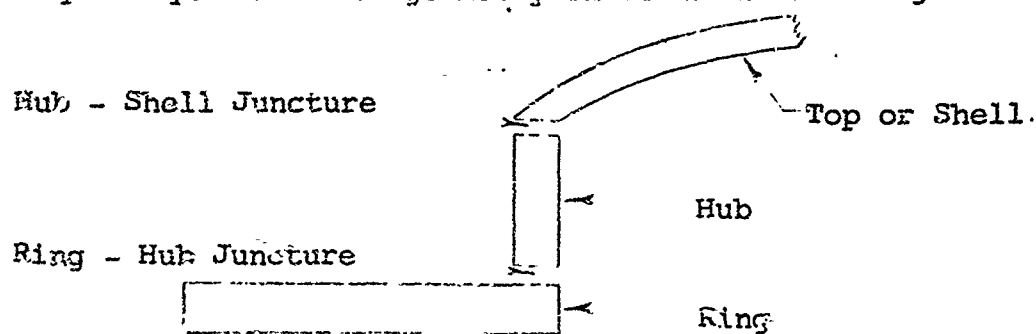


Figure 8-1 General cover geometry

When fluid pressure, initial clamping load and seal reaction load are applied to the cover, elastic deformation takes place in each member of the cover. The deformation of each member is treated separately. The internal stresses at these junctures are replaced by undetermined forces and moments and these, in turn, are treated as external forces in each independent analysis. Thus, a set of simultaneous deflection equations is developed. The solution of these equations is accomplished by the use of common boundary conditions: displacement and rotation at the junctures.

The derivation of the deflection relations, the application of the boundary conditions, and a detailed discussion of the entire analysis process is contained in Appendix VII. Because of the complex nature of the equations and the iterative process necessary for their solution, a digital computer solution is necessary. The type of computer routine, and the general solution of the problem is also discussed in the appendix. A solution for one particular configuration also is given in Appendix VII.

In its completed form the results can be presented in graphical or tabular form to enable a designer to determine the elastic displacements in the vicinity of the seal for any geometry of cover meeting the restriction of cylindrical symmetry, and for the various modes of seal contact:

- (1) total contact (i.e., flat gasket with bolt holes)
- (2) contact within the bolt circle
- (3) contact outside the bolt circle
- (4) contact both within and outside the bolt circle but not total contact.

These force and deflection results can be combined with the seal structural design criteria to yield a complete structural, and leakage performance analysis for the entire seal assembly.

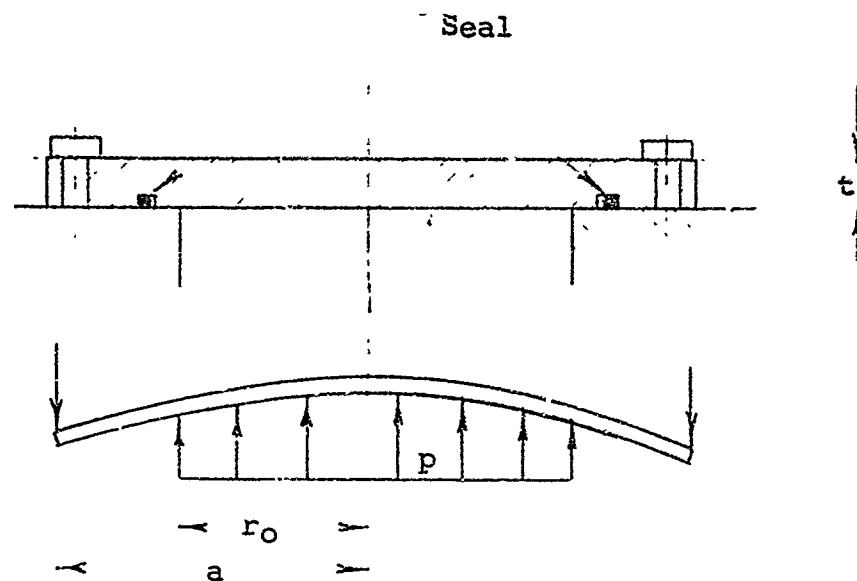


Figure 8-2 Flat cover plate geometry

Simplified Approach. The general approach can be used for any cover geometry having cylindrical symmetry simply by applying the proper boundary conditions. Since this work is not entirely completed at this time, a simplified approach applicable only to a flat plate cover is presented. The model used in this analysis is shown in figure 8-2.

The problem of a thin circular flat plate in the same manner as the cover described has been solved for small, elastic deflections (Ref. 8-3). The equations giving the deformation and slope of the plates are:

$$(r > r_o) \quad y = - \frac{3W(m^2-1)}{16\pi E m^2 t^3} \left[\frac{(12m+4)(a^2-r^2)}{(m+1)} - \frac{2(m-1)(a^2-r^2)r_o^2}{(m+1)a^2} - (8r^2 + 4r_o^2) \log \frac{a}{r} \right] \quad (8-1)$$

$$(r < r_o) \quad y = - \frac{3W(m^2-1)}{16\pi E m^2 t^3} \left[4a^2 - 5r_o^2 + \frac{r^2}{r_o} - (8r^2 + 4r_o^2) \log \frac{a}{r_o} - \frac{2(m-1)(a^2-r^2)r_o^2}{(m+1)a^2} + \frac{8m(a^2-r^2)}{m+1} \right] \quad (8-2)$$

$$(r > r_o) \quad \theta = \frac{-3W(m^2-1)}{16\pi E m^2 t^3} \left[\frac{-(24m+8)r}{m+1} + \frac{4r_o^2(m-1)r}{(m+1)a^2} - 16r \log \frac{a}{r} + 8r + \frac{4r_o^2}{r} \right] \quad (8-3)$$

$$(r < r_0) \theta = \frac{-3W(m^2-1)}{16\pi E m^2 t^3} \left[\frac{4r^3}{r_0^2} - 16r \log \frac{a}{r_0} + \frac{4(m-1)r r_0^2}{(m+1)a^2} - \frac{16mr}{(m+1)} \right] \quad (8-4)$$

where

y = deflection (in.)

θ = slope (radians)

$W = p\pi r_0^2$ = total pressure force (lb)

E = modulus of elasticity (psi)

$m = 1/\nu = 1/\text{Poisson's Ratio}$ (dimensionless)

t = plate thickness (in.)

a = outside radius of plate (in.)

r_0 = location of seal from axis (in.)

From the sealing standpoint, the location where deformations are of interest is right at the seal interface. The seal is located at a distance r_0 from the axis of the plate. Rewriting the equations in dimensionless form, and evaluating at $r = r_0$, we obtain a dimensionless slope parameter as a function of the ratio r_0/a , i.e.,

$$\frac{16 y_0 E m^2 t^3}{3 r_0^2 (m^2 - 1) a^2 p} = \left\{ \frac{(12m+4) \left[1 - \left(\frac{r_0}{a} \right)^2 \right]}{(m+1)} - \frac{2(m-1) \left[1 - \left(\frac{r_0}{a} \right)^2 \right] \left(\frac{r_0}{a} \right)^2}{(m+1)} - 12 \left(\frac{r_0}{a} \right)^2 \log \left(\frac{a}{r_0} \right) \right\} \quad (8-5)$$

and

$$\frac{16 E m^2 t^3 \theta_0}{3 r_0^2 a (m^2 - 1) p} = \left[\frac{(-12m+4)}{(m+1)} \left(\frac{r_0}{a} \right) + \frac{4(m-1)}{(m+1)} \left(\frac{r_0}{a} \right)^3 - 16 \left(\frac{r_0}{a} \right) \log \left(\frac{a}{r_0} \right) \right] \quad (8-6)$$

However, these dimensionless parameters are not the best for use in a comparison, since they contain a , r_0 , and p , which tend to cloud the results, while the stress, a useful parameter

for comparison purposes, is absent. The maximum stress in the flat plate takes place at the axis, i.e., $r = 0$, where the radial and tangential stresses are equal and given by:

$$S_r = S_t = S_{\max} = \frac{3r_o^2 p}{2mt^2} \left[m + (m+1) \log \frac{a}{r_o} - \frac{(m-1)}{4} \left(\frac{r_o}{a} \right)^2 \right] \quad (8-7)$$

from where:

$$t = \sqrt{\frac{3r_o^2 p}{2mS_{\max}}} \left[m + (m+1) \log \frac{a}{r_o} - \frac{(m-1)}{4} \left(\frac{r_o}{a} \right)^2 \right] \quad (8-8)$$

which shows that the thickness of the plate is also a function of r_o/a . This, of course, is to be expected, since larger plates (for larger apertures) must be thicker, even for the same pressure.

Substituting the result of equation (8-8) into equations (8-5) and (8-6), we obtain two new dimensionless parameters for the deflection and slope of the plate at the seal location, i.e.,

$$\frac{16 y_o E m^2}{3r_o^2 (m^2 - 1) a^2 p} \left(\frac{3r_o p}{2mS_{\max}} \right)^{3/2} = \frac{\left\{ \frac{(12m+4) \left[1 - \left(\frac{r_o}{a} \right)^2 \right]}{m+1} - \frac{2(m-1)}{m+1} \frac{1 - \left(\frac{r_o}{a} \right)^2}{2} - 12 \left(\frac{r_o}{a} \right) \log \left(\frac{a}{r_o} \right) \right\}}{\left[m + (m+1) \log \frac{a}{r_o} - \frac{(m-1)}{4} \left(\frac{r_o}{a} \right)^2 \right]^{3/2}} \quad (8-9)$$

and simplifying:

$$\frac{y_o E p^{1/2}}{a S_{\max}^{3/2}} = \frac{\left\{ \frac{(12m+4) \left[\left(\frac{a}{r_o} \right) - \left(\frac{r_o}{a} \right) \right]}{m+1} - \frac{2(m-1)}{m+1} \left[\left(\frac{r_o}{a} \right) - \left(\frac{r_o}{a} \right)^3 \right] - 12 \left(\frac{r_o}{a} \right) \log \left(\frac{a}{r_o} \right) \right\}}{\left[m + (m+1) \log \frac{a}{r_o} - \frac{(m-1)}{4} \left(\frac{r_o}{a} \right)^2 \right]^{3/2}} \quad (8-10)$$

and, similarly, for the slope:

$$\frac{\theta_o Ep^{1/2}}{S_{max}^{3/2}} = \frac{m^2 - 1}{4\sqrt{6m}} \frac{\left[\frac{(-12m+4)}{(m+1)} + \frac{4(m-1)}{(m+1)} \left(\frac{r_o}{a}\right)^2 - 16 \log\left(\frac{a}{r_o}\right) \right]}{\left[M + (m+1) \log \frac{a}{r_o} - \left(\frac{m-1}{4}\right) \left(\frac{r_o}{a}\right)^2 \right]^{3/2}}$$

The new deflection and slope parameters,

$$y'_o = \frac{y_o Ep^{1/2}}{aS_{max}^{3/2}}, \text{ and } \theta'_o = \frac{\theta_o Ep^{1/2}}{S_{max}^{3/2}},$$

are much simpler and are useful expressions since they contain only E , p , and S_{max} (also a in y'_o only) which are usually kept constant for comparisons. Thus, it becomes a simple matter to find the deflection and slope as a function of geometry for a given stress and pressure level, and a given material. The parameters y_o and θ'_o are plotted as a function of r_o/a in figures 8-3 and 8-4. Figure 8-4 shows that, for a given pressure, stress level and material, the slope at the seal location increases slightly with the geometry parameter r_o/a . Figure 8-3 illustrates the behavior of y'_o as the geometry parameter r_o/a varies, which shows that for a given material, fluid pressure, and stress level, the ratio y_o/a decreases with increasing r_o/a . However, since an increasing value of r_o/a is usually obtained as a becomes rather large, then it should be expected that for large flat plate covers, the actual deflection at the seal, y_o , will also be larger. For a given geometry (r_o/a), a larger cover will also show a correspondingly larger deflection.

This cover deformation analysis shows the deflections and slopes that should be expected at the seal location if the cover is of the flat plate type. By making similar analyses of other configurations, it will be possible to compare the relative merits and disadvantages of each design.

The preceding discussion yields a method of estimating flange deflection resulting from the influence of fluid pressure. The next important criterion is the means by which the cover plate is fastened to the pressure vessel. The most common type of fastener used in this type of application is the bolt. A great deal of information exists on bolt loading, preload, torque to load relationship for bolt-type fasteners. In the case of bolted pressure vessel covers using the types of seal discussed thus far, certain particular requirements are present which can be stated:

- (1) The bolts must be capable of providing the initial contact load at the sealing interface. The load is determined by the seal structural design.

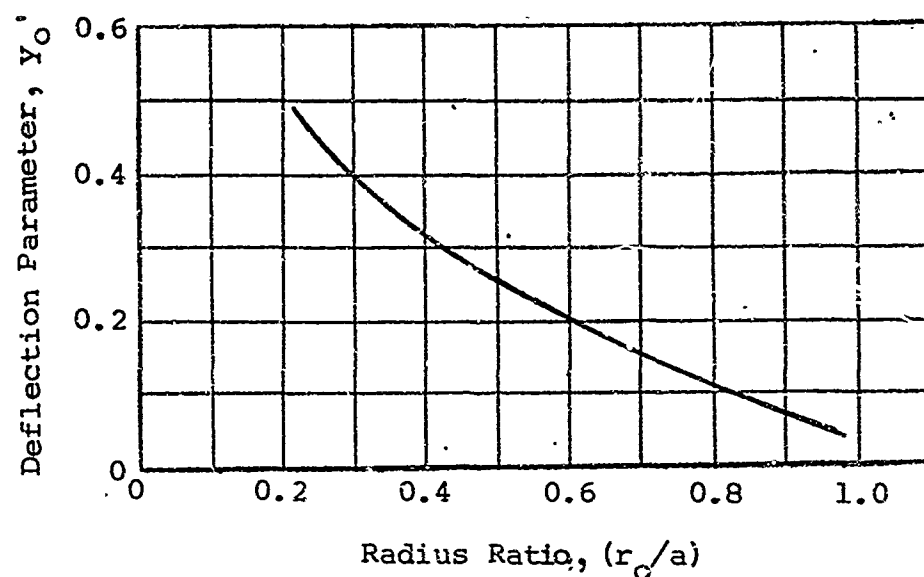


Figure 8-3 Deflection parameter versus radius ratio for a flat cover

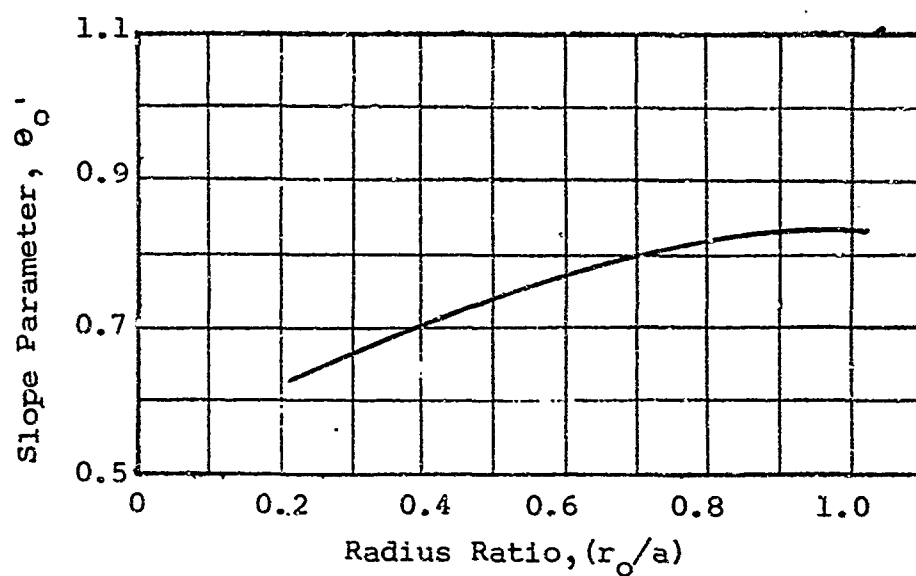
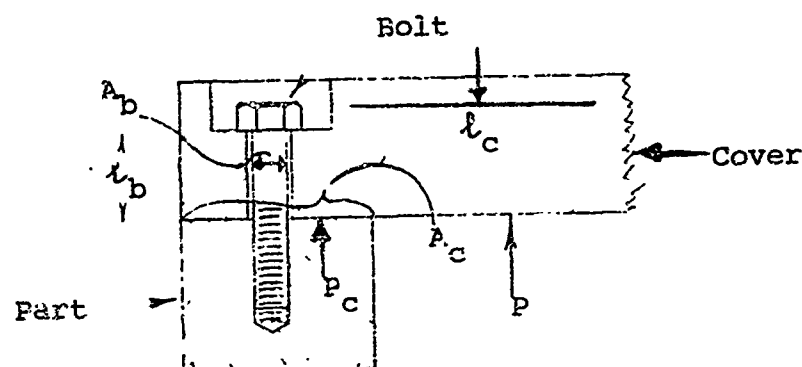


Figure 8-4 Slope parameter versus radius ratio for a flat cover

- (2) The bolts must be capable of withstanding the full fluid pressure force with tolerable elongation.
- (3) The bolts and other members of the seal and housing assembly must have carefully mated thermal properties.

To analyze the cover, we proceed as follows:



If a part is bolted in place and an initial tensile force P_0 is applied to the bolt, a corresponding compressive load is induced in the part. If no other forces are applied to the system, the load on the cover P_c and the bolt P_b are given by

$$P_b = P_0$$

$$P_c = P_0$$

If a load P is also applied to the cover, the relationship can now be expressed as

$$|P_b| = \frac{k_b}{k_b + k_c} P + P_0 \quad (8-11)$$

$$|P_c| = \frac{k_p}{k_b + k_c} P - P_0 \quad (8-12)$$

where k_b and k_c are the elastic constants of the bolt and cover.

$$k_b = \frac{A_b E_b}{l_b}$$

$$k_c = \frac{A_c E_c}{l_c}$$

where

A = effective area (in^2)

E = modulus of elasticity (psi)

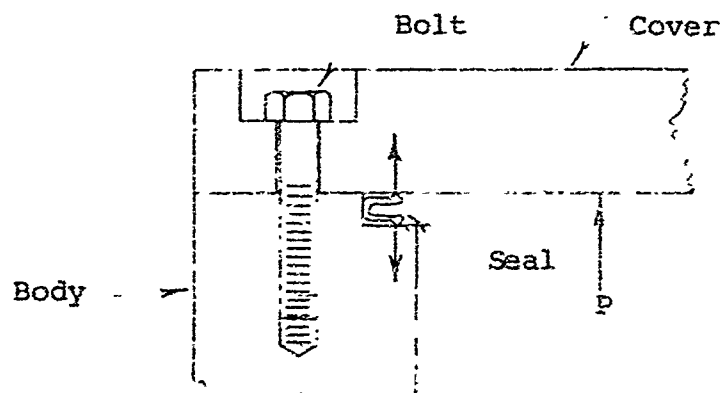
l = effective length (in.)

In the diagram shown, the effective contact area of the cover is much larger than that of the bolt. Thus, as long as compression is maintained on the cover, changes in load P will have a small effect on the bolt load P_b .

In practice, the initial load P_0 is usually made sufficiently large that, when load P is applied to the part, a compressive load P_p is still maintained. Maintaining a compressive load by application of the proper initial bolt load is extremely important in the use of flat gaskets for sealing. This subject has been under study in many fields and by many investigators (Ref. 8-4 and 8-5).

The use of sufficient initial bolt load is advantageous in reducing the effects of fatigue if the load P is fluctuating as in the case of varying pressure. In the case of varying load P the maximum and minimum bolt loads are found from equation (8-11) by substitution of the maximum and minimum values of P . From this relationship it can be seen that the maximum bolt load is increased because of the initial load. However, the minimum bolt load is considerably larger because of the presence of the initial load than it would be if there were no initial load present. The resultant effect is to reduce the range of load fluctuation in the bolt. Since they depend on the magnitude of the range of stress variation, the fatigue effects are also reduced.

When the cover plate, bolts and the seal reaction load are considered together, the relationship becomes more complex. Consider the following:



When the bolt is torqued so that the cover just barely touches the body, the entire seal contact load P_s is taken by the bolts and the corresponding bolt load is given by

$$P_b = P_s$$

where all loads are expressed as forces on each bolt. Any additional load P , such as that due to fluid pressure, is also taken directly by the bolt. In the presence of a load P , the bolt load is now given

$$P_b = P + P_s$$

The total bolt load variation will now be exactly the same as the variation in force P_s . The range of variation of the bolt force can be reduced if an initial compression is induced in the cover plate by increasing the bolt preload. Since the cover and body are usually much more massive than the seal, the compressive load induced in the cover by the additional bolt preload may not cause sufficient deflection to have a significant effect on the seal interface load P_s .

If the magnitude of the structural load P , due to fluid pressure or other causes, is known, the additional bolt preload P_o necessary to keep the cover in compression can be found from equation (8-11). Since a load P_s has already been applied to the bolt to deflect the seal, the total bolt load in the presence of load P can now be expressed as

$$P_b = \frac{k_b}{k_b + k_c} P + P_o + P_s \quad (8-13)$$

The maximum, minimum and average bolt loads can now be calculated and plotted on a working stress diagram or Goodman diagram to determine if these stresses are within the fatigue limits of the bolt material.

There may be cases where it is not possible to apply sufficient bolt preload P_o such that the cover remains in compression, because an excessive bolt load as given by equation (8-13) would occur. In these cases, the maximum allowable preload P_o can be determined from the relation $P_b = P + P_s + P_o$. In this relationship, P_b will be the maximum allowable bolt load determined from working stress considerations.

In addition to the consideration of bolt loading, the deflection or elongation of the bolts under load must also be considered. This elongation must be added to the cover deflection at the seal contact point to determine the total housing deflection at the sealing contact point. The allowable deflection at the sealing contact point is determined by the seal structure and

the seal interface criteria. Thus, either the seal structure or the housing design or both may have to be modified until an allowable deflection at the sealing interface point is achieved. The elongation of a bolt is given as

$$\delta = \frac{F_b l_b}{A_b E_b} \quad (8-14)$$

To minimize bolt elongation the free length of the bolt should be kept as small as possible. Also a short bolt length minimizes the effects of thermal expansion. Thus, bolt load, fatigue considerations, bolt elongation and bolt length must be carefully considered as part of the housing design.

8.2 Thermal Considerations

Thermal Expansion. The dimensional changes in the components comprising a housing and seal structure assembly due to changes in temperature of the assembly can exert a significant influence on the performance of a seal. The differences in expansion or contraction of the parts can often cause displacement equal to or larger than the permissible deflection of the seal structure.

The problem is even more complicated when large temperature fluctuations are expected. This occurs because the expansion characteristics of material change with magnitude of temperature. Table 8-1 (Ref. 8-6) gives the mean coefficient of thermal expansion for several, high-temperature fastener alloys. Figures 8-5, 8-6 and 8-7 (Ref. 8-7) and corresponding Tables 8-2, 8-3 and 8-4 give actual values of thermal expansion for various materials. The data on these curves are presented in per cent of change in length using 22°C (71.6°F) as a base. The shape of the curves indicates that the coefficient of thermal expansion increases with increasing temperature.

To minimize the problem of thermal expansion in a seal housing assembly, it is necessary to match the thermal expansion properties of the parts as closely as possible. This will minimize the effects of differential thermal expansion. Even if all of the parts were of identical material, the problem of differential thermal expansion would still exist because of the presence of temperature gradients in the seal and housing assembly.

The effects of poor matching of thermal properties can be illustrated by an example. Assume the following seal configuration:

Table 8-1

MEAN COEFFICIENT OF THERMAL EXPANSION* OF HIGH-STRENGTH,
HIGH-TEMPERATURE FASTENER ALLOYS AT VARIOUS TEMPERATURES
(after Reference 8-6)

Alloy	Temperature (°F)				
	600	800	1000	1200	1600
Titanium					
Ti-6 Al-4 V	4.8	5.0	5.3	5.5	5.8
Ti-7 Al-12 Zr	5.3	...	5.3	5.5	...
Stainless Steels					
Type 302	9.9	10.03	10.2	10.4	...
Type 403	5.71	6.20	6.61	6.72	...
PH 15-7 Mo	5.6	5.9	6.1
High-Strength Iron-Base Stainless Alloys					
A 286	9.6	9.72	9.84	9.95	...
AMS 5616	6.21	6.38	6.53
Unitemp 212	8.8	...	9.4	9.6	10.3
High-Strength Iron-Base Alloys					
AISI 4340	7.04	7.4	7.8
H-11 (AMS 6485)	6.9	7.1	7.3	7.4	...
AMS 6304	7.3	7.6	7.8
Nickel-Base Alloys					
Inconel X	7.5	7.7	7.9	8.1	9.0
Waspaloy	7.3	7.5	7.7	8.0	8.8
Rene 41	7.02	7.24	7.50	7.80	8.72

*All values are in units of in. per in. per deg F $\times 10^{-6}$.

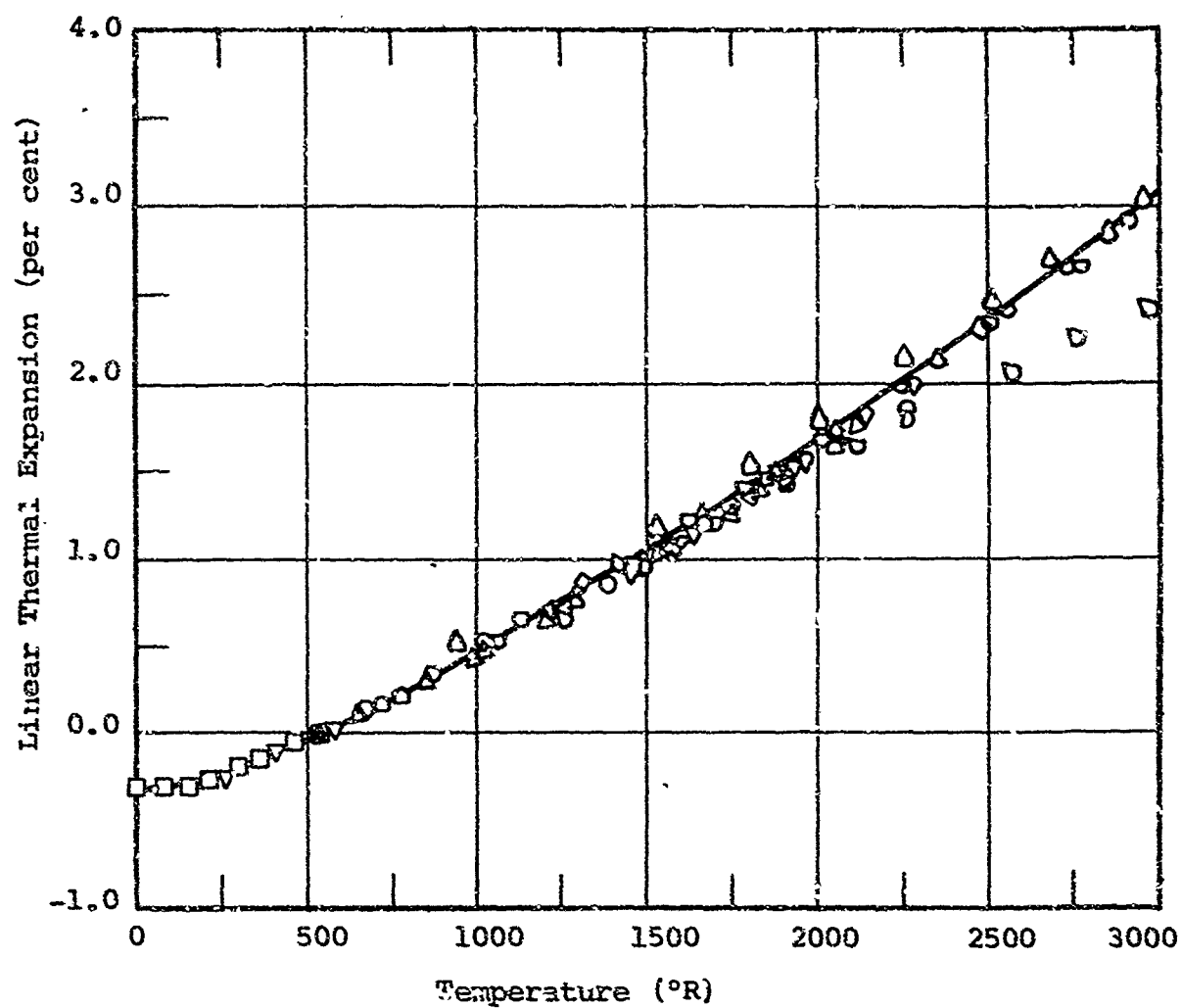


Figure 8-5 Linear thermal expansion for 17-7PH and similar metals (after Reference 8-7)

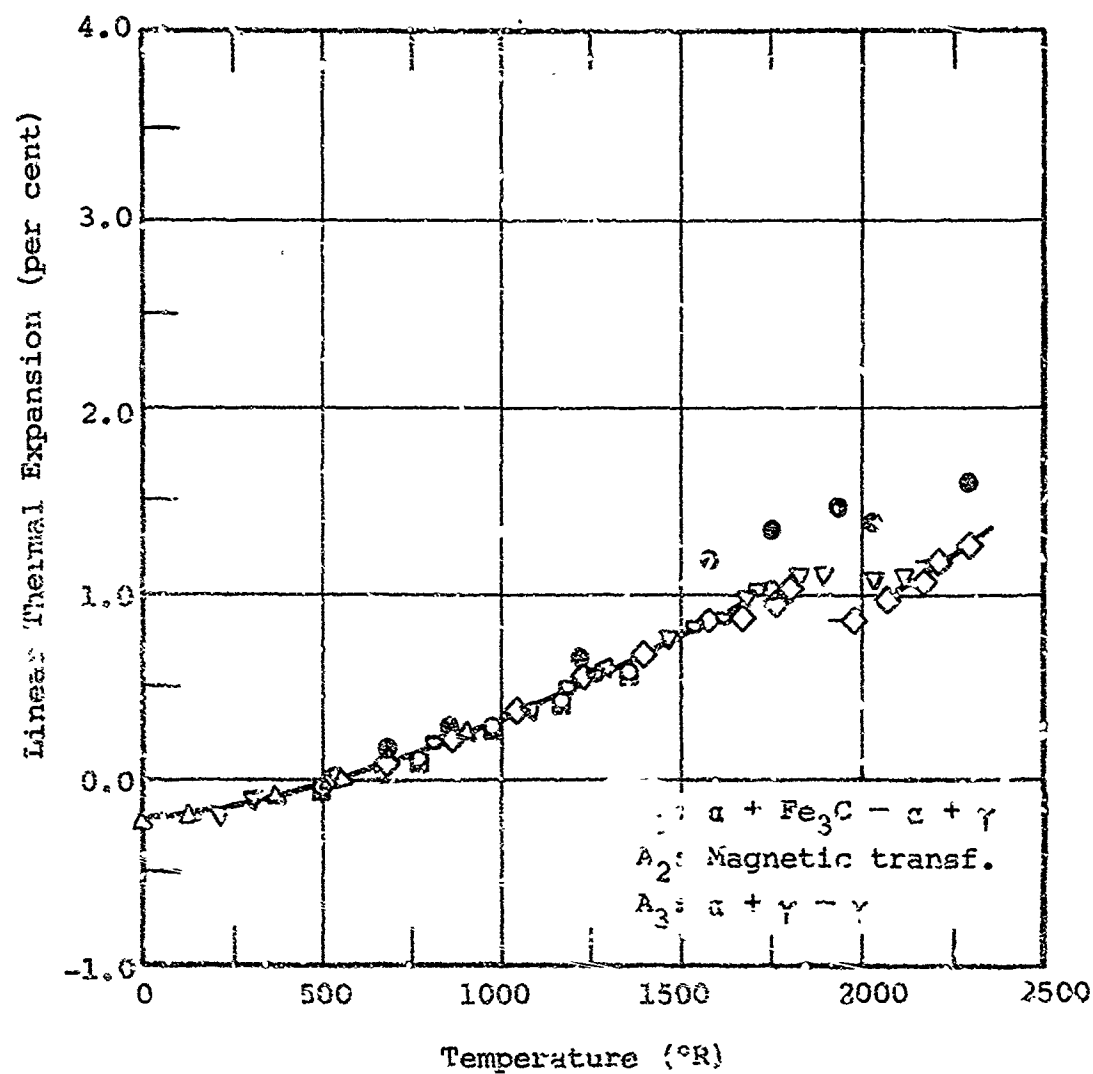


Figure 8-6 Linear thermal expansion for plain carbon steel
(after Reference 8-7)

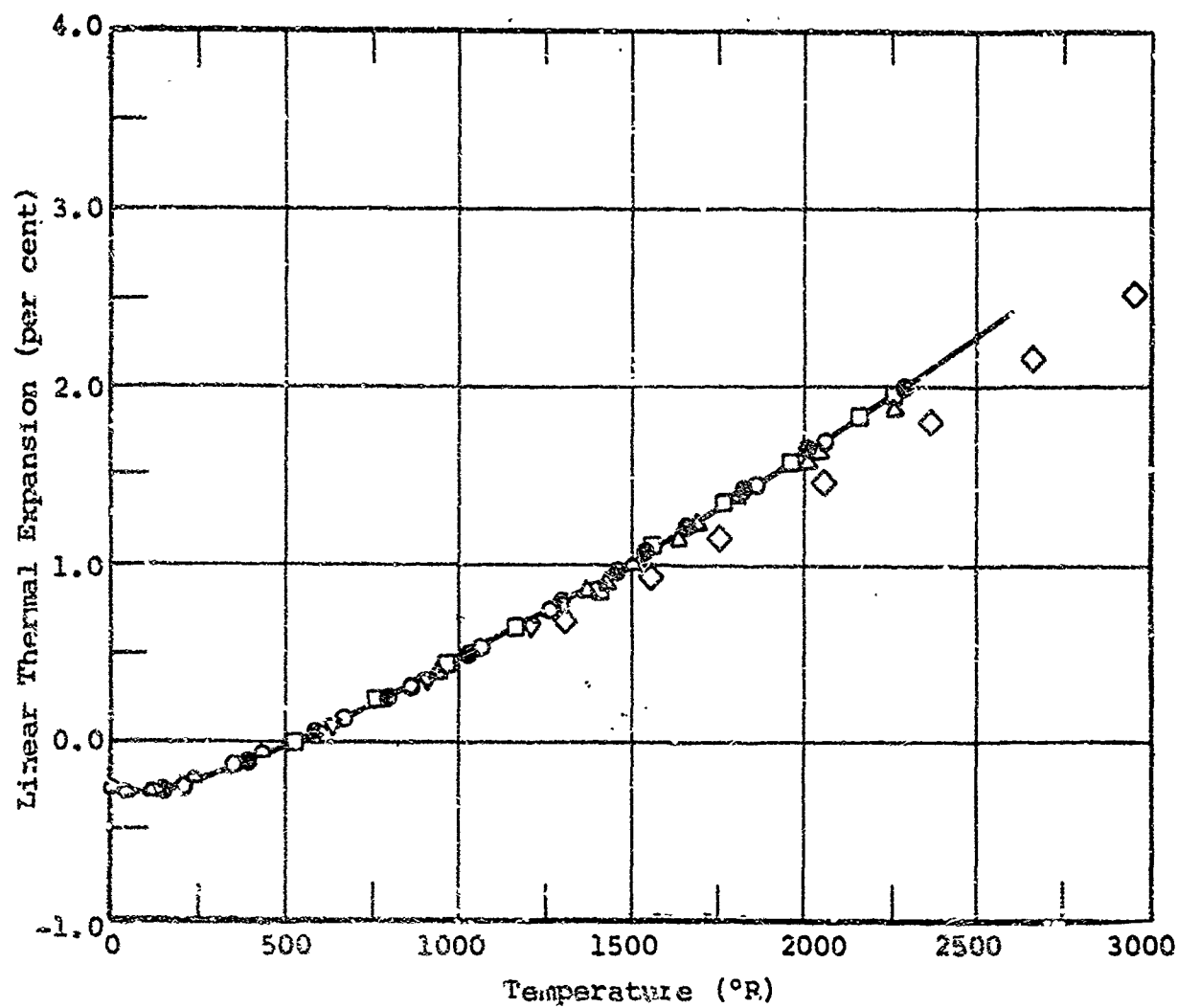


Figure 8-7 Linear thermal expansion for 304 stainless- and similar metals (after Reference 8-7)

Table 8-2

LINEAR THERMAL EXPANSION FOR 17-7PH AND SIMILAR METALS
(after Reference 8-7)

REFERENCE INFORMATION

Sym. No.	Investigator	Range, R	Material Composition	Test Method	Remarks
●	Kirby, H. W. and Sykes, C.	672-2752	17.04% Cr; 9.5% Ni; 1.22% Nb; 0.50% Si; 0.41% Mn; 0.11% C; 0.014% P, 0.011% S	Not given	Hot rolled, heated 1/2 hr. at 1050°C, air cooled
□	Altman, H. W., Rubin, T. and Johnston, H. L.	0-540	A. I. S. I. 304; 18.68% Cr; 8.84% Ni; 1.12% Mn; 0.43% Si; 0.06% Cu; 0.05% C; 0.031% N ₂ ; 0.023% S; 0.017% P	Interferometer	
△	Cornelius, H., Bungard, W. and Bollenrath, F.	852-1932	A. T. S. (Ger. desig.): 18.0-19.3% Cr; 9.2-10.3% Ni; 1.35-1.75% Ta, Nb; 0.70-0.72% Mn; 0.30-0.34% Si; 0.58-0.70% W; 0.13-0.14% C; p = 498.1 lb _m /ft ³	Dilatometer	Forged, heated to 1050°C, air cooled
◇	Ibid.	852-1932	S2S 8 (Ger. desig.): 17.6% Cr; 15.2% Ni; 2.2% Mo; 1.8% Cu; 1.06% total Ta and Nb; 0.1% C; p = 492 lb _m /ft ³	Same as above	Rolled, heated to 1050°C, air cooled
▽	Cornelius, H.	528-2112	17.4-17.6% Cr; 9.1-9.2% Ni; 1.75-1.81% Si; 1.13-1.20% Mn; 1.1-1.15% W; 0.44-0.48% C	Bollenrath type comparative dilatometer	Tested in vacuum at 1.5°C/min. rise
○	Perry, S.	360-528	72.85% Fe; 18.00% Cr; 9% Ni; <0.15% C; <0.60% Zr + Mo	Quartz tube dilatometer	Auth. est. accuracy ± 3.4%
◊	Lucks, C. F. and Doern, H. W.	210-2060	A. I. S. I. 347. Nominal: 17-19% Cr; 9-12% Ni; <0.08% C; % Nb = 10(±% C)	Quartz tube dilatometer	Hot rolled, annealed 1 hr. at 2000°F, water quenched. Tested in vacuum
◌	Ibid.	210-2260	A. I. S. I. 316. Nominal: 16-18% Cr; 10-14% Ni; 2-3% Mo	Same as above	Same as above
◐	Fieldhouse, I. B., Hedge, J. C. and Lang, J. I.	540-2909	A. I. S. I. 316	Telemicroscopes sighting on sample	Tested in He atmos.
◑	Ibid.	540-2690	A. I. S. I. 347. Mfg. anal. 17.82% Cr; 10.32% Ni; 1.62% Mn; 0.6% Si; 0.14% Mo; 0.13% Cu; 0.06% C; 0.018% ea. P, S	Same as above	Same as above
◒	Neimark, B. E.	528-2112	15.3-18.1% Cr; 9.82-12.3% Ni; 0-2.76% W; 0.43-0.88% Mn; 0.59-0.74% Si; 0.072% Mo; 0-0.45% Ti; 0.09-0.10% C	Quartz tube dilatometer	Tested at 2°C/min. rise. Results of three samples: 1) as received 2) austenitized 3) stabilized 10 hr. at 800°C. Agreement ± 2.5% of average value plotted
◓	Fieldhouse, I. B., Hedge, J. C. et al.	540-2521	Stainless Steel Type 17-7PH: 72.21% Fe; 17.30% Cr; 7.06% Ni; 1.11% Al; 0.60% Mn; 0.49% Si; 0.074% C	Telemicroscopes sighting on samples	

Table 8-3
LINEAR THERMAL EXPANSION FOR PLAIN CARBON STEEL

(after Reference 8-7)

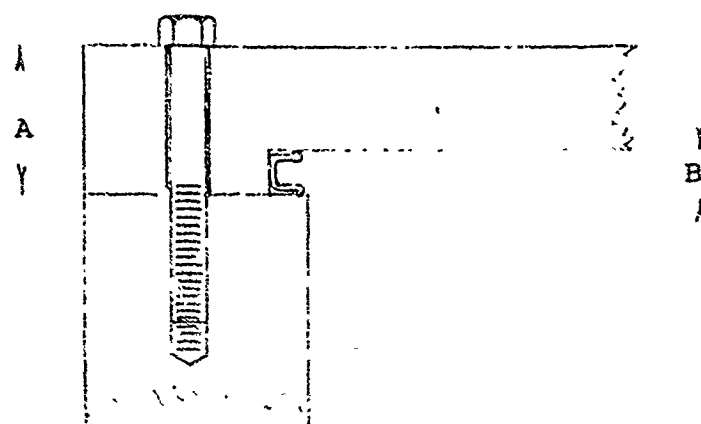
REFERENCE INFORMATION

By No.	Investigator	Range, °K	Material Composition	Test Method	Remarks
●	Andrew, J.H., Lee, H. et al.	492-1810	0.05% Mn; 0.04% C; 0.015% S; 0.01% Si; 0.005% P	Dilatometer	Normalized so that initial structure is ferrite and lamellar pearlite
□	Ibid.	492-1812	2.63% Mn; 0.16% C; 0.07% Si; 0.012% P; 0.010% S	Same as above	Same as above
△	Rosenfield, A.R. and Averback, B.E.	515-542	SAE 1020 steel. 0.89% Mn; 0.20% C; 0.17% Si; 0.064% S; 0.015% P	Strain gages glued to sample	Coeff. of exp. given as $11.1 \times 10^{-6}/^{\circ}\text{C}$ for 13-28°C
◇	Esser, J. and Eusterbrock, H.	528-2292	0.13% C; <0.03% O ₂ ; <0.02% Mn; <0.004% S; <0.0024% S	Comparative dilatometer; (Au standard)	Annealed 1 hr. at 700°C in vacuum, cooled slowly. ◇: heating; ◇: cooling
▽	Lucks, C.F. and Deem, M.W.	210-2110	SAE 1010 steel from U.S. Steel $p = 490 \text{ lb}/\text{in}^2$	Quartz tube dilatometer	Hot rolled. Tested in vacuum
○	Abe, Y., Kimura, K. and Saito, T.	528-2272	"Low carbon steel"	Not given here; refers to others	
○	Cornelius, H.	528-1752	0.46% Mn; 0.17% Si; 0.07% C; 0.014% S; 0.012% P	Comparative dilatometer	Tested in vacuum at 1.5°C/min. rise
○	Ibid.	528-1752	1.51% Mn; 0.34% Si; 0.08% C; 0.013% S; 0.012% P	Same as above	Same as above
△	Laquer, H.L.	0-540	SAE 1020 steel	Interferometer	Integrated values of unpublished thermal expansion coefficients by Allman, Rubin, and Johnston (1949-50)

Table 8-4
LINEAR THERMAL EXPANSION FOR 304 STAINLESS AND SIMILAR METALS
(after Reference 8-7)

REFERENCE INFORMATION

Ref.	Investigator	Ref.	Range, °R	Material Composition	Test Method	Remarks
58-5	Lucke, C. F. and Dean, H. W.	210-2060	AISI 301. Nominal: 16-18% Cr; 6-8% Ni		Quartz tube dilatometer	Hot rolled, annealed 1 hr. at 1900°F; water quenched. Tested in vacuum.
48-17	M. W. Kellogg Co.	520-2260	AISI 304: 18.43% Cr; 9.67% Ni; 1.14% Mn; 0.53% Si; 0.16% Cu; 0.069% C; 0.023% P; 0.016% S		Dilatometer	Solution heat treated 5/4 hr. at 1990-2170°F; water quenched, aged 48-50 hr. at 2400°F
53-127	Saunders, H. A., et al.	960-2260	AISI 310: Nominal: 24.2% Fe; 25.0% Cr; 20.5% Ni; <2.00% Mn; <1.5% Si; <0.25% C		Dilatometer	Arc melted, cast, heated for 24 hr. at 1800°F in vacuum. Data average of two heating and cooling cycles. Tested in vacuum.
57-156	Seibel, R. D. and Adams, G. L.	1260-2060	AISI 310: 46.59% Fe; 24.94% Cr; 19.60% Ni; 1.57% Mn; 0.37% Si; 0.062% C; 0.018% P, P.S.		Alumina tube dilatometer	Calibrated using Cu and Mo; tested at 350°F/min in vacuum.
56-97	Kefauver, H. C., Sprague, R. M. and Bennett, D. G.	544-1393	AISI 302: Nominal: 17.97-19.00% Cr; 8.00-18.00% Ni; 2.50% Mn max; 0.08-0.20% C		Interferometer	
51-65	Lucke, C. F., Thompson, H. B. et al.	150-1312	AISI 301: Nominal: 16.0-18.0% Cr; 6.07-8.00% Ni; 2.50% Mn max; 0.08-0.20% C		Quartz tube dilatometer	Hot rolled, annealed 1 hr. at 1900°F; water quenched.
52-77	Laquer, K. L.	0-521	AISI 304: Nominal: 18.20% Cr; 8-11% Ni		Viscan Interferometer	Work by Allman, Rubin, Johnston. Unpubl. 1948-1951.
53-35	Schneider, L. A.	530-2060	HP Grade Alloy; 21% Cr; 9% Ni		Not given	



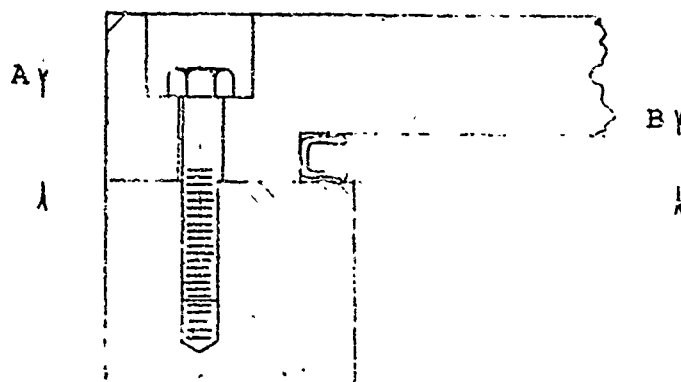
<u>Dimension</u>	<u>Material</u>	<u>Thermal Expansion at 1000°F</u>
Bolt free length A = 0.75 in.	304 SS	0.95% from figure 3-7
Groove height B = 0.25 in.	AM3 SS	7.2×10^{-6} in./in./°F from manufacturing literature
Seal height B = 0.25 in.	17-7PH SS	1% from figure 7-5

The thermal expansion of the various parts for a 1000°F change in temperature is

<u>Part</u>	<u>Expansion (in.)</u>
Bolt	0.00716
Groove height	0.0018
Seal height	0.0025

The groove height increases less than the seal height, however, as a result of the expansion of the bolts, there is a difference in displacement between the seal and the top of the groove of $(0.00716 + 0.0018) - 0.0025 = 0.0064$ in. In addition to this 0.00646 in., there may be additional displacement of the groove owing to pressure force deflection of the cover. It can be seen that haphazard selection of assembly materials can lead to serious performance problems. A differential expansion of 0.006 in. may be sufficient to separate the interface surfaces depending on the preload and resiliency of the seal structure.

Since the bolt free length is most often longer than the seal and groove height, it is possible to minimize the problem of differential expansion by choosing a shorter bolt length and a material with a lower thermal expansion coefficient as an example. Consider



<u>Dimension</u>	<u>Material</u>	<u>Thermal Expansion at 1000°F</u>
Bolt free length A = 0.375	1020 Stl	0.75% from figure 8-6
Groove height B = 0.25	AM3 SS	7.2×10^{-6} from manufacturer literature
Seal Height B = 0.25	17-7PH	1% from figure 8-5

The thermal expansion under these conditions is given as

<u>Part</u>	<u>Expansion (in.)</u>
Bolt	0.00271
Groove height	0.0018
Seal height	0.0025

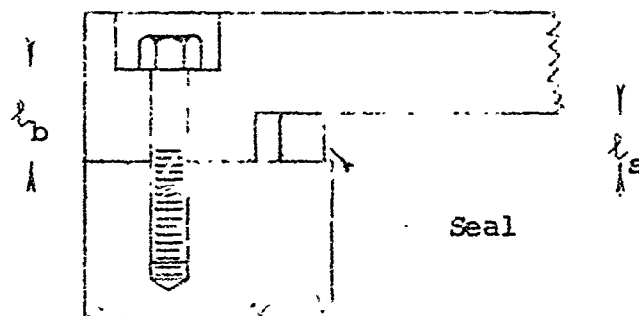
The total differential expansion in this case is $(0.0027 + 0.0018) - 0.0025 = 0.002$ in. This represents a considerable improvement. The differential expansion can possibly be compensated in the design of the seal structure. Sufficient initial elastic deformation of the seal structure can be provided so that after the thermal expansion takes place there will still remain sufficient elastic deflection in the seal structure to maintain adequate contact load at the sealing interface. In the case of pressure-actuated seals, the fluid pressure acting on the seal structure tends to increase the contact force.

The same type of procedure is necessary when the seal assembly is to be operated at extremely low temperatures. If the seal contracts at a greater rate than the groove or the bolts, interface separation could occur. If the flange or cover material contracts at a greater rate than the seal, the decrease in groove height may counteract the shrinkage of the flange at the bolt which tends to decrease the bolt clamping load.

The effect of pressure gradients must also be considered. If the seal temperature suddenly increases because of contact with a hot gas, a large temperature gradient can be created between the seal and the bolts. In this case there is a tendency

for the seal to expand at a much greater rate than the bolt. However, the seal is in contact with the cover and the expansion of the seal structure is restrained. This restraint against the expansion of the seal induces an additional load on the bolts. It is possible that this induced load can deform the bolts plastically. Thus, when the gradient decreases, there may be a substantial decrease in contact force at the sealing interface. If large thermal transients and large temperature gradients are expected in the seal and housing assembly, the thermally induced stresses on the bolts should be estimated. The results of this estimation may indicate that, because of effects of the temperature gradient, higher strength bolts are necessary. This would be indicated by an analysis in which temperature gradients are neglected. This estimation can be accomplished using the standard strength of materials approach using elastic theory or the increase in load can be estimated from empirical load deformation data. In the use of empirical data, the change in the seal dimension that is due strictly to thermal expansion can be estimated. The additional bolt load required to restrain this expansion is then assumed to be equal to the load required to produce the same change in seal dimension by deformation of the seal, and is obtained from the load versus deformation data.

A treatment of the problem by elastic theory is illustrated in the following example.



If the temperature of the entire assembly is raised by an amount ΔT , and the seal has a greater rate of expansion than the bolt, the restraint on the seal will induce an additional load on the bolt. From static equilibrium conditions the following conditions must hold.

- (1) The total compressive force on the seal must be equal in magnitude to the total additional tensile load on the bolts.
- (2) The elongation of the bolt due to the rise in temperature plus the stretching of the bolt due to the additional force must equal the expansion of the seal due to the rise in temperature minus the compression of the seal due to the additional load on the seal interface.

These relations may be expressed as follows.

Load relation:

$$F_b = F_s \quad (8-15)$$

Elongation relation:

$$\delta_{Tb} + \delta_{Fb} = \delta_{Ts} - \delta_{Fs} \quad (8-16)$$

The temperature expansion of the seal and the bolt can be expressed as

$$\delta_{Ts} = \alpha_s \ell_s \Delta T_s \quad (8-17)$$

$$\delta_{Tb} = \alpha_b \ell_b \Delta T_b$$

The deflection of the bolt and seal due to the forces are given by

$$\delta_{Fb} = \frac{F_b \ell_b}{A_b E_b} \quad (8-18)$$

$$\delta_{Fs} = \frac{F_s \ell_s}{A_s E_s}$$

Substituting relations (8-17) and (8-18) in (8-16) yields

$$\alpha_b \ell_b \Delta T_b + \frac{F_b \ell_b}{A_b E_b} = \alpha_s \ell_s \Delta T_s - \frac{F_s \ell_s}{A_s E_s} \quad (8-19)$$

Equation (8-19) shows the general relationship between the loads and deflections of the seal and bolts. In cases where no gradients exist in the assembly but a temperature change of the entire assembly is taking place, $\Delta T_b = \Delta T_s$. During a thermal transient, in general $\Delta T_b \neq \Delta T_s$. In the most extreme case of a thermal shock either ΔT_b or ΔT_s can be assumed to be equal to zero while the other assumes some finite value. In all cases the total forces must be equal. Thus, if the geometry and thermal expansion coefficients are known, the additional force that is due to any assumed temperature gradient condition can be calculated from equation (8-19). This thermally induced load must be added to the total bolt load including the preload, seal reaction, and pressure load. If the bolt yields, then larger bolts or higher strength bolts are required to withstand the thermally induced forces.

Table 8-5

MODULUS OF ELASTICITY* OF HIGH-STRENGTH, HIGH-
TEMPERATURE FASTENER ALLOYS AT VARIOUS TEMPERATURES

(after Reference 8-6)

Alloy	Temperature (°F)			
	70	1000	1200	1600
Titanium				
Ti-6 Al-4 V	16.5	---	---	---
Ti-7 Al-12 Zr	16.5	---	---	---
Stainless Steels				
Type 302	28.0	---	---	---
Type 403	29.0	---	---	---
PH 15-7 Mo	28.0	---	---	---
High-Strength Iron-Base Stainless Alloys				
A 286	29.1	23.5	21.1	18.9
AMS 5616	29.0	21.5	---	---
Unitemp 212	29.0	24.4	22.4	18.5
High-Strength Iron-Base Alloys				
AISI 4340	30.0	---	---	---
H-11 (AMS 6485)	30.6	23.0	16.0	---
AMS 6304	29.5	20.0	---	---
Nickel-Base Alloys				
Inconel X	31.0	25.0	23.0	---
Waspaloy	30.6	26.7	---	22.7
Rene 41	---	---	25.9	23.2

*All values are in units of 10^6 psi.

Table 8-6

**YIELD STRENGTH* OF HIGH-STRENGTH, HIGH-TEMPERATURE
FASTENER ALLOYS AT VARIOUS TEMPERATURES**
(after Reference 8-6)

Alloy	Temperature (°F)				
	70	800	1000	1200	1500
Titanium					
Ti-6 Al-4 V	120,000	75,600	54,000	---	---
Ti-7 Al-12 Zr	120,000	75,600	69,000	---	---
Stainless Steels					
Type 302	35,000	35,000	34,000	30,000	10,000
Type 403	145,000	110,000	95,000	38,000	9,700
PH 15-7 Mo	220,000	149,000	101,000	---	---
High-Strength Iron-Base Stainless Alloys					
A 286	95,000	95,000	90,000	85,000	---
AMS 5615	113,000	80,000	60,000	40,000	---
Unitemp 212	150,000	140,000	135,000	130,000	---
High-Strength Iron-Base Alloys					
AISI 4340	200,000	130,000	75,000	---	---
H-11 (AMS 6485)	215,000	175,000	155,000	---	---
AMS 6304	160,000	100,000	75,000	---	---
Nickel-Base Alloys					
Inconel X	115,000	---	---	98,000	40,000
Waspaloy	115,000	---	106,000	100,000	75,000
Rene 41	100,000	---	95,000	90,000	60,000

*All values are in psi.

Other Thermal Effects. In addition to the direct effects of thermal expansion, temperature changes exert more subtle influence on the seal and housing assembly because of the changes in physical properties caused by temperature changes. Tables 8-5 and 8-6 show the variation of modulus of elasticity and yield strength with temperature for several metals.

As the temperature increases the modulus of elasticity decreases, thus more deflection can be produced with a given force. Therefore, structures at high temperature are less rigid under the same loading as structures at lower temperatures. The decrease in yield strength at high temperatures must be carefully considered when designing a seal structure for high temperature applications. The yield strength and modulus of elasticity at the maximum operating temperature are suggested for use at design calculations.

Creep occurs when long periods of operation at elevated temperatures are encountered. Creep is the slow steady continuous plastic deformation that occurs in most metals at elevated temperatures at stress levels far below the yield strength of the material. Quantitative data on creep are extremely limited, and little is known about the theoretical basis of the phenomenon. A quantity known as creep strength is defined and some information is available. The creep strength is usually defined as a stress that produces an elongation at a temperature during a time interval. The creep strength of various metals based on a 0.1% elongation for 1000 hours at 800°F is given in Table 8-7 (Ref. 8-8).

Table 8-7
CREEP STRENGTH OF METALS
(after Reference 8-8)

Age Hardenable Stainless Steels	Creep Strength (psi)
17-4 PH	50,000
17-7 PH	40,000
PH15-7 Mo	95,000
17-14 CuMc	24,000
AM 350	91,000
AM 3SS	100,000
<u>Iron base superalloys (C_r-Ni)</u>	
A286 (.1% at 1000 hr, 1200°F)	30,000
16-25-6 (.1% at 1000 hr, 1200°F)	19,000

This information can not readily be used to interpolate and find the creep rate at other conditions of stress and temperature with a high degree of reliability. Often experimental evaluation

under a specific set of conditions is necessary to evaluate the creep properties of a material.

8.3 Dynamic Seal Housing

In dynamic applications, the interface load is much smaller than the contact loads in static applications. The seal configuration itself usually provides the necessary contact force. Examples of this are the deflection of the lip or the lip-type sliding seal and the hydrostatic balance force and the spring load on a typical face-type rotating seal. Thus the housing design does not contribute directly to the contact force as in the case of the cover plate and seal or in the various fluid conduit connectors.

The housings of dynamic seals must support the seal so that the proper positional relationship between the sealing contact surfaces is maintained. The housing must also withstand the fluid pressure and structural loads imposed on it.

In all dynamic seal housings, a static seal of some sort is present. The design criteria for this type of seal are the same as for any other static seal.

In all dynamic applications some secondary motion of the dynamic surface will be present. Secondary motion is defined as inherent but unnecessary and unwanted motion superimposed on the desired motion. Examples of this are:

- Radial movement of a rotating shaft due to bearing play, eccentricity, misalignment
- Radial movement of a sliding shaft due to these causes plus the effects of side loading, variations in straightness of the shaft.

In addition to these types of secondary motion, motion of the seal can be caused by shaft out-of-roundness and variations in shaft diameter.

To compensate for this secondary motion most dynamic contacting seals have supports with some flexibility built in. An example of this is the spring loading of a face-type seal. The spring-loaded face has freedom to wobble slightly about a plane perpendicular to the axis of rotation of the shaft. Thus, the face can follow the motions of the mating member of the seal configuration. The spring-loaded face can be either stationary or rotating depending on the seal configuration.

Secondary motion is usually undesirable from a seal standpoint because:

- (1) Periodic fluctuating motion may cause fatigue failure of some of the seal components
- (2) Separation of the sealing surface may occur because of inability of one of the surfaces to follow the motion of the other.

Thus, the reduction of secondary motion is of significant importance in the design of dynamic sealing devices. This means that bearing design must be considered as part of the over-all dynamic seal housing design problem.

In addition to these considerations which are common to all dynamic seal housing problems, in certain applications special functions must be designed into the dynamic seal housing. These include:

- seal cooling facilities
- supplementary lubrication
- interface flushing

Thus the designer of dynamic seal housing must consider not only those structural criteria described in the static seal housing discussion, but also the additional problems associated with dynamic seals. These problems can be summarized as

- seal support flexibility
- bearing rigidity or stiffness
- part roundness and straightness
- elimination or reduction of misalignment
- special housing functions

8.4 Observations

All of the design procedures and criteria discussed in this section concerning seal structure and housing design have one major goal. That goal is to provide and maintain the necessary interface contact load conditions so that adequate sealing is achieved at all operating conditions. The entire design process for sealing can now be placed on a systematic basis. Factors to consider in the design or analysis of housings and structures are:

- The operating temperature and fluid compatibility considerations will, in general, establish the field of choice of the seal interface materials. If plastics or rubber are satisfactory, they should be employed since these materials require a substantially

lower contact load than metallic seals. This can have a significant effect on the seal structure and housing.

- The design of the seal structure housing must be an iterative process. The shape of the seal and the interface load will determine the initial seal deflection. The minimum operational load will be determined by the deformation and the hysteresis characteristics of the seal material.

Interface deformation will be determined by the rigidity of the housing configuration and can be obtained from:

- Structural analysis of the housing configuration, either conduit connector or pressure vessel cover, including the values of yield strength and modulus of elasticity at the operating temperatures where applicable
- Load and deformation analysis of the housing fasteners
- Estimates of deflection and distortion due to differential thermal expansion caused by differences in the thermal properties of the materials, and temperature gradients in the housing and seal configuration
- Investigation of the thermally induced loads in the housing configuration.

If the housing deflection estimated by the criteria and methods suggested in this section is greater than the allowable deflection determined from the sealing interface and seal structure criteria, the design must be modified. Either the housing must be more rigid, or the seal structure redesigned for more deflection.

The choice of which member to modify must be made by the designer. Some important considerations in making the choice are:

- The relative difficulty of making the modification on either the seal or the housing
- Size of the seal (to allow greater deflection to stay within the structural limitations of the seal configuration, the size may have to be increased)
- Effect of normal manufacturing tolerances
- Weight considerations. A saving in increased weight may be achieved by using a larger seal which allows larger deflections rather than increasing the rigidity of the housing.

- Space limitations. In some applications space limitations either in the immediate vicinity of the seal or elsewhere will limit the allowable size of the various components of the seal and housing assembly
- Cost considerations. The use of a higher strength but higher cost material may solve certain structural problems if the increased cost can be tolerated.

8.5 References

- 8-1 Development of Mechanical Fittings Phases I and II Technical Documentary Report RTD-TDR-63-1115, Project 6753 Task 675304, Contract AF04(611)-817
- 8-2 Design Criteria for Zero Leakage Connectors for Launch Vehicles, Volumes 1-4, Contract NAS8-4012, 15 Mar 1963
- 8-3 R. J. Roark, Formulas for Stress and Strain, McGraw Hill, N. Y. 1954
- 8-4 Paul A. Bauer, Myron Glickman and Frank Iwatsuki, Analytical Techniques for the Design of Seals for Use in Rocket Propulsion Systems, Volumes I and II AFRL-TR-65-61 IIT Research Institute Chicago (May 1965)
- 8-5 American Society of Mechanical Engineers Pressure Vessel and Piping Design, Collected Papers, 1927-1959
- 8-6 Thomas C. Baumgartner, "High Temperature Joints" Machine Design 37 No. 2, 21 Jan 1965
- 8-7 A. Goldsmith, T. Waterman and H. Hirschhorn, Thermo-Physical Properties of Solid Materials, Volume 2 Macmillan Co. N.Y. 1961
- 8-8 "Materials Selector Issue" Materials in Design Engineering 58, No. 5 Mid-October 1963

9. INTERACTION OF SEALING PARAMETERS

In each of the preceding sections certain parameters affecting sealing were studied either individually or in groups. Most of the parameters influencing the seal as a singular device have been considered while other parameters induced by seal-related parts, such as the seal housing, have yet to be introduced. The purpose of this section is to interrelate the additional parameters and develop methods of predicting seal performance. The consideration of each type of seal would be a difficult task. Therefore, one seal, a static seal, was selected to portray the general procedures. This example should provide the systems designer with an understanding of the interaction of parameters and thus serve as a general guide in modifying the procedures for specific seal applications. These modifications in the analysis are demonstrated in Section 10 where a variety of seals are considered. Before proceeding, related information and its applicability to various seals is located in the following sections:

Interface Deformation and Leakage: Section 2
Seal Inspection and Fabrication Techniques: Section 6
Analytical Criteria for Seal Structures: Section 7
Criteria for Seal Housing: Section 8

9.1 General Considerations, Input Data

The interaction of parameters in static seals can be exemplified by choosing an arbitrary application and environmental conditions. Starting with these basic ingredients, a seal is developed by optimizing each parameter to produce a 10^{-6} cc per sec helium leakage seal. The application is to seal a simple, circular cover located over a 1.8-in.-diam aperture as might be found on many fluid system components. The environmental conditions are pressures up to 2000 psi and temperatures between -320°F and 1200°F.

9.2 Mode of Interface Deformation and Leakage

The first consideration is given to the materials and fabrication of the interface. The high temperature requirement eliminates plastic and rubber as possibilities, leaving metallics as the most likely candidates. The most feasible surface fabrication methods are:

Super polishing to produce an elastically deformed interface, Class I or II

Plastic deformation of rougher engineering surfaces, Class IV

The major difference between the two methods is the magnitude of the interface load required to obtain the desired leakage rate. With either possibility, the load must be a minimum from the standpoint of the seal structure and seal-related parts. The Class I or II interfaces require the least

load but have several disadvantages which eliminate them from consideration. First, the manufacture of Class I and II surfaces is usually slow and expensive with the results often uncertain because of the limitations of the inspection equipment and procedures. Secondly, the degree of cleanliness necessary for the successful operation of this type of seal is often difficult to achieve in practical applications. The remaining possibility is a fine finish Class IV surface pressed together until substantial plastic deformation occurs. Carrying this further, at least one of the materials must deform plastically suggesting that the interface be composed of a soft and hard material. The soft material being part of the demountable structure and the hard material forming the seal housing. This minimizes permanent deformation of the housing and permits at least this part of the sealing system to be reusable.

9.2.1 Material Selection

The selection of a seal-housing material should be based on high hardness and strength properties at elevated temperatures. The hardness is predicated on interfacial requirements while strength is predicated on minimum size and weight requirements of the parts being sealed. The material selected is AM355 having the following properties:

Temperature (°F)	Modulus of Elasticity, E (10 ⁶ psi)	Yield Strength (0.2% offset) (10 ³ psi)	Hardness
80	29.3	181	Rc 53
800	24.6	139	Meyer
1000		97	540,000 psi

A material for the seal should be selected on low hardness and high strength properties. Since these two properties are interrelated, a strength compromise is necessary based on the relative hardness of the mating (AM355) material. A suitable material is 17-7PH stainless steel having the following properties.

Temperature (°F)	Yield Strength (0.2% offset) (10 ³ psi)	Hardness
80	180	Brinell: 168
800	129	Meyer 238,000 psi
1000	76	

A comparison of the Meyer hardness of both materials at room temperature shows that the housing material is approximately twice the seal material. While no adequate criteria are available to predict an optimum difference in hardness, experiments have

shown that a factor of two is close to the minimum for the reusability of the harder surface. A smaller difference in hardness can be expected to produce substantial permanent deformation of both interface surfaces when pressed together.

Other parameters, not considered important in this example, a chemical compatibility of the materials, fluid sealed, and the environment.

9.2.2 Determination of the Interface Geometry

Two basic choices of interface geometry available are flat mating surfaces or a wedge-shaped surface mated against a flat surface. An optimum (low load) geometry was identified in Section II as a 60° wedge constructed from the softer material. The interface geometry is shown on figure 9-1.

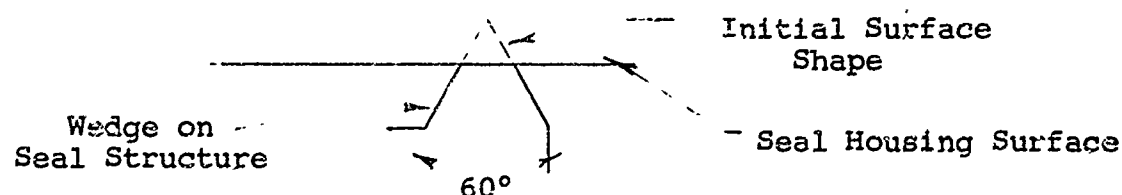


Figure 9-1 Typical geometry of the seal interface

The linear load - contact area relationship (figure 2-8) shows that a condition of constant average stress occurs at the interface when the wedge is deformed. This implies plastic flow of the seal material at the interface so that the relation

$$\frac{P}{A} = \sigma = \text{constant for a given material}$$

where

P = load/in. of circumference

A = contact area/in. of circumference

σ = normal stress

The stress σ is related to the Meyer hardness, σ_m , of the softer interface material by:

$$\sigma = C\sigma_m \quad (9-1)$$

where C is a constant that depends on the geometry of the wedge and is approximately 0.5 (figure 2-8).

Since the average contact stress is constant, we can expect good sealing with almost no load and almost line contact. This does not occur because of the irregularities on the contact

surfaces. A sufficient width of contact is necessary to "surround" enough of the scratches, valleys, gorges and other microscopic surface disturbances, and minimize the size of the leak path. A criterion for the proper contact width was established tentatively as 0.012 in. in Section 2. Combining the preceding requirements,

$$\sigma = C\sigma_m$$

$$C = 0.5$$

$$A = 0.012 \text{ in.}$$

the net load at the interface is

$$P = AC\sigma_m$$

$$\text{or } P = 0.006\sigma_m \quad (9-2)$$

Substituting the material properties of the softer interface material $\sigma_m = 238,000$ psi, the net load is $P = 1430$ lb per in. of interface circumference.

9.2.3 Preliminary Estimate of Leakage

If it is assumed that the contact load at the interface is constant, the leak path and conductance parameter for the interface will also be constant. Thus, the modified stress ratio can be computed and a conductance parameter derived from the empirical data presented in Section 2. The conductance parameter is then applied to the appropriate flow equation to predict leakage.

Since the load is known, the modified stress ratio is computed from the relation

$$\text{Modified Stress Ratio} = \frac{P^{2/n'}}{A_A} / \sigma_m \quad (9-3)$$

where

P = total load

A_A = apparent contact area

σ_m = Meyer hardness

n' = Meyer index

The properties of 17-7PH are $\sigma_m = 238,000$ psi and $n' = 2.2$. Equation (9-3) can be solved:

$$\text{Modified Stress Ratio} = \frac{143 \text{ J}^{2/2.2}}{0.012} / 238,000$$

$$= 0.26$$

Assuming that the interface surfaces are ground to $10 \mu\text{in.}$ PTV, the conductance parameter can be obtained from figure 2-46. An approximate value of the conductance parameter is

$$(h^3) \approx 1 \times 10^{-22} \text{ in}^3$$

Helium leakage can be calculated from the equation for transition flow (Subsection 2.6)

$$Q_o = \frac{\pi(D_o + D_i)(p_{in}^2 - p_{out}^2)}{12\mu p_o (D_o - D_i)} h^3 +$$

$$\frac{1.06\epsilon \lambda_o h^2 (p_{in} + p_{out})(D_o + D_i)}{\mu (D_o - D_i)}$$

where

Q_o = leakage rate ($\text{in}^3/\text{sec STP}$)

p_{in} = inlet pressure (psia)

p_{out} = outlet pressure = 14.7 psia

μ = viscosity of helium = $2.8 \times 10^{-9} \frac{\text{lb-sec}}{\text{in}^2}$

ϵ * ~ 0.9 for a single gas

λ_o = molecular mean free path of helium = $13.0 \times 10^{-6} \text{ in. STP}$

D_o = 2.006 in.*

D_i = 1.994 in.*

The predicted helium leakage as a function of pressure and temperature are:

* D_o and D_i are the outside and inside diameters on the interface. Assuming that the mean interface dimension is 2 in., the diameters are equal to $\pm 1/2$ the contact width of 0.012 in.

<u>Pressure</u> (psia)	<u>80°F</u>	<u>Temperature</u> <u>-320°F</u>	<u>1000°F</u>
114.7	3.01×10^{-6}	8.53×10^{-6}	1.47×10^{-6}
214.7	6.01×10^{-6}	1.7×10^{-5}	2.94×10^{-6}
514.7	1.54×10^{-5}	4.36×10^{-5}	7.52×10^{-6}
1014.7	3.26×10^{-5}	9.24×10^{-5}	1.59×10^{-5}
1514.7	5.075×10^{-5}	1.44×10^{-4}	2.48×10^{-5}
2014.7	7.05×10^{-5}	2.00×10^{-4}	3.44×10^{-5}

A review of the preceding data shows that the average leakage closely approximate the goal of 10^{-6} cc per sec. It should be noted that the empirical data developed in Section 2 yield correlation parameters estimated to be accurate within a factor of ± 10 . Thus, the preceding leakage rates may be expected to vary between 2×10^{-3} to 1.5×10^{-7} cc per sec over the temperature and pressure range.

9.3 Seal Housing Deformation

Since the seal housing is expected to deform from pressure and thermal expansion effects, it is necessary to estimate its magnitude before any consideration can be given to the shape of the seal structure. A bolted flat cover housing is selected as shown in figure 9-2.

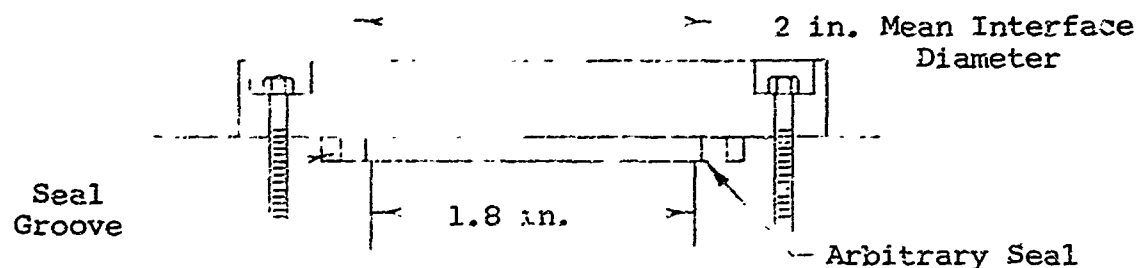


Figure 9-2 Flat cover geometry

Following the procedures outlined in Section 8, the deformation can be approximated using the simplified flat cover criteria. Since the diameter of the seal contact area is given, a bolt circle radius can now be assumed. Thus, the ratio r_o/a is established where r_o is the contact area radius and a the bolt circle radius. The flange or cover plate deflection parameter at the contact point can be obtained as a function of the ratio r_o/a from the data in figure 9-3. At this point, the designer must decide whether to design a housing for minimum weight (i.e., maximum stress), or maximum rigidity (i.e., minimum deflection). The following relationships are used in the analysis.

Deflection parameter:

$$y'_o = \frac{y_o E p^{1/2}}{a S_{\max}^{3/2}}$$

Flange thickness:

$$t = \frac{3r_o^2 p}{2m S_{\max}} \left[m + (m+1) \ln\left(\frac{a}{r_o}\right) - \frac{m-1}{4} \left(\frac{r_o}{a}\right)^2 \right]$$

where

t = flange or cover thickness (in.)

S_{\max} = maximum flange stress (psi)

p = fluid pressure (psi)

m = $1/\nu$

ν = Poisson's Ratio = 0.3

Assume

$$\frac{r_o}{a} = 0.5,$$

therefore $a = 2$.

Minimum Weight Design will be obtained for adverse operating conditions (i.e., $p = 2000$ psi, $t = 1000^\circ\text{F}$). The minimum weight will be achieved when the cover is designed for the highest allowable stress. Assume $S_{\max} = 50,000$ psi, thus giving a safety factor of 2. From figure 9-4, when $r_o/a = 0.5$, y'_o equals 0.26. The deflection at the contact point is given as

$$y_o = \frac{a (S_{\max})^{3/2} y'_o}{E p}$$

when the known values are substituted:

$$\begin{aligned} y_o &= \frac{(2) \{(50,000)^{3/2}\} (0.26)}{(24.6 \times 10^6) \quad 2000} \\ &= 0.00528 \text{ in.} \end{aligned}$$

The cover thickness is given by

$$t = \frac{3r_o^2 p}{2m S_{\max}} \left[m + (m+1) \ln(a/r_o) - \frac{(m-1)}{4} (r_o/a)^2 \right]$$

$$= \frac{(3)(1)(2000)}{(2)(3.33)(50,000)} 3.33 + 4.33 \ln 2 - \left(\frac{2.33}{4}\right) (1/2)^2$$

$$= 0.333 \text{ in.}$$

Maximum Rigidity Design. Assume a maximum deflection at the seal interface, $y_o = 0.001$. Again, for

$$\frac{r_o}{a} = 0.5; y'_o = 0.26$$

Solving the deflection parameter relationship for S_{\max} ,

$$S_{\max}^{3/2} = \frac{y_o^{EP^{1/2}}}{ay'_o} = \frac{(0.001)(24.6 \times 10^6)(2000)^{1/2}}{2(0.26)}$$

$$= 2115 \times 10^3$$

$$S_{\max} = 14,940 \text{ psi}$$

Cover thickness,

$$t = \frac{3r_o^2 p}{2mS_{\max}} 3.33 + (4.33) \ln\left(\frac{a}{r_o}\right) - \frac{(m-1)}{4} \left(\frac{r_o}{a}\right)^2$$

$$= \frac{(3)(1)(2000)}{(2)(3.33)(14,940)} 3.33 + 4.33 \times .59 - \frac{2.33}{4 \times 4} = 0.61 \text{ in.}$$

$$= 0.61 \text{ in.}$$

Thermal Distortion. The maximum rigidity design will be assumed. As further input data for the required initial deflection, the thermal distortion will be estimated. In the seal and housing configuration under consideration, the critical problem in differential thermal expansion is the difference in expansion between the unthreaded length of the bolts and the seal structure itself. This expansion at a temperature of 1000°F can be estimated using figure 9-2 and assuming:

Bolt, Plain Carbon Steel, unthreaded length
 $l_b = 0.75 \text{ in.}$

Seal, 17-7PH

Housing, AM 335

Housing Groove height, C, 0.25

From figure 8-5, the linear expansion of 17-7PH steel at 1000°F is 0.96 per cent. From figure 7-9 the linear expansion of plain

carbon steel at 1000°F is 0.72 per cent. The average thermal expansion coefficient of AM 355 steel in the range from 68 to 1150°F is given as 7.2×10^{-5} .

Estimated expansion for a 1000°F change in temperature:

Bolt; 0.0054 in.

Groove; 0.0018 in.

Seal; 0.0024 in.

Thus, the bolt elongation is 0.003 in. greater than the seal elongation. This situation can be improved by decreasing the free length of the bolt. If a bolt free length of 0.375 in. is assumed, the bolt elongation would be 0.0027 in. The difference in expansion is now only 0.0003 in.

Additional consideration must be given to bolt elongation due to pressure loading. Since the seal contact diameter is 2 in., the pressure loading on the bolts is given by

$$\pi PD^2 = F_b$$

where P_b is the bolt load due to pressure. At this point the designer must make a reasonable assumption for the bolt size and number of bolts.*

Assume eight 3/8-16NC bolts having a stress area of 0.0678 sq in. The total bolt area of eight bolts is 0.542 sq in. For the thermal consideration, the unthreaded length of the bolts should be 0.375 in. Thus, the bolt elongation is

$$\delta_b = F_b h_b / A_b E$$

where

δ_b = bolt elongation (in.)

A_b = total bolt area (in.²)

P_b = total bolt load due to pressure (lb)

$$F_b = \frac{\pi(2)(2000)}{4} = 6280 \text{ lb}$$

$$\delta_b = \frac{(6280)(0.375)}{(0.541)(30 \times 10^6)} = 0.00015 \text{ in.}$$

* Reference 9-1 is suggested for optimization methods in bolt selection and sizing.

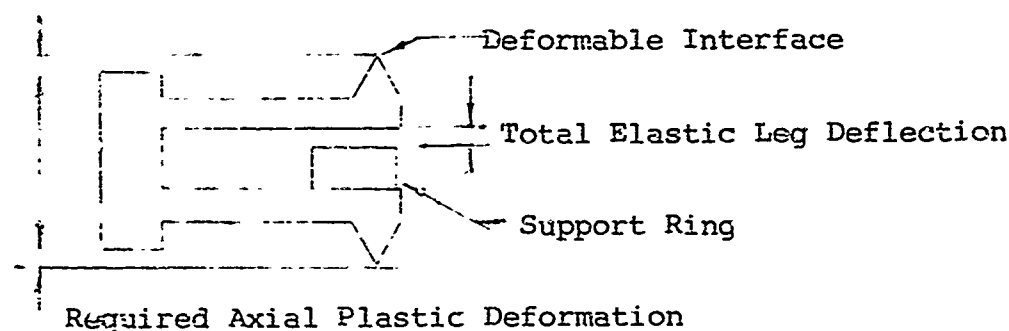
The estimated pressure and thermal deflection can now be used to establish the deformation of the seal structure. To ensure sufficient sealing contact force under all operating conditions, it is necessary to apply predeformation to the seal. Thus, the elastic reaction and the pressure actuation load are additive at the seal interface. To achieve this situation, the initial seal deflection must be greater than the thermal and pressure deflections in the housing. The previous estimations show that the total expected housing deformation due to cover deflection and bolt elongation given by $P_b + y_o$.

$$P_b + y_o = 0.00015 + 0.001 \approx 0.002 \text{ in.}$$

The differential thermal expansion for a 1000°F change in temperature is given as 0.0003 in. Thus, the total housing deformation can be assumed to be 0.0015 in.

9.4 Structure Criteria

The procedures outlined in Section 7 can be used to develop a seal configuration once a basic shape has been selected. The presence of thermal and pressure deformation on the seal housing suggests that the seal be pressure-energized to compensate for the deformation. The seal shape must be sufficiently resilient, as typified by the lip-type seal. Having selected this shape, the procedures can now be employed. Before proceeding, however, some thought must be given to the requirements. The procedures, as outlined, attempt to keep the stresses in the seal leg within the elastic limits of the material. In many cases an attempt to achieve the initial interface loading and maximum housing deformation solely by elastic deflection leads to unreasonably large seal dimensions. This problem can be overcome by the use of an auxiliary support for the cantilever leg of the seal. This concept is shown as follows.



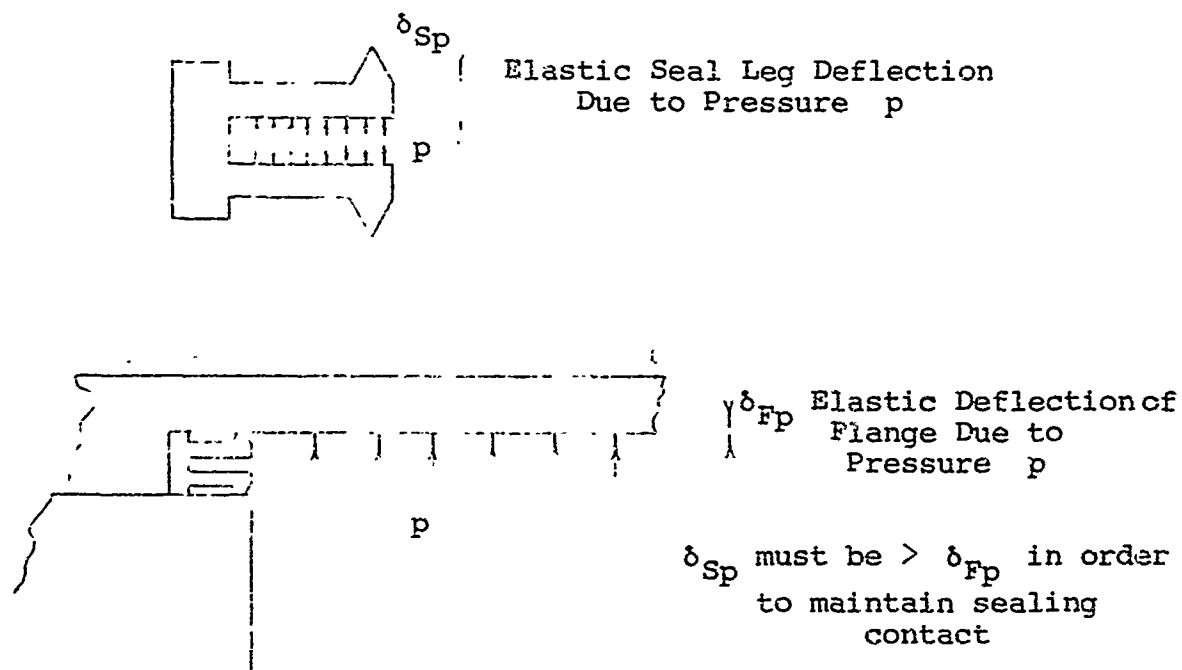
The seal legs deform elastically when the wedge tips are brought into contact with the mating housing surface. When the seal legs come in contact with the support ring, an additional

increase in contact load plastically deforms the wedge but not the seal legs. Since the leg does not have to support the entire contact load, it can be made compact, with reasonable dimensions.

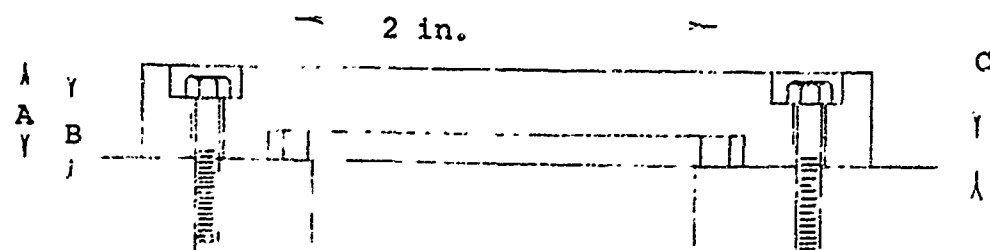
When a support ring is used, the primary design consideration for the seal leg is to allow sufficient flexibility and contact at the interface plastically under thermal and pressure deformation.

To assure sealing contact when full design pressure is encountered, the cantilever leg of the seal must be capable of a greater deflection under pressure than the mating surface.

Thus, the seal contact will not be broken. This concept is shown schematically in the sketch.



Thermal expansion is a particularly important consideration at low pressures when there is insufficient load due to pressure actuation. An estimate must be made of the maximum separation that can occur due to differential thermal expansion caused by temperature gradients and differences in thermal expansion coefficients of the various materials. The seal leg must then be designed with sufficient elastic pre-deflection of the leg so that a contact load remains when the maximum separation occurs. The housing example shown on figure 9-3 illustrates the importance of this consideration.



l_b = bolt unthreaded length
= 0.375 in.

Dimension (in.)	Identification	Material	Thermal Expansion Coefficient
A = 1	Flange thickness	AM 355	6.44×10^{-6}
B = 0.75	Bolt length	304	9.6×10^{-6}
C = 0.25	Seal height and cavity height	17-7PH	5.6×10^{-6}

Figure 9-3 Housing dimensions

If the structure shown on figure 9-3 were heated uniformly to 1000°F, the following dimensional changes would occur.

Dimension	Room Temp.	1000°F	Change
A	1	1.0064	0.0064
B	0.750	0.7572	0.0072
C for seal	0.25	0.2514	0.0014
C for flange	0.25	0.2524	0.0024

Thus, there would be a total separation of $0.0072 + 0.0024 - 0.0014 = 0.0082$ in.

From this example it can be seen that close matching of the thermal expansion properties of the material is important. Also, the example illustrates a simplified method of determining the necessary initial seal predeflection. In this particular example, it would have been necessary to design the seal structure with sufficient initial predeflection so that a relaxation of 0.0082 in. would still leave the leg in a state of deflection such that the elastic reaction force would provide sufficient contact load. In most cases due to the high initial contact load required to deform the contact surface and the hysteresis effects of the seal material, the elastic reaction load of the cantilever portion of the seal will still provide adequate sealing contact load. Also the example points out the problems that could arise from differential thermal expansion. The problem of differential thermal expansion can be minimized by close matching of the thermal expansion coefficients of the materials, however, it cannot be eliminated entirely because of the presence of thermal gradients in the structure.

Some flexibility in the design of the seal structure can be attained if the requirement that the initial deflection of the

seal leg produce only elastic bending stresses is relaxed. By allowing the initial deflection to cause some plastic bending of the legs, the manufacturing tolerances on the parts need not be as strict. Even when plastic bending of the legs takes place, there will be some elastic recovery of leg. Thus the seal leg may be designed so that the elastic recovery of the leg is sufficient to provide the necessary contact load when thermal expansion takes place. Caution should be exercised when using this procedure because of the uncertainties involved in plastic deformation. The amount of elastic recovery may not be sufficient to offset the expansion of the housing due to thermal effects. Also, fracture of the leg at the point of highest bending stress may occur if excessive yielding is allowed to occur. The additional plastic leg deflection usually should not be allowed to exceed 50 per cent of the maximum elastic leg deflection.

The discussion thus far can now be summarized to establish an analytical procedure.

- A thermal and pressure-induced deflection analysis of the housing configuration will yield the maximum housing deflection. The elastic recovery of the seal leg should be greater than the largest expected housing deformation at the interface.
- Applying the contact load and deflection as input information, the seal dimensions can be determined from the nomograph charts, or from simple beam theory as described in Section 7.
- If this procedure yields large over-all seal dimensions, the contact load is too large for completely elastic beam reactions. The use of a support device is suggested.
- If a support device is used, the housing deformation may cause the leg to lose contact with the loading ring. The elastic and pressure reaction loads will then be the only loading at the interface. The minimum load required for adequate sealing after a large load has been applied to the seal surface can be determined from hysteresis data contained in Section 2. The leg deflection resulting from the maximum conditions of thermal and pressure deformation of the housing can be used as input for the nomograph design procedure. If a satisfactory design cannot be achieved, more stringent deflection limitations on the housing may be necessary.

The method of structural analysis chosen for the seal example is simple beam theory. In the range of leg length to thickness ratios envisioned, the nomographs in Section 7 cannot be employed without extending their range.

Assuming that an initial load P is applied to a uniform cantilever beam, the deflection at the free end is

$$y = \frac{1}{3} \frac{Pl^3}{EI}$$

where $\bar{I} = t^3/12 =$ moment of inertia per in. of circumference,

$E = 29 \times 10^6$ psi for 17-7PH stainless steel

$$y = \frac{4P}{E} \left(\frac{l}{t}\right)^3 \quad (9-4)$$

The bending stress

$$S_b = \frac{MC}{I}$$

where

$$C = t/2$$

$$M = Pl^2$$

$$S_b = \frac{6P}{t^2} \quad (9-5)$$

Substituting known quantities into equation (9-4), the leg length to thickness ratio is

$$\frac{l}{t} = \sqrt[3]{\frac{Ey}{4P}} = \sqrt[3]{\frac{(29 \times 10^6)(0.0015)}{4(1430)}}$$

where the important input information is

$$y = 0.0015 \text{ in.}$$

$$P = 1430 \text{ lb/in.}$$

$$\frac{l}{t} = 1.97$$

At this point, several assumptions for the leg length can be made, and the bending stress calculated as shown on Table 9-1.

Table 9-1

BENDING STRESS AS A FUNCTION OF LEG LENGTH TO THICKNESS RATIO

l (in.)	t (in.)	t^2 (in. ²)	l/t^2	σ_b (psi)
0.200	0.1015	1.03×10^{-2}	19.4	166,500
0.125	0.0888	7.9×10^{-3}	22.2	190,500
0.150	0.0761	5.79×10^{-3}	25.9	222,000
0.125	0.0635	4.03×10^{-3}	31.0	266,000

A review of Table 9-1 shows that the geometrical aspect ratio between leg length and thickness is not consistent with the maximum stress. A unwieldy shape occurs at low stress while the maximum yield strength of 17-7PH is exceeded at a more realistic ratio. The calculations also show that the entire initial load of 1430 lb per in. cannot be supported by elastic loading. Plastic bending stresses in the leg should be avoided if possible in order to retain maximum seal resilience and because the fatigue life of a part is severely limited by repeated plastic deformation.

A solution to the loading problem is obtained with the use of a support ring, as shown in figure 9-4. The height of the support ring is such that the bending of the legs are limited to elastic deformation. When the legs are in contact with the support ring, the balance of the initial load is transmitted through the support ring.

To achieve pressure energization, the seal legs must be capable of deflecting under pressure a distance greater than the total housing deflection. This is necessary so that the contact area of the seal remains in contact with the flange under the condition of maximum housing deformation. Again, simple beam theory can be used to determine the proper leg configuration.

From simple beam theory, the deflection of the free end of a cantilever beam under uniformly distributed loading is given (Ref. 9-1) by

$$y = \frac{1}{8} \frac{Pl^3}{EI}$$

where P is the total beam loading per in. of circumference.

In the case of pressure loading, the total beam load can be expressed as

$$P = lp$$

where

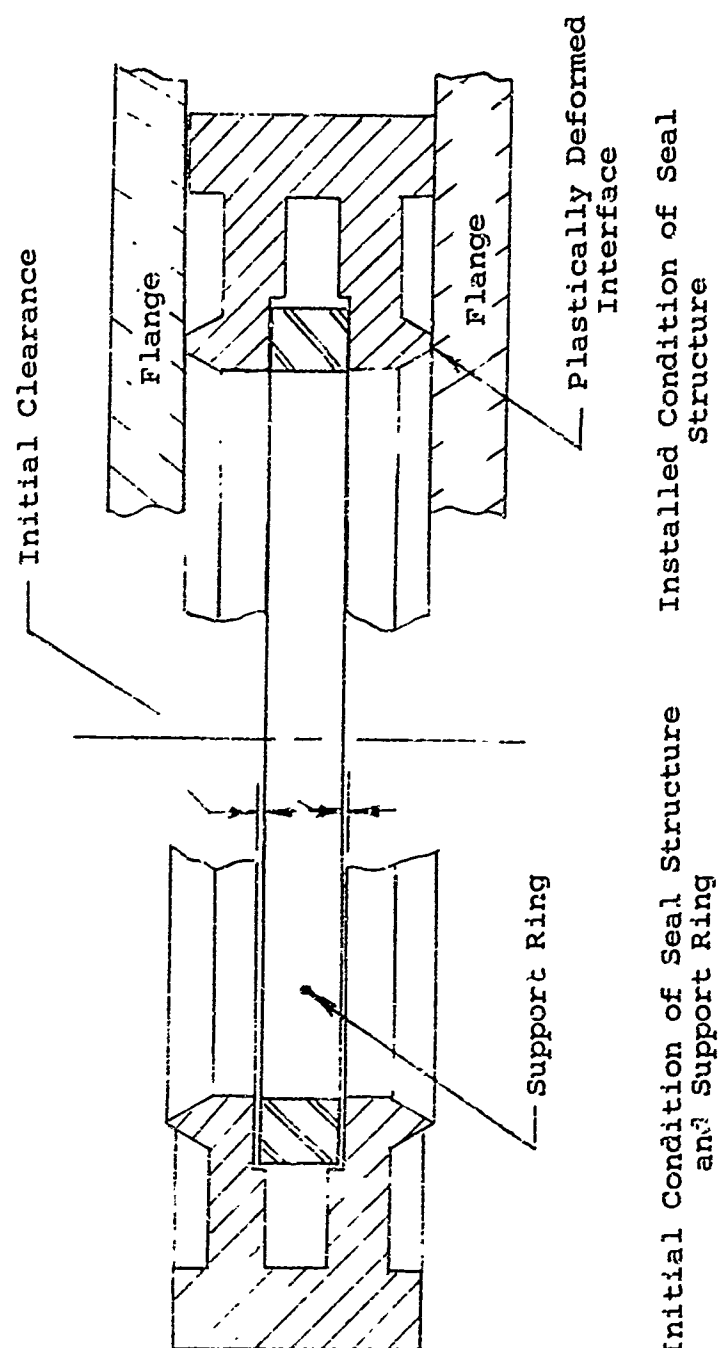


Figure 9-4 Functional aspects of the seal structure and support ring

p = fluid pressure (psi)

l = leg length (in.)

Thus, the deflection can be expressed as

$$y = \frac{3}{2} \frac{p l^4}{E t^3} \quad (9-6)$$

The total housing deflection under pressure at the seal contact point is estimated as 0.0013 in. for a fluid pressure of 2000 psi. To assure the desired flexibility under pressure, assume that each leg must deflect 0.002 in. under pressure

Thus

$$0.002 = \frac{3}{2} \frac{2000}{29 \times 10^6} \frac{l^4}{t^3}$$

and

$$t = 0.372 l^{4/3} \quad (9-7)$$

The bending stress at the fixed end of the leg for this case can be calculated from the relation (Ref. 9-1)

$$M = \frac{1}{8} P l = \frac{1}{8} p l^2$$

where

$$P = p l$$

Bending stress is given as

$$S_b = \frac{M C}{I} = 0.75 P \left(\frac{l}{t} \right)^2 \quad (9-8)$$

Several arbitrary values of length can be chosen and the deflection and bending stress calculated as shown on Table 9-2.

Table 9-2

BENDING STRESS DUE TO FLUID PRESSURE AS A FUNCTION OF
LEG LENGTH TO THICKNESS RATIO

$l(\text{in.})$	$l^{4/3}$	$t(\text{in.})$	(l/t)	$(l/t)^2$	σ_b at 2000 psi
0.200	0.117	0.0435	4.60	21.2	31,600
0.175	0.0968	0.0360	4.86	23.6	35,400
0.150	0.0796	0.0296	5.06	25.6	38,400
0.125	0.0624	0.0232	5.39	29.0	43,500

The bending stresses for any of these leg configurations are acceptable. Under actual operating conditions, the bending stress due to the applied pressure will tend to counteract the initial bending stress due to the predeflection of the seal leg. The additional load at the interface resulting from the fluid pressure is given as

$$R = \frac{3}{8} P$$

where R = reaction load due to fluid pressure per in. of circumference.

Assume

$$l = 0.175 \text{ in.}$$

$$D = 2 \text{ in.}$$

$$p = 2000 \text{ psi}$$

Then

$$R = 131 \text{ lb/in.}$$

Any of the l/t ratios in Table 9-2 meet the pressure deflection requirements. Since an initial predeflection of 0.0015 in. per leg accounts for thermal and pressure deflection of the housing, the leg configuration must now be checked for initial bending stresses. This can be done with the simple beam relationship

$$y = \frac{Pl^2}{3EI} = \frac{4P}{E} \left(\frac{l}{t}\right)^3$$

Since y is known, the bending load at the free end of the leg P can be calculated and the bending stress can also be calculated.

$$s_b = \frac{MC}{I} = \frac{6P}{t^2}$$

The bending stress due to a leg deflection of 0.0015 in. is shown on Table 9-3 as a function of arbitrarily chosen leg lengths.

Table 9-3

BENDING STRESS DUE TO A DEFLECTION OF 0.0015 IN. AS A
FUNCTION OF LEG LENGTH TO THICKNESS RATIO

(in.)	t(in.)	(l/t)	(l/t) ²	(l/t) ³	t ² (in. ²)	l/t ²	F(lb/in.)	S _b (psi)
0.2000	0.0435	4.60	21.2	97.6	18.9x10 ⁻⁴	105	111.5	71,000
0.1750	0.0360	4.86	23.6	114.8	12.9x10 ⁻⁴	136	95	77,500
0.1500	0.0296	5.06	25.6	129.5	8.76x10 ⁻⁴	170	84	86,000
0.125	0.0232	5.39	29.0	156.5	5.38x10 ⁻⁴	224	69.6	93,600

Where thermal expansion takes place, the flange movement will tend to reduce the contact load caused by initial plastic deformation of the seal wedge. The only remaining contact load will be that due to the elastic bending force of the beam. The elastic bending stress shown in Table 9-3 is quite low at the maximum predeflection of the leg. To increase the elastic reaction force, the leg must be made stiffer. At this point a reasonable arbitrary leg configuration can be chosen using these values as guidelines.

Assume:

$$l = 0.175 \text{ in.}$$

$$t = 0.055 \text{ in.}$$

The bending stress, elastic bending load, and pressure deflection must now be rechecked.

Elastic Bending Load for $y = 0.0015$ in.:

$$P = \frac{Ey}{4(l/t)^3} = \frac{(29 \times 10^6)(0.0015)}{4\left(\frac{0.175}{0.055}\right)^3} = 339 \text{ lb/in.}$$

Bending Stress:

$$S_b = 6P (l/t^2) = (6)(339)(0.175/0.00303) \\ = 117,500 \text{ psi}$$

Pressure Deflection at 2000 psi:

$$y = \frac{3 p l^4}{2 E t^3} = \frac{(3)(2000)(0.175)^4}{(2)(29 \times 10^6)(0.055)^3} \\ = 0.000581 \text{ in.}$$

The total housing deflection from both pressure and thermal expansion is estimated to be 0.0016 in. If the seal is subjected to an initial deflection of 0.0015 in. per leg, an equivalent preload of 0.0007 in. per leg will remain for a total equivalent of 0.0014 in.

The remaining elastic bending load is given

$$P = \frac{E y}{4} \left(\frac{t}{l} \right)^3 = 158 \text{ lb/in.}$$

This load plus the contact load due to the effects of fluid pressure may marginally provide an adequate interface load under the conditions of maximum temperature and pressure.

The seal leg configuration has now been completely determined.

The initial height of the wedge and the axial wedge deformation required to give the proper contact width must now be determined. It is assumed that geometrically similar wedges will deform plastically in a similar manner. A interface deflection to width ratio of 0.65 is an experimental approximation for a 60 deg wedge obtained by combining data on figures 2-8 and 2-12. The total initial axial deformation of two wedges in the seal housing is $2 \times 0.65 \times 0.012 \approx 0.016$ in. The wedge shape and size have now been determined.

Next to be considered is the radial or hoop rigidity of the seal structure. The radial deflection must be held to a minimum to minimize relative motion at the interface. The hoop stress in the web can be approximated by:

$$S_H = \frac{PD_w}{2t_w}$$

where

S_H = hoop stress (psi)

D_w = web ID (in.)

t_w = web thickness (in.)

P = fluid pressure (in.)

The web ID is given by

$$D_w = D + 2$$

Thus,

$$D_w = 2.00 + (2)(0.175) = 2.350$$

The circumferential web elongation is given by

$$\delta_c = \frac{S_H L_w}{E}$$

where

t_w = web circumference

$$\approx \pi D_w$$

The diametral elongation is given by

$$\delta_D = \frac{1}{\pi} \delta_c$$

The criterion that the web thickness be not less than the leg thickness may be used as a first approximation in the web design.

Assume a web thickness,

$$t_w = 0.060 \text{ in.}$$

The hoop stress at 2000 psi is

$$S_H = \frac{(2000)(2.35)}{(2)(0.060)} = 39,200 \text{ psi}$$

The circumferential elongation,

$$\delta_c = \frac{39,200 \pi (2.35)}{(29.0 \times 10^6)} = 0.010$$

$$\delta_o = \frac{\delta_c}{\pi} = 0.0318$$

This value of δ_D is greater than 25 per cent of the interface width. Increasing the web thickness will decrease the elongation.

Then, let

$$t_w = 0.120 \text{ in.}$$

Therefore,

$$\delta_D = 0.00159 \text{ in.}$$

At this point all of the important seal dimensions have been established, viz;

seal leg ID	2.000 in.
seal leg thickness	0.055 in.
seal leg length	0.175 in.
initial leg deflection	0.0015 in.
wedge profile angle	60 deg
wedge axial deformation	0.016 in.
web ID	2.350 in.
web thickness	0.120 in.

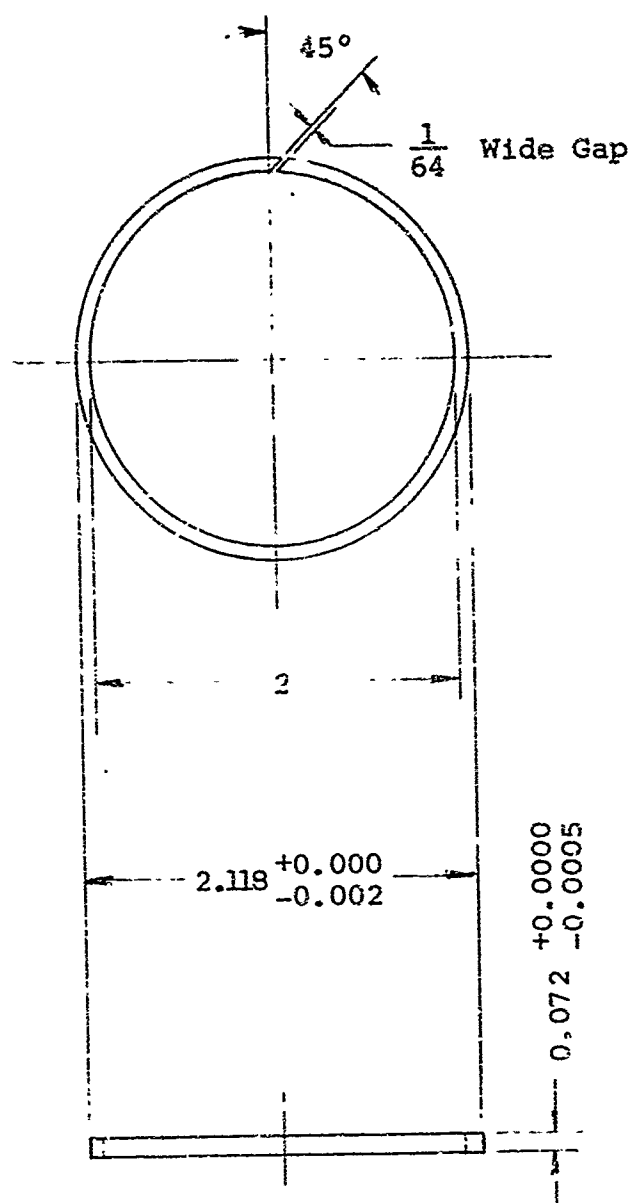
The support ring can be a simple gap cut ring. The ring thickness is critical since the clearance between the ring and the legs of the seal will determine the initial leg deflection. Heat treatment of the support ring is necessary to increase its tensile yield strength if a high strength alloy is not used. This is necessary so that when the ring is contracted on installation into the seal, it will spring back to its original shape. The prototype seal and support ring based on these design requirements are shown on figures 9-5 and 9-6.

The increase in leakage associated with a corresponding decrease in interface stress is defined as a hysteresis effect. This topic was discussed in Reference 9-2 and Section 2.

In Subsection 9.4, the minimum elastic bending load at a maximum temperature and pressure was given as 158 lb per in. This is approximately 11 per cent of the maximum initial load imposed. From experimental observations, it is felt that this load reduction is a borderline case. Thus, it may be expected that leakage may substantially increase at elevated temperature and pressure. No criteria are available to predict this increase in leakage.

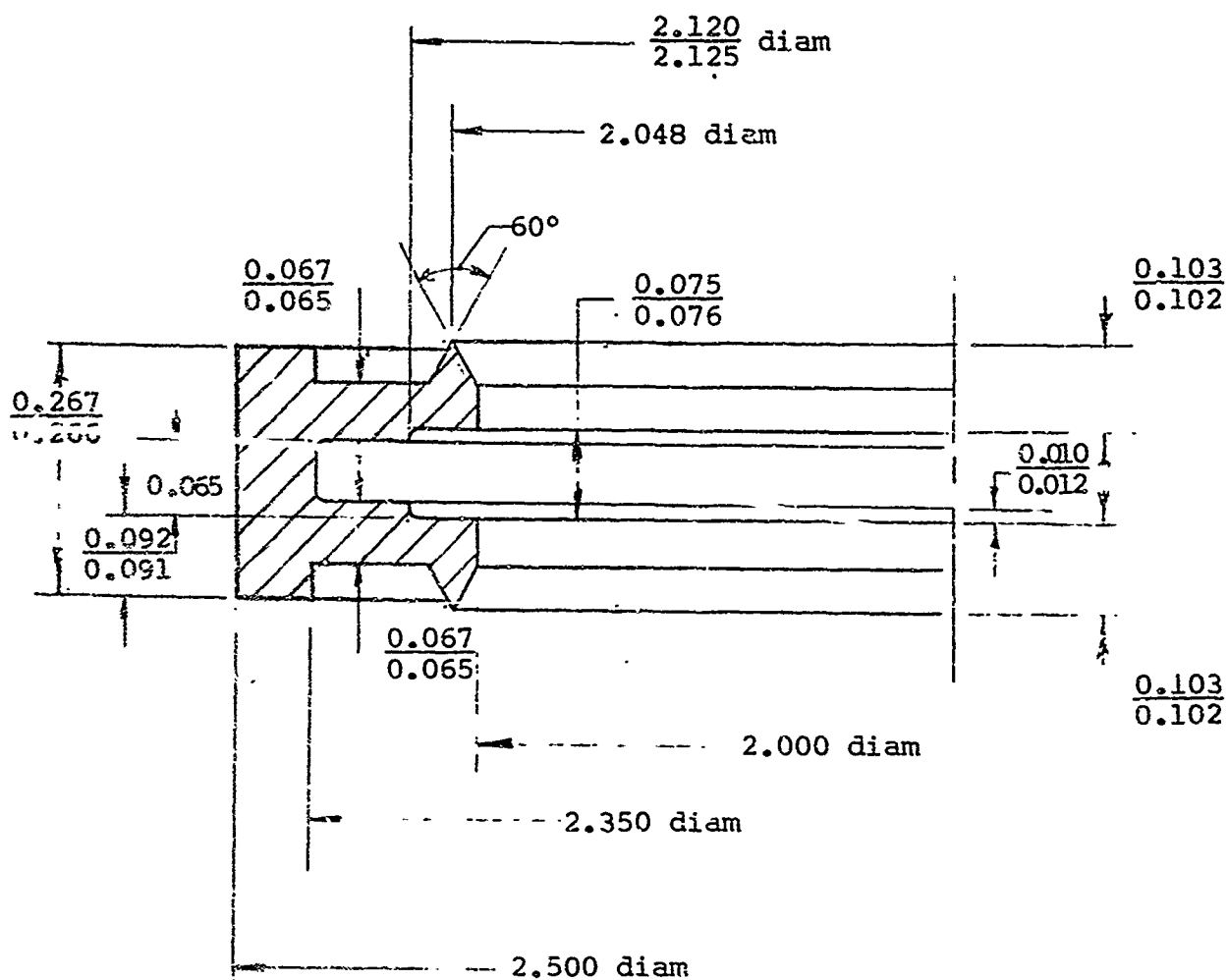
9.5 Experimental Evaluation

The IITRI wedge seal is composed of two parts: the main structure (figure 9-5) and an interface support ring (figure 9-6). Six of these seals were fabricated for the purpose of experimental evaluation whereby the results of Subsection 9.1 through 9.4 can be verified. The principal verification



Material 1090 or 1095 Stl.

Figure 9-5 Support ring



Material 17-7PH

All decimal dimensions ± 0.005 unless otherwise specified

Figure 9-6 IITRI wedge seal

experiments pertain to the structural deformation and leakage of the seal under the environmental conditions stated in Subsection 9.1.

9.5.1 Structural Deformation Experiments

The procedures and apparatus employed in the structural deformation experiments are discussed in Appendix IV. Essentially, the experiment consists of measuring the axial deformation as a function of applied load. In the wedge seal, two important deformations are the plastic deformation of the interface and the elastic deformation of the structure.

Before proceeding, it must be pointed out that the performance predictions in Subsection 9.4 were based on material properties given in handbook. The actual properties materials differed considerably. The difference has an important effect on the seal performance. To show the effect, corrected calculations are presented in this report and the reader is invited to compare them with the results in Section 9.2.1. The new material hardness considered are:

	<u>Actual</u>	<u>Assumed</u>
AM 355 Housing Material	Brinell 433 (Rc 46)	540,000*psi (Rc 53)
17-7PH Seal Structure Material	352,000 psi* (Brinell 242)	238,000 psi* (Brinell 168)

An objective in the design of the seal was to obtain a 0.012 in. width of interface contact. The original estimated interface load was determined as $P = 1430$ lb per inch of seal circumference. Applying the actual hardness of the 17-7PH material, a revised loading is obtained from equation (9-2)

$$P = 0.006\sigma_m$$

$$P = 0.006 \times 352,000 = 2120 \text{ lb per in.}$$

*Meyer Hardness

A comparison of this result with experimental data, shown on figure 9-7, indicates a close correlation. Additionally, the experimental load-deflection characteristics, shown on figure 9-8 correlate with the theoretical prediction in that the axial deflection is approximately one-half the interface width.

9.5.2 Leakage Experiments

The wedge seals were installed in the evaluation apparatus described in Appendix VII. The mating interface surfaces were ground and lapped to an average roughness of $7\mu\text{in. PTV}$.

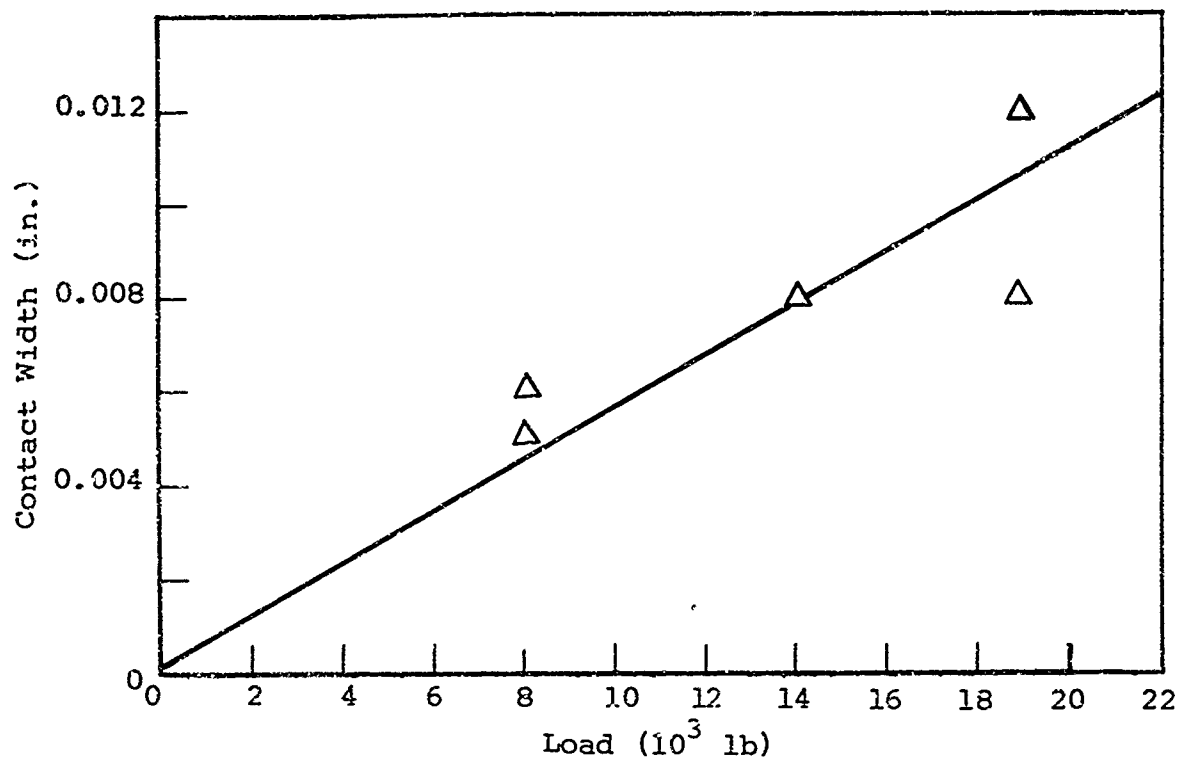


Figure 9-7 Contact width as a function of load IITRI wedge seal 3

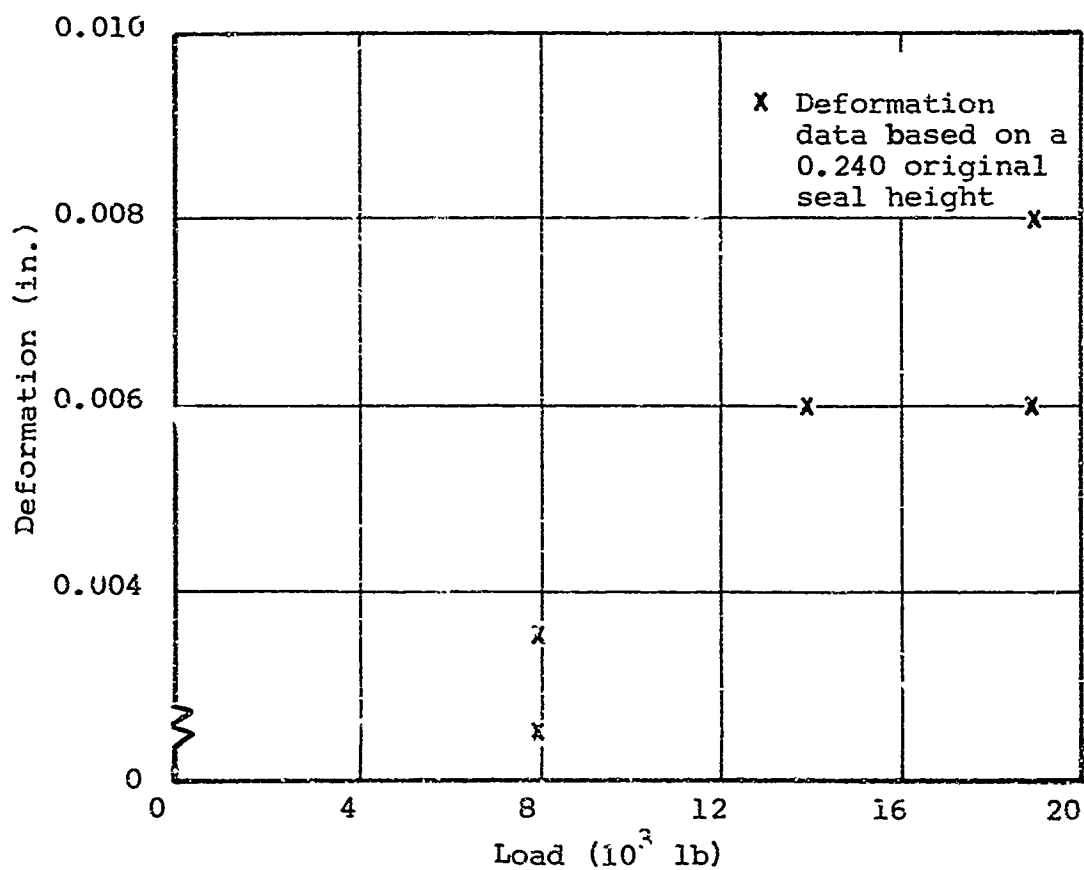


Figure 9-8 Load deformation data, IITRI wedge seal 3

Two of the seals were subjected to leakage performance evaluation under conditions of varying fluid pressure and temperature. The relatively large mass of the evaluation apparatus prevented rapid changes in temperature. However, the apparatus did impose large thermal gradients because of its size. The effects of the thermal gradients are probably more severe than the time rate of temperature variation.

During the heating cycle, hot gas from an oxyacetylene flame was circulated through the heating coils. A large thermal gradient occurred between the bottom of the test chamber and the seal cavity. When the seal cavity was at a temperature of 760°F, the bottom of the test chamber was 1480°F. For safety purposes the chamber was not heated beyond 1500°F. Thus, the maximum seal cavity and interface temperature was limited to ~700 to 770°F.

Cooling of the seal area was achieved by immersing the lower half of the apparatus in liquid nitrogen. Again, the rate of temperature change was slow.

A comparison of the predicted and experimental leakage rates can be made without further corrections for material properties. The conductance at maximum deformation is assumed to be $(h^3) = 10^{-22} \text{ in}^3$. Consequently, the leakage predictions of Subsection 9.2.3 are still valid. A comparison of results is shown on Table 9-4.

Table 9-4

ACTUAL AND PREDICTED LEAKAGE RATES OF HELIUM FOR THE
IITRI WEDGE SEAL

Pressure (psia)	80°F		-205°F		720°F	
	$Q_{\text{theo.}}$ (cc/sec, STP)	$Q_{\text{act.}}$ (cc/sec, STP)	$Q_{\text{theo.}}$ (cc/sec, STP)	$Q_{\text{act.}}$ (cc/sec, STP)	$Q_{\text{theo.}}$ (cc/sec, STP)	$Q_{\text{act.}}$ (cc/sec, STP)
114.7	3.01×10^{-6}	5.62×10^{-6}	5.01×10^{-6}	-----	1.69×10^{-6}	-----
214.7	6.01×10^{-6}	-----	1×10^{-5}	2.35×10^{-5}	3.38×10^{-6}	1.87×10^{-6}
514.7	1.54×10^{-5}	2.34×10^{-4}	2.56×10^{-5}	1.37×10^{-4}	8.66×10^{-6}	1.09×10^{-5}
1014.7	3.26×10^{-5}	5.93×10^{-4}	5.43×10^{-5}	7.15×10^{-4}	1.93×10^{-5}	8.12×10^{-5}
1514.7	5.07×10^{-5}	8.43×10^{-4}	8.45×10^{-5}	-----	2.35×10^{-5}	1.07×10^{-3}
2014.7	7.05×10^{-5}	-----	1.17×10^{-4}	-----	3.97×10^{-5}	3.49×10^{-3}

The leakage results on Table 9-4 show a good correlation between actual and predicted leakage rates within the range of criteria applicability. At this point a detailed discussion of the seal performance will further demonstrate the applicability of the design criteria.

Figure 9-9 shows leakage results at room temperature for IITRI Seal 5. The actual measurements are within the expected deviation of the predictions (one order of magnitude). When heated, the seal showed a rapid increase in leakage at 200 psi. This is shown in figure 9-10. This behavior is attributed to the fact that the seal cover plate was bolted to the test chamber with 304 stainless steel bolts. Type 304 stainless steel has a thermal expansion of 0.65 per cent at 700°F. The thermal expansion of the seal structure (17-7PH) at 700°F is also 0.65 per cent at 700°F.

From the bolt length and seal height dimensions given

$$L_b = 0.375 \text{ in. bolt length}$$

$$C = 0.25 \quad \text{seal height,}$$

the thermal expansion at the parts at 700°F is estimated to be

$$\text{Bolt expansion} = 0.0065 \times 0.375 = 0.00244 \text{ in.}$$

$$\text{Seal expansion} = 0.0065 \times 0.25 = 0.00162 \text{ in.}$$

The difference in thermal expansion is 0.00082 in. There could be even a greater differential thermal expansion which would be caused by temperature gradients within the housing structure. It is quite likely that the bolts may be at a higher temperature than the seal. The test chamber is heated from the outside by the hot gas flowing in the coils. Thus, the heat flow path through the housing into the bolts causes the bolts to be at a higher temperature than the seal cavity. The thermal expansion may be sufficient to offset the initial deflection of the seal legs. Coupled with a pressure deflection of the housing cover and bolts, a substantial reduction in contact loading can occur, resulting in higher leakage rates. If complete separation of the contact surfaces occurred, the leakage rate would be disastrously high.

Leakage past Seal 1 is shown on figure 9-11. It may be observed that most of the leakage rates were within or close to the expected leakage rate range over the entire temperature range. This seal was evaluated under exactly the same conditions as Seal 5. However, the bolts on the cover were replaced by plain carbon steel bolts having a thermal expansion of 0.46 per cent at 700°F. This represents a substantial improvement in the thermal expansion problem. As the temperature increases, the bolts will expand less than the seal. Thus, a positive contact stress will always be present at the seal contact area. If the seal expansion is greater than that of the bolts, the seal contact stress will increase, resulting in a decrease in leakage with increasing temperature as shown on figure 9-12.

The shape of the curve in figure 9-12 can be attributed to the unsteady heat transfer situation. Since the assembly is heated from the outside, the bolts heat up first and begin to expand.

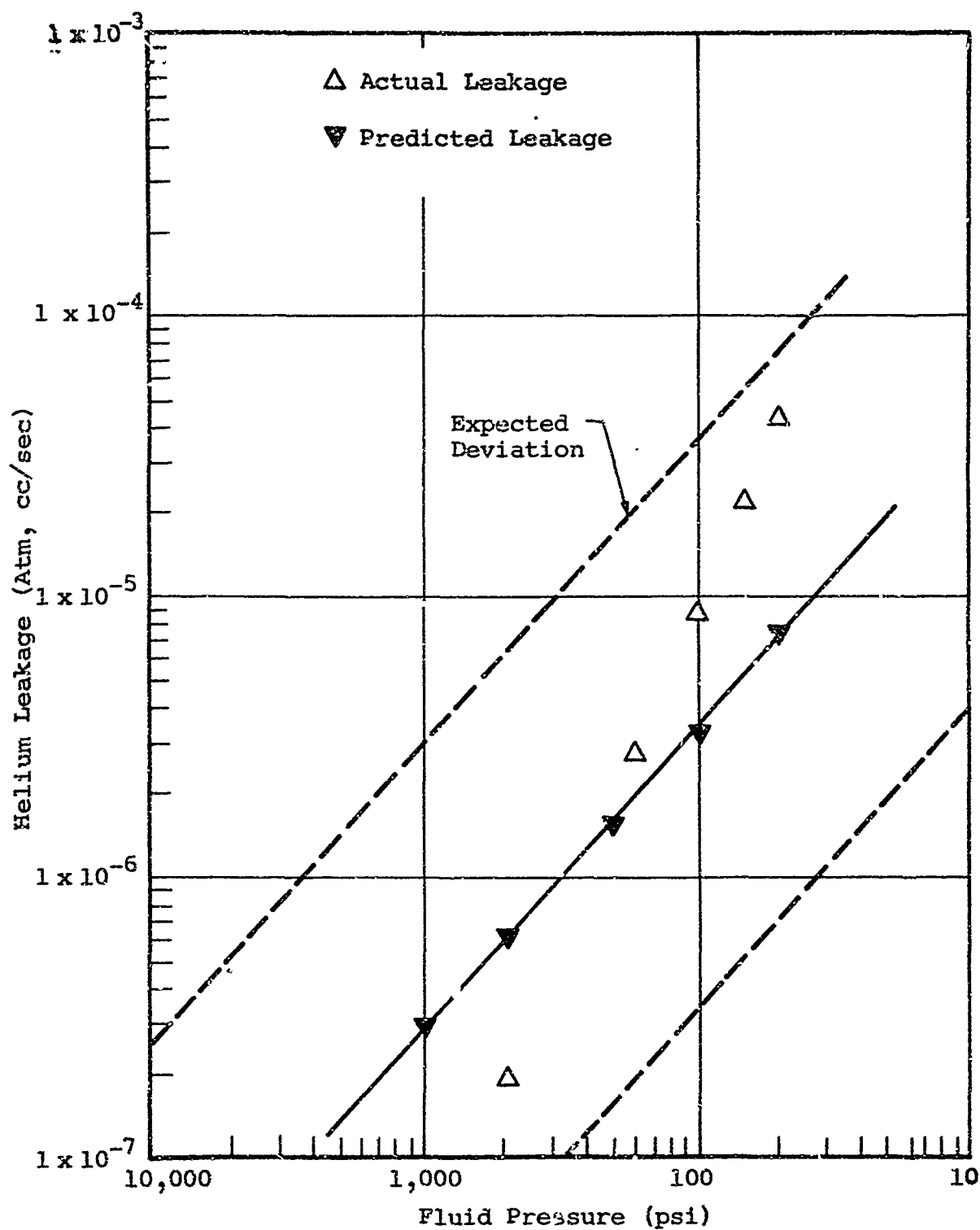


Figure 9-9 Helium leakage at 80°F for IITRI wedge seal 5

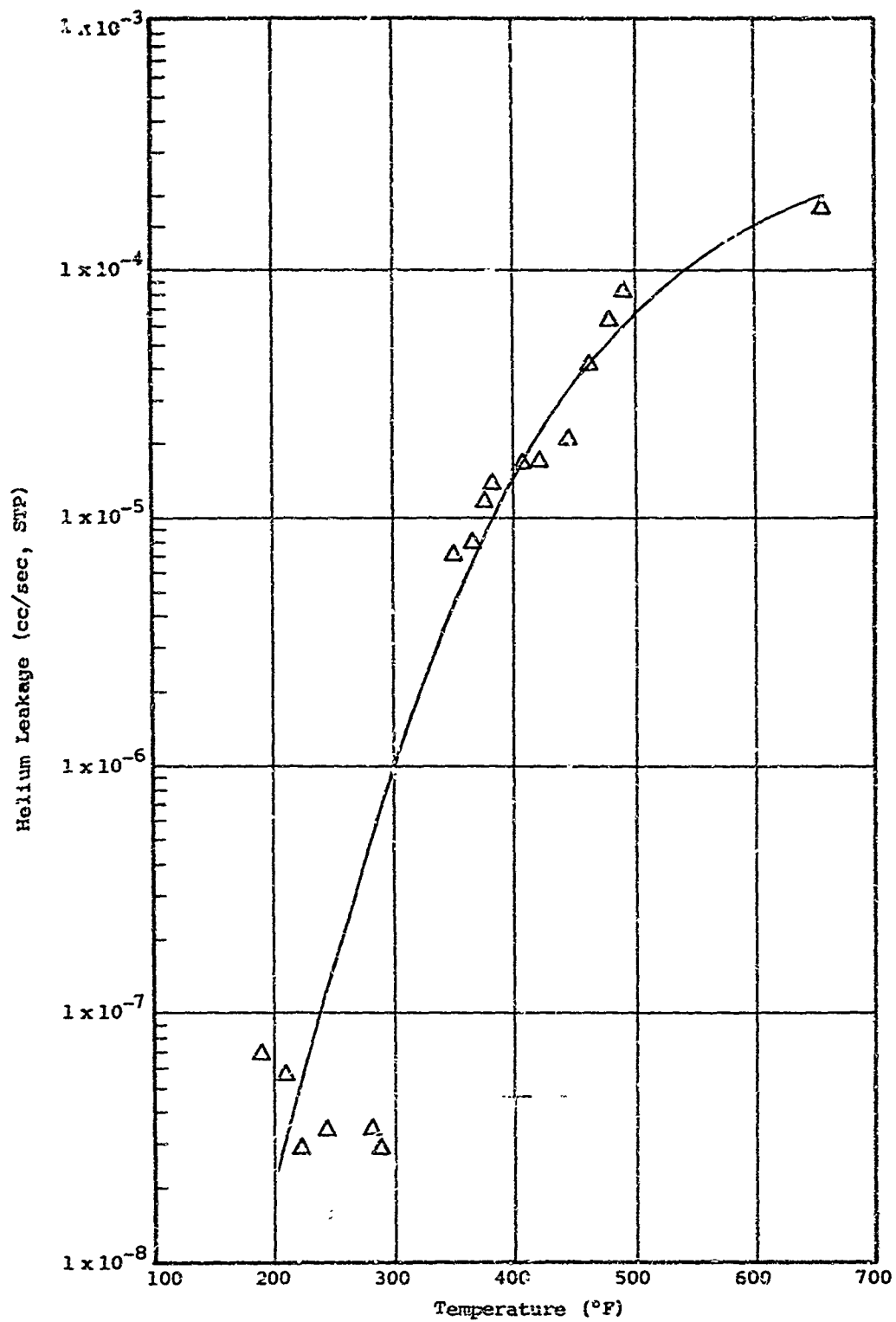


Figure 9-10 Helium leakage versus gas temperature at 200 psi
IITRI wedge seal 5
Total elapsed time during temperature rise = 140 min

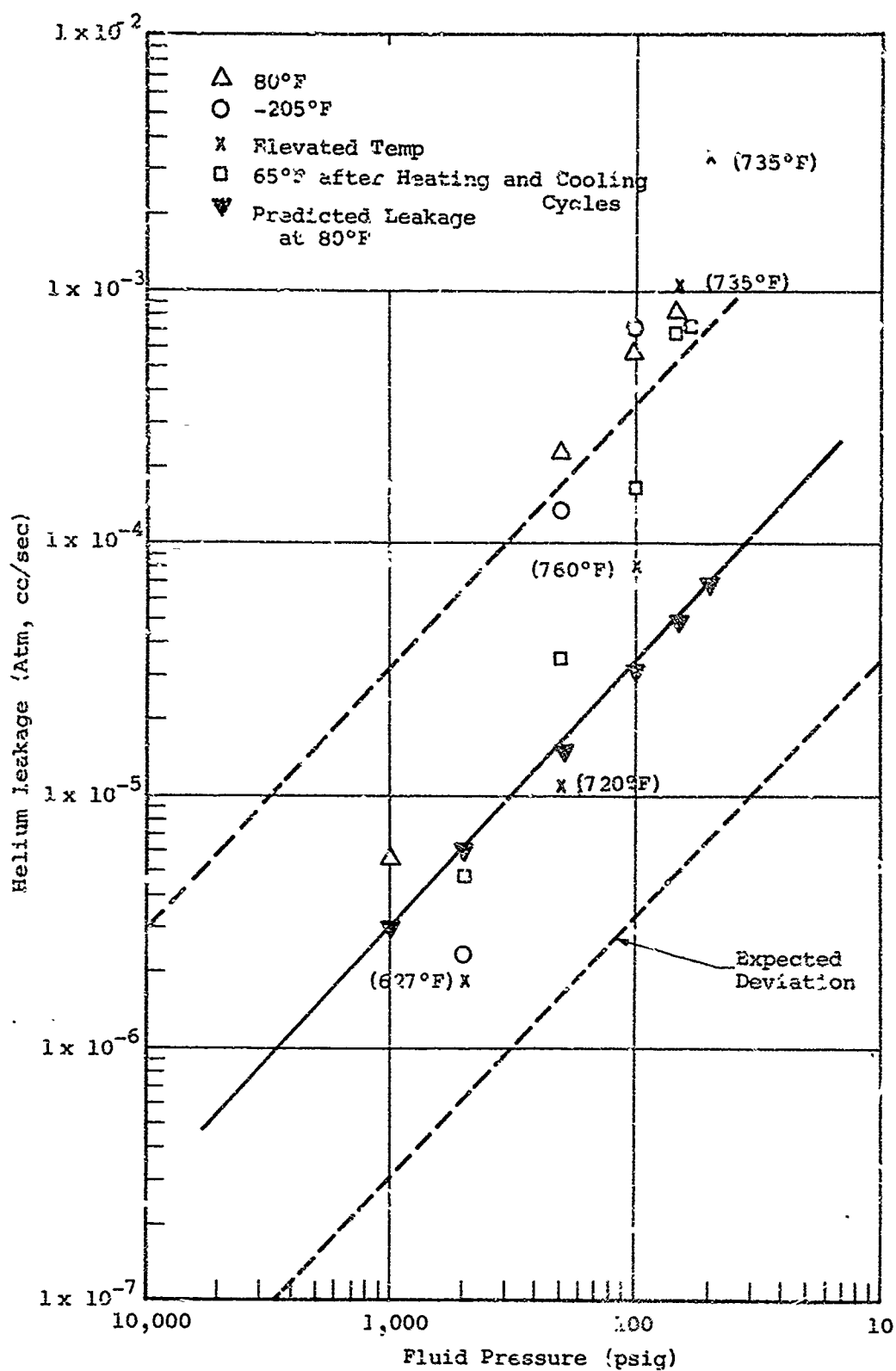


Figure 9-11 Helium leakage as a function of pressure
at various temperatures IITRI wedge seal 1

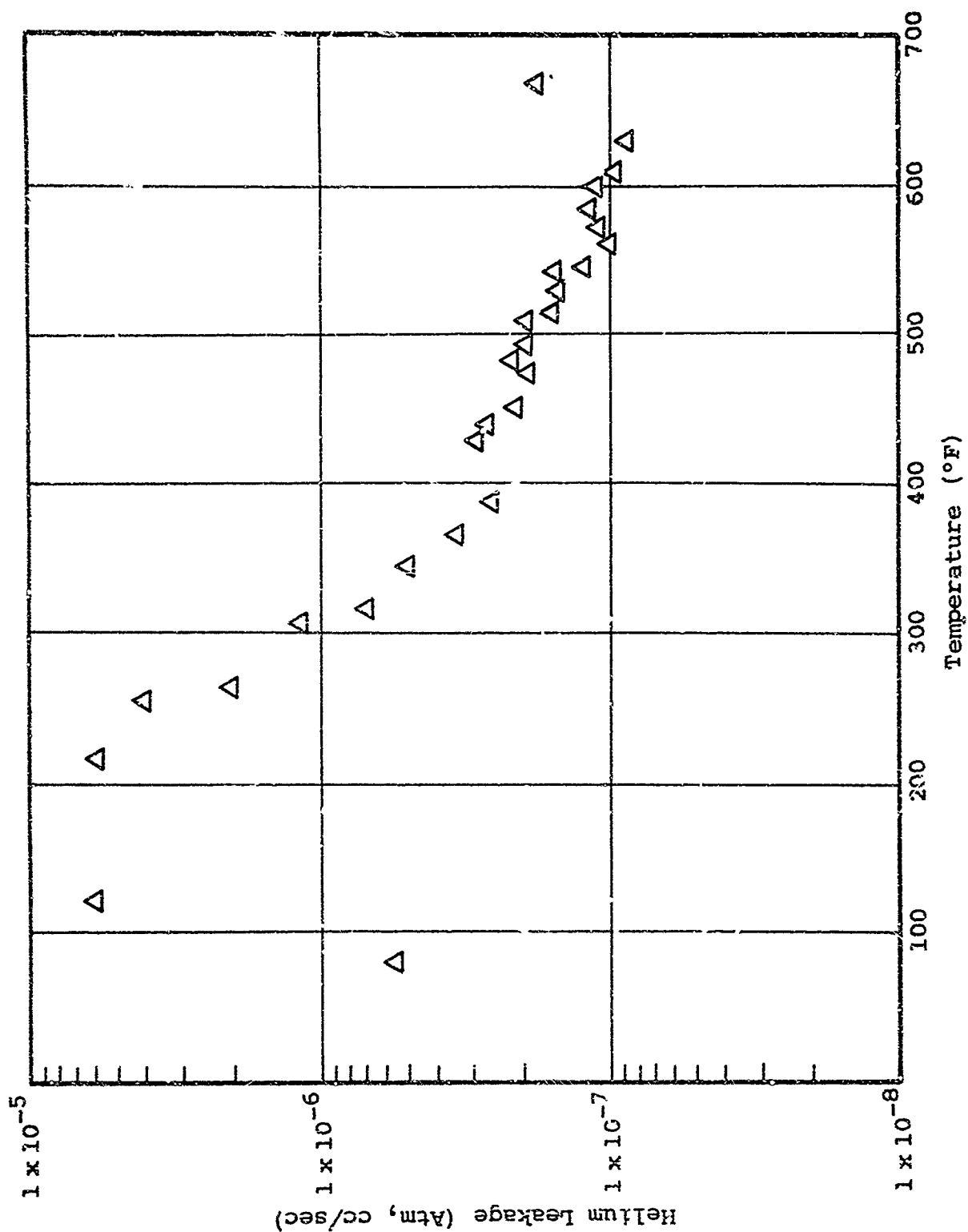


Figure 9-12 Helium leakage as a function of gas temperature at 200 psi
 IITRI wedge seal 1
 Total elapsed time during heating: 6 hr

As heat flows into the test chamber, the seal cavity heats up. Since the thermal expansion coefficient is greater for the seal material than for the bolts, the expansion of the seal begins to equal and possibly exceed that of the bolts. This tends to maintain a steady or increasing contact stress at the seal contact area. The result is a steady or decreasing leakage rate with increased temperature. Thus, the leakage rates are determined by the nature of the unsteady heat flow as well as the thermal properties of the materials.

The low temperature behavior of Seal 1 is shown on figure 9-13. The practically constant leakage rate shown on the curve indicates good matching of the thermal properties of the materials. Since the chamber is cooled from the outside, the thermal gradient also assists in maintaining contact load because the bolts shrink at a faster rate than the seal. Thus, a positive contact stress will be maintained on the seal interface.

An important observation can be made regarding the critical nature of the relationship between the thermal deformation properties of the materials. The magnitude of the thermal expansion of the various parts of the seal assembly can mean the difference between the success or failure of a seal design under conditions of varying temperature. The thermal expansion coefficients of the materials at the expected operating temperatures should be as close as possible depending upon gradient effects. Also, the differences in thermal expansion properties of the materials may be offset by proper sizing of the components. For example, if the bolt thermal expansion coefficient is greater than that of the seal or flange material, the differential thermal expansion may be minimized by keeping the bolt free length as small as possible. Another possibility for overcoming the problems of differential thermal expansion in the IITRI Wedge Seal is to replace the support ring with a ring that fits extremely closely at room temperature but has a significantly greater thermal expansion coefficient than the seal material. Thus, as the temperature increases, the center ring will tend to expand faster than the seal material. If the ring expansion is matched properly with the seal cavity, and/or bolt expansion at the proper contact, stress can be maintained at the seal contact area.

9.6 References

- 9.1 E. C. Rodabaugh, Developmental Mechanical Fittings, Phases I and II, RTD-TDR-63-1115, AF04(611)-8176 Battelle Memorial Institute (Dec. 1963)

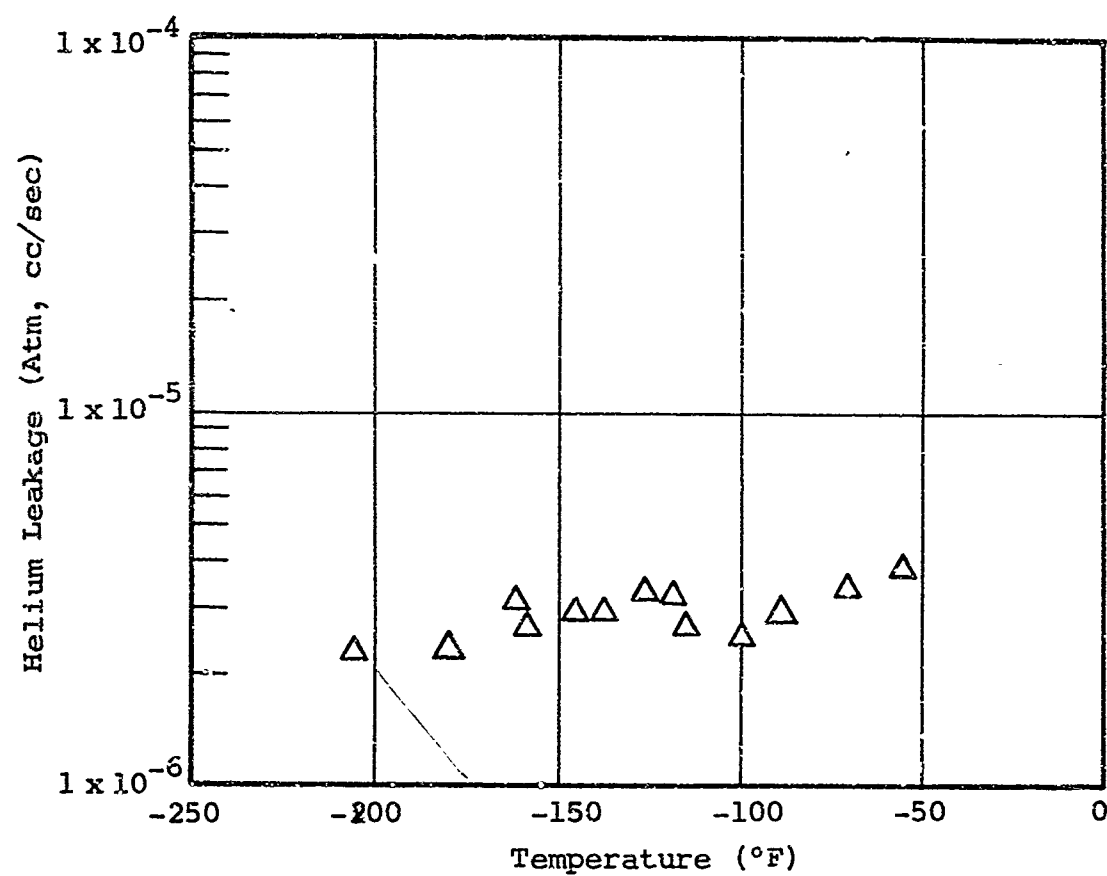


Figure 9-13 Helium leakage as a function of gas temperature
at 200 psi

IITRI wedge seal 1

Total elapsed time during cooling: 5 hr

10. ANALYTICAL PREDICTION AND EXPERIMENTAL VERIFICATION OF LEAKAGE PERFORMANCE ON ADDITIONAL SEALS

A comprehensive analysis of a static seal was developed in Section 9 as a general outline for the systems designer. Following the same outline other seals, wherein modifications in the analysis are required because of the complexity of the seal or simplifications in the approach, are considered. The seals considered are generally commercially available items. Thus, most of the input information, such as geometry, applied loads, and material, is predetermined with leakage performance as the only unknown factor. This differs from the analysis in Section 9 in that leakage was an input condition and the seal was designed to meet this requirement.

In this presentation, the seal structure is first analyzed to determine the interface loading, using as an input the environmental and housing deformation effects utilized in the experimental verification phase. The next step is to predict the leakage rate by applying the interface criteria contained in Sections 2 and 3. Following these theoretical predictions, experimental results are compared to show the success achieved. The following outline identifies the seals evaluated and the location of the pertinent discussion.

<u>Seal Type</u>	<u>Seal Description</u>	<u>Section</u>
Static	Navan Naflex - Teflon coated	10.1
Static	Cook Airtomic - Metallic	10.2
Static	Wiggins - Metallic	10.3
	Haskel - Metallic	10.3
	Hydrodyne - Metallic	10.3
	United Aircraft - Metallic	10.3
	Pressure Science - Metallic	10.3
Sliding	IITRI Lip-Type - Metallic	10.4

10.1 Navan* Naflex Seal

10.1.1 Description

A 2-in. nominal diameter Naflex groove flange seal was composed of a 4340 steel structure covered with a 0.004-in. coating of Teflon. The geometry of the metallic structure is shown in figure 10-1. The manufacturer's identification of this seal is VD261-0030-0036, and it was recommended for the following applications:

Temperature: -425 to 300° F

Pressure: 5000 psi

Fluid: Liquid oxygen, nitrogen, hydrogen, air;
gaseous oxygen, nitrogen, hydrogen,
helium, air; water and corrosive liquids.

The seal was assumed to be installed in a cavity having a depth of 0.148 in. as recommended by the manufacturer. From the free dimensional height of the seal, as shown in figure 10-1, the initial axial seal deformation is 0.1697 - 0.1480 in. or approximately 0.022 in., neglecting any effects of the Teflon coating.

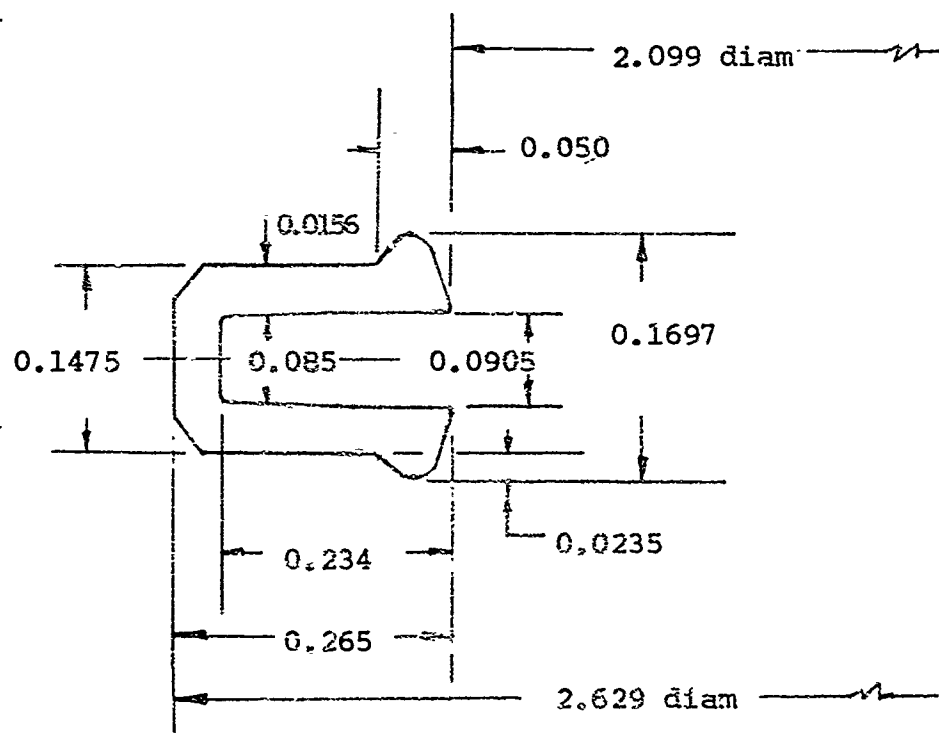


Figure 10-1 Two-inch diameter Navan seal
(Part No. VD261-0030-0036)

*Marketing subsidiary of North American Aviation, Incorporated.

10.1.2 Structural Analysis

The deformation of the seal structure is assumed to be elastic and the influence of the Teflon coating is neglected. The analysis is accomplished using the nomographic approach described in Section 7. The nomenclature is identical and the reader should refer to the step-by-step procedures.

From figure 10-1

$$L = 0.1425 \text{ in.}$$

$$l = 0.234$$

$$2H_F = 0.1697$$

$$\text{Groove depth} = 0.148$$

$$2h = 0.1475 - 0.0850 = 0.0625$$

$$h = 0.0312 \text{ in.}$$

Then

$$\frac{l}{h} = \frac{0.234}{0.0312} = 7.5$$

The initial deflection is given by

$$2Y_e = 2H_F - 0.148$$

$$2Y_e = 0.1697 - 0.148 = 0.0217$$

$$Y_e = 0.0108 \text{ in.}$$

Since all the geometric properties of the seal are known, figure 7-11 of Section 7 can be used to determine the contact load.

First calculate the deflection parameter

$$\frac{Y_e E}{1-\nu^2}$$

where

$$E = 30 \times 10^6$$

$$\nu = \text{Poisson's Ratio} = 0.3$$

$$\text{Deflection parameter} = \frac{(0.0108) (30) (10^6)}{1 - 0.3^2} = 35.6 \times 10^4$$

The contact load per unit circumference can be determined from figure 7-12 by dividing the deflection parameter by the known (l/h) ratio. This operation, shown by the solid line on the nomograph, yields a load:

$$R_s = 210 \text{ lb/in. of circumference}$$

The advertised average contact load is 150 lb/in. of circumference.

10.1.3 Experimental Verification of the Structural Analysis

The results of the load-deflection experiment performance on a Teflon-coated seal are shown in figure 10-2. The maximum load applied at the maximum deflection of 0.020 in. is 1525 lb. Thus, the reaction on contact load per inch of interface contact is given as

$$R_s = \frac{1525}{\pi_3 D_i} = 242 \text{ lb/in.}$$

where

$$D_i \approx 2.0 \text{ in.}$$

This value is in fair agreement with the theoretical contact load of 210 lb per in. predicted in the design analysis. The straight-line loading curve indicates that most of the deflection of the seal legs is an elastic process. This is further substantiated by the fact that only 0.005 in. permanent set was exhibited by the seal after complete release of the load. Part of this is attributed to plastic deformation of the Teflon coating. The preceding results are in close agreement with the manufacturer's literature shown on figure 10-3 and the theoretical analysis.

10.1.4 Interface Contact Area

Teflon is fairly deformable under compression. However, because of the spherical interface contact surface it is difficult to estimate the contact area that will result from plastic flow of the Teflon under the compressed contact load.

The design curves of Section 2 show that for unconfined materials the corrected stress ratio approaches asymptotically a value less than 0.4. This means that as the load increases, the material flows plastically until the apparent contact area

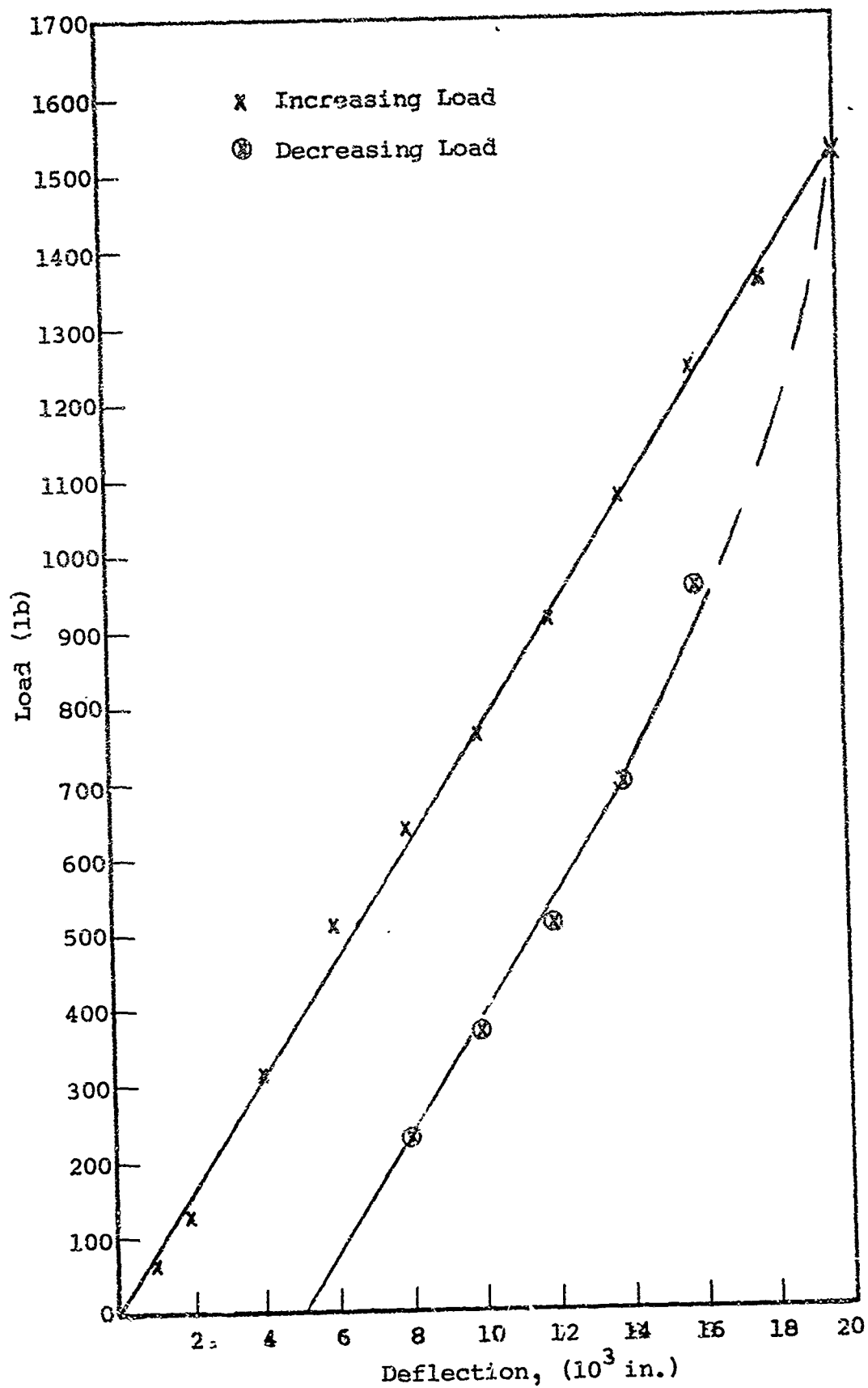


Figure 10-2 Load deflection characteristics of a Naflex seal

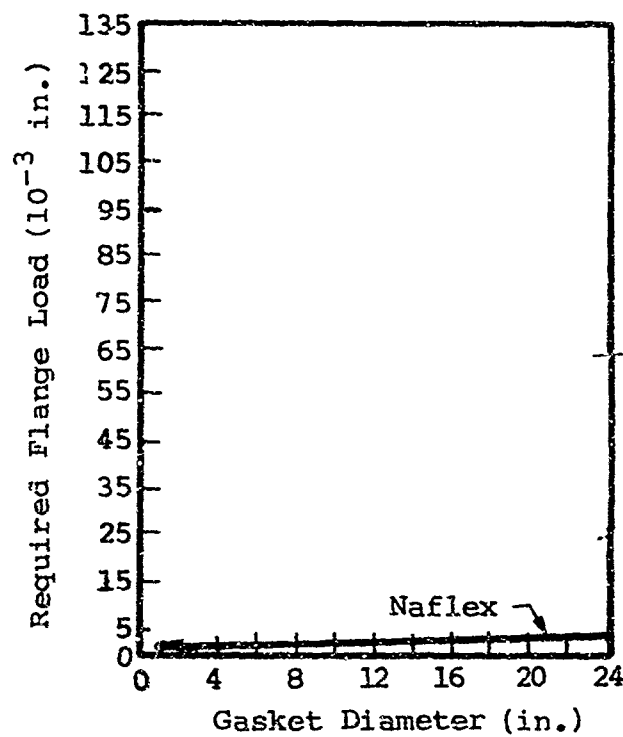
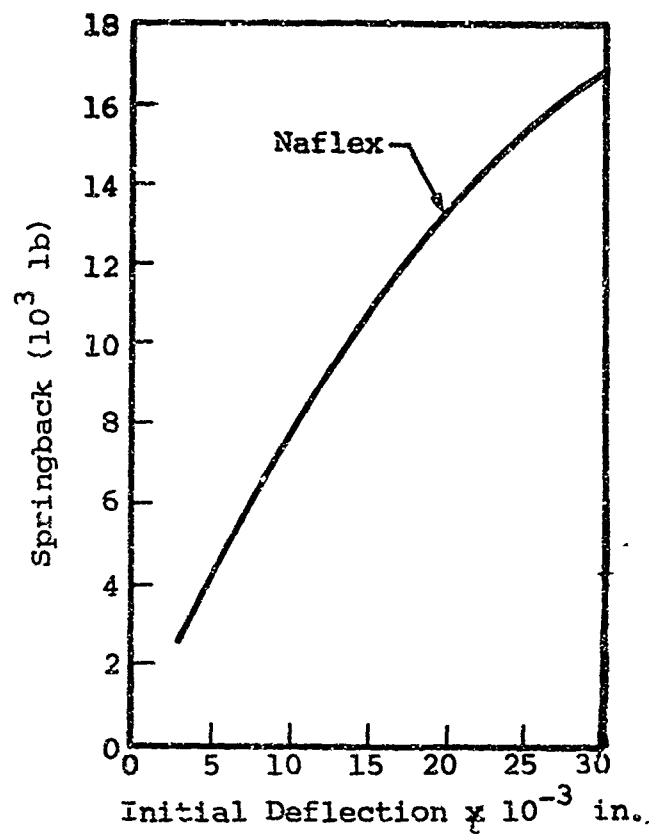


Figure 10-3 Structural performance data from the Naflex seal catalog

is large enough to support the load. Since Teflon is rather easily deformed under a compressive load, a stress ratio will be assumed and the leakage will be calculated. This leakage will be compared with the experimental results and the comparison will serve as a check on the validity of the initial assumption.

Assume the corrected stress-ratio is given by

$$\frac{W^{2/n'}}{A_A} / \sigma_m = 0.30$$

where

$$\sigma_m = 3870 \text{ psi}$$

$$n' = 2.8$$

$$A_A = \text{apparent area of contact}$$

$$W = \text{total applied load} = R_S \pi D$$

$$R_S = 210 \text{ lb/in. of circumference}$$

$$D = 2 \text{ in.}$$

Then $A_A = 0.1465 \text{ in}^2$ and the width of contact,

$$\bar{A} = \frac{A}{\pi D} = 0.0234 \text{ in.}$$

Figure 10-4 is a photomicrograph of the seal interface after experimental temperature and pressure cycling. The contact area extends from the bottom of the dark band to the top of the photo. The mating surface was unidirectional ground AM 355. The linear finish marks can be seen impressed into the Teflon surface. The dark band is assumed to be caused by the beginning of thermal decomposition of the Teflon coating.

The contact area width of the seal shown in figure 10-4 is 0.030 in. This also compares fairly well with the predicted value. Since the actual contact load on the seal was greater than the predicted load, it is expected that the contact area would be greater than the predicted value.

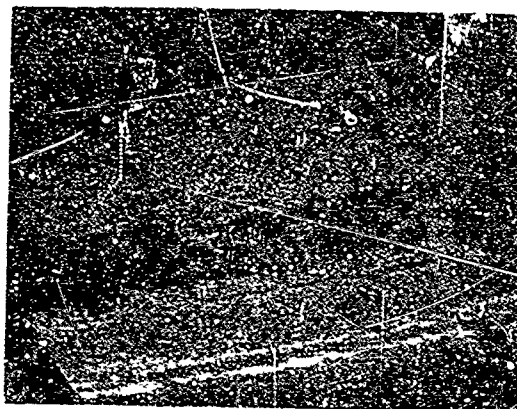


Figure 10-4 Experimentally observed contact area of a Naflex seal

10.1.5 Leakage Prediction

The design curves of Section 2 indicate a conductance parameter of $h^3 = 1 \times 10^{-22}$ in the neighborhood of a stress ratio equal to 0.3.

The helium leakage can now be predicted from the flow equation:

$$Q_o = \frac{(D_o + D_i)(P_{in}^2 - P_{out}^2)}{12\mu(D_o - D_i)p_o} h^3 + \frac{0.958\eta\lambda_o(P_{in} + P_{out})(D_o + D_i)}{\mu(D_o - D_i)}$$

where

$$D_o = 2 \text{ in.} + \bar{A}$$

$$D_i = 2 \text{ in.} - \bar{A}$$

The leakage predictions as a function of temperature and pressure are shown on Table 10-1.

The preceding calculations were based on the assumption that the contact load remains constant and equivalent to the initial seal deformation. In an actual application, the load does vary due to pressure and thermal deformation of the housing and seal structure. The critical effects occur at the higher temperature limit of 300° F, assuming that the seal is installed at normal temperatures. To estimate the effects of load variations, the characteristics of the experimental apparatus, described in Appendix V, are used as guidelines.

Table 10-1

LEAKAGE PREDICTION OF A NAFLEX SEAL

Pressure (psia)	@ 80°F	@ -320°F	@ 300°F
	Helium Leakage Rate (cc/sec, STP)		
114.7	8.85×10^{-7}	2.5×10^{-6}	6.77×10^{-7}
214.7	1.77×10^{-6}	5.0×10^{-6}	1.35×10^{-6}
414.7	3.58×10^{-6}	1.01×10^{-5}	2.74×10^{-6}
514.7	4.44×10^{-6}	1.25×10^{-5}	3.39×10^{-6}
614.7	5.49×10^{-6}	1.55×10^{-5}	4.19×10^{-6}
814.7	7.46×10^{-6}	2.11×10^{-5}	5.71×10^{-6}
1014.7	9.44×10^{-6}	2.67×10^{-5}	7.22×10^{-6}
1214.7	1.16×10^{-5}	3.28×10^{-5}	8.87×10^{-6}
1414.7	1.38×10^{-5}	3.90×10^{-5}	1.05×10^{-5}
1614.7	1.60×10^{-5}	4.52×10^{-5}	1.22×10^{-5}
1714.7	1.72×10^{-5}	4.86×10^{-5}	1.31×10^{-5}
1814.7	1.84×10^{-5}	5.21×10^{-5}	1.41×10^{-5}
2014.7	2.04×10^{-5}	5.77×10^{-5}	1.56×10^{-5}

The experimental flange or cover plate was designed for a 0.001-in. deflection under pressure. Since the seal structure deflection was 0.020-in., the effects of pressure on the load reduction due to flange separation is negligible. This corresponds to a load reduction of 7 per cent and is well within the 50 per cent limits of hysteresis stress relaxation.

The differential thermal expansion at 300° F can be estimated from the average coefficients of thermal expansion of the seal structure and bolt materials. The bolt elongation at 300° F is obtained from Section 8 as 0.15 per cent. The thermal expansion coefficient of 4340 steel is $6.3 \mu\text{in. per in.}^\circ\text{F}$ and

$$\text{Bolt expansion: } 0.375 \text{ in.} \times 0.0015 = 560 \mu\text{in.}$$

$$\text{Seal structure expansion: } 0.1475 \times 6.3 \times 10^{-6} (300-80) = 704 \mu\text{in.}$$

The bolt expansion exceeds the seal expansion by .00036 in. Thus, the total deflection change resulting from thermal and pressure causes is negligible compared to the initial elastic deflection of the seal legs. The reduction in contact load because of the deflection change is also negligible. Thus, it can be concluded that the predicted leakage rates based on the initial load will not change as a result of pressure or thermal distortions.

10.1.6 Experimental Performance

The experimental procedures are described in Section 9.5.2 and Appendix V.

Figures 10-5 through 10-8 show the results of leakage evaluation of the Naflex seal. Room temperature results, shown on figure 10-5, and the low temperature results, shown on figure 10-6, are in close agreement with the predicted leakage rates. The actual results are well within the one order of magnitude deviation that is expected from the predicted leakage rates. Figure 10-7 shows the variation of leakage with decreasing temperature and constant 1000-psi pressure.

Figure 10-8 shows the leakage at elevated temperature for the seal. The actual leakage is approximately two orders of magnitude greater than the predicted leakage. This disagreement is attributed to the thermal decomposition of the Teflon coating. While precautions were made to monitor and limit the maximum temperature of the seal, it was not possible to ensure an absolute limit. An average temperature close to the seal interface was 375° F, which may not have represented the actual temperature. The possibility that the interface temperature was higher than 375° F was evidenced by liquid residue on the housing surfaces.

The Naflex seals were subjected to pressure cycling experiments in addition to the thermal cycling evaluation. The seal was placed in a test housing and subjected to fluctuating pressures of 0 to 1900 psi at a rate of 30 cycles per minute using hydraulic oil as the sealed fluid. The experimental apparatus is shown in figures 10-9, 10-10 and 10-11.

After 50,250 pressure cycles, oil seepage was observed around the outer diameter of the spacer. The cycling was continued until 73,500 cycles were completed. At this time, the experimental housing was disassembled as shown in figure 10-10. Oil was visible on the spacer. The complete assembly after cleaning is shown in figure 10-11, and a view of the seal contact interface after 73,500 pressure cycles is shown in figure 10-12.

Figure 10-12 shows the Teflon coating has been completely worn away from the contact interface. Since the contact loading provided by the deflection of the seal legs is insufficient to provide adequate contact stress for metal-to-metal sealing, substantial seal leakage occurred.

The wearing away of the Teflon coating is attributed to flexing of the seal and creep under the influence of the pressure pulses. Approximately 0.0035-in. radial expansion of the seal and approximately 0.001-in. axial bolt deflection can be expected for a pressure pulse of 2000 psi. Thus, a substantial amount of relative motion under high contact stress takes place at the interface. The effects of this relative action are visible in

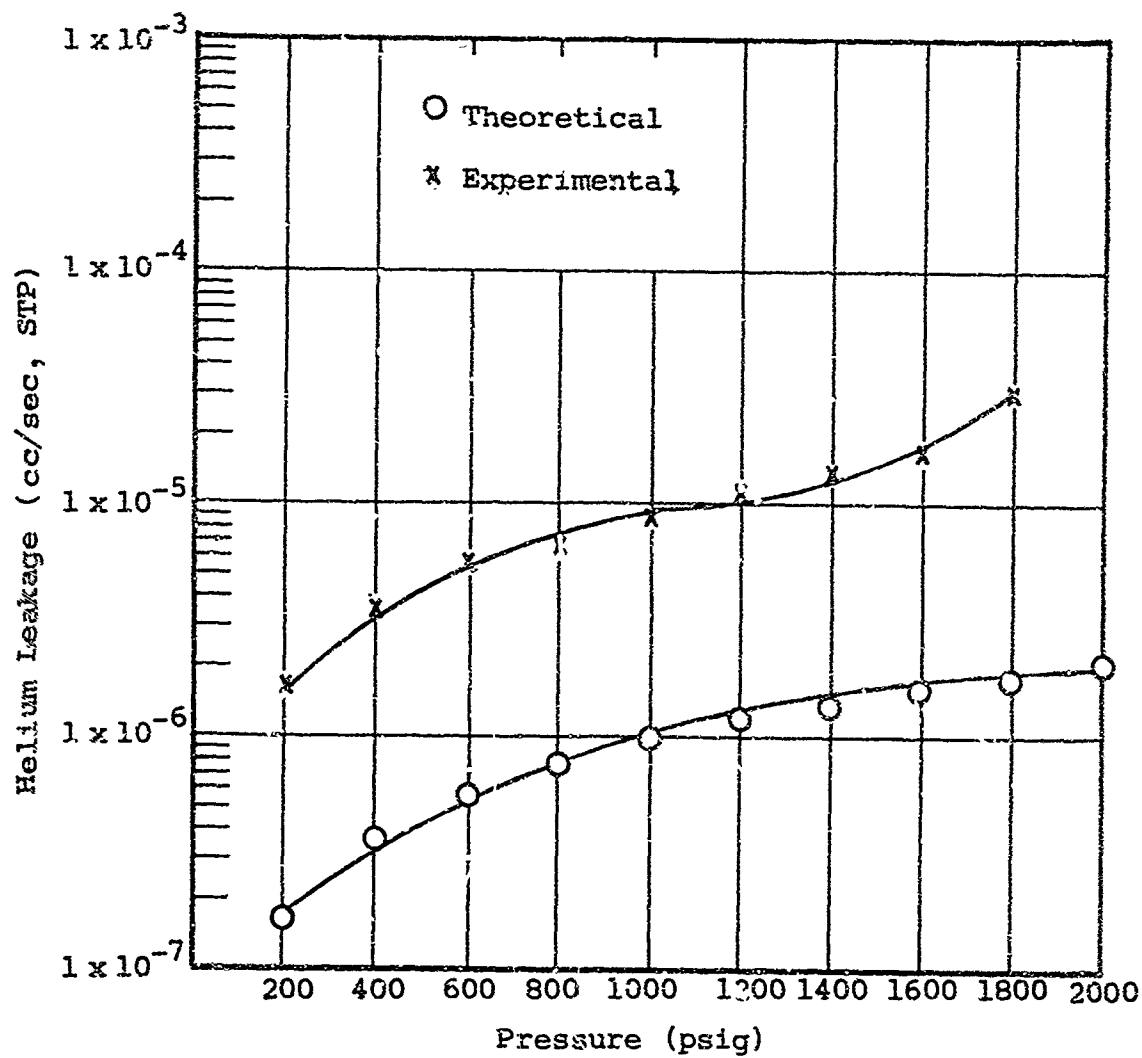


Figure 10-5 Leakage of a two-inch Naflex seal at 80°F

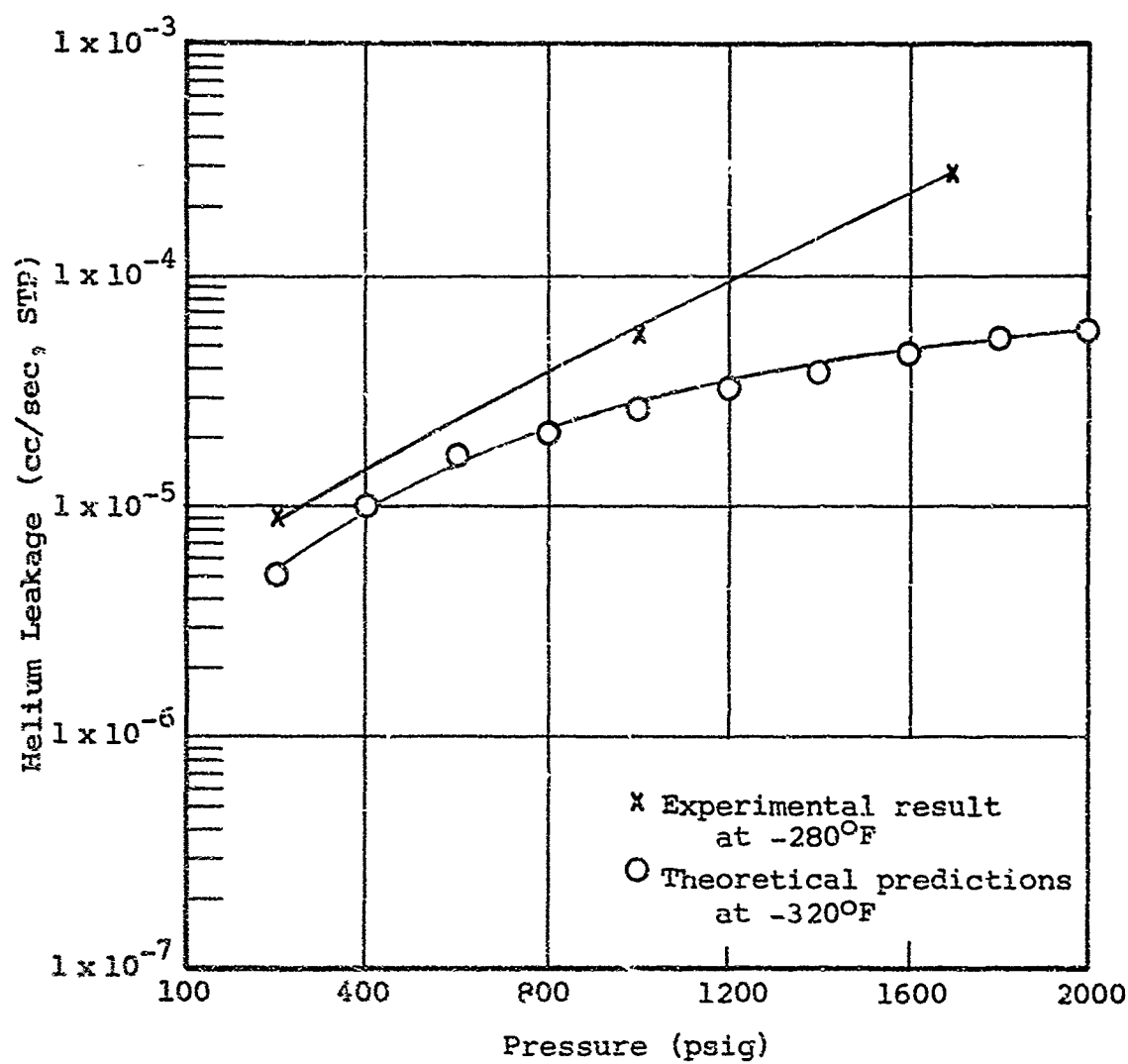


Figure 10-6 Leakage of a Naflex seal at low temperatures

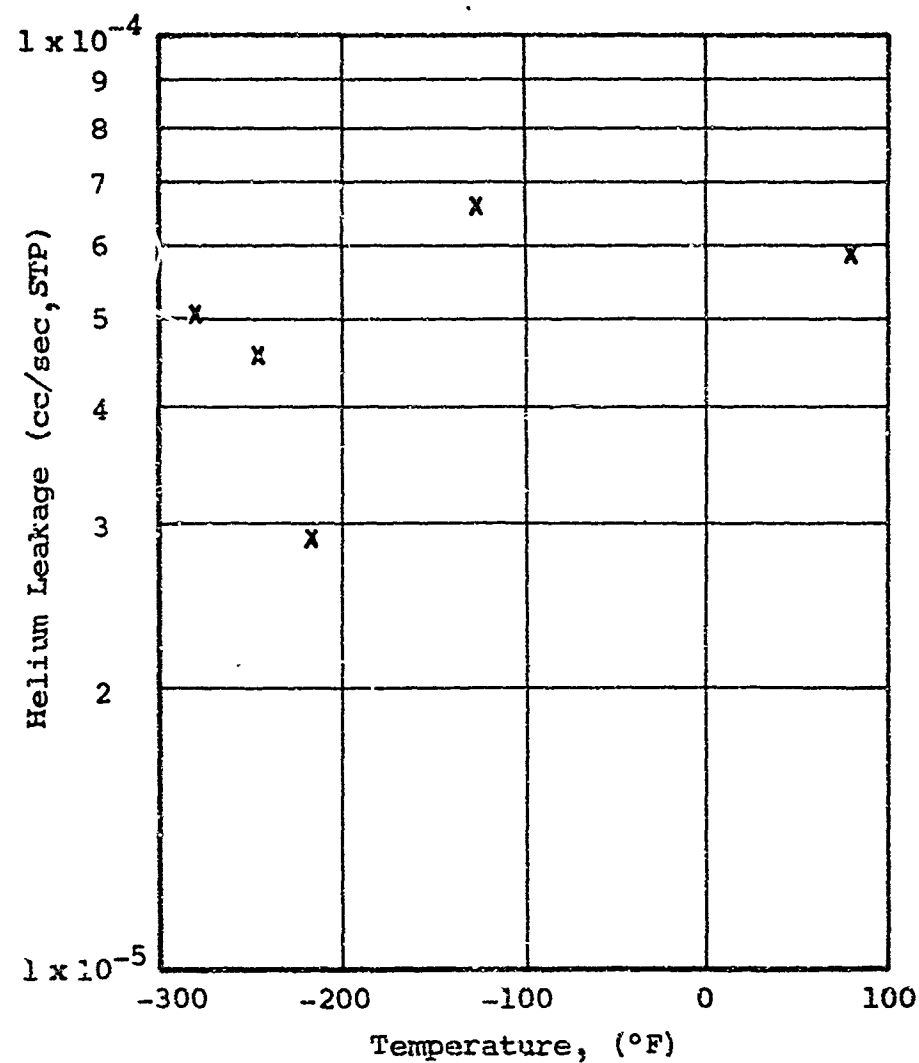


Figure 10-7 Leakage of a Naflex seal as a function of temperature for a fluid pressure of 1000 psig

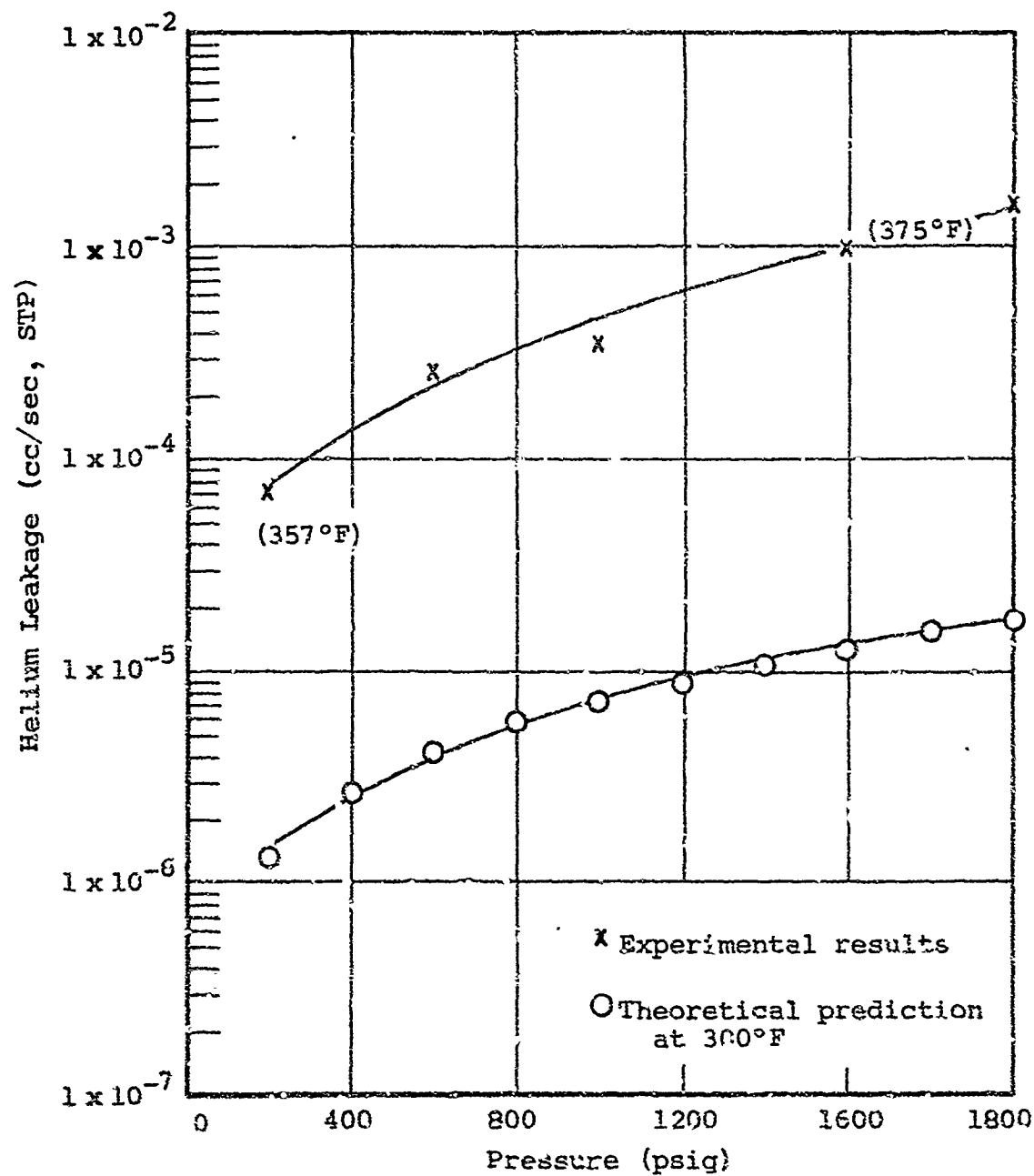


Figure 10-8 Leakage of a Naflex seal at elevated temperature

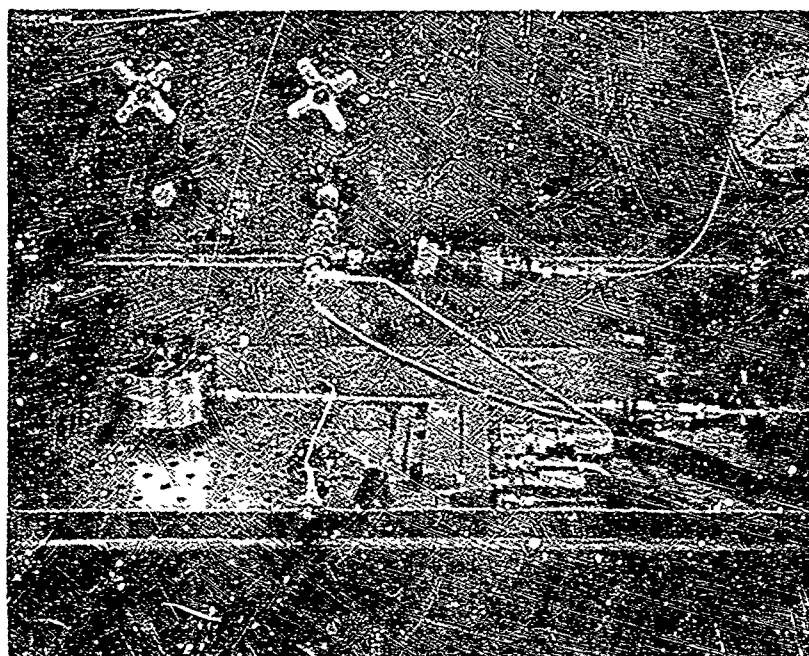


Figure 10-9 Pressure cycling apparatus

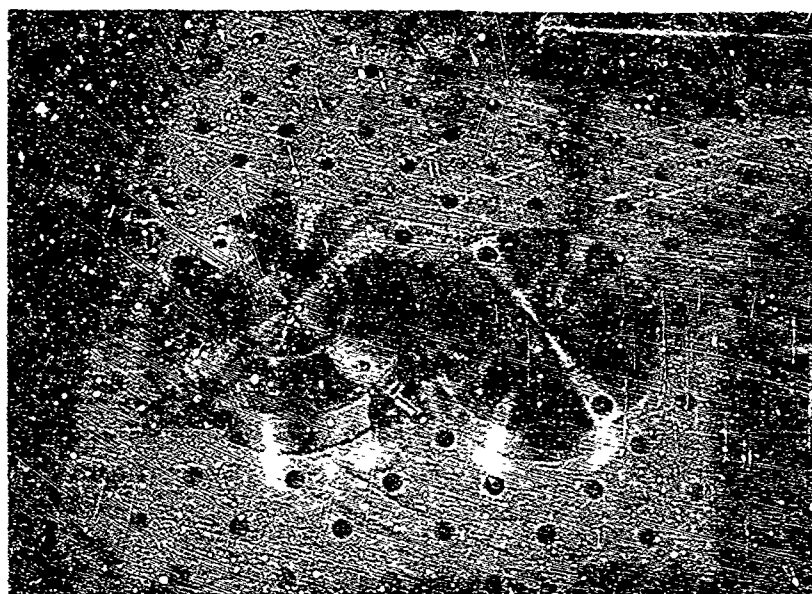


Figure 10-10 Experimental apparatus disassembled
after 73500 pressure pulsation cycles

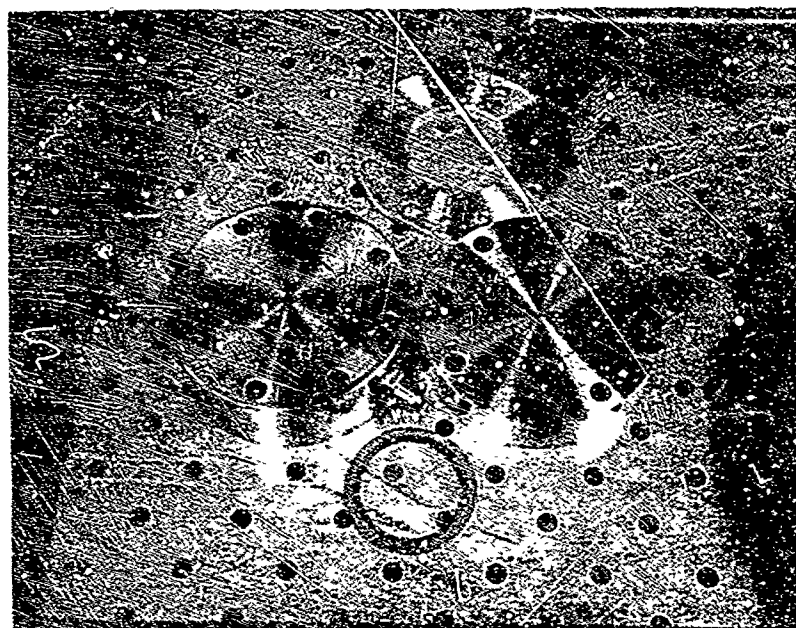


Figure 10-11 Pressure cycling housing
completely disassembled

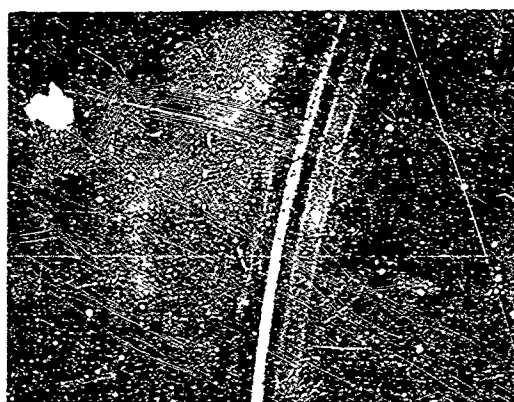


Figure 10-12 Contact interface of Teflon-coated seal
after 73,500 pressure pulsation cycles

figure 10-11. The circular impressions on the flange plates are due to the relative motion and the metal-to-metal contact occurring after the Teflon coating was worn away.

The most important implication of these results is that in applications where severe pressure pulsations are expected, the seal and housing must be made more rigid than in applications where few or no pulsations are present. This is necessary to reduce the amount of relative motion that takes place, and to eliminate wear that damages and destroys the interface.

10.1.7 Observations

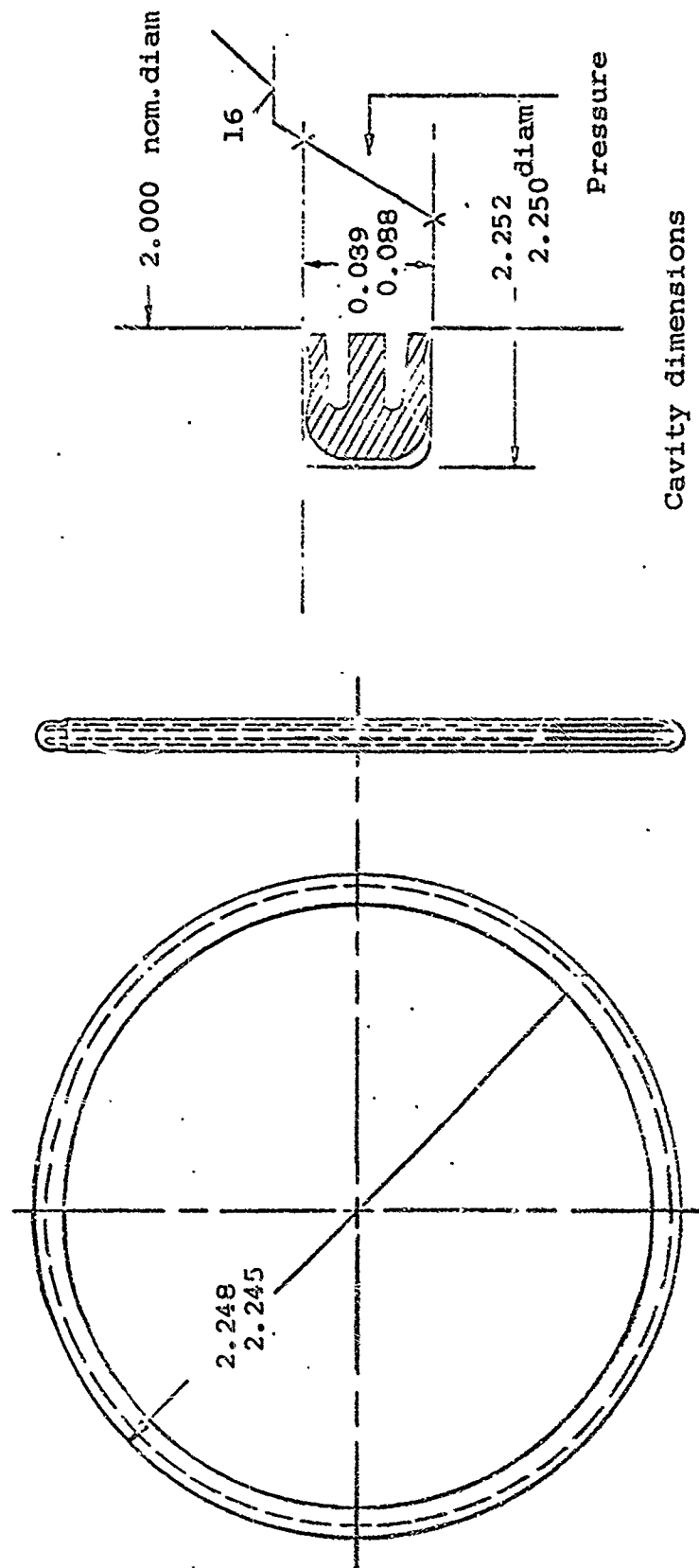
The close agreement between the actual and predicted leakage rates and between the actual and predicted contact areas further substantiates the phenomenon demonstrated by the conductance parameter - modified stress ratio relationships. As the load is increased on an unconfined material, plastic flow will take place in such a way that the full plasticity hardness stress is never reached. The stress ratio asymptotically approaches a value less than 0.4.

The theoretical leakage predictions and actual rates indicate that the leakage flow varies directly with the pressure drop across the seal interface indicating molecular flow. The actual leakage rate characteristics, shown on figures 10-5, 10-6 and 10-8, show this type of variation also.

The results of this evaluation point out the advantages of maintaining large elastic deflection on the seal leg. Since the initial elastic leg deformation is much larger than the subsequent pressure and thermal deflection of the housing, these deflections do not substantially influence the loading of the seal. Thus, as long as the temperature remains within the tolerable limits of the seal material, sealing performance should not be affected to a significant degree by thermal variations.

10.2 Cook Airtomic Seal

The Cook seal is an edge-contact seal, as shown in figure 10-13, designated to seal helium at temperatures between -320°F and 1200°F and pressures up to 2000 psi. The manufacturer claims that the legs produce a line contact interface. Actually, the interface is formed by a wedge at the tip of the seal leg which plastically deforms the mating surface. The seal structure is made from AMS-5734, a high-strength, high-hardness steel. Thus, the mating of the seal edge with another hard material (AM-355) produced permanent deformation of the seal cavity surfaces. While the seal may be reusable, the mating surface cannot be reused. In addition, the magnitude of the interface deformation was not expected to produce a minimum leakage rate since the loading was low, producing a very narrow interface width normal to leakage flow. The seal, however, does possess



Seal material: AMS-5734, prec. ht. treat at 1325°F for 16 hr,
a-c operating conditions: helium gas at 1200°F max. and 2000 psi max.

Patent pending

Figure 10-13 Cook static seal, type FW

one interesting feature. This is inherent in its shape, whereby the hoop or radial expansion of the main body of the structure is compensated by the straightening of the concave legs. The resulting deformation under pressure should produce no movement at the interface. A center stiffening member is provided to give radial stabilizing to the structure.

Two of the seals of this type were subjected to an experimental leakage evaluation and found to leak excessively ($\sim 10^2$ cc/sec STP). An inspection of parts showed a difference in leg thickness. One leg was approximately twice the thickness of the other, causing uneven leg deflection. The thinner leg collapsed completely producing interface contact over the entire leg surface, resulting in low contact stresses. This, in turn, caused excessive leakage. From the discussion in Section 7, the seal leg deflection varies with the cube of the thickness. Consequently, a leg thickness variation factor of two produces a deflection variation of eight.

A further inspection of six remaining seals showed identical variations. A comparison, therefore, between theoretical and actual performance was not possible. The fabrication of thin seal legs is difficult from the standpoint of achieving close dimensional tolerances. Section 6 should be reviewed to gain a further insight into the tolerance limits which can be achieved by various machining processes.

10.3 Evaluation of Additional Commercially Available Seals

10.3.1 Description

Eleven additional static seals were evaluated theoretically, and experimentally under less stringent environmental conditions than the seals discussed in Section 9 and Subsection 10.1. The seals are identified as follows.

<u>Seal</u>	<u>Manufacturer</u>	<u>Part No.</u>	<u>Figure</u>
X-1	Wiggins Oil Tool Co.	2140-131	10-14
X-2	3424 East Olympic Boulevard	2540-3250	
X-3	Los Angeles 23, California		
K-1	Haskei Engineering	H54-21	10-15
K-2	1236 South Central Avenue	H54-24	
	Glendale 4, California		
W-1	Hydrodyne Division of Donaldson	8100-29-0701	10-16
E-1	7350 North Coldwater Canyon	9100-29-0701	10-17
E-2	North Hollywood, California	9100-29-0101	
O-1	United Aircraft Products	U-2410-02875	10-18
O-2	Box 1035	U-2420-02500	
	Dayton, Ohio		
C-1	Pressure Science Incorporated	10111-0003	10-19
	11642 Old Baltimore Pike		
	Beltsville, Maryland		

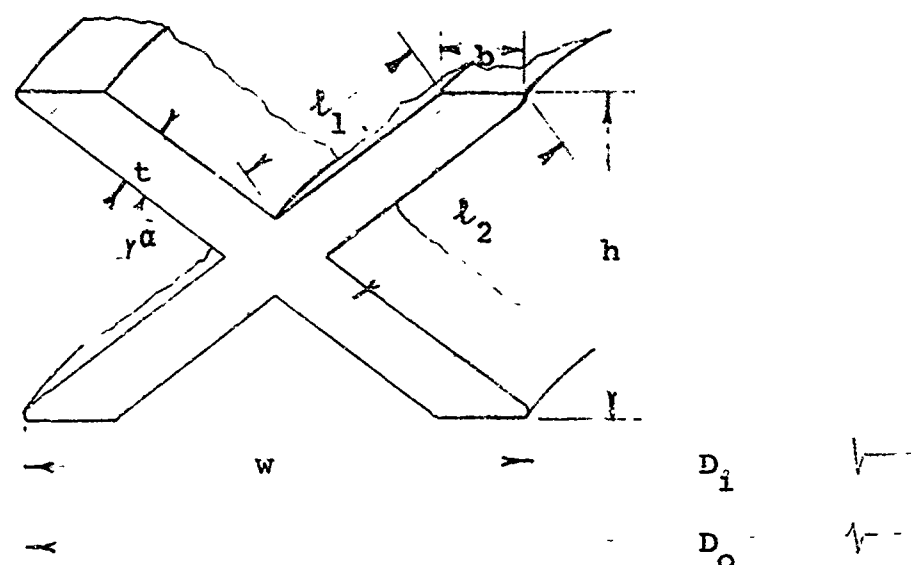


Figure 10-14 X-shaped seals

Seal	Structure Material	Plating	D_o	D_i	h	b (in.)	w (in.)
X-1	Stainless Steel	AG	1.540	1.250	0.1385	0.011	0.145
X-2	Stainless Steel	AG	3.632	3.245	0.1838	0.022	0.1935
X-3	6061T6 Aluminum	None	1.878	1.565	0.1536	0.012	0.1565

Seal	t (in.)	α	l_1 (in.)	l_2 (in.)	l (in.)	Mean Circumference (in.)	Interface Contact Area (in ²)
X-1	0.017	46°1'	0.088	0.096	0.092	4.3825	0.1298
X-2	0.026	47°	0.110	0.126	0.118	10.8024	0.4739
X-3	0.020	39°4'	0.031	0.122	0.102	5.4083	0.1298

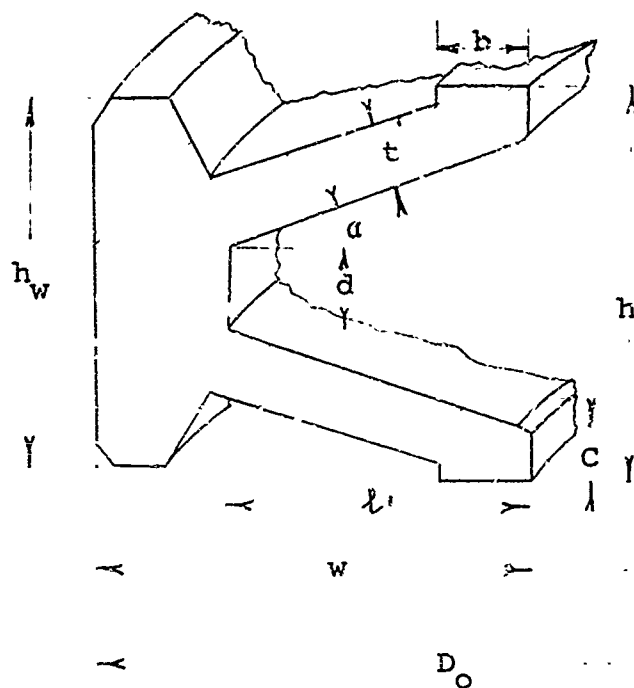


Figure 10-15 K-shaped seals

Seal	Structure Material	Plating	D_o (in.)	D_i (in.)	w (in.)	h (in.)	h_w (in.)	b (in.)	t (in.)
K-1	Inconel X	Silver	1.313	1.113	0.100	0.096	0.091	0.0164	0.012
K-2	Inconel X	Silver	2.188	1.1	0.100	0.095	0.091	0.0185	0.0135

Seal	α	t'	t	c (in.)	d (in.)	Contact Circum. (in.)	Interface Contact Area (in. ²)
K-1	20° 16'	0.065	0.069	0.008	0.032	3.5481	0.582
K-2	17° 16'	0.065	0.068	0.0155	0.025	6.3036	0.1165

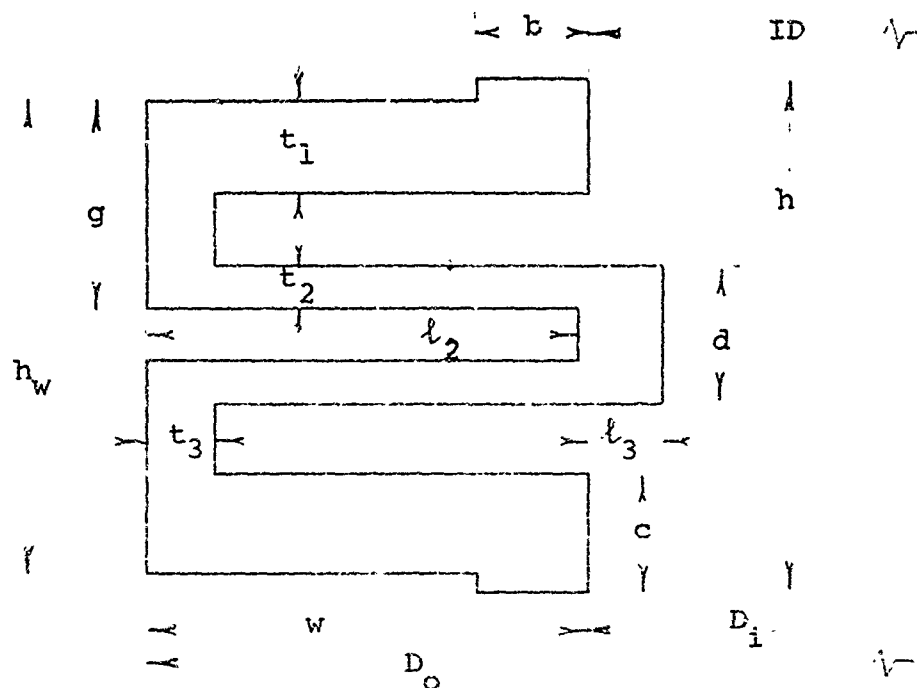


Figure 10-16 W-shaped seals

Seal	Structure Material	Plating	D_o (in.)	D_i (in.)	ID (in.)	h	h_w (in.)	b (in.)
W-1	Stainless Steel	Silver	2.002	1.863	1.829	0.1015	0.086	0.0225
W-2	Inconel X	Silver	1.690	1.550	1.580	0.1015	0.0785	0.0240
W-3	Inconel X	Silver	1.690	1.550	1.580	0.1015	0.0785	0.0226

Seal	t_1 (in.)	t_2 (in.)	t_3 (in.)	t_1 (in.)	t_2 (in.)	t_3 (in.)	t_4 (in.)	c (in.)
W-1	0.047	0.058	0.013	0.0135	0.012	0.0095	0.0115	0.0145
W-2	0.047	0.059	0.013	0.0135	0.012	0.0095	0.0115	0.0145
W-3	0.047	0.059	0.013	0.0135	0.012	0.0095	0.0115	0.0145

Seal	d (in.)	Contact Circum. (in.)	Interface Contact Area (in. ²)
W-1	0.036	6.0052	0.1351
W-2	0.036	5.0391	0.1209
W-3	0.036	5.0284	0.1136

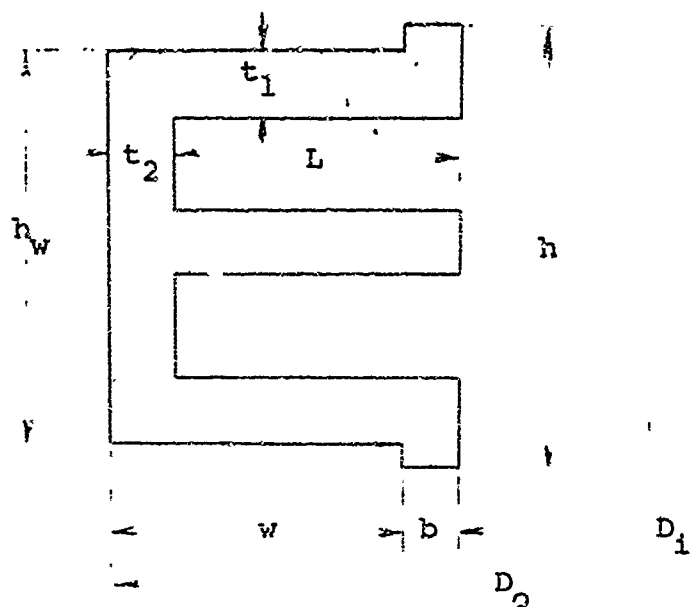


Figure 10-17 E-shaped seals

Seal	Structure Material	Plating	D_0 (in.)	D_1 (in.)	b (in.)	h (in.)	h_w (in.)
E-1	Inconel X	Silver	2.00	1.863	0.0095	0.1005	0.0945
E-2	Inconel X	Silver	2.000	1.863	0.0096	0.1010	0.0936
E-3	6061T6 Aluminum	None	2.497	2.362	0.0070	0.1008	0.0930

Seal	L (in.)	t_1 (in.)	t_2 (in.)	Contact Circum. (in.)	Interface Contact Area (in. ²)
E-1	0.045	0.020	0.0235	5.8826	0.0559
E-2	0.047	0.020	0.0215	5.8830	0.0565
E-3	0.049	0.020	0.0185	7.4425	0.0521

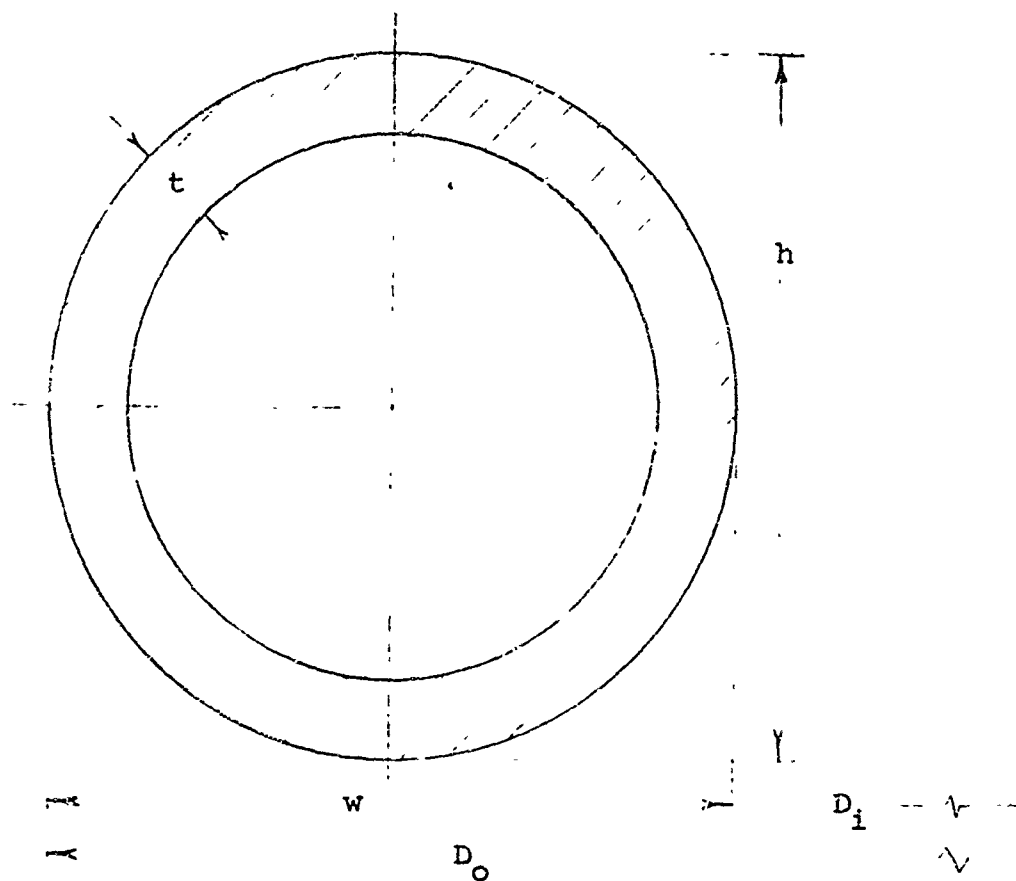


Figure 10-18 O-shaped seals

Seal	Structure Material	Plat- ing	D_o (in.)	D_i (in.)	w (in.)	h (in.)	t (in.)	Contact Circum. (in.)
O-1	Stainless 321 Steel	None	1.502	1.376	0.063	0.063	0.012	4.5145
O-2	Stainless 321 Steel	None	2.875	2.631	0.122	0.122	0.010	8.6488
O-3	Stainless 321 Steel	None	2.502	2.255	0.1235	0.126	0.020	7.4723

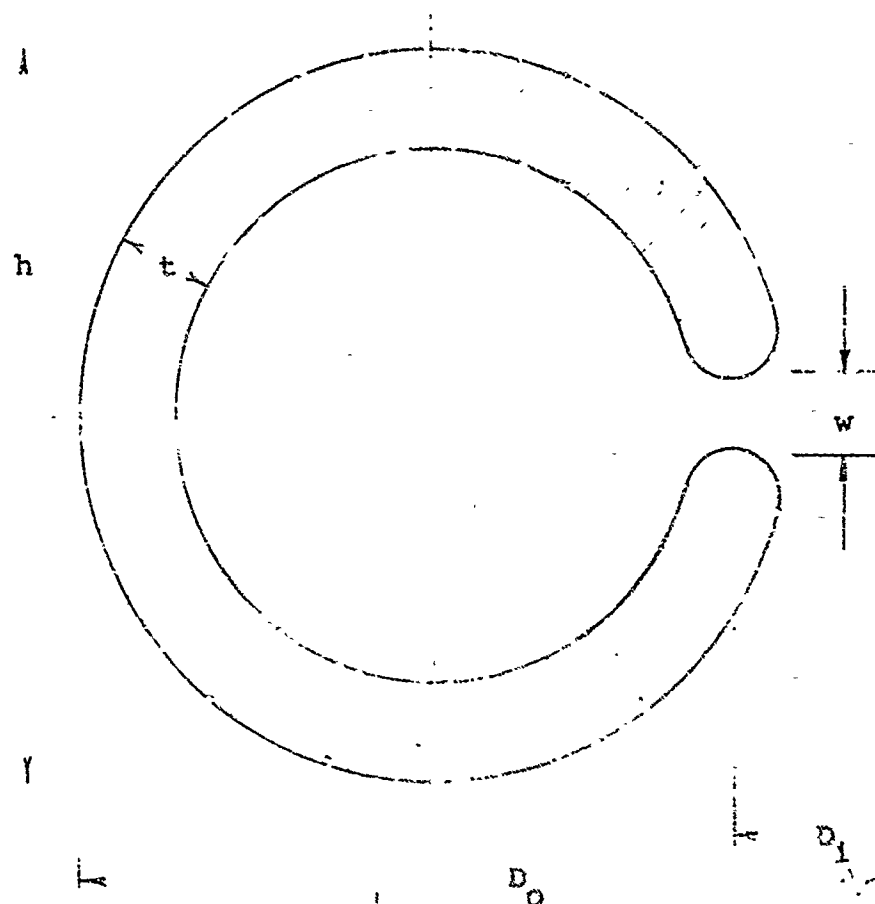


Figure 10-19 C-shaped seals

Seal	Structure Material	Plating	L_o (in.)	R_1 (in.)	w (in.)	h (in.)	t (in.)	Contact Circum. (in.)
C-1	Stainless Steel	Silver	0.364	0.210	0.007	0.0946	0.012	6.8453
C-2	Stainless Steel	Silver	0.990	0.836	0.007	0.0867	0.015	2.8378

10.3.2 Structural Analysis

The procedure used on each seal was to analyze the flexible member of the seal as a cantilever beam and assuming that all the structural deflections were elastic. By using the basic equation for the deflection of the free end of a cantilever beam,

$$y = \frac{Pl^3}{3EI}$$

where

y = deflection (in.)

P = total load (lb)

E = modulus of elasticity (psi)

I = moment of inertia (in⁴)

l = effective beam length

A deflection constant can be derived for any seal configuration. The deflection constant used in the beam analysis of the seals relates the load to the total seal deflection in the form

$$\bar{P} = Ky$$

where

\bar{P} = contact load per unit circumference (lb/in.)

K = deflection constant (psi)

y = tip deflection of seal leg normal to contact surface (in.)

The simple beam approach taken was utilized to illustrate more clearly the use of simple beam theory in the analysis of seal shapes. Because the configurations are complicated, the direct use of the nomographs (Section 7) was not feasible.

In cases where the seal leg is inclined with respect to the mating surface, as shown in figure 10-20(a), the friction force imposes axial and transverse loads on the assumed beam, as shown in figure 10-20(b).

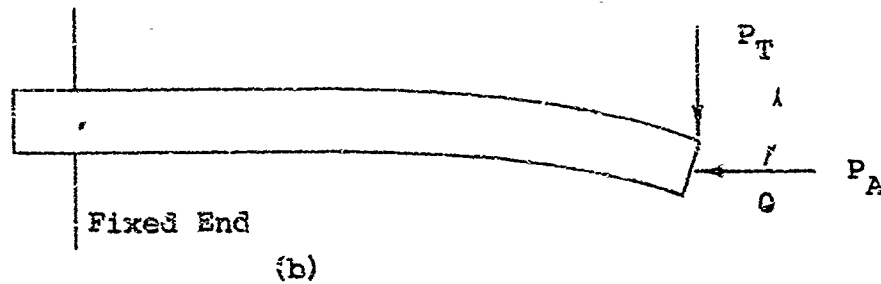
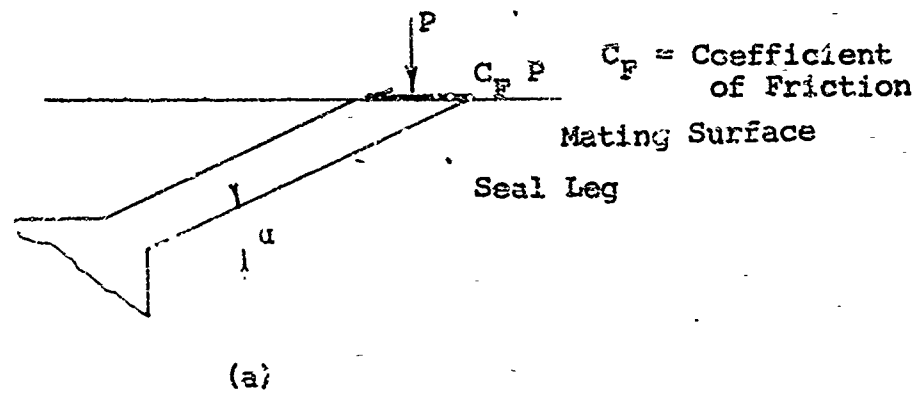


Figure 10-20 Beam with axial and transverse loading

An approximate formula for the maximum bending moment that is due to the combined effect of the axial and transverse loads is

$$M' = M(1 \pm \beta P_A L^2 / EI)^{-1}$$

where

M = bending moment due to P_T

P_T = transverse load

P_A = axial load

$\beta = 1/3$ for a cantilever beam

For $P_A = 0$; $M' = M$. The minus sign is used when P_A is a compressive load.

A more precise analysis for relatively long and slender beams yields the result

$$y_{\max} = \frac{P_T}{P_A} (j \tan U - 1)$$

$$\theta = \frac{P_T}{P_A} \left(\frac{1 - \cos U}{\cos U} \right)$$

where

$$j = (EI/P_A)^{0.5}$$

$$U = 1/j$$

Since the preceding equations are nonlinear, it would be desirable to be able to neglect the effects of the axial load. If $P_A \ll 3EI/L^2$ then $M' \approx M$. If the error in the bending moment calculation is to be less than 5 per cent, then P_A must be less than $0.125 EI/L^2$. This test applied to the subject seal shapes showed that transverse loading effects can be neglected. A derivation of the deflection constant K for each seal is presented in Appendix VI.

The effects of the fluid pressure on the contact stress must also be considered. It is assumed that the seal leg behaves elastically under the influence of the fluid pressure. Thus, the problem of the reaction force at the contact area that is due to the fluid pressure is a statically indeterminate problem. However, since the beam is assumed to behave elastically, the reaction force will be a function of the pressure and the geometry. The derivation of the effects of pressure on the contact stress of each seal is contained in Appendix V. The effect of fluid pressure on the contact stress is given in the form

$$\sigma = \sigma_i + C_R \Delta P$$

where

σ = contact stress (psi)

σ_i = initial contact stress (psi)

ΔP = pressure difference across seal leg (psi)

C_R = constant depending on geometry of seal

Table 10-2 summarizes the deflection coefficients, K' , and the pressure actuation constant, C_p along with the experimentally determined deflection coefficient. A description of the experimental determination of the deflection coefficients is described in Appendix IV.

The relative magnitude of fluid pressure is small compared with the initial contact stress for the X-seals. Additionally, the shape of the O- and C-seals do not lend themselves to the type of analysis necessary to calculate the coefficient C_p . For these reasons, C_p was neglected for the X-, O-, and C-seals.

Table 10-2

LOADING PROPERTIES OF SEAL CONFIGURATIONS

Seal	$K'(\times 10^3)^*$	$K'(\times 10^3)^*$ experimental	C_p
X-1	60	96	
X-2	102	159	
X-3	27	48	
K-1	21.3	61	0.533
K-2	31.3	20	0.557
W-1	18.8	32	0.597
W-2	18.8	26	0.592
W-3	18.8	32	
E-1	96.0	47	1.876
E-2	78.5	42	1.800
E-3	21.4	22	2.659
O-1	14.2	34	
O-2	134	113	
O-3	261	99	
C-1	21.0	71	
C-2	116.7	74	

* K' = Spring Scale of Seal per inch of circumference
= lb/in/in

10.3.3 Leakage Prediction

The establishment of the interface loading enables the systems designer to predict the interface contact area and normal stress. From this information the design charts in Section 2 of the report can be employed to predict a conductance parameter. This, in turn, permits the calculation of leakage using the leakage flow equation.

The modified stress ratio at the interface was determined by the theoretical deflection constant K' or from the experimental deflection constant and the known deflection of the seal. The contact area is usually known from the initial seal geometry as shown on figures 10-14 through 10-17. The interface material and the surface finish are also given qualities. Thus, the ratio can be calculated

$$\frac{W^{2/n'}}{A_A} / \sigma_m$$

Most of the seals evaluated were plated, thus, the Meyer hardness of soft plating was used in calculating the modified stress ratio.

The load-deflection experimental results (Appendix IV) show that most of the seals deflect elastically throughout the range of their specified deflection. The metal O-rings, however, undergo considerable plastic deformation. Thus, the establishment of a deflection constant is meaningless in the range of plastic deformation. The required load and contact area at the specified seal deflection were determined experimentally on similar seals, and used in the calculation of leakage predictions. In cases where a wide disagreement between experimental and theoretical deflection constants existed, the experimental results were used in the calculation of the modified stress ratio.

Once the modified stress ratio was determined for a particular seal configuration, the conductance parameter for that configuration was determined from the design curves of Section 2 for the proper surface finish. With the conductance parameter determined, the leakage was then calculated using the relationship

where

D_o = outside diameter of contact area

D_i = inside diameter of contact area

$$Q_o = \left(\frac{\pi h^3 (D_o + D_i) (p_{in}^2 - p_{out}^2)}{12\mu (r_o - r_i) p_o} \right) \left(\frac{(1 + 12.76\epsilon p_o \lambda_o)}{(p_{in} - p_{out}) h} \right)$$

A summary of the preliminary calculations leading to the final leakage calculation are shown on Table 10-3. Also shown are theoretical and experimental helium leakage rates at a 100-psi sealed fluid pressure. The experiments were conducted by mating each seal against 1141 steel flanges having a Meyer hardness of 308,000 psi. Additionally, Table 10-3 summarizes

- The surface finish of the harder interface surface used in the experiments and also the theoretical calculations
- The Meyer hardness of the softer interface material used in the calculations.

Another approach in arriving at the conductance parameter is also possible. In seals where the initial contact area is a flat surface as shown, the deflection of the seal leg may cause a condition of nonuniform contact.

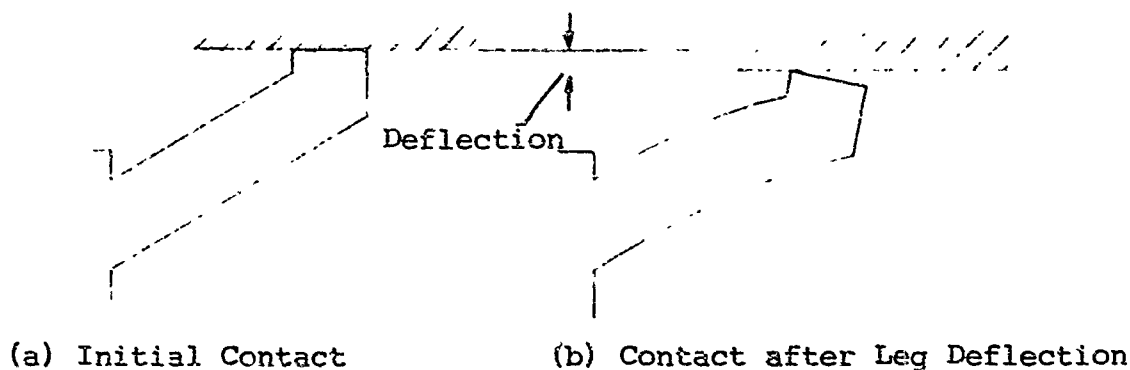


Figure 10-21 Nonparallel interface contact

This type of contact could cause extremely high contact stresses over a small portion of the initial contact area. Full plasticity could occur in this small portion of the initial contact area.

The design in Section 2 indicates that a finite limit of modified stress ratio exists in the case of unconfined interface contact. These curves asymptotically approach modified stress ratios of 0.2 and 0.3. By assuming a limiting stress ratio the contact area resulting from the full plasticity condition caused by the type of contact postulated in figure 10-21(b) can be

estimated. The relationship

$$\frac{W^{2/n'}}{A} / \sigma_m$$

is used to estimate the contact area since it is assumed that all the other variables are known. When the contact area is calculated the inside and outside diameters of the contact area can also be estimated from the initial seal geometry. These values and the conductance parameter determined by the limiting value at the stress ratio (approximately $h^3 \approx 10^{-22} \text{ in}^3$) are then used in the leakage equation to calculate the leakage. This approach is discussed mainly for the purpose of indicating an alternate procedure. The results using either method do not differ widely.

In all of the subsequent leakage prediction calculations presented in this section, the contact was assumed to be uniformly distributed over the entire geometric contact area. In the case of the O- and C-ring seals, however, the area of interface contact was determined by assuming nonparallel contact and following the preceding procedures. A comparison of theoretical and predictions and experimental leakage rates for each seal configuration is summarized on figures 10-22 through 10-27.

These results indicate a close correlation between theoretical and experimental results (within one order of magnitude) for most of the seals evaluated.

10.3.4 Observations

The following observations can be made from the preceding results:

- The assumption of uniform contact across the apparent interface contact area yields good prediction results
- The design curves of Section 2 of the report can be used to predict leakage in the laminar flow region as well as in the molecular flow region. The leakage curve of figures 10-22 through 10-27 shows that the flow rate varies approximately as the square of the pressure drop, thus indicating laminar compressible flow.
- The close correlation between the leakage predictions based on experimentally determined deflection constants and the actual leakage rates indicates a useful method of seal evaluation. The actual load-deflection characteristics of a given seal can usually be determined in a fairly straightforward manner, without the use of highly specialized equipment. One method is

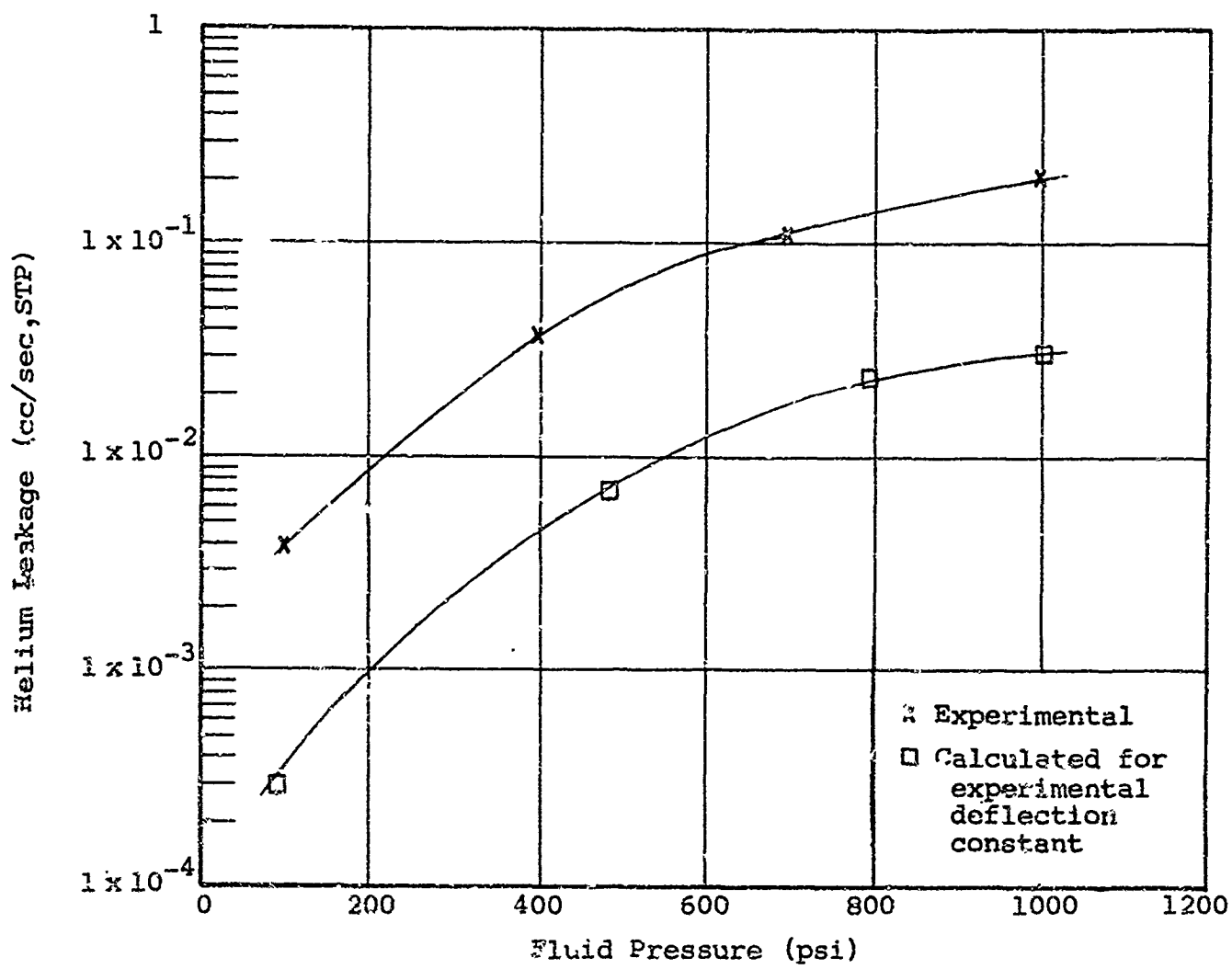


Figure 10-22 Helium leakage as a function pf pressure for K-1 seal

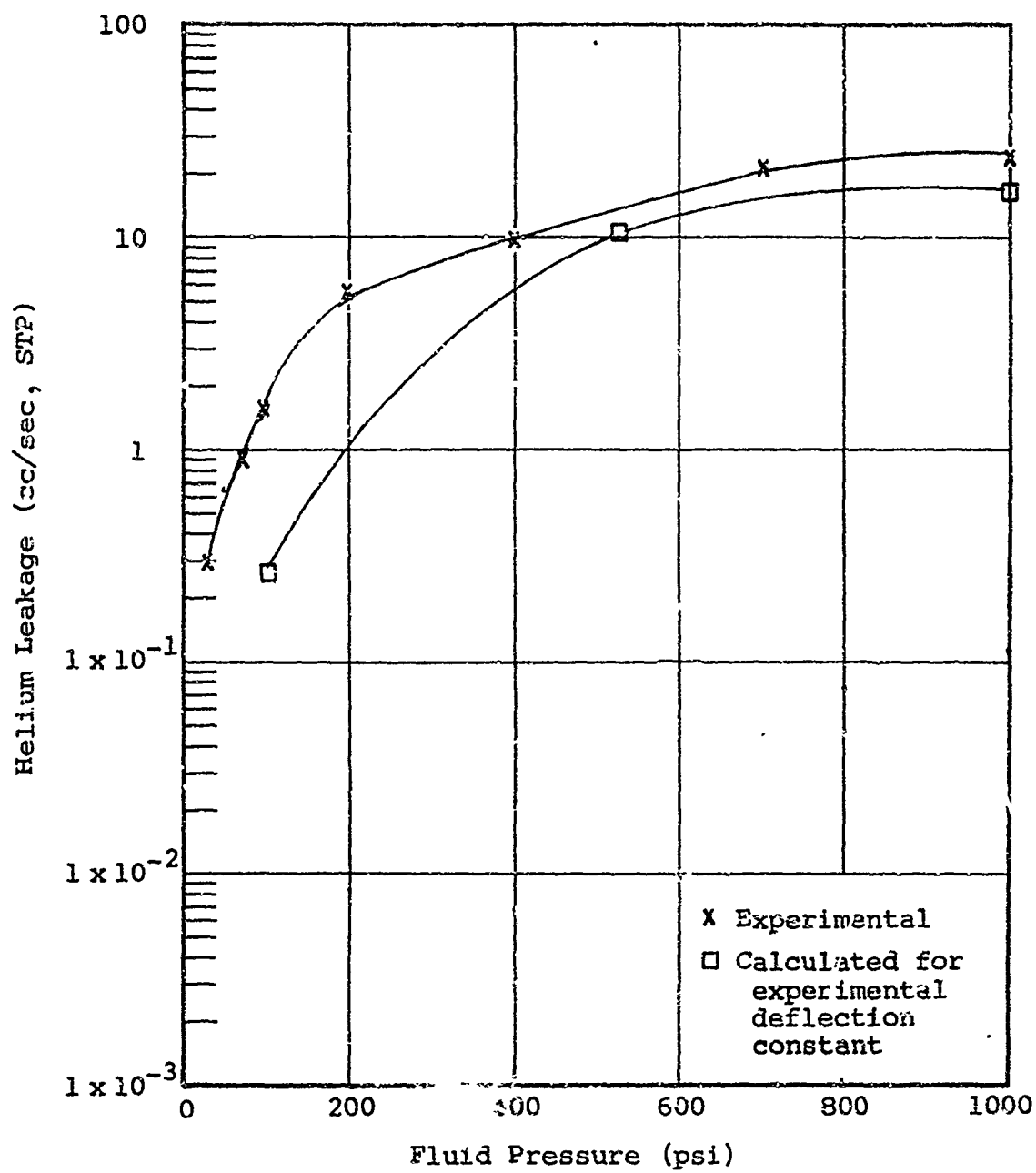


Figure 10-23 Helium leakage as a function of pressure for K-2 seal

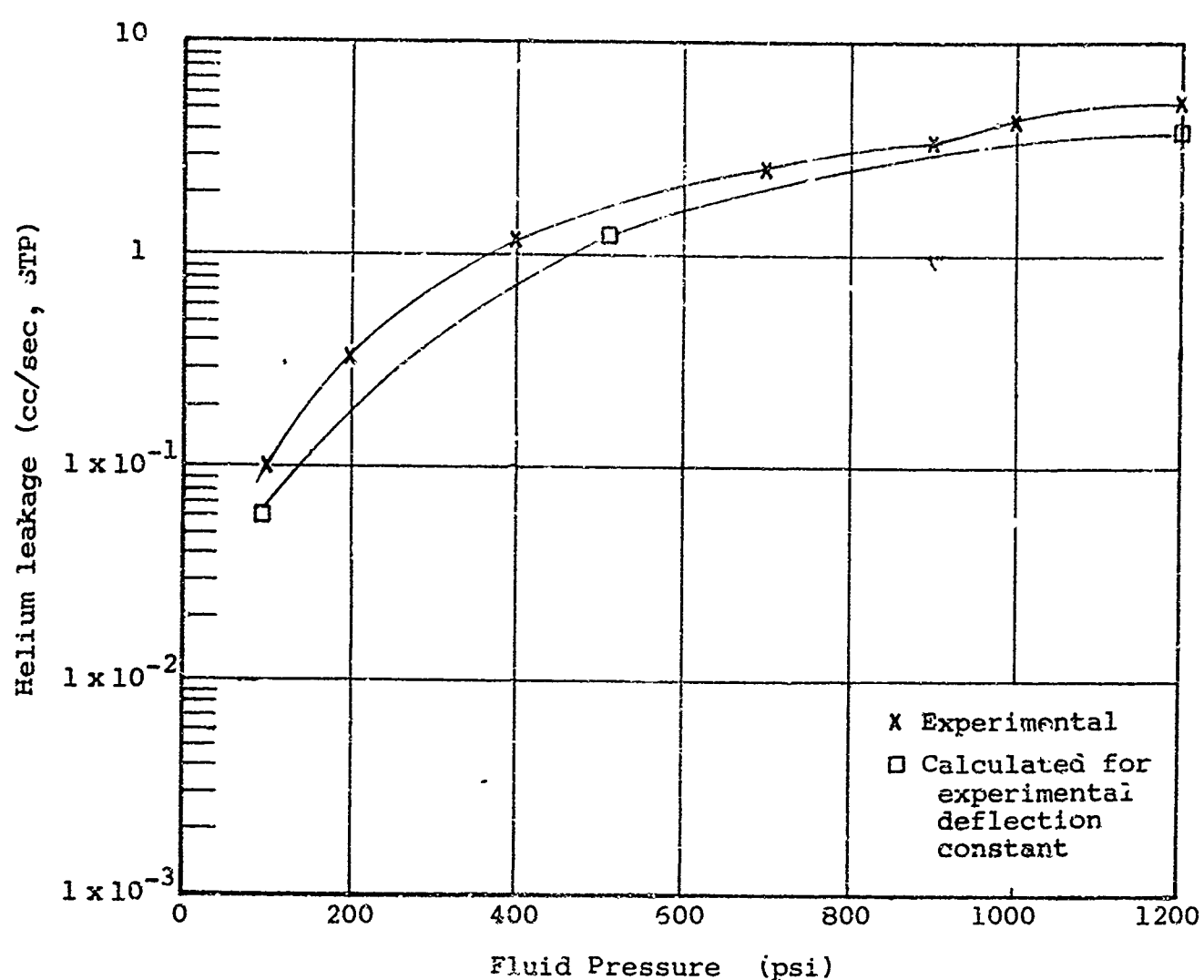


Figure 10-24 Helium leakage as a function of pressure for W-1 seal

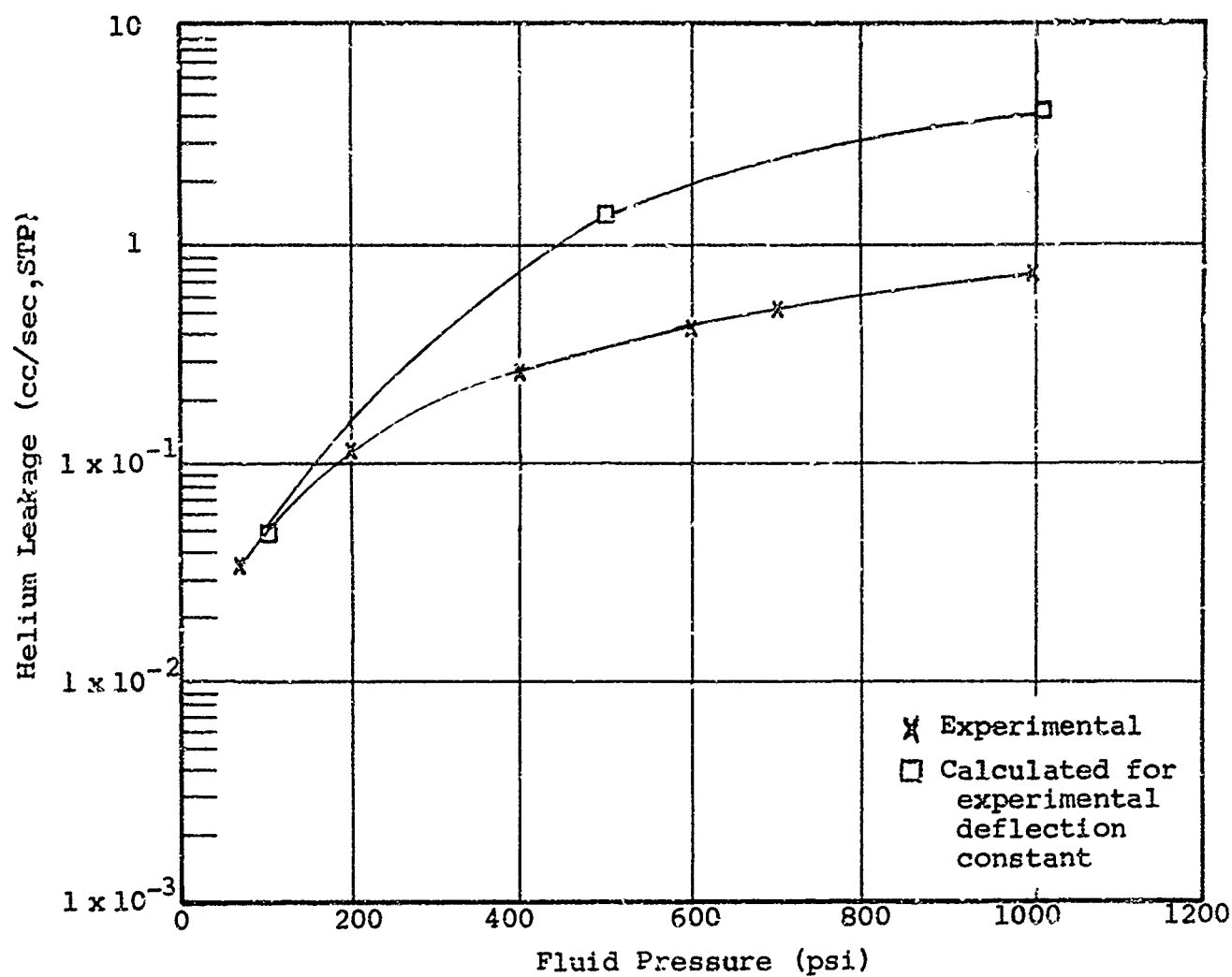


Figure 10-25 Helium leakage as a function of pressure for W-2 seal

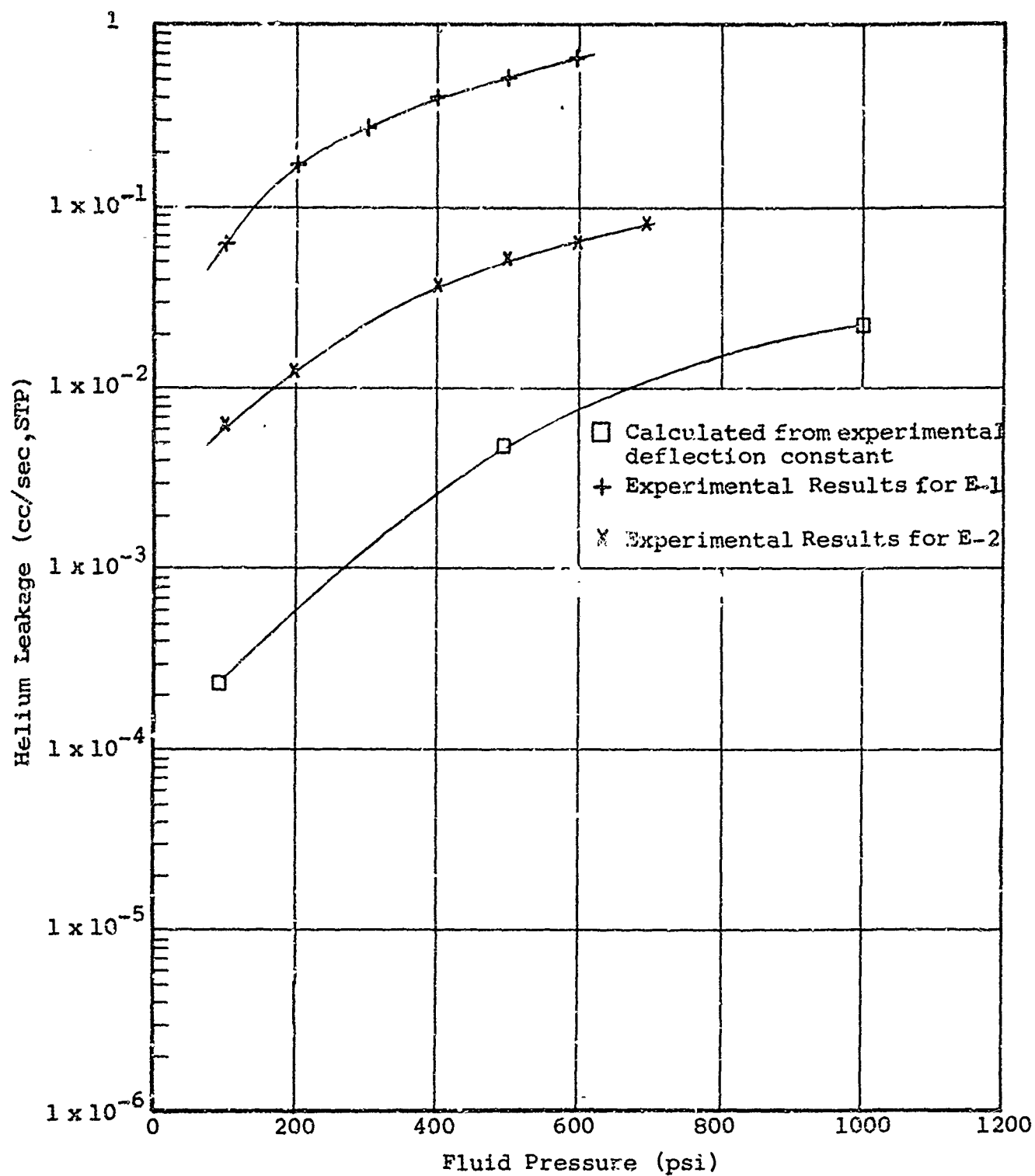


Figure 10-26 Helium leakage as a function of pressure for E-1 and E-2 seals

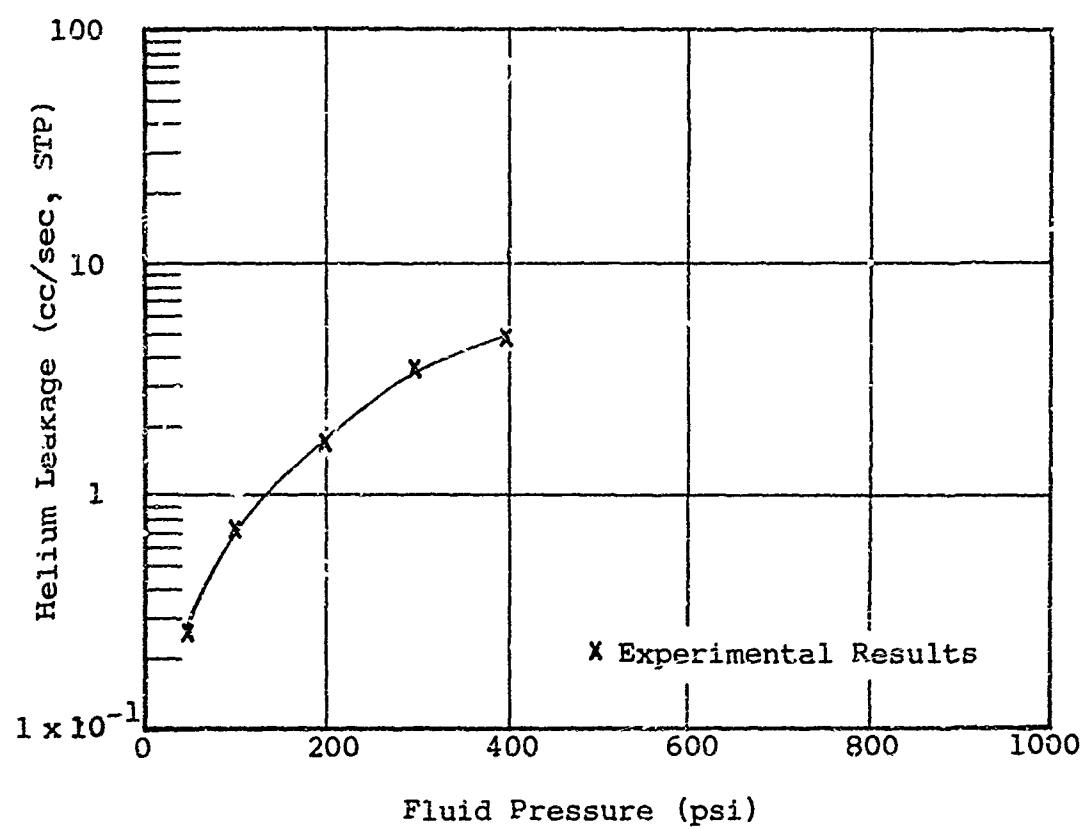


Figure 10-27 Helium leakage as a function of pressure for O-1 seal

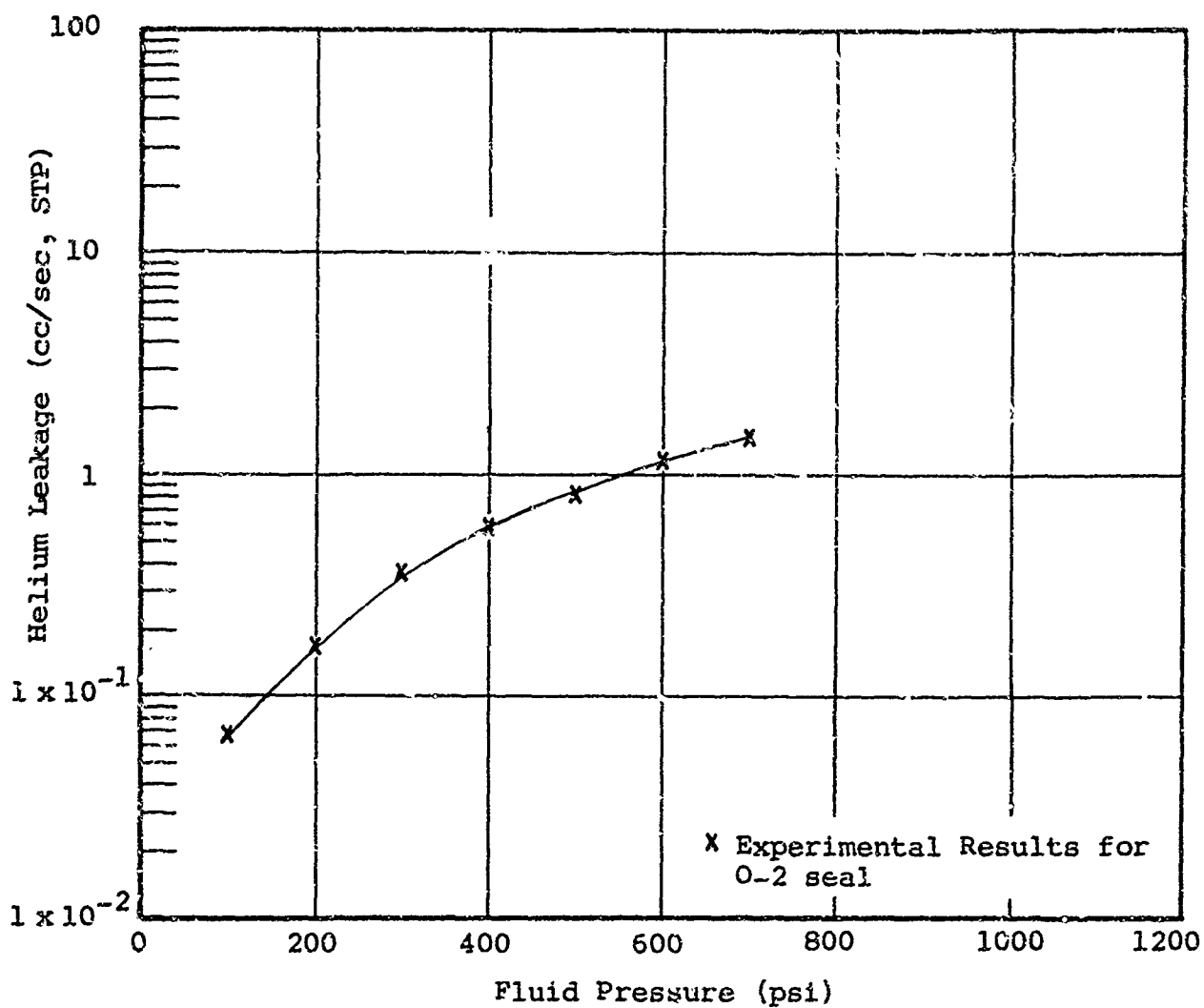


Figure 10-28 Helium leakage as a function of pressure for O-2 seal

Table 10-3

SUMMARY OF THEORETICAL AND EXPERIMENTAL LEAKAGE RATES
FOR VARIOUS SEAL CONFIGURATIONS

Seal	K (Exp) (lb/in. x 10 ³)	C.R.C. (mean) (in.)	K' (Exp) (lb/in./in. x 10 ³)	γ	P Load per in. circumference (lb/in.)	b Interface Depth** (in.)	P/A _A (psi)	Meyer Hardness of the Softer Interface Material (psi)
X-1	420	4.38	96	0.005	480	0.022	21,800	112,000
X-2	1714	10.8	159	0.0083	1320	0.044	30,000	112,000
X-3	260	5.4	48	0.006	286	0.024	11,920	159,000
K-1	215	3.55	61	0.0064	390	0.0164	23,600	112,000
K-2	123	6.3	20	0.0055	110	0.0185	5,960	112,000
W-1	191	6.0	32	0.0048	154	0.0225	6,840	112,000
W-2	133	5.04	26	0.0059	153	0.024	6,380	112,000
W-3	160	5.03	32	0.005	160	0.0226	7,120	112,000
E-1	276	5.88	47	0.0051	240	0.0095	25,200	112,000
E-2	247	5.88	42	0.0064	269	0.0095	28,200	112,000
E-3	163	7.44	22	0.0035	77	0.007	11,000	159,000
O-1	153	4.51	34	0.029	310*	0.0038	---	202,000
O-2	980	8.65	113	0.034	890*	0.0110	---	202,000
C-1	60	0.85	71	0.007	222*	0.005	---	112,000
C-2	210	2.84	74	0.008	300*	0.0067	---	112,000

* Calculated using actual load as given in Appendix V.

** Total depth of all seal interfaces. Usually b except for x seals where the depth is 2b.

*** Meyer index assumed equal to 2.

+ Obtained from figures 2-46 and 2-47.

(a) Lapped surface

(b) Ground surface

Note: $rms \approx \frac{PTV}{4}$.

Table 10-3 (Cont.)

P/A_A $n^{1/2}$ m Modified Stress Ratio	Surface Finish of the Harder Interface Surface (μ in. PTV)	Conductance Parameter (h^3) ⁺	Calculated Helium Leakage Rate, Q_T (cc/sec STP at 100 psi)	Experimental Leakage Rate, Q_E (cc/sec STP at 100 psi)
0.20	10 (a)	2×10^{-22}	2×10^{-5}	2.6×10^{-5}
0.27	10 (a)	1×10^{-22}	1×10^{-5}	6.2×10^{-7}
0.075	10 (a)	3×10^{-17}	4×10^{-2}	---
0.21	75 (b)	2×10^{-20}	3×10^{-4}	4×10^{-3}
0.053	75 (b)	4×10^{-16}	3×10^{-1}	1.6
0.061	10 (a)	4.5×10^{-17}	6×10^{-2}	1×10^{-1}
0.057	10 (a)	5×10^{-17}	5×10^{-2}	3.6×10^{-2}
0.064	10 (a)	4×10^{-17}	4×10^{-2}	---
0.26	75 (b)	2×10^{-21}	2×10^{-4}	6.2×10^{-3}
0.25	75 (b)	2×10^{-21}	2×10^{-4}	6.2×10^{-2}
0.070	10 (a)	3.2×10^{-17}	2×10^{-1}	93
0.4 (assumed)	10 (a)	1×10^{-22}	5×10^{-5}	7.4×10^{-1}
0.4 (assumed)	50 (b)	1×10^{-22}	3×10^{-5}	6.8×10^{-2}
0.4 (assumed)	10 (a)	1×10^{-22}	7×10^{-6}	---
0.4 (assumed)	10 (a)	1×10^{-22}	2×10^{-5}	---

described in Appendix IV. In general, the determination of the actual load deflection characteristics of a seal is a simpler and less involved procedure than leakage evaluation. Thus, in cases where it is not desirable or possible to perform a structural analysis of the seal configuration, it is possible to estimate the leakage performance of a seal, usually to within one order of magnitude, by using experimental load deflection data. Thus, the actual leakage evaluation may be eliminated. However, in any complete seal evaluation, the housing characteristics must be carefully considered in estimating the seal leakage. In the preceding performance estimates, the influence of seal housing deformation was neglected.

10.4 IITRI Lip-Type Sliding Seal

10.4.1 Description

Two lip-type seals, as shown in figure 10-29, were constructed to seal over a 2.00-in. reciprocating shaft. The structural analysis leading to the dimensions of the seal is presented as an example for a Case I structure in Section 7. The seals were fabricated from AISI 414 stainless steel to seal liquids or gases up to 1000 psi.

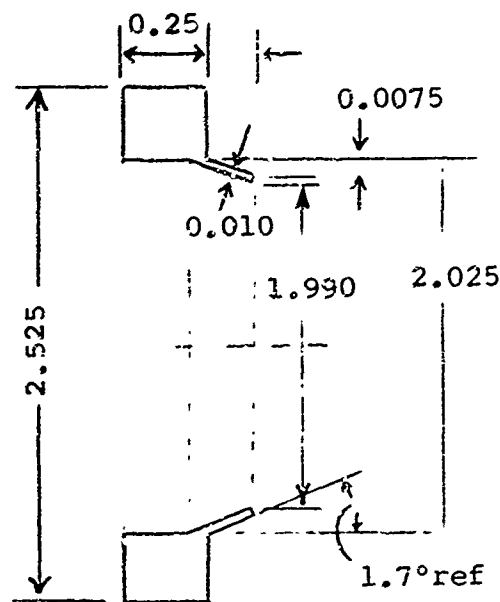


Figure 10-29 Dimensions of a lip-type sliding seal

10.4.2 Experimental Evaluation

The apparatus employed in the following experiments is described in Appendix VI. The experiments were conducted in two phases involving gas and liquids as the sealed fluid. The first phase was an investigation into the degree of interface contact which can be achieved by the flexible lip pressing against a shaft. This consisted of sealing a gas or liquid at pressures up to 600 psi, and measuring the leakage flow at various stroke positions of the shaft and angular orientation of the shaft with respect to the seal. The second phase was an investigation of the effects of wear and interface loading on leakage during long term sliding. Additionally, the fatigue characteristics were experimentally investigated through pressure impulse and sliding cycling.

Phase I Leakage Experiments

The first experiment was conducted with the shaft in a fixed position and the pressure varied. At low pressures, shown in figure 10-30, Seal 1 exhibited substantial leakage indicating poor contact. When the pressure was increased to 100 psi, the leakage began to decrease reaching a minimum of 19 cc per sec at a pressure of 300 psi. As the pressure increased, the leakage rose steadily with the pressure. For Seal 2 at 50 psi, the leakage could not be detected with a mercury bubble leak meter, thereby indicating a leakage of less than 0.001 cc per sec. With an increase in pressure, the leakage increased to 0.077 cc per sec at 100 psi. The rate of change of leakage decreased only slightly at higher pressures with a leakage of 26.2 cc per sec at 600 psi.

A nitrogen gas experiment was also conducted to measure more precisely the variation of leakage rate with various shaft positions. The leakage was measured at nine positions corresponding to one inch increments of stroke. The results, figures 10-31 and 10-32, show that the leakage rate varies considerably over the distance of only 1 in.

Leakage past the lip seals was also measured at periodic intervals during a 280 inch-stroke cycle. Leakage at each interval was measured at three positions of the piston rod. The positions were the two extreme stroke positions and the center position. Figures 10-33 and 10-34 show the leakage characteristics as a function of total stroke. The piston velocity was 4 inches per second during the stroke interval. The piston positions, shown on figures 10-33 and 10-34, refer to the stroke distance in inches from the fully retracted position. The leakage measurements show a slight decrease with increasing sliding distance except for those measurements made at rod position 1 of Seal 2. Rod position 1 of Seal 1 does not appear on figure 10-34 as a necessity due to leakage rates beyond the capabilities of the flow measuring equipment. Although Seal 1 showed a greater decrease in leakage than Seal 2, the leakage of Seal 1 was greater than Seal 2 at the termination of the experiment.

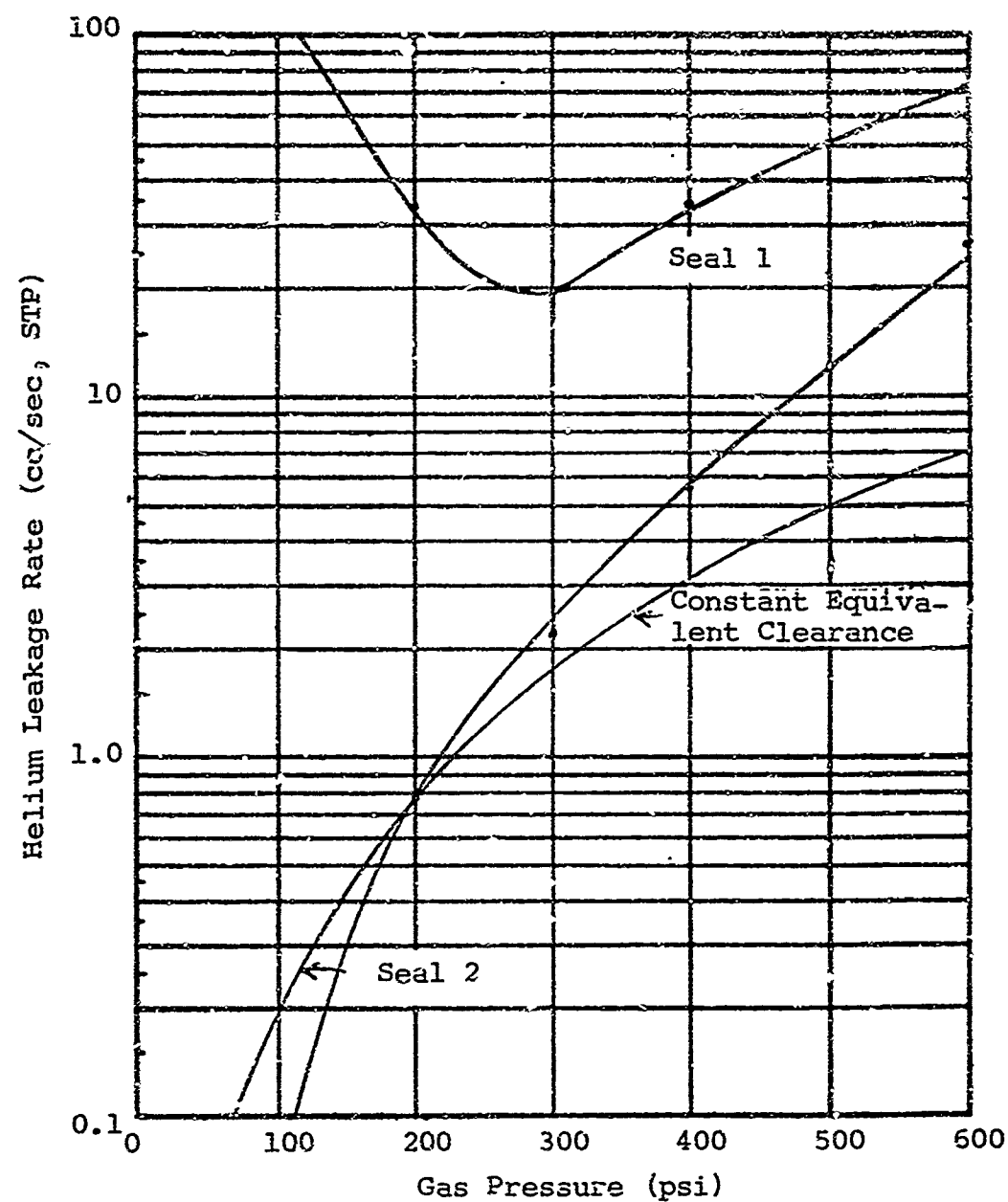


Figure 10-30 Leakage as a function of gas pressure for metallic lip seals

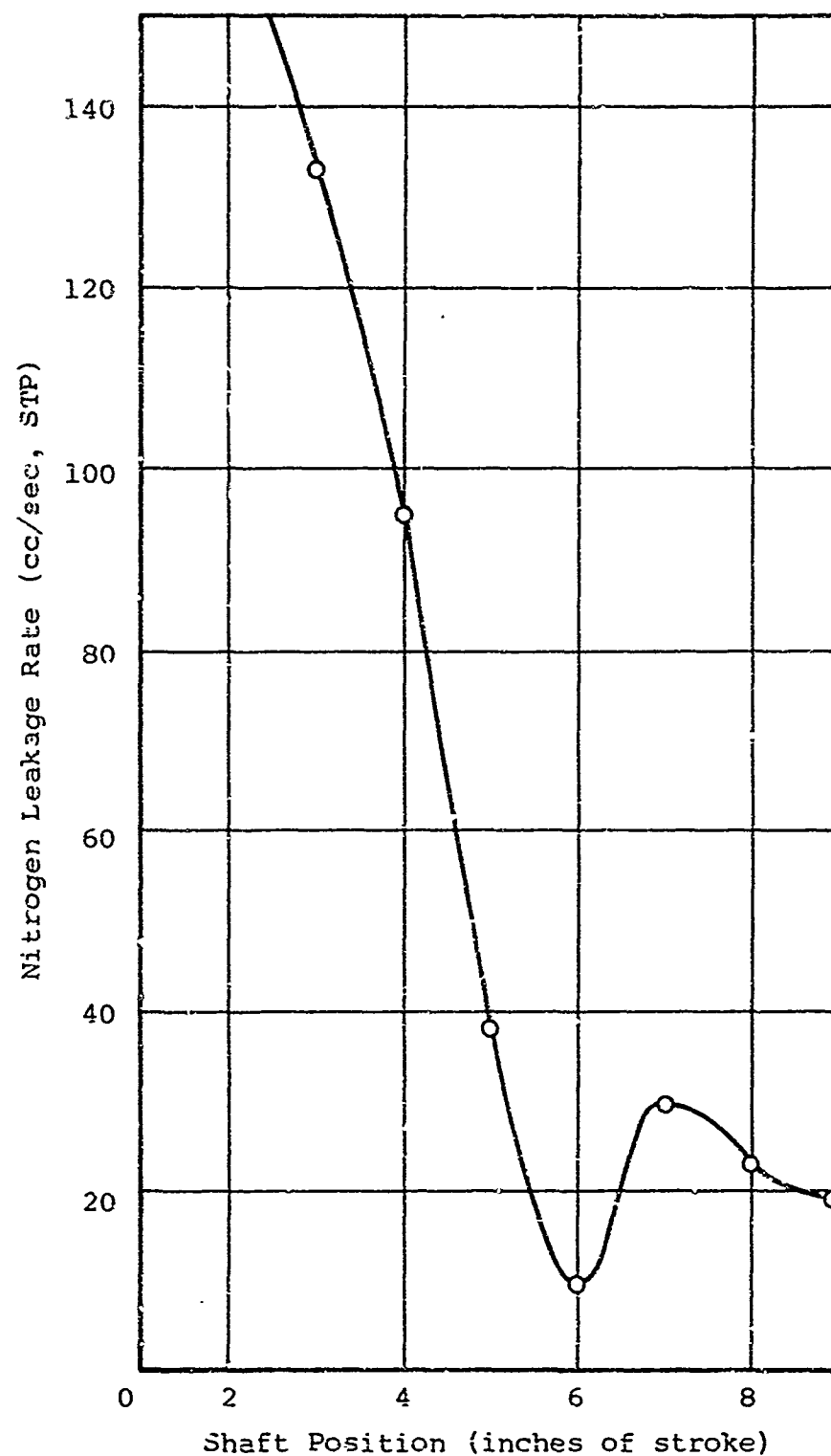


Figure 10-31 Gas leakage as a function of shaft position in seal 1 at 300-psi gas pressure

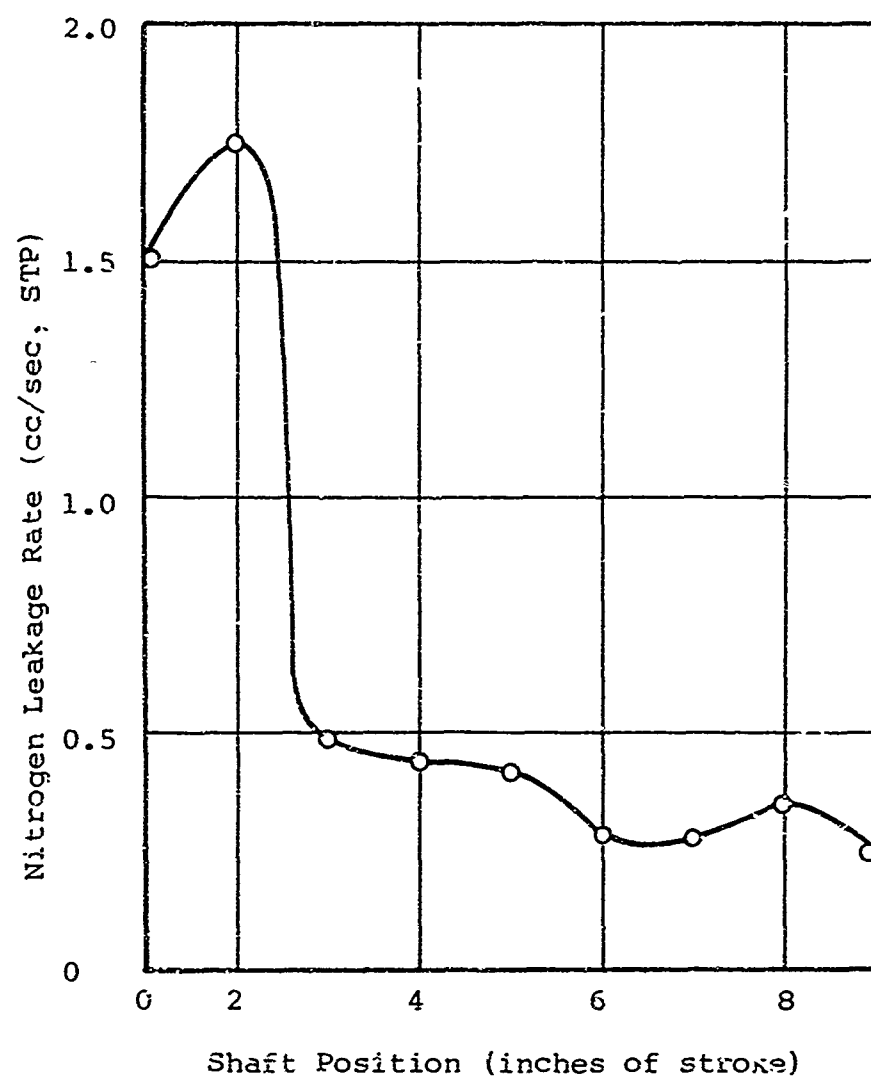


Figure 10-32 Gas leakage as a function of shaft position for seal 2 at 300-psi gas pressure

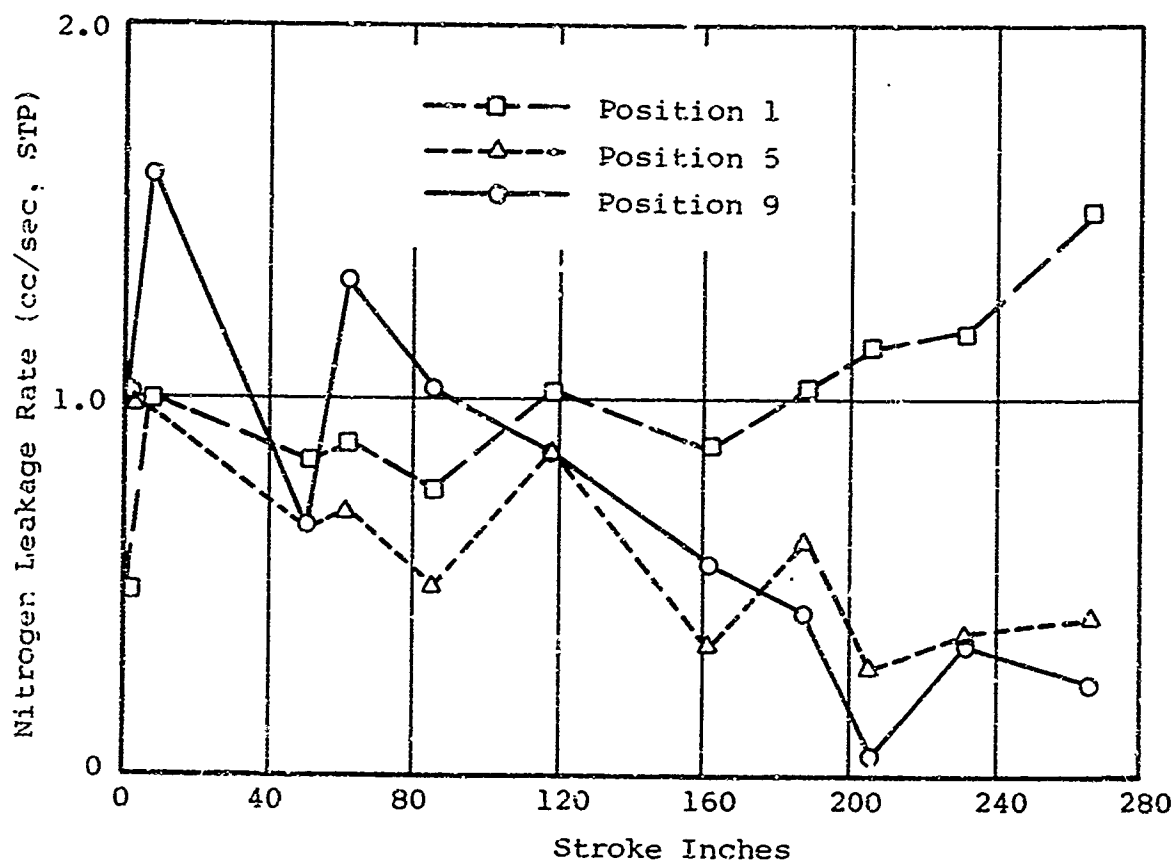


Figure 10-33 Leakage variation during sliding for seal 2 at 300-psi gas pressure

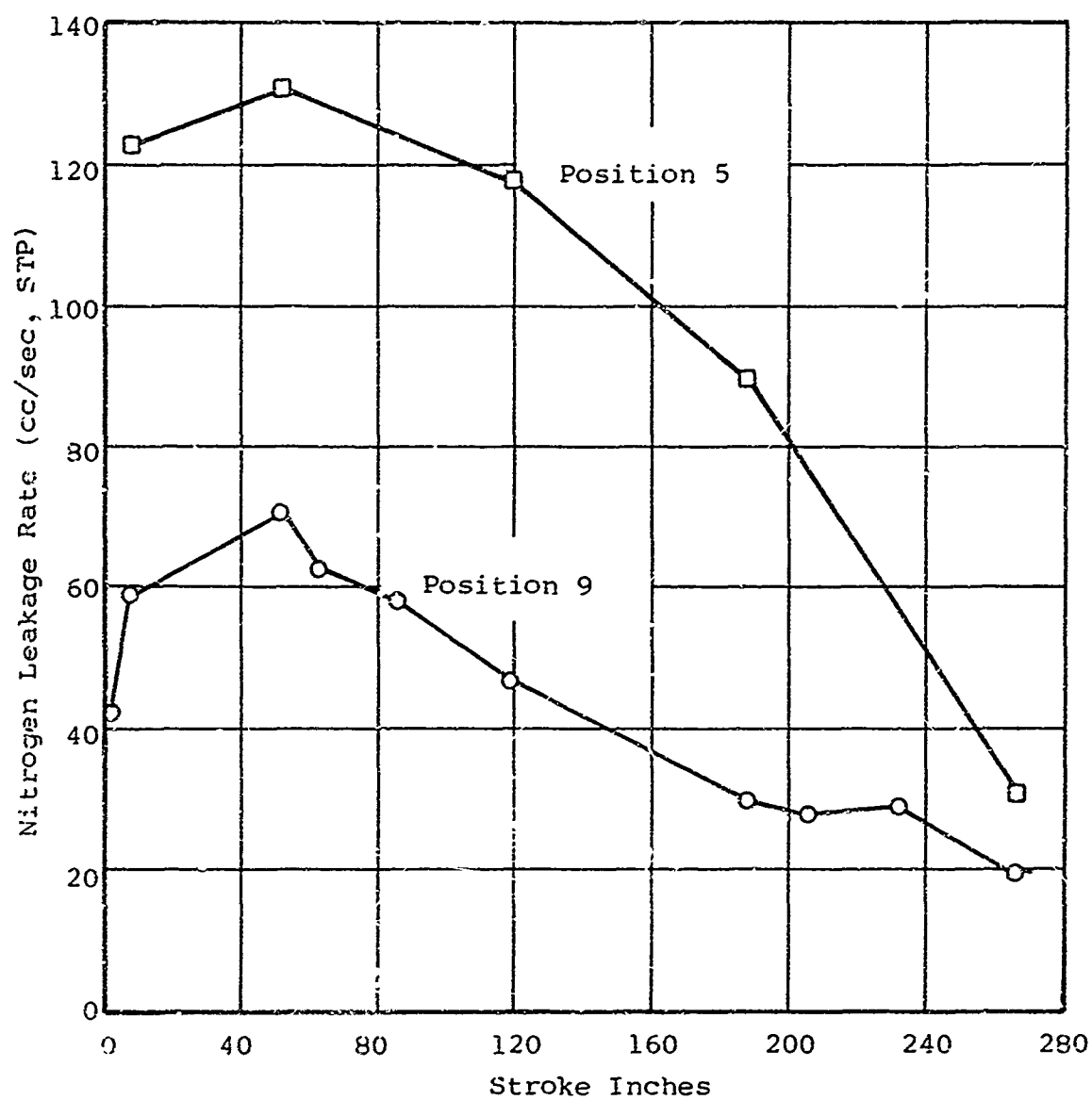


Figure 10-34 Leakage variation during sliding for seal 1 at 300-psi gas pressure

Phase II Leakage Experiments

The experimental apparatus was filled with an oil having a viscosity of 8.03×10^{-6} lb-sec per sq in. at 100° F. The pressure of the sealed oil was varied between 100 and 600 psi. Leakage was measured by collecting it in a graduated cylinder while the apparatus was being cycled. Since the leakage is collected over a long period of time, between two and three hours, the leakage rates obtained were an average value for the time period. The oil leakage characteristics were similar to the gas leakage results.

The first experiment was the measurement of leakage rate at fluid pressures between 100 and 600 psi. The results are shown on Table 10-4 and figure 10-35. The shape of the liquid leakage curves in figure 10-35 are very similar to the corresponding characteristics observed with gas leakage as shown on figure 10-30. One of the seals has a much higher leakage rate than the other at low pressures, but approaches the other at high pressures. Above 300 psi, both curves have the same shape indicating that the initial differences that caused the wide difference in the leakage rates of the two seals at low pressures have been almost eliminated by the effects of the pressure acting on the cantilever section of the seal. The conductance clearance is initially low and rises until 400 psi where it begins to decrease. For Seal 2, the conductance clearance is initially high at 100 psi, and decreases up to 200 psi. The conductance clearance remains constant until 400 psi, where it again decreases. Thus, 400 psi is apparently the pressure at which the pressure actuation of the seals becomes effective.

The sealed fluid pressure was then increased to the 1000 psi design limit of the seals, and a stroke cycling experiment was initiated. Even though the seals were operated for almost four million stroke-inches, there was very little change in the leakage rate. The sliding speed was varied during periodic intervals between 3.3 and 10 ips. The total number of stroke inches at 1000 psi at the end of the experiment was 3.73×10^6 in.. The total distance of sliding under all environmental conditions is over four million inches. The results are shown in Table 10-5 and figure 10-36. It was observed that there was virtually no change in the sealing characteristics of the seals. The large increase in leakage for Seal 2 after two million stroke-inches was a result of replacing a Teflon secondary shaft seal on that shaft. The oil that leaked past the seal is collected in a small cavity between the test seal and commercial Teflon shaft seal where the shaft enters the test chamber. The leakage is channeled out a port in the bottom of the cavity and is collected and measured in a graduated cylinder. Any oil that passes through the secondary seal would not be measured. Until the reading at two million stroke-inches, the leakage past the secondary seal did not appear to be sufficient to affect the leakage measurements. At that point, the leakage measurement

Table 10-4

VARIATIONS IN OIL LEAKAGE FOR VARYING APPLIED PRESSURES

Applied Pressure (psi)	Total Stroke Inches in Oil	Oil Leakage Seal 1 (cc/sec)	Seal 2 (cc/sec)	Equivalent Clearance Seal 1 (μ in.)	Seal 2 (μ in.)	Cycles per Minute
100	11,170	5.55×10^{-5}	7.31×10^{-4}	33.5	79.1	8.67
200	13,050	1.53×10^{-4}	6.12×10^{-4}	40.3	64.1	8.67
300	14,600	3.67×10^{-4}	8.0×10^{-4}	48.8	63.4	8.6
400	16,610	6.81×10^{-4}	9.03×10^{-4}	55.6	61.1	9.35
500	18,590	5.77×10^{-4}	6.81×10^{-4}	49.7	52.5	9.44
600	20,500	4.87×10^{-4}	5.42×10^{-4}	44.4	46.0	9.38

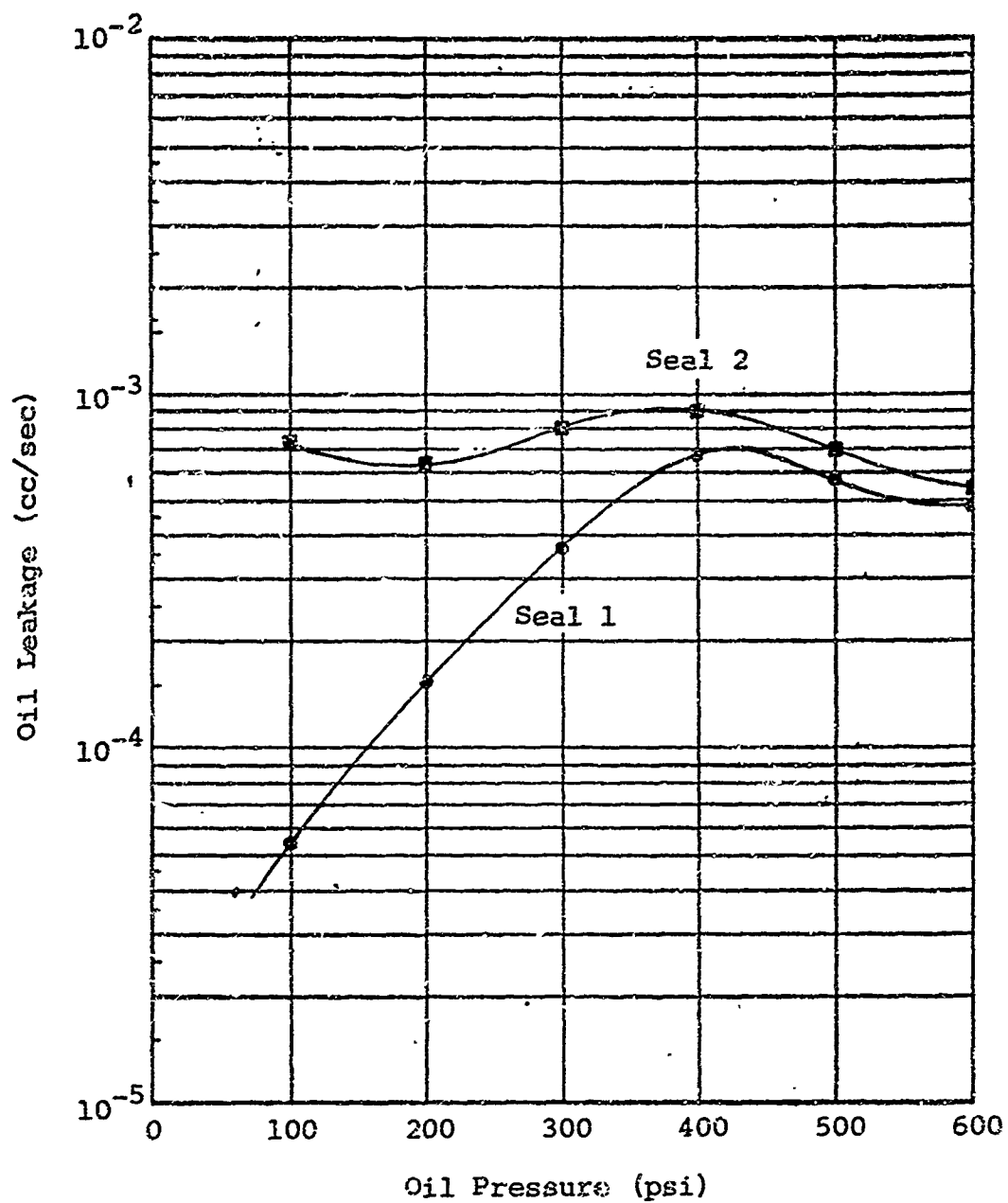


Figure 10-35 Oil leakage for various pressures for metallic lip seals

Table 10-5

OIL LEAKAGE AS A FUNCTION OF TIME AT 1000-POUNDS-PER-SQUARE-INCH PRESSURE

Total Stroke Inches @ 1000 psi	Cycles per Minute	Leakage Seal 1 (cc/sec)	Seal 2 (cc/sec)	Equivalent Clearance Seal 1 (μ in.)	Seal 2 (μ in.)
1.27 x 10 ⁵	36.7	1.96 x 10 ⁻³	7.37 x 10 ⁻⁴	61.9	44.6
4.84 x 10 ⁵	39.4	2.38 x 10 ⁻³	6.95 x 10 ⁻⁴	66.0	43.8
8.84 x 10 ⁵	39.7	2.04 x 10 ⁻³	6.67 x 10 ⁻⁴	62.6	43.2
1.297 x 10 ⁶	39.3	2.21 x 10 ⁻³	7.6 x 10 ⁻⁴	64.4	45.1
1.31 x 10 ⁶	12.46	7.22 x 10 ⁻⁴	5.29 x 10 ⁻⁴	44.3	40.0
1.62 x 10 ⁶	39.6	2.15 x 10 ⁻³	7.09 x 10 ⁻⁴	63.8	44.0
2.02 x 10 ⁶	39.0	2.52 x 10 ⁻³	-----*	67.3	-----
2.26 x 10 ⁶	39.7	2.07 x 10 ⁻³	2.2 x 10 ⁻³	63.0	64.3
2.81 x 10 ⁶	37.9	2.11 x 10 ⁻³	2.23 x 10 ⁻³	63.4	64.6
3.33 x 10 ⁶	0.0**	8.35 x 10 ⁻⁵	1.11 x 10 ⁻⁴	22.1	23.8
3.73 x 10 ⁶	35.4	2.18 x 10 ⁻³	1.85 x 10 ⁻³	64.0	60.6

* Teflon secondary seal leaking badly, replaced for subsequent measurements of leakage

** Stationary at position 5

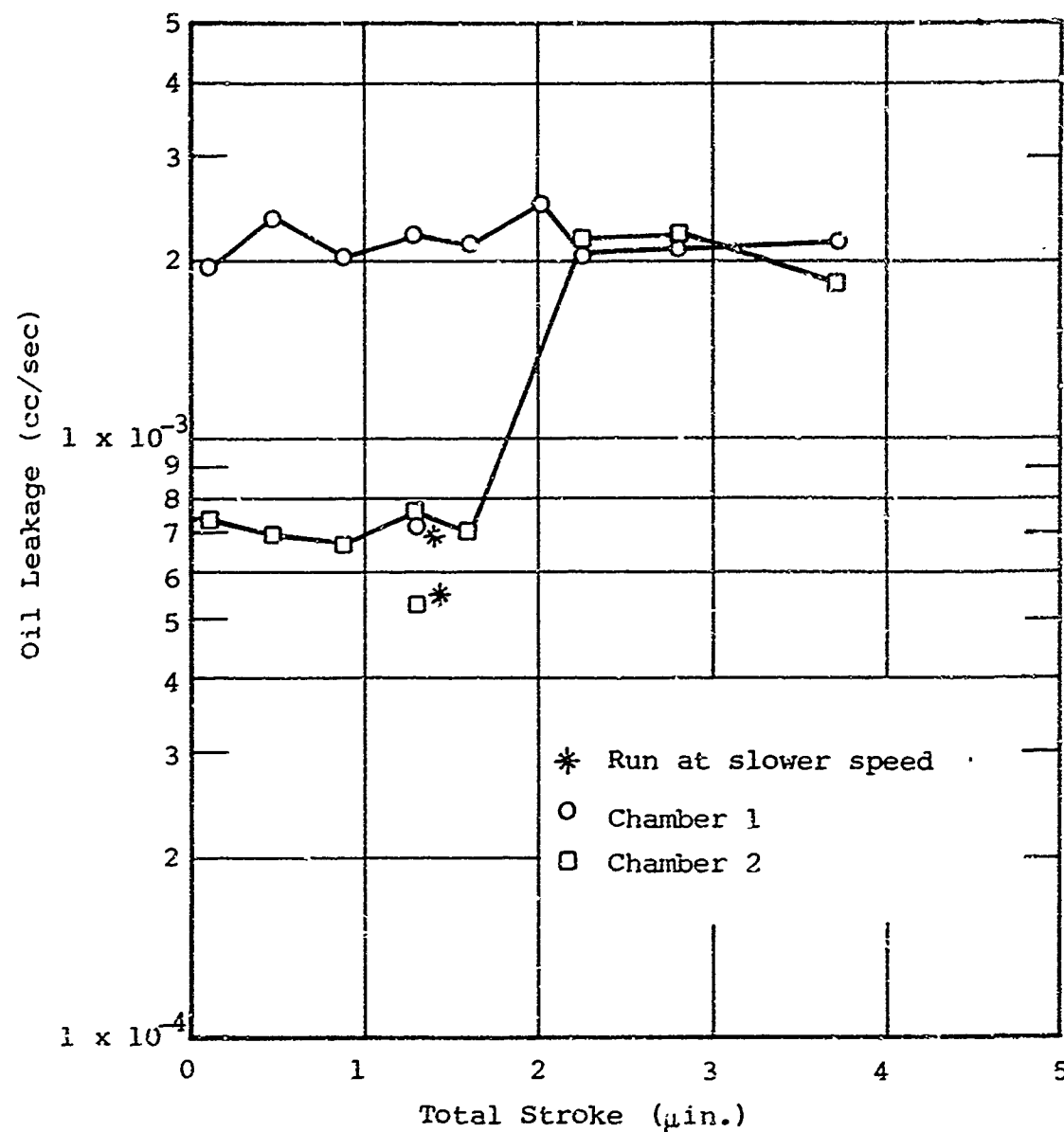


Figure 10-36 Oil leakage at 1000-psi pressure differential as a function of total stroke-inches for metallic lip seal

dropped drastically and it was decided to replace the Teflon elements of the secondary seals. That increase in the subsequent readings indicates that some of the oil may have been past the secondary seal and that the previous measurements were slightly in error.

Sliding velocity was found to have a profound effect on the leakage rate. Most of the measurements were made at a sliding speed of 10 ips. At this speed, the leakages were around 2×10^{-3} cc per sec, and the equivalent clearances were in the range of 60 - 64 μ in. When the speed was reduced to 3.3 ips, the leakages dropped to 7.22×10^{-4} and 5.29×10^{-4} cc per sec. The equivalent clearances dropped to 44.3 and 40.9 μ in. With no motion, the leakage rates were still lower -- 8.35×10^{-5} and 1.1×10^{-4} -- and the equivalent clearances were 22 - 24 μ in. Figure 10-37 shows the leakage variations with sliding speed.

Friction Measurements, Wear, and Interface Contact Loading

The measurement of the friction force during sliding at various gas pressures was made by monitoring the hydraulic pressure to the piston actuators necessary to produce sliding. Knowing the piston area, the friction force could be calculated. From 100 to 600-psi gas pressure, the friction force increased in even increments for every 100-psi increase in gas pressure. A normal contact force was calculated from the friction force using an assumed value of 0.5 for the value of the coefficient of dry friction.

A contact area at each value of fluid pressure was estimated by assuming that the width of interface contact at each pressure was equal to the difference between active length of the seal leg at that pressure and the initial length of the leg. The theoretical active length as a function sealed fluid pressure was determined from the structural analysis in Section 7 of the report. Since the normal load is estimated from the friction force and the coefficient of friction, and interface contact stress can also be estimated. The value of the coefficient of friction is based on experimental results contained in Appendix II. A visual inspection of the seals after 267,500 stroke-inches at 300 psi seal fluid pressure showed a small area of wear near the tip of the lip. Small scratches from previous experiments and from installation made the determination of the exact contact area uncertain. However, the average width of the worn area was less than 1/6 in. The theoretical stress and deflection analysis of the seal leg shows that the active length of the seal should be 0.15 in. at a sealed pressure of 300 psi. Since the free length of the leg is 0.25 in., theoretically the length of contact of the leg should be approximately 0.1 in. This is in fair agreement with the observed interface wear area.

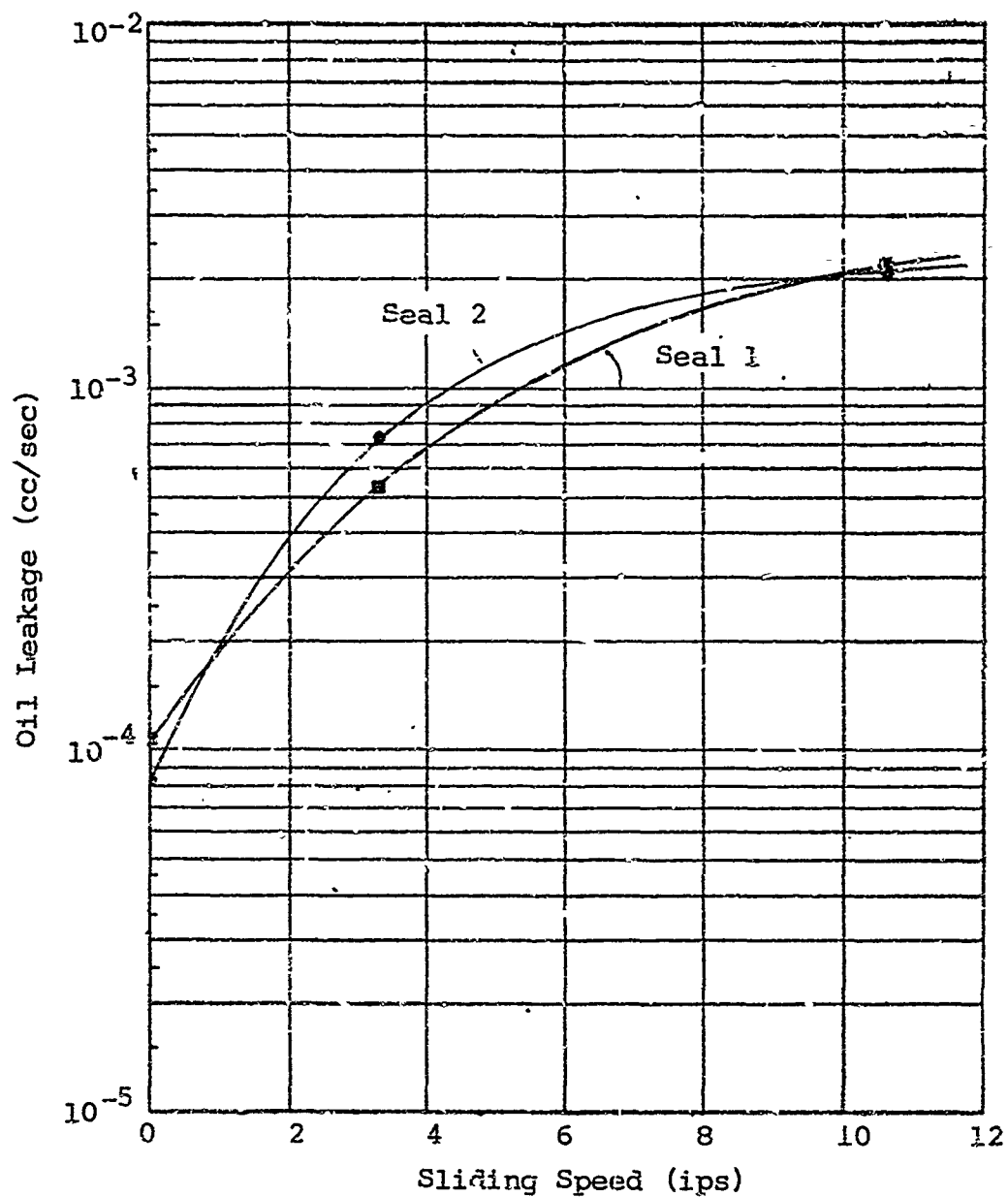


Figure 10-37 Oil leakage at 1000 psi for varying sliding velocities for metallic lip seals

It can be accepted that to keep wear to a minimum in sliding contact application, contact stress must be kept low. This interior is verified by the results of sliding wear investigations contained in Appendix II. When the contact stress on a pair of Nitralloy sliding surfaces was increased from 100 to 200 psi, a rapid increase in wear occurred. Another almost unavoidable effect of high contact stress is an increase in friction force.

The calculated values of contact stress for the lip seals given in Tables 10-6 and 10-7 are relatively low from the sealing viewpoint. These values of contact stress have been shown in previous work to have little effect on the asperity deformation in metal-to-metal contact. The major effect of the low contact stresses in sealing is to minimize the effects of gross surface topography variations such as waviness and out of roundness.

Profilometer measurements on the lip seals showed an initial out of roundness of ~ 0.001 to 0.002 in. at the seal tip. The equivalent clearances calculated from the measured leakage values given in Tables 10-4, 10-5, 10-6 and 10-7 are in most cases less than the measured shaft out of roundness of 0.0001 to 0.0002 in. This indicated that the flexibility of the lip does allow a fair degree of conformity with the sliding shaft.

The flexibility of the reed does allow pressure actuation to occur. This is illustrated on figure 10-30 for Seal 1. The leakage for this seal actually decreases with increasing fluid pressure from 100 to 300 psi. Beyond 300 psi, the leakage increases. The decrease in leakage may be attributed to the action of the pressure forces on the leg, bringing it into closer conformity with the shaft.

In the ideal case of a perfectly round shaft, the degree of conformity is limited by the surface roughness of the shaft and seal. Thus, the effect of pressure actuation will be to reduce the leakage path by deforming the seal and eliminating the effect of its out-of-roundness, and to approach a constant leakage path height, in this case, limited by the surface roughness. The leakage rate will vary as the square of the pressure difference for the condition of laminar compressible flow and constant leakage path height.

A theoretical curve of leakage as a function of pressure difference for constant leakage path clearance is also shown in figure 10-30 based on the equivalent clearance calculated for Seal 2 at 200-psi gas pressure. From the similarity in the shape of this curve and the experimental leakage curves, it appears that a condition of constant leakage path is approached

Table 10-6

SEALING CHARACTERISTICS OF METALLIC LIP SEALS

Seal No.	Pressure (psi)	Leakage (cc/sec, STP)	Theoretical Contact Area (in. ²)	Friction Force (lb)	Contact Stress (psi)	Flow Conductance Parameter (in. ³)	Equivalent Clearance (in.)
1	50	84.5	0.264	26.4	200	7.53×10^{-11}	4.21×10^{-4}
1	100	125	3.83	27.9	146	3.78×10^{-11}	3.35×10^{-4}
1	200	33.3	0.527	30.8	117	3.4×10^{-12}	1.5×10^{-4}
1	300	19.9	0.603	33.7	112	1.03×10^{-12}	1.01×10^{-4}
1	400	34.2	0.647	36.6	113	1.07×10^{-12}	1.03×10^{-4}
1	500	51.2	0.685	39.6	116	1.08×10^{-12}	1.04×10^{-4}
1	600	72.6	0.697	42.5	122	1.09×10^{-12}	1.04×10^{-4}
2	50	---	0.264	26.4	200	---	---
2	100	0.077	0.383	27.9	146	2.34×10^{-14}	2.86×10^{-5}
2	200	0.78	0.527	30.8	117	8.0×10^{-14}	4.3×10^{-5}
2	300	2.2	0.603	33.7	112	1.14×10^{-13}	4.85×10^{-5}
2	400	5.5	0.647	36.6	113	1.72×10^{-13}	5.55×10^{-5}
2	500	12.4	0.685	39.6	116	2.62×10^{-13}	6.4×10^{-5}
2	600	26.2	0.697	42.5	122	3.91×10^{-13}	7.3×10^{-5}

Table 10-7

RESULTS OF CONTINUED CYCLING OF LIP SEAL AT 300-PSI GAS PRESSURE

Seal	Position	Leakage (cc/sec,STP)	Contact Stress (psi)	Leakage Conductance Parameter (in. ³)	Total Stroke- Inches	Equivalent Clearance (in.)
2	1	1.00	109	4.86 x 10 ⁻¹⁴	7,260	3.64 x 10 ⁻⁵
	5	0.97		4.71 x 10 ⁻¹⁴		3.61 x 10 ⁻⁵
	9	1.6		7.78 x 10 ⁻¹⁴		4.26 x 10 ⁻⁵
1	9	59.0	109	2.87 x 10 ⁻¹²	7,260	1.42 x 10 ⁻⁴
2	1	1.02	95.5	4.96 x 10 ⁻¹⁴	119,800	3.66 x 10 ⁻⁵
	5	0.87		4.23 x 10 ⁻¹⁴		3.48 x 10 ⁻⁵
	9	0.86		4.18 x 10 ⁻¹⁴		3.46 x 10 ⁻⁵
1	5	118.1	95.5	5.75 x 10 ⁻¹²	119,800	1.79 x 10 ⁻⁴
	9	47.2		2.39 x 10 ⁻¹²		1.33 x 10 ⁻⁴
2	1	1.5	97.2	7.3 x 10 ⁻¹⁴	267,500	4.18 x 10 ⁻⁵
	2	1.75		8.51 x 10 ⁻¹⁴		4.39 x 10 ⁻⁵
	3	0.49		2.38 x 10 ⁻¹⁴		2.87 x 10 ⁻⁵
	4	0.44		2.14 x 10 ⁻¹⁴		2.77 x 10 ⁻⁵
	5	0.42		2.04 x 10 ⁻¹⁴		2.72 x 10 ⁻⁵
	6	0.29		1.41 x 10 ⁻¹⁴		2.42 x 10 ⁻⁵
	7	0.28		1.36 x 10 ⁻¹⁴		2.38 x 10 ⁻⁵
	8	0.35		1.7 x 10 ⁻¹⁴		2.56 x 10 ⁻⁵
	9	0.24		1.17 x 10 ⁻¹⁴		2.26 x 10 ⁻⁵
1	3	133.0	97.2	6.47 x 10 ⁻¹²	267,500	1.86 x 10 ⁻⁴
	4	95.0		4.61 x 10 ⁻¹²		1.66 x 10 ⁻⁴
	5	30.8		1.5 x 10 ⁻¹²		1.14 x 10 ⁻⁴
	6	9.75		4.74 x 10 ⁻¹³		7.8 x 10 ⁻⁵
	7	29.7		1.44 x 10 ⁻¹²		1.13 x 10 ⁻⁴
	8	23.1		1.23 x 10 ⁻¹²		1.04 x 10 ⁻⁴
	9	19.2		9.34 x 10 ⁻¹³		9.76 x 10 ⁻⁵

as expected. Further evidence of a fairly constant leakage path, or a limit on the conformability of the lip is shown by the close comparison between the values of equivalent clearance calculated from both gas and oil leakage results. Thus, the leakage results indicate that, while the pressure force can overcome to a large extent, the effects of the initial out-of-roundness of the flexible lip, certain limits exist on the conformability of the seal to the mating surface.

The flexibility of the seal leg allows it to conform to variations in the position of the shaft. A dial indicator was mounted near the seal in order to measure the amount of wobble in the shaft. The shaft in seal chamber 1 showed a displacement of 0.0004 in. as it moved from one end point to the other; the shaft in seal chamber 2 showed a displacement of 0.0001 to 0.0002 in. These values are considerably larger than the values of equivalent clearance shown in Table 10-7 which are derived from the experimental results. The value of clearance for the seal in seal chamber 1 ranges from 7.8×10^{-5} to 1.86×10^{-4} in., and the clearance for the seal in seal chamber 2 ranges from 2.26×10^{-5} to 4.26×10^{-5} in. The calculated clearance is less than the shaft side movement. This indicates the ability of the seal to function in the presence of a limited amount of shaft side motion.

The phenomenon of decreasing gas leakage with time, shown in figures 10-31 and 10-32, is somewhat similar to the slight decrease in leakage that occurred in the initial stages of the investigation of sliding wear desired in Appendix II. The decrease in leakage is attributed to the additional conformity caused by a small amount of wear occurring at the interface. In the case of the Nitralloy as a function of Nitralloy sliding wear experiments (Appendix II) a steady state condition was achieved after approximately 50,000 stroke-inches at 100 psi contact stress. After this steady state wear process had been reached, leakage and friction remain practically constant for 47,200 stroke-inches of sliding. These values increased only after the contact stress was increased to 200 psi.

The relatively constant lip seal leakage rate achieved during the long oil leakage experiment (figure 10-36) shows that a steady state wear condition was also achieved.

The contact stress was greater than in the gas leakage evaluation of the lip seal since the oil pressure was 1000 psi. However, this was a case of lubricated sliding. In any event the results do show that a steady-state wear process can be achieved if the proper conditions of contact stress are present.

The lip seals were also subjected to rapid pressure cycling evaluation to determine the fatigue characteristics of the design. In this experiment the shaft of the sliding seal apparatus was held stationary at its midstroke position. The sealed chambers were alternately pressurized to 1000 psi and vented by a solenoid valve. The pressure rise from 200 to 1000 psi in the pres-

sure chambers took approximately 20 msec. Thus, the seals were subjected to shock loading. The solenoid valve was oscillated at a rate of 30 cycles per minute. Leakage from each seal is shown on Table 10-8. Because of the extremely low leakage rate, leakage was collected over long periods of time, usually several hours. The results shown on Table 10-8 represent average leakage rates over many impulse cycles. The relatively constant and low leakage rate indicates that the seal has the ability to function under severe shock loading conditions.

Table 10-8

RESULTS OF PRESSURE SHOCK TEST ON METALLIC LIP SEALS

Cycles	Leakage Rate (cc/sec)	
	Chamber 1	Chamber 2
12,100	2.3×10^{-5}	2.3×10^{-5}
16,460		
25,700	1.9×10^{-5}	2.8×10^{-5}
31,050		
46,590	1.7×10^{-5}	2.8×10^{-5}
52,470		
53,310	Experiment Terminated	

Pressure rise 200 psi to 1000 psi

Approximate rise time 20 msec

Pulsing rate 30 per min.

11. CRITERIA FOR THE USE OF ADHESIVES AND SEALANT MATERIALS IN SEAL APPLICATIONS

The information presented in this section is not intended as a comprehensive survey of all adhesives and sealants. Rather, it is a superficial survey to identify sealants and adhesives that can be used as sealants along with some information about their properties and applications. The general applications of these materials are in the interfaces of demountable, semi-demountable, and nondemountable seals, depending on the properties of the materials. The purpose of such materials is to clog the interface void spaces thus minimizing leakage.

11.1 Adhesives

The materials usually encountered in rocket propellant systems are mostly metals, together with some elastomers and plastic materials. The adhesives used in rocket propellant systems, therefore, would be those that can successfully bond metals, plastics and elastomers to each other or to themselves. Adhesives capable of bonding these materials with a reasonable strength include:

- epoxides
- phenolics
- isocyanates (urethanes)
- cyanoacrylates
- neoprene rubber bases
- polysulfide elastomer bases
- silicone elastomer bases
- nitrile rubber bases
- butyl rubber bases
- ceramics
- hot melts (phenoxy, phenol formaldehyde, polyvinyl acetate, polyethylene, etc)
- such combinations as epoxy phenolic and phenolic elastomers

Of these adhesives, only the epoxides, phenolics, isocyanates, cyanoacrylates, and ceramics polymerize or set after cure into hard and rigid solids, more or less infusible and insoluble. The hot melts, as the name indicates, soften up at higher temperatures and are limited in application to a certain temperature range. Some of the elastomers, such as silicone bases, have surprisingly high thermal resistance. In general, however, elastomers tend to soften or deteriorate rather quickly with temperature.

Because no one adhesive has the required properties to bond all materials of interest, or to give the best performance for all possible conditions, more than one adhesive are often combined to obtain a system combining the properties or characteristics of the individual constituents. For instance, the rigid, highly cross-linked and temperature resisting structure of phenolics is combined with the more elastic structure of elastomers to yield a phenolic elastomer capable of higher deformation, good resistance to shock loads, and a relatively high thermal resistance. This is an improvement over both individual components, i.e., the rigid and somewhat brittle phenolic, and the pure elastomer with its low temperature resistance.

The properties of adhesives can be modified in many ways, as by the addition of: 1) diluents to decrease viscosity, 2) fillers to increase viscosity, decrease shrinkage, 3) plasticizers and flexibilizers to increase elasticity of the bond, or 4) resinous modifiers to alter the basic chemical character of the adhesive base. The proper combination of these different constituents, to obtain the best adhesive system for a given application, is usually referred to as formulation.

The best adhesive for a particular application cannot be determined solely from the standpoint of physical properties of the adhesive. Many other characteristics, of which cure is probably the most important, must be taken into consideration. With the exception of hot melts and ceramics, all adhesives set by polymerization, and this reaction must be induced by heat or the presence of the proper catalyst. The time required for the reaction to be completed and the application of heat when needed, constitutes the cure.

If a relatively large structure is to be bonded, and the strongest bond can be obtained with an adhesive that requires high temperature cure, it may be very difficult or impractical to heat the whole structure to the required temperature. In such a case, a room-temperature-curing adhesive may be indicated.

11.2 Sealants

Sealants are used to make structural joints leak-tight, and/or electrically insulated. Because they must adhere to the surfaces they seal, they have common characteristics with adhesives. Actually the same chemical species are many times used in both applications, the only difference being the function, i.e., if the main purpose is to support a load, it would be termed an adhesive; if to fill a void or close an interstice, it would be called a sealant.

Since the load-supporting requirements in a sealant are usually small or totally lacking, strength is a property that can be sacrificed to obtain other more desirable characteristics.

This actually increases the freedom in selecting and using adhesive materials for sealing applications.

Sealants that may have possible applications in the aerospace field parallel the list of adhesives previously considered. Some of the important ones are:

- epoxides
- phenolics
- silicones
- polysulfides
- isocyanates
- nitriles
- neoprene
- ceramics

Since, in general, sealants will be in contact with fluids, one of the most important considerations in selecting the proper material for a given application is chemical compatibility. Useable temperature range is probably next in importance, and practical considerations such as cure, handling and surface preparation, physical strength, aging, toxicity, permeability, and, in some cases, color and odor must also be taken into consideration. Typical properties are shown on Tables 11-1, 11-2 and 11-3 obtained from Reference 1.

It is difficult to generalize about the chemical resistance of sealants. Since there are many polymer systems and compounding ingredients available for making a wide variety of sealants, there is a sealant and a method of sealing to satisfy almost every need. Chemical resistance depends not only on the nature of the material, but also on surface erosion rate and permeation, and on temperature. Furthermore, chemical effects can be of two types; irreversible chemical attack and swelling in water or solvent.

In general, epoxides, phenolics, polyethylenes, and dense glazed ceramics are considered chemically resistant. Among the rubbers, neoprene and butyl are resistant by virtue of low permeability, and silicone because of its hydrophobic nature.

In order of decreasing heat resistance, sealants can be listed as:

- (1) ceramics
- (2) silicones
- (3) phenolics

- (4) epoxys
- (5) organic rubbers

Ceramics are the only systems for temperatures above 1000°F. Silicones can probably go up to 600°F, while phenolic-nitrile-epoxy combinations have been reported usable for short times up to 500 to 600°F. Epoxides are usually limited to 400 to 500°F.

Low temperatures can also introduce severe problems; since polymeric materials, in general, tend to stiffen and embrittle with low temperatures. Silicones and polyurethanes perform rather well at low temperatures.

Typical present aerospace applications of sealants are: sealing of propellant tanks, coatings, door and hatch seals, and other cabin and bulkhead seals. Methods of applications vary from hand spraying, brushing and troweling, to pressure gun application and simply "fill and drain." Most of these applications are of a more-or-less permanent nature, i.e., the parts being sealed are seldom, if ever, taken apart. Modern sealants are rarely used in applications where the seal is taken apart frequently or occasionally. This is probably due to the rather high physical strength of most modern sealants, which would make disassembly difficult. Most gasketing and pipe compounds consist simply of highly filled unsaturated oils, and are quite different chemically from the sealants here considered.

This is perhaps one area where further development might be profitable. If a modern sealant can be developed, with good thermal resistance, suitable chemical properties, excellent adhesion, but a very low cohesive strength, then it could be used for helping seal reusable seals, since easy disassembly would be possible. Although there seems to be a trend in this direction, no presently available system can satisfy this need.

11.3 References

- 1-1 "Elastomeric Sealants - Where and How to Use Them,"
Materials in Design Engineering, 61, No. 2, 87, (1965).

Table 11-1

MECHANICAL PROPERTIES OF ELASTOMERIC SEALANTS

Material	Adhesion (lb-in.)	Shrinkage (%)	Elongation (%) (ASTM D 412)	Tensile Strength (psi)	Shear Strength (psi)	Abrasion Resistance
Butyl	-----	0-3	600-800	2500-3000	150-200	Good
Chlorosulfonated Polyethylene	15-100	10-20	75-125	500-600	40-100	Exc
Fluoroelastomer	-----	3	150-325	1200	125-175	Good-Exc
Neoprene	50-75	-----	200-350	1000-1500	-----	Exc
Polysulfide	7-50	1-3	150-500	50-125	125-175	Fair-Good
Silicone	20-40	0.2-0.6	50-150	400-750	250-350	Fair-Good
Urethane	18-30	0.1	250-600	100-3000	125-350	Exc

Table 11-2

ENVIRONMENTAL AND ELECTRICAL PROPERTIES OF ELASTOMERIC SEALANTS

Material	Temp Range (°F)	Aging Prop.	Weather- ability	Chemical Resistance			Dielectric Strength (v/mil)	Vol Res (ohm-cm)
				Alkalis	Acids	Solvents		
Butyl	-80-300	Good	Good	Good	Good	Poor	250-600	10 ¹⁶
Chloro- sulfonated polyethylene	-45-300	Exc	Exc	Exc	Good- Exc	Fair	300-600	10 ¹¹
Fluoro- elastomer	-65-450	Exc	Exc	Poor	Exc	Good	300-450	10 ¹¹
Neoprene	-45-300	Good- Exc	Good	Fair- Good	Good	Fair	300-600	10 ¹¹
Polysulfide	-60-275	Good	Good	Fair	Fair	Good	250-350	10 ¹¹ - 10 ¹²
Silicone	-60-700	Good- Exc	Exc	Poor- Fair	Fair- Good	Poor	400-600	10 ¹⁴ - 10 ¹⁵
Urethane	-60-300	Good	Good	Fair	Poor	Fair- Good		

Table 11-3
PROCESSING CHARACTERISTICS OF ELASTOMERIC SEALANTS

Material	Available Forms	Method of Application	Curing Conditions
Butyl	One component solvent types, tapes, contact bonding	Calking gun, spread coating, trowel, putty knife	Rm temperature, long time for complete cure
Chlorosulfonated Polyethylene	One and two component systems with solvent	Calking gun, brush, spatula, spread coating	Rm temperature, 1-14 days
Fluoroelastomer	One and two component	Calking gun, spatula, brush, spread coating	Rm temperature, 24 hours
Neoprene	One and two component	Brush, calking gun, spread coating	Rm temperature, 7-14 days, cures by solvent evaporation
Polysulfide	One and two component cans and prepared cartridges	Calking gun, brush, trowel, putty knife, spread coating	Rm and elev temperature
Silicone	One or two component liquids in tubes, prepared cartridge cans	Calking guns and tubes, spatula, putty knife	Cures at rm or elev temperature by chemical reaction
Urethane	Two component liquids cured by chemical reaction	Calking gun, brush, trowel, putty knife	Rm or elev temperature

12. EMPIRICAL CORRELATION OF PARAMETERS FOR RUBBER INTERFACES

In identifying and correlating the parameters that influence the leakage path in plastically deformed metals and plastics and elastically deformed metals (Section 2), we did not include rubber materials for two reasons. First, the deformation of rubber materials is expected to be completely elastic, even on the microscopic scale. Secondly, the parameter correlation was based on the hardness (plastic flow), a property having no real analogy in rubber. In developing criteria for rubber seals, we have used the same general format, i.e., considering the interface as an independent part of the seal and correlating the parameters that influence interface deformation.

12.1 Material Properties and Interface Deformation

Rubber materials are most often characterized by their heterogeneous composition. The molecular composition of these materials varies widely and it is beyond the scope of the present work to include a discussion of this topic. Even on the macroscopic scale, the materials vary widely, depending upon the basic material and fillers. Consequently, a discussion of the behavior of rubber materials is relegated to their gross volume properties.

Volume properties of rubber materials are more numerous and less comprehensive than those associated with other materials. For example, volume properties are often measured by cold bending a specific shape O-ring at a given temperature; flexural fatigue is measured by continuously rotating a ring over a set of rollers; and compatibility is measured by volume change in specific fluids. These properties, plus many others, are measured according to specific test requirements which are standardized. It would not be profitable at this point to discuss each standardized test criterion because:

- There are several standards and each is quite complicated.
- The volume properties obtained from these tests produce relative data. The results are beneficial when one material is compared with another but not for a quantitative description of the properties of the materials.
- Most of these properties, while influential to the sealing interface, are not the predominant factors in sealing. Since the state-of-the-art of rubber sealing can be termed undeveloped, it is more advantageous to develop basic criteria using no more parameters than necessary.

Because of the preceding problems, rubber materials are assumed to be homogenous, i.e., each material is constructed in a chemically similar manner and with volume properties that are not

relative but can be given in a quantitative manner. Of particular interest are those properties that are related to interface deformation.

The two properties, assumed significant, are the modulus of elasticity and hardness. It is recognized that the deformation of rubber is complex, dependent upon the geometry of the material nonlinear with load. Consequently, rubber does not possess a true modulus of elasticity as defined for metals in Section 2. For simplicity, however, it is assumed to exist and describes either an average stress-strain slope or a point slope. Since the modulus depends upon a varying definition from one condition and material to another, it is seldom used as a material property in commercial practice.

Hardness, on the other hand, is often used to describe a rubber material. The term hardness, however, is a misnomer when viewed as a plastic deformation characteristic as in metals. Actually, the hardness of rubber is a relative measure of its elastic properties. The most common measurement is the Shore hardness test.

Shore hardness is measured with an instrument known as a durometer. The instrument is composed of a spring-loaded indenter having a specific shape. The indenter is pressed against a rubber surface and an almost constant rate spring loads the indenter and deforms the rubber surface to a depth determined by the "hardness" (elastic nature) of the material. The depth of the penetration is measured by a dial indicator calibrated in units apparently arbitrarily chosen and which have become standardized over a period of years. A number of instruments are available for various materials. Table 12-1 contains a summary of the various durometer instruments.

12.2 Surface Topography and Interface Deformation

In Section 2, it was stated that rubber materials deform elastically and suggested that 100 per cent interface contact between a rubber and a solid surface will occur when the normal contact stress σ , is equal to the modulus of elasticity E . The relative deformation was defined as

$$\% \frac{h_o - h_f}{h_o} = \frac{\sigma}{E} \times 100\% = E \times 100\% \quad (12-1)$$

where h_f = final leak path dimension

h_o = initial leak path dimension

$$\sigma = \frac{P}{A_A} = \frac{\text{Load}}{\text{Apparent Contact Area}}$$

Table 12-1
SHORE HARDNESS MEASURING INSTRUMENTS (Ref. 12-1)

Durometer		Mainspring	Indentor	For Use on:
Quadrant Style	Round Style			
Type A Code QA (ASTM D676 & ASTM D1706)	Type A-2 Code XA	822 gm	Frustum cone	Soft vulcanized rubber and all elastomeric materials. Natural rubber, GR-S, GR-I, Neoprene, nitrile rubbers, Thiokol, flexible polyester cast resins, polyacrylic esters, etc. Also used for wax, felt, leather and other materials.
Type B Code QB	Type B-2 Code XB	822 gm	Sharp 30° included angle	Moderately hard rubber such as typewriter rollers, platens, etc. Also used for testing "green" ceramic tile.
Type C Code QC	*	10 lb	Frustum cone	Medium hard rubber and plastics.
Type D Code QD (ASTM D1484 & ASTM D1706)	*	10 lb	Sharp 30° included angle	Hard rubber and the harder grades of plastics such as rigid thermoplastic sheet, Plexiglas, polystyrene, vinyl sheet, cellulose acetate and thermosetting laminates such as Formica. Also paper filled calender rolls, calender bowls, etc. Also preform hardness of phenolic molding materials.
Type O Code QO	Type O-2 Code XO	822 gm	3/32 in. Sphere	Soft printers rollers, Artgum, etc. Also medium density textile windings of rayon, Orlon, Nylon, etc.
Type OO Code QOO	*	4 oz.	3/32 in. Sphere	Sponge rubber and plastics. Also low density textile windings. Not for use on foamed latex.

*Not available in round style durometer.

If it is assumed that h_o is equivalent to the initial surface roughness, then the leak path dimension is solely a function of the load and modulus. Proceeding further, consider a rubber gasket pressed against a solid under varied assumed ratios of σ/E and solid surface roughness, h_o . The leak path dimension, h_f , can be calculated from equation (12-1). Since the leakage rate may be expected to vary with $(h_f)^3$, the relative effects of parameters on leakage can be described as shown on Table 12-2.

Table 12-2

RELATIVE EFFECT OF PARAMETERS ON LEAKAGE ASSUMING $(h_f)^3 \sim Q$

$\frac{\sigma}{E}$	Surface Roughness, h_o , ($\mu\text{in.}$)		
	10	80	300
	$h_f^3 (\text{in}^3)$		
0.1	720 (10^{-18})	370 (10^{-15})	270 (10^{-12})
0.2	640 (10^{-18})	260 (10^{-15})	240 (10^{-12})
0.4	215 (10^{-18})	110 (10^{-15})	180 (10^{-12})
0.6	64 (10^{-18})	32 (10^{-15})	120 (10^{-12})
0.8	8 (10^{-18})	4.1 (10^{-15})	60 (10^{-12})
1.0	0	0	0

A review of Table 12-2 shows that, theoretically, the initial surface finish of the solid should have a substantial effect on leakage. For example, at a given contact stress, the leakage rate for an 80 $\mu\text{in.}$ surface should be three orders of magnitude less than a 300 $\mu\text{in.}$ surface. Experimental leakage measurements on a butyl gasket of 70 Shore A mated against 80 and 300 $\mu\text{in.}$ steel surfaces showed an insignificant difference at low contact stresses but greater variation at high stresses. These results, shown on figure 12-1, do not conform to the theoretical predictions on Table 12-2 where the largest variation occurs at low stress while zero leakage is predicted at the same stress or $\sigma/E = 1$. This discrepancy cannot be theoretically explained solely on the basis of surface deformation around asperities. Apparently the substrate has a substantial influence.

The experimental deviation of leakage in the higher stress region (>800 psi) is attributed to permeation leakage variations within the rubber material. This effect is demonstrated by the flattening of the curve where leakage becomes virtually independent

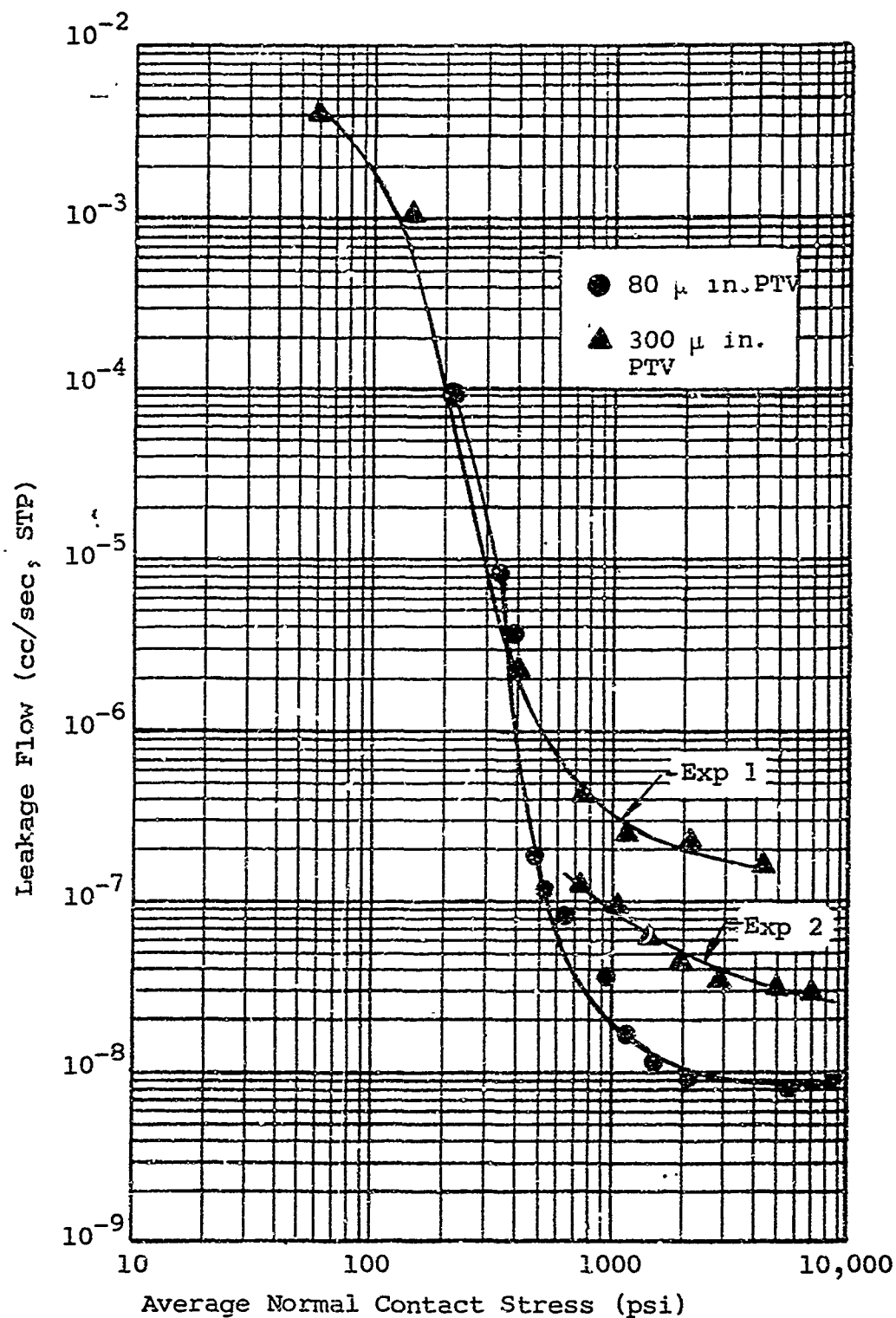


Figure 12-1 Leakage characteristics of butyl materials mated against 80 and 300 μ in. PTV turned steel surfaces

Based on the experimental results obtained, it may be concluded that surface finish is not an important factor in sealing with rubber materials. Further experimental investigations are necessary before sufficient evidence will be obtained to completely substantiate this conclusion.

A detailed description of the conductance parameter is contained in Section 2.5. Rather than repeat the development and significance of this parameter, the reader should refer to that section for the details. However, one aspect of the conductance parameter must be qualified when applied to very soft materials.

418

A summation of forces action at one interface is:

$$P_n - \int_{x=0}^{x=X} bp(x) dx - \int_{x=0}^{x=X} b\sigma(x) dx = 0 \quad (12-2)$$

where

P_n = net flange load

$\sigma(x)$ = contact stress at any point x

$P(x)$ = fluid pressure at any point x

b = depth of the interface normal to flow

If the second term is negligible with respect to the first and third terms, the average stress at the interface becomes

$$\sigma_{avg} = \frac{P_n}{Xb} \quad (12-3)$$

The preceding discussion is particularly pertinent to the development of empirical correlations from experimental leakage measurements. In the process of measuring leakage through sealing interfaces, the influence of the pressure gradient force must be minimized.

12.4 Correlation of Parameters

The parameters influencing rubber interfaces can be identified as load, apparent geometry, and the relative hardness of materials. Each of these parameters is to be correlated together by the conductance parameter. The parameters of chemical composition of materials, surface topography, and fluid pressure forces in the interface are tentatively neglected.

To achieve such a relationship between parameters, leakage experiments were made on flat rubber gaskets and the conductance parameter was calculated. Because of the range and variation in leakage data, it was impossible to perform a manual correlation of results. Consequently, a mathematical curve-fitting method was employed. The procedures are described in Appendix VIII. To portray the over-all development of criteria, a flow chart is presented in figure 12-3.

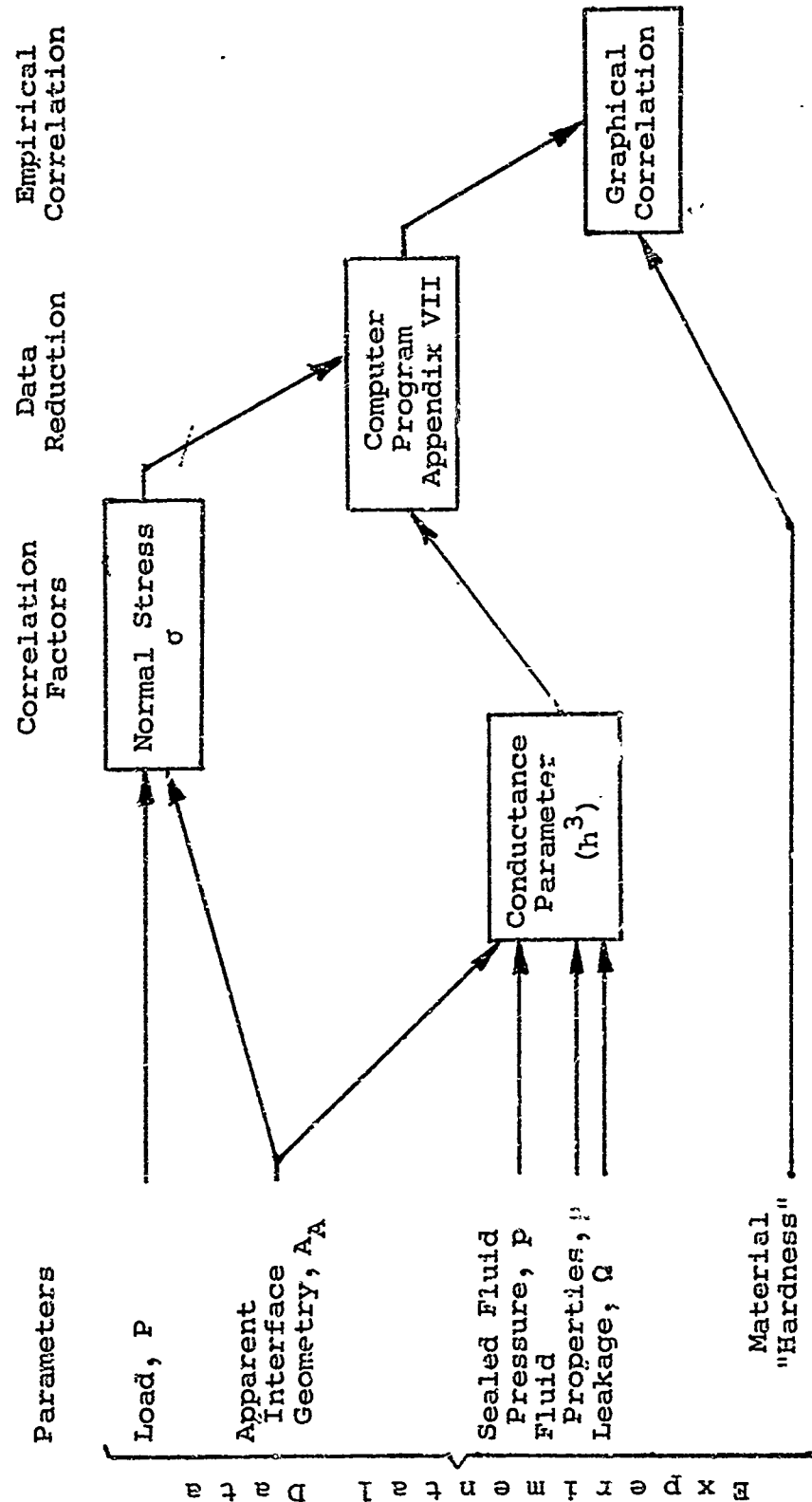


Figure 12-3 Flow chart of the correlation process for rubber interface parameters

12.4.1 Leakage Experiments

Leakage experiments were made using the apparatus shown schematically on figure 12-4. Circular rubber gaskets possessing an almost square cross section were installed into the fixture and a variable load was applied to the flanges. The radial movement of the gasket was restrained by an inner and outer retaining ring. Thus, the load applied was distributed over a fixed area of gasket surface.

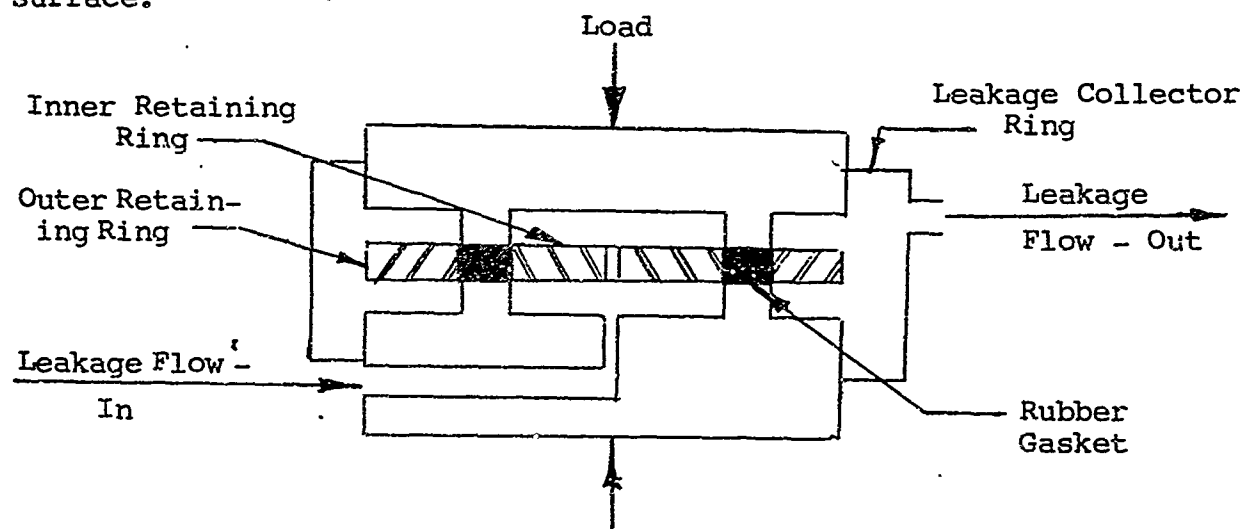


Figure 12-4 Rubber gasket evaluation apparatus

Two methods of measurement were employed to measure helium leakage introduced at 34 psia into the center of the gasket. A capillary-tube bubble-displacement method was used to measure leakage-flow into the cavity above 10^{-3} cc per sec. When leakage rates below 10^{-3} cc per sec were encountered, a CEC leak detector was employed. The latter measurement method is based on a leakage out principle and accomplished by collecting gasket leakage using a collector ring surrounding the experimental apparatus.

Butyl, Viton, Buna-N, and Silicone gaskets were evaluated. The gasket dimensions were 2.50-in. OD, 2.23-in. ID, and 0.125-in. thick. The hardness of the materials is given as:

Experimental Number	Rubber	Hardness Shore A
R-1	Butyl	67
R-4	Butyl	67
R-3	Silastic	62
R-2	Viton	65-75
R-5	Viton	70-75
RU-4	Buna N	68

The leakage results for the various materials as functions of the normal contact stress are shown on figures 12-5, 12-6, 12-7, and 12-8. The leakage characteristics below 2000 psi contact stress are generally similar for all materials evaluated. At higher contact stresses, the leakage rate does not change appreciably with contact stress. The leakage characteristics in this region were attributed to permeation effects.

12.4.2 Empirical Correlation

Leakage data were reduced by the data reduction process described in Appendix VII. The results obtained were in the form of mean leakage values as a function of normal interface contact stress. These data were reduced to form a mean conductance parameter-stress relationship by applying the theoretical leakage flow equation described in Section 2. The conductance parameter identified as (h^3) in.³ was further reduced by obtaining the cube root and defining the result as the conductance clearance, h . The mean conductance clearance is shown on figure 12-9. The relationship shows that the conductance clearance varies almost inversely with contact stress. An equation, describing the curve on figure 12-9 is

$$h = \frac{7.1 (10^{-4})}{\sigma} \quad (\text{for a 70 Shore-A Material}) \quad (12-4)$$

where h is measured in inches and σ in pounds per square inch.

The influence of material hardness was determined by combining the mean leakage data for 70 Shore-A materials with leakage data of varying hardness materials contained in Reference 12-2. A leakage rate of 1×10^{-4} cc per sec was chosen as a reference leakage rate. The corresponding interface stress was then related to the Shore A hardness, as shown on figure 12-10. The relationship between hardness and contact stress is approximately

$$\sigma = 2.74 (10^{-4}) H^{3.25} \quad (12-5)$$

where the units are σ in psi and H as Shore-A hardness.

Since the leakage rate is constant and a function of the conductance parameter,

$$Q_{70} = f(h_{70}^3) = Q_{90} = f(h_{90}^3) = \dots = Q_n = f(h_n^3) \quad (12-6)$$

where the subscript represents hardness and

$$h_{70} = h_{90} = \dots = h_n \quad (12-7)$$

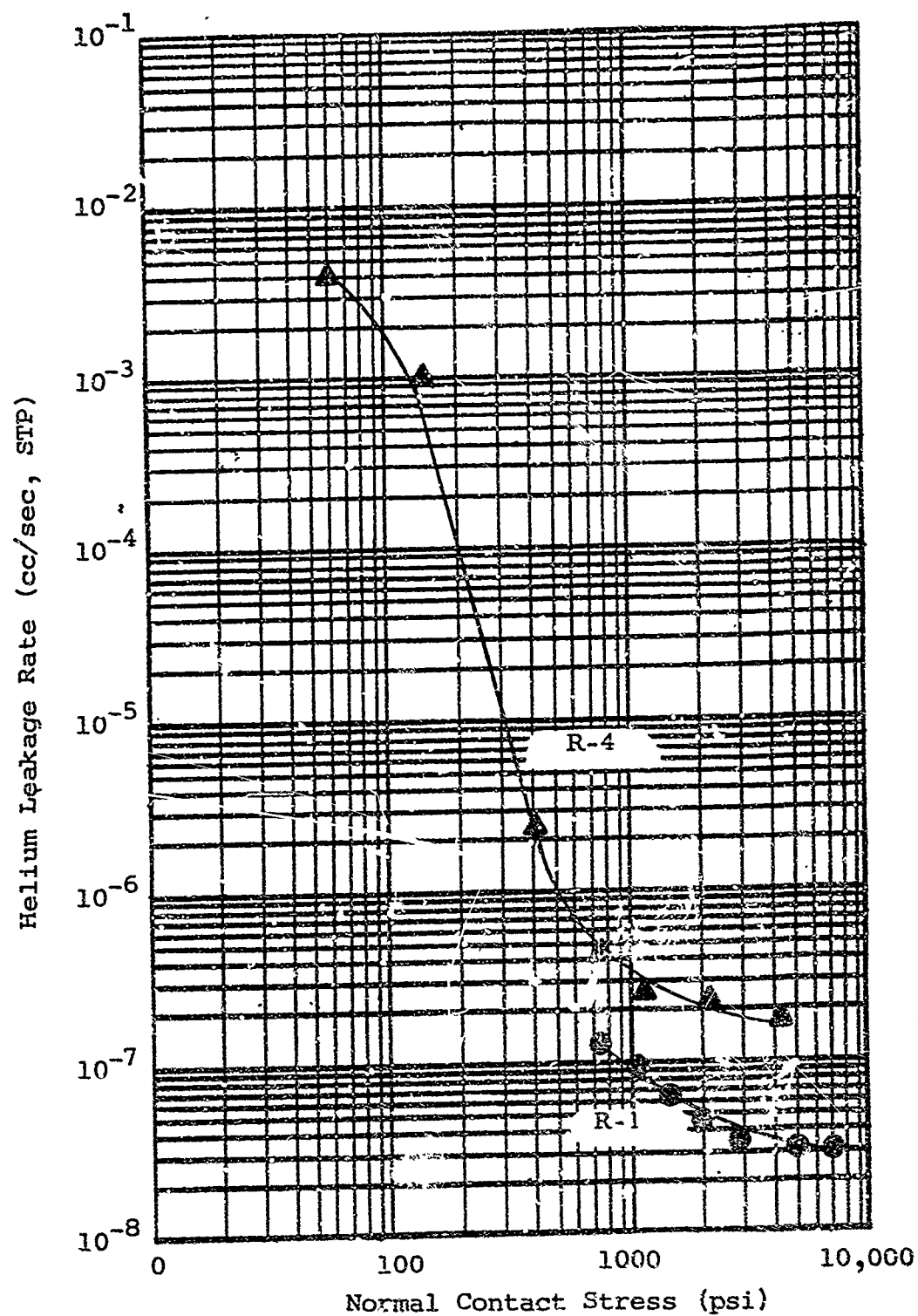


Figure 12-5 Leakage characteristics of butyl materials mated against a 100-PTV turned steel surface

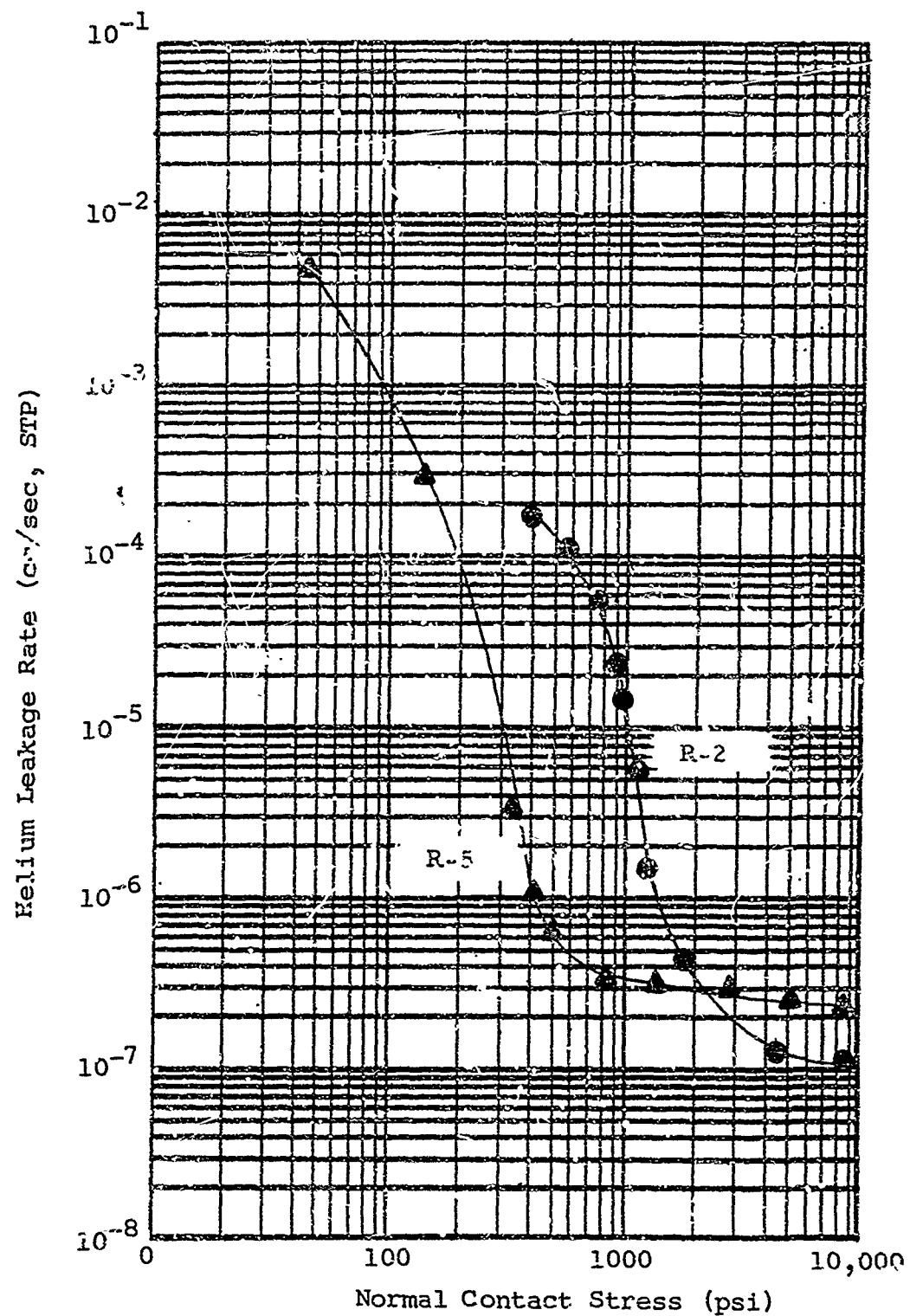


Figure 12-6 Leakage characteristics of Viton materials mated against a 100-PTV turned steel surface

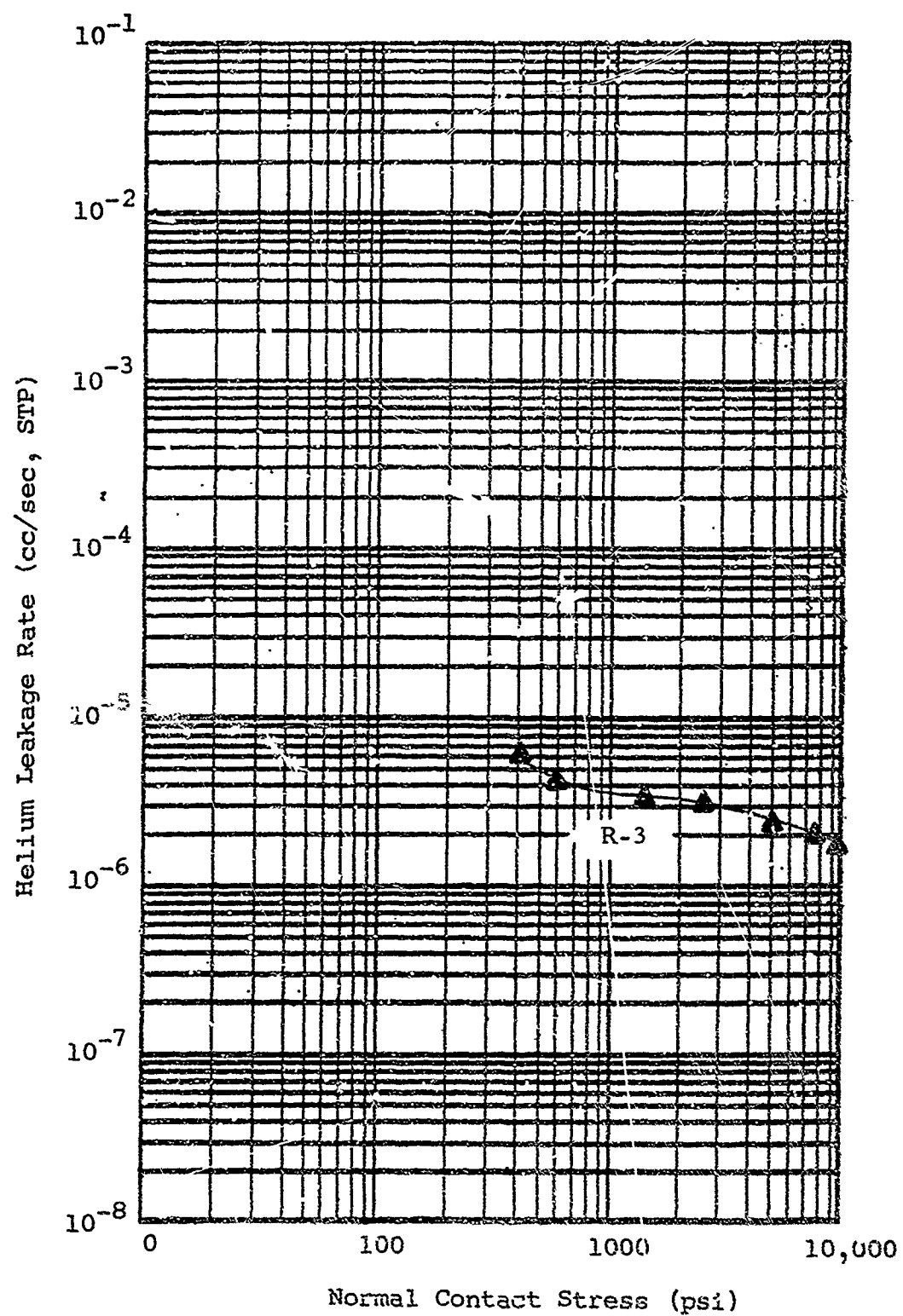


Figure 12-7 Leakage characteristics of silastic materials mated against a 100-PTV turned steel surface

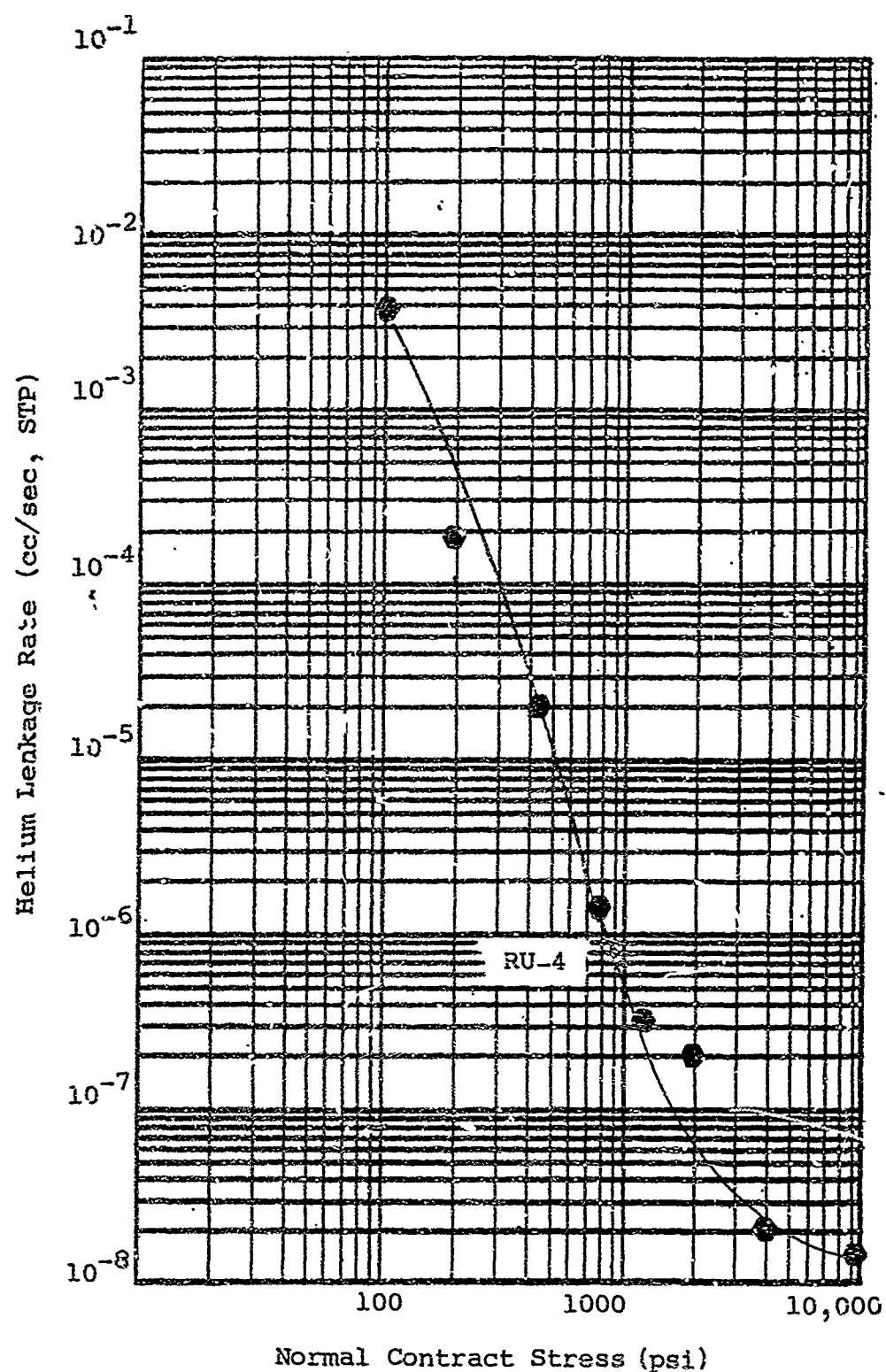


Figure 12-8 Leakage characteristics of Buna N materials mated against a 100-PTV turned steel surface

When the relationship given by equation (12-4) is assumed, the conductance clearance for a 70 Shore-A material at the stress shown on figure 12-10 is

$$h = \frac{7.1(10^{-4})}{270 \text{ psi}} = 2.63 \text{ } \mu\text{in.} \quad (12-8)$$

Applying the conditions imposed by equation (12-7)

$$h_{70} = 2.63 \times 10^{-6} = h_{90} = \frac{K_{90}}{\sigma_{90}} = h_n = \frac{K_n}{\sigma_n} \quad (12-9)$$

Substituting the data shown on figure 12-10 into equation (12-9) yields values of the constant K , as shown on figure 12-11. The conductance clearance for any rubber material is

$$h = \frac{K_f(H)}{\sigma}$$

where $K_f(H)$ is obtained from figure 12-11. An approximation for the functional relationship $K_f(H)$ was obtained by curve fitting techniques;

$$h = \frac{5.7 \times 10^{-10} H^{3.25}}{\sigma} \quad (12-10)$$

A review of the preceding expression shows that each of the interface parameters is represented. It must be emphasized that the formula is derived from a minimum of experimental data and, therefore, its validity must be accepted with caution.

12.5 Observations

The interface deformation of rubber is almost proportional to the applied load. This is demonstrated by the inverse relationship between the leakage path (conductance clearance) and contact stress as shown on figure 12-9. The hypothesis of elastic deformation is supported by this result.

At low normal loading, equivalent to stresses less than 1000 psi, the predominant leakage occurs at the interface formed by the rubber and solid materials. Higher loads produce close conformability at the interface and the leakage rate reaches an almost constant value, suggesting the predominance of permeation flow. A correlation can be made between the experimentally obtained helium permeation flow rates and air permeabilities for various materials. A direct correlation cannot be made because of the complexity of the permeation path and confined gasket geometry. Table 12-3 shows the experimental results compared to air permeability.

The permeability of an elastomer by gases, particularly air, is of interest where rubber components are required to maintain gases under pressure at room as well as elevated temperatures. Such applications occur in bladders used to contain a pressurized gas and in mechanical seals that must prevent leakage and pressure loss. Aside from the loss of pressure, the deterioration of the rubber caused by the permeating gases, particularly oxygen, is of concern.

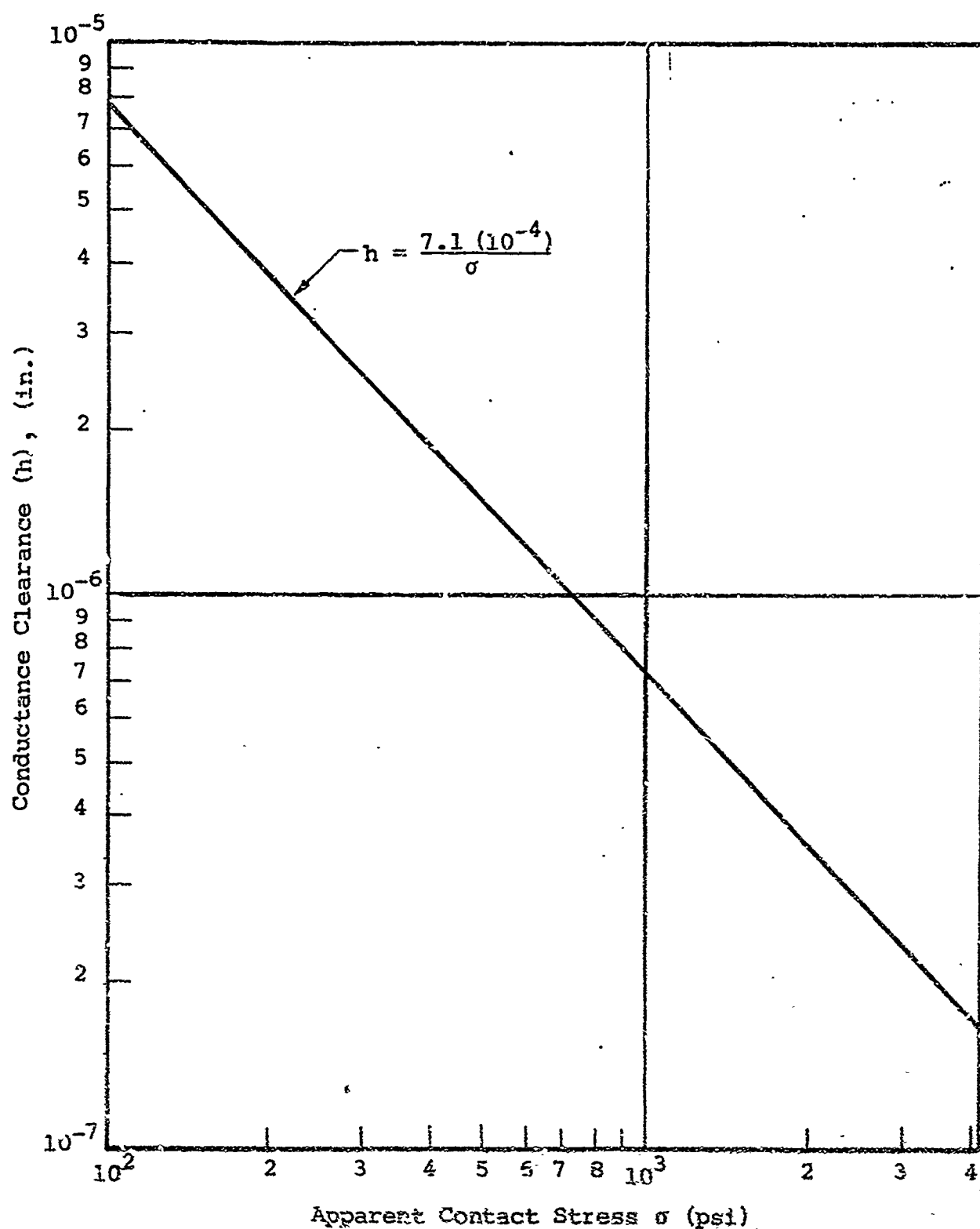


Figure 12-9 Mean relationship between the conductance clearance and apparent contact stress for 70 Shore A rubber materials

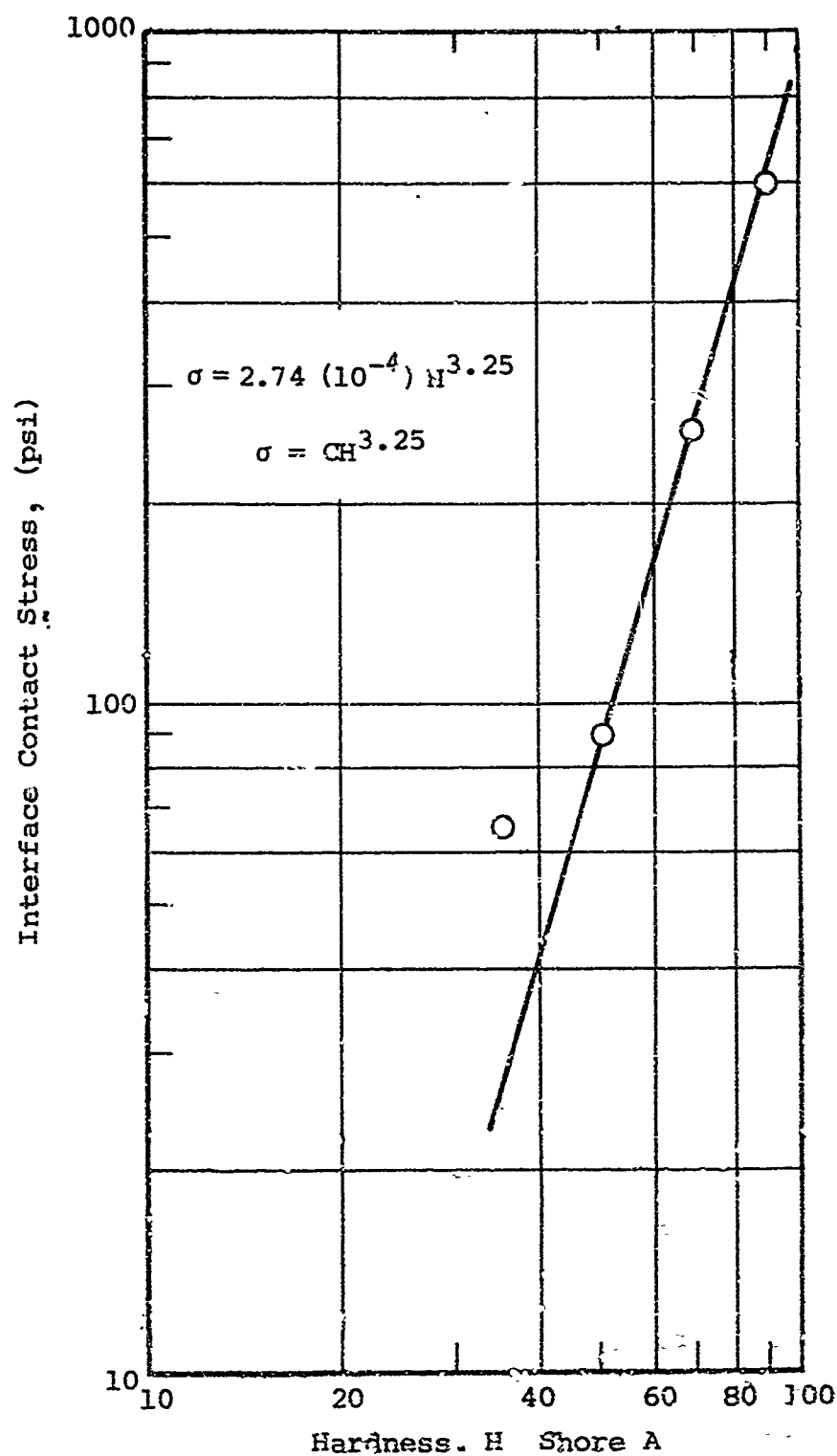


Figure 12-10 Variation of contact stress with hardness for geometrically identical Buna-N rubber gaskets at an arbitrarily selected leakage rate of 10^{-4} cc/sec (STP)

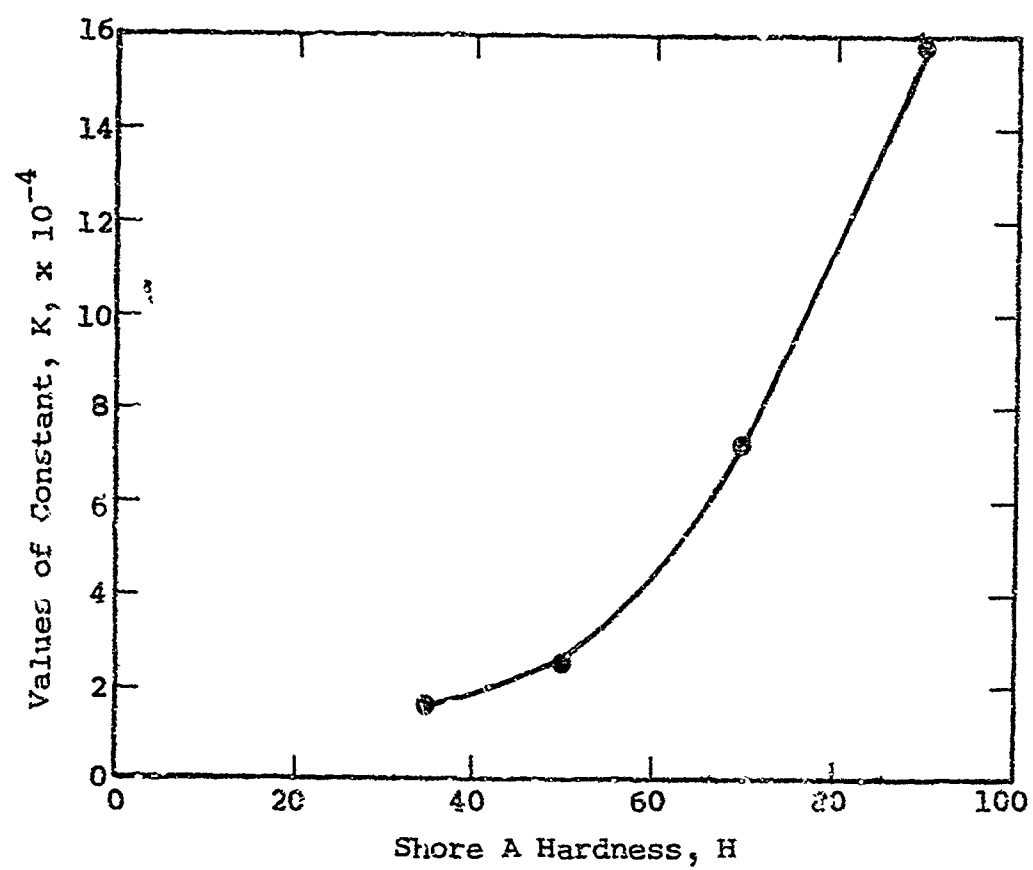


Figure 12-11 Relationship between the constant in equation (12-9) and hardness

Table 12-3

PERMEATION COMPARISON FOR RUBBER MATERIALS

Rubber	Air Permeability at one atmosphere and 176°F (cc/sec/cm ² /cm) (Ref. 12-3)	Experimental Helium Leakage Rates at a Stress of 7000 psi (cc/sec STP)
Butyl	$3.2 - 4.6 \times 10^{-8}$	3×10^{-8}
Viton	8.8×10^{-8}	2×10^{-7}
Silicone	$3.5 - 4.7 \times 10^{-6}$	2×10^{-6}
Buna-N	6×10^{-8}	1.5×10^{-8}

Permeability is expressed as the volume of gas, corrected to standard conditions (0°C, 760-mm mercury), that permeates a specimen of one square centimeter area, one centimeter thickness in one second. For low permeability, a rubber should contain maximum loading of filler and minimum loading of plasticizer. Laminar-type fillers are most suitable for retarding permeability. Table 12-4 presents the air permeability rates for the major elastomer groups at five temperatures. The absence of data for the higher temperatures, indicates that many of the elastomers had deteriorated beyond the point of being able to test them.

Figure 12-12 presents permeability temperature curves for six elastomers and shows that Vyram N-5400 and butyl rubber have the lowest permeability rates. At room temperature, the permeability of silicone rubber is 1000 times greater than that of butyl. This is reduced to 20 times at 400°F. The permeability of butyl, polyurethane, and silicone rubbers to nitrogen is substantially the same as for air.

12.6 References

- 12-1 Shore Instrument and Manufacturing Company Inc. Bulletin Catalog R-12 Jamaica, New York
- 12-2 A. Kehn and F. A. Tsuki, Investigation of Structural Sealing Parameters and Concepts for Spacecraft Seals, AFFDL-TR-65-88, IIT Research Institute, Chicago (Apr 1965)
- 12-3 WADC Report TR-56-331, Gas Permeability of Elastomers, Part II, Section VI.

Table 12-4

AIR PERMEABILITIES AT VARIOUS TEMPERATURES, VARIOUS ELASTOMERS (Ref. 12-3)

Elastomer	Permeability $\times 10^7$				
	at 75°F	176°F	250°F	350°F	400°F
Natural rubber	0.49	4.4	7.1	20.7	26.2
SBR	0.25	2.9	4.7	15.4	---
Neoprene	0.09-0.10	0.98-1.7	2.6-3.0	7.3	---
Butyl	0.02	0.32-0.46	1.3-1.8	5.6-6.1	10.0
Nitrile	0.13	0.8	2.2	6.6	---
Thiokol	0.02	0.37	1.6	melted	---
Hypalon	0.72	0.73	2.3	6.2	---
Poly ethane (polyester type)	0.05	0.97	3.1	7.1	melted
Silicone	11-33	35-47	---	69-113	74
Fluorocarbon	1.5	9.6	24	49	---
Vyram	0.007	0.24	0.56	5.1	---
Kel-F 3700	---	0.8	3.4	15.6	---
Viton A	---	0.88	3.6	14.6	---
Acrylon EA-5	0.16	1.5	3.7	10.2	---
Hycar 4021	0.19	1.8	4.8	9.4	---
Methacrylate	---	---	---	---	16.3
Adiprene C	---	2.3	3.8	16.6	---
Carboxy	---	2.4-2.6	2.3-5.2	7.1-14	---

Permeability is expressed in cubic centimeters of air (corrected to STP conditions) per second which would permeate through one square centimeter of vulcanizate one centimeter thick ($\text{cc/sec/cm}^2/\text{cm}$) with one atmosphere of pressure difference.

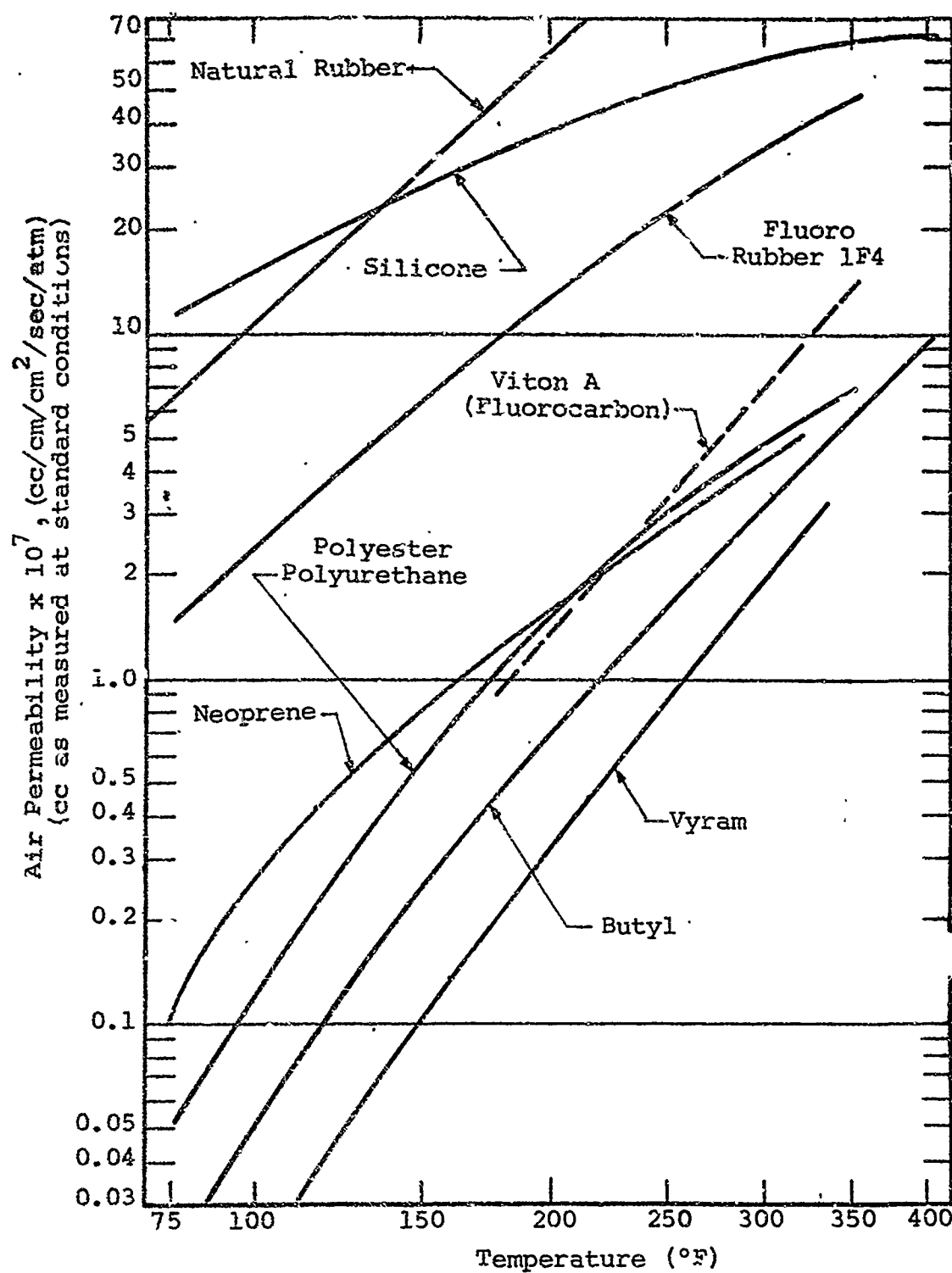


Figure 12-12 Air permeabilities of elastomers at elevated temperatures (Ref. 12-3)

13. APPLICATION OF RUBBER INTERFACE CRITERIA

The criteria derived in Section 12 are applied to a rectangular and a circular cross-sectional seal. A method of analysis, which yields the leakage performance as a function of sealed fluid pressure, is shown. In addition, experiments performed on identical seals to demonstrate the reliability of the criteria are described.

Several general assumptions appear in the analysis:

- The relationship between conductance clearance and contact stress was derived from the assumption that the conductance clearance represented a descriptor of a large interface (experimental gasket surface) and the contact stress was uniformly distributed over the surface. In the following analysis the conductance is assumed to be a point function. That is, the stress and conductance clearance at any point in the interface varies, but the relationship between the variables is constant and denoted by the average relationship. Hence, equation (12-10), Section 12, can be rewritten

$$h(x) = \frac{5.7 \times 10^{-10} H^{3.25}}{\sigma(x)} \quad (13-1)$$

- All forces, including the pressure gradient, are considered to be acting in the interface. These forces, shown on figure 13-2 and described by equation (13-1), can be restated in terms of stress and pressure acting simultaneously at any point x in the interface by

$$\frac{P_N}{bX} - p(x) - \sigma(x) = 0 \quad (13-2)$$

where P_N/bX is the net, average, externally applied stress acting at the interface.

- The external loading of the seal structure can in some cases be assumed transmitted hydrostatically throughout the structure. The types of loading include initial deformation, pressure deformation of the structure, pressure deformation of seal housing, and any other mechanical loading device. Seal structures particularly suited for this assumption are those which do not significantly deform during operation.
- The conductance clearance obtained from equation (13-1) is introduced into the laminar flow equation

to calculate a leakage rate. The equation has the general form

$$W = \frac{\rho b(h(x))^3}{6\mu} \frac{dp}{dx} \quad (13-3)$$

Other flow equations, for flow through hypothetically separated uniform surfaces, can also be employed depending upon the mode of flow encountered.

- The application of equation (13-1) into equation (13-3) produces problems associated with boundary conditions in the integration process. This occurs when $\sigma(x) \rightarrow 0$. At this time $h(x) \rightarrow \infty$. If $h(x)$ becomes sufficiently large, separation of the interface surfaces is implied. To overcome this problem, the maximum conductance clearance is assumed equivalent to the PTV roughness of the solid surface as h_{\max} . Equation (13-1) can be revised to the form

$$h(x) = \frac{5.7 \times 10^{-10} H^{3.25}}{a + \sigma(x)}$$

where

$$a = \frac{5.7 \times 10^{-10} H^{3.25}}{h_{\max}} \quad \text{when } \sigma = 0 \text{ at } h = h_{\max}$$

and

$$h(x) = \frac{5.7 \times 10^{-10} H^{3.25}}{\frac{5.7 \times 10^{-10} H^{3.25}}{h_{\max}} + \sigma(x)} \quad (13-4)$$

To show the relative significance of the constant, a , the following is assumed

$$H = 70 \text{ Shore A}$$

$$h_{\max} = 46 \mu\text{in. PTV roughness}$$

$$a = 15.4$$

The inclusion of the constant changes the empirical relationship but the order of magnitude of effects is small when σ is large in comparison.

- The leakage rate prediction is obtained by combining equations (13-2), (13-3) and (13-4).

- The conductance clearance equation (13-1) applies to any rubber material. In most cases, high contact loading produces permeation flow. Thus, limitations must be placed upon equation (13-1) from the standpoint of minimum leakage prediction. The permeation rate can be estimated from the data in Section 12 and the procedures and data contained in Volume II, of Reference 13.1.
- The rubber material must be devoid of all contaminants including large surface scratches. If a grease lubricant is applied to the surfaces, the properties of the lubricant should be initially used to predict its flowrate through the interface.

13.1 Rectangular Seal Ring

The general case of a rectangular cross-section ring is chosen for analysis. The ring is assumed to be confined between two flanges, as shown on figure 13-1. The radial displacement of the rubber is constrained by two substantial rings.

If the curvature of the seal ring is neglected, the geometry of flange A can be represented as a rectangular flange with no leakage past the edges. This approximation is valid when the ring width is small compared with the diameter. The approximate geometry is shown in figure 13-2.

Forces Acting at the Interface

$$\frac{P_N}{bX} = \frac{P - \frac{p\pi D_1^2}{4}}{bX} = p(x) - \sigma(x) \quad (13-5)$$

where

P_N/bX = average net interface stress

X = width of interface in the direction of leakage flow

b = depth of interface normal to flow

P_N = net load

P = flange load

p = sealed fluid pressure

$p(x)$ = fluid pressure at any point x

$\sigma(x)$ = normal stress at any point x

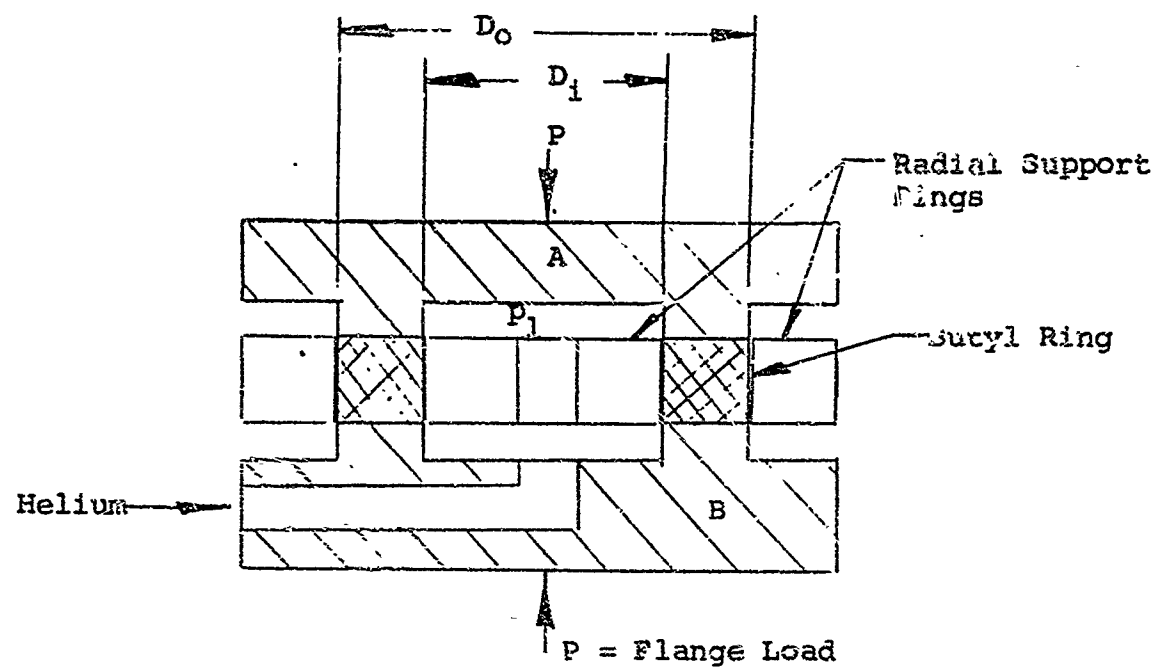


Figure 13-1 Experimental apparatus for evaluating rubber materials

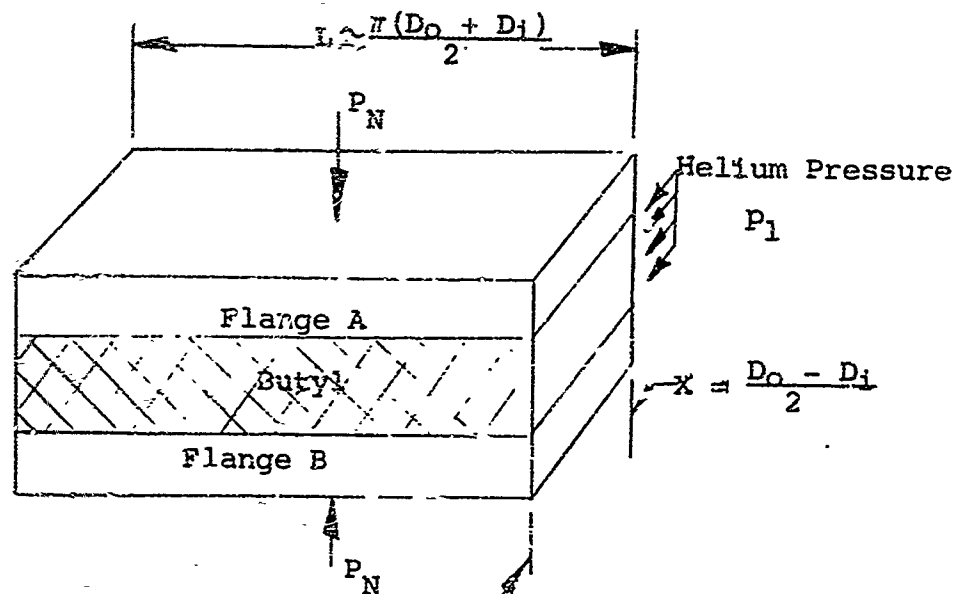


Figure 13-2 Approximate geometrical representation of the seal interface

The weight rate of flow simultaneously through two interfaces, shown on figure 13-1, under the assumptions of laminar, compressible flow is:

$$W = \rho Q = \frac{\rho b h^3}{6\mu} \frac{dp}{dx} \quad (13-6)$$

Rearranging terms;

$$W \int_0^X dx = \int_{p=p}^{p=p_0} \frac{b h^3 p dp}{6\mu R T} \quad (13-7)$$

Combining equations (13-4), (13-5) and (13-7)

$$W = - \frac{b 1.85(10^{-28}) H^{9.75}}{6X\mu R T} \int_{p=p_1}^{p=p_0} \frac{p}{\left[a + \frac{p_N}{bX} - p\right]^3} dp \quad (13-8)$$

Integration yields

$$W = \frac{b 1.85(10^{-28}) H^{9.75}}{6X\mu R T} \left\{ \frac{a + \frac{p_N}{bX} - 2p_0}{2 \left(a + \frac{p_N}{bX} - p_0\right)^2} - \frac{a + \frac{p_N}{bX} - 2p_1}{2 \left(a + \frac{p_N}{bX} - p_1\right)^2} \right\} \quad (13-9)$$

where

$$a = \frac{5.7 \times 10^{-10} H^{3.25}}{h_{\max}}$$

If the following actual identities are substituted into equation (13-9), the volume leakage rate at ambient conditions can be calculated. The results are shown graphically on figure 13-3 along with comparative experimental data.

Butyl Rubber Seal

$$H = 70 \text{ Shore A}$$

$$h_{\max} = 46 \mu\text{in. PTV}$$

$$p_1 = 360 \text{ psia}$$

$$p_0 = 14.7 \text{ psia}$$

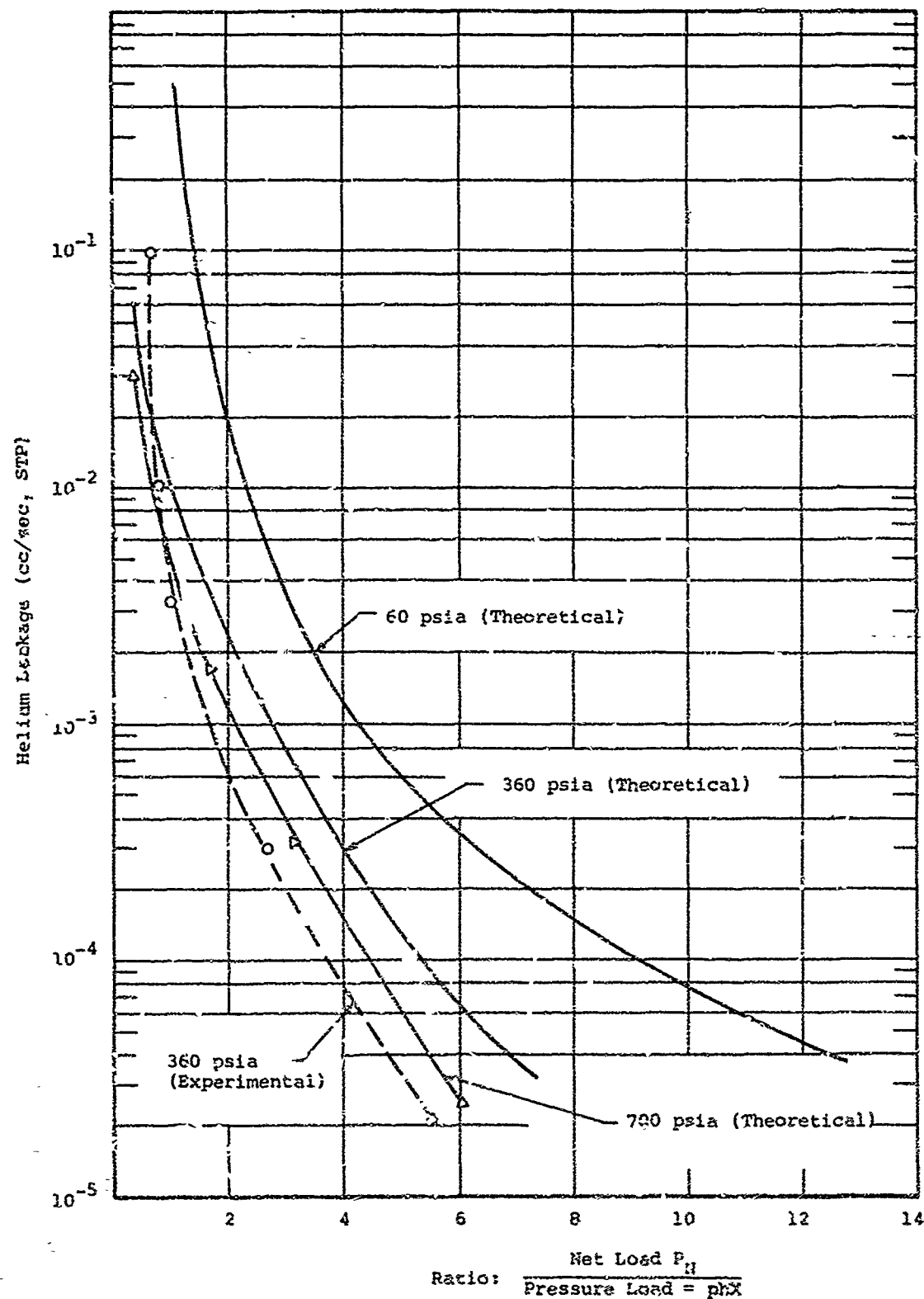


Figure 13-3 Theoretical and experimental leakage characteristics of a butyl rubber ring. The net interface load is normalized to the maximum pressure load to show the relative effects of increasing load. Pressure difference across the ring is shown as a parameter.

$$\mu = 2.83 \times 10^{-9} \text{ lb-sec/in.}^2 \text{ viscosity of helium}$$

$$X = (D_o - D_i)/2 = 0.134 \text{ in.}$$

$$D_o = 2.500 \text{ in.}$$

$$D_i = 2.232 \text{ in.}$$

$$r = \frac{\pi(D_o - D_i)}{2} = 7.42 \text{ in.}$$

$$Q_o = \frac{W}{\gamma_o} \text{ and } RT = \frac{p_o}{\gamma_o}$$

$$\gamma_o = \text{specific weight of helium}$$

13.2 O-Ring Analysis

The analysis of an O-ring departs slightly from that applied to the rectangular ring. The difference arises from the fact that the rectangular ring possesses an interface geometry that remains constant. The interface geometry of the O-ring, on the other hand, changes with applied load. The method of attack is twofold. First, experimental load-deformation characteristics can be utilized. Secondly, a theoretical prediction can be calculated. Since the first approach is more reliable, experimental data will be employed initially.

The general case of an O-ring in a groove, as shown in figure 13-4, is considered.

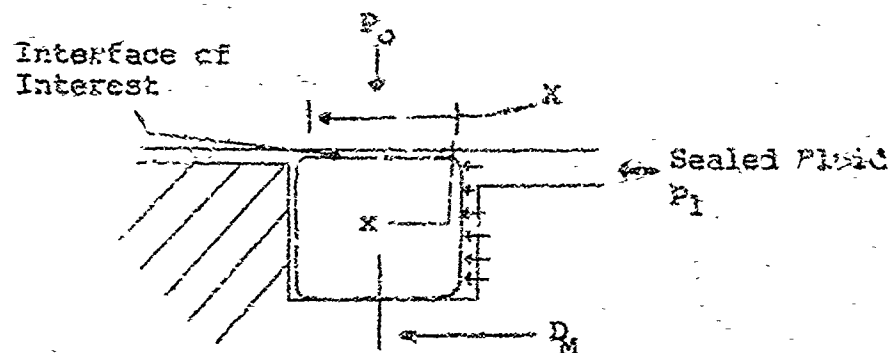


Figure 13-4 Cross section of an O-ring installed in a groove

An initial load P_o is applied to the ring, producing a deflection equivalent to the height of the seal cavity. A corresponding preload stress is P_o/Xb . The application of fluid

pressure, p , results in a hydrostatic transfer of this load to the interface. The net contact stress at the interface is assumed

$$\frac{p_o}{Xb} + p = p_{(x)} + \sigma_{(x)} \quad (13-10)$$

where $b = \pi D_m$

Since the conductance clearance is

$$h_{(x)} = \frac{1.85(10^{-28}) H^{3.25}}{a + \sigma_{(x)}} ,$$

and the gas leakage flow is

$$W = \frac{pb(h_{(x)})^3}{6\mu} \frac{dp}{dx}$$

these equations can be combined and integrated to yield

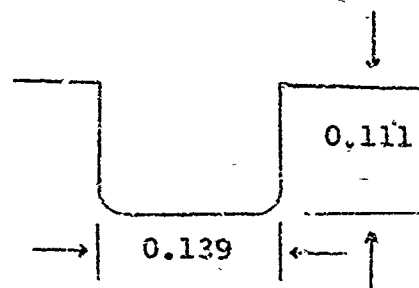
$$W = \frac{b \cdot 1.85(10^{-28}) H^{3.25}}{6XRT} \left\{ \frac{a + \frac{p_o}{Xb} + p - 2p_o}{2 \left(a + \frac{p_o}{Xb} + p - p_o \right)} \right. \\ \left. - \frac{a + \frac{p_o}{bX} - p_1}{2 \left(a + \frac{p_o}{bX} \right)} \right\} \quad (13-11)$$

where

$$a = \frac{5.7 \times 10^{-10} H^{3.25}}{h_{\max}}$$

Before proceeding in calculating the leakage rate, a typical configuration must be selected and the experimental deformation characteristics determined. The cavity and seal dimensions are shown on figure 13-5.

Cavity



Note: O-ring fills 94% of the groove when deflected

Seal

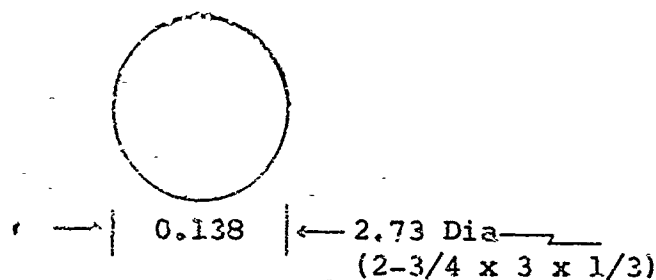


Figure 13-5 Dimensions of the 70 Shore A seal and cavity

The experimental deformation characteristics are shown on figure 13-6 as a function of contact stress. The initial stress interface at the maximum deformation is $P_0/bX = 430$ psi. For comparison, the deformation of an unsupported O-ring is shown to provide an insight into the effects of the seal cavity.

Leakage may now be calculated from equation (13-11) by applying the conditions

$H = 70$ Shore A

$h_{max} = 46 \mu\text{in. PTV}$

$P_1 = \text{variable}$

$P_0 = 14.7$ psi

$\mu = 2.83 \times 10^{-9} \frac{\text{lb-sec}}{\text{in}^2}$ viscosity of helium

$X = \text{from figure 13-7}$

$b = \text{from figure 13-7}$

$D_m = 2.87$ in.

Calculations for all internal pressures show that the leakage is in the permeation region. It can be concluded that O-rings installed in standard cavities provide minimum leakage less than 10^{-6} cc per sec.

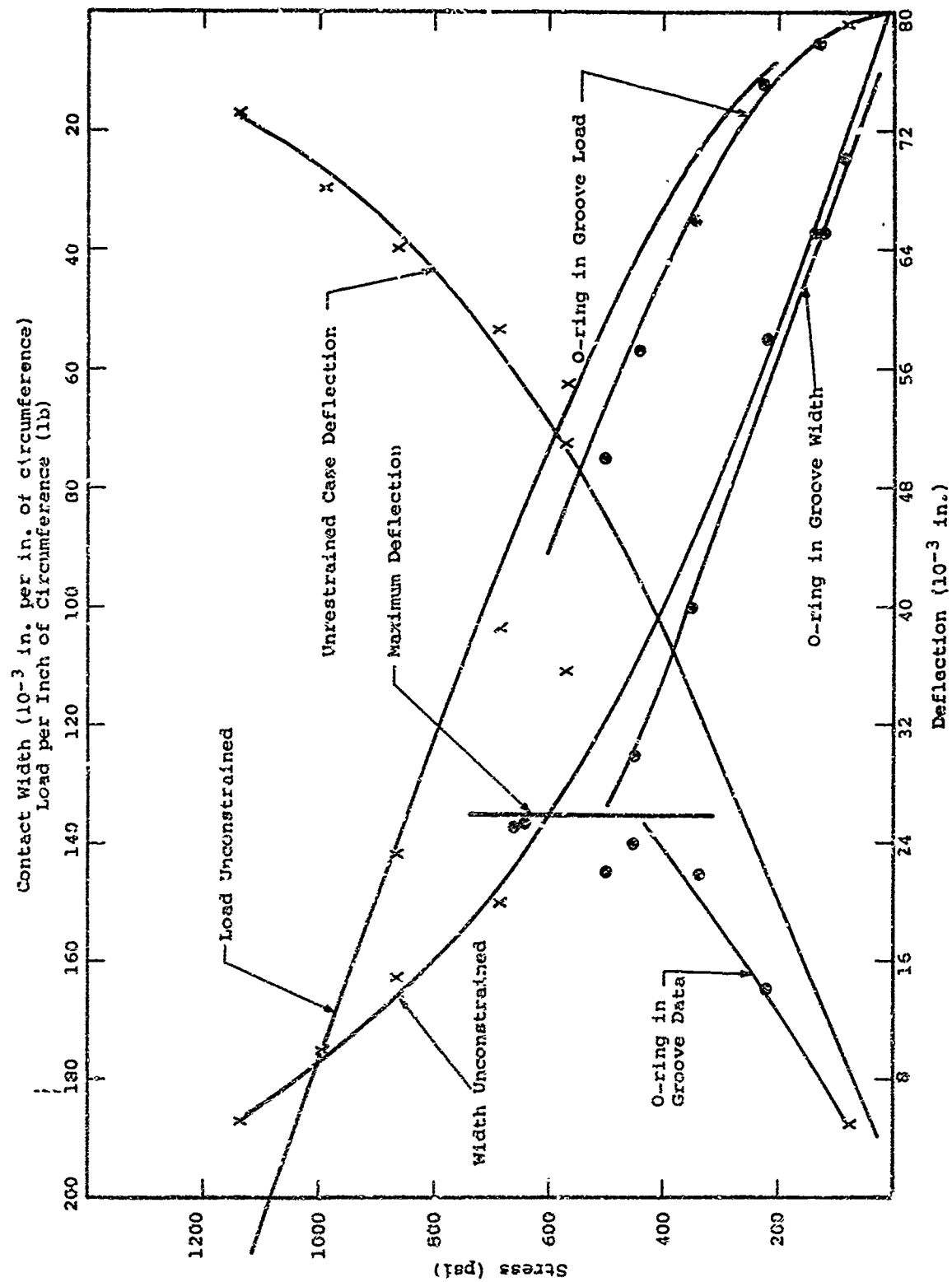


Figure 13-6 Deformation data for a 2-3/4 x 3 x 1/8 70 Duro O-ring

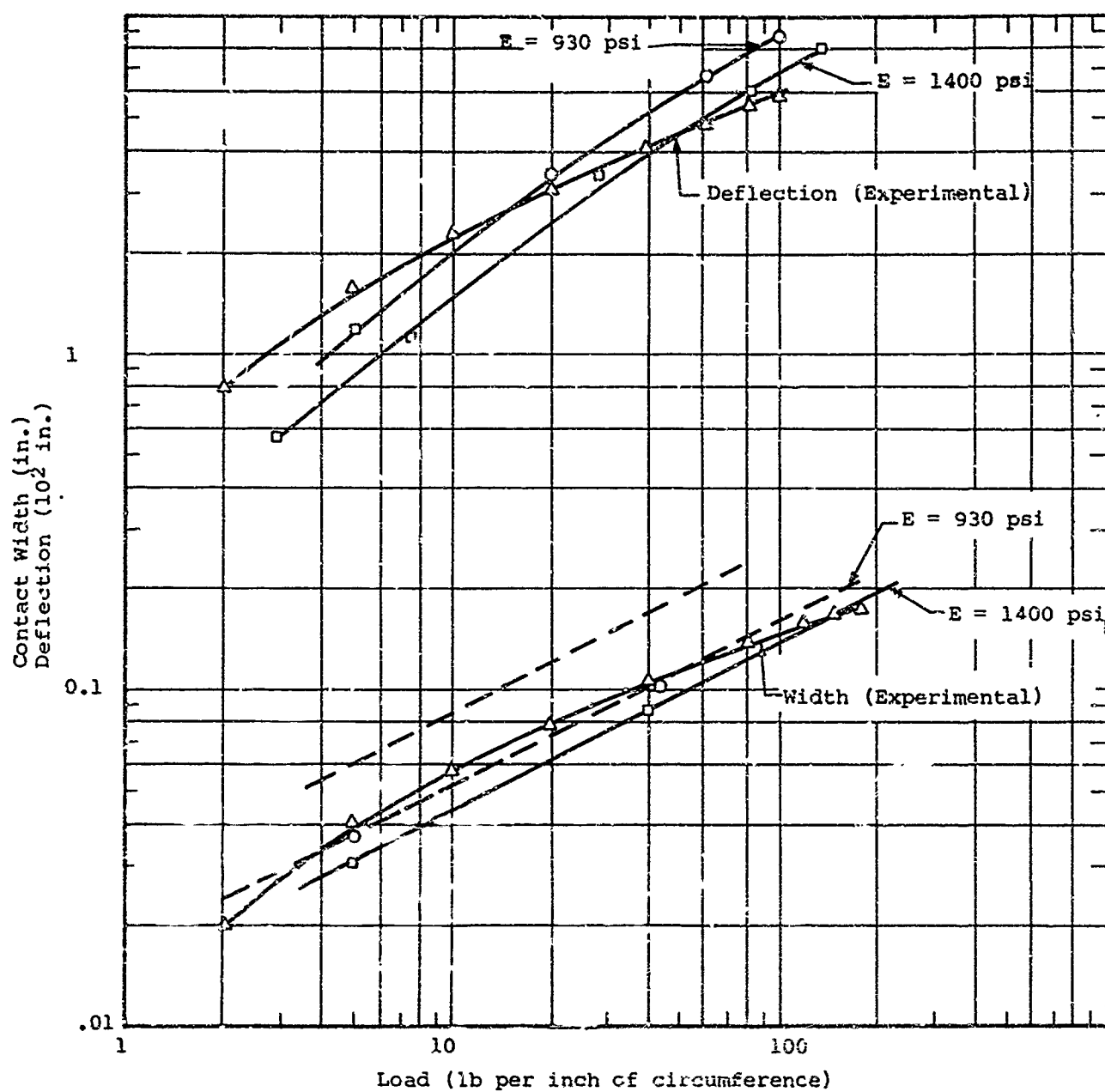
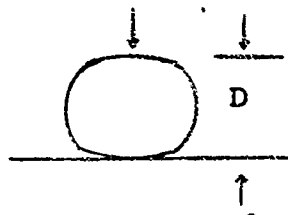


Figure 13-7 Experimental and approximate deformation characteristics of an 70 Shore A O-ring (2-3/4 x 3 x 1/8)

An approximate method for determining the area, X , of C-ring contact can be obtained by accident from the Hertzian elastic analysis of a cylinder pressed against a flat plate (Ref. 13.2).

The geometry is



the width of contact, X

$$X = 1.6 \sqrt{PD \frac{1-v^2}{E}} \quad (13-12)$$

the deflection

$$\Delta D = 4P \left(\frac{1-v^2}{\pi E} \right) \left(\frac{1}{3} + \ln \frac{2D}{X} \right) \quad (13-13)$$

where

v = Poisson's ratio for rubber ≈ 0.5

E = modulus of elasticity for rubber

Equations (13-12) and (13-13) can be evaluated by assuming values of modulus of elasticity. The calculations for two values are shown on figure 13-7 along with the corresponding experimental results. A close comparison can be observed between load and contact width. The effect of modulus variation is not substantial. The prediction of deflection, however, does not correlate satisfactorily with the experimental results. Considering the error induced in the experimental measurements, the results may be acceptable. It should be noted that the elastic analysis accidentally predicts the deformation. The analysis is based on a cylinder which retains its shape. The rubber seals, however, deform substantially. Equations (13-12) and (13-13) have been verified for other diameter and material seal rings. In each case a reasonably close correlation was obtained. Materials having a hardness between 65 and 85 Shore A have an apparent modulus of elasticity of 900 to 1100 psi, based on curve fitting procedures as shown on figure 13-6. This appears to correlate closely with the normal contact stress at which interface leakage ceases as shown typically on figure 12-1. Thus, the elastic strain may be assumed as 100 per cent and $\sigma = E$.

13.3 References

- 13-1 Paul A Bauer, Myron Glickman, and Frank Iwatsuki;
Analytical Techniques for the Design of Seals for
Use in Rocket Propulsion Systems, Volume I and II,
AFRPL-PR-65-61, IIT Research Institute, Chicago,
Illinois (May 1965)
- 13-2 R. Roark, Formulas for Stress and Strain, McGraw-Hill,
1954

14. CONCLUSION

The conclusions reached during this program can be divided into two categories. The first is composed of those conclusions derived with respect to the development of design criteria, specifically the development of analytical tools for the systems designer. The second category contains conclusions pertinent to minimum leakage sealing, for example 10^{-2} cc per sec of gas flow. An additional distinction is made between static and dynamic seals.

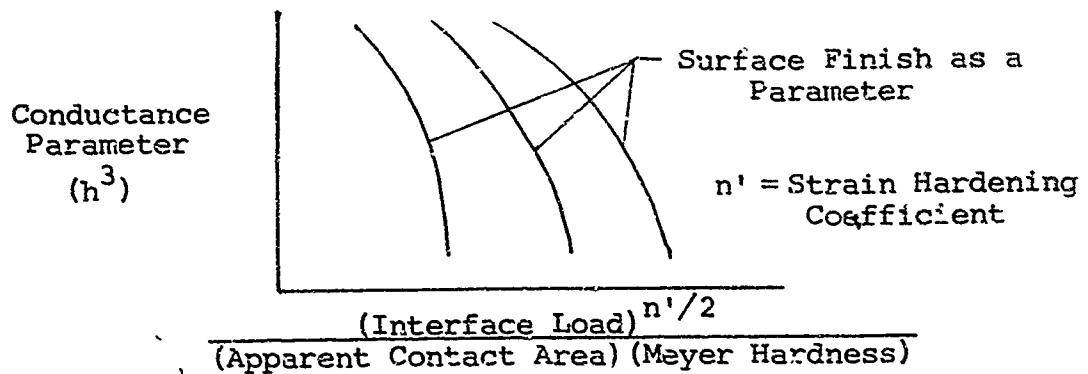
14.1 Design Criteria

14.1.1 Static Seals

The correlation of parameters influencing leakage through an interface can be described as successful even though the results have an estimated accuracy of \pm one order of magnitude. This statement is supported by the following arguments.

- It is the first comprehensive attempt to correlate parameters. Also, it is the first criterion available for systems designers which can be used to quantitatively predict leakage.
- The parameters are not uniquely defined, hence, variation in results can be expected. The most significant variation is attributed to the lack of an adequate description of surface finish.
- The correlations are based on experimental leakage measurements, which vary at least one order of magnitude in accuracy. This is not a large variation in that the leakage range of interest varied over ten orders of magnitude.

The method of parameter correlation is particularly suitable for use by the systems designer. The presentation is in the form of design charts where the conductance parameter is used as a basis for the correlation. The charts which have the form:



contain all of the important parameters describing the leakage path. These include material properties, load, interface geometry and surface topography. Thus, for any interface where the preceding conditions are known, the designer can predict leakage. Leakage is given as

$$Q = f \text{ (conductance parameter, sealed fluid pressure, fluid properties, and gross geometry of the interface)}$$

The functional relationship in this expression is given by an assumed state of fluid flow through hypothetically separated surfaces.

The application and reliability of the criteria were demonstrated by comparing theoretical (empirical) leakage predictions with experimental measurements of many selected seals. The criteria were successfully applied by treating each part of the seal independently. The parts included the interface, seal structure and seal housing. The results of each part were then superimposed to yield leakage performance.

While comprehensive criteria for all varieties of seal structures and housing were not feasible, the most typical were selected for study and the most influential parameters were identified. Procedures for analysis, using simple beam theory, were sufficiently adequate to predict interface loading.

The criteria for elastic rubber sealing interfaces were approached in the same general manner as the metallic and plastic criteria. It is the first criterion which has been developed to predict leakage flow through rubber interfaces. This criterion, applicable to static and dynamic seals, contains a number of areas yet to be investigated. Because of the close correlation of experimental results with theoretical calculations in several seal applications, it is recommended that additional studies be made.

14.1.2 Dynamic Seals

Criteria for interfacial seals in sliding and rotating applications were developed by combining principles of fluid mechanics with concepts of friction and wear. The criteria are in the form of parametric relationships yielding a description of the average wear fragment size generated at the interface. Through information contained in the literature plus experimental evidence, it was concluded that wear fragments produce separation of the interface surfaces. The gap formed by the fragments is equivalent to the leakage path. Hence, leakage varies with the size of the fragments.

Experimental investigations of wear fragment generation show that the fragments are large in number and in size. An estimate

of the wear particle diameters for sliding systems can be obtained from material surface energy considerations;

$$d = 2.3 \times 10^{-4} \frac{W_{ab}}{H} \text{ in.}$$

where

W_{ab} = surface energy in (ergs/cm²)

H = hardness in (kg/mm²)

A review of the literature and experimental evidence has shown that the average particle diameter for the best combination of sliding materials is ~50 to 100 μin.

An estimate of the number of particles generated, N , can be obtained by experimentally determining wear coefficients, k , using the formula

$$N = \frac{kP}{3Hd^3}$$

where P is normal surface loading and the wear rate is equal to Nd^3 . From the preceding formulas, the magnitude of wear and particle size can be estimated. The leakage rate through a seal can, therefore, be determined by applying the appropriate flow equation derived from principles of fluid mechanics.

In view of the substantial separation of interface surfaces by wear fragments and the apparent lack of methods for reducing the fragment size, alternative methods of sealing can be considered at least for rotating shaft seals. Interstitial seals, such as the hydrostatic and hydrodynamic seals, offer this improvement in that there is virtually no wear and lower frictional power losses. The criteria for these seals have not reached a satisfactory state of development considering the problems involved and their possible importance in producing lower leakage performance than interfacial seals.

14.2 Minimum Leakage Sealing

14.2.1 Static Seals

Minimum leakage is usually desirable with minimum interface loading. This can be achieved by elastically deforming rubber or metallic materials. At higher loads, metals and plastics can be employed through plastic deformation of the materials.

Elastic deformation of metallic surfaces requires the surfaces to be very highly polished with few surface disturbances smaller than 1 μin. The waviness must be approximately the same value, depending upon the geometry of the

substrate material. These surfaces are difficult and expensive to produce and susceptible to handling damage and foreign contaminants. The performance of the elastically deformed interface can be superior to the plastically deformed interface. The performance, however, is unreliable because of factors over which one has little control. In addition, the elastic seal surface is difficult to evaluate in large diameter seals (greater than 4 in.) due to limitations of inspection techniques.

Plastic deformation of the sealing interface offers reliable performance, but at the expense of very high contact loads. Minimum leakage can be achieved when the interface loads approach the Meyer hardness of the materials. Hence, materials with low hardness are preferable to harder materials. To illustrate this point, the Meyer hardness, σ_m , of plastics is ~4000 psi compared with over 1,000,000 psi for hard metals. An average elastic stress for rubber materials is ~1000 psi.

The shape or geometry of the interface should lend itself to gross plastic deformation. Most commercial seals have relatively flat interface surfaces, which, when pressed together, produce microscopic deformation of the asperities. Consequently, large loads must be imposed before sufficient plastic deformation of the leakage path can be realized for minimum leakage. Wedge-shape interfaces, on the other hand, produce substrate and surface deformation upon the first application of load. Consequently, full plasticity occurs. The most beneficial shape of the interface appears to be a 60-deg wedge, however, other shapes offer similar advantages.

Minimum leakage through wedge-deformed interfaces depends upon the load applied, material properties and the resulting width of contact normal to the average direction of leakage flow. On the basis of limited experiments, the width of contact must not be less than 0.012 in. This suggests that the ability to produce minimum leakage is a function of the load per unit length of circumference and the material properties. For minimum leakage, an approximation for the load per inch of circumference is $P = 0.012 \sigma_m$. Thus, a metal with a hardness of 100,000 psi would require an interface load of 1200 lb per in. This loading is normal and may be excessive in some applications. Design innovations whereby mechanical advantage can be utilized can overcome this problem. For example, in the Battelle bobbin-type connector seal (Ref. 14-1), the normal loading is produced on a radial surface rather than an axial surface. In this case, the axial load is less than the radial load.

Minimum leakage is associated with the deformation of the softest material forming the interface. Hence, surface platings and coatings will govern the deformation process while the substrate has little or no effect.

Whether the interface deformation be elastic or plastic, the topography of the surface must be a minimum. Rough surfaces greater than $10\mu\text{in.}$ PTV should possess a lay pattern normal to the direction of leakage flow. Surface waviness, usually a controlling factor in rough interfaces, must be a minimum. Unfortunately, waviness is machine-produced, and minimizing it depends on the fabrication process and quality of the machine tool. Surface finishes less than $10\mu\text{in.}$ can be multidirectionally oriented. These surfaces are produced by precision machine tools where waviness is approximately the same as the roughness.

The effects of contaminants are most pronounced on elastically deformed metal interfaces. The detrimental contaminant size is estimated as $1/20$ micron. On the other hand, plastically deformed interfaces can tolerate contaminants equivalent in size to the maximum rough variations. For a $10\mu\text{in.}$ PTV surface, the contamination level would be $1/4$ micron. While the contaminant size is still small, the chances of removal are improved by exceptional cleanliness procedures. The removal of $1/20$ -micron particles is, indeed, difficult if not impossible. It can be stated, therefore, that plastically deformed interfaces are less susceptible to small contaminants and, therefore, more reliable.

The seal structure must be resilient to compensate for thermal and pressure deformations of the seal and seal-related housing. Many commercial seals are pressure-energized to produce this effect, although the philosophy behind it is usually one of attempting to increase the deformation at the interface. The influence of additional pressure loading in commercial seals is almost negligible. To clarify the requirements for a seal structure, the following can be stated:

- The structure must be capable of imposing the initial interface load required for minimum leakage.
- The structure must maintain approximately 50 per cent of the initial load when the interface is plastically deformed $\frac{W^{2/n'}}{A_A} \sigma_{II} > 0.1$.

This effect is defined as an hysteresis phenomenon attributed to the relative influence of elastic structure to plastic interface deformation. Thus, the seal structure must provide a minimum load when deformations occur as the result of individual thermal or pressure effects or combined effects.

- Thermal effects are difficult to estimate theoretically and, hence, some experimental development is necessary for those seal applications where large temperature variations occur. A selection of materials offering thermal compensation effects can overcome this problem. It should be noted that the so-called pressure energization of the structure is not applicable in this case. Therefore, the seal structure and surrounding parts must be designed on a compromise basis with interface load a rigid requirement.
- Fluid pressure deformation of the structure and seal-related parts can be compensated for by designing the structure so that it deforms elastically to the limits or maximum deformation. If thermal effects are small in comparison, the interface pressure loading is often sufficient to produce the minimum interface load.

14.2.2 Dynamic Seals

Interfacial seals were described as contacting-type seals where one face rubs against the other. It was concluded that fragments resulting from wear are of such a size and number that substantial separation of the seal surfaces occurs. These fragments, even under well-lubricated conditions, have an average size generally not less than $50\mu\text{in.}$ and can range to $10,000\mu\text{in.}$ Consequently, interfacial seals could be more appropriately classed as fixed clearance seals where the wear fragment size determines the size of the leakage path. To achieve minimum leakage, the fragment size must be as small as possible. This can be accomplished through low contact loads and a choice of rubbing materials having low surface interaction. Low surface interaction can be achieved with hard materials having low energy of adhesion, preferably a metal rubbing against a nonmetal, e.g., hardened steel against aluminum oxide.

Hydrostatic or hydrodynamic seals offer improved leakage performance by producing a smaller leakage path than that produced in interfacial seals. The criteria for these seals have not been fully developed and, additionally, pertain primarily to rotating shaft seals.

Sliding seals appear relegated to the interfacial variety because of the nature of the motion and the problems associated in the fabrication of seals and seal-related parts. Since most sliding seals are cylindrical, the problem is one of fabricating and inspecting cylindrical surfaces. To achieve minimum leakage, the maximum mismatching (out-of-roundness of both interface surfaces) must be at least less than the average size of the wear fragments. This suggests out-of-roundnesses less than 0.0001 in. In some cases this can be achieved, depending on the

geometry of the cylindrical parts. In any event, inspection instrumentation and procedures must be improved before reliable advances in fabrication can be achieved.

Even with optimum criteria, it seems unlikely at the present time that leakage rates of 10^{-6} cc per sec of gas leakage can be achieved without resorting to such devices as liquid barriers. A review of the criteria for static seals shows that substantial surface loading and deformation are required to achieve this leakage rate. These requirements placed on dynamic seals would undoubtedly produce severe wear and large debris fragment size.

14.3 Recommendations

As a result of the preceding work, several areas requiring further investigation have emerged.

14.3.1 Static Seals

Improvements in the empirical correlations between sealing parameters should be continued. This work could proceed as follows:

- Additional experimental data from all sources should be combined and compared with the present correlations. This should improve its reliability.
- The methods of correlation should be improved by incorporating statistical methods of data analysis.
- The interrelationship of parameters could be formulated from improved theory of deformation and methods of surface inspection and identification.

Additional details on the effect of the plastic deformation of wedge interfaces should be combined with particular emphasis on the minimum width of interface contact for minimum leakage.

The merits of changing parameter description from volume properties to surface properties or possibly combining both together should be re-appraised. Surface parameters suggested for study include:

- Surface oxides and other contaminants and their mechanical properties, crystal structure, and degree of coherence with the substrate.
- Influence of adsorbed gases and their effect on surface elastic properties.

- Effect of oxides on dislocation movement.
- Variation of surface energy with strain.

Development of techniques for visual observation of the interface should be continued with a view to determining the nature of the leak paths. A radiographic technique appears promising.

A concise distinction between the laminar, transition, and molecular flow regimes should be obtained. This could be accomplished experimentally by leakage measurements through varied finish interface surfaces. This information can produce additional corrections in the design criteria and also lead to a description of the leakage path. For example, the leakage characteristics will show whether the leakage paths are composed of few large interconnecting void spaces or a large number of small void spaces.

The criteria developed for rubber seals contained a number of gaps, which should be eliminated.

- The importance of surface finish is not clearly defined.
- The effect of wedge shaped interfaces, including the O-ring shape requires definition.
- The influence of contaminants must be established.

14.3.2 Dynamic Sealing

Additional experimental correlations of wear particle size and the relationship between load, material hardness, and surface energy should be obtained for verification and expansion of the data.

The influence of friction energy loss on the mean asperity junction temperature should be definitely established. It is felt that this can be accomplished by viewing formation of localized vaporization at given relative velocity and loading of the surfaces.

Mechanical methods of removing wear debris particles from contacting interfaces should be studied. This is suitable for rotating seals. Grooves in the interface may aid in the expulsion of the particles, thereby minimizing their effect on surface separation.

If a critical surface temperature does exist when wear occurs, then the commonly employed pv factor (pressure-velocity relationship) may be considered a constant for given combinations of materials. However, the relationship should include other geometrical, material property, and heat loss corrections. The development of reliable pv relationships would provide the systems designer with an insight into the wear rate of materials as a function of rubbing velocity.

The wear of circular-plate rubbing surfaces should be investigated with a view to determining the effect of pressure and leakage flow on the debris particle generation and resulting surface topographical variations. A radiographical study of monitoring wear particle sizes and number of particles should be conducted concurrently with this investigation.

Design criteria for hydrostatic and hydrodynamic seals should be developed, based on theory and experimental verification. The experimental verification is particularly important because of instability and other dynamic factors not readily predictable.

14.4 References

- 14-1 E.C. Rodabaugh, "Development of Mechanical Fittings," Report RTD-TRD-63-115, Battelle Memorial Institute, (Dec 1963)

APPENDIX I
EXPERIMENTAL RESULTS OF STATIC GASKET EXPERIMENTS

APPENDIX II
EXPERIMENTAL INVESTIGATION OF SLIDING CONTACT
AND LEAKAGE OF A SEALING INTERFACE

APPENDIX III
EFFECTS OF PHASE CHANGES ON LEAKAGE RATES
THROUGH ROTARY FACE SEALS

APPENDIX IV
EXPERIMENTAL LOAD DEFLECTION CURVES

APPENDIX V
CRITERIA FOR COMPONENT COVERS

APPENDIX VI
STRUCTURAL ANALYSIS OF SEALS AND DERIVATION
OF FACTOR K

APPENDIX VII
DESCRIPTION OF STATIC
AND SLIDING SEAL EXPERIMENTAL APPARATUS

APPENDIX VIII
DEVELOPMENT OF A COMPUTER CODE
FOR ESTABLISHING EMPIRICAL DATA
FROM EXPERIMENTAL DATA

APPENDIX I

EXPERIMENTAL RESULTS OF STATIC GASKET EXPERIMENTS

The apparatus used in the static gasket leakage experiments is described briefly and graphical results of experiments conducted by IITRI, Rocketdyne and General Electric are presented in this appendix.

I-1. Experimental Apparatus and Procedures

The general procedures used in the experimental evaluation of static interfaces are described in Reference I-1 and are not repeated. A new evaluation fixture was constructed, however, and the details of it are contained herein.

Figure I-1 shows a schematic view of the experimental apparatus. The equipment consists of a base plate which contains a displacement transducer and its appropriate electrical connector, a port for introducing pressurized fluid media, and a port for connecting a leakage measuring instrument. A bellows welded to the base plate acts as an elastic member, allowing deflection of apparatus with the application of load as well as a leakage collector. A V-band clamp and O-ring with their appropriate mating ring and plate are attached to the upper end of the bellows and base plate. This feature allows assembly of the upper and lower flanges between which an experimental gasket is placed. The lower flange is centered with respect to the base plate and transducer by a locating recess in the base plate. The upper flange and gasket are free floating and held in place during assembly by the loading apparatus. The V-band clamp is tightened after load application but before the introduction of pressurized fluid.

The displacement transducer is a LVDT and provides an electrical output proportional to linear displacement. The motion of the upper flange with respect to the lower flange upon application of load is the displacement measured. Contact between transducer core and upper flange is assured by spring loading the core and core extension assembly. The transducer is zeroed or balanced after the flanges and gaskets are assembled but before any load is applied.

Seals on all connectors, electrical and mechanical, are O-rings. Dual O-ring seals are used between the lower flange and the fixture base. A cavity between the two seal rings is evacuated to eliminate leakage between the inlet and outlet at the bottom of the lower flange.

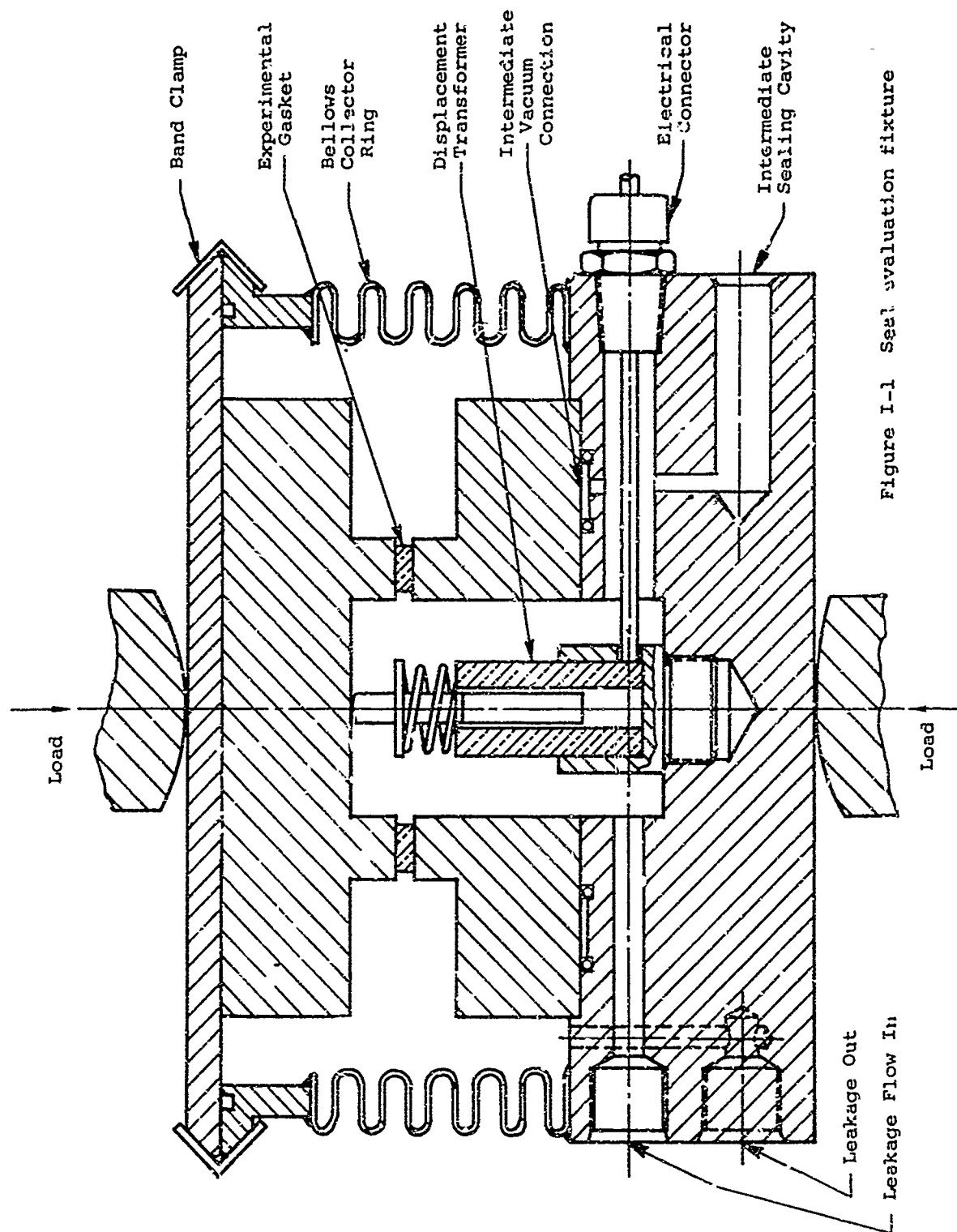


Figure I-1 Seal evaluation fixture

I-2 Experimental Results

The presentation of the following detailed experimental results is not a requisite in the attainment of the objectives of this report. The important information, deduced from these results, is presented in Section 2. Consequently, they have no immediate value. However, further development of design criteria will no doubt continue and the availability of the detailed results will enhance this effort. Also, the results, while not of interest to the systems designer, should be of interest to those doing research on seals. Some of the data have already been presented in the literature in the form of leakage-stress correlations. These data with new leakage data were rearranged in a new format using the conductance parameter as a variable. These data are presented in this form for the first time.

Complete identification of the source of data and other definitions are contained in Section 2. The data for each experiment are identified by a code designation. In addition, the gasket material and surface finish are included to complete the identification. The source of information can be deduced from the letter prefix of the code designation: R - represents data from Rocketdyne Division North American Aviation and GE - represents data from General Electric Co. The balance of the data was obtained by IITRI.

I-3 References

- I-1 Paul A. Bauer, Myron Glickman and Frank Iwatsuki, Analytical Techniques for the Design of Seals for Use in Rocket Propulsion Systems, Volume I and II, AFRPL-TR-65-61, IIT Research Institute, Chicago (May 1965)

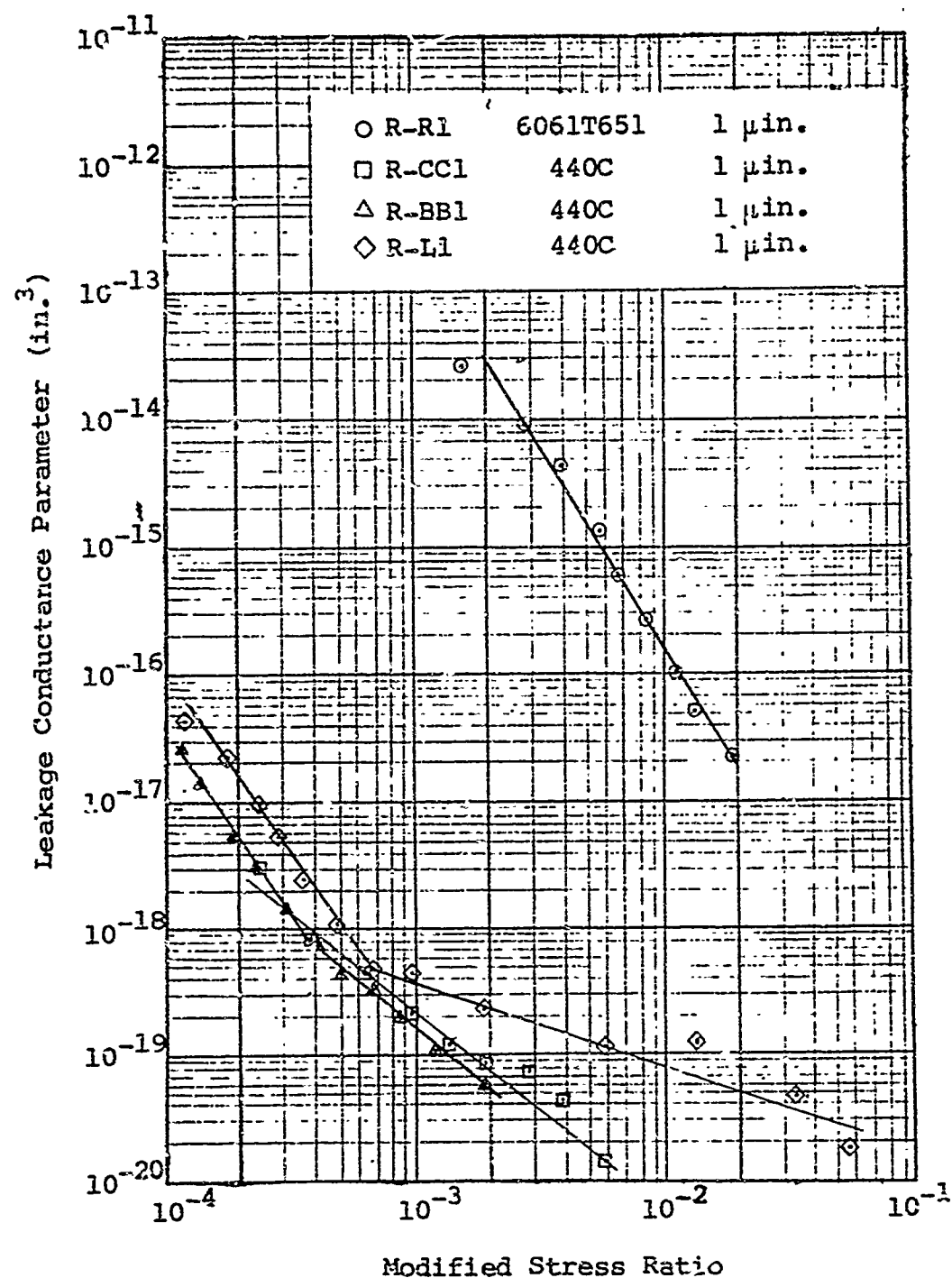


Figure I-2 Conductance parameter - modified stress ratio for 1-μin. PTV seal surfaces

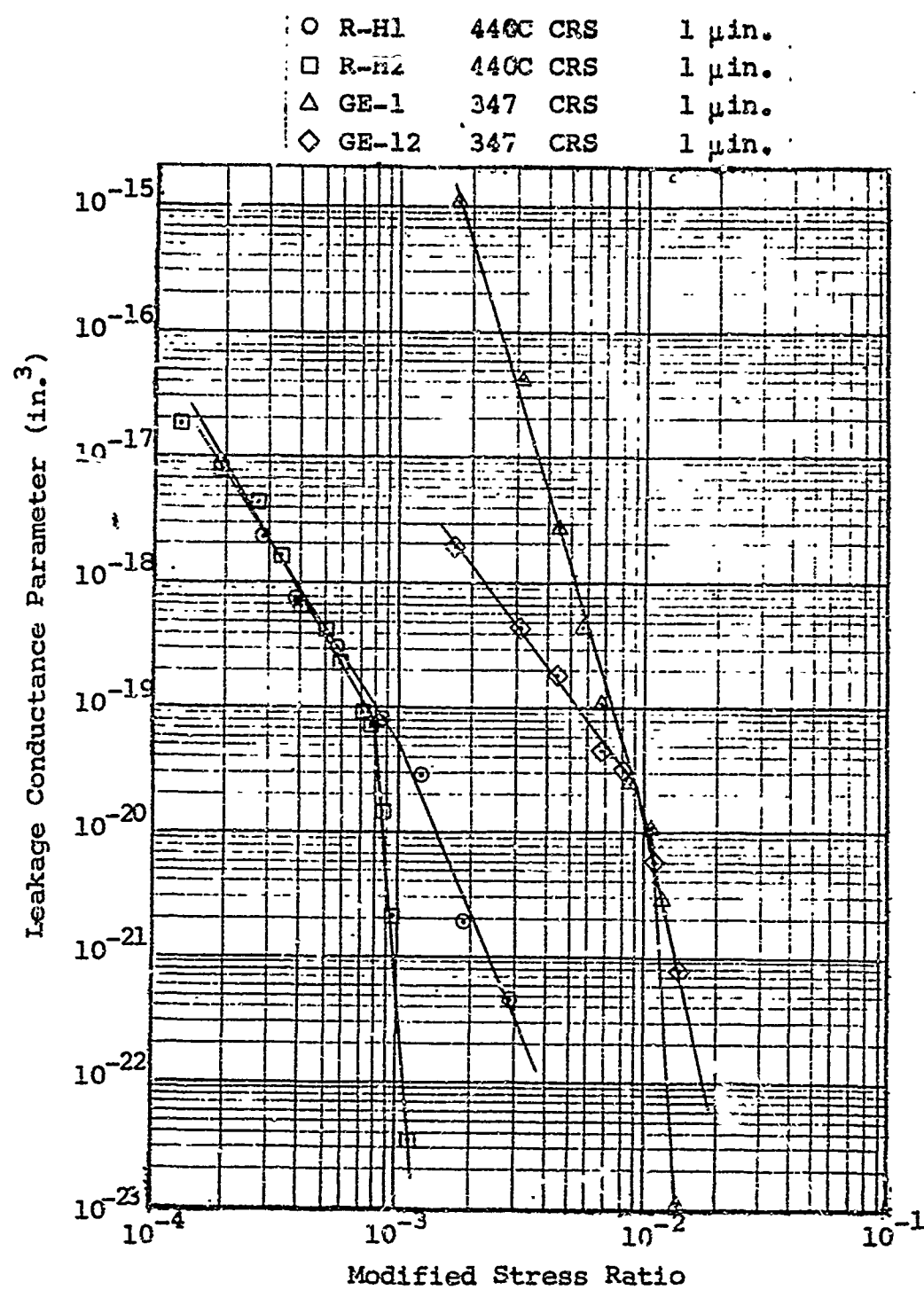


Figure I-3 Conductance parameter - modified stress ratio for 1- μ in. PTV seal surfaces

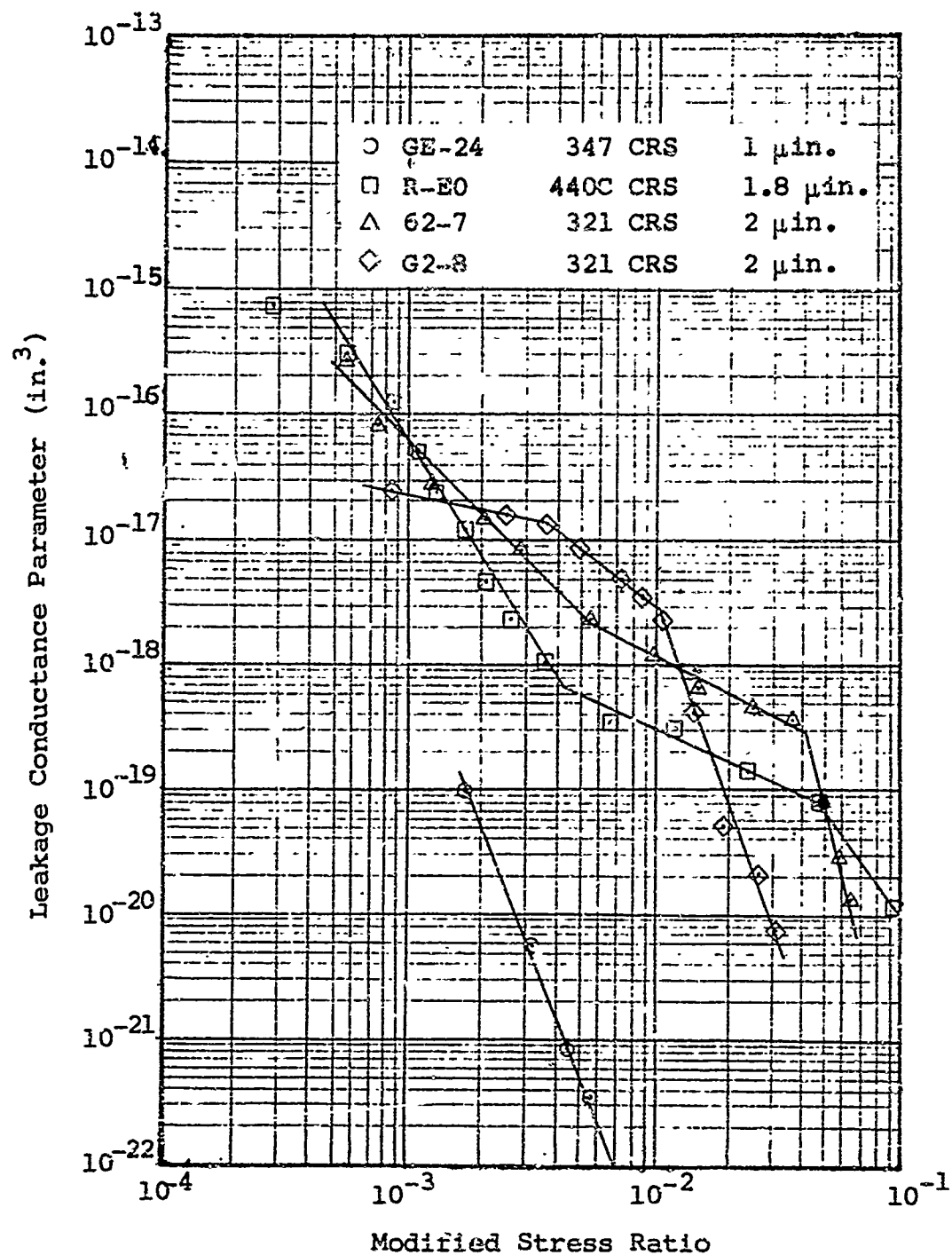


Figure I-4 Conductance parameter - modified stress ratio for 1-2-μin. PTV seal surfaces

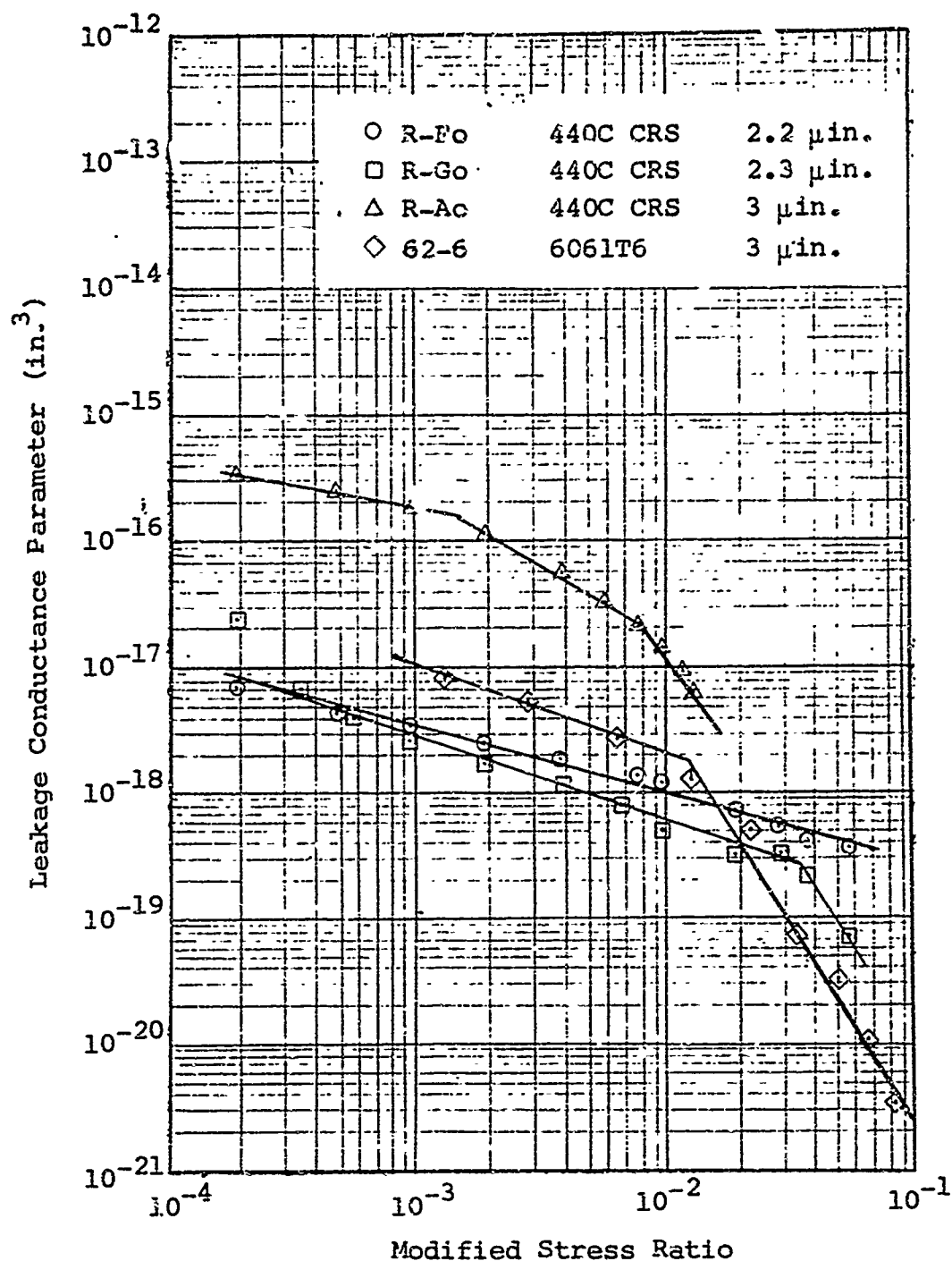


Figure I-5 Conductance parameter - modified stress ratio for 2.2-3-μin. PTV seal surfaces

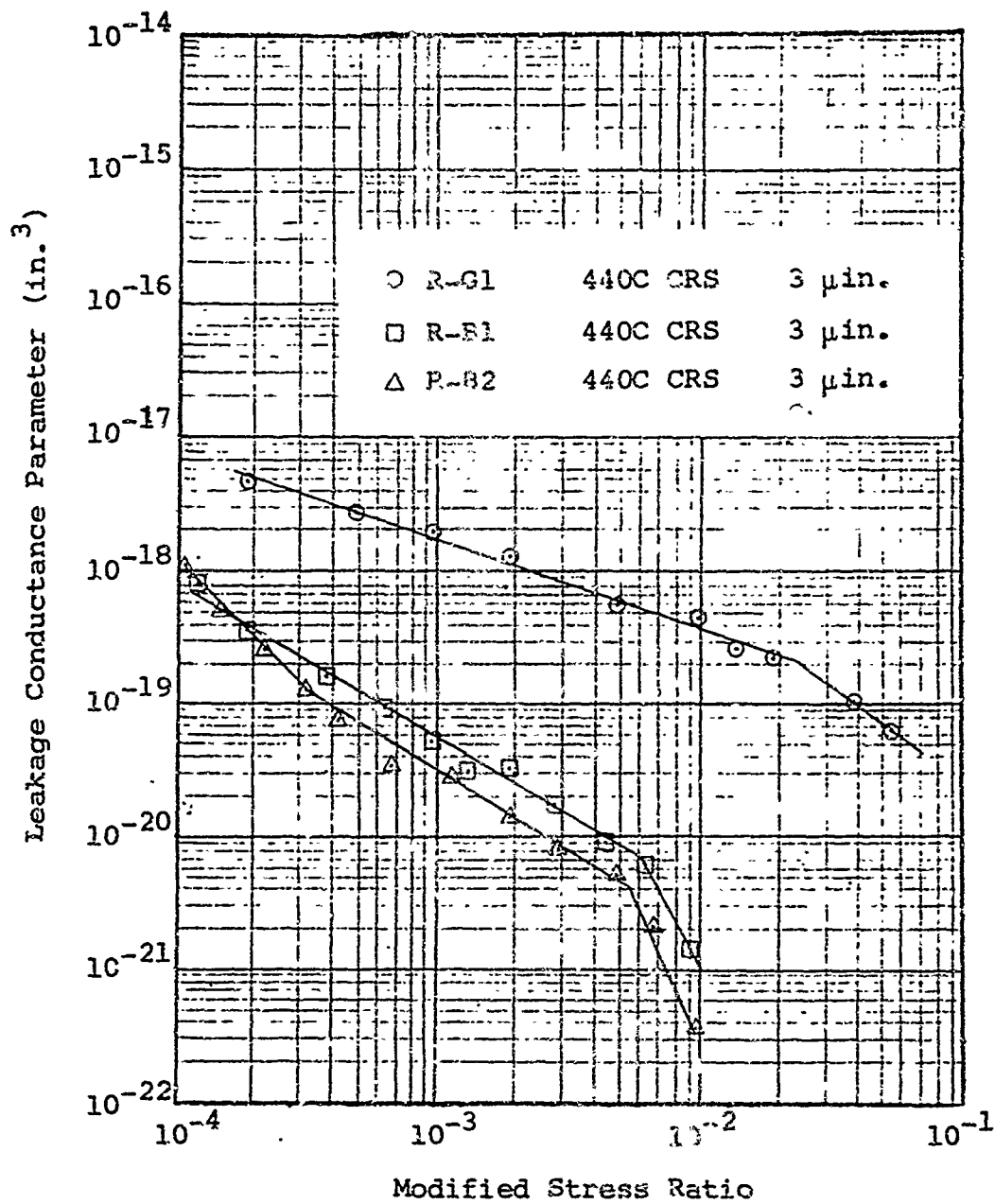


Figure I-6 Conductance parameter - modified stress ratio for 3-μin. PTV seal surfaces

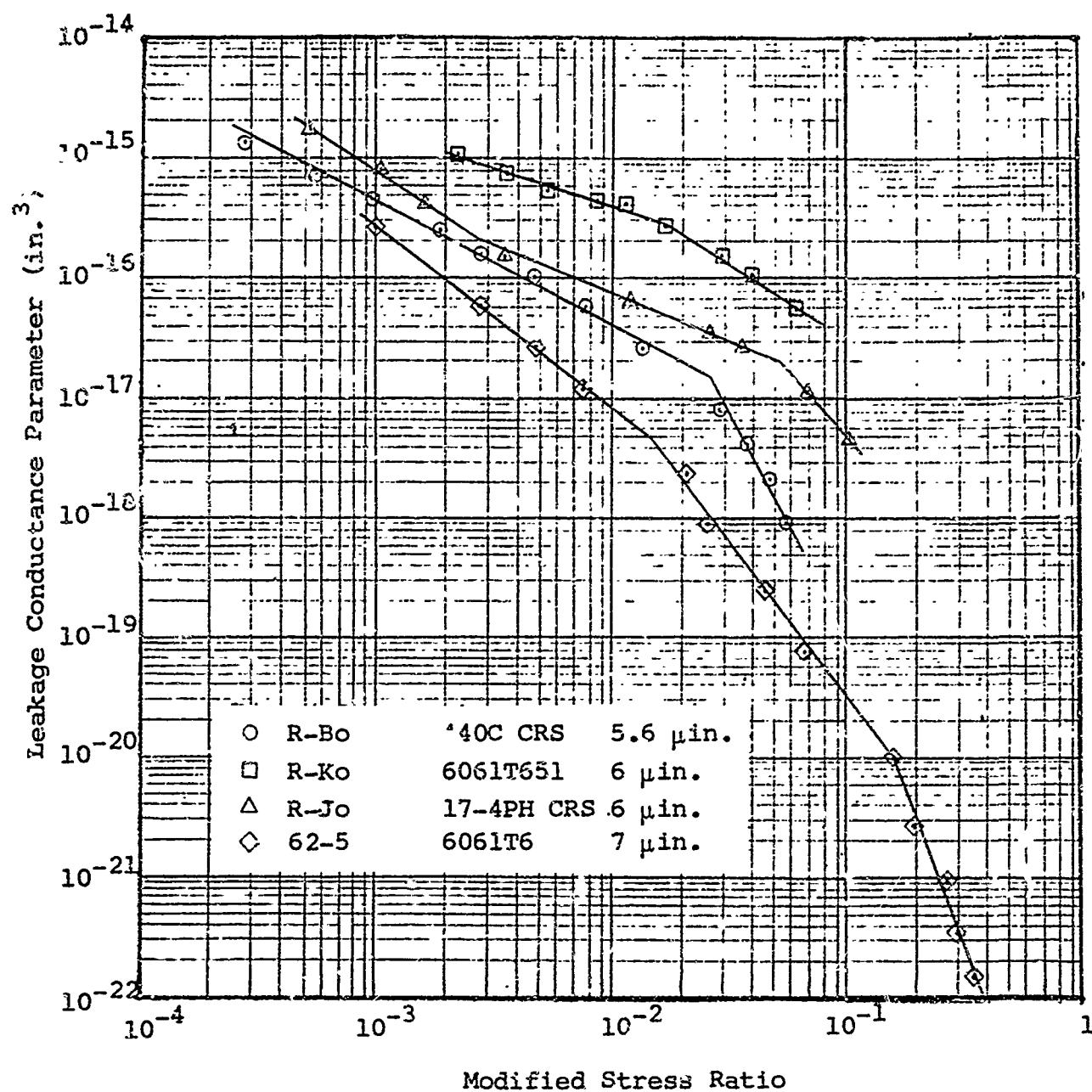


Figure I-7 Conductance parameter - modified stress ratio for 5.6-7-μin. PTV seal surfaces

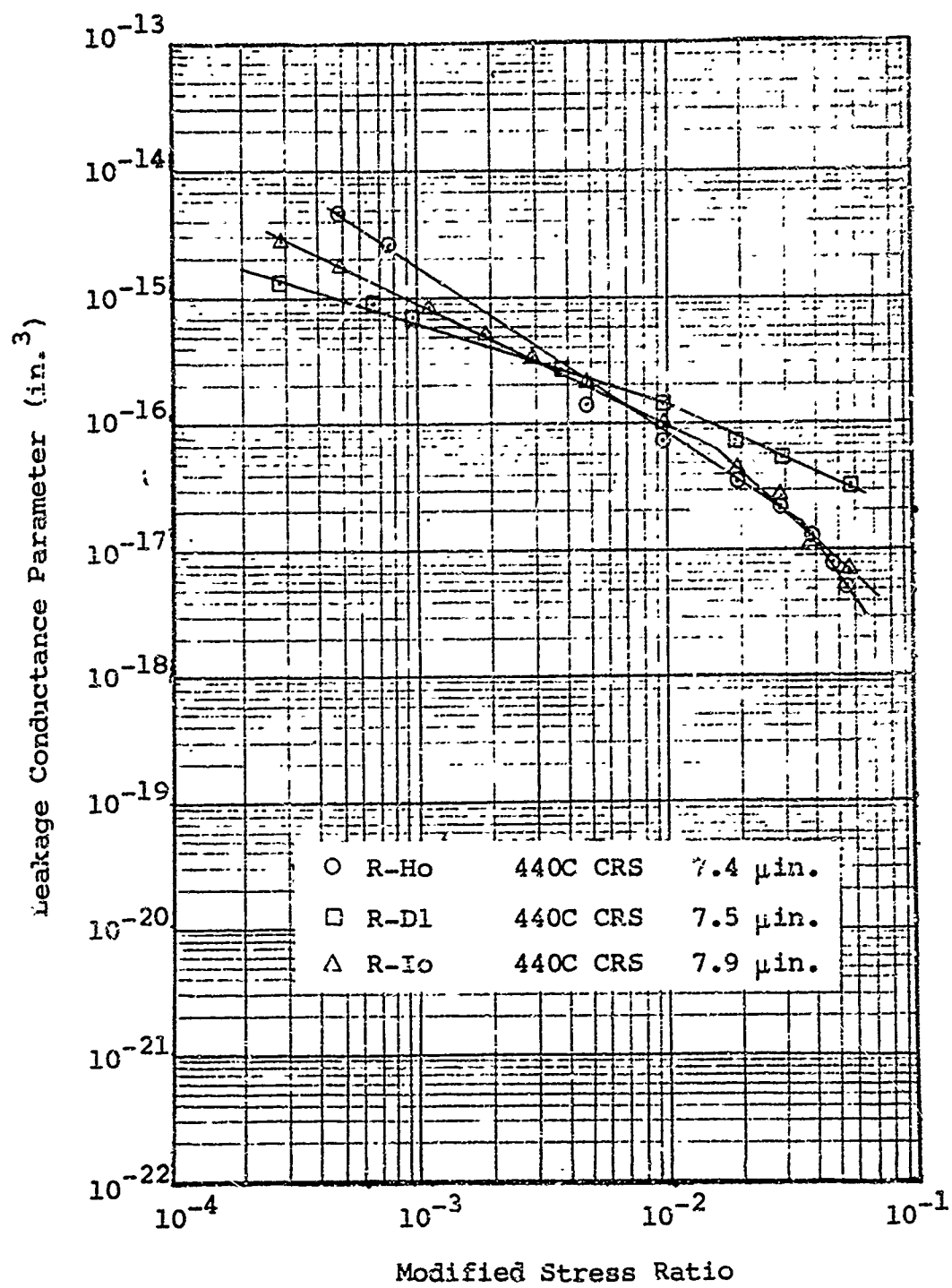


Figure I-8 Conductance parameter - modified stress ratio for 7.4 - 7.9-μin. PTV seal surfaces

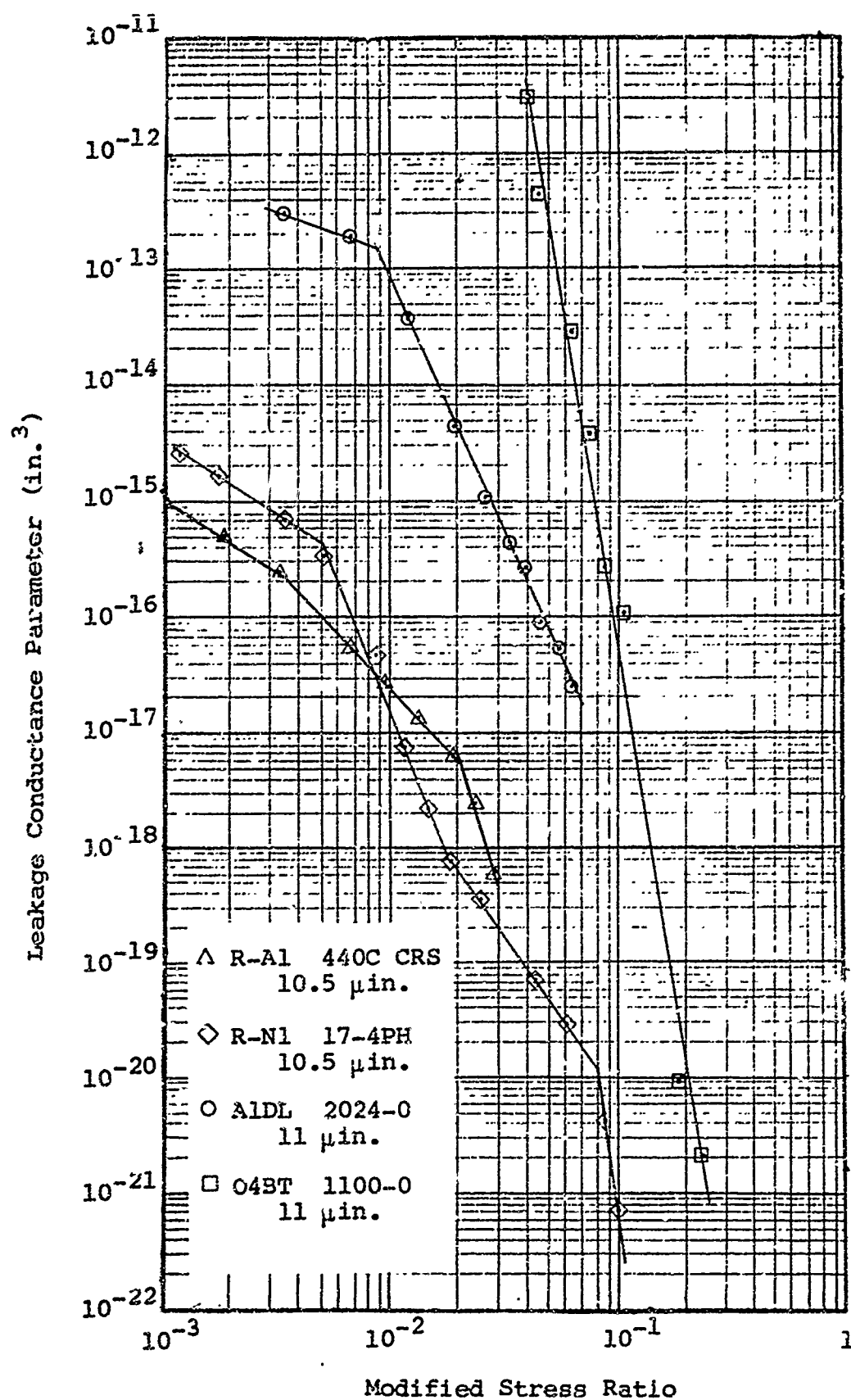


Figure I-9 Conductance parameter - modified stress ratio for 10.5 - 11-μin. PTV seal surfaces

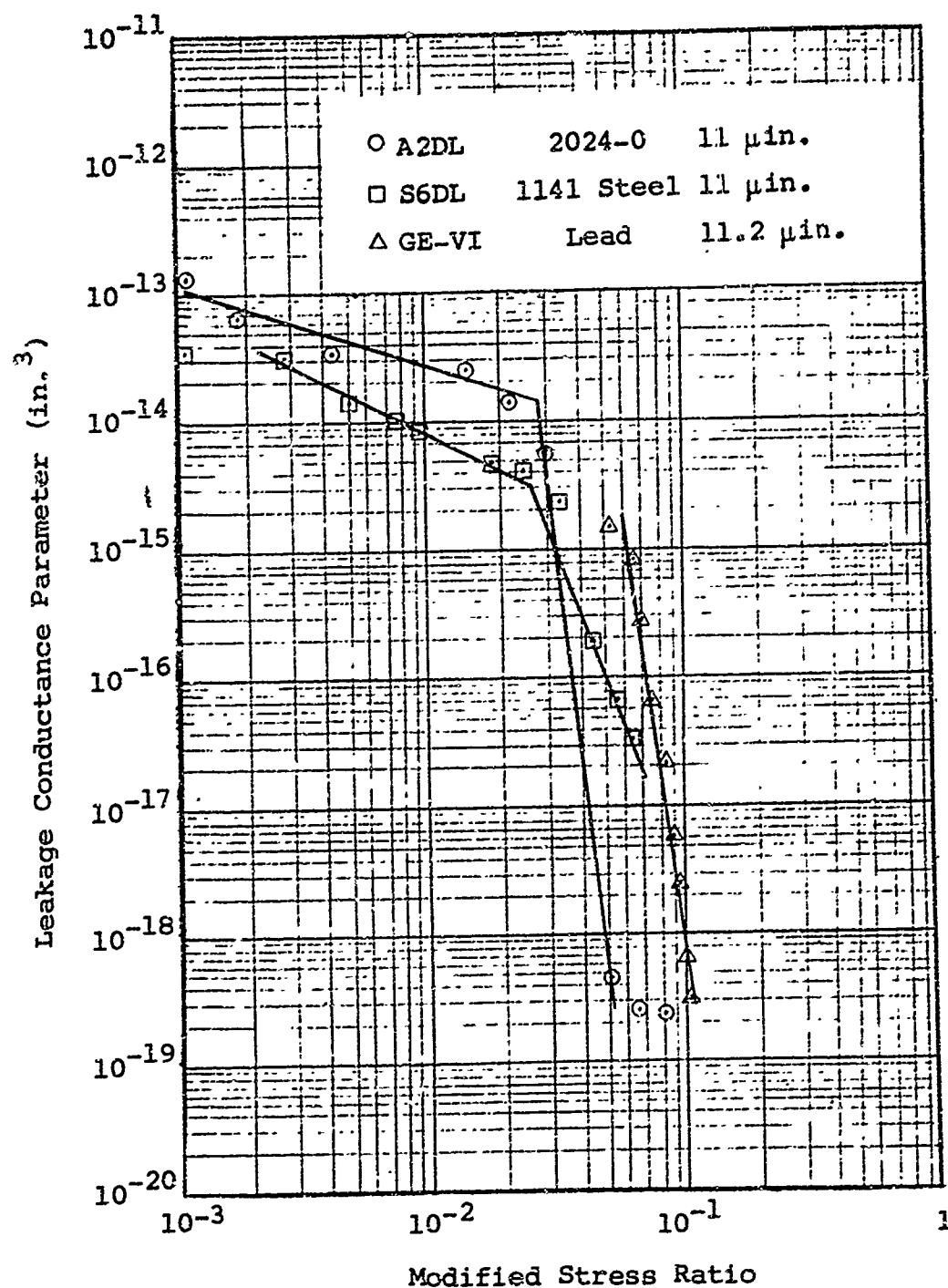


Figure I-10 Conductance parameter - modified stress ratio for 11-11.2-μin. PTV seal surfaces

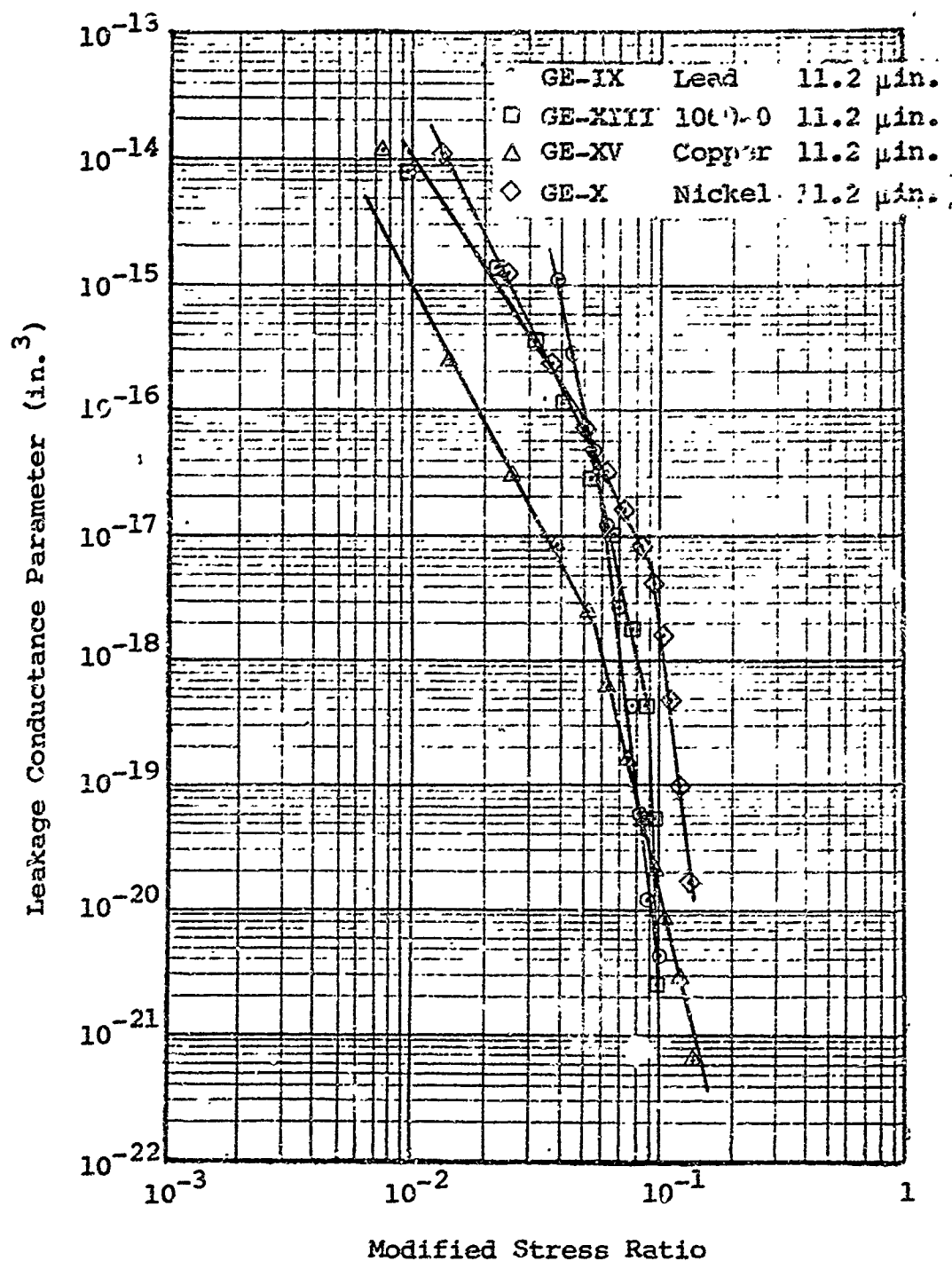


Figure I-11 Conductance parameter - modified stress ratio for 11.2-μin. PTV seal surfaces

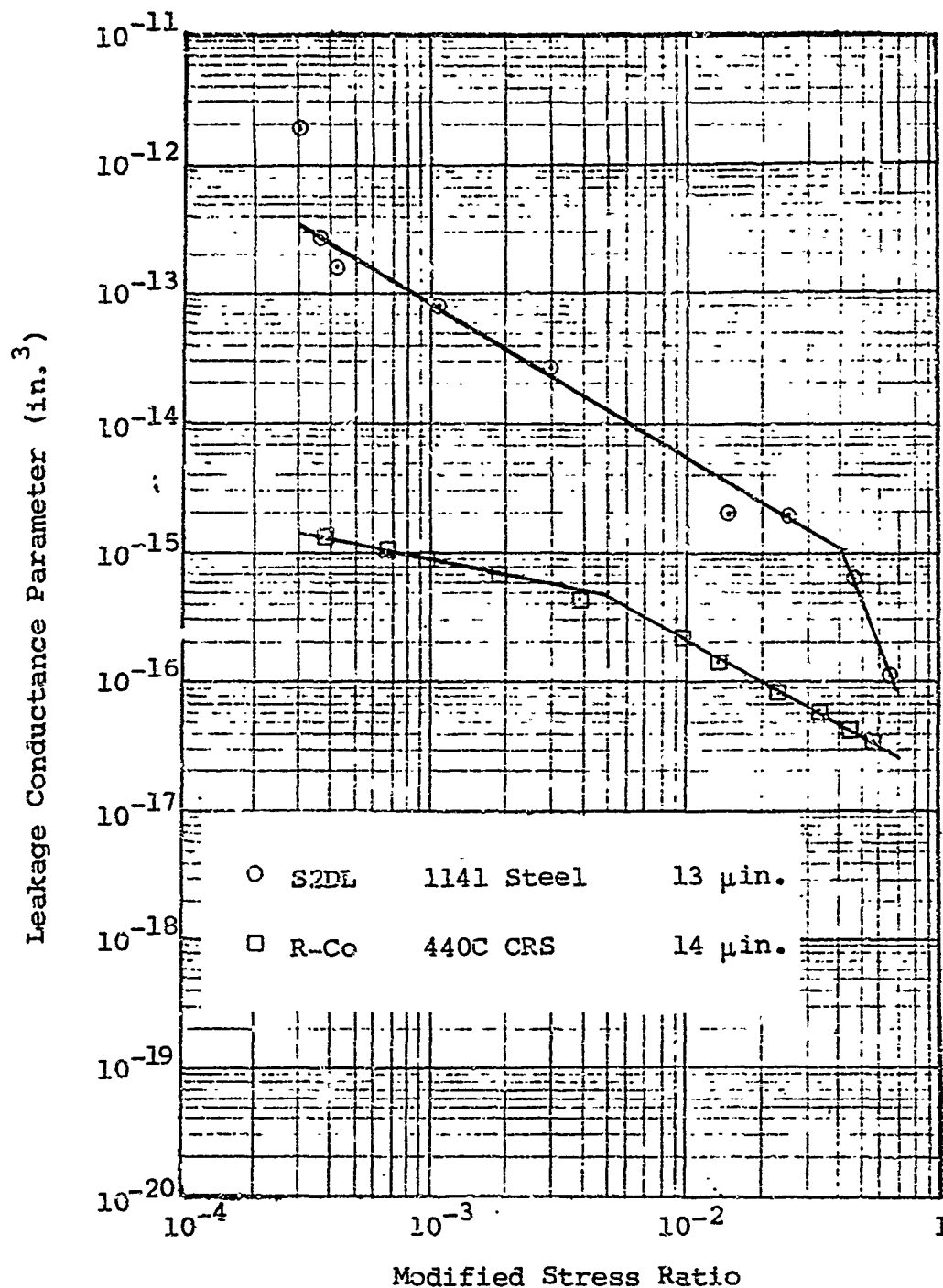


Figure I-12 Conductance parameter - modified stress ratio for 13 - 14-μin. PTV seal surfaces

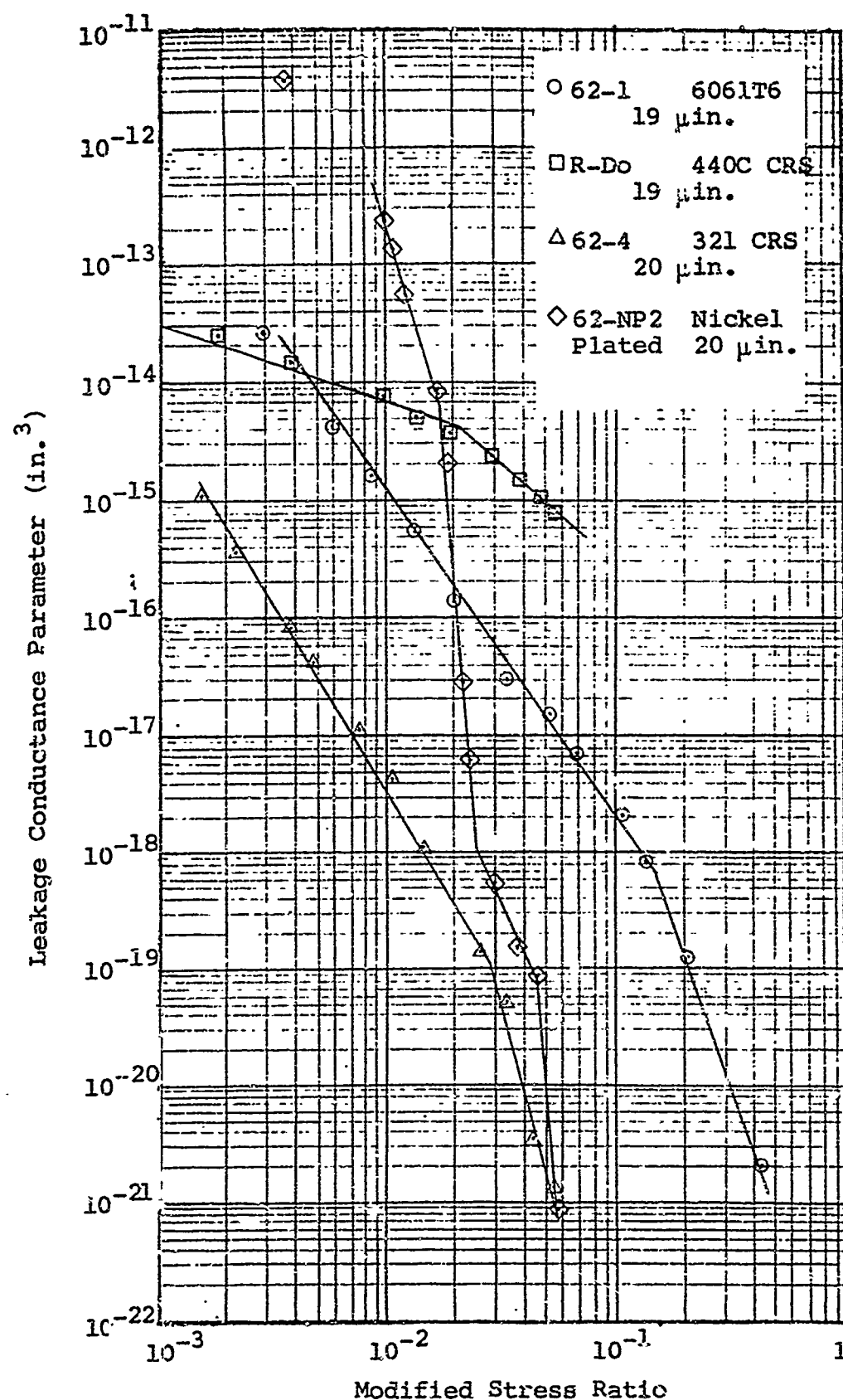


Figure I-13 Conductance parameter - modified stress ratio for 19 - 20- μ in. PTV seal surfaces

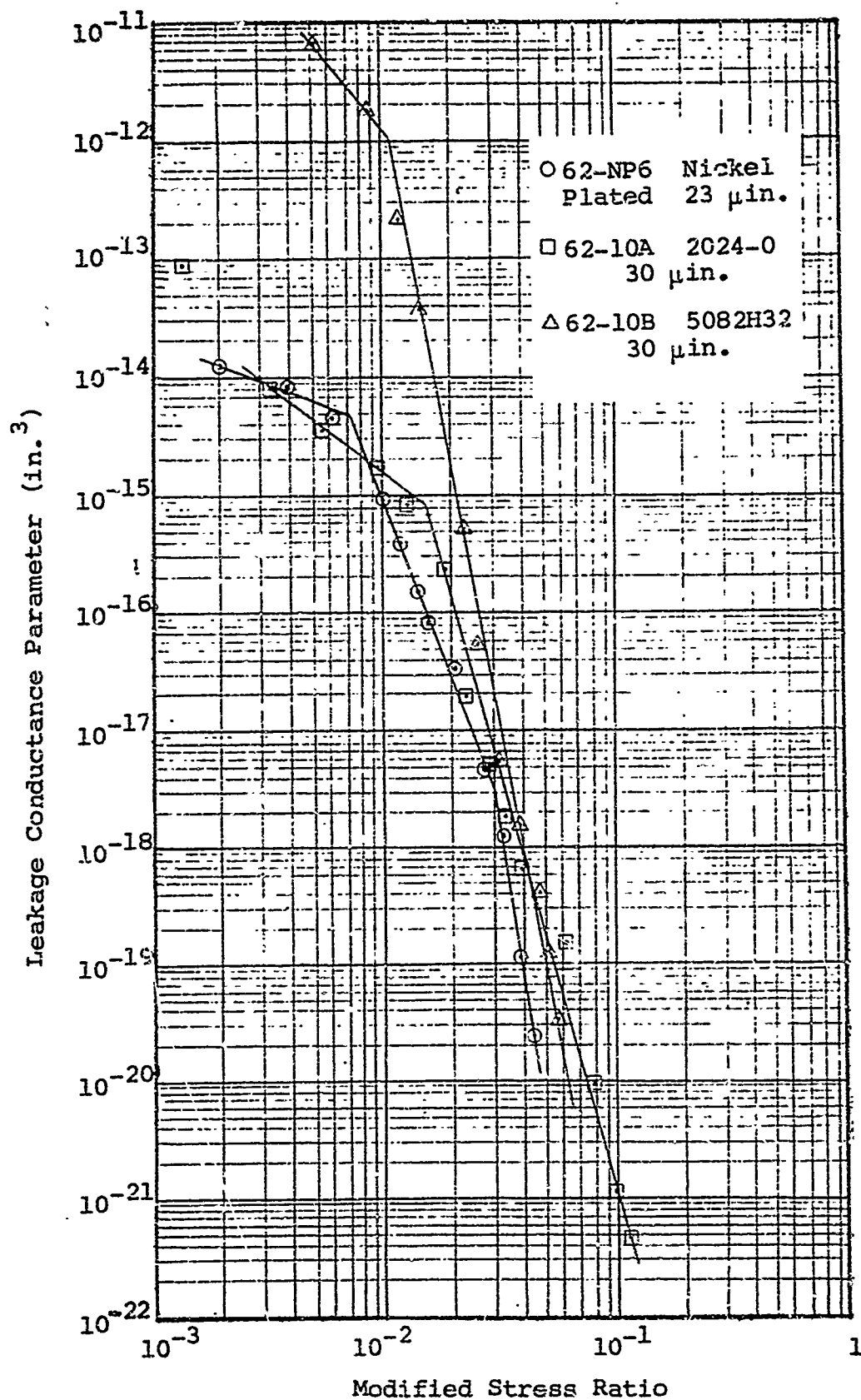


Figure I-14 Conductance parameter - modified stress ratio for 23 - 30- μ in. PTV seal surfaces

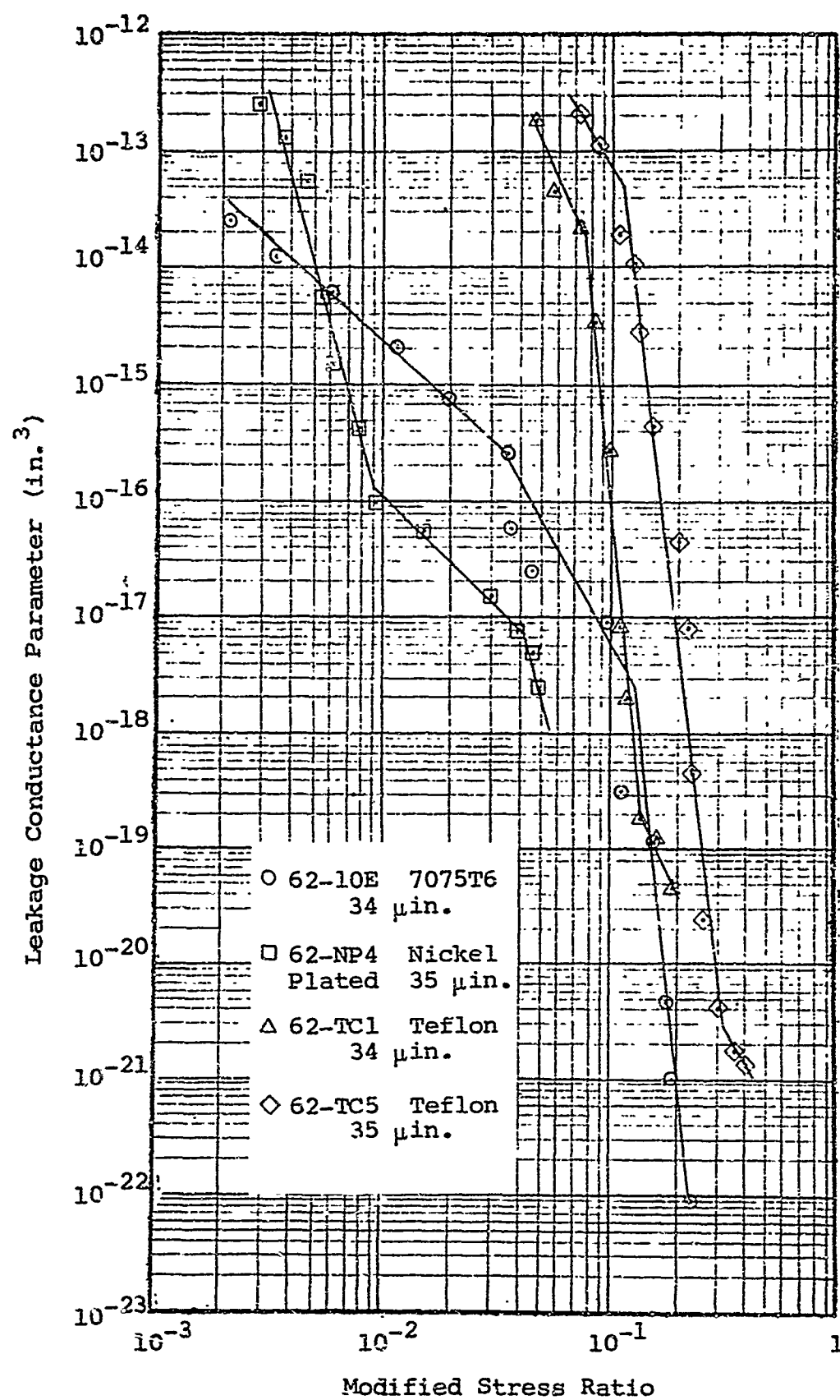


Figure I-15 Conductance parameter - modified ratio ratio for 34 - 35-μin. PTV seal surfaces

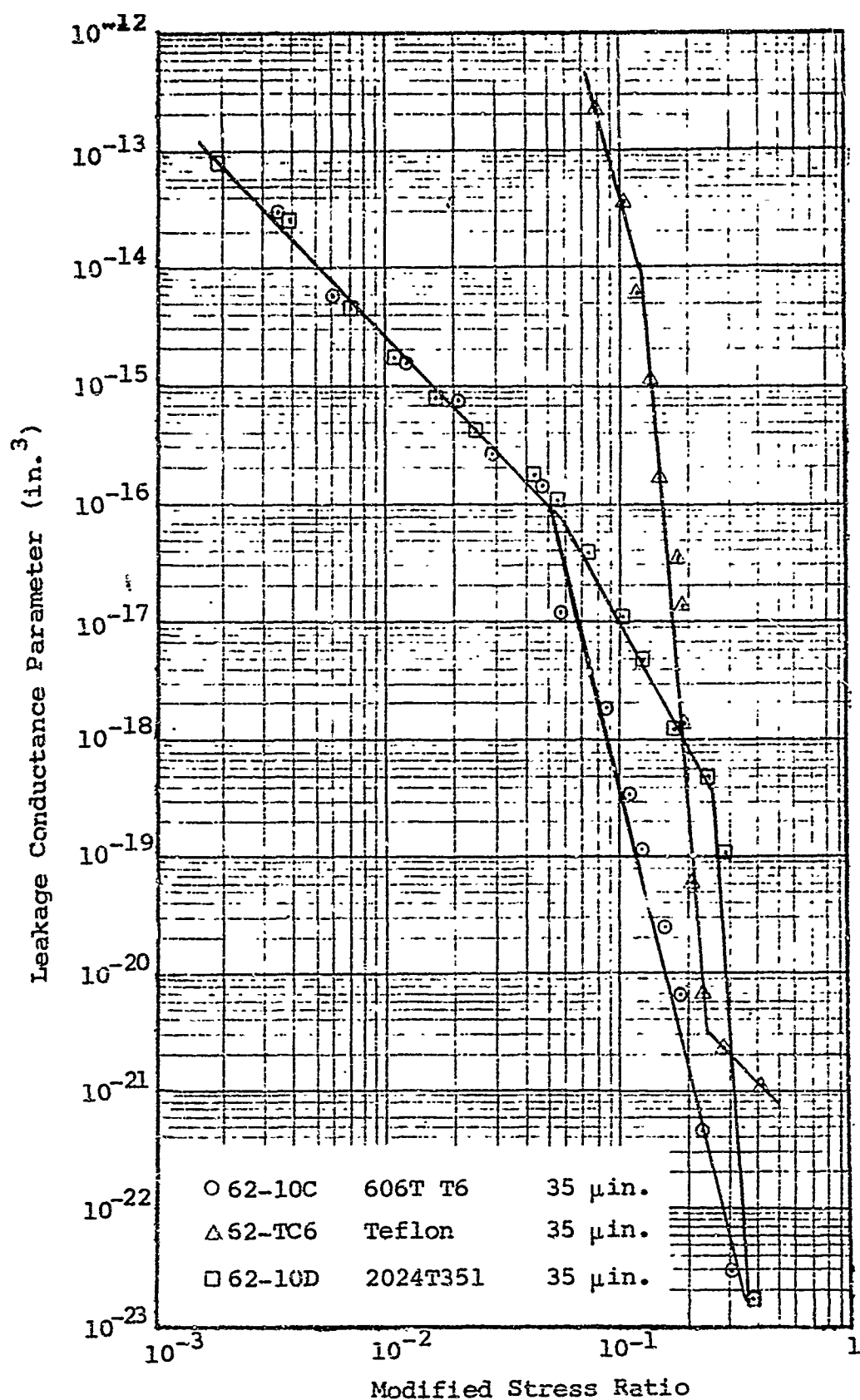


Figure I-16 Conductance parameter - modified stress ratio for 35-μin. PTV seal surfaces

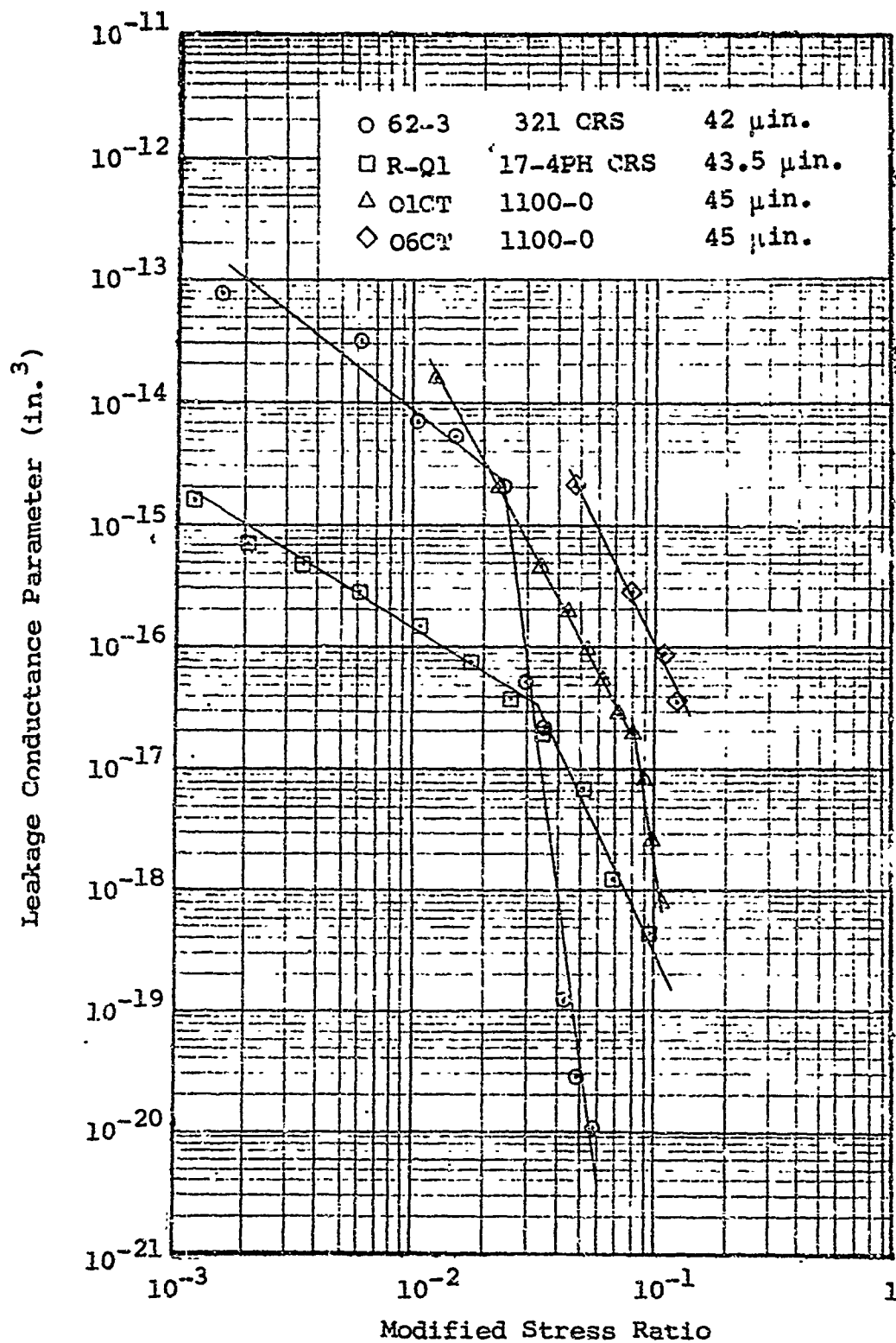


Figure I-17 Conductance parameter - modified stress ratio for 42 - 45-μin. PTV seal surfaces

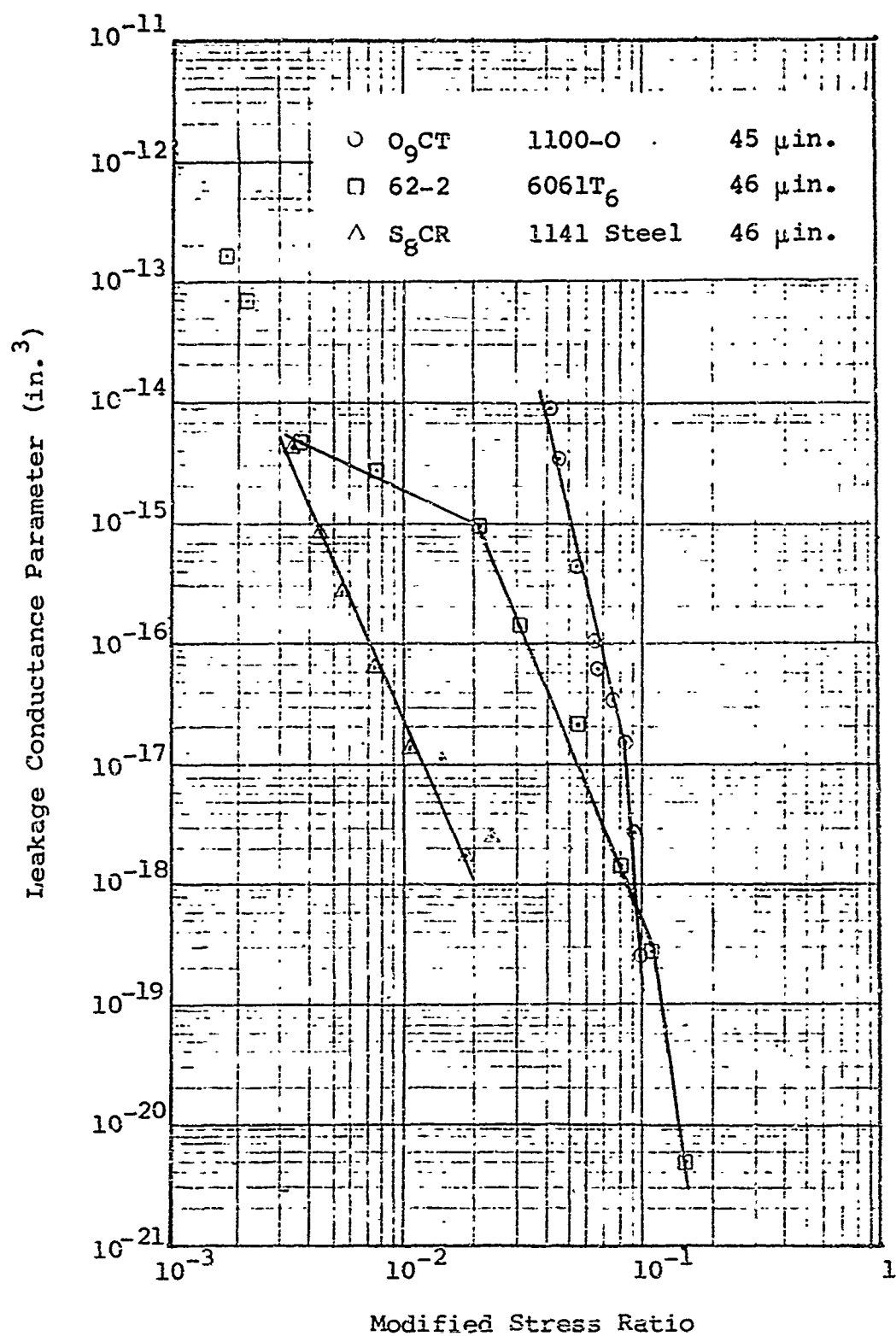


Figure I-18 Conductance parameter - modified stress ratio for 45 - 46 $\mu\text{in.}$ PTV seal surfaces

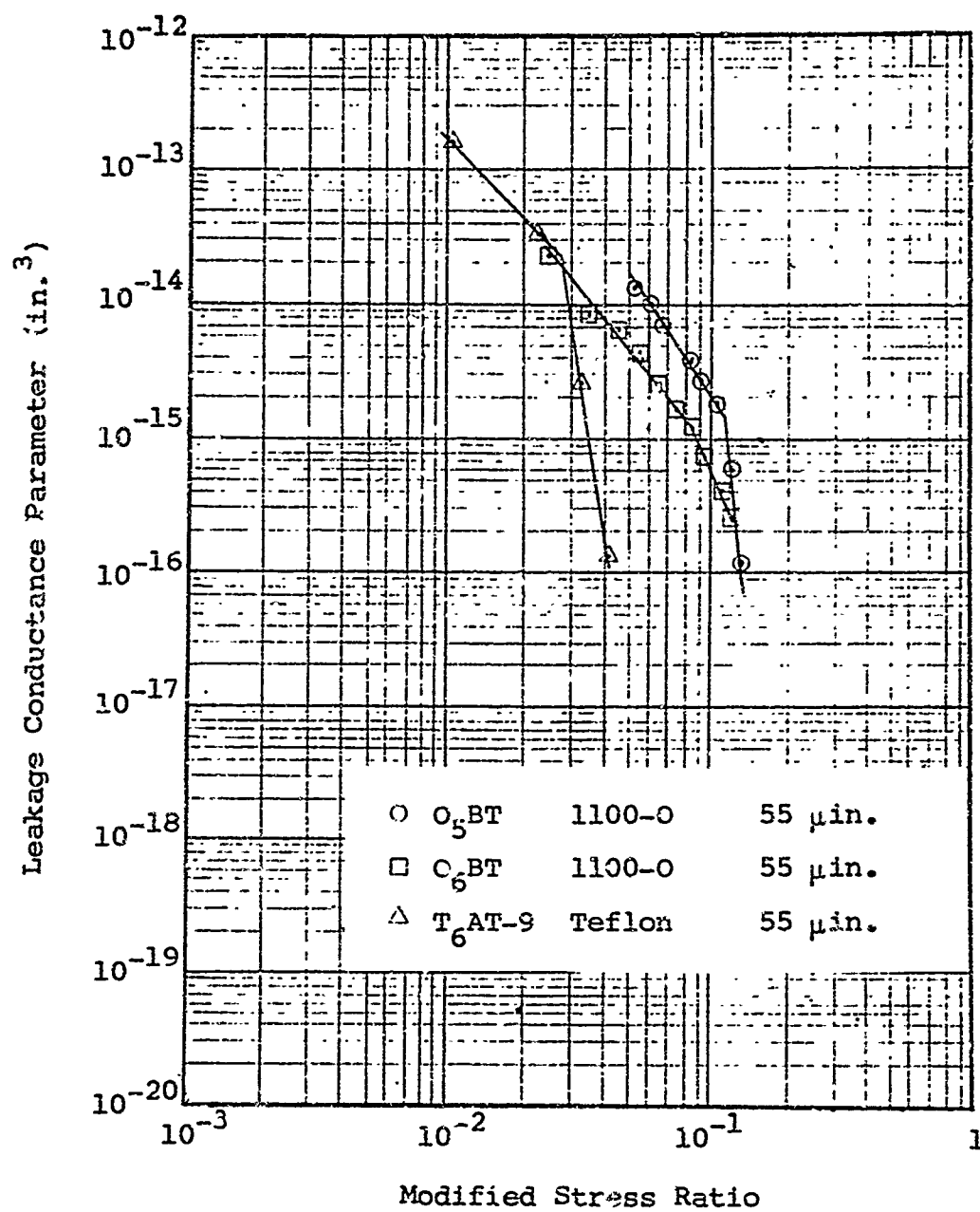


Figure I-19 Conductance parameter - modified stress ratio for 55-μin. PTV seal surfaces

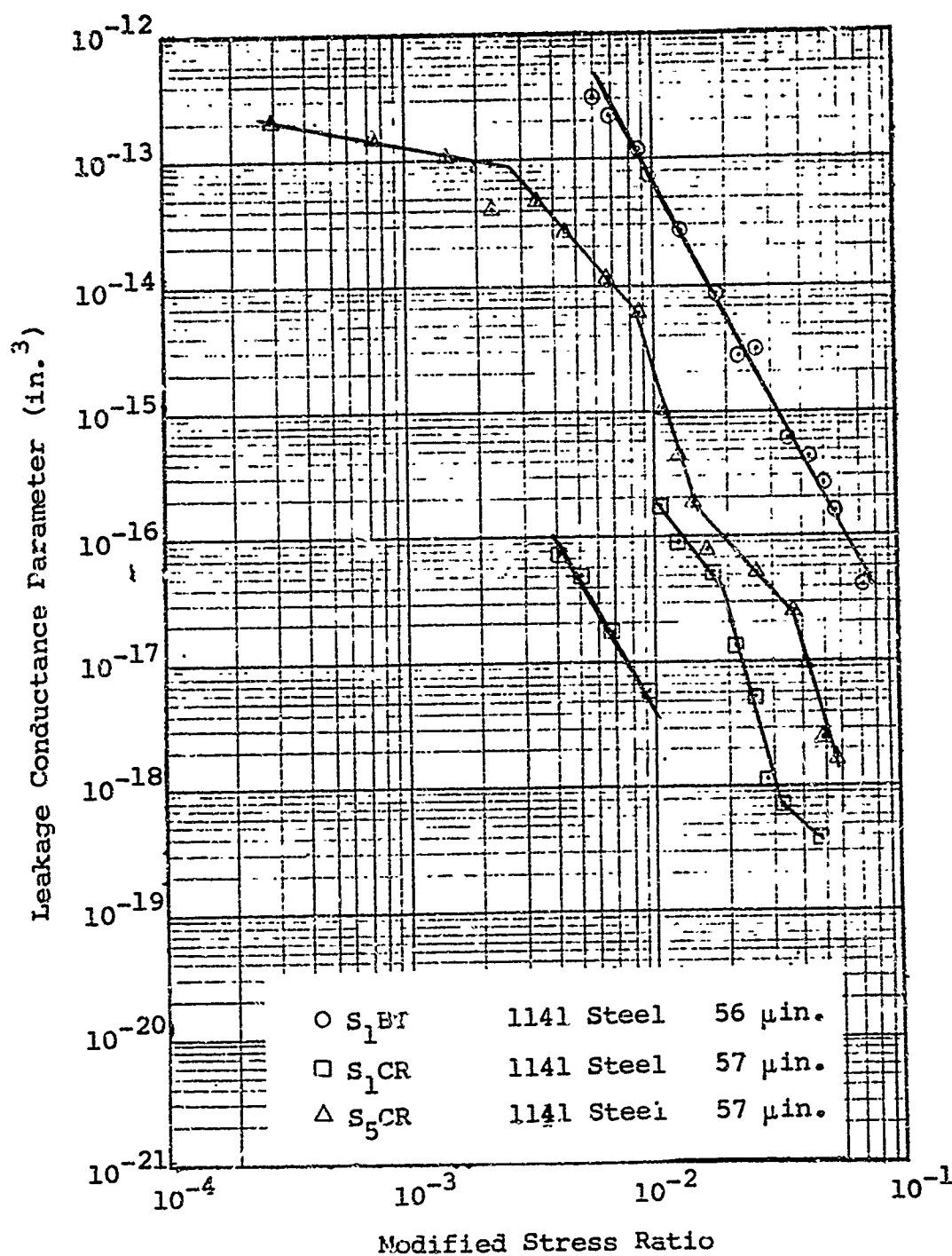


Figure I-20 Conductance parameter - modified stress ratio for 56 - 57 μ in. PTV seal surfaces

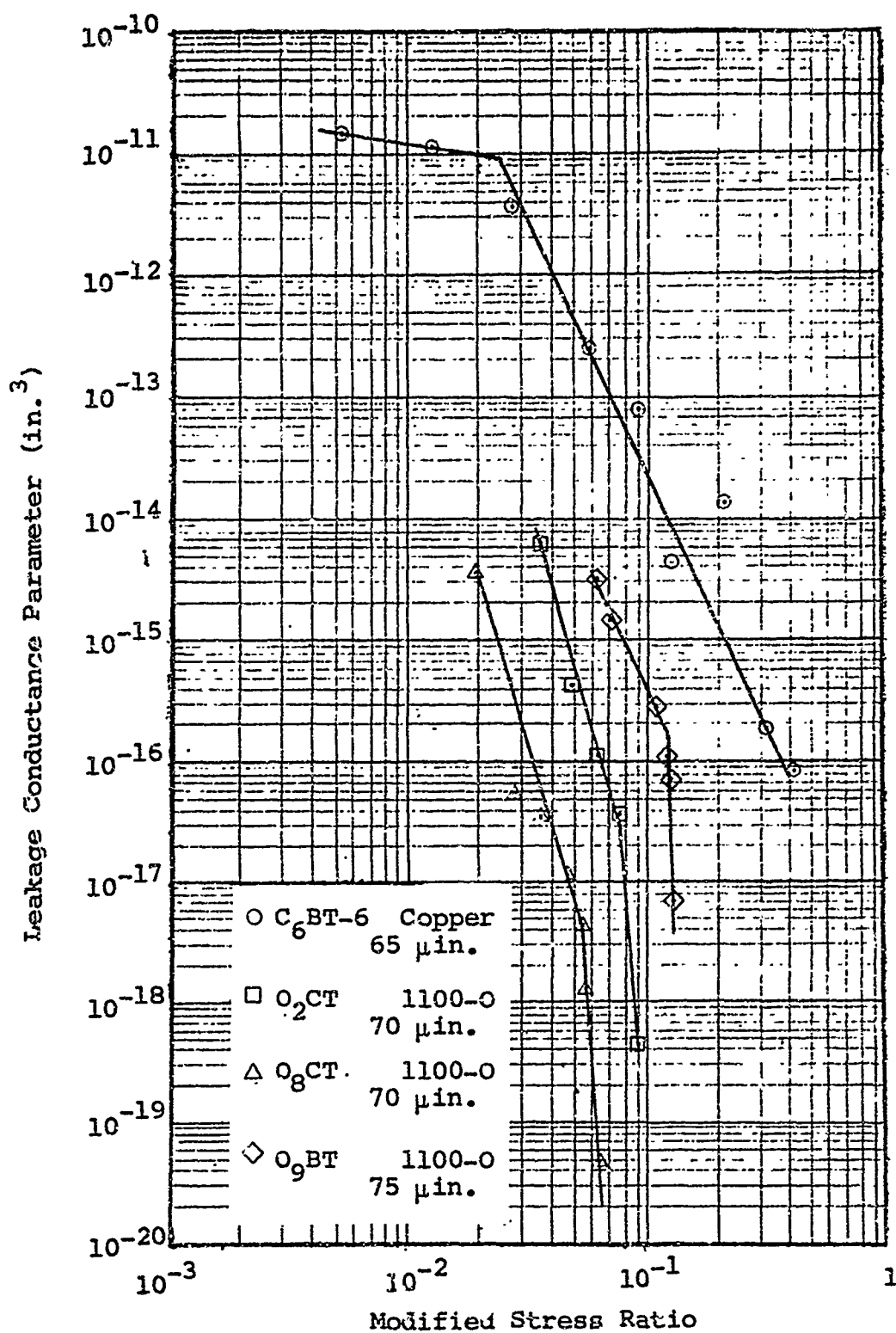


Figure I-21 Conductance parameter - modified stress ratio for 65 - 75-μin. PTV seal surfaces

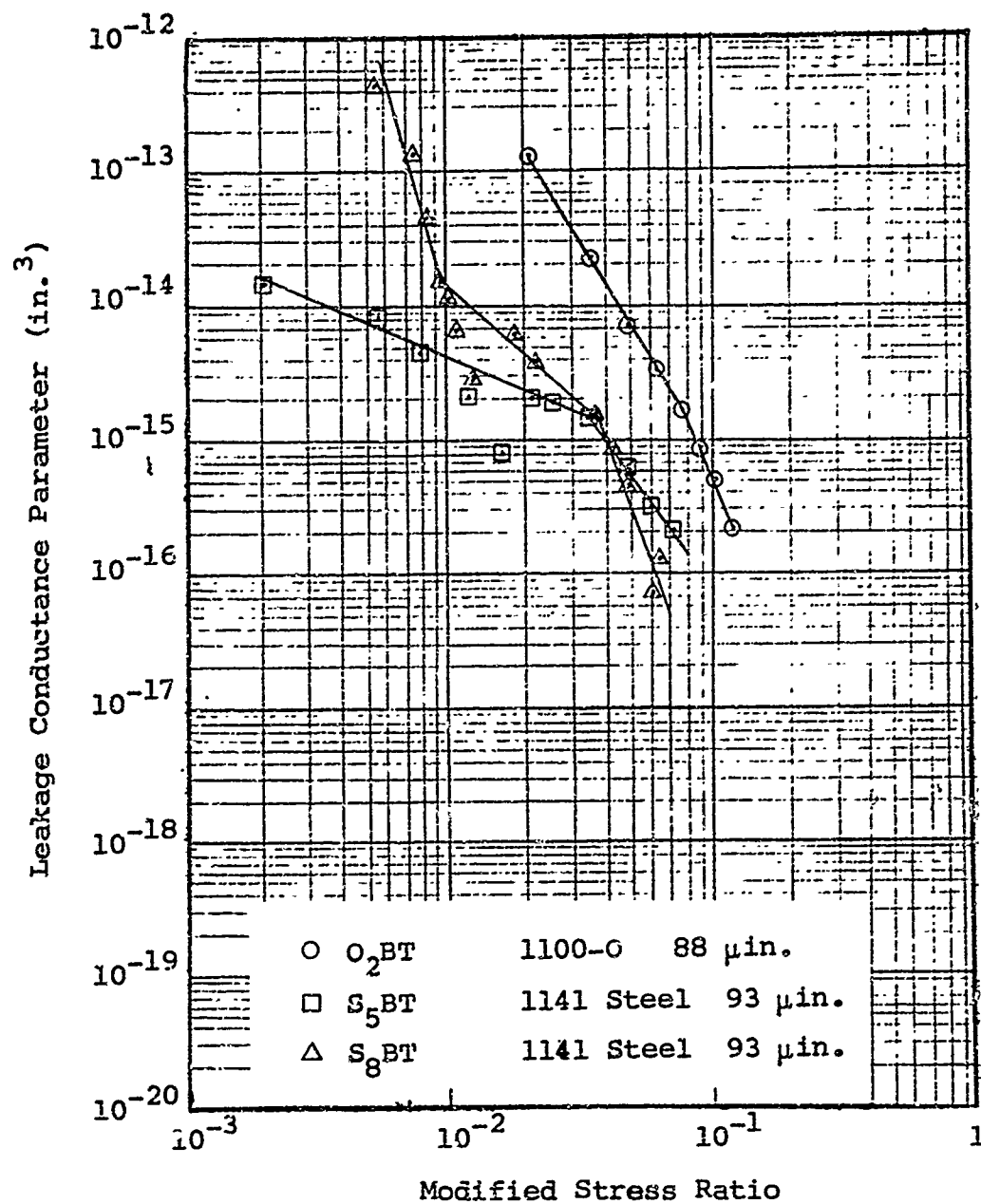


Figure I-22 Conductance parameter - modified stress ratio for 88 - 93-μin. PTV seal surfaces

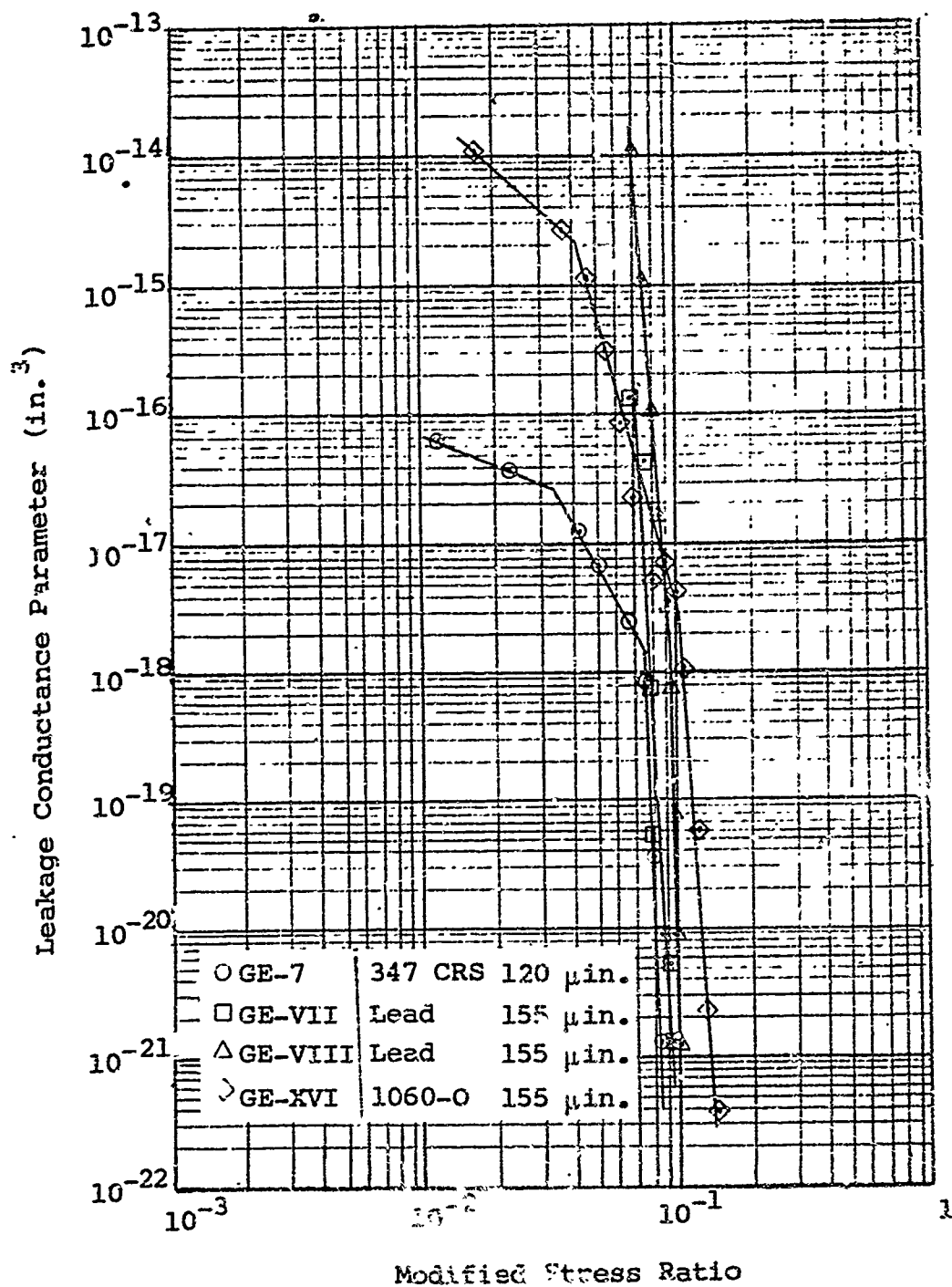


Figure I-23 Conductance parameter - modified stress ratio for 120 - 155-μin. PTV seal surfaces

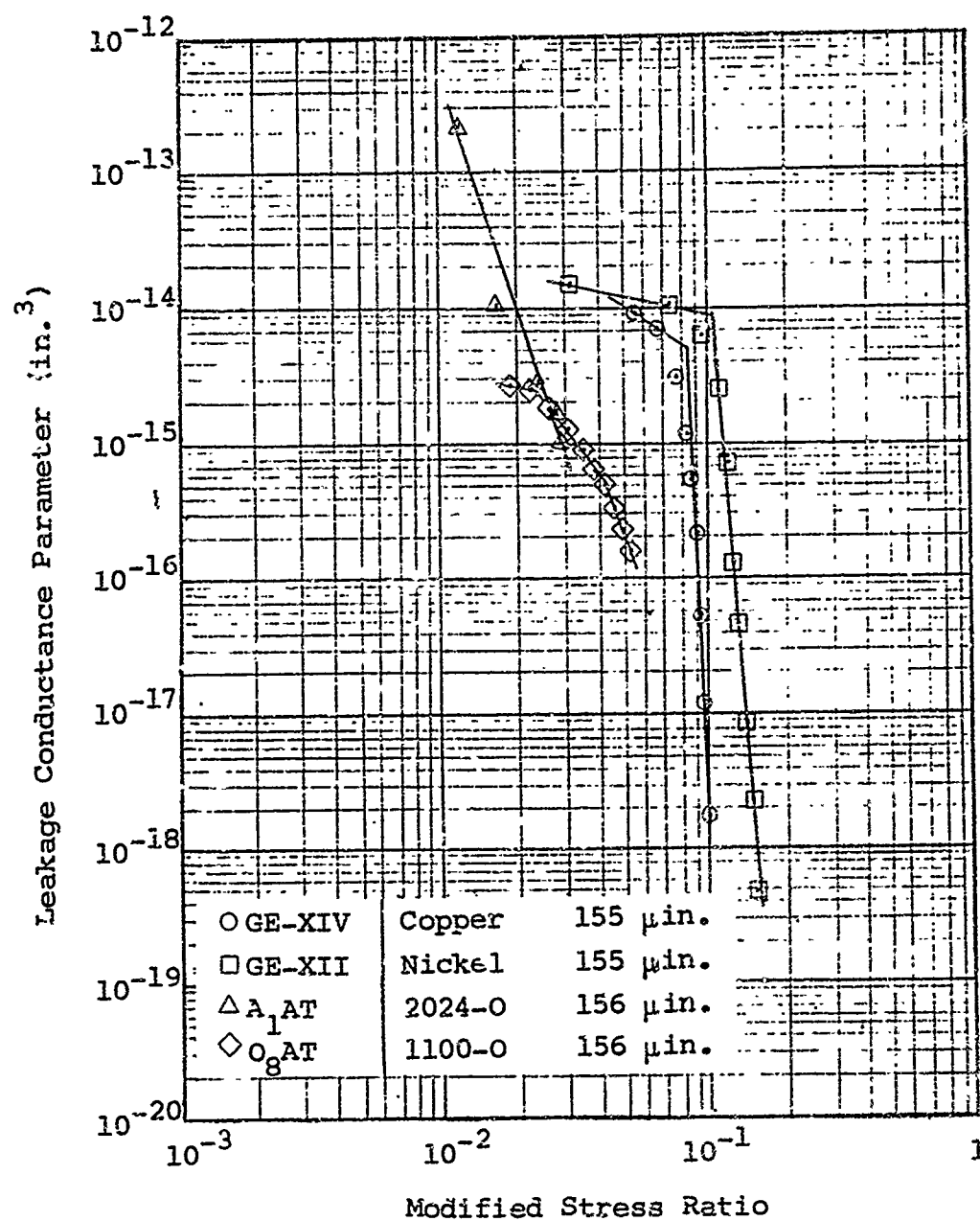


Figure I-24 Conductance parameter - modified stress ratio for 155 - 156-μin. PTV seal surfaces

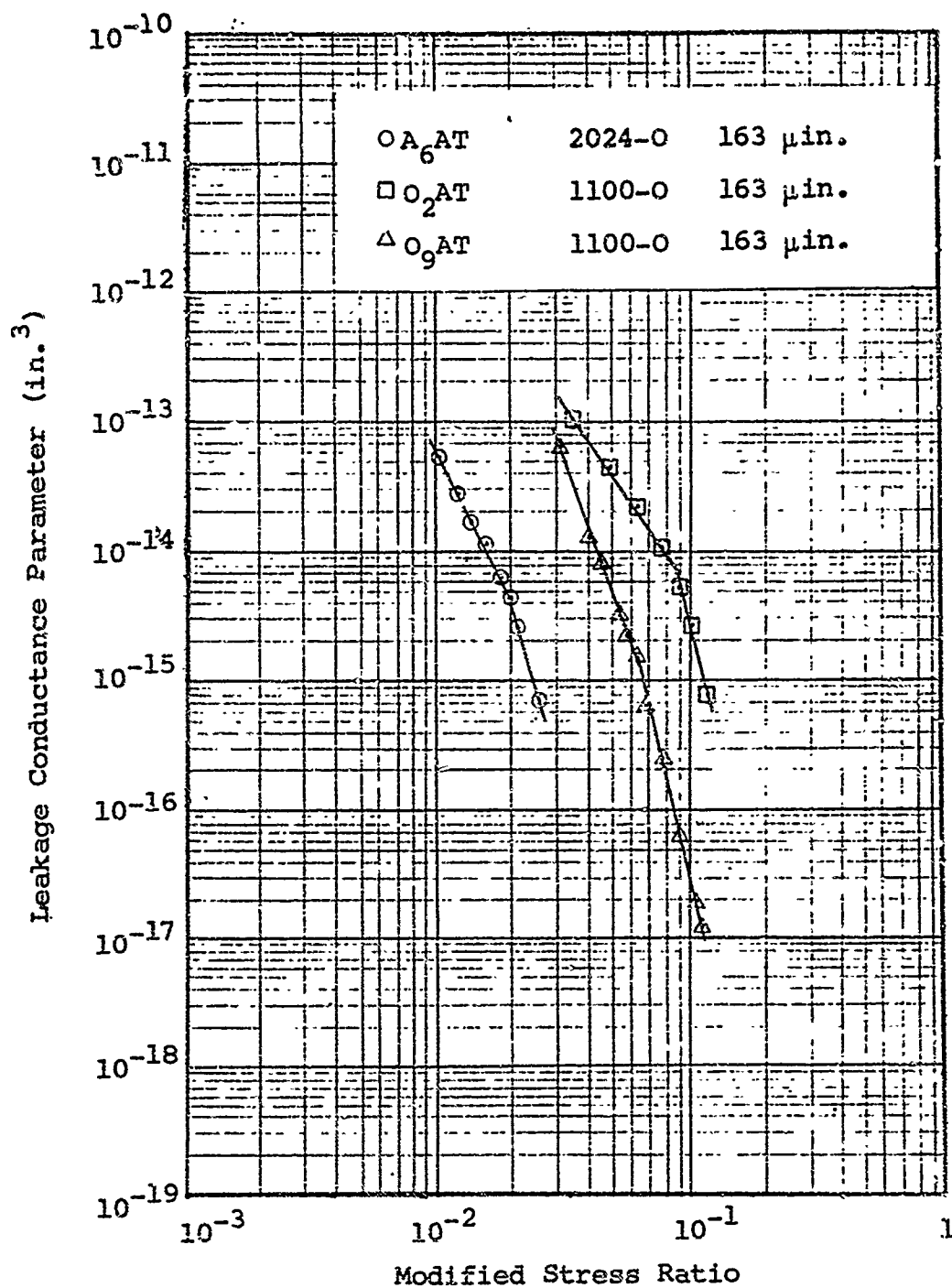


Figure I-25 Conductance parameter - modified stress ratio for 163-μin. PTV seal surfaces

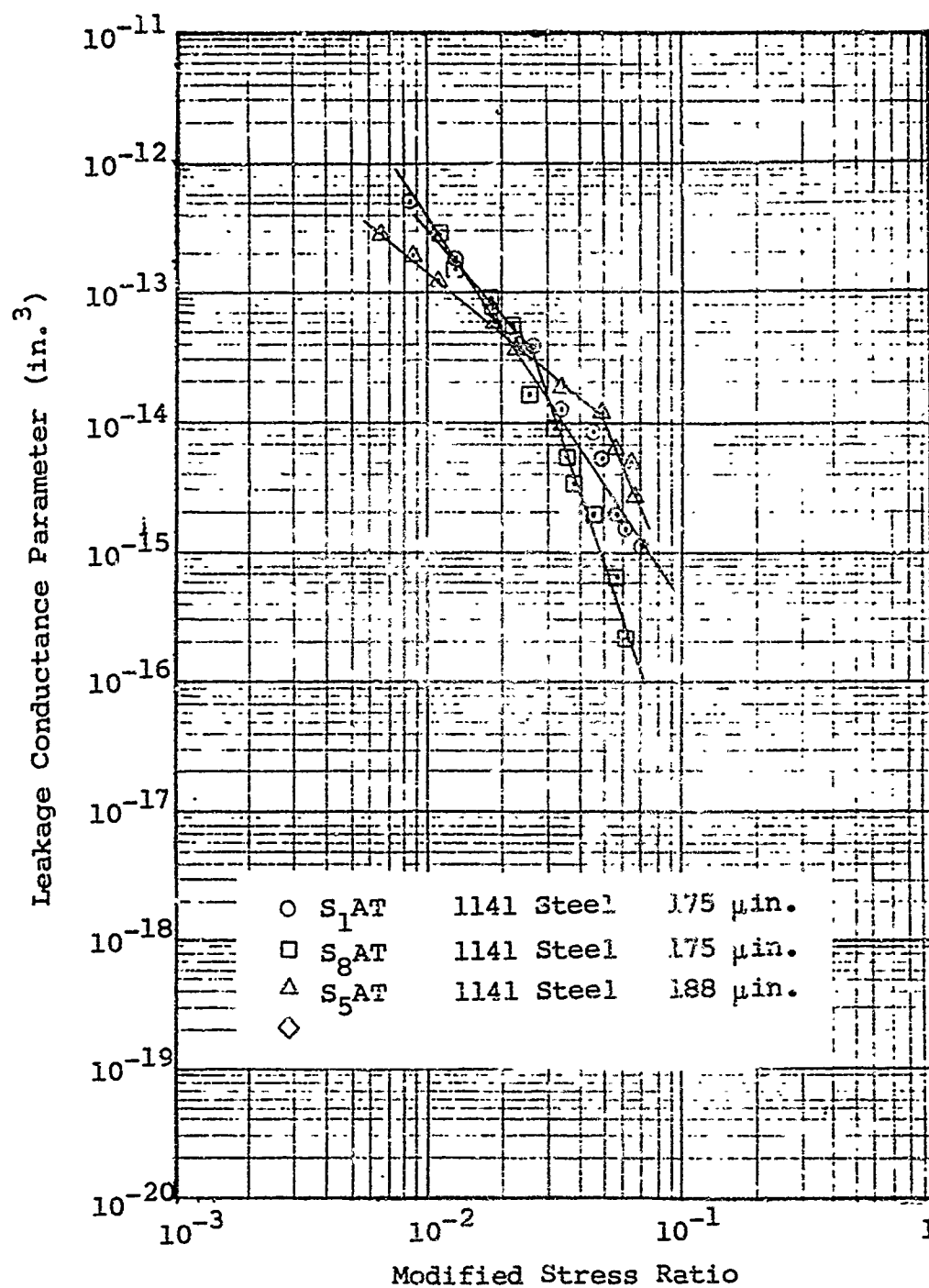


Figure I-26 Conductance parameter - modified stress ratio for 175 - 188-μin. PTV seal surfaces

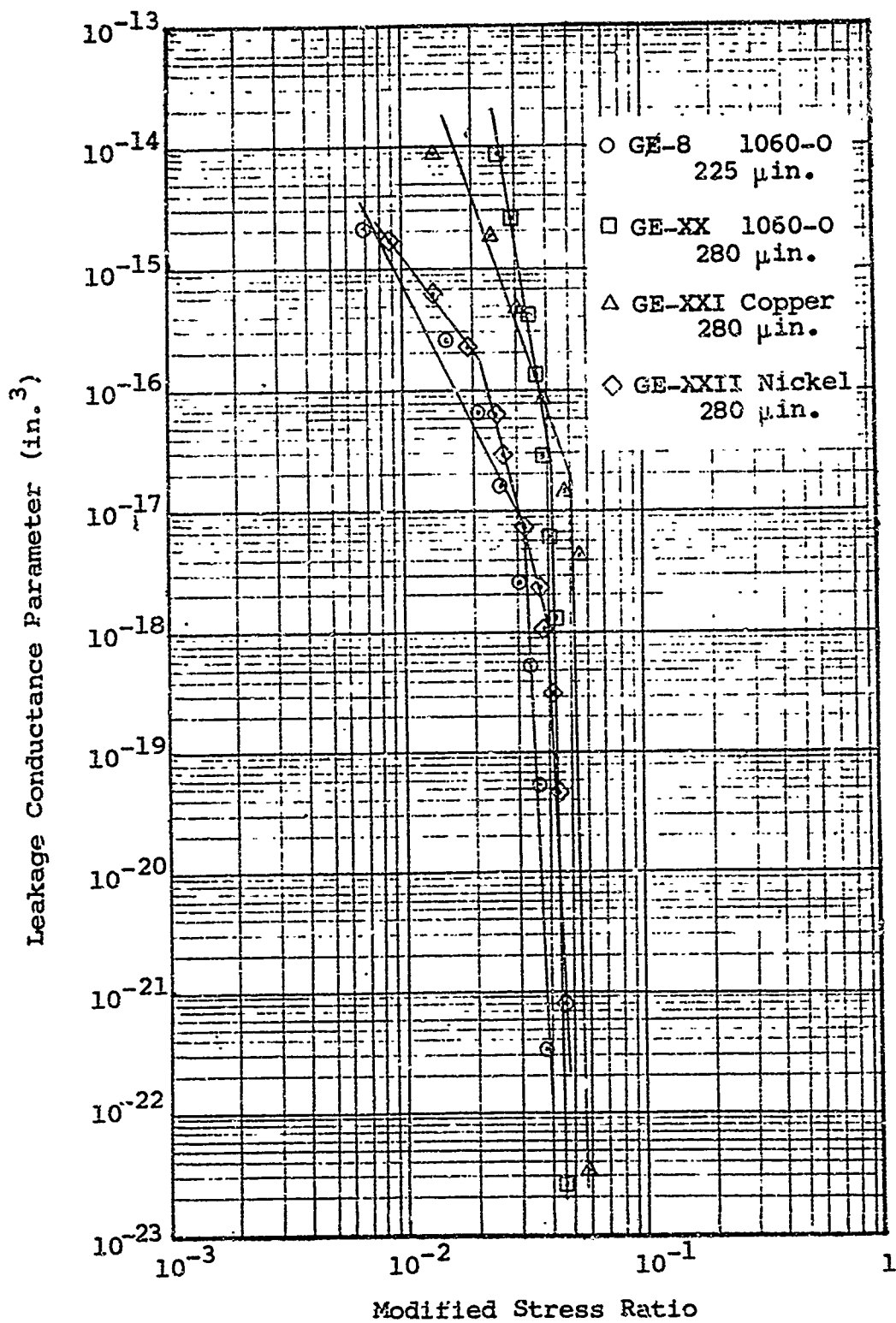


Figure I-27 Conductance parameter - modified stress ratio for 225 - 280-μin. PTV seal surfaces

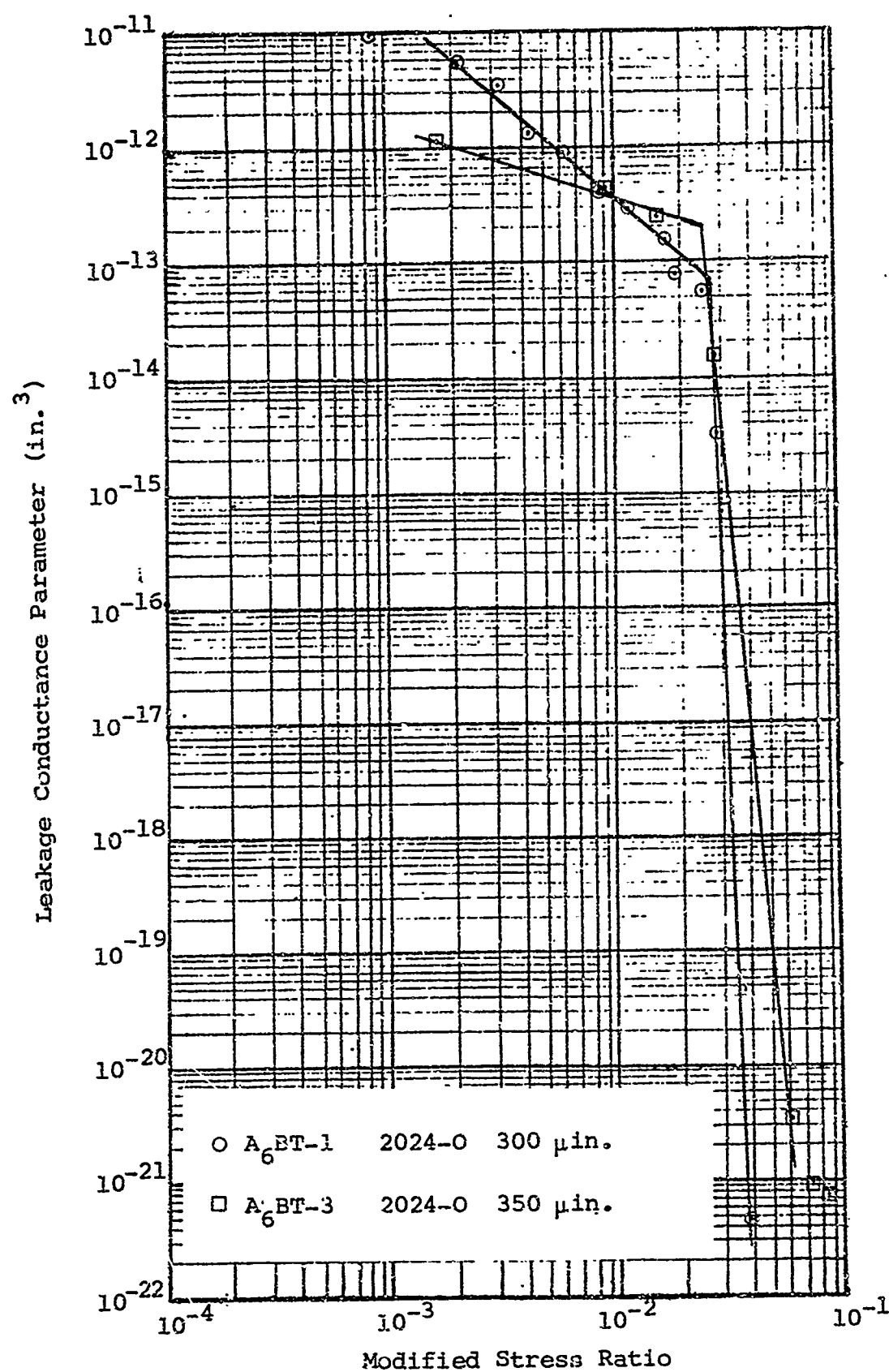


Figure I-28 Conductance parameter - modified stress ratio for 300 - 350-μin. PTV seal surfaces

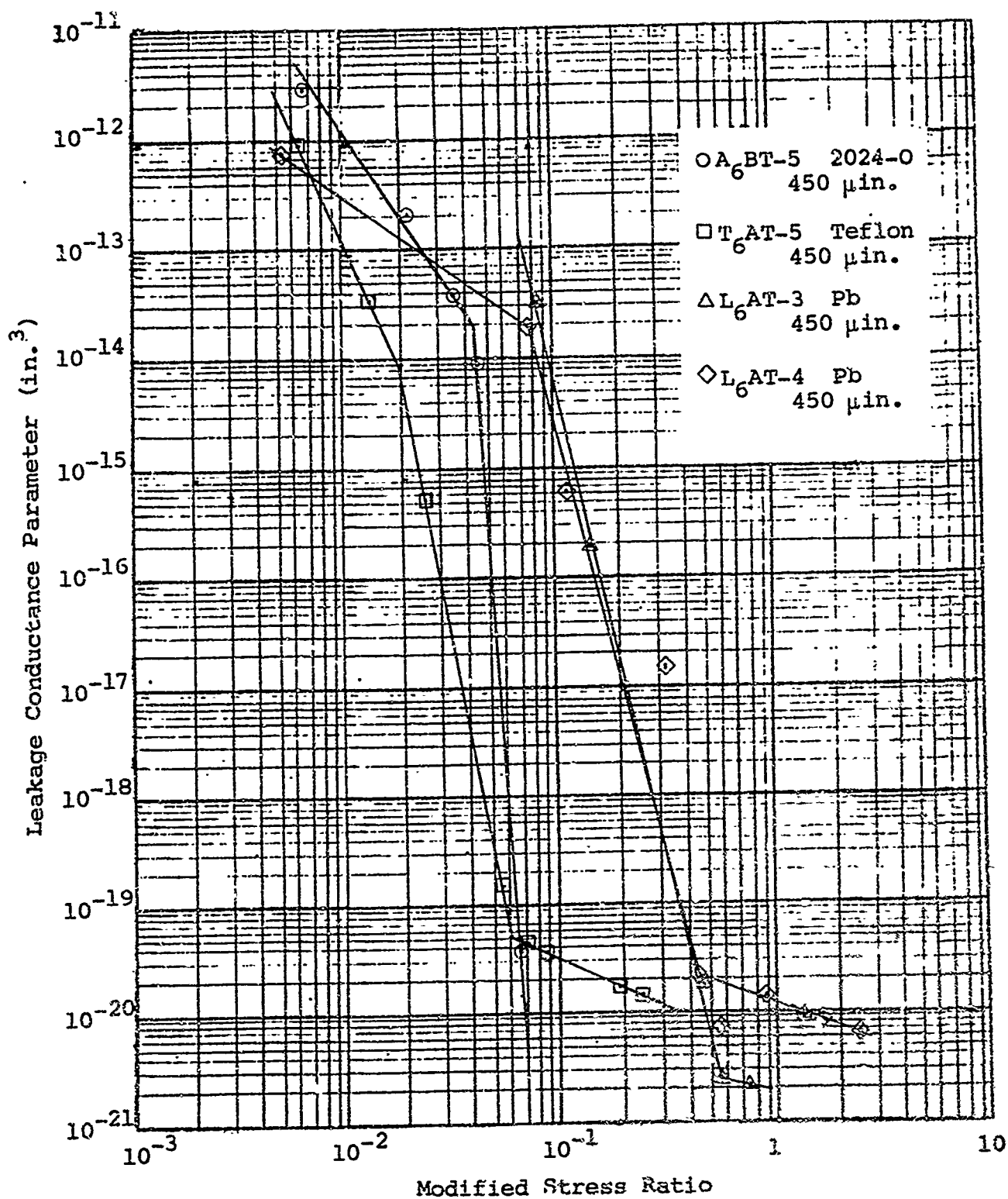


Figure I-29 Conductance parameter - modified stress ratio for 450-μin. PTV seal surfaces

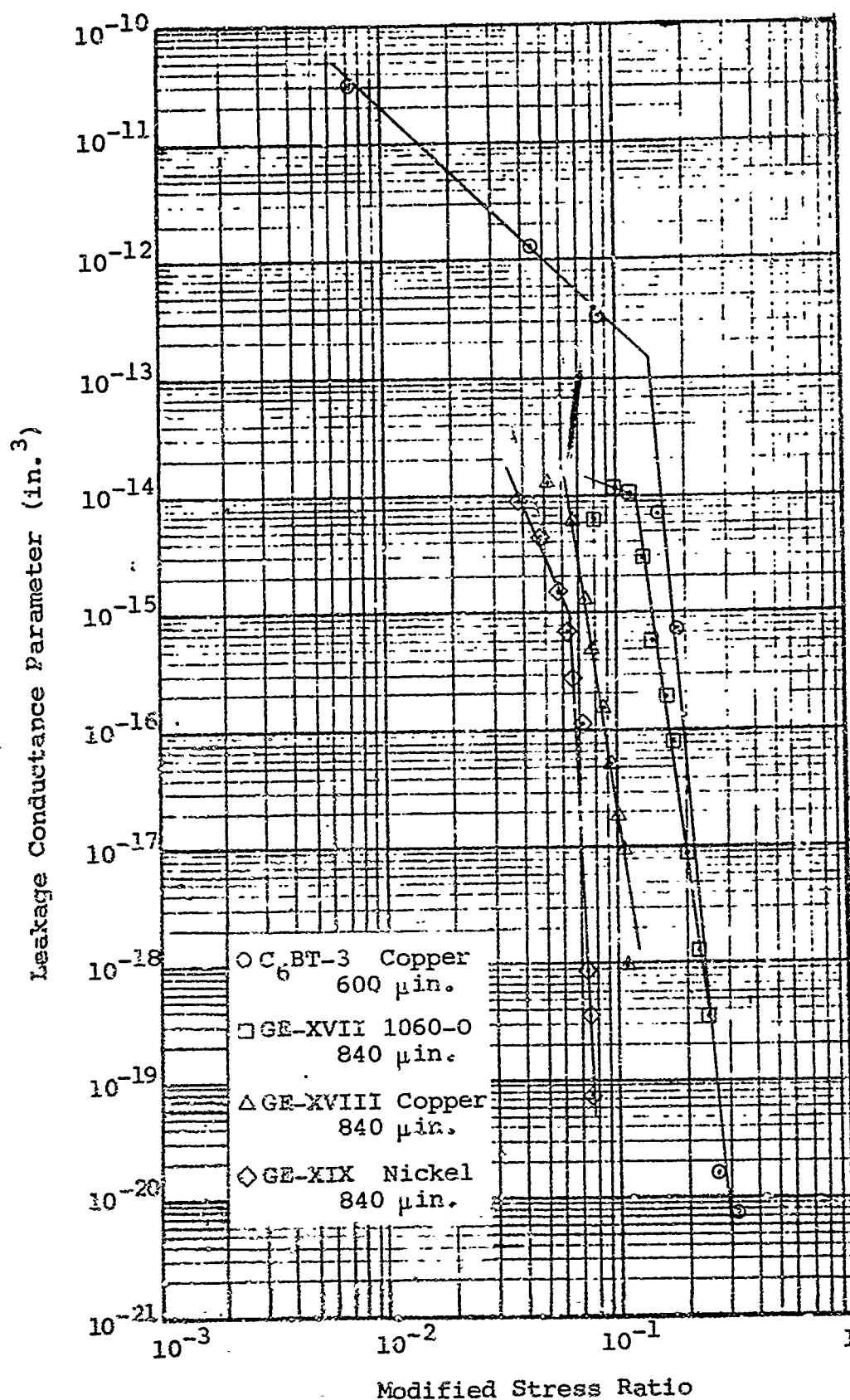


Figure I-30 Conductance parameter - modified stress ratio for 600 - 840-μin. PTV seal surfaces

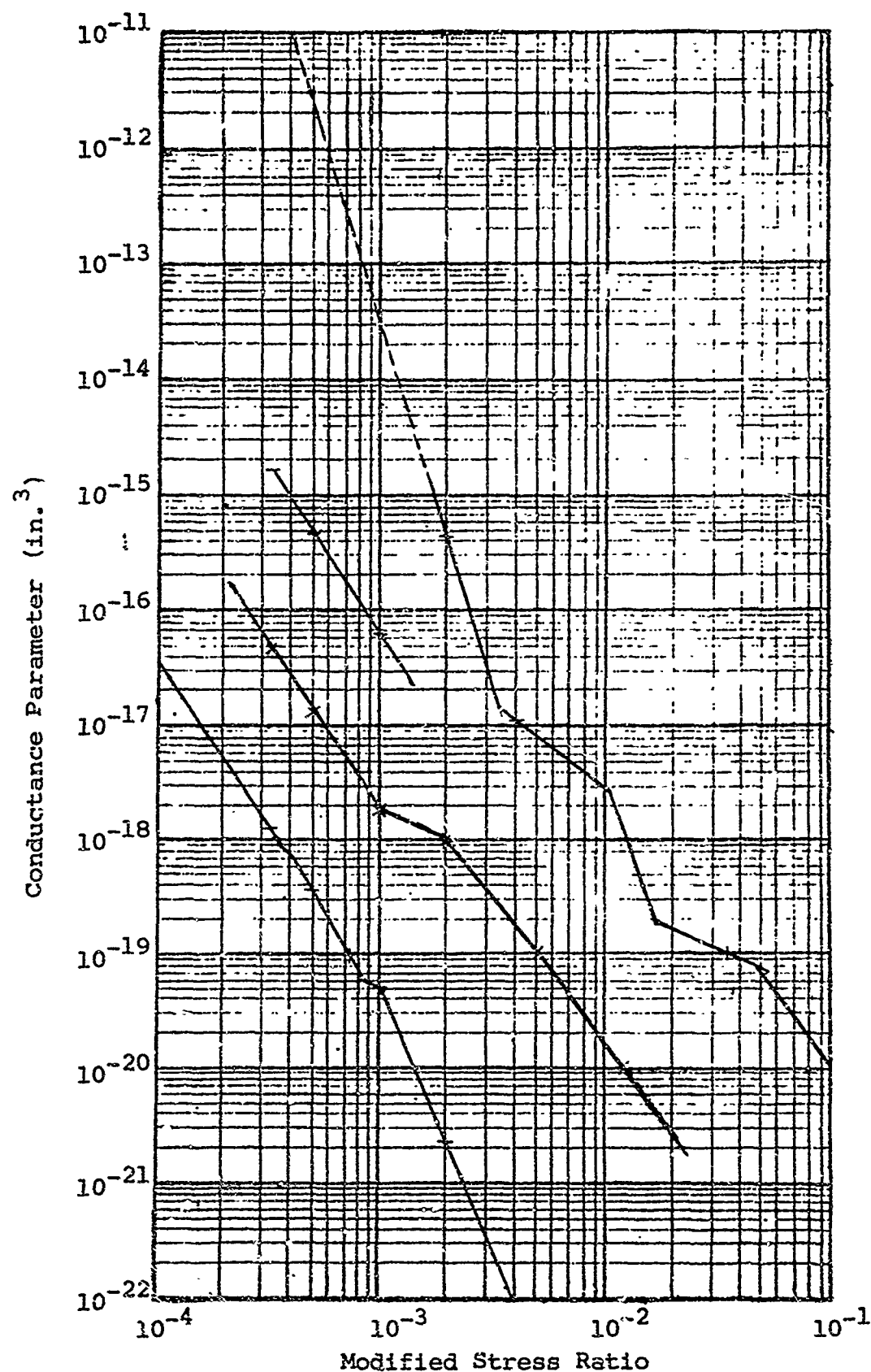


Figure I-31 Conductance parameter - modified stress ratio for lapped and polished seals having a 0-2- μ in. PTV roughness

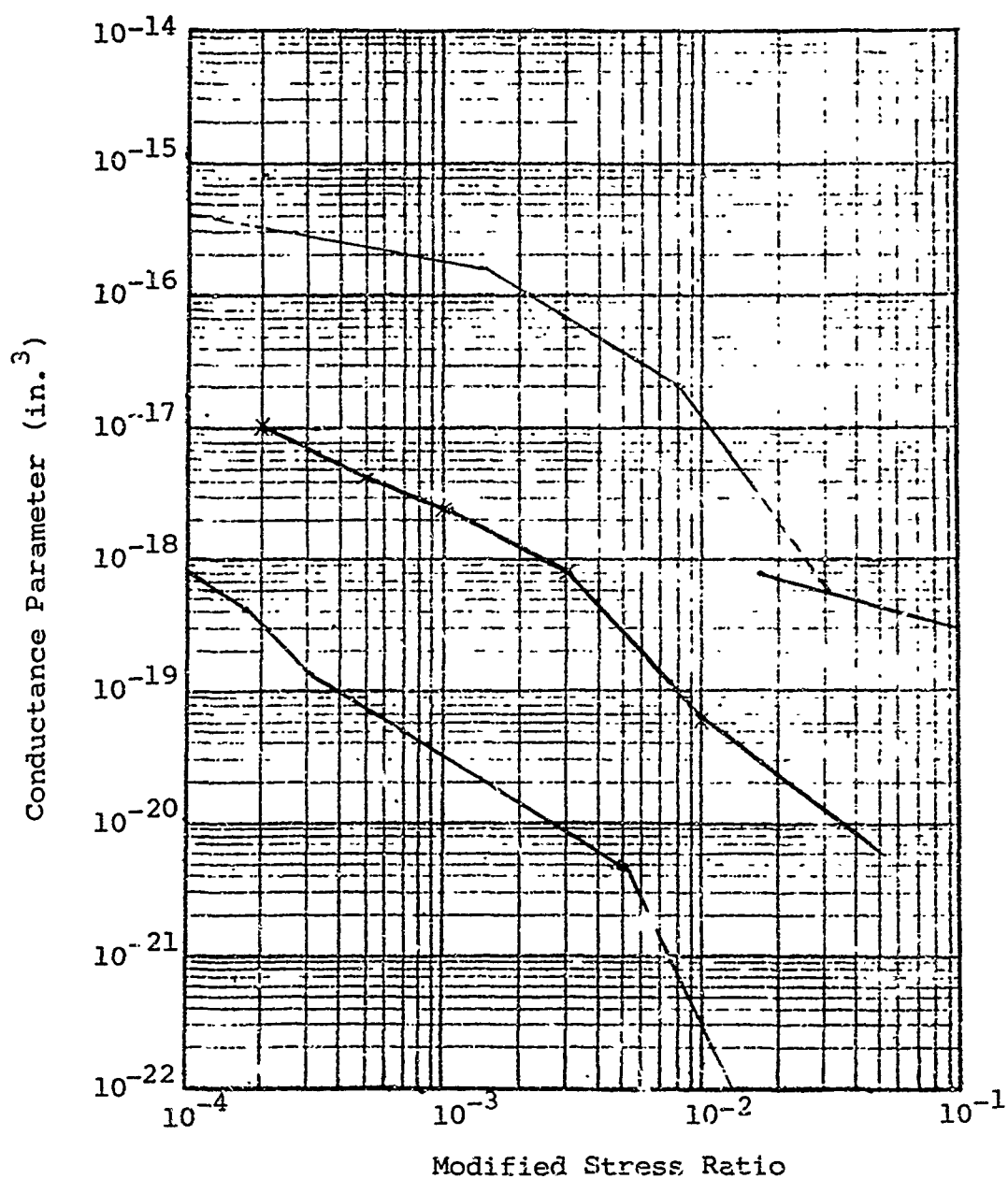


Figure I-32 Conductance parameter - modified stress ratio for lapped and polished seals having 2-5- μ in. PTV roughness

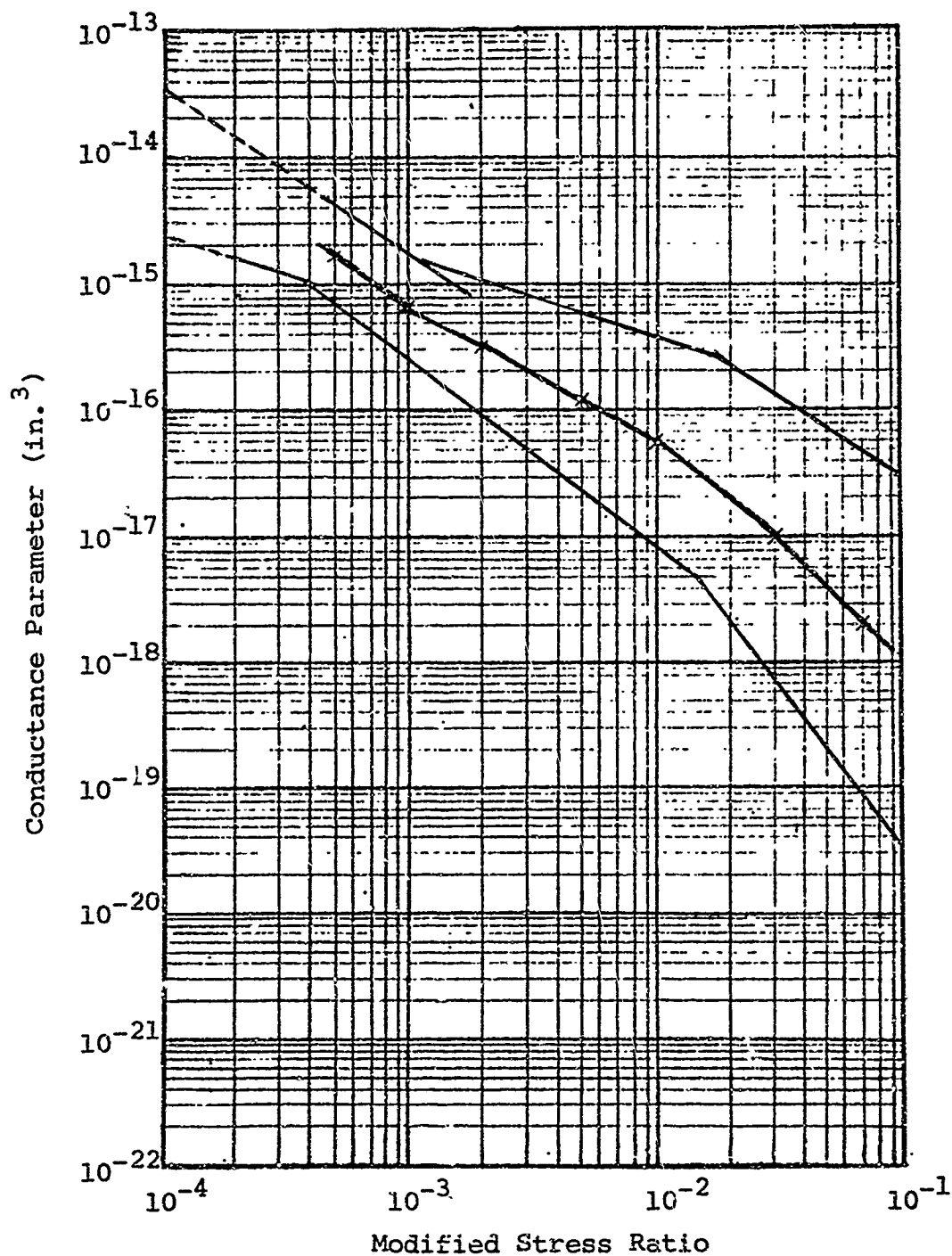


Figure I-33 Conductance parameter - modified stress ratio for lapped and polished seals having a 5 - 10- μ in. PTV roughness

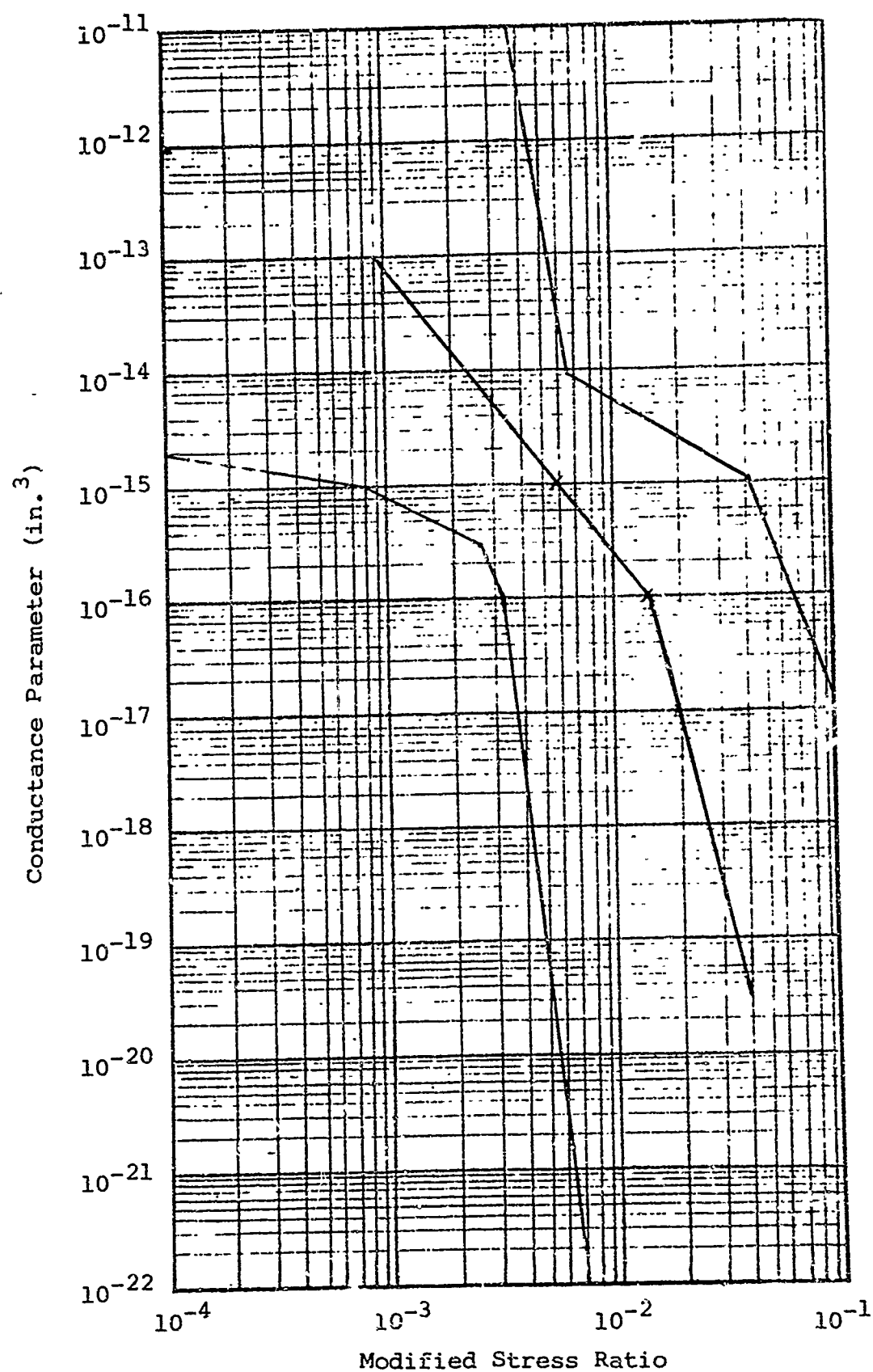


Figure I-34 Conductance parameter - modified stress ratio for lapped and polished seals having a 10 - 30- μ in. PTV roughness

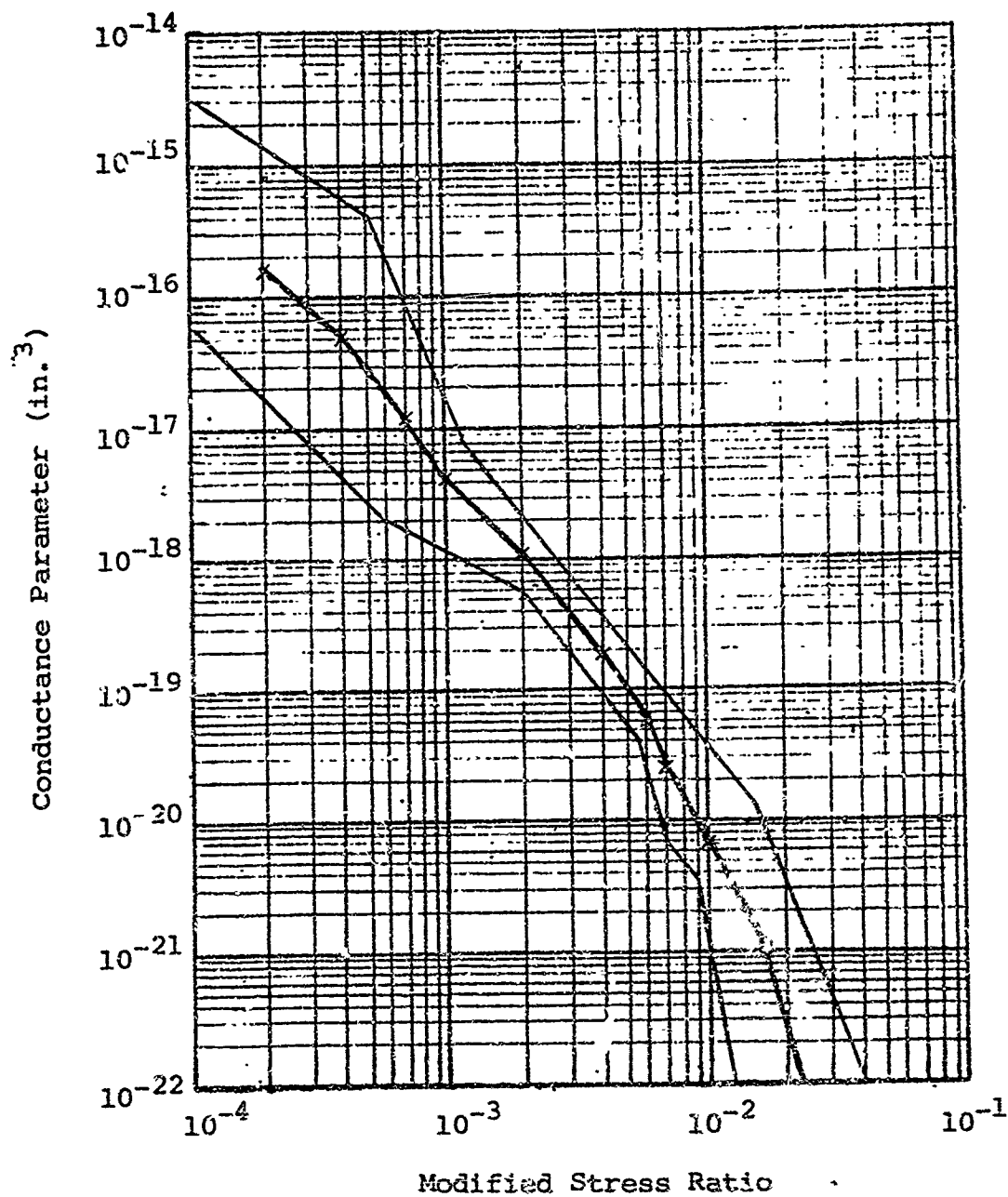


Figure I-35 Conductance parameter - modified stress ratio for turned seals having a 0-10.5- μ in. PTV roughness

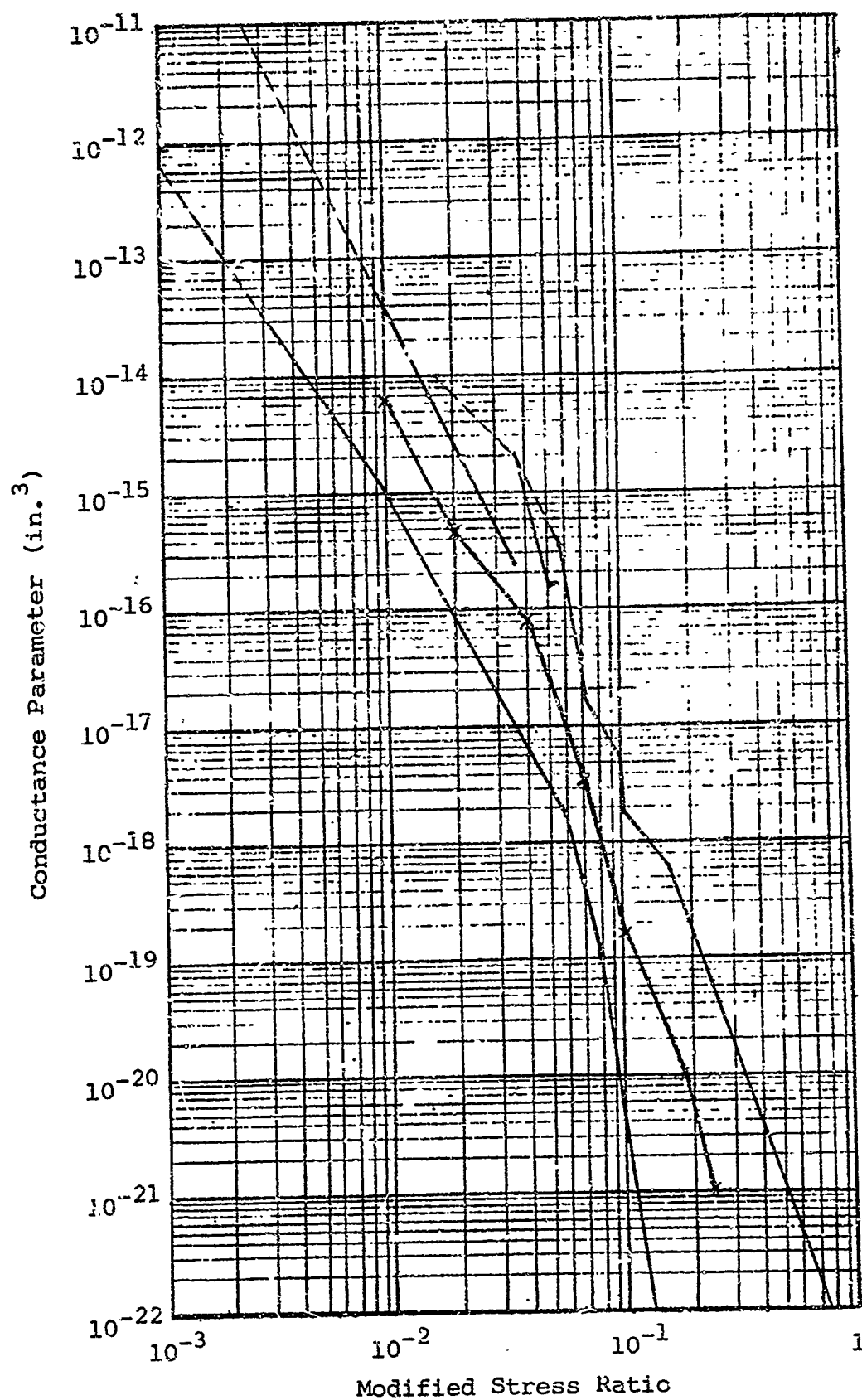


Figure I-36 Conductance parameter - modified stress ratio
for turned seals having a 11-30- μ in. PTV roughness

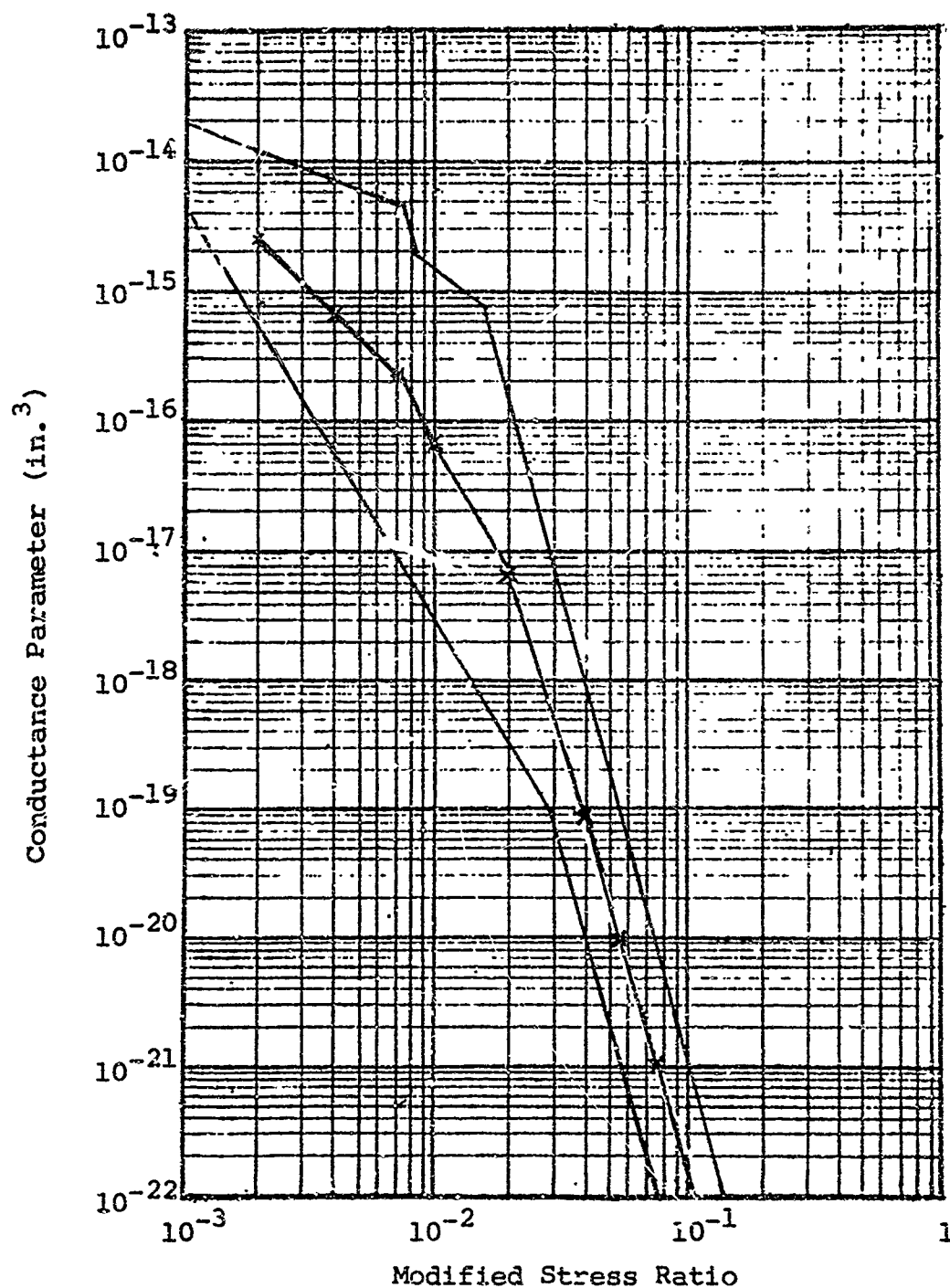


Figure I-37 Conductance parameter - modified stress ratio for turned seals having a 20 - 30- μ in. PTV roughness

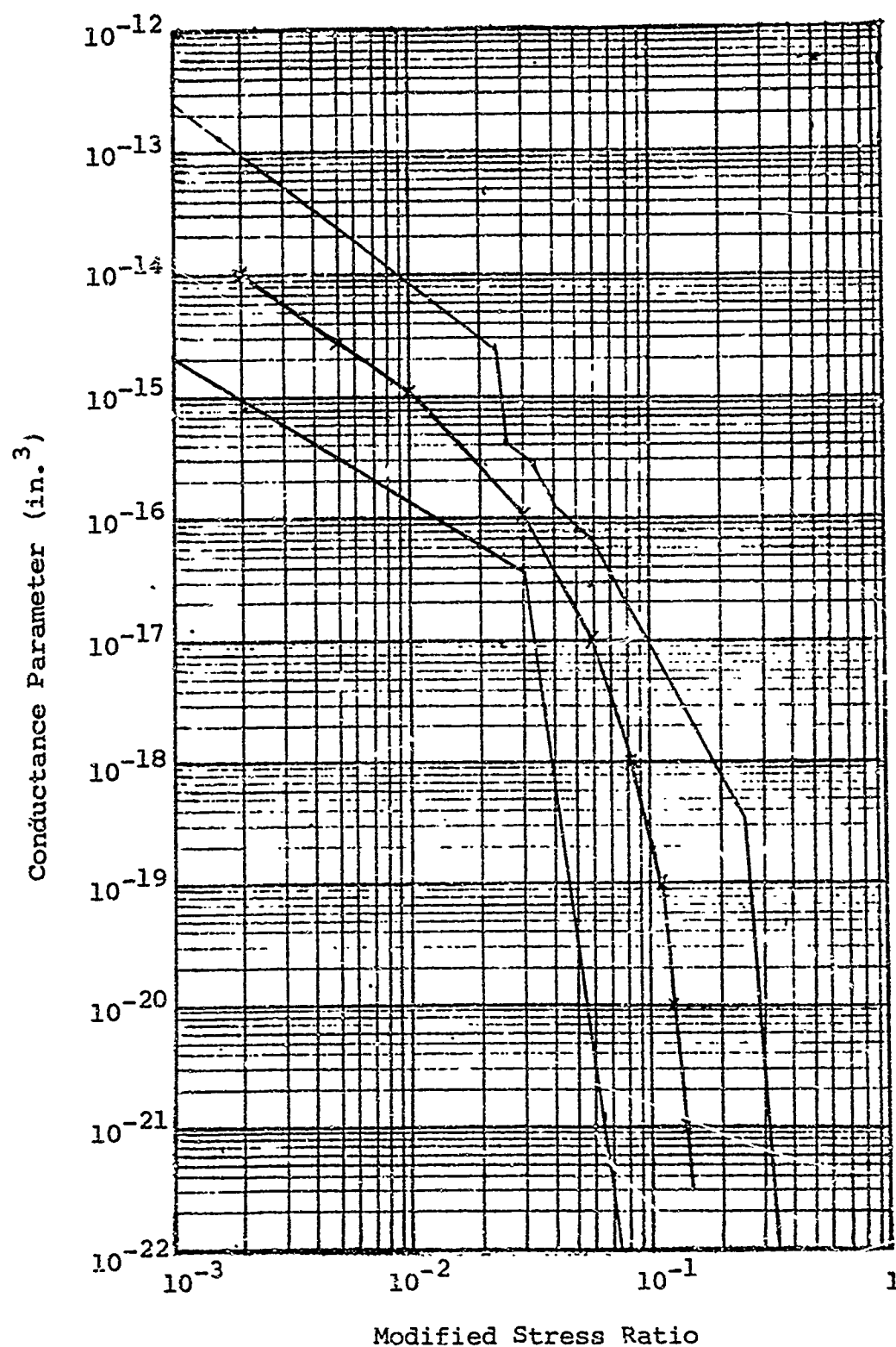


Figure I-38 Conductance parameter - modified stress ratio for turned seals having a 30 - 50- μ in. PTV roughness

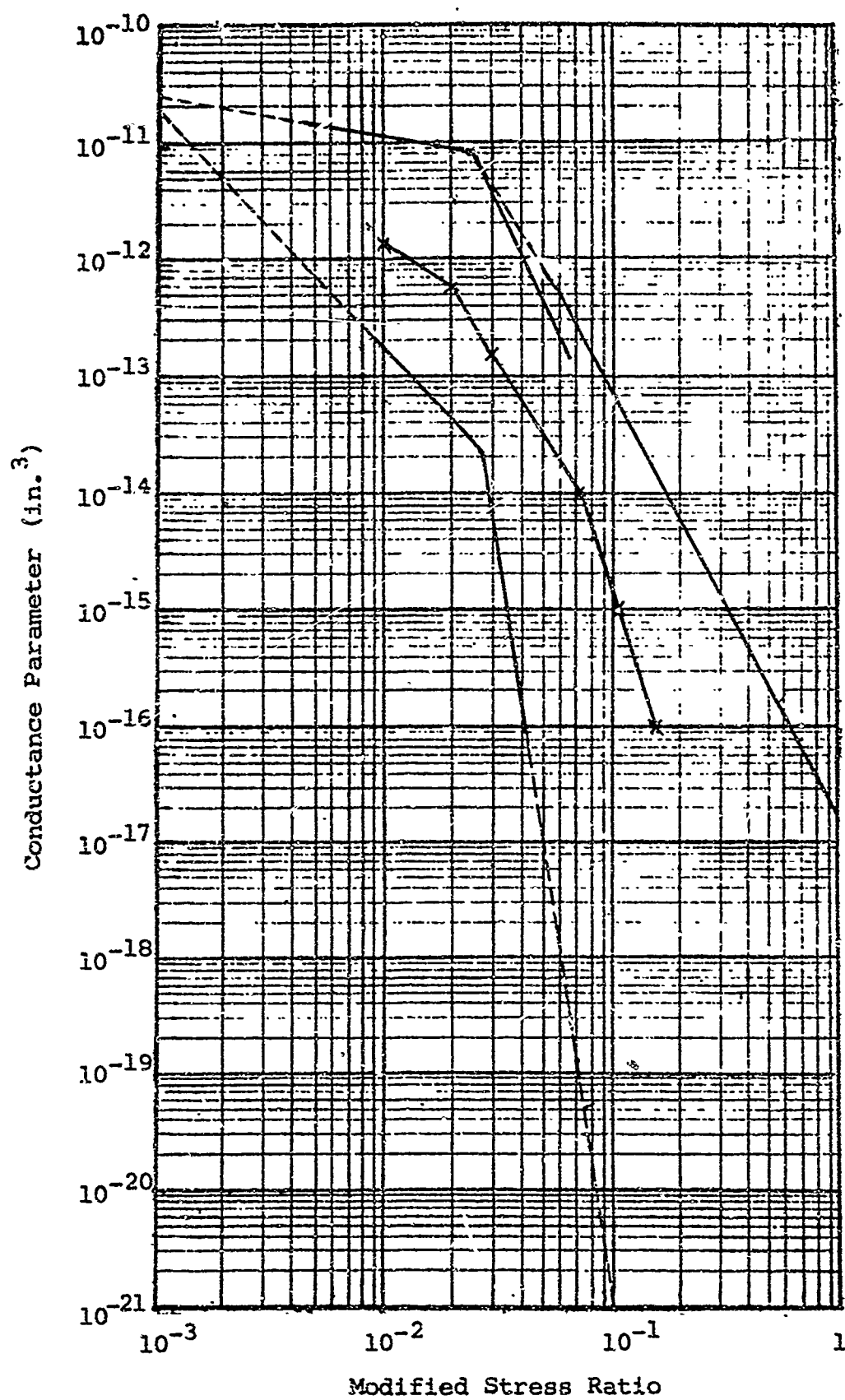


Figure I-39 Conductance parameter - modified stress ratio for turned seals having a 50 - 75- μ in. PTV roughness

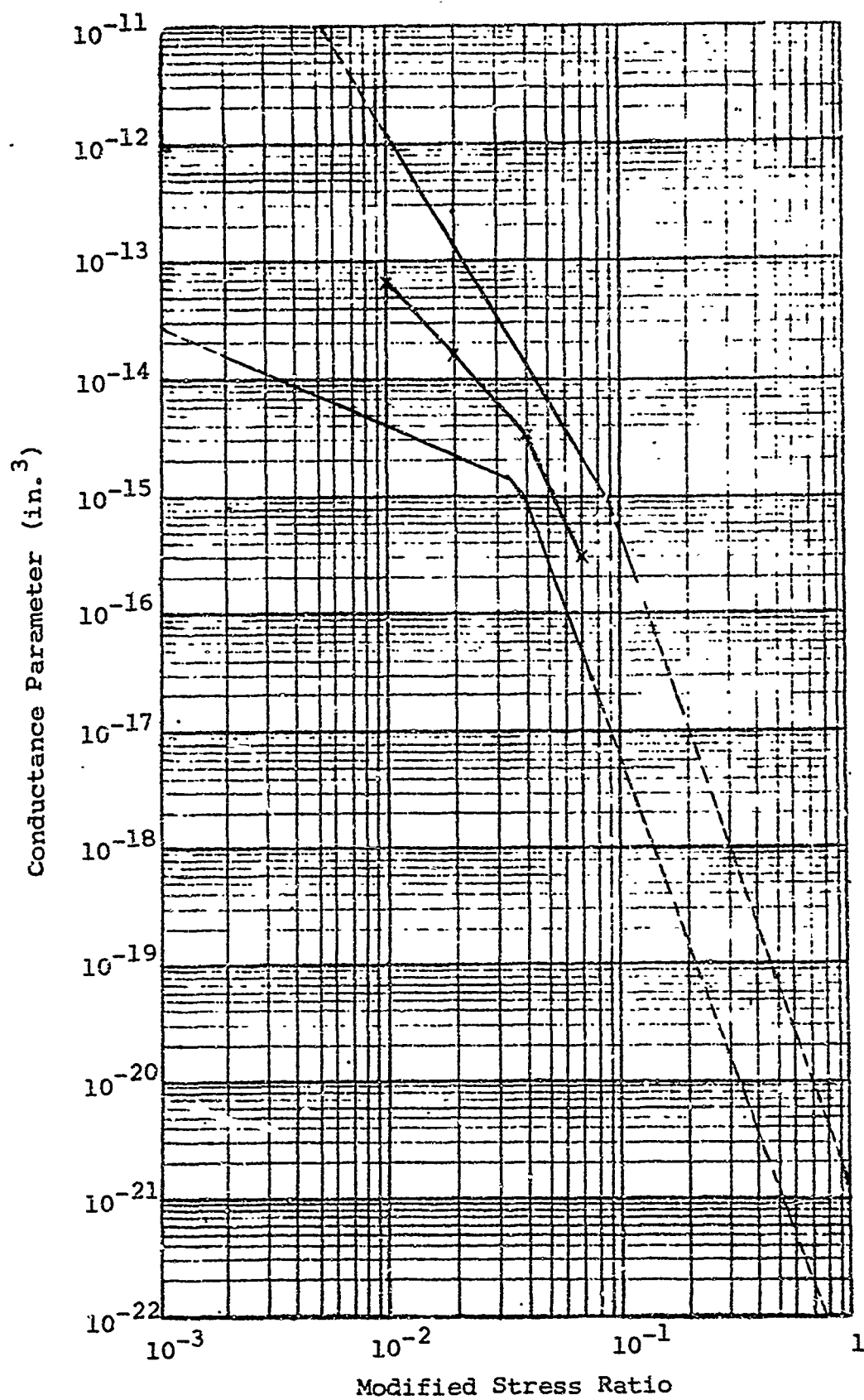


Figure I-40 Conductance parameter - modified stress ratio for turned seals having a 75 - 100- μ in. PTV roughness

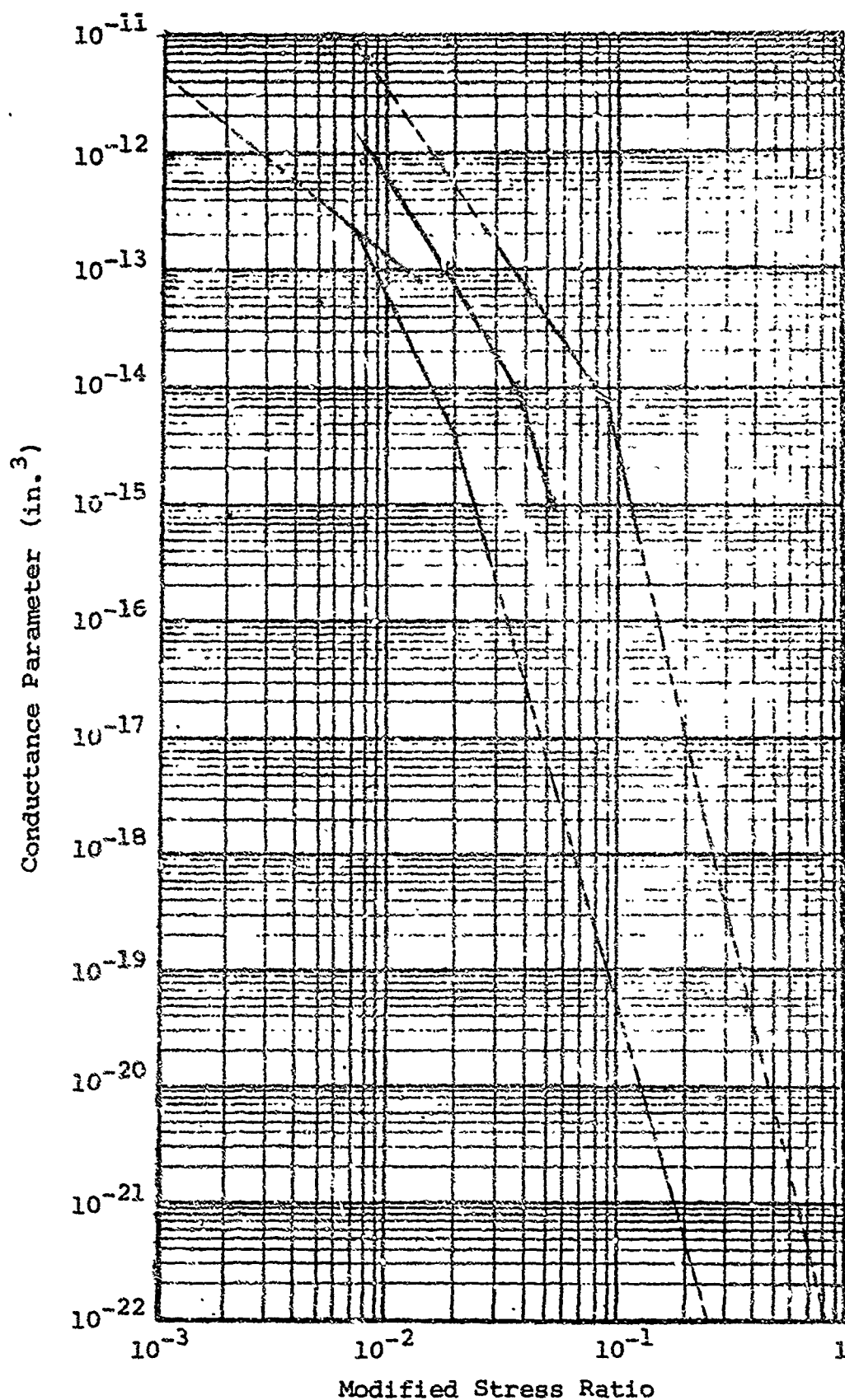


Figure I-41 Conductance parameter - modified stress ratio for turned seals having a 100 - 200- μ in. PTV roughness

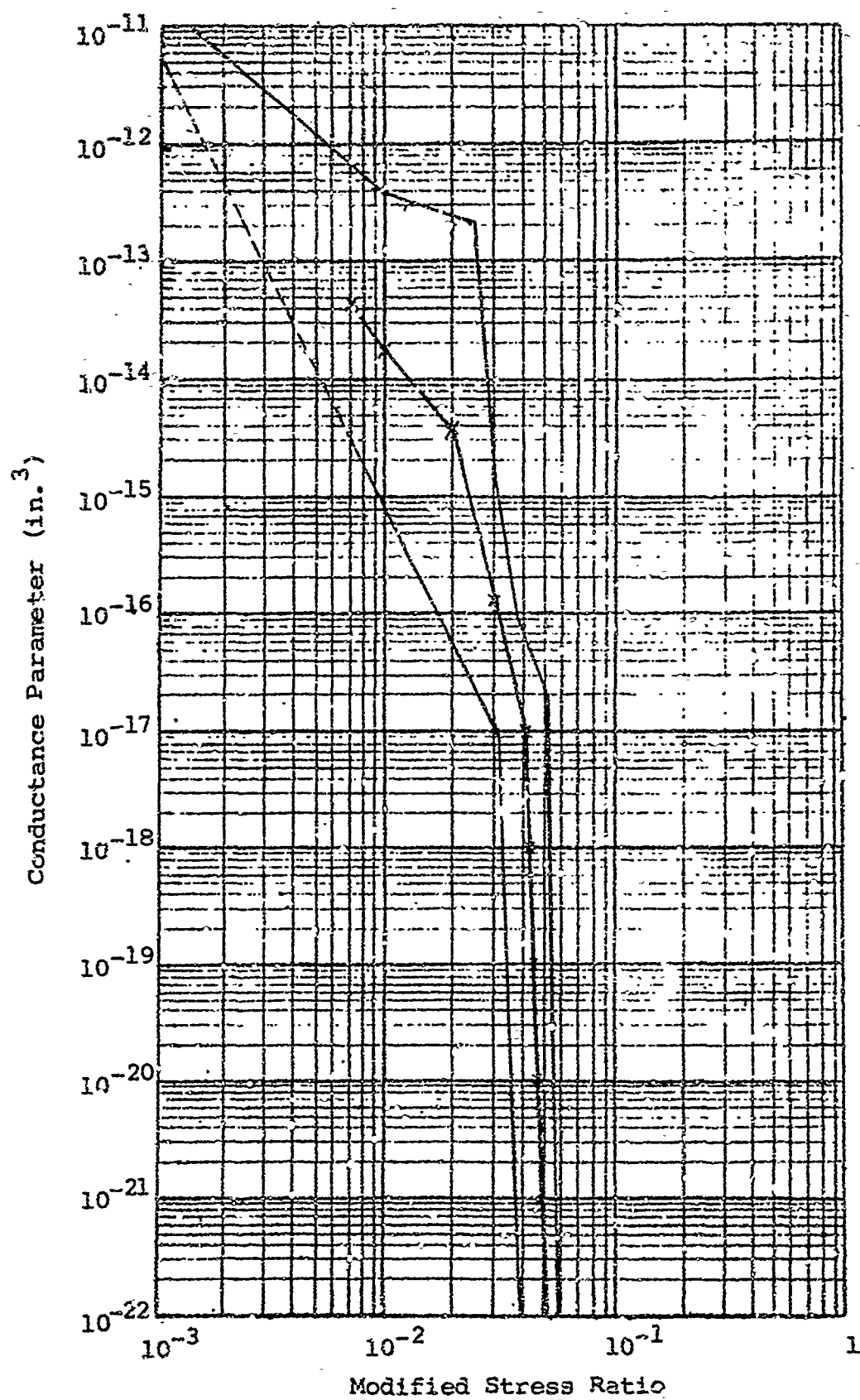


Figure I-42 Conductance parameter - modified stress ratio for turned seals having a 200 - 400- μ in. PTV roughness

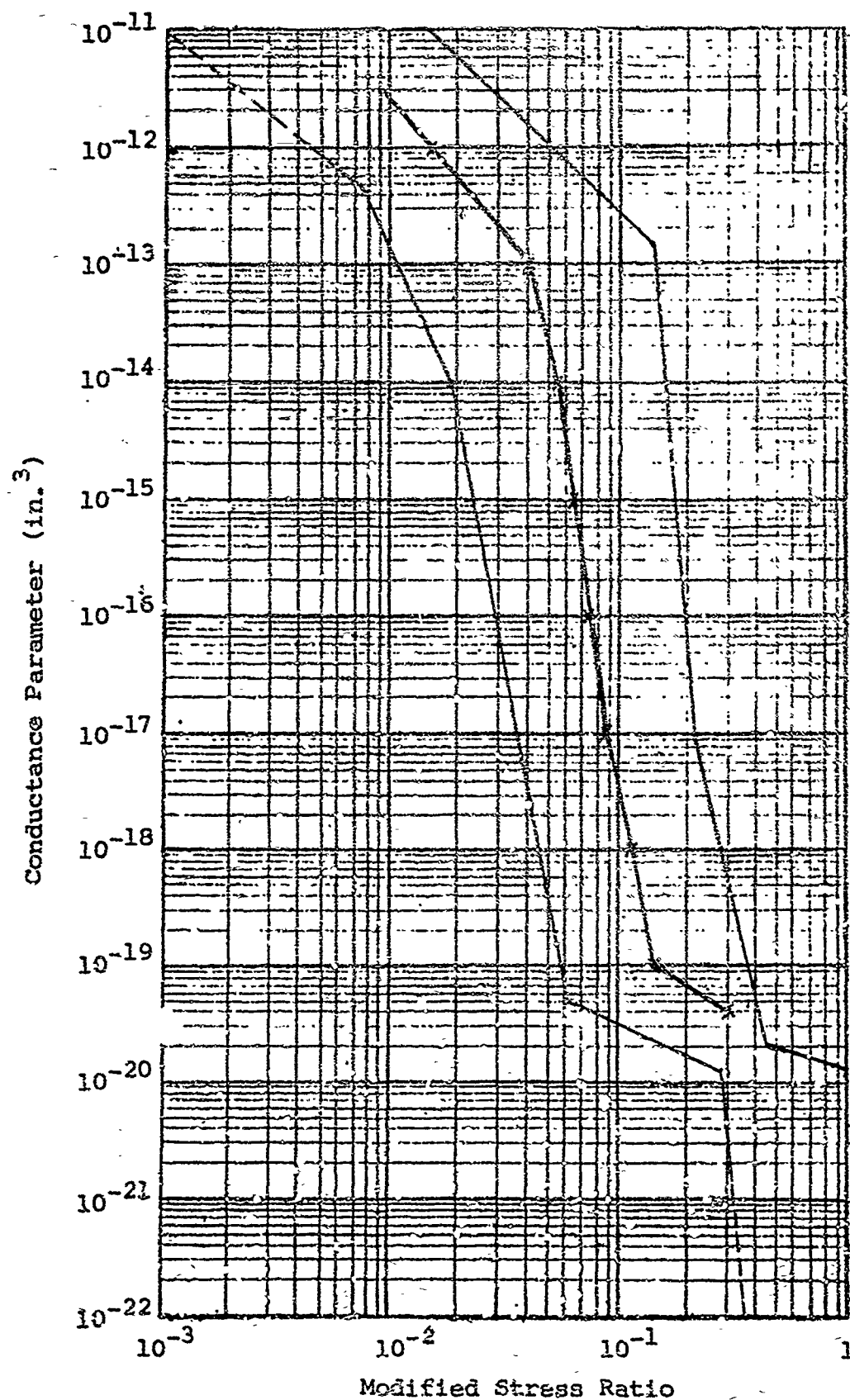


Figure I-43 Conductance parameter - modified stress ratio for turned seals having over 400- μ in. PTV roughness

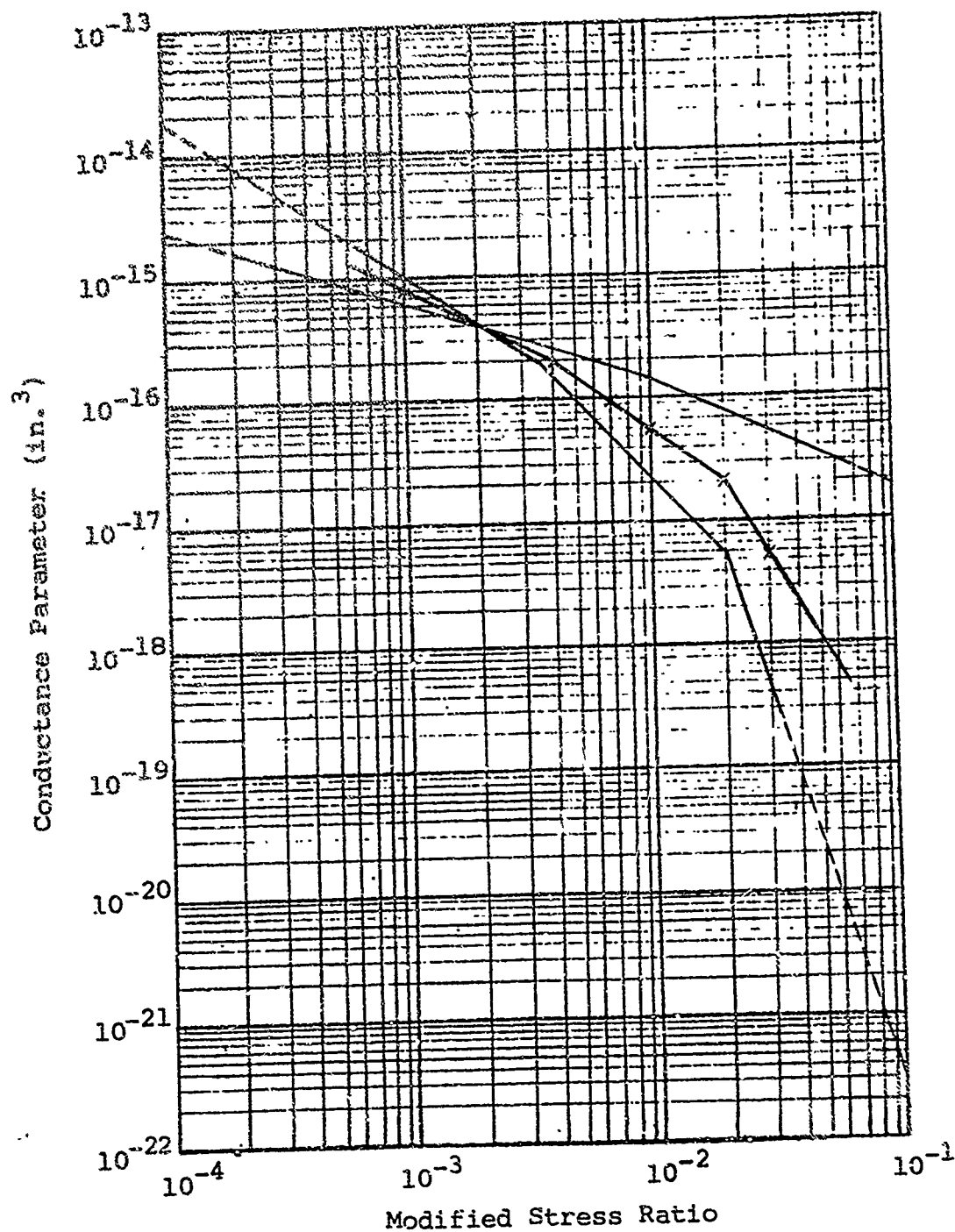


Figure I-44 Conductance parameter - modified stress ratio for ground seals having a 0-10.5- μ in. PTV roughness

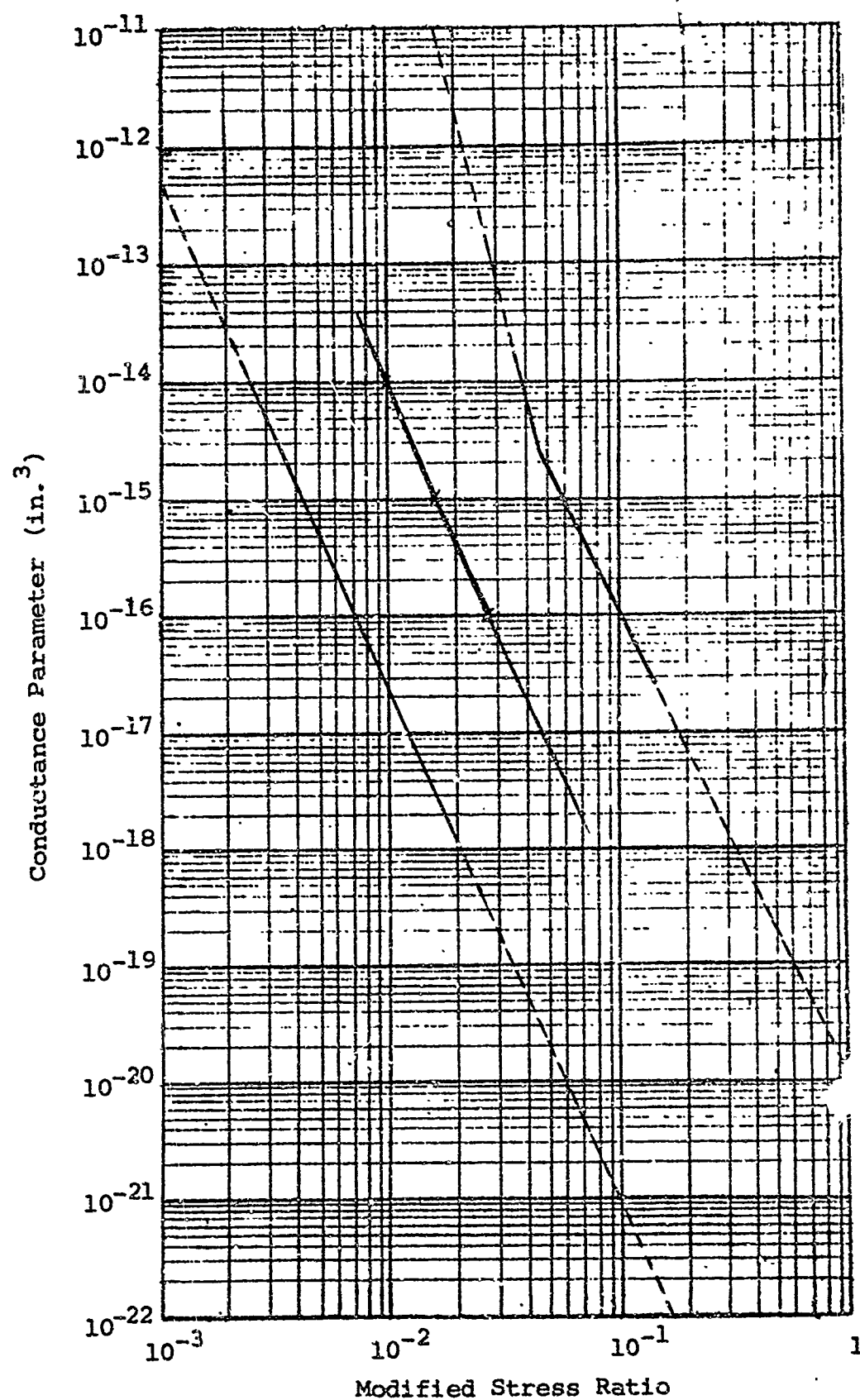


Figure I-45 Conductance parameter - modified stress ratio for ground seals having 11 - 50.µin. PTV roughness

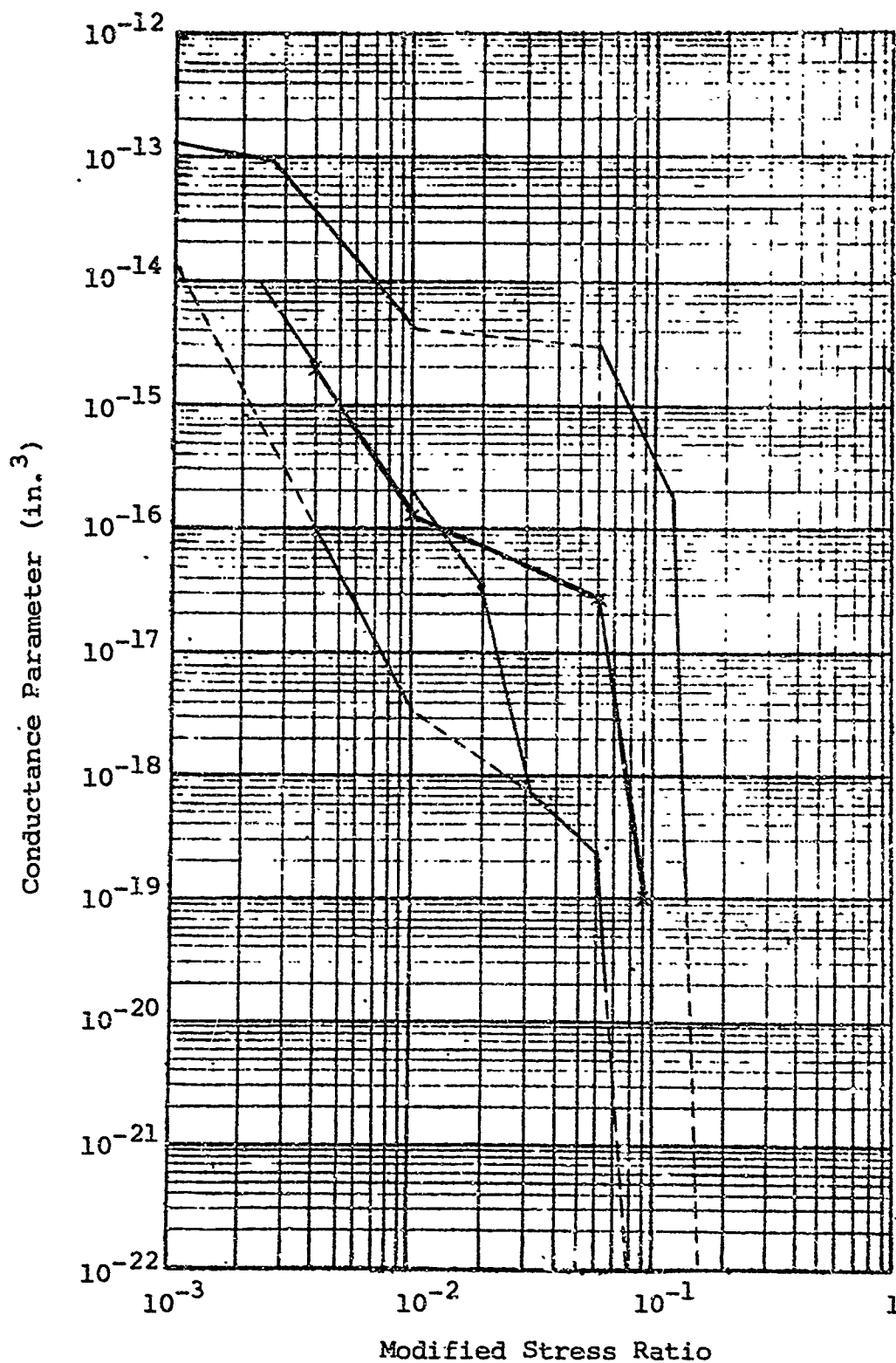


Figure I-46 Conductance parameter - modified stress ratio for ground seals having 50 - 100- μ in. PTV roughness

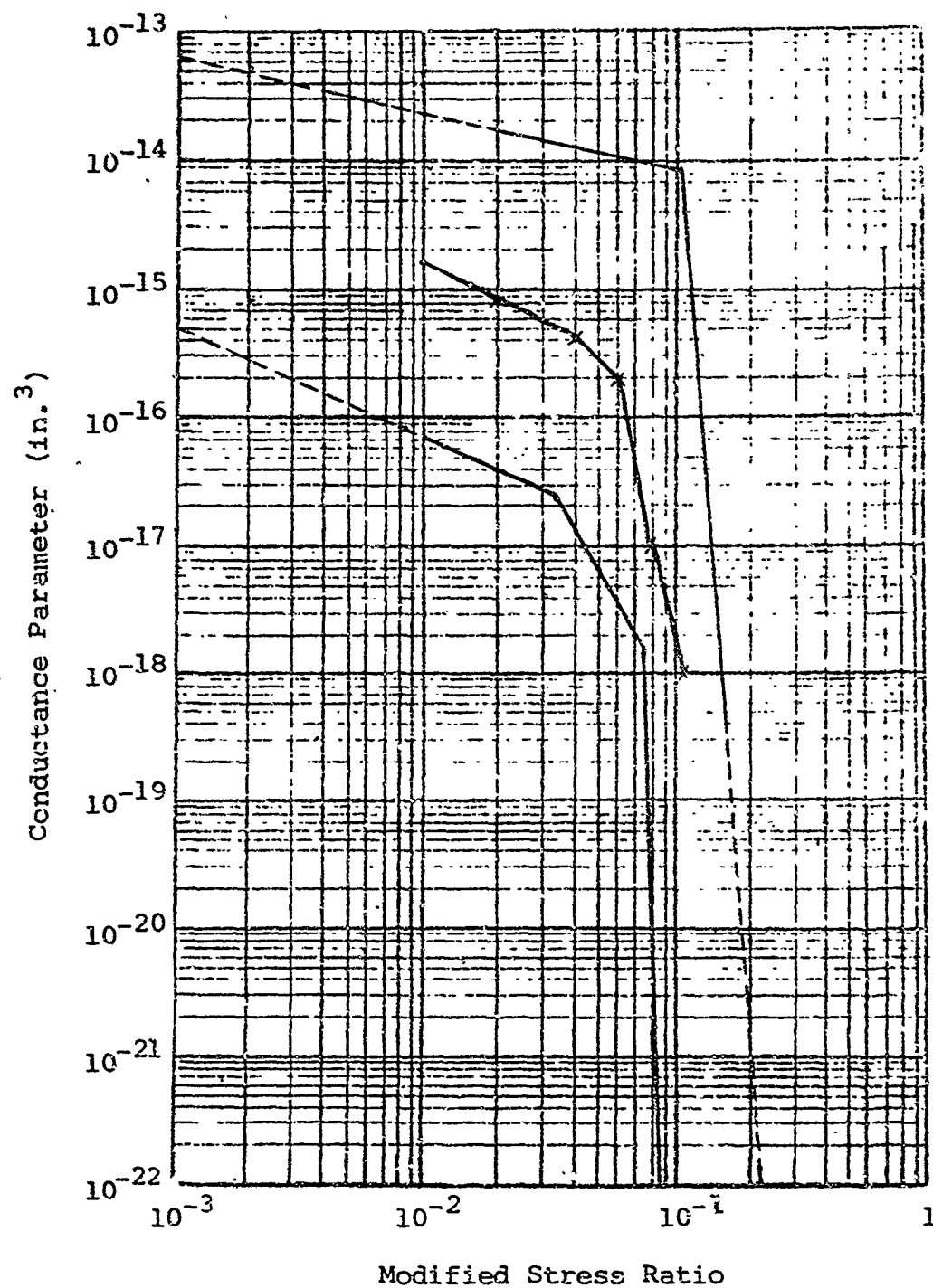


Figure I-47 Conductance parameter - modified stress ratio for ground seals having 100 - 200- μ in. PTV roughness

APPENDIX II

EXPERIMENTAL INVESTIGATION OF SLIDING CONTACT AND LEAKAGE OF A SEALING INTERFACE

Leakage flow occurs between any two metallic surfaces through the interconnection of void spaces formed by the topographical variations on the mating surfaces. Rubbing contact continuously disturbs the chance orientation of the void spaces and, additionally, produces a change in the topography of the surfaces through the various mechanisms of wear. The purpose of this study, therefore, was to investigate the influence of the parameters affecting the leakage path as related to dynamic seals. Since the changes in the leakage path are essentially produced by the wear processes, the influencing parameters can be identified as:

- material properties
- contact forces
- rubbing velocity
- initial surface topography
- degree of lubrication.

Each of these parameters is definable and may be independently studied. The problem, however, is to relate the effects of the parameters to the leakage path. One approach is to experimentally measure the surface topography resulting from rubbing contact under varied conditions. Past experience, however, has shown that there is not necessarily a relationship between leakage path and topography. Another approach is to measure leakage flow through the rubbing interface and indirectly relate it to the influencing parameters. The approach selected as most promising combines both methods. Since the interface leakage path is difficult to describe quantitatively, leakage measurements were used to calculate a conductance parameter and, when coupled with measured surface topography, provided a relative description of the leakage path.

With the important parameters for study and methods of correlation identified, it was necessary to develop an experimental apparatus that would permit the measurement and variation of parameters.

II-1 Experimental Apparatus

The requirements of the experimental apparatus may be stated:

- The rubbing contact must be such that the leakage flow is in the same direction as the rubbing action. This situation reproduces the action of a dynamic sliding seal.

- Leakage through the interface must be measurable. A single interface is a necessity.
- The forces acting at the interface must be measured and controlled.
- Sliding velocity must be controlled.
- Friction force must be measured.
- Wear rates must be measured without dismantling the apparatus.

When each of the requirements was considered, the apparatus concept was almost self-determined and very few alternatives were permissible. The design that emerged consisted of a hollow cylindrical shaft sliding within a circular ring. The interface of interest was formed by the inside diameter of the ring and the outside diameter of the piston. The apparatus is shown schematically in figure II-1. Figure II-2 is an external view of the apparatus and associated equipment; the experimental parts are shown on figures II-3 and II-4. Since the design and operation of the apparatus were so closely associated with the validity of results, detailed design information is presented in the following sections.

II-2 Leakage Flow and Measurement

In the experiments described in this appendix, air was used as the sealed fluid. Leakage flow through the ring-shaft interface was determined by measuring the flow into the sealed fluid chamber shown on figure II-1. The instrumentation used was a tapered tube flow-meter, although other instruments could have been employed depending upon the range of leakage flow. In addition to the ring-shaft interface, a rubber O-ring was used to seal the opposite end of the shaft. The purpose of this seal was to minimize compression effects resulting from shaft reciprocation. The leakage past this seal was insignificant, consequently no pressure loading occurred on the shaft.

II-3 Interface Loading

The experimental ring and shaft were fabricated to provide a very close slip fit when assembled. Hence, the cylindrical interface surfaces were technically unloaded in the free state. Loading of the surfaces was obtained by applying pressure to the outer periphery of the ring and elastically deforming the ring into contact with the shaft. The pressurization was accomplished by an air-oil intensifier system. Oil leakage past the ring was prevented by O-rings located at the side faces of the ring.

Deformation of the ring against the shaft produced contact loading. When the stresses in the ring and shaft remain below the elastic limits of the materials, apparent contact stress at

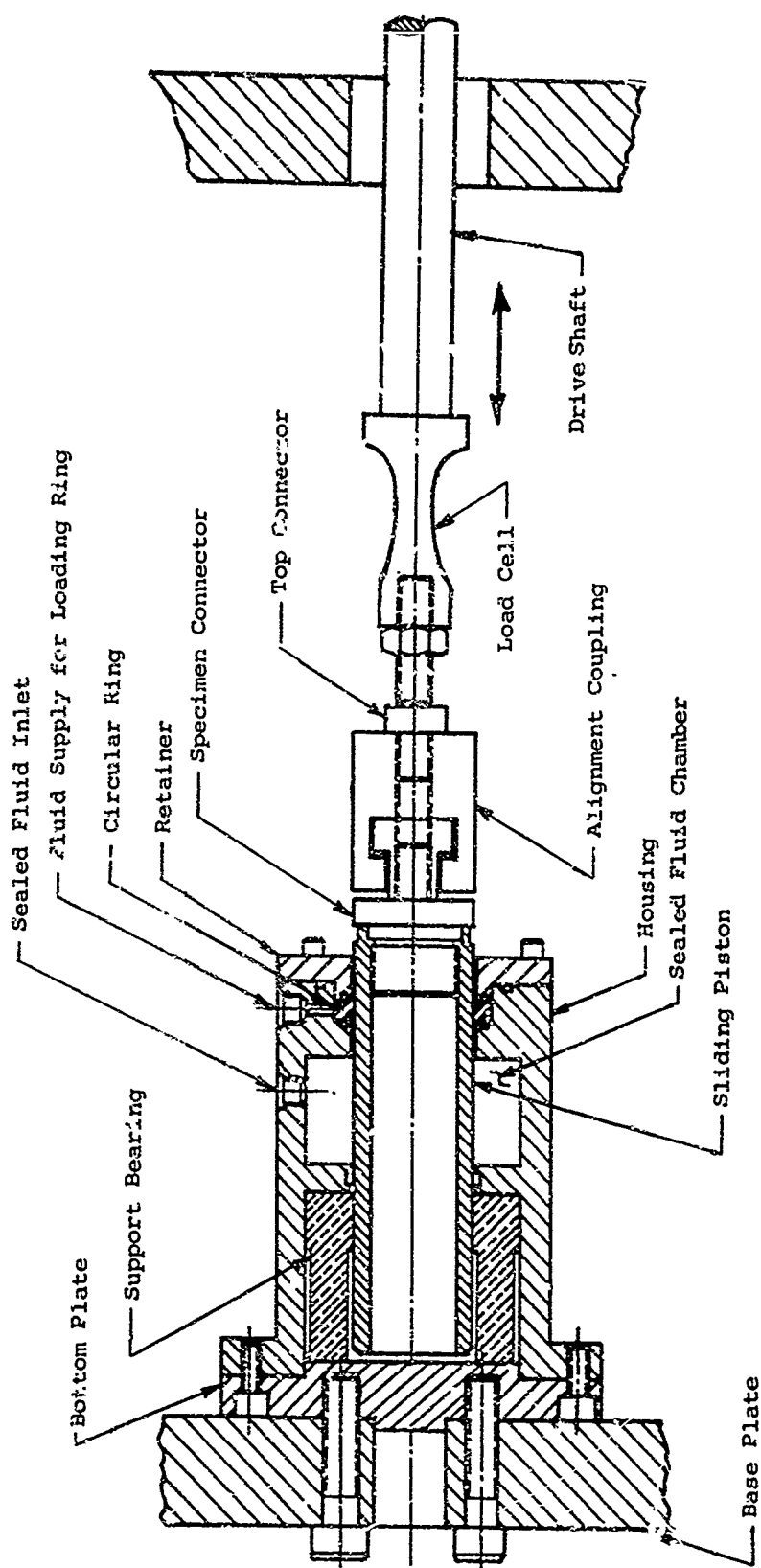


Figure II-1 Sliding wear experimental apparatus

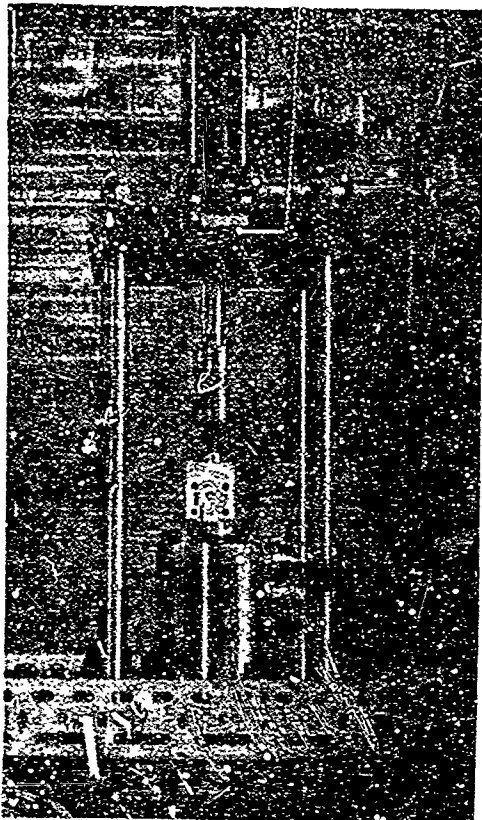


Figure II-2 Experimental sliding wear and leakage evaluation apparatus



Figure II-3 Seal and loading ring for sliding wear and leakage apparatus

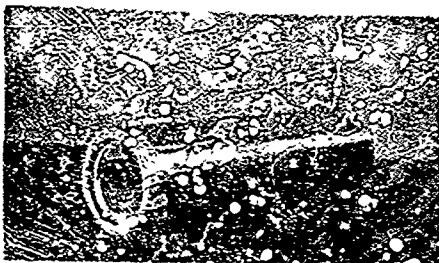


Figure II-4 Sliding piston for sliding wear and leakage apparatus

the seal interface can be expressed as a function of the fluid pressure applied to the outside diameter of the seal ring, the geometry, elastic moduli of the materials, and the tangential stress on the inside of the shaft. An analysis providing this functional relationship was derived on the basis of the deformation of two circular rings. In this case, the hollow shaft was assumed to be a ring.

Strain gages were mounted tangentially on the inner surface of the shaft approximately midway between ends. Measurement of the stress level permitted calculation of the interface stress. In addition, the ring deformation analysis was substantiated by observing the effects of radial pressure on the external ring to the measured tangential strain on the inside of the shaft.

Under conditions of sliding, the gages were located directly under the outer ring at only one position of the shaft. By continuously monitoring strain during sliding operation, the peak value was obtained and used in the calculations of the interface loading.

The elastic deformation analysis of the ring and shaft was based on the assumption that the long shaft could be represented by a narrow ring. The effects of the shaft length may have introduced an error that would tend to produce greater loads at the interface than the analysis predicts. No attempt was made to compensate for the shaft length. In any event, the method of load evaluation does provide consistent relative load values. The following analysis of two concentric rings (figure II-5) was employed in the determination of contact loads.

The net radial deflection of the outer ring can be expressed as

$$\delta_o = \delta_o(P) - \delta_o(S_i) \quad (II-1)$$

According to Roark (Ref. II-1) $\delta_o(P)$ and $\delta_o(S_i)$ can be expressed as

$$\delta_o(P) = \frac{Pa_o}{E_o} \frac{(2b_o^2)}{(b_o^2 - a_o^2)} \quad (II-2)$$

$$\delta_o(S_i) = \frac{S_i a_o}{E_o} \left[\frac{b_o^2 + a_o^2}{b_o^2 - a_o^2} - \nu \left(\frac{a_o^2}{b_o^2 - a_o^2} - 1 \right) \right]$$

When equation (II-2) is substituted in equation (II-1),

$$\delta_o = \frac{Pa_o}{E_o} \frac{(2b_o^2)}{(b_o^2 - a_o^2)} - S_i \frac{a_o}{E} \left[\frac{b_o^2 + a_o^2}{b_o^2 - a_o^2} - \nu \left(\frac{a_o^2}{b_o^2 - a_o^2} - 1 \right) \right] \quad (II-3)$$

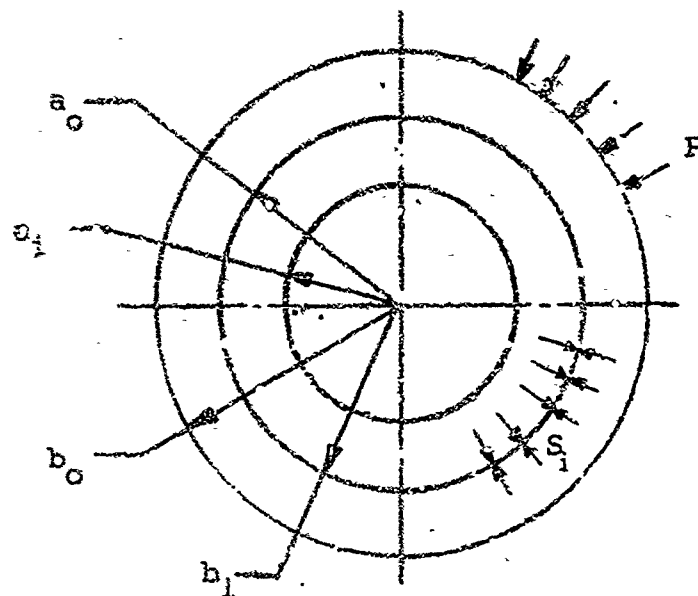


Figure II-5 Deformation of concentric rings

- a_i = ID of inner ring
- a_o = OD of inner ring
- b_i = ID of outer ring
- b_o = OD of outer ring
- E_i = Young's modulus inner ring
- E_o = Young's modulus outer ring
- P = applied pressure on outer ring
- S_i = contact stress at the interface
- ν = Poisson's ratio
- δ_i = net radial deflection of inner ring
(change in outside radius)
- δ_o = net radial deflection of outer ring
(change in inside radius)
- $\delta_o(P)$ = deflection due to P
- $\delta_o(S_i)$ = deflection due to S_i

The radial deflection of the outside diameter of the inner ring can be expressed as

$$\delta_i = \frac{S_i b_i}{E_i} \left(\frac{a_i^2 + b_i^2}{b_i^2 - a_i^2} - \nu \right) \quad (\text{II-4})$$

but if contact is to be achieved and maintained under load,

$$\delta_i = \delta_o. \quad (\text{II-5})$$

Then, substituting equations (II-3) and (II-4) into (II-5),

$$\begin{aligned} \frac{S_i b_i}{E_i} \left[\frac{a_i^2 + b_i^2}{b_i^2 - a_i^2} \right] - \nu &= \frac{P a_o}{E_o} \frac{(2b_o^2)}{b_o^2 - a_o^2} - \\ &\frac{S_i a_o}{E_o} \left[\frac{b_o^2 + a_o^2}{b_o^2 - a_o^2} - \nu \left(\frac{a_o^2}{b_o^2 - a_o^2} - 1 \right) \right] \end{aligned} \quad (\text{II-6})$$

Solving for S_i ,

$$S_i = \frac{P \left[\frac{a_o (2b_o^2)}{E_o (b_o^2 - a_o^2)} \right]}{\frac{b_i}{E_i} \left[\frac{a_i^2 + b_i^2}{b_i^2 - a_i^2} - \nu \right] + \frac{a_o}{E_o} \left[\frac{b_o^2 + a_o^2}{b_o^2 - a_o^2} - \nu \left(\frac{a_o^2}{b_o^2 - a_o^2} - 1 \right) \right]} \quad (\text{II-7})$$

Substitution of known geometry and material properties will give a direct relation between an external pressure P and the contact stress at the interface.

II-4 Initial Installation and Wear Compensation

Since the ring and shaft formed an initial interface clearance, fluid pressure was initially applied to the ring to obtain contact at the desired interface load. Calculations show that large clearances (0.001 in.) require high fluid pressures (~10,000 psi). Additionally, the large deformation could be permanent, thus upsetting the theoretical load relationships. In the process of rubbing contact, material was removed from the inside diameter of the ring and the outside diameter of the shaft. Consequently, the radial loading of the interface was decreased. To compensate for the material removal, the fluid pressure acting on the outside of the ring had to be increased again. It was necessary, therefore, that the parts have a very close initial fit

so that maximum wear could be compensated without permanent deformation. It should be noted that a small amount of wear does not markedly influence the elastic deformation analysis based on the initial past geometry. Thus, the magnitude of wear at any time during the sliding process can be estimated from calculations using the experimental ring pressure data required to produce a given strain on the inside of the shaft. The following calculations show the relative effects of clearance.

To determine: feasibility of using pressurized ring

Assume: two steel rings

$$a_o = 0.875$$

$$a_1 = 0.625$$

$$b_o = 1.125$$

$$b_1 = 0.875$$

$$E = 30 \times 10^6$$

$$Y = 0.26$$

From equation (II-7),

$$S_1 = 0.746P \quad (II-8)$$

However, for this equation to be valid, the rings must be in contact. If there is an initial radial clearance between the rings, an initial pressure P_i must be applied to bring the rings into contact. Then, equation (II-8) may be expressed as

$$S_1 = 0.746(P_T - P_i)$$

where

P_T = total applied pressure

P_i = pressure required for initial contact.

Values of P_i for known values of initial radial clearance can be calculated from the radial deflection equation

$$\delta_o = \frac{Pa_o}{E} \frac{2b^2}{(b_o^2 - a_o^2)}$$

For this example,

$$\delta_o = 0.147 \times 10^{-6}P$$

The maximum internal circumferential compressive stress S_c occurs at the inside diameter of the outer ring and is given by

$$S_c = \frac{P 2b_o^2}{b_o^2 - a_o^2} = 5.06P.$$

The pressure and compressive stress necessary to establish contact are shown for several values of radial clearance.

Radial Clearance, δ_o (in.)	Applied Pressure, P_i (psi)	Maximum Circumferential Stress in the Outer Ring, S_c (psi)
0.0001	681	3450
0.0002	1362	6810
0.0004	2720	13780
0.0017	11500	60000

The preceding results show the necessity of achieving a close initial fit between the ring and piston. A minimum clearance requires low applied pressure and produces minimum stress in the ring. Thus, greater compensation can be obtained for material removed as a result of wear.

II-5 Driving Mechanism

The sliding shaft was driven by a hydraulic cylinder producing constant velocity contact except at the point of stroke reversal. Provisions for stroke length and speed were incorporated into the driving apparatus.

A close fitting sleeve bearing supported the sliding member and minimized the wobble or sideways movement of the shaft. The ring was supported on the sides by O-rings, thereby producing a semifloating action aiding the alignment of parts.

A load cell was coupled between the driving cylinder and shaft to facilitate friction measurements. Self-aligning couplings were used to prevent misalignment.

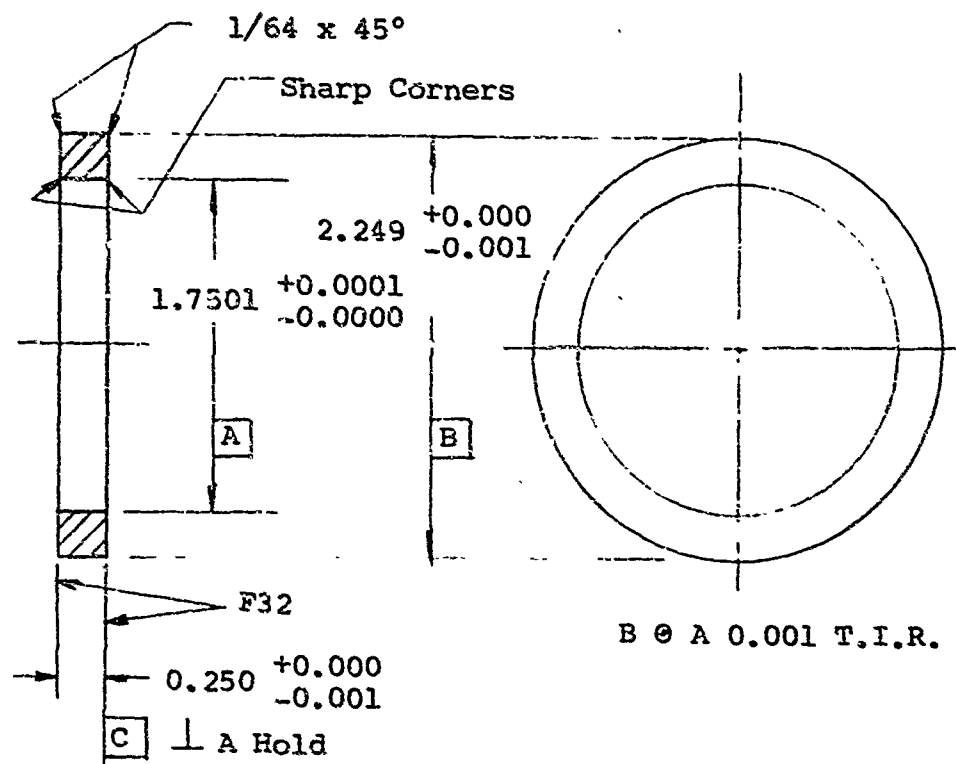
II-6 Experimental Parts

Nitralloy 135 was selected for the ring and shaft. This material was chosen on the basis of wear characteristics, ease of fabrication, and general compatibility with most of the fluids used in rocket systems. While mating of identical materials is not good practice from a minimum wear viewpoint, other factors had to be considered and a compromise reached. Factors influencing the material selection were:

- The magnitude of surface damage due to wear should be sufficiently large that measurements could be made without exceeding the sensitivity of instrumentation. Time-dependent effects in the rubbing process should be short term to minimize the duration of the experimental work.
- The cylindrical parts should be readily fabricated. Although at first glance this would appear a simple problem, if we consider the requirements for minimum leakage, the problem is indeed difficult. First, the finish of the surfaces forming the interface must be a minimum: This may be assumed to be less than 3 μ in. Secondly, the out-of-roundness of the ring and shaft must be a minimum; preferably the same variation as the roughness. Thirdly, the interface surfaces should slide parallel to one another, hence the deviation from straightness of the shaft and ring must also be a minimum. When each of these factors was considered, roughness was the only condition obtainable. Influencing factors were the machinability of the materials and the instrumentation used in the inspection process. An improved combination of mating materials would require at least one surface being much harder than the other. For minimum wear this would suggest a material such as tungsten carbide. This, in turn, induces machining problems adversely affecting roundness and straightness. Nitralloy 135, however, offered substantial hardness (Rc70), yet permitted finishing by optimum grinding techniques. The inspection problems were twofold. First, no adequate definition of roundness and straightness was available. The instrumentation used consisted of a Micrometrical rotary Proficorder which traces a surface contour in a single plane. The alignment of the plane with respect to a mean center of the cylindrical surfaces was not possible without new concepts of measurement. Additionally, the minimum resolution of measurement was 10 μ in., based on the capabilities of the mechanical and electrical parts of the instrument. Details of the ring and shaft (figures II-6 and II-7) show the fabrication objectives. The actual results of part fabrication are contained in the following section along with the experimental results.

II-7 Experimental Results and Observations

The experimental study was conducted in three phases. The first phase consisted of unlubricated sliding contact at a normal apparent stress of 100 psi for 470,000 stroke-in. The second phase consisted of an additional 178,000 stroke-in., unlubricated at a normal apparent contact stress of 200 psi. The phase-III work was conducted on a new ring and shaft at a stress of 100 psi for 2,533,000 stroke-in. with a lubricant. The velocity of sliding was 2.8 ips. Unlubricated experiments were conducted with air as the sealed fluid, thus the interface was continuously supplied with oxidizing media. The lubricated surface experiments were conducted



Note: 1. Nitralloy 135 modified: 6-hr heat treatment

2. Surface A: Surface Finish: 5- μ in. PTV
or 1- μ in. CLA

Roundness - Maximum variation 20 μ in.
on a two-lobed surface at
any cross section. Maxi-
mum variation from a
straight line center not
to exceed 20 μ in.

Figure II-6 Seal ring

with a mineral oil as a lubricant. The lubricant was externally applied to the shaft surface by a wick applicator. Static leakage measurements were obtained with air preceding the application of the lubricant.

Phase I Experiments. The experimental ring was brought into intimate contact with the shaft by increasing the fluid pressure on the periphery of the ring. The pressure was adjusted until the strain value measured at the inside surface of the shaft was equal to the theoretical strain produced by a uniformly distributed normal surface stress of 100 psi. When the proper strain was obtained, the sealed chamber was pressurized to 20 psi with air. Leakage was measured with the shaft static and during sliding. Figure II-8 shows the variation of leakage with total sliding distance.

Initial sliding contact produced a considerable amount of ferric oxide debris. The debris continued to be generated at a decreasing rate during the first 20,000 stroke-in. of contact. Finally, the formation of debris became unobservable and remained this way during the remaining 450,000 stroke-in. of operation. The initial surface finish of the shaft was 3-4 μ in. and, subsequently, increased to 5-7 μ in. at the termination of sliding. At the completion of the experiment, when the parts were inspected little surface damage was observed. During the period of debris formation, however, random scratches in the shaft surface were observed. These scratches were often filled with debris particles giving the surface a dark and rather worn appearance. After debris formation ceased, the shaft surface appeared highly polished with a light reflectivity greater than that produced by the fabrication process. Microscopic measurement of the wear debris particles showed the debris particles to be in the range of 50 to 100 μ in. in average dimensions. Table II-1 shows the changes in surface topography and average dimensions during the experiment.

Table II-1

EFFECTS OF WEAR ON RING AND SHAFT DIMENSIONS
AND SURFACE FINISH

Part	ID (in.)	Maximum Out-of-Roundness Peak-to-Valley (μ in.)	Peripheral Roughness Peak-to-Valley (μ in.)
Ring			
Initially	1.7477-3	150	5
after experiment	1.7481	150	10
Shaft			
Initially	1.7470-2	50	3-4
after experiment	1.7470-1	50	5

Accurate measurement of the parts after the cycling experiment showed an increase in the average ring diameter of 0.00035 in. and a decrease in the average shaft diameter of 0.00005 in. Thus, the average diametral clearance was increased by 0.0004 in. This increase required an additional 0.0002 in. of radial deflection to bring the ring into contact with the shaft and corresponded to an increase in hydraulic pressure applied to the ring to maintain the proper value of strain in the shaft. An increase of 2000-psi hydraulic pressure was required to maintain the nominal contact stress of 100 psi (as indicated by the strain on the inside of the shaft) by the time the end of the run was reached. This increase was required to provide the additional radial deformation of the ring to make up for the increase in clearance resulting from wear which approximates the rate of material removal. In addition, the wear rate was correlated by dimensional measurements. The estimated wear rate for the ring and shaft was 8×10^{-10} cu in. per in.

The theoretical increase in pressure necessary to provide an additional 0.0002 in. of radial deflection is 1350 psi. Thus, there was a fair correlation between the theoretical pressure increase and the actual pressure increase. The difference between the two was probably due to the out-of-roundness of the parts.

A coefficient of friction was calculated from the apparent contact stress based on the measured strain. During the initial 20,000 stroke-in. of sliding, the coefficient of friction varied between 1 and 8. Continued sliding showed a decrease in friction to values ranging between 0.15 and 0.90. Figure II-8 shows the characteristics of friction with sliding distance. The initial high coefficient of friction was attributed to the wedging of debris particles between the interface surfaces. Since the ring and shaft were not very resilient, substantial resistance to sliding motion could have been generated. It should be noted that the decrease in friction coefficient occurred when observable debris formation ceased.

Leakage data, shown on figure II-8, were used in calculating conductance parameter and, subsequently, were converted into the form of an equivalent channel dimension, which is the cube root of the conductance. The equivalent dimension ranged from 106 to 120 μ in. during the experiment. Results obtained during the first 15,000 stroke-in. are shown in Table II-2.

A comparison of the maximum surface roughness variation of 10 μ in. with the equivalent dimension obtained from leakage measurements shows that the surface roughness effect on leakage must have been insignificant. The out-of-roundnesses of the cylindrical surfaces, as shown on Table II-2, were of the same order of magnitude as the equivalent dimension. Average out-of-roundness of both parts was 100 μ in. The topography of the ring could be described as a three-lobed surface while the shaft possessed two lobes. Figure II-9 shows an exaggerated schematic view of the piston and ring.

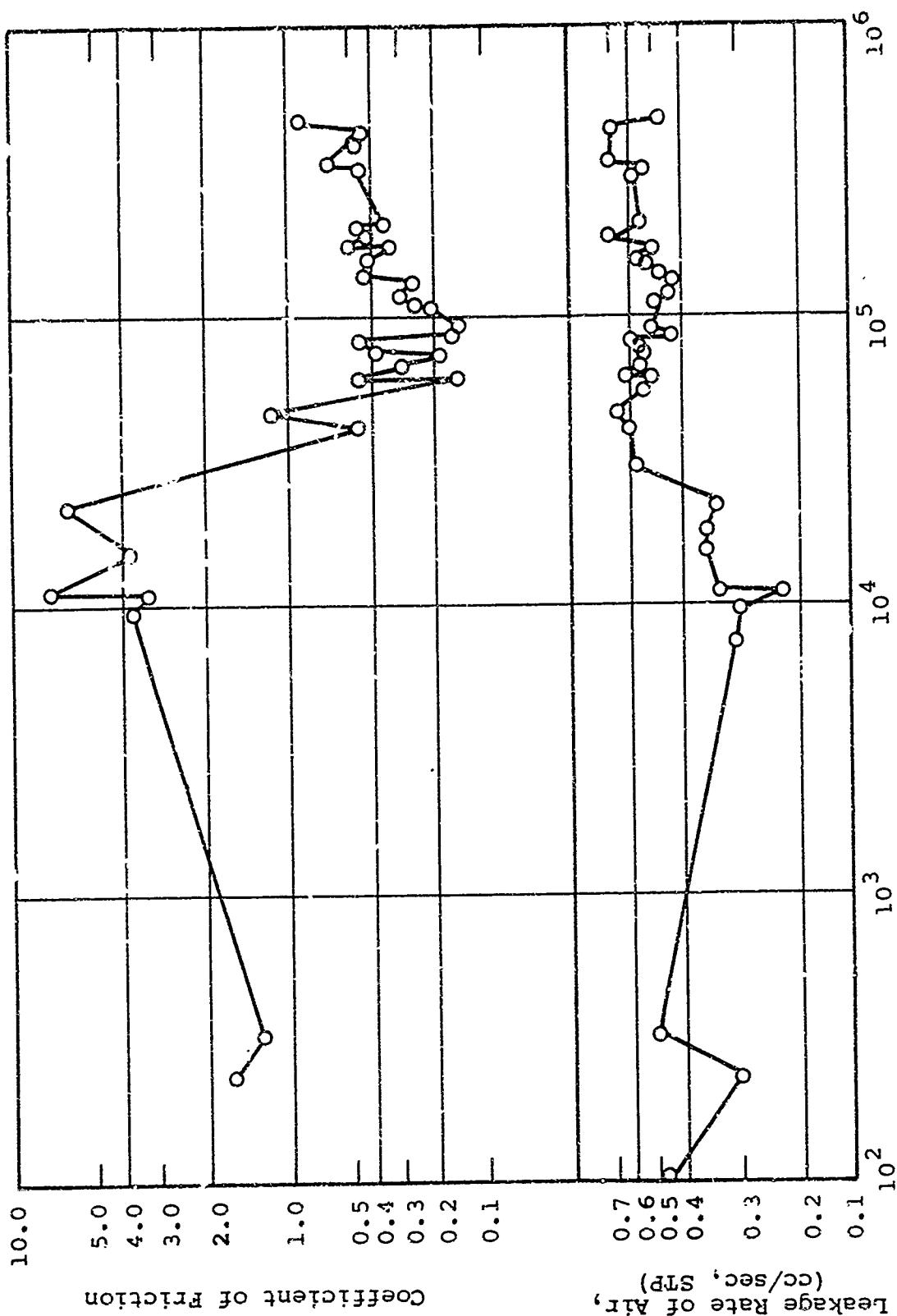


Figure II-8 Leakage rate and friction characteristics of Nitralloy sliding on Nitralloy as a function of total sliding distance

Table II-2

VARIATION OF LEAKAGE WITH CUMULATIVE SLIDING OF THE PARTS UNDER LOAD

Sealed Fluid Pressure (psi)	Leakage Rate (cc/sec)	Total Stroke-in. Traveled	Flow Conductance Parameter (h^3) (in.^3)	Equivalent Clearance ($\mu\text{in.}$)
20	0.475	---	1.245×10^{-12}	106.5
20	0.250	230	6.53×10^{-13}	87
20	0.500	327	1.31×10^{-12}	109.6
20	0.362	7,417	5.87×10^{-13}	88.5
20	0.250	9,517	6.53×10^{-13}	87
20	0.175	11,092	4.62×10^{-13}	77.6
20	0.150	15,337	3.93×10^{-13}	70.4

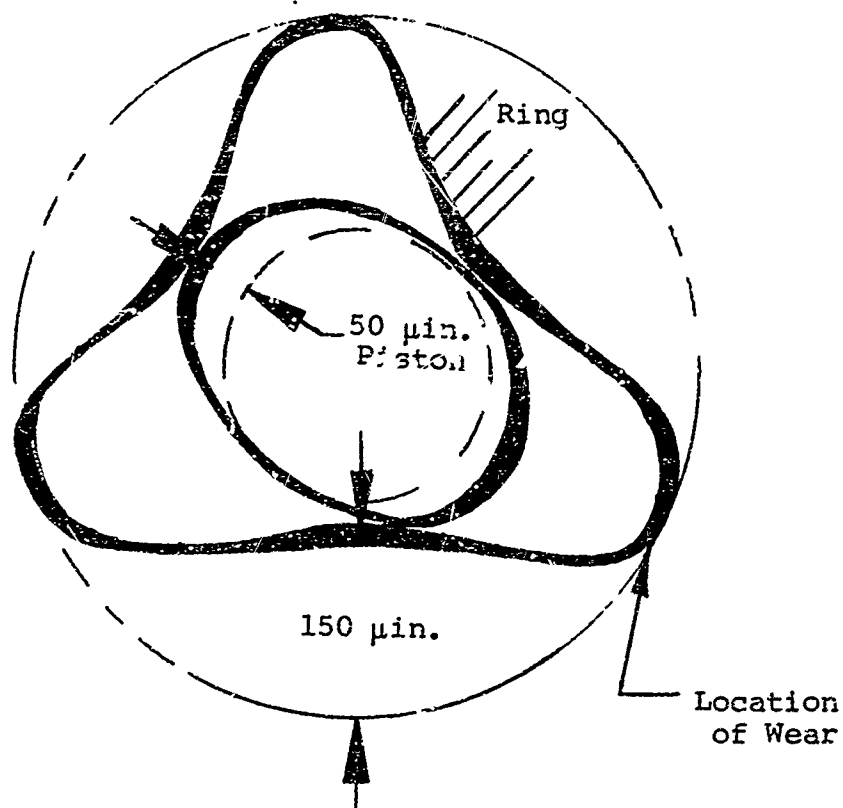


Figure II-9 Exaggerated view of piston and ring geometry

It was reasoned that the ring did not uniformly deform against the shaft when substantial surface variations were present. Hence, it would appear that nonuniform contact and wear resulted. Microscopic examination of the surfaces, however, showed uniform wear

with no evidence of localized contact. It was concluded, therefore, that wear debris particles generated at the points of rubbing contact were substantially large so that when the particles were transferred to the area of no contact similar surface damage was generated.

The effects of out-of-roundness of the piston outside diameter and ring inside diameter were investigated by rotating the piston in 90-deg increments and measuring leakage. A change in leakage was observed, indicating that uniform contact had not been achieved. The variation of leakage with the relative position of parts is shown on Table II-3.

Table II-3

VARIATION OF LEAKAGE WITH ANGULAR POSITION OF PARTS

Sealed Fluid Pressure (psi)	Contact Stress (psi)	Angle of Rotation (deg)	Leakage rate of air (cc/sec, STP)
18	96	0	0.69
18	96	90	0.33
18	96	180	0.39
18	96	270	0.18
18	96	360	0.41

Phase-II Experiments. Sliding experiments utilizing the same parts as in Phase I were conducted for an additional 178,000 stroke-in. An increase in normal contact stress to 200 psi caused an increase in leakage, coefficient of friction and quantity of wear particles generated. Leakage and coefficient of friction results are shown in figures II-10 and II-11.

The increased interface loading disrupted the equilibrium wear process that previously existed. Increased generation of wear debris led to the conclusion that the wear rate was also increasing. The calculation of coefficients of friction greater than unity occurring during this period of increased wear-particle generation further supported the assumption of the wedging of wear particles in the contact interface. Figure II-12 shows typical oxide particles generated during sliding. The average particle size is between 50 and 100 μ in.

Additional evidence of the rapid wear was the increase in the fluid pressure on the ring required to produce the interface contact stress. Initially, the 200-psi contact stress was produced by a fluid pressure of 5,750 psi, increasing to 7,500 psi during the experiment. The average wear rate was 7×10^{-4} cu in. per in.

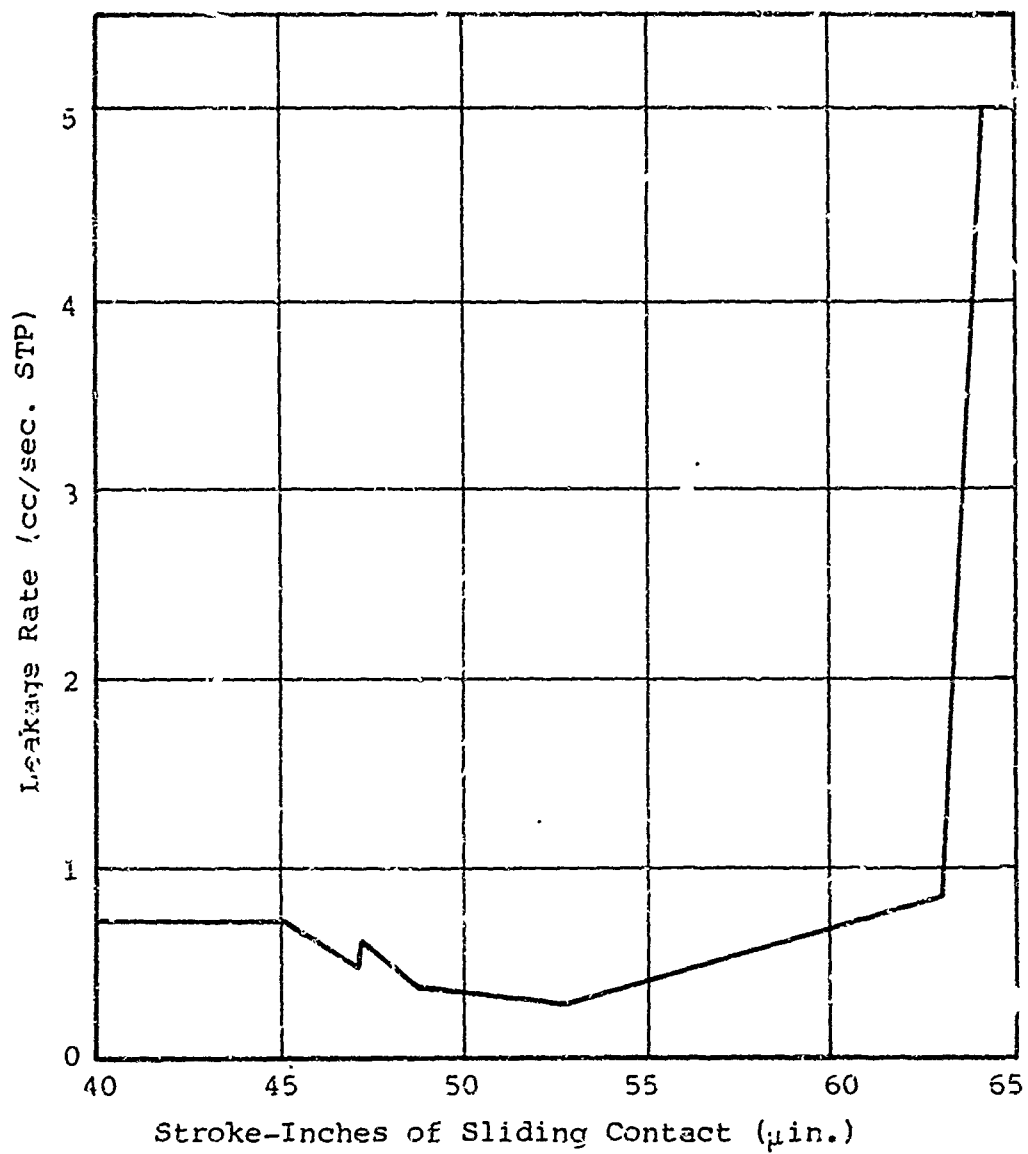


Figure II-10 Leakage rate of Nitralloy sliding on Nitralloy as a function of total sliding distance

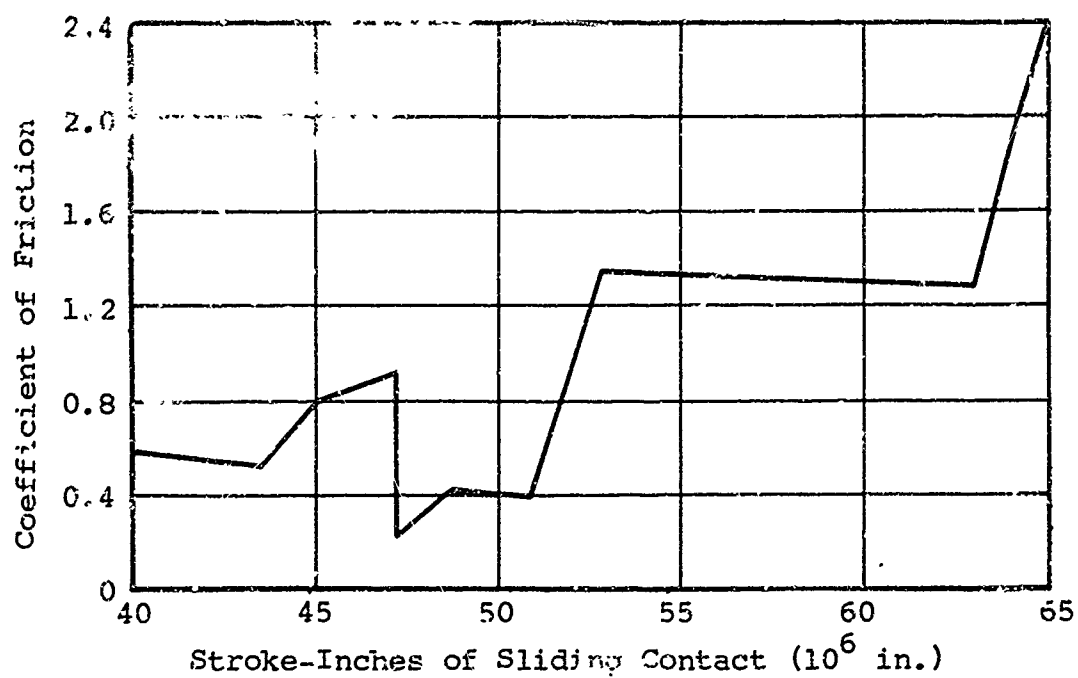
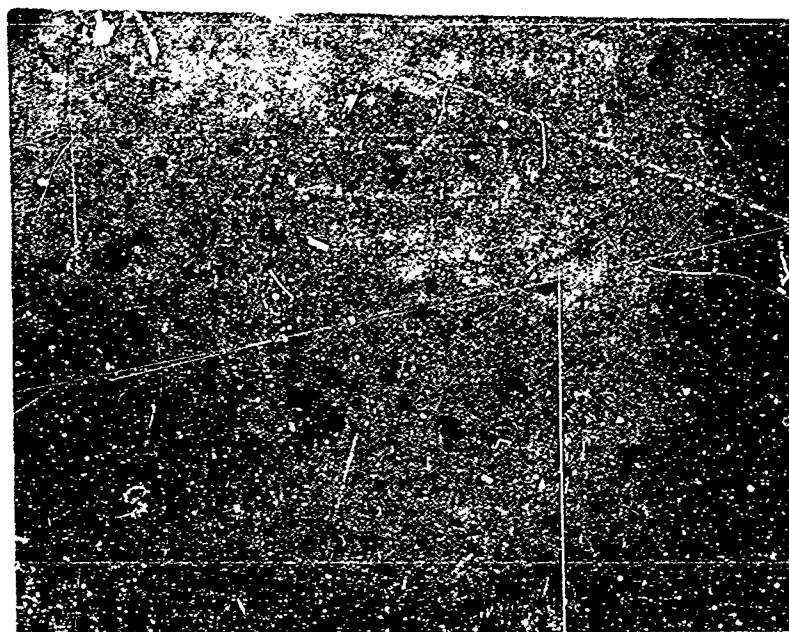


Figure II-11 Friction characteristics of Nitralloy sliding on Nitralloy as a function of total sliding distance



—→ | | ←— 0.0005 in.

Figure II-12 Photomicrograph of wear particles collected after 178,483 stroke-inches at 200-psi contact stress

(Magnification: 960X)

An inspection of parts at the completion of the experiment (Table II-4) showed that the wear process affected the roundness and surface roughness. The corresponding increase in leakage substantiates the increase in out-of-roundness. This may be seen by comparing the equivalent channel dimensions, shown on Table II-5, with the inspection results.

A review of the general behavior of the increased interface load experiment led to the conclusion that equilibrium wear was not obtained during the experiment. The conclusion was based on the continued formation of wear debris through the experiment. Unfortunately, the experiment had to be terminated before this hypothesis could be proved.

Table II-4

VARIATION OF LEAKAGE WITH CUMULATIVE SLIDING OF THE PARTS
UNDER LOAD FOR CONTACT STRESS OF 200 PSI

Fluid Pressure (psi)	Leakage Rate (cc/sec)	Total Stroke-In. Traveled	Flow Conductance Parameter (h^3) (in. ³)	Equivalent Clearance (μ in.)
20	0.623	473,028	1.63×10^{-12}	127
20	0.635	487,893	9.6×10^{-13}	98.5
20	0.32	489,751	8.4×10^{-13}	94
20	0.325	508,669	8.5×10^{-13}	94.5
20	0.275	528,334	7.2×10^{-13}	89.5
20	0.85	630,434	2.22×10^{-12}	149
20	5.0	642,162	1.31×10^{-11}	236
20	5.0	650,559	1.31×10^{-11}	236

Table II-5

EFFECTS OF WEAR ON RING AND SHAFT DIMENSIONS AND SURFACE FINISH

Part	Stroke-In. Traveled	Contact Surface Diameter (in.)	Maximum Out-of-Roundness Peak-to-Valley (μ in.)	Peripheral Roughness Peak-to-Valley (μ in.)
Ring	0	1.7477-8	150	5
	470,000 Phase I	1.7481	150	10
	650,559 Phase II	1.7490-2	200	20
Shaft	0	1.7470-2	50	3-4
	470,000 Phase I	1.7470-1	50	5
	650,559 Phase II	1.7468-9	130	10

Phase-III Experiments. A new set of sliding parts was employed in this investigation to determine the effects of lubrication on sliding contact. A mineral oil without additives was used as the lubricating fluid. An initial inspection of the ring and shaft showed the ring was out-of-round diametrically and, in addition, was tapered on the inside diameter. The out-of-roundness of parts was 140 μ in. while the surface roughness of parts was less than 2 μ in. peak-to-valley. Figure II-13 shows the taper dimensions of the ring.

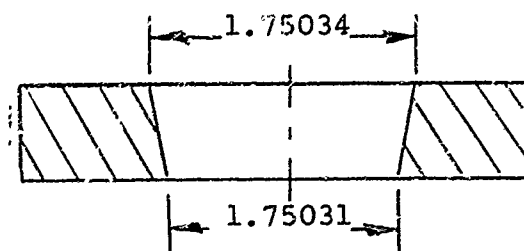


Figure II-13 Taper dimensions of the ring

The shaft possessed an out-of-roundness of 20 μ in. with a diameter variation between ends of the shaft of 1.75036 and 1.75037 in. Therefore, by combining the smallest ring dimension with the largest shaft dimension an interference of 60 μ in. was produced. The surface roughness of the shaft was 2 μ in. peak-to-valley.

Since an initial interference between parts occurred, the interface was prestressed radially. Consequently, a 500-psi external pressure on the ring produced a 100-psi average radial stress. Air leakage as a function of contact stress is shown on Table II-6. The results show an equivalent channel dimension variation between 55 and 100 μ in. and that improved conformability occurred between the ring and piston as compared with the Phase I results. This condition was attributed to a two-lobed surface on the new ring and the slight decrease in out-of-roundness.

At the completion of 2,533,000 stroke-in. of sliding contact, the parts were examined for wear and dimensional change. The peripheral roughness on the ring and shaft had increased from 2 to 4 μ in. while the out-of-roundness was unchanged. Because of the very small topographical changes, no change in leakage occurred. Wear had the form of very shallow scratches running axially along the ring and shaft surface. The scratches were uniform around the periphery. The estimated wear rate was 2.5×10^{-12} cu in. per in.

Table II-6

LEAKAGE VARIATION WITH POSITION FOR NEW RING AND SHAFT

Fluid Pressure (psi)	Leakage Rate (cc/sec, STP)	Contact Stress (psi)	Angular Shaft Position* (deg)	Leakage Conductance Parameter (in. ³)	Equivalent Clearance (μin.)
20	0.30	25.0	0	7.68×10^{-13}	92
20	0.195	47.9	90	5.11×10^{-13}	80
20	0.40	35.8	180	1.048×10^{-12}	101
20	0.20	32.1	270	5.24×10^{-13}	80.6
20	0.065	46.4	270	1.7×10^{-13}	55

* Shaft rotation clockwise as viewed from above.

II-8 Summary

The following observations can be made from the experimental results.

- The resistance to fluid flow is formed by mating contact irregularities. The contact can be described as roughness or waviness contact using the commercial definition of the two terms. The experiments showed that leakage through cylindrical metallic interfaces will be influenced largely by the degree of waviness or out-of-roundness of the mating surfaces. To achieve minimum leakage, however, the surfaces should be in uniform roughness contact. The inability to achieve roughness contact was attributed to limitations in surface fabrication and inspection techniques. Since these problems were not part of this study, they are discussed separately at the end of this appendix.
- The rubbing of Nitralloy on Nitralloy can be described as mild wear when normal loads up to 250 lb (200 psi) are applied to the surfaces with or without lubrication. The amount of surface damage was relatively small. For example, the peripheral surface roughness increased from 2 μin. to 5 μin peak-to-valley. Had the sliding parts been in more intimate contact, this would cause a small increase in leakage.

- Equilibrium wear occurs when operating conditions remain unchanged. A change in contact load, however, does upset the wear process and produces a change in wear rates. Figure II-14 shows a comparison between the total wear and wear rates for conditions of 100 and 200-psi normal contact pressure. The change in wear rate preceding equilibrium is attributed to the time-dependent transfer of materials and subsequent oxidation, the reduction in the number of junctions formed by adhesion, the increase in actual contact area through the process of wear.
- The generation of wear debris particles occurs predominantly during nonequilibrium sliding. The particles range from very small ($<1 \mu\text{in.}$) to $150 \mu\text{in.}$ with an average size of $100 \mu\text{in.}$ The particles may have been singular or small particles that coalesced into larger ones. There was no direct evidence of particle structure. However, wear occurred uniformly in all cases despite the apparent nonuniform contact developed by the out-of-roundness of parts. Since the equivalent channel dimensions were greater than $100 \mu\text{in.}$, it must be concluded that the particles, however formed, act as a singular large particle. Hence, it also must be concluded that wear debris particles can have a significant effect on leakage by causing the surfaces to separate and accommodate the particle.
- Friction coefficients greater than unity and as high as 10 can occur if the geometry of the sliding elements is such that the wear debris particles cannot readily deform the surface and substrate. During nonequilibrium sliding, the coefficient of friction was greater than unity. This was accompanied by larger wear rates and particle size. During equilibrium wear, the friction coefficient was close to values reported in the literature (i.e., 0.55). No observable debris was generated.
- Lubrication of the surfaces produced a two-order-of-magnitude decrease in wear rate. However, the surface damage was not significantly different from the unlubricated case and in the range of $3\text{--}5 \mu\text{in.}$ In the absence of wear debris and mismatched surfaces, the leakage path should be relatively unaffected by the conditions of sliding. The initial surface finish of $2\text{--}3 \mu\text{in.}$ appears to be an optimum for this material, considering the small amount of topographical change due to sliding.

II-9 Comments on the Fabrication and Inspection of Cylindrical Surfaces

An objective in any seal application is to achieve zero leakage. Although this objective is not attainable, it is important to know how close to this objective we can achieve. In the case of cylindrical sealing interfaces, the objective is complete

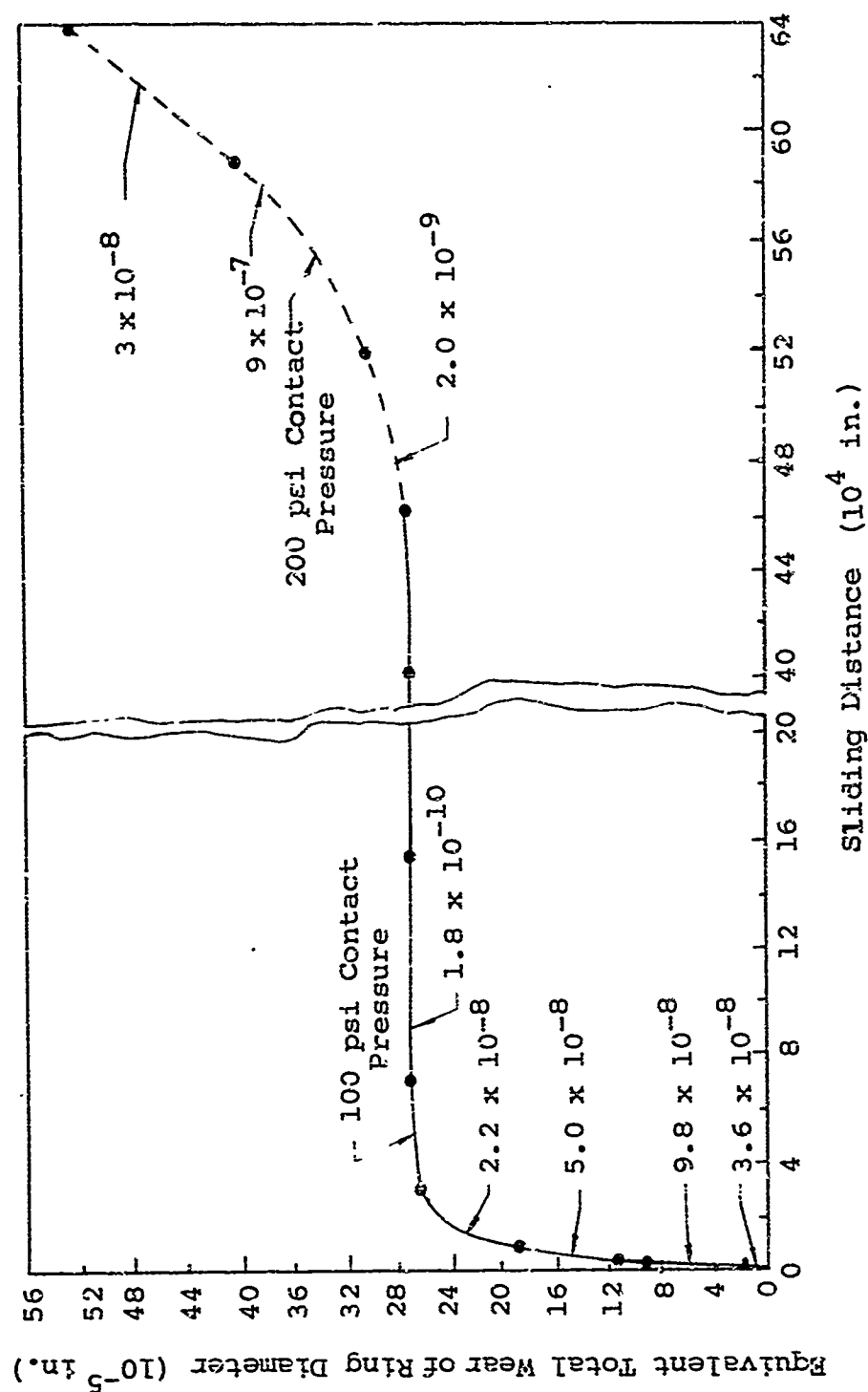


Figure II-14 Total wear of a Nitralloy-135 ring sliding in an air environment (Wear rates, shown between adjacent data points, are given in units of cu in. per in.)

surface contact on the smallest microscopic scale possible. The factors that limit the attainment of this objective are many: some of which have yet to be defined. In the present state-of-the-art, however, most of these problems are not significant simply because no satisfactory solution has been found for the most predominant problem -- the fabrication process. Once the fabrication problem has been solved, the remaining factors will take on new significance.

The generation of precision cylindrical surfaces is not really a difficult task provided that precision is defined and can be substantiated by measuring instruments. This, then, forms the basis of the entire problem, which can be restated:

- How do you make precise cylindrical surfaces?
- How do you define a precise cylindrical surface?
- How do you measure a cylindrical surface?

First to be considered is the measurement of a cylindrical surface. The state of development of measuring instrumentation may be described as unsatisfactory. Specifically, the available instruments do not offer sufficient accuracy, sensitivity, and flexibility with respect to size and geometry needed for present day seal and bearing technology. These statements, of course, must be accepted on the basis of known commercial devices, and exclude the possibility of unique methods developed without wide recognition. Possibly the best instruments available are the Micrometrical Rotary Proficorder and the Taylor and Hobson Tallyrond. Both instruments measure variations in distance from a center point reference generated by a hydrostatically suspended shaft, as shown in figure II-15. These instruments are capable of tracing the variations of a circular surface in a single plane by means of a stylus-actuated transformer and other electrical apparatus. The instruments are not capable of tracing the entire surface using a single fixed center reference. In addition, wobble and eccentricity of the hydrostatic bearing may occur, thereby limiting the sensitivity of planar measurement. By a system of reindexing the part being traced, the influence of bearing centerline variation can be detected but not positively substantiated. Considering the limitations imposed by the bearing, stylus, electrical apparatus, and structural parts, the instruments are capable of planar measurements to 3 μ in. with some degree of reliability. Other limitations are the diameter, length of the part, and access to surfaces in complex parts.

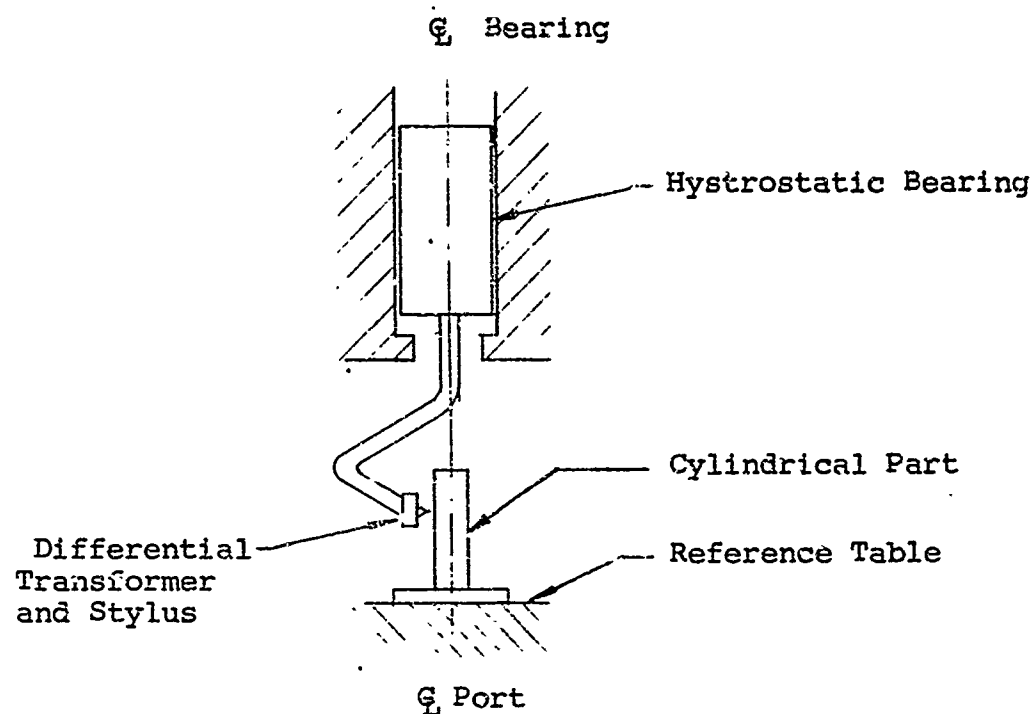


Figure II-15 Schematic view of a circular tracing instrument

The next question considered is how to define a cylindrical surface. As stated, the planer tracing instruments cannot scan accurately along the axis of even a simple cylindrical surface. Hence, planer traces of two sections of a cylinder, as shown in figure II-16 cannot be related together because the reference centers are not the same. Hence, to define a surface it is necessary to establish a hypothetical center from which all planer measurements can be made. At present, this cannot be accomplished.

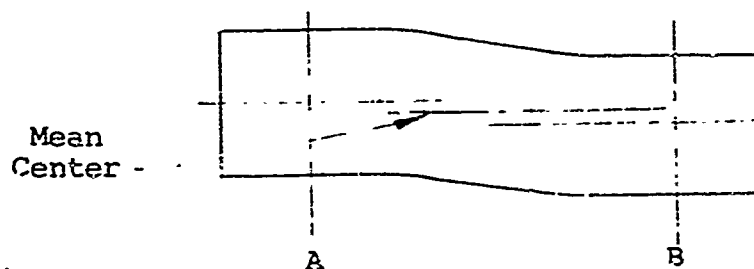


Figure II-16 Nonalignment of planar centers

A method suggested for achieving a center is to traverse the stylus axially on an optical flat reference surface. The procedure would be as follows:

- (1) Starting at the edge of a surface, a planer trace is made around the periphery of the surface. A center of the plane would be established based on a minimum rms deviation. This center would be referenced to the optical flat plane and axis of the hydrostatic bearing. This feature of automatically establishing a mean center is presently available in Taylor and Hobson equipment. In this case, however, all output from the tracing stylus would be recorded on magnetic tape.
- (2) Having established the center of the first plane, the stylus would be relocated axially, whereupon successive planer traces would be made and additional centers established. After the entire surface has been scanned in discrete planes, the mean center data would be used to compute a mean line center. This would require the development of computer equipment.
- (3) After the mean line center is established, the taped output would be replayed and the variations from the mean center could thus obtain at any point on the surface.

The final question to be considered is how to produce precise cylindrical surfaces. The term precise may be assumed to be 5 μ in. variation on any dimension. The purpose of this discussion is not to describe the processes but rather to describe the problems. Generally, if a part can be measured, the part can be fabricated to the required dimensions by common methods such as grinding, honing, polishing and other superfinishing processes. Part geometry can impose limitations on the degree of precision, however. As an example, the shafts used in the sliding wear experiments (figure II-7) were readily fabricated to finishes of 2 μ in. and out-of-roundness of the mating ring obtainable was 120 μ in. The difference was attributed to the bulk of material involved and thermal deformation during the finishing process. The factors that can limit dimensional variations are:

- The method of supporting the work piece. Easily deformable structures can be distorted by clamping or fixturing in the machining process.
- Inspection procedures. If the part must be removed from the machine for inspection, it is difficult to realign the part when further processing is necessary. Hence, the development of simultaneous finishing and inspection equipment would be beneficial.

- Thermal deformation due to ambient and finishing effects.
- Structural rigidity of the part itself. Deformation during the finishing process can produce considerable dimensional variations.
- Capability of the finishing machine with respect to the tool material and shape and other mechanical effects such as learning runout, shaft misalignment, and vibration.
- Size, weight, and geometry of the part. In general, small parts can be made to greater precision than large parts.

As a result of the lack of success in obtaining suitable rings and shafts for use in the wear experiments, a survey was made to determine whether substantial improvements could be realized. A survey letter (figure II-17) was submitted to twenty-five manufacturers and users of precision forming equipment. In addition, personal and follow-up letter contacts were made to clarify several of the questions. In brief, however, the survey was not beneficial. No valuable data were obtained and none of the firms showed a willingness to produce the ring and shaft parts. One interesting reply was received and is quoted in part because it substantiates much of the preceding discussion. This reply was received from a leading manufacturer of aerospace products.

"These (seals) are of our own design and manufacture for reasons which are partly related to the subject of your questions, namely that you can build quality into a seal surface but you can't inspect it in. The quality is maintained by controlling the attitude of the producers and the methods by which they produce.

"Air Force quality control philosophy doubly insures this to be the case by treating all drawing requirements as black or white and pretending that features of the highest possible precision can be fully described and controlled on a drawing and a system which requires 'corrective action' when the feature can be found to exceed the drawing requirements in any particular. When you are doing the best you can already then the 'corrective action' ends up as a relaxation of drawing tolerance which must be offset by an 'underground' campaign to try to keep doing the best possible rather than yielding to the strong temptation to use the new drawing tolerance for cost saving and letting the Engineering Department worry about what to do with the parts.

"This same situation exists in almost all manufacture. We have been in business for many years and many customers, such as Boeing, North American, Convair, Douglas, Lockheed, etc. have tried to write fully definitive specifications. Some of these are so big as to make the Sears catalog look like a casual flyer. None of them ever came close to insuring a useable product from us, and some of the most voluminous were most lacking.

Gentlemen:

This letter is a request for information concerning the capabilities of your company in fabricating cylindrical surfaces to very precise tolerances. The objectives are two fold: (1) to obtain and assess tolerance data on cylindrical surfaces having varying dimensions, and (2) to obtain a cost quotation on a specific set of parts.

Our interest in obtaining this information is occasioned by a research program we are conducting under Contract AF 04(611)-9704 with the United States Air Force, Rocket Propulsion Laboratories, Edwards Air Force Base, California. The research program is entitled, "Investigation of Leakage and Sealing Parameters."

This program is a study of variables influencing static and dynamic seals with a view towards the development of design criteria for component designers. The information being generated will be included in an "Aerospace Fluid Component Designers Handbook."

One of the most influencing parameters affecting sealing is the ability to fabricate seal parts to exacting tolerances, including dimensional and topographical. We have already surveyed the literature and industry in an attempt to establish the limits of fabrication capabilities. The data obtained has yielded only the best general commercial information. We know that parts have been fabricated with greater precision but it has been impossible for us to completely identify:

- The influence of part size
- The methods of inspection
- The method of fabrication
- The amount of trial and error involved in fabrication
- The best procedures for specifying dimensional variations taking into account the methods of inspection

If the preceding information could be gathered together, it would assist the component designer in incorporating seals and bearings in the hardware. Most important, it would improve seal performance and ensure the successful completion of a space mission. In addition, the design information would be of benefit to all other critical sealing applications.

The area most devoid of information is the fabrication and inspection of cylindrical surfaces. To assist in obtaining data, two typical parts have been selected for study. These parts, shown on Figs. 1 and 2, consist of a shaft and ring. The surfaces of concern are the outer surfaces of the rod and the inner surface of the ring. Two charts are attached to this letter which list the information required for various dimensions of the parts. Spaces are provided to fill in the appropriate data.

It is realized that the completion of the attached tables may require considerable time and effort. Also, the tables may not be suitable for the inclusion of all data, and possibly, some data may be considered proprietary. Therefore, any data you can furnish would be appreciated. Since your company is one of several selected for this survey, we will forward a summary of the results. Source of information will not be divulged unless permission to do so is indicated.

In addition, we would appreciate a cost quotation to produce the parts shown on attached drawings 6062-7 and 6062-8*. We will have these parts fabricated for experimental seal evaluation. Cost will not be of major consideration. The important consideration is the ability to produce the parts to specifications which can be substantiated by your past experience. If improved tolerances can be achieved, please specify.

Your assistance in this survey will be greatly appreciated from our own standpoint, and, certainly, will improve the state-of-the-art of sealing by providing the component designer with useful information. Please do not hesitate in contacting me if any additional information is required.

* Figures II-6 and II-7.

Figure II-17 Form letter requesting information on fabricating cylindrical surfaces to very precise tolerances

"I sense that you already realize that it is impossible to dimension a high precision right circular cylindrical surface in a practical manner. For one thing, you will never be able to decide where the axis of the part is when you go to inspect it. One can specify a maximum allowable deviation from a true surface, but this is too laborious for inspection to use in small quantity manufacture. In our shop, it forces the inspector to put the part on the Tallyrond and run a series of charts at different sections along the piece. Then he must somehow decide what these charts mean after being arranged along an optimum axis which he must choose. I don't know who would simultaneously have both the skill and patience to do such work on a continuous basis. Even then, the accuracy of the test machine is not good relative to the best quality plate lapping our shop can do."

In summary, the need for improved fabrication techniques and inspection instrumentation must be satisfied before improvements in sealing and bearing technology can be realized. Additionally, reliable specifications must be generated to provide the component designer with real information and not simply objectives which are "compromised" during fabrication.

II-10 References

- II-1 R.J. Roark, Formulas for Stress and Strain 3rd Ed. p. 276, McGraw-Hill (1954).

APPENDIX III
EFFECTS OF PHASE CHANGES ON LEAKAGE RATES
THROUGH ROTARY FACE SEALS

III-1 Introduction

It has been fairly well established by experimental observation that changes of phase occur within the interfacial film of rotary face seals. These changes of phase are to be anticipated upon consideration of the high local heating which must occur in the very narrow clearance of a rapidly rotating shaft seal. Not only is heat produced by the hydrodynamic viscous dissipation within the lubricant film, but also the occurrence of boundary lubrication in spots may produce additional frictional heat release. The vaporization produced by this local heating may be the reason for the effectiveness of face seals in the reduction of leakage. There are a number of explanations for expecting vaporization to result in reduced leakage. One obvious explanation is that the face seal may be considered a type of labyrinth seal since the surface irregularities are of the order of magnitude as the average clearance and produce a tortuous flow passage. It is well-known that a labyrinth seal is far more effective for reducing leakage of vapors than of liquids. This effectiveness is due to the much greater specific volume of a gas, so that for a given mass flow rate the leakage velocity is increased and results in a greater pressure drop. In addition, the labyrinth with its numerous changes in flow passage area produces turbulence and flow expansion in the diverging area sections with consequent inefficient flow and higher pressure drop.

Vaporization in rotary face seals has been reported to appear either as bubble trails or as concentric "cavitation trails." In view of the large number of cavitation trails observed -- Battelle Memorial Institute reports 180 to 280 trails per inch -- it is conceivable that surface tension forces alone can account for a considerable pressure drop. For example, L. Bernd (Ref. III-1), using the classical concept of capillary forces dependent upon contact angles, has computed that a $1/16$ in. seal width will support 1320-psi water pressure drop for a Stellite-faced runner (rotating against a stationary carbon-graphite seal face) with a 20- μ in. clearance and 180 cavitation trails per inch.

It should be recognized that a computation of this type proves nothing unless supported by experimental observation. Unfortunately, detailed experimental substantiation is difficult

because of the near impossibility of measuring contact angles in the dynamic case, or for that matter, even an effective clearance width. However, the computation does indicate the possibly important role of vaporization phenomena and accompanying surface tension in dynamic face seals.

In attempting to understand the basic mechanisms involved in relatively little-understood phenomena, such as those represented by the rotary face seal, there are two pitfalls to be avoided; oversimplification and overgeneralization.

Overgeneralization is less objectionable because it merely leads to extra, eventually unnecessary computations. On the other hand, oversimplification and forced fitting of experimental data to inapplicable theory can result in completely overlooking important phenomena. An oversimplification that may be particularly misleading is to extend the use of friction factors and coefficients as employed in conduit flows with contractions and expansions to the rotary seal problem. There is also little justification for using the idea of surface tension as a static equilibrium concept, or in the usual concepts of cavitation theory as employed in turbomachinery and lubrication engineering.

By undesirable overgeneralization in this context, examples are provided by the complicated rheological models of modern continuum mechanics, or complex kinetic theory models. The following discussion will attempt to avoid either extreme; however, it is preferable to err on the side of overgeneralization.

III-2 Surface Tension

Because surface tension may play a key role in the sealing properties of face seals in which film vaporization occurs, the classical concept of surface tension will be reviewed in terms of static equilibrium, followed by a discussion of the extension of the concept to nonequilibrium phenomena.

III-2.1 Static Equilibrium Surface Tension

The existence of the property of surface tension is easily demonstrated by placing a flat plate vertically into a dish of liquid. The liquid will be deflected at the plate, say a rise h_0 , and a constant angle α will be formed as shown in figure III-1. If it is hypothesized that there is a force T per unit width tangential to the surface, then the theoretical shape of the liquid surface can be computed from a simple force balance.

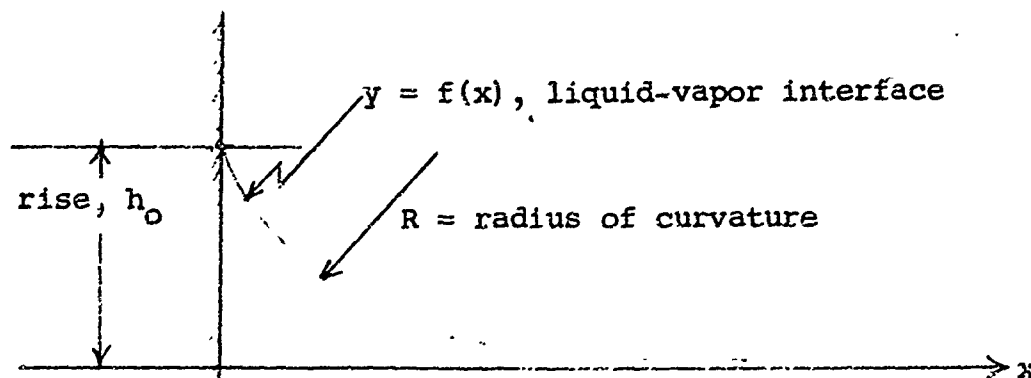


Figure III-1 Liquid attachment to a vertical plate

The force per unit area normal to the surface is easily shown to be T/R , and equating this force to the component of the weight force of the raised liquid column yields the balance of forces

$$T/R = \rho g y.$$

Defining the capillary constant to be $c = 2 T/\rho g$, and from the well-known formula for the radius of curvature

$$R = \frac{(1 + y'^2)^{3/2}}{y''},$$

the differential equation for the capillary curve is obtained

$$y'' = \frac{4y}{c^2} (1 + y'^2)^{3/2}. \quad (\text{III-1})$$

The first integral of this equation is

$$\frac{1}{1 + y'^2} = c_1 - \frac{2}{c^2} y^2. \quad (\text{III-2})$$

From the boundary condition that far from the plate, the surface becomes horizontal, $y = 0 = y'$, the integration constant c_1 is unity, so that

$$\frac{1}{1 + y'^2} = 1 - \frac{2}{c^2} y^2$$

At the wall, $x = 0$, the slope $y' = -\cot\alpha$, and $y = h_0$, so from the above equation

$$h_0 = c \frac{1 - \sin\alpha}{2} \quad (\text{III-3})$$

A second integration yields the solution for the capillary curve

$$x + c^2 - y^2 - c^2 - h_0^2 = \frac{c}{2} (\cosh^{-1} \frac{c}{y} - \cosh^{-1} \frac{c}{y_0}) \quad (\text{III-4})$$

This curve may actually be observed experimentally, justifying the assumption that T is a constant over the gas-liquid interface, and indicating further that the two essential physical parameters in this static example are $T/\rho g$ which is dependent upon the gas and liquid, and the angle of contact α dependent upon the solid boundary and liquid. A direct extension of this example to two plates, yields a situation which appears very much akin to the face-seal problem.

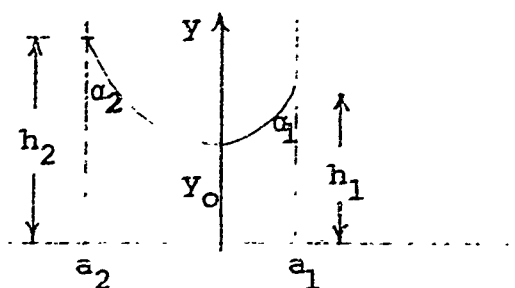


Figure III-2 Liquid attachment between two plates

The clearance between the plates is a ; the origin is placed at the minimum $y = y_0$. The same differential equation (III-1) for the capillary curve applies as for the single plate. From the first integral, equation (III-2) the boundary condition at the origin, $x = 0$, is zero slope $y' = 0$, so that

$$\sin\alpha_1 = c_1 - \frac{2}{c^2} h_1^2$$

Combining the two equations above gives

$$\begin{aligned} h_1^2 - y_0^2 &= c^2 \frac{1 - \sin\alpha_1}{2} \\ &= h_{01}^2 \end{aligned} \quad (\text{III-5})$$

where from comparison with equation (III-3) the distance h_{01} is the height the liquid film would rise up a single wall at $x = a_1$.

The first integral, equation (III-2) becomes

$$\frac{1}{1 + y'^2} = 1 - \frac{2}{c^2} (y^2 - y_0^2)$$

so that

$$\frac{dy}{dx} = \frac{2 c^2 (y^2 - y_0^2) - (y^2 - y_0^2)^2}{c^2 - 2(y^2 - y_0^2)} \quad (\text{III-6})$$

The substitution

$$y^2 - y_0^2 = c^2 \cos^2 \phi \quad (\text{III-7})$$

will transform the integral of equation (III-6) to a standard form for elliptic integrals.

Integration gives the equation for the surface

$$x = \frac{c}{k} \left(1 - \frac{k^2}{2}\right) F(k) - F(k, \phi) - E(k) - E(k, \phi) \quad (\text{III-8})$$

where $E(k, \phi)$ is the elliptic integral of the second kind, with k the modulus and ϕ the amplitude, and $E(k)$ is the complete elliptic integral; $F(k, \phi)$ is the elliptic integral of the first kind, and $F(k)$ the complete integral of the first kind. The constant k is

$$k^2 = c^2 / (y_0^2 - c^2).$$

From the boundary conditions at the walls

$$\cos \phi_1 = h_{01}/c = (1 - \sin \phi_1)/2$$

$$\cos \phi_2 = h_{02}/c = (1 - \sin \phi_2)/2$$

$$a_1 = \left(\frac{c}{k} - \frac{ck}{2}\right) F(k) - F(k, \phi_1) - \frac{c}{k} E(k) - E(k, \phi_1)$$

$$a_2 = \left(\frac{c}{k} - \frac{ck}{2}\right) F(k) - F(k, \phi_2) - \frac{c}{k} E(k) - E(k, \phi_2)$$

The unknowns in the above equations are y_0 , a_1 , and a_2 . The equations can be solved by trial. Select a pair (a_1 , a_2) such that the sum equals the clearance. Since ϕ_1 and ϕ_2 are known from the contact angles, the above two equations can be solved independently (by trial) for the values of k , say k'_1 and k'_2 . The two values should be the same; if not, repeat until $k'_1 = k'_2$, resulting in the proper value of k . This value of k in turn yields y_0 , and if desired, the values of h_1 and h_2 follow from y_0 and h_{01} and h_{02} .

If the clearance between the two plates is considered to be very narrow ($a \ll c$), then for equation (III-8), taking the limit $a \rightarrow 0$ and $c \infty$ it can be shown (Ref. III-2) that the height to which the fluid rises is

$$y_0 = \frac{T}{\rho g a_1} \cos \alpha_1; \text{ (approx)} \quad (\text{III-9})$$

The equivalent pressure supported by the film is

$$\Delta p = \rho g y_0$$

so that

$$\Delta p = \frac{T}{a_1} \cos \alpha_1 = \frac{T}{a_2} \cos \alpha_2 \quad (\text{III-10})$$

Hence, the distances a_1 and a_2 , measured from the walls to the point of minimum film, can be determined from the equations:

$$a_1/a_2 = (\cos \alpha_1) / (\cos \alpha_2) \quad (\text{III-11})$$

$$a_1 + a_2 = 2a \quad (\text{III-12})$$

A geometrical picture illustrating the action of the surface tension in a very narrow clearance may be obtained from the following consideration. It is easily shown from static equilibrium that at any point on the film, with radius of curvature R , that the pressure supported by the film tension is

$$\Delta p = T/R.$$

For a film of constant curvature R , figure III-3 illustrates the geometrical relationship

$$a = R \cos \alpha.$$

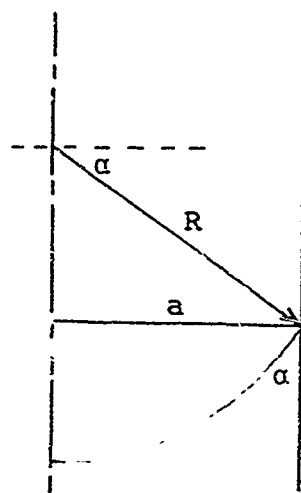


Figure III-3 Geometrical relation between clearance, contact angle, and film radius of curvature for a narrow clearance

Consequently, the approximation involved in deriving equation (III-10) from the exact equation (III-8) implies that the film radius of curvature be considered constant, with the values

$$R = a_1 / \cos \alpha_1 = a_2 / \cos \alpha_2$$

Equations (III-10), (III-11), and (III-12) may be used to compute the pressure drop Δp supported by the interfacial film between the liquid and vapor phases for two parallel plates with very narrow clearance. All that need be known is the surface tension T , the contact angles α_1 and α_2 at the walls, and the clearance $2a$.

A useful physical explanation for the creation of a definite angle of contact α may be made (Ref. III-3) from consideration of the balance of distinct surface tension forces existing between the liquid and its vapor T_{lv} , the liquid-solid T_{ls} , and the vapor-solid T_{vs} as shown in figure III-4.

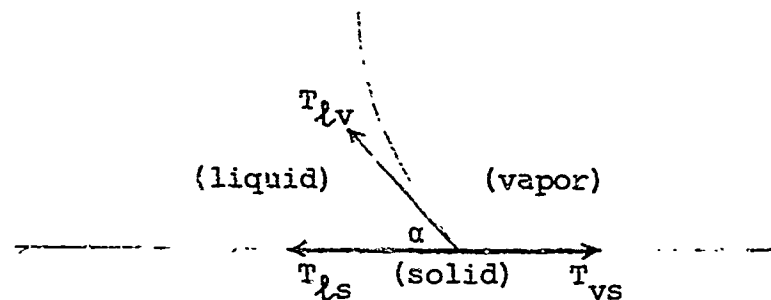


Figure III-4 Creation of contact angle by the three distinct surface tension forces

From equilibrium of the forces shown in figure III-4, it is evident that

$$T_{lv} \cos \alpha = T_{vs} - T_{ls} \quad (\text{III-13})$$

For the liquid to "wet the wall" ($\alpha < 90^\circ$) it may be observed that the necessary condition is that T_{vs} be greater than T_{ls} .

The above physical interpretation of the angle of contact resulting from the three surface tension forces will provide the basis for consideration of surface tension in a moving rather than a static fluid.

III-2.2 Surface Tension in a Moving Fluid

Extending the concept of surface tension described above for static equilibrium to the slow radial leakage flow existing in the narrow clearance of a rotary face seal, the force diagram (figure III-4) changes somewhat as a result of the wall shear stress. For slow motion, the surface stresses can be as assumed to be in equilibrium and the body forces can be neglected. The vapor-phase, because of its lower density, can be expected to have a much greater velocity than the liquid phase, and consequently will be subjected to a much higher wall shear

stress. Also, since the vaporization will most likely occur in regions of minimum clearance where the frictional heat generation is greatest, the constricted flow passage area (figure III-5) will cause a further increase in the vapor velocity compared to the slow liquid velocity.

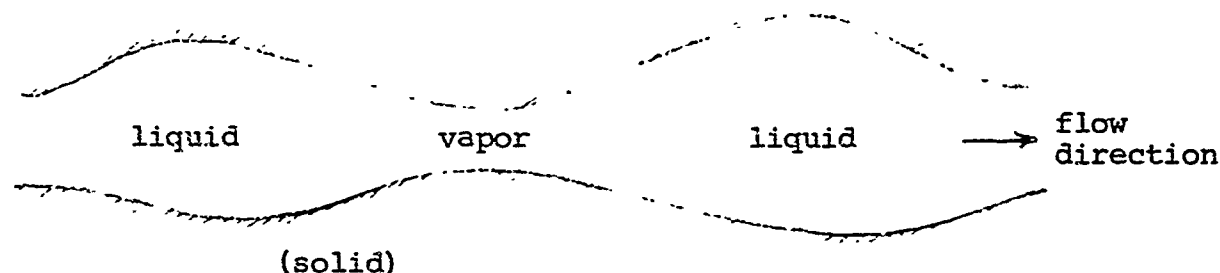


Figure III-5 Vapor generation at points of minimum clearance

At the interface shown in figure III-6, the wall shear effectively reduces T_{vs} and causes an increase in the contact angle α .

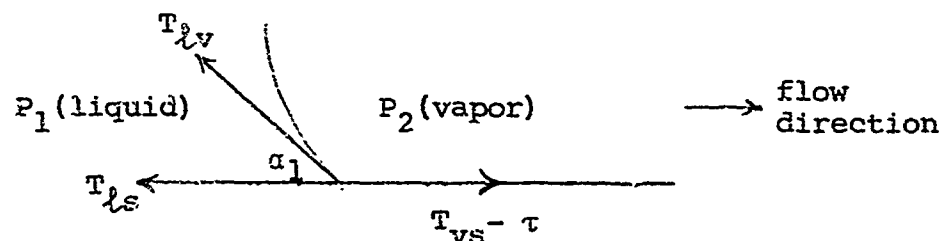


Figure III-6 The dynamic contact angle for vaporization

Consequently, equation (III-13) which involves the static contact angle α , must be modified for the dynamic contact angle α_1 .

$$T_{lv} \cos \alpha_1 = (T_{vs} - \tau) - T_{ls} \quad (\text{III-14})$$

In accordance with equation (III-10), the effect of the fluid motion is to decrease the pressure drop

$$(\tilde{P}_2 - \tilde{P}_1)$$

supported by the surface tension, since $\cos \alpha_1$ is reduced (T is the liquid-vapor surface tension T_{lv} , and α_1 is now the dynamic contact angle).

$$\tilde{P}_2 - \tilde{P}_1 = \frac{T}{a} \cos \alpha_1$$

The opposite side of the vapor cavity, where the vapor condenses to a liquid, is shown below in figure III-7.

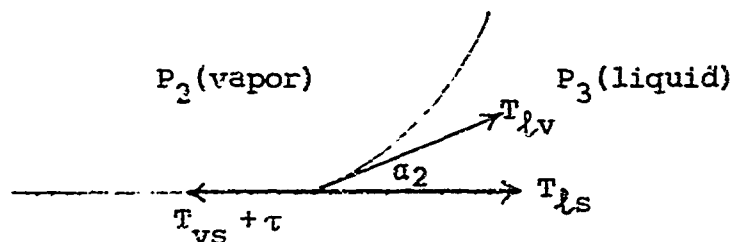


Figure III-7 The dynamic contact angle for condensation

In this case, the net effect of the leakage flow is to increase $\cos \alpha_2$

$$T_{lv} \cos \alpha_2 = (T_{vs} + \tau) - T_{ls} \quad (\text{III-15})$$

and the pressure increment supported by the surface tension is

$$\tilde{P}_2 - \tilde{P}_3 = \frac{T}{a} \cos \alpha_2$$

As a result, the combined pressure drop supported by the two interfacial films is

$$\tilde{p}_1 - \tilde{p}_3 = \frac{T}{a} (\cos \alpha_2 - \cos \alpha_1) \quad (\text{III-16})$$

This net pressure increment for the interfaces at both ends of the vapor cavity is a finite positive value for the physical mechanism described above, since the effect of the vapor wall friction is to increase $\cos \alpha_2$ and diminish $\cos \alpha_1$.

The form of equation (III-16) is that used by L. Bernd, mentioned previously, from which he computed the pressure drop of 1320 psi for the 1/4-in. face seal with 180 cavitation trails per inch.

III-2.3 The Role of Surface Tension under Nonequilibrium Conditions Instability of the Interface

For the concept of the pressure differences sustained by the alternate interfacial surface tensions described above, a stable equilibrium configuration and steady state conditions were assumed. It is questionable whether this simple model provides an adequate representation of the complex phenomena actually involved. The first question to be raised concerns the stability of the interface. The following simplified analysis indicates that instability of the interface is likely.

The Reynolds equation of lubrication theory applied to the average fluid velocity through the clearance of width $2a$ yields the relations

$$\bar{u} = - \frac{2a}{3\mu} \frac{\partial p}{\partial r} \quad (\text{III-16})$$

$$\bar{w} = - \frac{2a}{3\mu} \frac{\partial p}{\partial z} + a W \quad (\text{III-17})$$

where W is the tangential velocity of the rotating face seal.

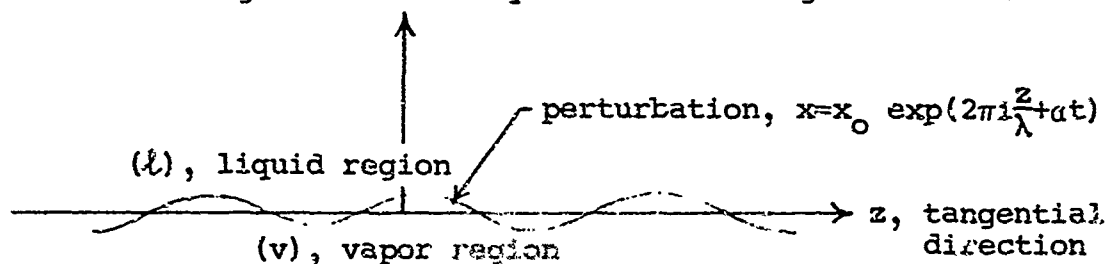


Figure III-8 Perturbation of interface

A small perturbation of the interface between the vapor and liquid, as shown in figure III-8, is assumed of amplitude x_0 , wavelength λ , and amplification factor α .

$$x = x_0 \exp \left(i \frac{2\pi}{\lambda} z + \alpha t \right) \quad (\text{III-18})$$

The film is considered to be unstable to small disturbances under those conditions which yield a positive value for α .

The continuity equation is

$$\frac{\partial \bar{u}}{\partial r} + \frac{\partial \bar{w}}{\partial z} = 0 \quad (\text{III-19})$$

and so the pressure must satisfy the Laplace equation

$$\frac{\partial^2 p}{\partial r^2} + \frac{\partial^2 p}{\partial z^2} = 0 \quad (\text{III-20})$$

The perturbation velocity of the interface is obtained from equation (III-18)

$$\tilde{u} = \frac{\partial x}{\partial t} = \alpha x_0 \exp \left(i \frac{2\pi}{\lambda} z + \alpha t \right) \quad (\text{III-21})$$

Assuming no change of phase to be taking place at the interface, the radial velocity components must be equal for the two phases:

$$-\frac{2a}{3\mu_l} \frac{\partial p_l}{\partial r} = -\frac{2a}{3\mu_v} \frac{\partial p_v}{\partial r} = \bar{u} + \tilde{u} \quad (\text{III-22})$$

where \bar{u} is the average velocity of the film radially outward. It is easily shown by separation of variables (i.e., assume product solution of form $p = R(r) Z(z)$) that a solution of the Laplace equation for the pressure is the product of two factors satisfying the ordinary differential equations

$$\begin{aligned} R'' - CR &= 0 \\ Z'' + CZ &= 0. \end{aligned}$$

From these two equations it may be observed that if one factor is periodic (depending upon the sign of the arbitrary constant C) the other factor is exponential. Choosing the disturbance

to be of the periodic form

$$\exp \left(i \frac{2\pi}{\lambda} z \right),$$

the coefficient in the above ordinary differential equation is $C = 2\pi/\lambda$ and the R-factors must be of the exponential form

$$\exp \left(\pm \frac{2\pi}{\lambda} r \right).$$

For the disturbance to die at large positive r -values in the liquid, the minus sign in the exponent is chosen; and similarly for the vapor, the plus sign in the exponent is chosen so the disturbance will die at large negative r -values. Integration of equation (III-22) gives

$$p_L = -\frac{3\mu_L}{2a} \bar{u}r + \frac{\alpha x_0 \lambda}{2\pi} \exp \left(-\frac{2\pi}{\lambda} (r - iz) + \alpha t \right)$$

$$p_V = -\frac{3\mu_V}{2a} \times \bar{u}r - \frac{\alpha x_0 \lambda}{2} \exp \left(\frac{2\pi}{\lambda} (r + iz) + \alpha t \right)$$

At the interface $r = x$, the pressure in the liquid is

$$\begin{aligned} p_L &= -\frac{3\mu_L}{2a} \times \bar{u} + \frac{\alpha \lambda}{2\pi} \exp \left(-\frac{2\pi}{\lambda} x \right) \\ &= \frac{3\mu_L}{2a} \times \left(\bar{u} + \frac{\lambda}{2\pi} \right); \text{ (approx)} \end{aligned}$$

and, in the vapor, the pressure is

$$p_V = \frac{3\mu_V}{2a} \times \left(\bar{u} - \frac{\alpha \lambda}{2\pi} \right); \text{ (approx)}$$

Consequently,

$$\frac{\partial p_L}{\partial x} = -\frac{3\mu_L}{2a} \left(\bar{u} - \frac{\alpha \lambda}{2\pi} \right)$$

$$\frac{\partial p_V}{\partial x} = -\frac{3\mu_V}{2a} \left(\bar{u} + \frac{\alpha \lambda}{2\pi} \right)$$

(III-23)

The pressure drop sustained by the surface tension can be assumed to be*

$$p_v - p_l = T \left(\frac{1}{a} - \frac{\partial^2 x}{\partial z^2} \right) = T \frac{1}{a} + \left(\frac{2\pi}{\lambda} \right)^2 x \quad (\text{III-24})$$

In this expression the curvature due to the radial location r on the face seal is small for $r \ll a$, and the slope $\partial x / \partial z$ of the perturbation of the interface is small compared to unity, so that,

$$\frac{\partial p_v}{\partial x} - \frac{\partial p}{\partial x} = T \left(\frac{2\pi}{\lambda} \right)^2$$

Combining equations (III-23) and (III-24) yields the stability equation:

$$\frac{3}{2a} \frac{\alpha \lambda}{2\pi} (\mu_l + \mu_v) = \frac{3}{2} \frac{\bar{u}}{a} (\mu_l - \mu_v) - T \left(\frac{2\pi}{\lambda} \right)^2 \quad (\text{III-25})$$

The interface is unstable for positive α , which occurs when the right-hand side of (III-25) is greater than zero. Hence, to be unstable, it is necessary that the vapor viscosity be less than the liquid viscosity (for the flow from vapor to liquid); it may also be noted that the surface tension has a stabilizing influence.

If the space between the seal is not of uniform clearance, but consists rather in a tortuous and intermittent flow path, than a representative clearance k may be used (analogous to a permeability coefficient in a porous medium) and the same basic Reynolds-type equation (III-17) will apply analogous to the Darcy law for a porous medium,

$$\vec{q} = - \frac{k}{\mu} \Delta p.$$

Obviously, the same type of stability equation (III-25) will result; however, a special interpretation must be given to the surface tension term.

*The negative sign is used since the surface tension supports the higher pressure on the vapor side for negative curvature of the assumed perturbation wave.

Radial Leakage Through an Unstable Interface

For an unstable interface, the vapor phase may be considered to penetrate the liquid in such a way that only a fraction of the liquid is forced through the clearance. This type of phenomenon was observed by Taylor (Ref. III-4) in a study of cavitation in journal bearings in which occurred long vaporized striations in the direction of rotation between the shaft and a transparent bushing.

If the vapor is considered to pass with a velocity U through the liquid, as shown in figure III-9, the equations of motion for the liquid may be derived in the following way.

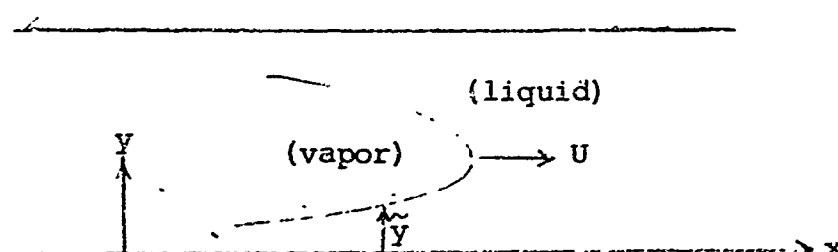


Figure III-9 Vapor penetration of the liquid

The Navier-Stokes equation for the liquid is:

$$\rho \frac{d\vec{q}}{dt} = \rho \vec{f} - \Delta p + \mu \Delta^2 \vec{q}$$

For a small Reynolds number ($\rho a U / \mu = \text{inertial/viscous forces}$) the inertial force $\rho d\vec{q}/dt$ may be neglected. The gravity force also is considered small compared with the viscous force, so that the body force \vec{f} can be neglected. Under these conditions, the Navier-Stokes equation becomes

$$\begin{aligned} p_x &= \mu (u_{xx} + u_{yy}) \\ p_y &= \mu (v_{xx} + v_{yy}) \end{aligned} \quad (\text{III-26})$$

where subscripts indicate partial derivatives.

The surface tension at the interface will be considered significant, and the following dimensionless parameters are assumed small compared with $\mu U/T$:

$$\frac{\rho g a^2}{\mu U} = \text{gravity/viscous force}$$

$$\frac{\rho g a^2}{T} = \text{gravity/surface tension}$$

$$\frac{\rho g a U}{T} = \text{inertial/surface tension}$$

The continuity equation is

$$0 = u_x + v_y \quad (\text{III-27})$$

and the boundary condition at the wall ($y = 0$) is

$$0 = u = v \quad (\text{III-28})$$

The boundary condition at the interface is obtained from local equilibrium of the surface stress forces shown in figure III-10.

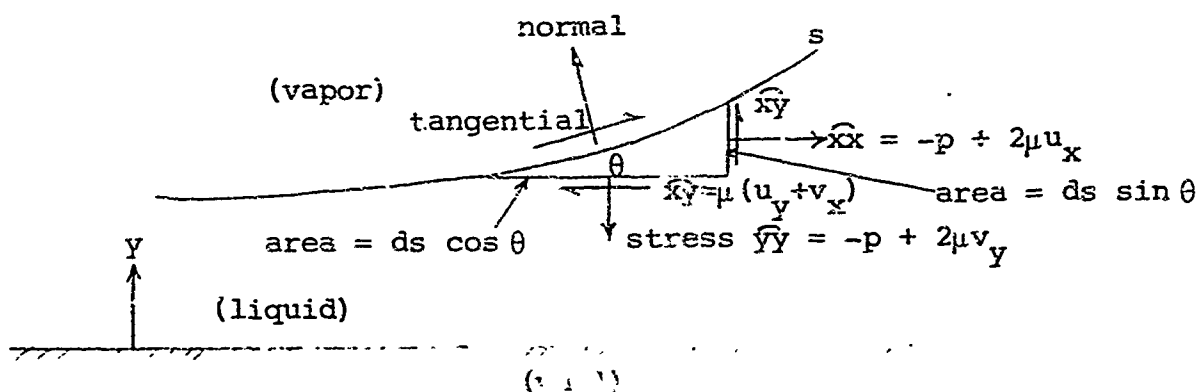


Figure III-10 Stresses in the liquid at the interface

The curvature of the interface (at $y = y$) is

$$k = y''/(1 + y'^2)^{3/2} = y''/(1 + y'^2)^{3/2} \quad (\text{III-29})$$

Equating the surface tension force component to the stress components in the normal direction gives

$$\begin{aligned} Tk &= yy \cos^2 \theta - 2xy \sin \theta \cos \theta + xx \sin^2 \theta \\ &= -p + 2\mu (v_y \cos^2 \theta + u_x \sin^2 \theta) - 2\mu (u_y + v_x) \sin \theta \cos \theta \end{aligned} \quad (\text{III-30})$$

The shear stress exerted by the vapor at the interface is assumed to be zero, so the summation of stress forces in the tangential direction gives

$$\begin{aligned} 0 &= xy \sin^2 \theta + xx \sin \theta \cos \theta - xy \cos^2 \theta - yy \sin \theta \cos \theta \\ 0 &= (u_y + v_x)(\cos^2 \theta - \sin^2 \theta) + 2(v_y - u_x) \sin \theta \cos \theta \end{aligned} \quad (\text{III-31})$$

The following relations may be substituted into equation (III-30)

$$\tan \theta = y', \quad \sin \theta = \frac{y'}{1 + y'^2}, \quad \cos \theta = \frac{1}{1 + y'^2}$$

And equation (III-30) will reduce to

$$\frac{-Tk-p}{2\mu} = \frac{(u_y + v_x)y' - v_y - u_x y'^2}{1 + y'^2}$$

Using the continuity equation (III-27) and the identities

$$\begin{aligned} u' &= u_x + u_y y' \\ v' &= v_x + v_y y' \end{aligned}$$

the boundary condition at the interface for the normal stresses becomes

$$\frac{-Tk-p}{2\mu} = \frac{u' + v' y'}{1 + y'^2}; \quad \text{at } y = \tilde{y} \quad (\text{III-32})$$

The boundary condition at the interface for the tangential stresses becomes

$$0 = (u_y + v_x) - 4 u_x \frac{y'}{1 - y'^2} ; \text{ at } y = \tilde{y} \quad (\text{III-33})$$

The Navier-Stokes equation may now be integrated in the y -direction. Letting

$$\tilde{p}' = \tilde{p}_x + \tilde{p}_y \tilde{y}',$$

the Navier-Stokes equation (III-26) is

$$u_{yy} - \frac{1}{\mu} \tilde{p}' = u_{xx} + \frac{1}{\mu} (p_x - \tilde{p}_x - \tilde{p}_y \tilde{y}')$$

Integration of the left-hand side of (III-34) from \tilde{y} to y gives the impression

$$u_y - \tilde{u}_y - \frac{1}{\mu} \tilde{p}' (y - \tilde{y})$$

where u_y is obtained from boundary condition (III-33).

Integrating again from $y = 0$ to y gives (using the wall boundary condition (III-28))

$$u - \tilde{u}_y y - \frac{1}{\mu} \tilde{p}' \left(\frac{y^2}{2} - y \tilde{y}' \right)$$

Integrating a third time, and noting that the radial liquid leakage flow Q_l per unit width is

$$Q_l = 2 \int_0^{\tilde{y}} u \, dy,$$

the following equation is obtained:

$$Q + \frac{2\tilde{y}^3}{3\mu} \tilde{p}' = \tilde{y}^2 \left(4\tilde{u}_x \frac{y'}{1-\tilde{y}'^2} - \tilde{v}_x \right) + \int_0^{\tilde{y}} \int_0^y \int_0^y \frac{1}{\mu} (p_x - \tilde{p}') - u_{xx} \, dy \, dy \, dy \quad (\text{III-35})$$

The kinematic boundary condition for no diffusion across the interface requires the equality of the normal velocity components of the two phases. If the velocity in the x-direction of the vapor phase is assumed to be uniform of magnitude U , then

$$U \sin\theta = \tilde{u} \sin\theta - \tilde{v} \cos\theta$$

or

$$(U - \tilde{u})\tilde{y}' = \tilde{v} \quad (\text{III-36})$$

Symmetry about the mean center line of the flow in the x-direction is assumed, as shown in figure III-11, and the leakage flow rate ahead of the vapor is $Q = 2a \bar{u}$.

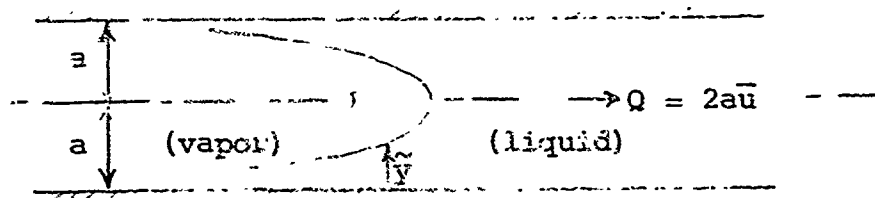


Figure III-11 Liquid-vapor flow configuration

The balance of flow rates is then

$$2U(a - \tilde{y}) - Q_l = Q. \quad (\text{III-37})$$

Differentiation with respect to x gives (since Q is independent of x)

$$Q_l' = 2U\tilde{y}'$$

Also, the derivative of the liquid flow rate may be obtained from the integral

$$\begin{aligned} Q_l'/2 &= \frac{d}{dx} \int_0^{\tilde{y}(x)} (x, y) dy, = \int_0^{\tilde{y}} u_x dy + \tilde{u} \tilde{y}' \\ &= \int_0^{\tilde{y}} v_x dy + \tilde{u} \tilde{y}' = -\tilde{v} + \tilde{u} \tilde{y}' \end{aligned}$$

Comparison of the above two expressions for the derivative Q_l' demonstrates the consistency of the kinematic boundary condition (III-36) and the flow rate balance (III-37). The flow balance, then, may be expressed as

$$Q_l/2 = U (\tilde{y} - c) \quad (\text{III-38})$$

where c is a constant,

$$c = (1 - \frac{\bar{u}}{U}) a \quad (\text{III-39})$$

Approximate Solution

In the region where \tilde{y}' is small, the liquid flow will be very nearly parallel, and u_{xx} will be negligible (compared to u_{yy}); the pressure variation in the y -direction will be small so that p_x will very nearly equal \tilde{p}' . Also, the tangential shear \tilde{u}_y , as well as \tilde{v}_x , at the interface will be small, so that equation (III-35) for the liquid leakage is approximately

$$\frac{Q_l}{2} + \frac{\tilde{y}^3}{3\mu} \tilde{p}' = 0$$

The normal stress from equation (III-33) is approximately

$$\begin{aligned} \tilde{p} &= -Tk \\ &= -T\tilde{y}'' \end{aligned}$$

Differentiating with respect to x and combining with equation (III-38) gives for the equation of the interface in the region of small slope

$$\begin{aligned} y''' &= -\frac{p}{T} = \frac{3\mu}{2T} \frac{\tilde{y}'}{\tilde{y}^3} \\ &= \frac{3\mu U}{T} \frac{(\tilde{y} - c)}{\tilde{y}^3} \end{aligned} \quad (\text{III-40})$$

This equation demonstrates that the shape of the interface depends upon the dimensionless ratio of the viscous to the surface tension force $\mu U/T$. Designating the liquid layer thickness to be $\tilde{y} = b$, where $\tilde{y}''' = 0$, then the constant c must be equal b .

$$c = b \quad (\text{III-41})$$

and, from equation (III-39)

$$\frac{b}{a} = \frac{U - \bar{u}}{U} \quad (\text{III-42})$$

At the position where $\tilde{y} = b$, it is important to note that $Q_L = 0$, so that the fraction m of the liquid remaining within the clearance space in the region where the vapor passes through the liquid is given by

$$m = \frac{b}{a} \quad (\text{III-43})$$

Introducing the dimensionless variables

$$Y = \frac{\tilde{y} - b}{b} ; X = \frac{x}{b}$$

equation (III-40) becomes

$$Y''' = \frac{3\mu U}{T} \frac{Y}{(Y + 1)^3}$$

Since $Y \ll 1$, the following approximation holds,

$$Y''' = \frac{3\mu U}{T} Y$$

A solution of this ordinary differential equation is given by the exponential

$$Y = e^{kX}$$

and substitution into the differential equation shows that

$$k = (3\mu U/T)^{1/3}$$

Taking the second derivation

$$\frac{Y''}{b} = \left(\frac{k}{b}\right)^2 e^{kX}$$

The origin of the x -axis is arbitrary, so choosing $X = 0$ in this region and since the curvature is nearly constant ($y'' = \text{constant}$),

the following approximate relation can be expected:

$$\frac{b}{a} = C \left(\frac{3\mu U}{T} \right)^{2/3}$$

Based upon dimensional reasoning, applied to a rotating journal bearing, Taylor (Ref. III-4) assumes that the fraction of liquid remaining in the clearance is

$$m = F_1 \left(\frac{\mu U}{T} \right)$$

From experiments he obtained approximately

$$m = 0.85 \mu U/T$$

On this basis it is possible for values of $\mu U/T > 1$, that less than one-third of the liquid in the clearance will be forced out.

The average leakage flow velocity ahead of the interface follows from the Reynolds approximation

$$\bar{u} = \frac{a^2}{3\mu} \frac{dp}{dx}$$

For this value approximately equal to the interface velocity U , it is evident that

$$m \sim 1/T$$

Hence, on the basis of this mechanism, the leakage reduction that is due to the passage of the vapor through the liquid phase can be expected to be reduced for liquids with smaller vapor tension values; also, apparently viscosity plays only a small role in the reduction caused by cavitation phenomena. It may be noted that in this interpretation the angle of contact has no influence.

Discussion

An exact solution to the complete boundary value problem as posed above would yield the relationship between m and $\mu U/T$, and also the pressure drop δp between the interior of the vapor cavity and the pressure in the passage ahead of the cavity. Taylor gives this pressure drop based upon dimensional reasoning in the form

$$\delta p = - \frac{\mu U}{a} F_2(\mu U/T)$$

This pressure drop in the vicinity of the nose of the bubble, is shown in the hypothesized pressure distribution plot of figure III-12.

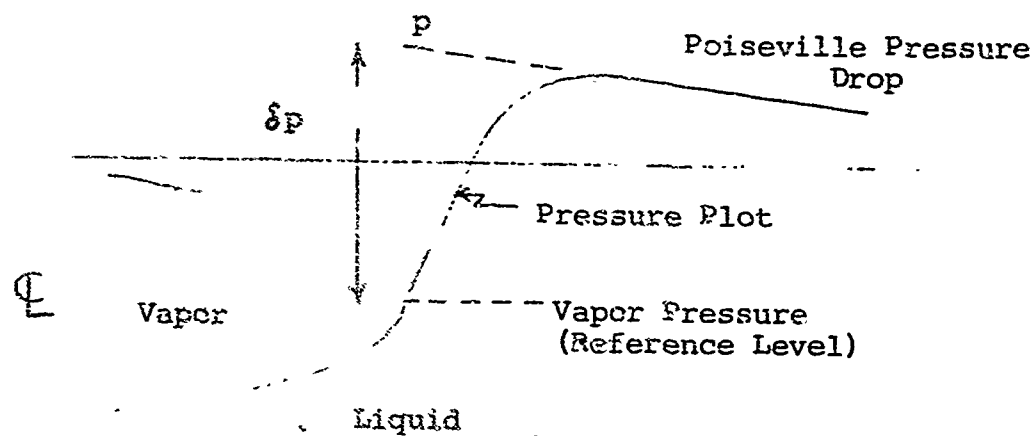


Figure III-12 Pressure distribution ahead of the vapor cavity

A more accurate solution of the complicated boundary value problem would be of questionable value at this stage of the analysis, because the actual mechanism depends to a large extent upon the irregular geometry of the seal faces which is not established. For example, the surface of the face seal of the softer material may have dominant undulations in the radial direction resulting from grooves cut by the relative rotation of the harder material. In this case, the generation of vapor can be expected to appear in the concentric cavitation trails as reportedly observed. Secondary undulations in the tangential direction of motion of the rotor will result in an alternate widening and narrowing of the clearance space. A given fluid element leaking radially outward, will thus pass along a flow path of varying cross-sectional area, and the vapor interface penetrating the liquid region in the wider section will force its way through, leaving a significant portion (say $\sim 2/3$) of liquid remaining in the section. In this event the leakage would be only a fraction of that expected if the entire liquid region were forced out ahead

of the vapor interface. When the passage area is reduced, the vapor flow is cut off and only liquid remains. The cycle is repeated as the passage widens, with the vapor again pushing through the liquid as illustrated in figure III-13.

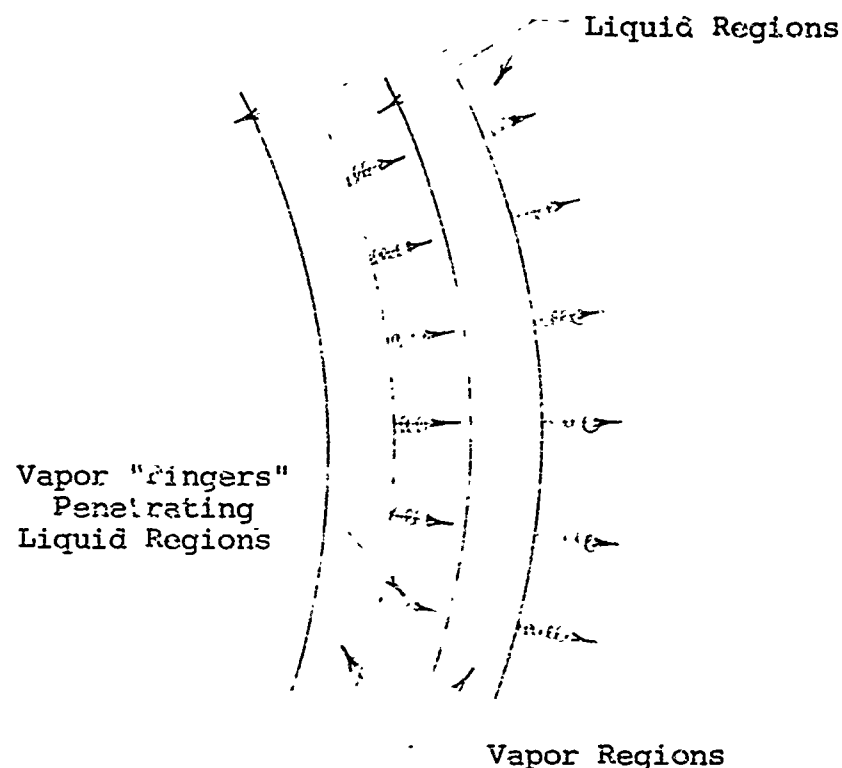


Figure III-13 Alternate regions of vapor penetration through the liquid phase

For a rotary face seal that contains a high pressure exerted at the inner radius, the vaporization phenomena can be expected to occur predominantly in the regions of the outer radii where the pressures are lower. The effect of the vaporization will be to raise the pressures in these outer regions above that which would occur for a purely liquid leakage flow. The higher pressure gradients developed, as shown in figure III-14, will tend to reduce the leakage flow rate.

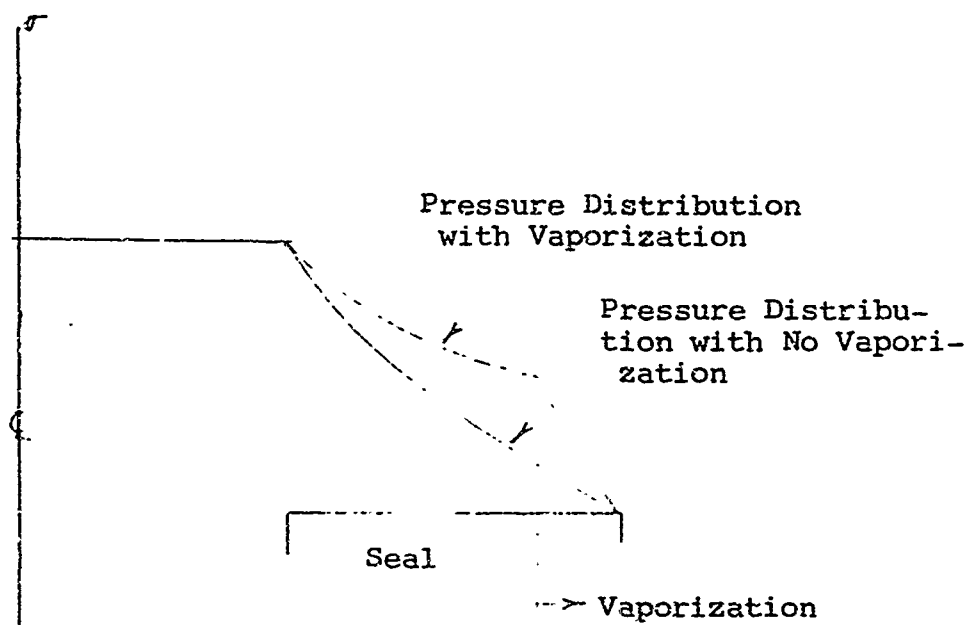


Figure III-14 Increased pressure gradients caused by vaporization

It may be remarked that since the total pressure force acting on the seal is greater if cavitation occurs, the compressive forces on the seal should be adjusted so that the vaporization does not cause an increased clearance. Obviously, if this should occur, the reduction in the leakage rate, expected on the basis of the vaporization phenomena, will not be achieved.

III-3 Two-Phase Leakage Flows

III-3.1 The Liquid and Vapor Phases Treated Separately

The high pressure fluid contained by the rotary face seal is considered to be initially in the liquid state. As the leakage progresses radially outward through the seal, the pressure drops, and ultimately vaporization conditions may be reached. Since the viscous dissipation, produced by the shear stresses opposing the rotary motion, generates temperature gradients in the transverse y -direction, vaporization will probably first occur only at one of the walls. The fluid will remain in the liquid phase along the cooler of the two walls, so that the liquid and vapor phases will flow concurrently. However, if the walls are treated as

approximately adiabatic, then the phase change will occur simultaneously across the entire flow passage, so that the leakage flow may be treated as a purely vapor flow. In this event, the analysis is less complicated and will be presented first. In the following section, the case of concurrent two-phase flow is analyzed.

Adiabatic Liquid Leakage

For a single phase occurring over any given cross-sectional area of the flow passage, if the clearance is sufficiently narrow and is not rapidly varying, the velocity profile for the radial leakage flow is parabolic. The leakage flow is considered to be small, so that the radial velocities are small compared to the tangential velocity W of the rotor. The velocity profile for the tangential flow is linear as shown in figure III-15.

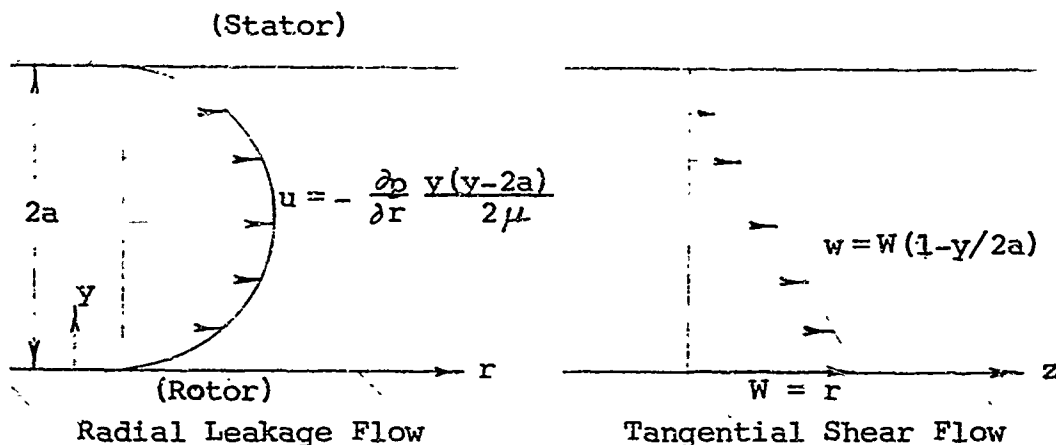


Figure III-15 Velocity profiles in lubricating film

The volume rate of leakage flow in the radial direction is

$$Q = \frac{4\pi}{3\mu} a^3 r \frac{dp}{dr} \quad (\text{III-44})$$

Considering the clearance $2a$ and the viscosity μ to be constant throughout the flow passage from the inner radius r_1 to the outer radius r_2 , integration yields

$$Q = \frac{4\pi a^3}{3\mu} \frac{p_2 - p_1}{\ln(r_2/r_1)} ; (\text{approx}) \quad (\text{III-45})$$

Since μ is a function of temperature, an improved computation of the leakage rate can be made if the temperature variation is determined. Assuming that the total viscous dissipation energy is absorbed by the fluid, increasing the internal energy and producing elevated temperatures (i.e., adiabatic heating, no wall losses) then

$$\tau \, 2\pi \, r \, dr \, W = \rho c_v Q dt$$

or

$$\frac{dT}{dr} = \frac{\pi \omega^2 r^3}{\rho c_v Q a} \mu(T) \quad (\text{III-45})$$

This equation follows directly from the more general equation (III-83) for zero temperature gradients at the walls, and the velocity gradient $\partial w / \partial y = -w_0 / 2a$ for the linear profile. The temperature distribution can be determined as a function of r from numerical integration of equation (III-46) starting from the inner radius r_1 at temperature T_1 . It may be observed that the temperature rises as the fourth power of the radius if the viscosity is considered to be constant.

Based upon the temperature distribution computed from equation (III-46) the pressure distribution can be found from the numerical integration of the equation (III-44)

$$\frac{dp}{dr} = - \frac{3Q}{4\pi a^3} \frac{\mu(T)}{r} \quad (\text{III-47})$$

The integration starts from the specified p_1 at the inner radius r_1 to a computed value p_2 at the outer radius r_2 . If the computed pressure is greater than the actual pressure, the approximate Q should be increased and a new pressure distribution computed. In this way Q can be adjusted until the correct p_2 is computed. An improved temperature distribution may then be computed and a corresponding improved pressure distribution, yielding a final value for leakage flow Q .

Adiabatic Leakage with Phase Change

Examination of the radial pressure and temperature distribution will reveal whether the vapor pressure has been reached at any radial location, for the dropping pressure and increasing temperature as shown in figure III-16. The vapor pressure is a specified function of the temperature.

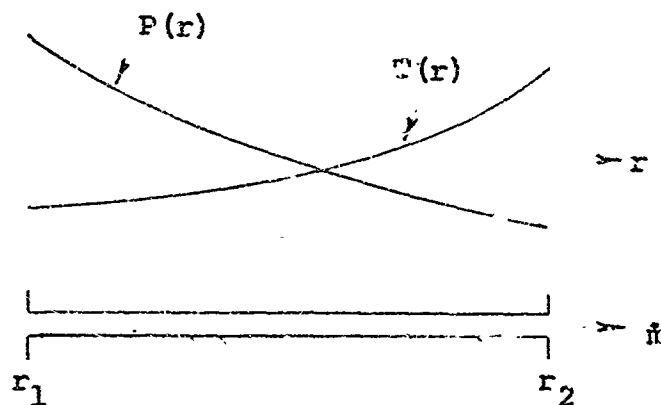


Figure III-16 Radial pressure distribution for liquid leakage

If vaporization does occur at some radial position, then the equation (III-47) for the pressure distribution at greater radii must be modified since the density can no longer be considered constant.

$$\frac{dp}{dr} = - \frac{p}{\rho_v} - \frac{3Q}{4\pi a^3} \frac{\mu_v}{r} \quad (\text{III-48})$$

The pressure gradient will be greater in the vapor phase because of the greatly reduced density, with the result that the leakage flow will be reduced.

Rather than attempt to calculate the leakage flow for a specified pressure drop by an iteration procedure as described for the single-phase flow, it is easier to find the corresponding pressure drops for a range of specified leakage flows and make a graph of the results. Then, from the graph, the leakage flow for a corresponding specified pressure drop, may be read directly.

Hence, for the specified mass leakage flow \dot{m} , the radial pressure and temperature distribution for the liquid phase can be determined from numerical integration of equation (III-46) and either (III-47) or (III-48), depending upon whether the fluid is in the liquid or vapor phase. From the radial location r' where vaporization first occurs, out to the location r'' where the phase

change is completed, the frictional energy dissipation is transformed into the latent heat λ of vaporization. The distance from r' to r'' may be estimated from the heat balance

$$\int_{r'}^{r''} W_T 2\pi r dr = \lambda \dot{m}$$

So that

$$r''^4 - r'^4 = \frac{4a\lambda\dot{m}}{\pi\mu\omega^2}$$

The approximate distance $r'' - r'$ will be small and represents the transition zone in which the liquid is changing to the vapor phase. The initial temperature at r'' will likely be slightly above the vaporization temperature and the liquid will initially be supersaturated. The pressure drop due to the momentum change in the transition region will result in a corresponding saturation temperature drop in accordance with the Clausius-Clapyron equation. To a first approximation the pressure and temperature in the small transition region may be assumed to remain at the constant saturation values.

The vapor leakage flow may then be determined by numerical solution of the simultaneous equations (III-46) and (III-47). The energy equation (III-46) should be modified so the dissipative friction work increases the enthalpy, h , of the fluid

$$\frac{dh}{dr} = \frac{\pi\omega^2 r^3}{\dot{m}a} \mu \quad (\text{III-49})$$

and the momentum balance (III-47) is

$$\frac{dp}{dr} = - \frac{3\dot{m}}{4\pi a^3} \frac{\mu}{\rho r} \quad (\text{III-50})$$

The physical properties of the vapor must be known. For example, if the vapor is steam, for the computed enthalpy and pressure increments the Mollier diagram or steam tables will yield the corresponding temperature rise; and the density ρ and viscosity μ are determined as functions of T and p . In this manner, the temperature and pressure profiles through the rotary seal may be computed with \dot{m} as a parameter

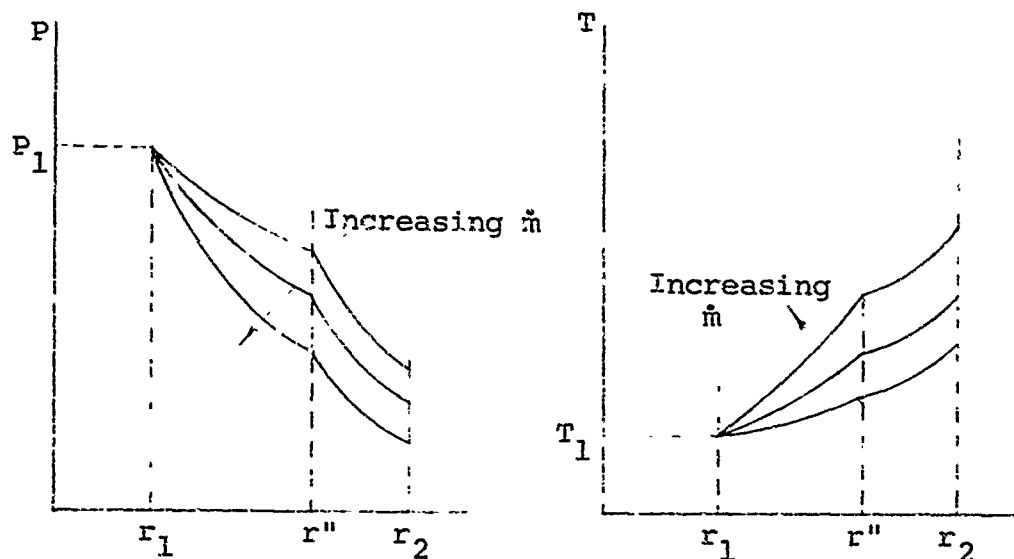


Figure III-17 Radial pressure and temperature distributions with a phase change at r''

Nonadiabatic Leakage Flow Computation

If heat is conducted through the walls, the energy equation (III-46) or (III-49) must be modified (see equation (III-83) to the form

$$\frac{c_v dT}{dr} = \frac{dh}{dr} = \frac{2\pi r}{\dot{m}} \frac{\omega^2 r^2}{2a} \mu - K_2(T-T_2) - K_1(T-T_1) \quad (\text{III-51})$$

where K_1 and K_2 are the heat transfer coefficients, and T_1 and T_2 are the temperatures at the stator and rotor walls. The radial distribution of T_1 and T_2 must be determined from separate computations of the temperature distributions in the rotor and stator materials.

The radial temperature and pressure distribution may be determined from the numerical solution of the simultaneous equations (III-50) and (III-51) together with the steady-state heat conduction equations within the rotor and stator materials. Numerical and graphical techniques exist for solving the Laplace equations for the temperature distributions in the stator and rotor; however, the numerical procedure will be quite cumbersome because the boundary condition at the interface involves the unknown temperatures T_1 and T_2 . The solution to this problem can be obtained to a practical degree of accuracy through the use of numerical techniques and a high-speed digital computer.

It may be noted that the assumption of adiabatic walls represents the limiting case in which the temperature increase in the radial direction is a maximum. The other limiting case, in which the least temperature rise would occur, is represented by the assumption that the walls be maintained at their initial temperature. The analysis of this limiting case or isothermal walls requires explicit consideration of the temperature distribution across the channel. Whereas in equation (III-51), the temperatures are considered to be functions of r alone, where T is a representative temperature of the fluid at radial location r , actually the heat flux through the wall is $k(\partial T/\partial y)$ and the equation should be (letting $Y = y/a$)

$$\rho c_v u \frac{\partial T}{\partial r} dy = k \frac{\partial T}{\partial y} + \mu \left(\frac{W}{2a}\right)^2 Y + c_1 \quad (\text{III-52})$$

If it is assumed, as a first approximation, that $\partial T/\partial r$ is parabolic (letting $Y = y/a$)

$$\frac{\partial T}{\partial r} = Ar^2 + BY + C$$

The velocity distribution is also parabolic

$$u = \frac{2}{3} \bar{u} (2 - Y) Y$$

where \bar{u} is the average velocity,

$$\bar{u} = \frac{3}{2} u_{\max} = Q/4\pi r a$$

Integration of equation (III-52) with respect to Y gives the temperature distribution across the channel

$$\begin{aligned} & \frac{2}{90} \rho c_v \bar{u} a^2 AY^6 + \frac{3}{2} (B-2A)Y^5 + \frac{5}{2} (C-2B)Y^4 - 10CY^3 + \\ & \qquad \qquad \qquad 4(4A + 4B + 5C)Y \\ & = k(T_1 - T + \frac{\Delta T}{2} Y) - \frac{\mu W^2}{8} (Y^2 - 2Y) \end{aligned} \quad (\text{III-53})$$

where $\Delta T = T_2 - T_1$.

The heat fluxes out through the walls are

$$\begin{aligned} -k \frac{\partial T}{\partial y}_1 &= -k \frac{\Delta T}{2a} - \frac{\mu W^2}{4a} + \frac{4}{9} \rho c_v \bar{u} a \frac{4}{5} (A+B) + C \\ k \frac{\partial T}{\partial y}_2 &= k \frac{\Delta T}{2a} - \frac{\mu W^2}{4a} + \frac{4}{9} \rho c_v \bar{u} a \frac{4}{5} (2A + \frac{3}{2}B) + C \end{aligned}$$

For the special case in which $\Delta T = 0$, the condition for the heat fluxes to be equal is that

$$B = -2A$$

The temperature distribution is then

$$\begin{aligned} & \frac{2}{90} \rho c_v \bar{u} a^2 AY^6 - 6AY^5 + \frac{5}{2} (4A + C) Y^4 - 10CY^3 - 4(4A-5C)Y \\ & \qquad \qquad \qquad = k (T_1 - T) - \frac{\mu W^2}{8} (Y^2 - 2Y) \end{aligned} \quad (\text{III-54})$$

and the radial temperature gradient is

$$\begin{aligned} \frac{\partial T}{\partial r} &= A (Y - 2) Y + C \\ &= \left(\frac{\partial T}{\partial r} \right)_{\max} (2-Y) Y + C (Y-2) Y + 1 \end{aligned} \quad (\text{III-55})$$

where the constant C is the linear rate that the temperature increases radially along the wall.

The heat flux through the wall is

$$\begin{aligned} -k \frac{\partial T}{\partial y}_1 &= k \frac{\partial T}{\partial y}_2 = -\frac{\mu W^2}{4a} + \frac{4}{45} \rho c_v \bar{u} a \left(\frac{\partial T}{\partial r} \right)_{\max} + C \end{aligned} \quad (\text{III-56})$$

For isothermal walls the constant C is zero.

III-3.2 Concurrent Liquid and Vapor Flow

In the analysis of the previous subsection, the change of phase from a liquid to a vapor state was assumed to take place over a relatively short transition distance. In this way the complex problem involving the presence of both phases at the same channel section is avoided. Before the transition region is reached the leakage flow is completely liquid, and after the transition region the leakage is completely vaporized. In some cases, the transition zone may extend over an appreciable distance. When this occurs, the concurrent flow of both the liquid and vapor phases in the same channel section must be treated.

Because of the narrowness of the clearance and the consequent predominance of the viscous forces in comparison to the inertial forces, the liquid phase is assumed to exist as a film along one or both of the walls. This assumption is consistent with the previous analysis of interfacial stability, in which the vapor was considered to penetrate the liquid, leaving a liquid layer remaining along the walls.

In general, one of the faces will be cooler than the other face. As a result, a liquid layer will be present on the cooler face concurrent with a vapor layer contiguous to the warmer face. If the liquid layer is along the rotor, the analysis is more complex because the centrifugal forces in the liquid phase may not be negligible compared to the shear forces in the vapor phase. On the other hand, if vaporization occurs on the rotor face, the centrifugal forces may be neglected. This latter, more simple case will be treated next.

Vaporization Along the Rotor Face

If the stator is maintained at a lower temperature than the rotor, the liquid layer will lie along the stator face and vaporization will take place along the rotor face. The tangential and radial velocity distributions are shown in figure III-18.

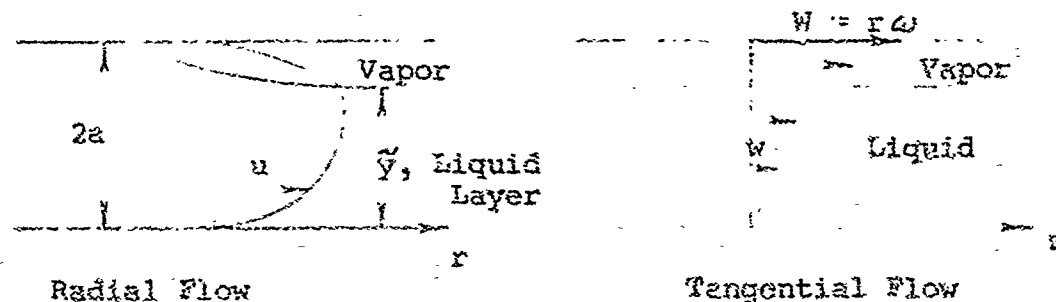


Figure III-18 Two-phase velocity distribution, vaporization on rotor face

The tangential velocity distribution is linear, and the condition that the shear stresses at the interface match is

$$\mu \frac{\partial w}{\partial y} = \mu_v \frac{\partial w_v}{\partial y} \quad (\text{III-57})$$

From these conditions

$$w = \frac{c_1}{\mu} y \quad ; y < \tilde{y} \quad (\text{III-58})$$

$$w_v = \frac{c_1}{\mu_v} (y - 2a) + W \quad ; y > \tilde{y}$$

The constant c_1 is obtained by matching the velocities at the interface ($y = \tilde{y}$).

$$c_1 = \frac{\mu_v W}{2a - (1 - \mu_v/\mu) \tilde{y}} \quad (\text{III-59})$$

The radial velocity distribution is

$$v = \frac{1}{2\mu} \frac{dp}{dr} (y^2 + c_2 y) \quad ; y < \tilde{y}$$

$$v_v = \frac{1}{2\mu} \frac{dp}{dr} (y^2 - 4a^2 + c_2 (y - 2a)) \quad ; y > \tilde{y} \quad (\text{III-60})$$

where

$$c_2 = -2a \frac{1 - (1 - \mu_v/\mu) (\frac{\tilde{y}}{2a})^2}{1 - (1 - \mu_v/\mu) \frac{\tilde{y}}{2a}} \quad (\text{III-61})$$

It is of interest to note that the maximum velocity occurs at the position

$$\frac{y_{\max}}{a} = - \frac{c_2}{2a} \quad 1$$

Hence, the maximum velocity always occurs above the center line, on the rotor side, and the position at which the maximum occurs at the interface is the solution of the quadratic equation

$$\left(1 - \frac{\mu}{\mu_v}\right) \left(\frac{\tilde{y}}{a}\right)_c^2 + 4 \left(\frac{\tilde{y}}{a}\right)_c - 4 = 0$$

For liquid layers less than this critical value, the maximum velocity occurs in the vapor phase; and for liquid layers greater than the critical value, the maximum velocity occurs in the liquid phase.

The frictional heat generated by the tangential shear stresses, minus the wall losses, is transformed into latent heat of vaporization. From integration of equation (III-85)*

$$\begin{aligned} -\frac{\lambda}{2\pi r} \frac{dm}{dr} &= \mu \left(\frac{\partial w}{\partial y}\right)^2 \tilde{y} + \mu_v \left(\frac{\partial w_v}{\partial y}\right)^2 (2a - \tilde{y}) + k \left. \frac{\partial T}{\partial y} \right|_1^2 \\ &= \mu \left(\frac{\partial w}{\partial y}\right)^2 \left(\tilde{y} + \frac{2a - \tilde{y}}{\mu_v/\mu}\right) + k \left. \frac{\partial T}{\partial y} \right|_1^2 \end{aligned} \quad (\text{III-62})$$

The liquid mass flow rate is

$$\dot{m}_L = 2\pi r \rho \int_0^{\tilde{y}} u \, d\tilde{y}$$

so that

$$\begin{aligned} \frac{d\dot{m}_L}{dr} &= 2\pi \rho \int_0^{\tilde{y}} \frac{\partial}{\partial r} (ru) \, d\tilde{y} + r \left(u(r, \tilde{y}) \frac{d\tilde{y}}{dr}\right) \\ &= \frac{\dot{m}_L}{r} + 2\pi r \int_0^{\tilde{y}} \frac{\partial u}{\partial r} \, d\tilde{y} + u(r, \tilde{y}) \frac{d\tilde{y}}{dr} \end{aligned} \quad (\text{III-63})$$

*Also see the right-hand side of equation (III-83), which represents the integral of (III-85).

Also, since the total leakage flow \dot{m} is constant,

$$\dot{m} = \dot{m}_l + \dot{m}_v$$

it is apparent that

$$\frac{d\dot{m}_l}{dr} = - \frac{d\dot{m}_v}{dr} \quad (\text{III-54})$$

so that

$$\frac{d\dot{m}_l}{dr} = -2\pi \int_y^{2a} \frac{\partial}{\partial r} (r\rho_v u_v) dy - r\rho_v u(r, \tilde{y}) \frac{d\tilde{y}}{dr}$$

The radial derivative of the vapor density is small so

$$\frac{d\dot{m}_l}{dr} = - \frac{\dot{m} - \dot{m}_l}{r} - 2\pi r\rho_v \int_y^{2a} \frac{\partial}{\partial r} u_v dy - u(r, \tilde{y}) \frac{d\tilde{y}}{dr} \quad (\text{III-65})$$

Equations (III-62), (III-63), and (III-65) provide the equations for the numerical determination of the rate of change of the liquid layer thickness \tilde{y} , and the pressure p with the radius. To perform this computation the heat losses through the walls must be determined from an independent computation.

Vaporization Along the Stator Face

If the cooling characteristics of the rotor are better than for the stator, then vaporization will initially occur along the stator face. The tangential velocity distribution will be linear, but of different slopes in the two phases as shown in figure III-19.

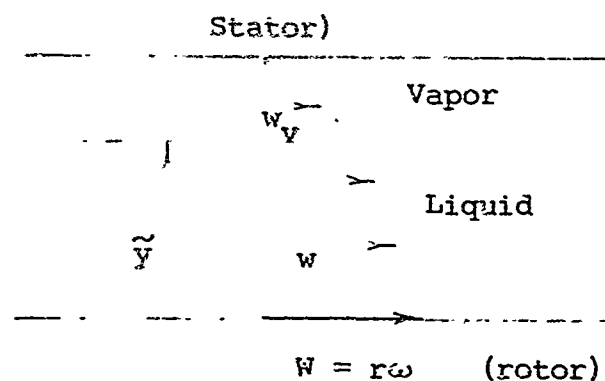


Figure III-19 Tangential velocity distribution, vaporization on stator face

It is apparent from the figure that the shear stress at the interface yields the ratio

$$\frac{\partial w_v}{\partial y} : \frac{\partial w}{\partial y} = \mu : \mu_v$$

The velocity distribution for the liquid is

$$w = r\omega (1 + c_1 y) ; y < \tilde{y} \quad (\text{III-66})$$

and for the vapor is

$$w_v = r\omega \frac{y-2a}{c_2} ; y > \tilde{y} \quad (\text{III-67})$$

where

$$c_1 = \frac{\mu_v}{\mu c_2}$$

$$c_2 = \tilde{y} \left(1 - \frac{\mu_v}{\mu}\right) - 2a$$

The velocity distribution in the radial direction for the vapor phase is obtained from the integration of the equation of motion, which neglecting inertial forces is

$$\frac{\partial p}{\partial r} = \mu_v \frac{\partial^2 u_v}{\partial y^2} ; y > \tilde{y}$$

Integration results in the parabolic distribution (using the fact that $u_v = 0$ at $y = 2a$):

$$u_v = \frac{1}{2\mu_v} \frac{\partial p}{\partial r} y^2 - (2a)^2 + c_3(y-2a) ; y > \tilde{y} \quad (\text{III-68})$$

For the liquid film adjacent to the rotor, the centrifugal forces should possibly be included in the equation of motion since they may be comparable to the viscous forces experienced in the vapor phase.

$$\frac{\partial p}{\partial r} = \mu \frac{\partial^2 u}{\partial y^2} + \rho w^2/r ; y < \tilde{y}$$

$$= \mu \frac{\partial^2 u}{\partial y^2} + \frac{\rho w^2}{r} (1 + c_1 y)^2$$

Integrating twice with respect to y (using the fact that $w = W$ at $y = 0$), the velocity distribution for $y < \tilde{y}$ is given by

$$\frac{dp}{dr} \frac{y^2}{2} = \mu(u-W) + \frac{\rho W^2}{12r} \cdot \frac{2}{1} (1 + c_1 y)^4 - 1 + c_4 y \quad (\text{III-69})$$

The two constants of integration c_3 and c_4 are determined from the interface boundary conditions

$$\left. \begin{aligned} u &= u_v \\ \mu \frac{\partial u}{\partial y} &= \mu_v \frac{\partial u_v}{\partial \tilde{y}} \end{aligned} \right\} \text{ at } y = \tilde{y}$$

These conditions result in the simultaneous equations

$$c_3 + c_4 = - \frac{\rho W^2}{2rc_1} (1 + c_1 \tilde{y})^3 = -A$$

$$(y-2a) c_3 + \frac{\mu_v}{\mu} y c_4 = \mu_v W - \frac{\rho W^2}{12rc_1} \frac{\mu_v}{\mu} (1 + c_1 \tilde{y})^4 - 1$$

$$+ \frac{dp}{dr} \left(\frac{\mu_v}{\mu} - 1 \right) \frac{\tilde{y}^2}{2} + 2a^2 = B$$

Solving for the integration constants gives

$$c_3 = \frac{\frac{\mu_v}{\mu} \tilde{y} A + B}{c_2}$$

$$c_4 = - \frac{B + (\tilde{y}-2a)A}{c_2} \quad (\text{III})$$

Hence, the velocity distribution in the radial direction is given by equations (III-68) and (III-69) at any location r , in terms of the liquid film thickness, the pressure gradient, fluid properties, and rotational speed and clearance.

To determine the variation of the pressure and liquid film thickness \tilde{y} with the radial distance, further relationships

involving energy and mass balances must be employed. The energy equation (III-85) yields the temperature distribution across the liquid film

$$k \frac{\partial^2 T}{\partial y^2} = \left(\frac{\partial w}{\partial y} \right)^2 = - (r c_1)^2 \quad (\text{III-71})$$

Integrating twice from $y = 0$ to $y = \tilde{y}$, and using the boundary conditions that $T = T_r$ at the rotor face and $T = T_{\text{sat}}$ at the vapor, yields

$$T - T_r = \Delta T \frac{y}{\tilde{y}} - \bar{k} \frac{(r c_1)^2}{2} (y - \tilde{y})y ; y < \tilde{y} \quad (\text{III-72})$$

where

$$\Delta T = T_{\text{sat}}(p) - T_r$$

The temperature distribution across the film is parabolic and is shown in figure III-20.

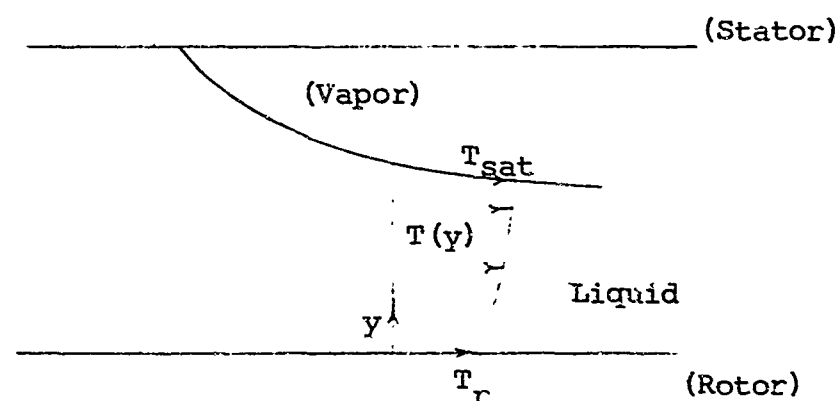


Figure III-20 Temperature distribution across liquid film

The temperature gradient at the vapor-liquid interface (at $y = \tilde{y}$), indicates a heat flux out of the liquid layer. This heat flux causes surface boiling, so that the liquid leakage flow rate \dot{m} is

reduced; assuming that the total surface heat flux is converted to latent heat of vaporization, the energy balance for an elemental radial distance dr is

$$2\pi r dr k \frac{\partial T}{\partial y} \bigg|_{y=y} = -\lambda \frac{d\dot{m}_l}{dr} dr$$

Evaluating the temperature gradient at the interface from equation (III-72) gives

$$\frac{d\dot{m}_l}{dr} = \frac{\pi r}{\lambda} (r_0 c_1)^2 \tilde{y} - k \frac{\Delta T}{2\tilde{y}} \quad (\text{III-73})$$

Since

$$\dot{m}_l = 2\pi r \rho \int_0^{\tilde{y}} u dy$$

the derivative of the liquid phase leakage flow in the radial direction is

$$\frac{d\dot{m}_l}{dr} = 2\pi \rho \int_0^{\tilde{y}} \frac{\partial}{\partial r} (ru) dy + r u(r, \tilde{y}) \frac{d\tilde{y}}{dr} \quad (\text{III-74})$$

The total leakage flow \dot{m} is the sum of the liquid and vapor phases,

$$\dot{m} = \dot{m}_l + \dot{m}_v$$

and since the total leakage flow is independent of the radial position

$$\frac{d\dot{m}_v}{dr} = -\frac{d\dot{m}_l}{dr} \quad (\text{III-75})$$

The derivative of the vapor phase leakage flow in the radial direction is

$$\frac{d\dot{m}_v}{dr} = 2\pi \int_{\tilde{y}}^{2a} \frac{\partial}{\partial r} (r \rho_v u_v) dy - r \rho_v u_v(r, \tilde{y}) \frac{d\tilde{y}}{dr} \quad (\text{III-76})$$

Since the liquid and vapor velocities at the interface are equal

$$u_v(r, \tilde{y}) = u(r, \tilde{y}) \quad (\text{III-77})$$

The above three equations combine to give:

$$\frac{dm}{dt} = 2\pi r \rho_v u(r, \tilde{y}) \frac{d\tilde{y}}{dr} - \frac{2a}{y} \frac{\partial}{\partial r} (r \rho_v u_v) dy \quad (\text{III-78})$$

From the value of the derivative of the liquid leakage flow obtained from equation (III-73), the pair of simultaneous equations (III-60) and (III-64) can be solved for the rate of change of the film layer thickness \tilde{y}' and the pressure gradient p'' . The details of the computation are discussed next.

III-4 The Energy Equation

Detailed discussions of the basic hydrodynamic energy equation are available in the standard works on hydrodynamics (e.g., Lamb, Milne-Thomson), and in specialized works (e.g., Ref. III-5, III-6) in lubrication engineering. The energy equations that are to be used in the analysis of rotary face seals can be explained simply by drawing a small element and making an energy balance of the work done by the viscous stresses, and the heat conducted and stored, including the latent heat if changes of phase occur.

However, to see which terms are neglected and what assumptions are being made, the development of the energy equation in a more general form will be briefly sketched in this section. We begin with the "principle of work and kinetic energy," which follows directly from the equation of motion and states that "the rate of change of kinetic energy of a moving volume is equal to the rate that work is being done on the volume by external forces diminished by a dissipation term involving the interaction of stress and deformation."

$$\frac{dK}{dt} = \vec{v} \cdot \vec{q} \, da - \vec{T} : \vec{D} \, dv \quad (\text{III-79})$$

where K , the kinetic energy, is the volume integral

$$K = \frac{1}{2} \rho \, q^2 \, dv$$

The work of the external forces is represented by the surface integral of the product of the velocity \vec{q} and the stress vector \vec{t} ; the external body forces are neglected. The stress vector is

$$\vec{t} = \vec{n} \cdot \vec{T}$$

where \vec{n} is the unit outer normal and \vec{T} is the stress tensor. The dissipation is represented by the product of the stress

tensor and the deformation tensor \bar{D}^*

$$D_{ij} = \frac{1}{2} (v_{i,j} + v_{j,i})$$

The first law of thermodynamics states that the dissipation diminished by the net heat conduction out is transformed into the thermodynamic internal energy U

$$\bar{T} : \bar{D}^* dv = - \nabla \cdot k \nabla T dv + \frac{dU}{dt}$$

Letting E be the sum of the internal and kinetic energy, and applying the divergence theorem to the surface integral of (III-79), the energy equation is obtained in the form

$$0 = \frac{dE}{dt} - \nabla \cdot k \nabla T dv - \nabla \cdot (T \cdot \vec{q}) dv \quad (\text{III-80})$$

where

$$E = \rho e dv$$

and

$$\frac{dE}{dt} = \rho \frac{De}{Dt} dv$$

For steady flow

$$\frac{dE}{dt} = \rho \vec{q} \cdot \nabla e dv$$

From the continuity equation for steady flow

$$\nabla \cdot \rho \vec{q} = 0$$

so that

$$\frac{dE}{dt} = \nabla \cdot \rho e \vec{q} dv$$

Hence, the differential equation form of (III-80) is

$$0 = \nabla \cdot \rho e \vec{q} - \nabla \cdot k \nabla T - \nabla \cdot (T \cdot \vec{q}) \quad (\text{III-81})$$

since the volume is arbitrary, the integrand must be identically zero.

For the very narrow clearance of the rotary seal, derivatives across (in the y-division) the clearance channel dominate. However, while the derivatives of the velocity in the radial and tangential directions are neglected in comparison to the y-direction, the temperature variation in the radial direction is of interest, so the radial temperature gradient is retained.

$$0 = \rho u c_v \frac{dT}{dr} = k \frac{\partial^2 T}{\partial y^2} - \frac{\partial}{\partial y} (y x u + y z w) \quad (\text{III-82})$$

For low leakage flow relative to the high rotary speed of the seal, the frictional dissipation of the leakage flow is small compared to the tangential shear stress dissipation so that

$$\rho u c_v \frac{dT}{dr} = k \frac{\partial^2 T}{\partial y^2} + \frac{\partial}{\partial y} \left(\mu \frac{\partial w}{\partial y} w \right)$$

For a linear tangential velocity distribution

$$\frac{\partial}{\partial y} \left(\mu \frac{\partial w}{\partial y} w \right) = \mu \left(\frac{\partial w}{\partial y} \right)^2$$

Integration across the clearance (from $y = 0$ to $y = 2a$) gives

$$\frac{\rho Q}{2\pi r} c_v \frac{dT}{dr} = k \frac{\partial T}{\partial y} \Big|_0^{2a} + \mu \left(\frac{\partial w}{\partial y} \right)^2 \Big|_0^{2a} \quad (\text{III-83})$$

Two-Phase Leakage in Rotary Seals

Because of the narrow clearance, the liquid phase is assumed to be in a film along the cooler of the two walls. The temperature of the vapor phase is assumed to be the saturation temperature corresponding to the local pressure. The variation of the temperature in the radial direction is then small, since almost all of the dissipative energy will be absorbed in the latent heat of vaporization. The saturation temperature changes gradually with the change in pressure in accordance with the Clausius-Clapeyron equation

$$\begin{aligned} \frac{dT_{\text{sat}}}{dp} &= \left(\frac{1}{p_v} - \frac{1}{p} \right) \frac{T_{\text{sat}}}{\lambda} \\ &= \frac{T_{\text{sat}}}{\lambda p_v} ; \text{ (approx)} \end{aligned} \quad (\text{III-84})$$

Hence, considering the radial variation of temperature to be small, the energy equation for a linear tangential velocity distribution is reduced to

$$0 = k \frac{\partial^2 T}{\partial y^2} + \mu \left(\frac{\partial u}{\partial y} \right)^2 \quad (III-85)$$

III-5 References

- III-1 General Electric Company, Advanced Technology Laboratories, "Study of Dynamic and Static Seals for Liquid Rocket Engines," NASA Contract No. NAS 7-102, 1963.
- III-2 Landau and Lifshitz, Fluid Mechanics, p. 336, Pergamon Press, 1959.
- III-3 Prandtl and Tietjens, Fundamentals of Hydro- and Aeromechanics, McGraw-Hill, 1934, Chapter 4.
- III-4 Taylor, G., "Cavitation of a Viscous Fluid in Narrow Passages," J. Fluid Mech., 16, No. 4, 545-632, (1963).
- III-5 Pinkus and Sternlich, Theory of Hydrodynamic Lubrication, Chapter 1.
- III-6 Gross, Gas Film Lubrication, Chapter 2.

APPENDIX IV

EXPERIMENTAL LOAD-DEFLECTION CURVES

The compressive load-deflection experimental apparatus and procedure are fairly simple and straightforward. The apparatus consists of a hydraulic press, two pistons that fit snugly into a hollow circular casing, a load cell and recorder, and a dial indicator gage calibrated in units of 0.0001 in.

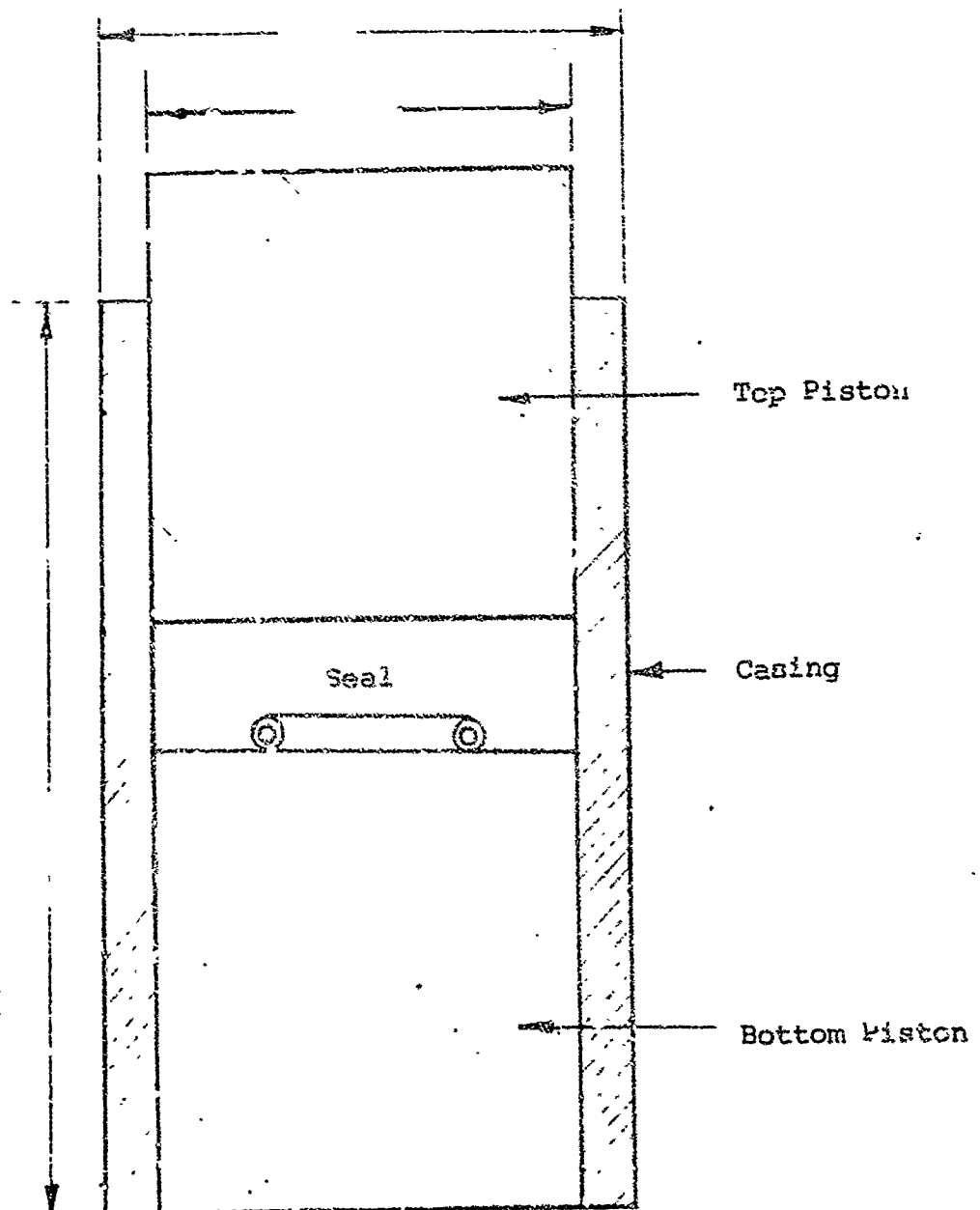


Figure IV-1 Cross section of load-deflection piston assembly

The seal to be evaluated is centered between the pistons as shown in figure IV-1, and the assembly is placed in the hydraulic press. The load cell is placed between the ram of the press and the top piston, and connected to the recorder. The dial indicator is fastened rigidly to the press and placed vertically on the top piston. The load cell and dial indicator give the loads and corresponding deflections, respectively.

The results of experiments on seals described in Section 10.3 are plotted as load versus deflection on figures IV-2 through IV-15. Several of the curves do not begin linearly but arch at a relatively steep slope as shown on figure IV-5. This can be accounted for as follows:

- warping of the seal
- high spots along the seal
- general setting-in of the assembly.

It was noticed that this initial nonlinearity only occurs for new seals.

The slopes of the predominantly linear portions of the curves are the spring constants of the seals given as K . Of course, errors in the readings of loads and deflections exist. With respect to the load, errors occur from:

- a slight inherent inaccuracy in the load cell
- difficulty in reading the load from the paper record due to the finite width of the ink trace
- error arising from balancing, zeroing, and drifting of the recorder.

In the first two cases, the percentage error generally depends on the total magnitude of the load, becoming less as the magnitude increases. It can be assumed that the error never exceeds ± 5 per cent and is probably insignificant in most instances if proper care is taken.

With respect to the deflection, errors occur from:

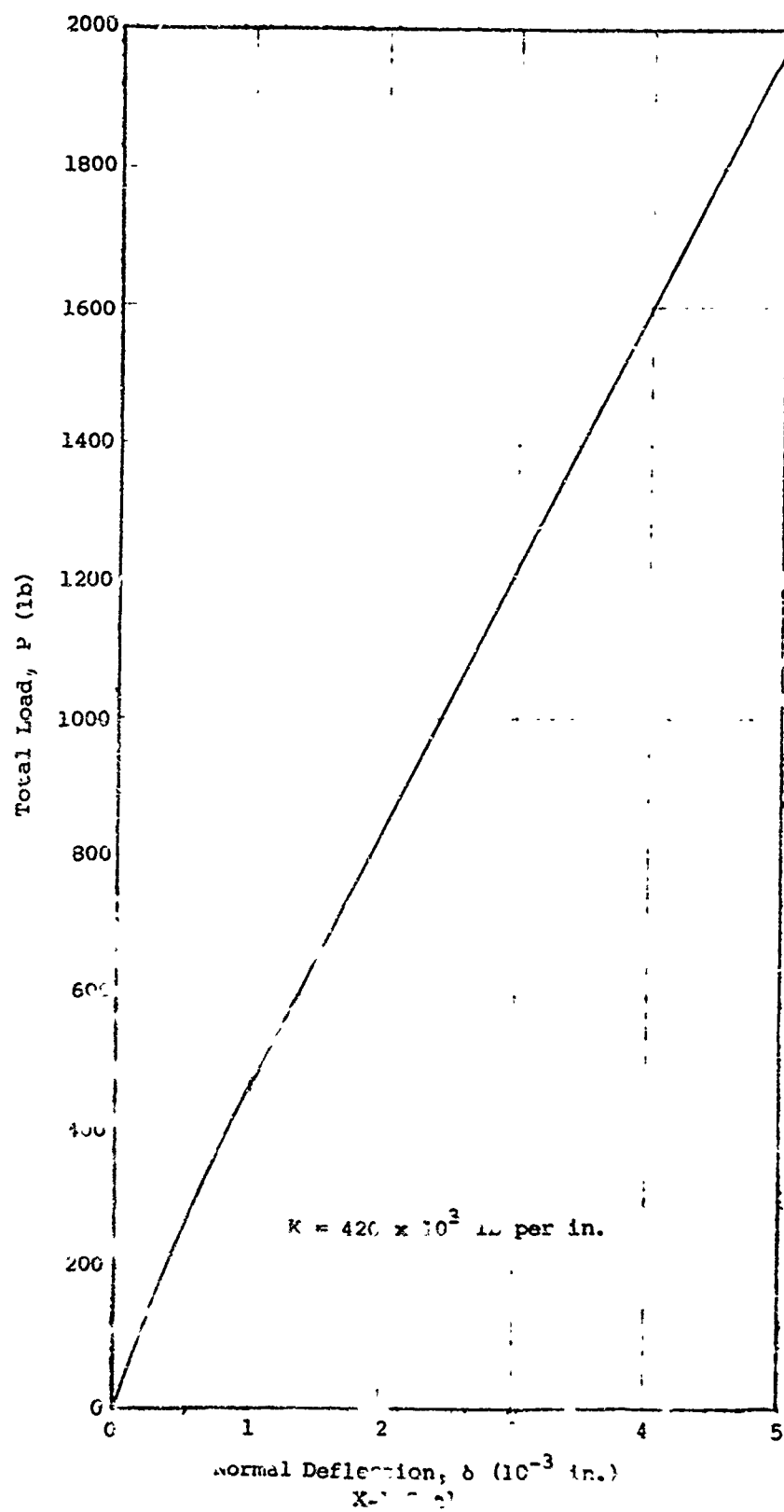
- inherent inaccuracy of the dial indicator (negligible)
- inability to align the indicator stem perfectly vertical on the top piston (very small if proper care is taken)

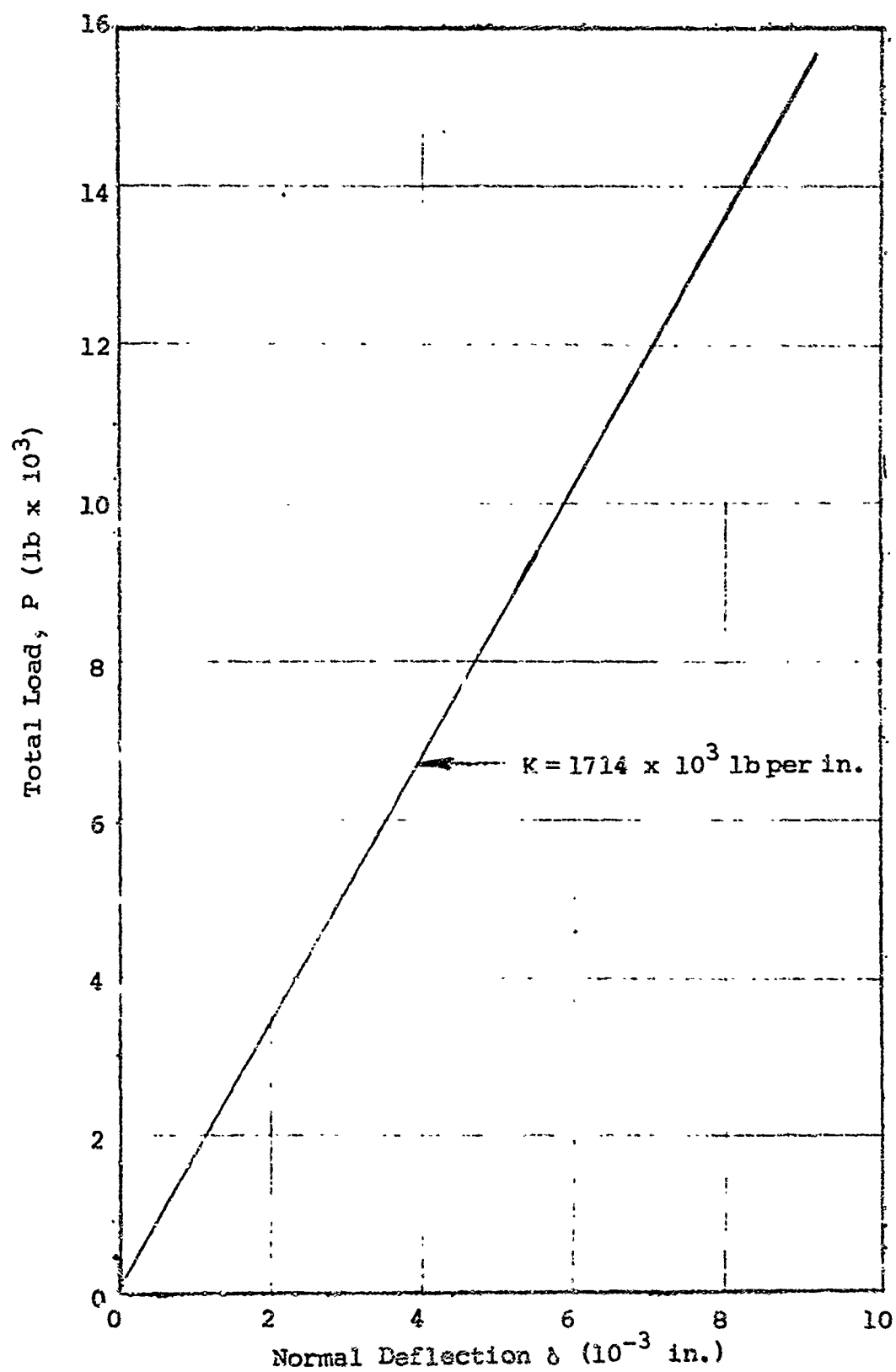
- difficult in rigidly fastening the indicator to a rigid body (also very small if the system's behavior is felt out before testing)
- tilting of the assembly during compression

The tilting effect may tend to be significant if warping and high spots are prevalent. However, as a result of the 0.0005-in. fit of the pistons in the casing, it can also be assumed to be small.

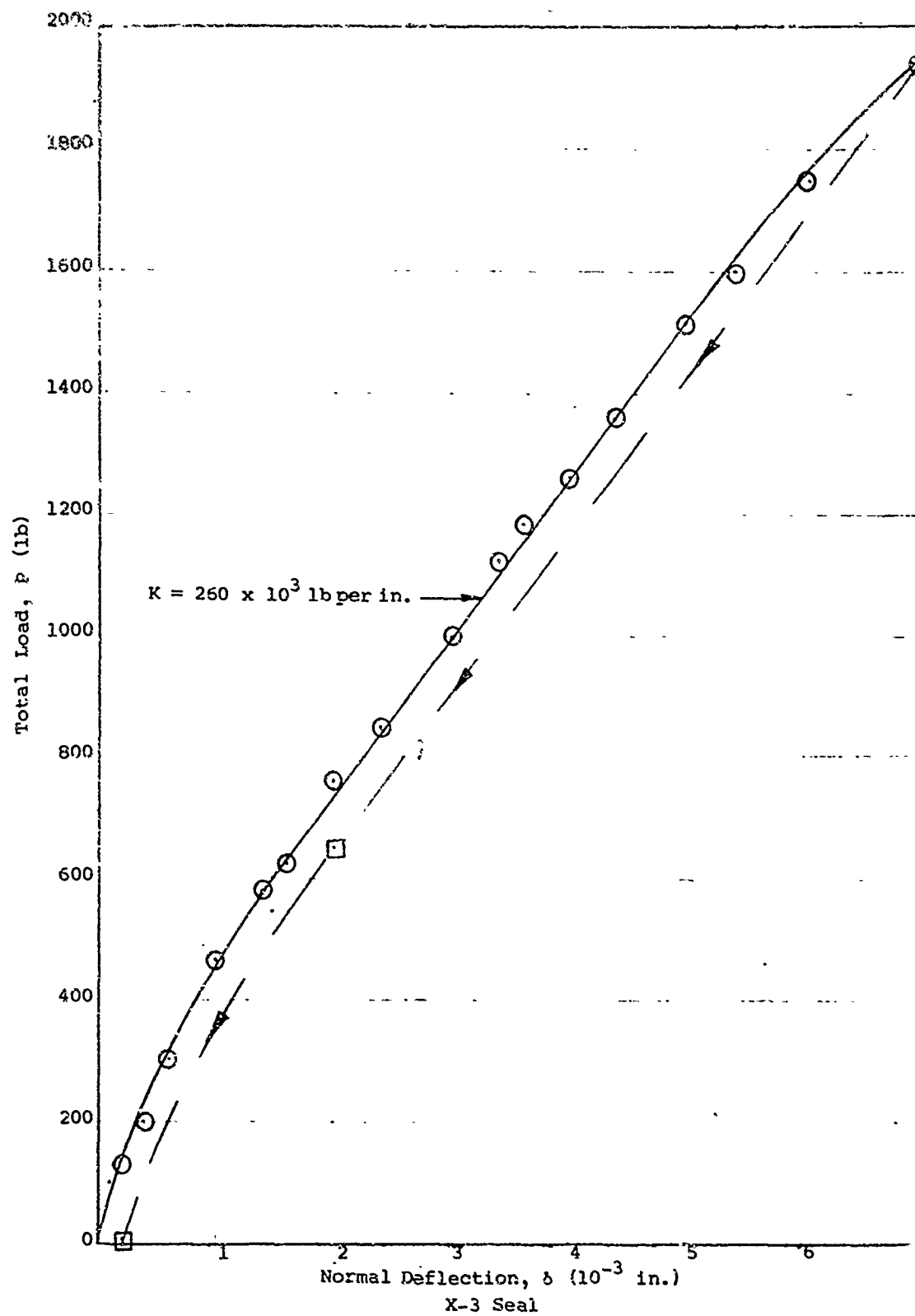
The spring constants depend on the slope of the linear portions of the curves and, thus, on the ratios of load differences to deflection differences. This would tend to diminish errors in any readings so that the errors in the spring constants can be reasonably assumed to be negligible. Furthermore, the fact that the data points lie in a very linear or smooth curve fashion indicates the accuracy of the tests. Drawing straight lines and smooth curves through the data points tends to average out any errors.

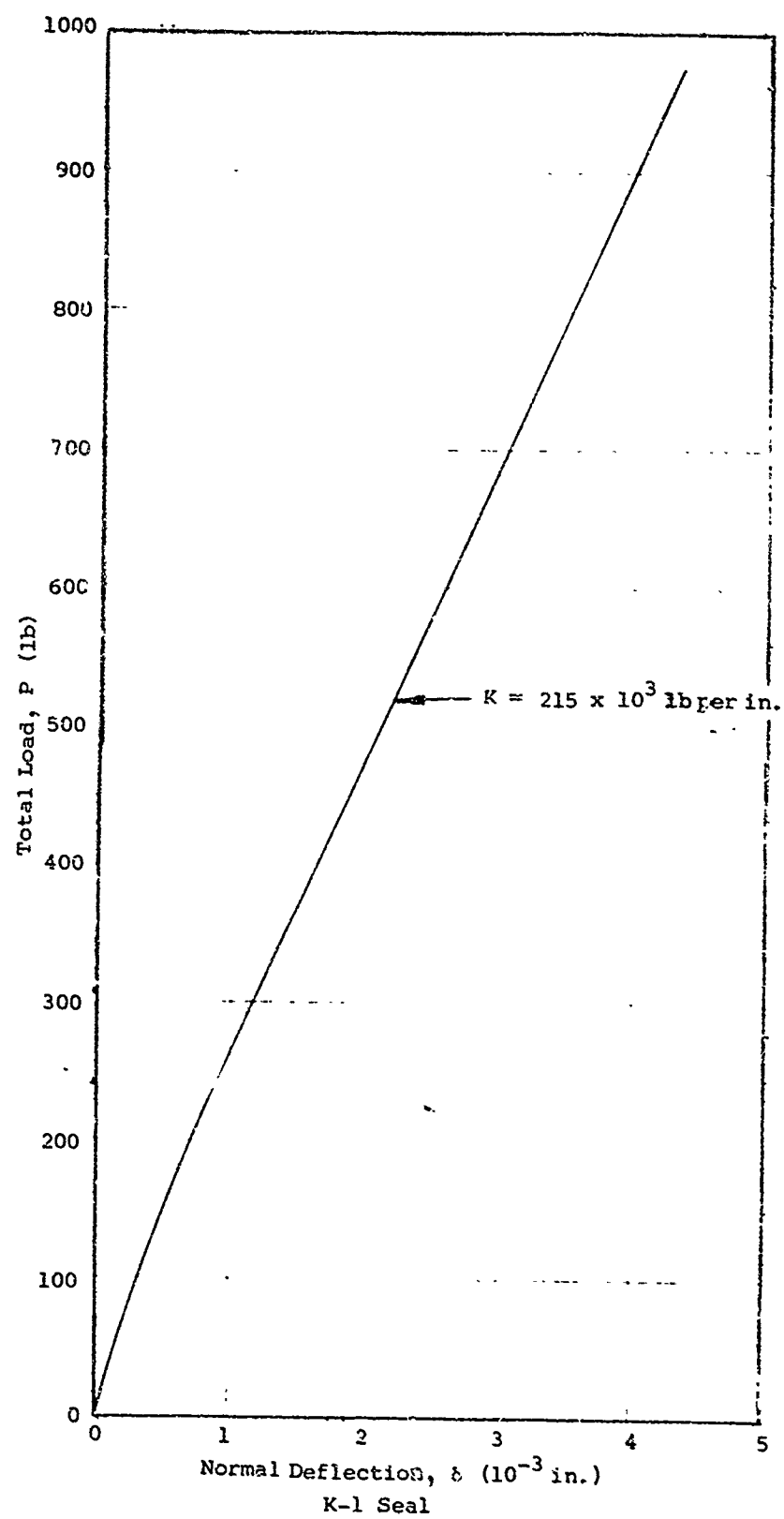
Following are the experimental load-deflection curves for the various seals considered. In one case, the W-2 seal, two graphs are included. These graphs are curves of two similar seals. On several of the graphs more than one curve, representing several trials of the same seal, are shown.

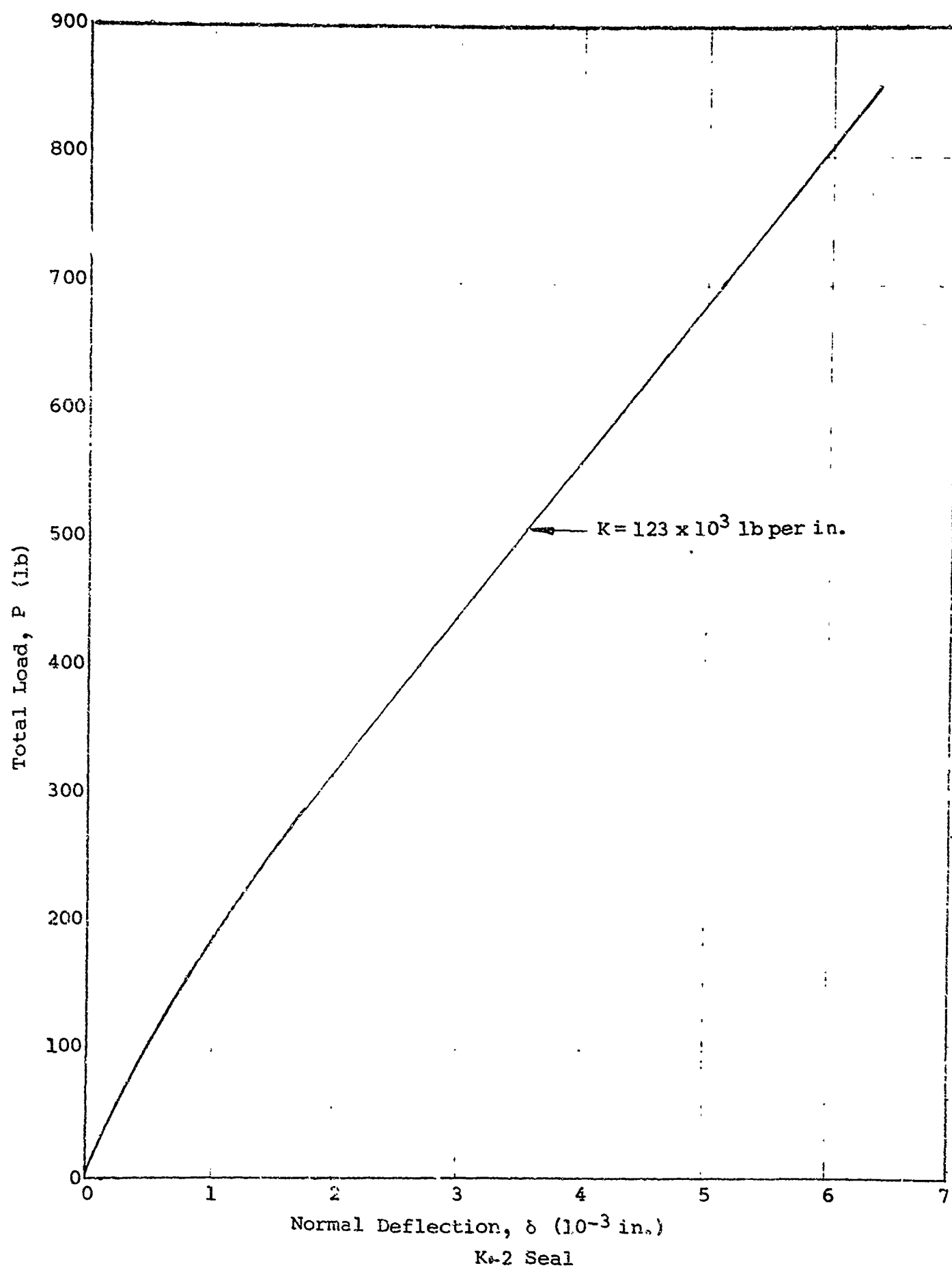


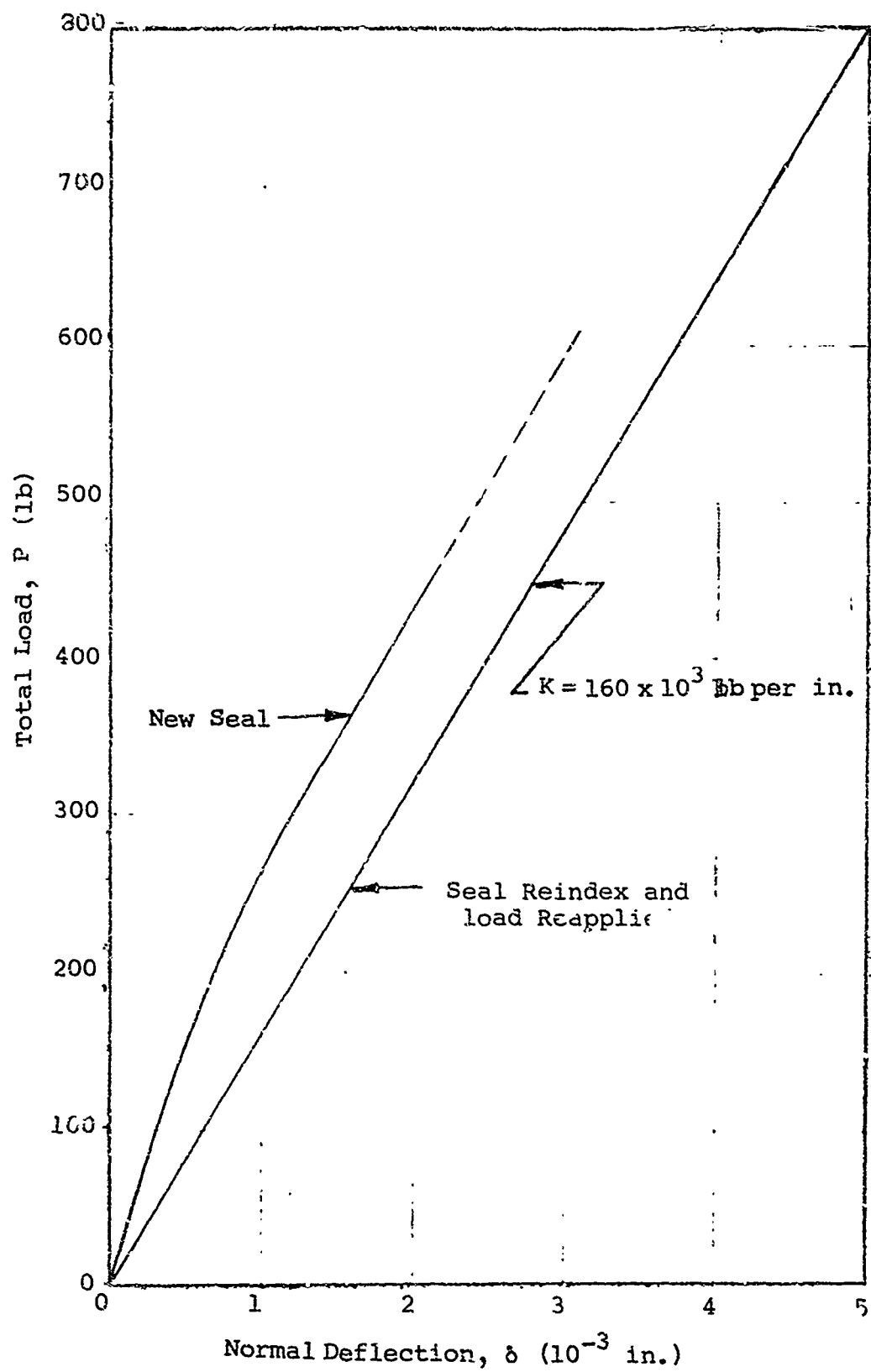


X-2 Seal.

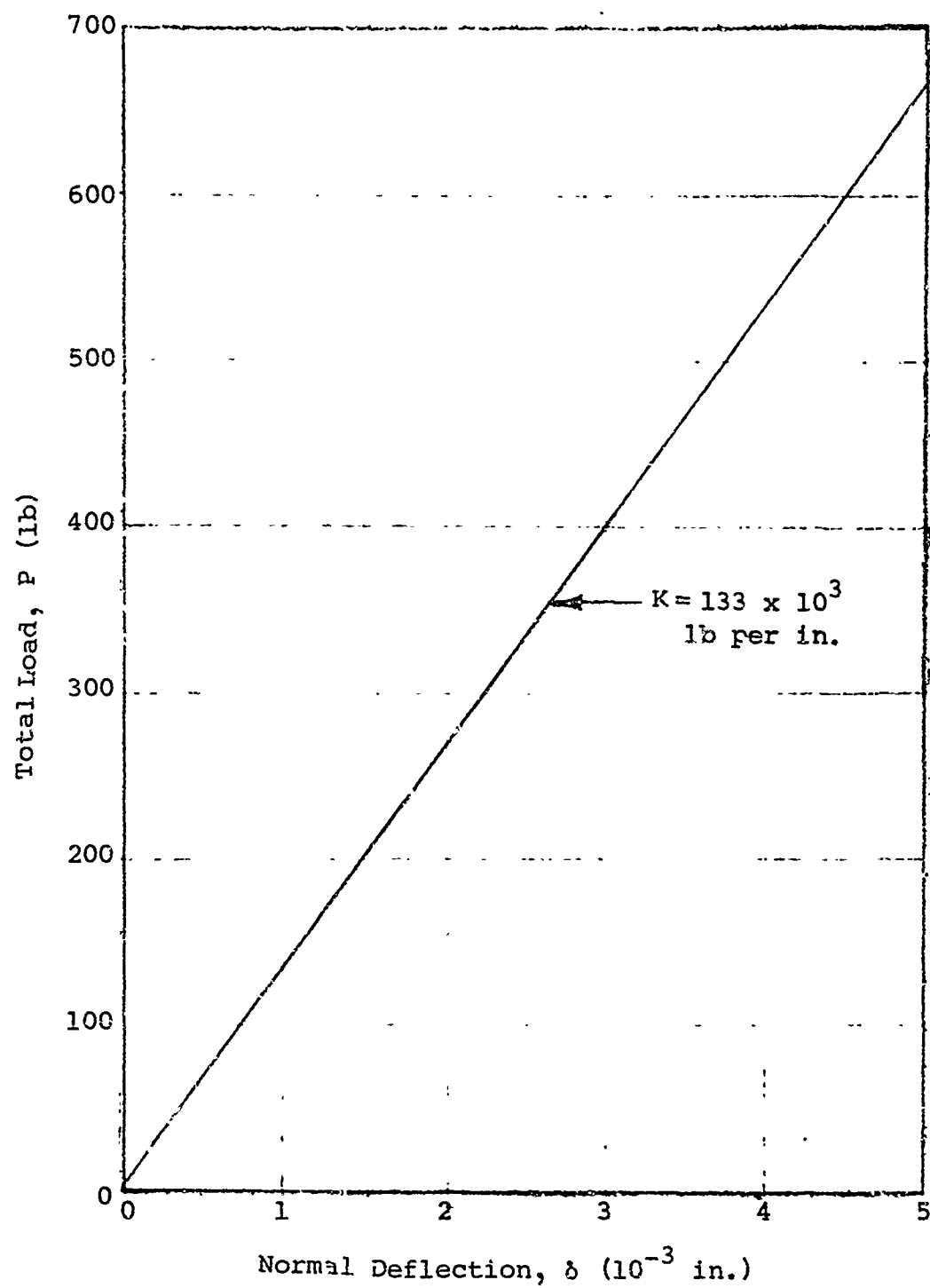




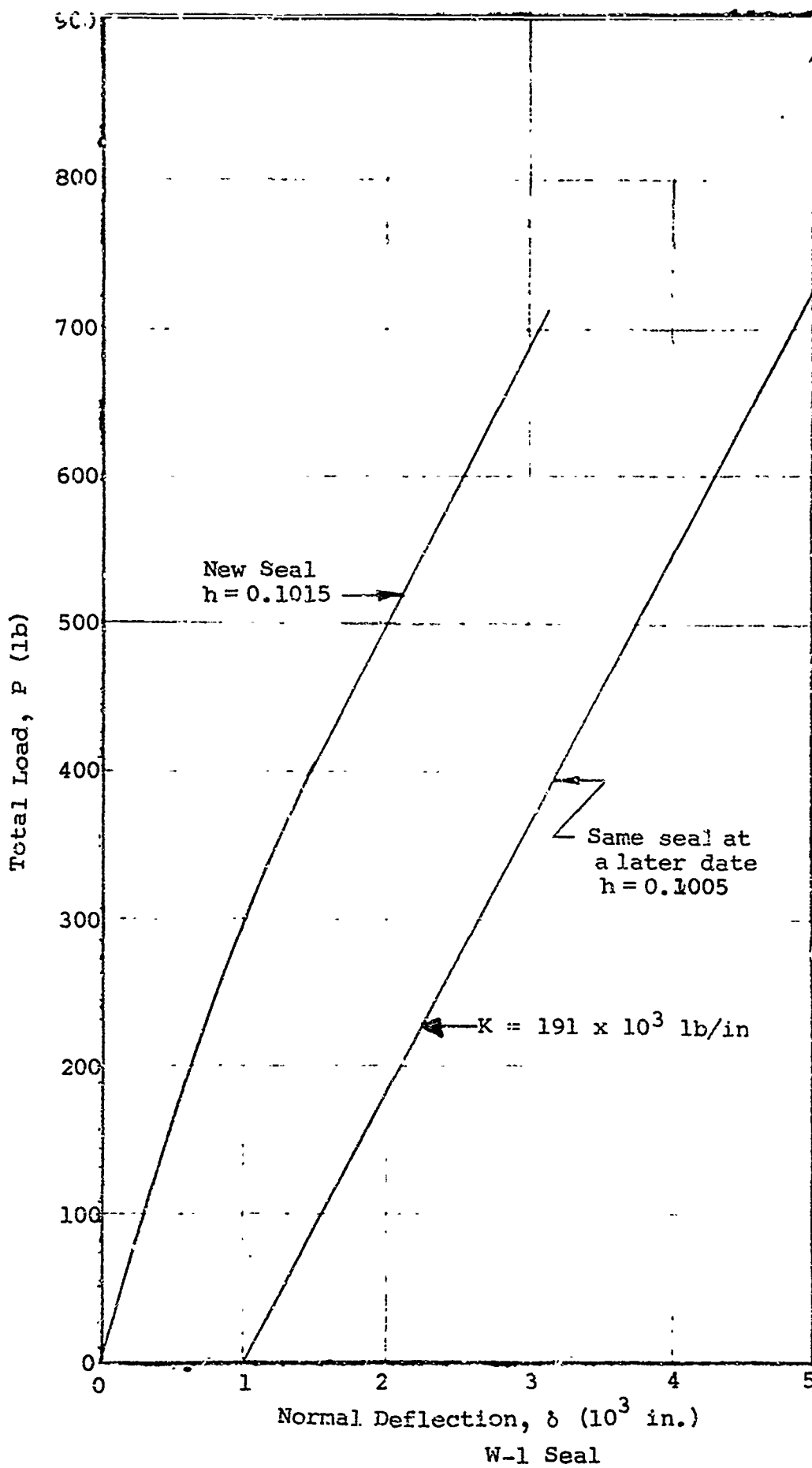


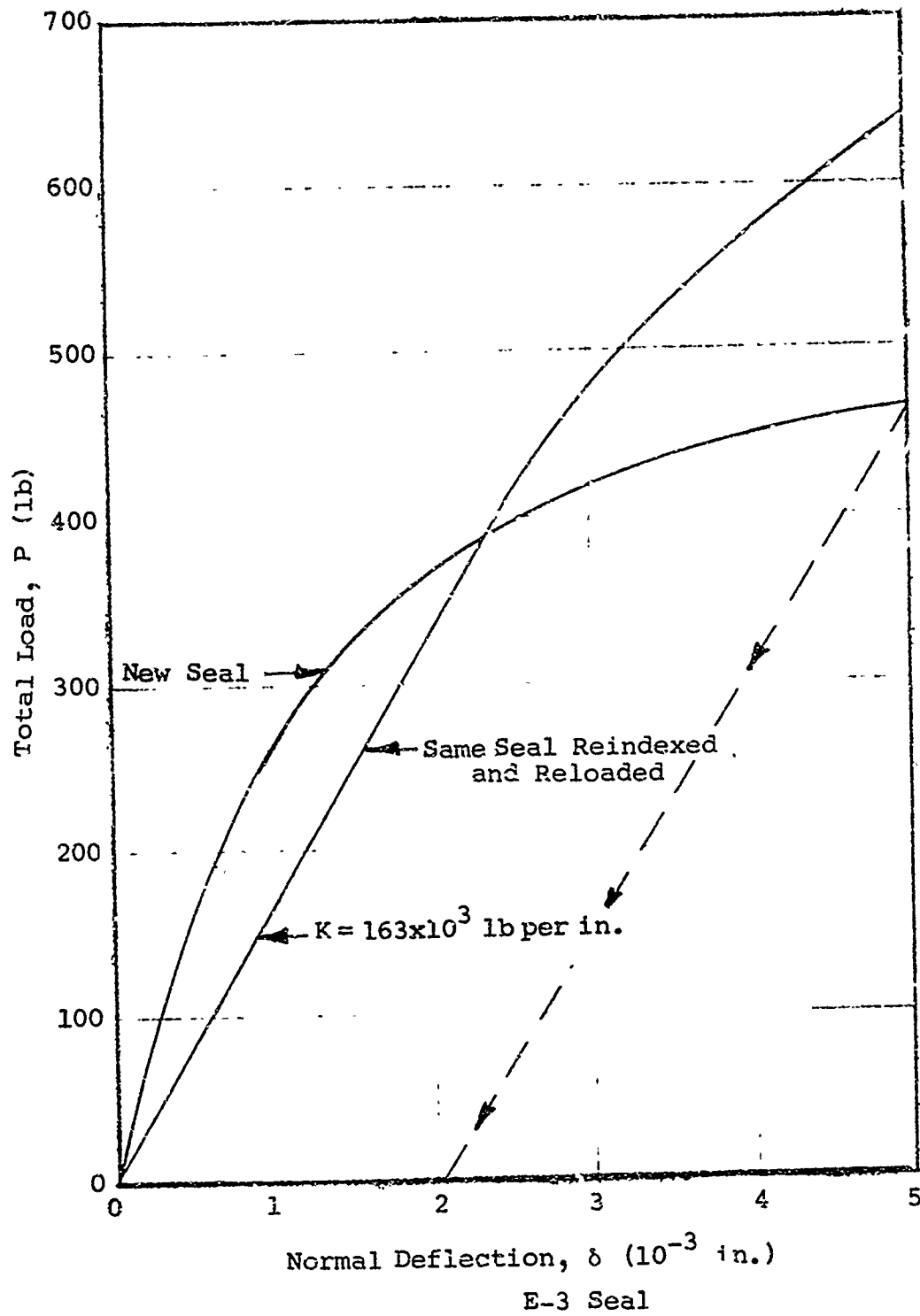


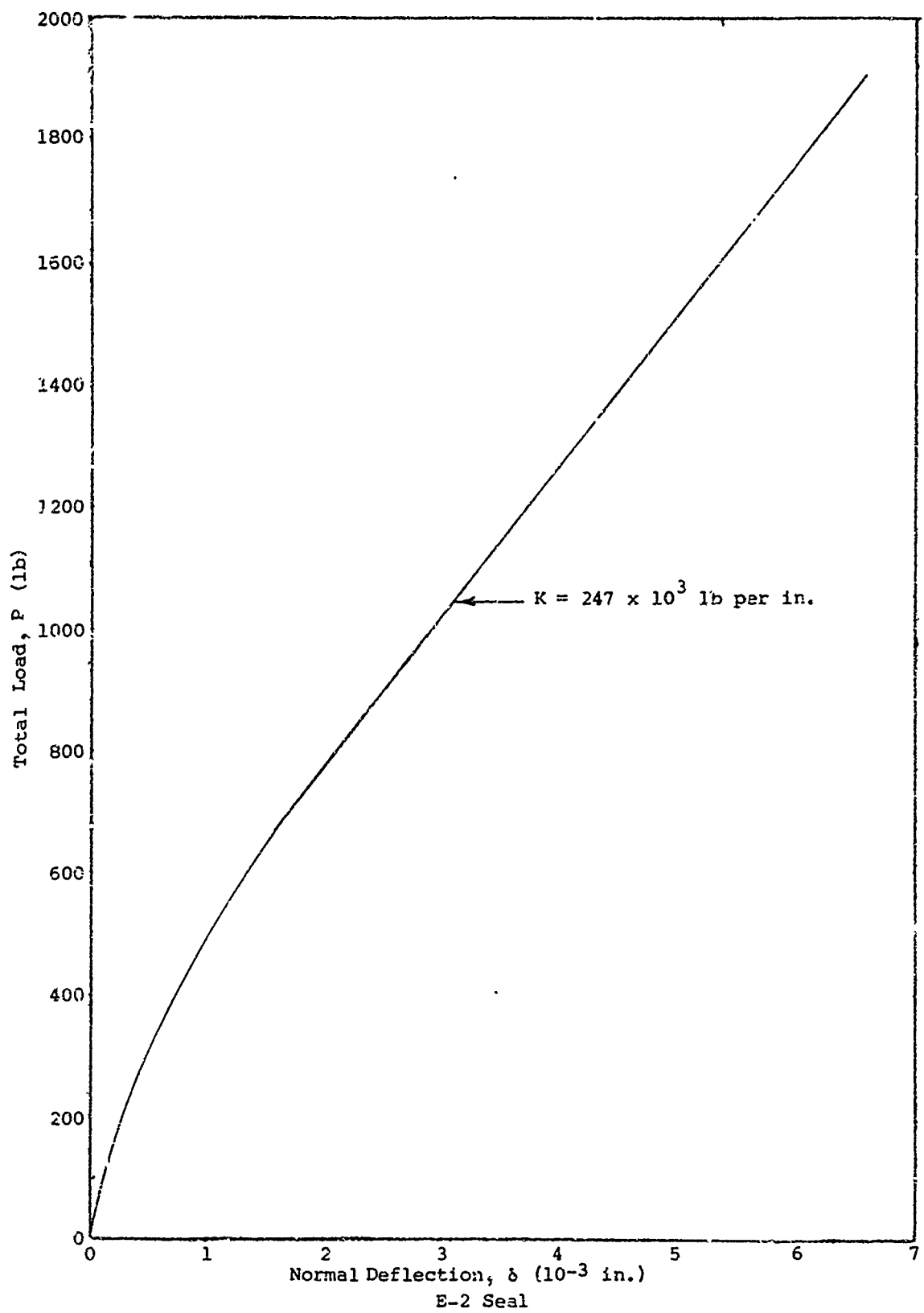
W-3 Seal

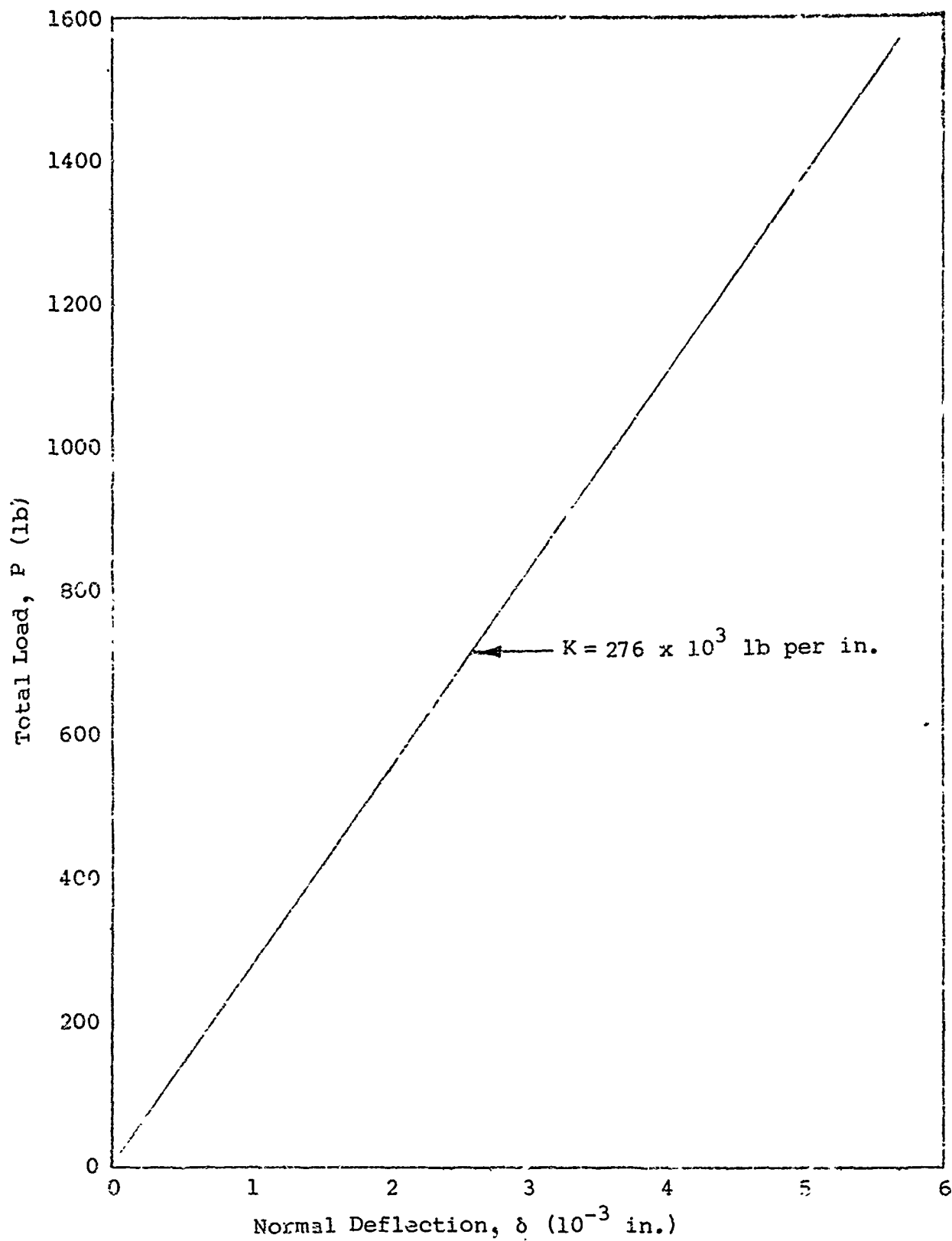


W-2 Seal

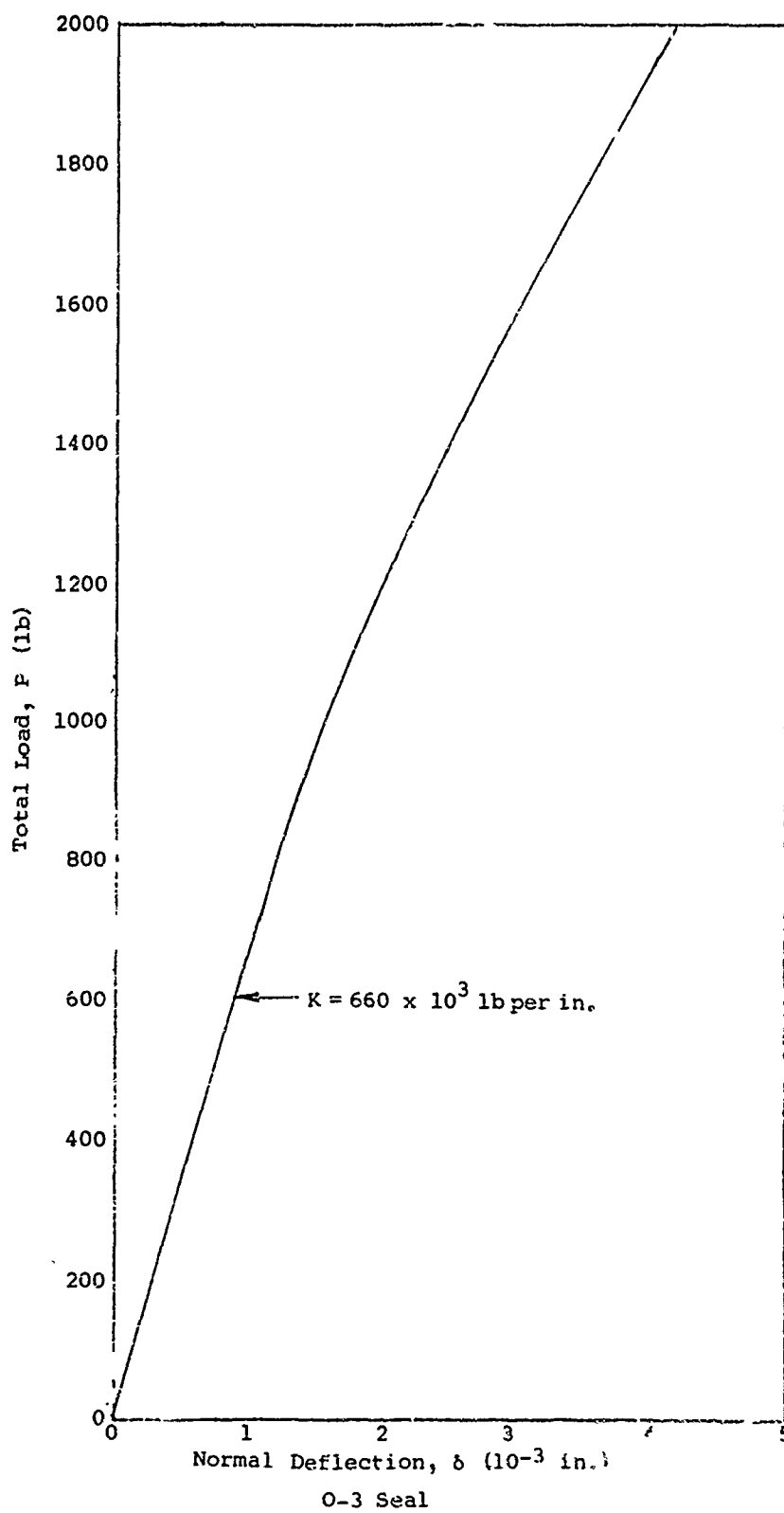


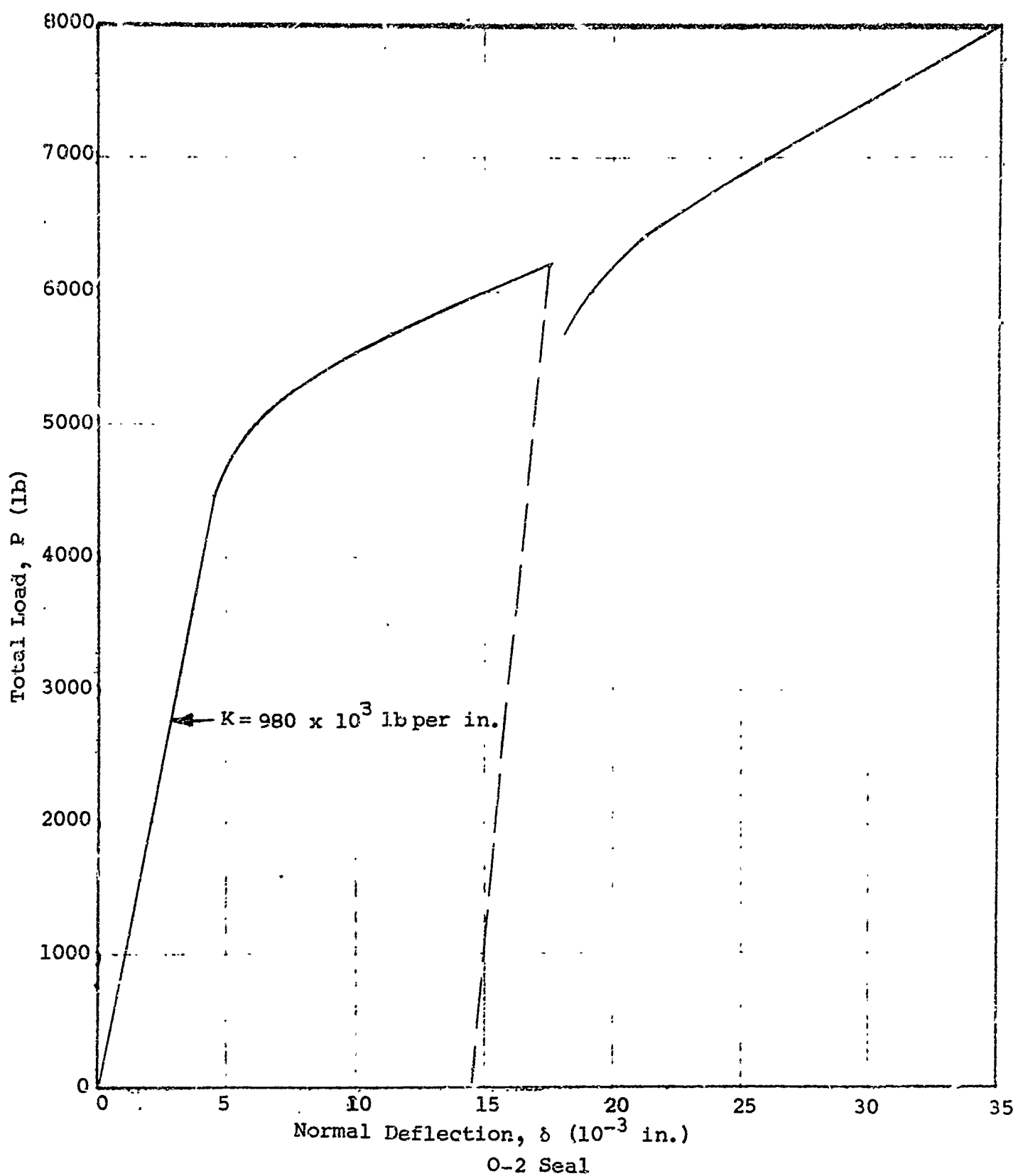




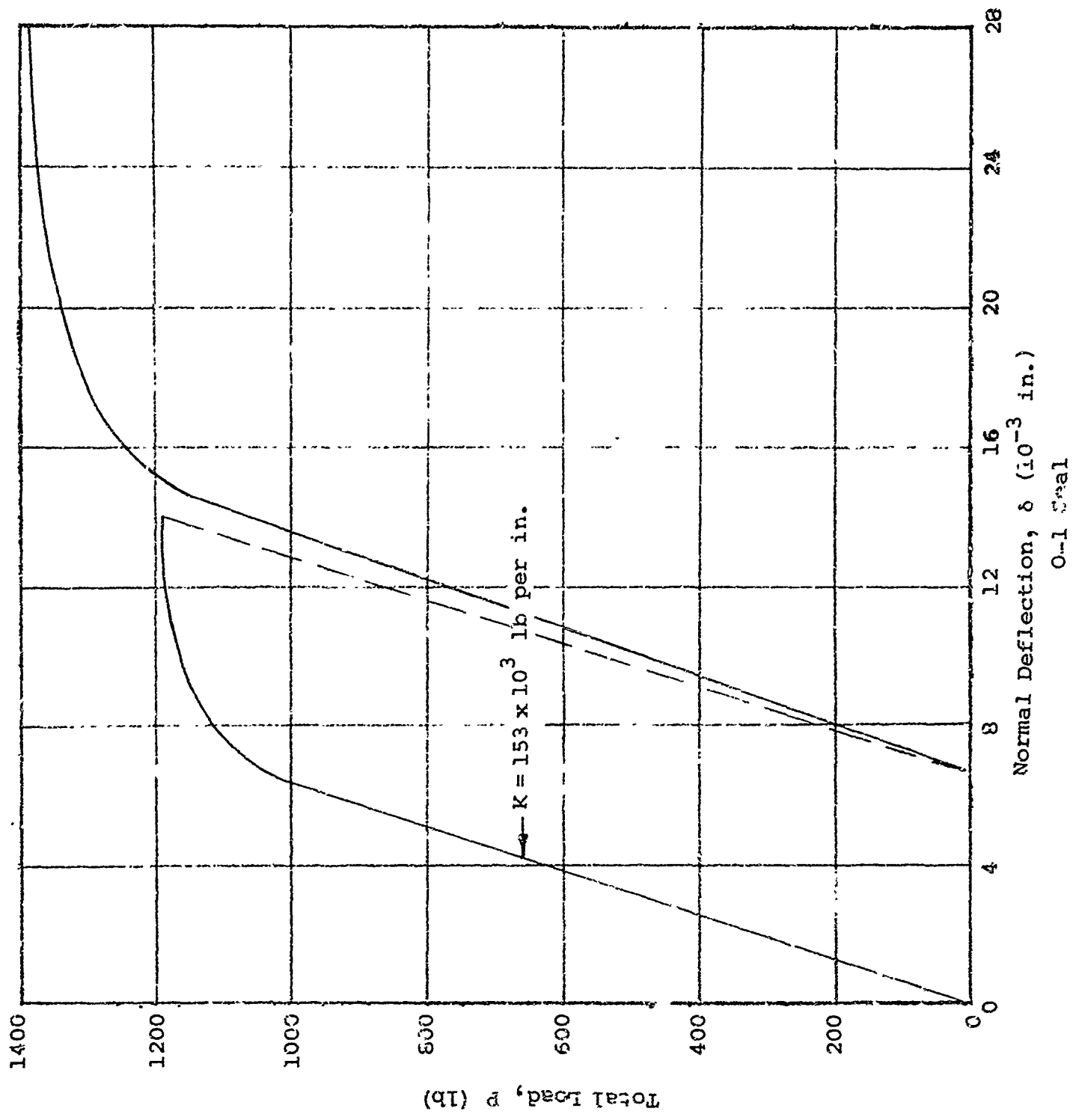


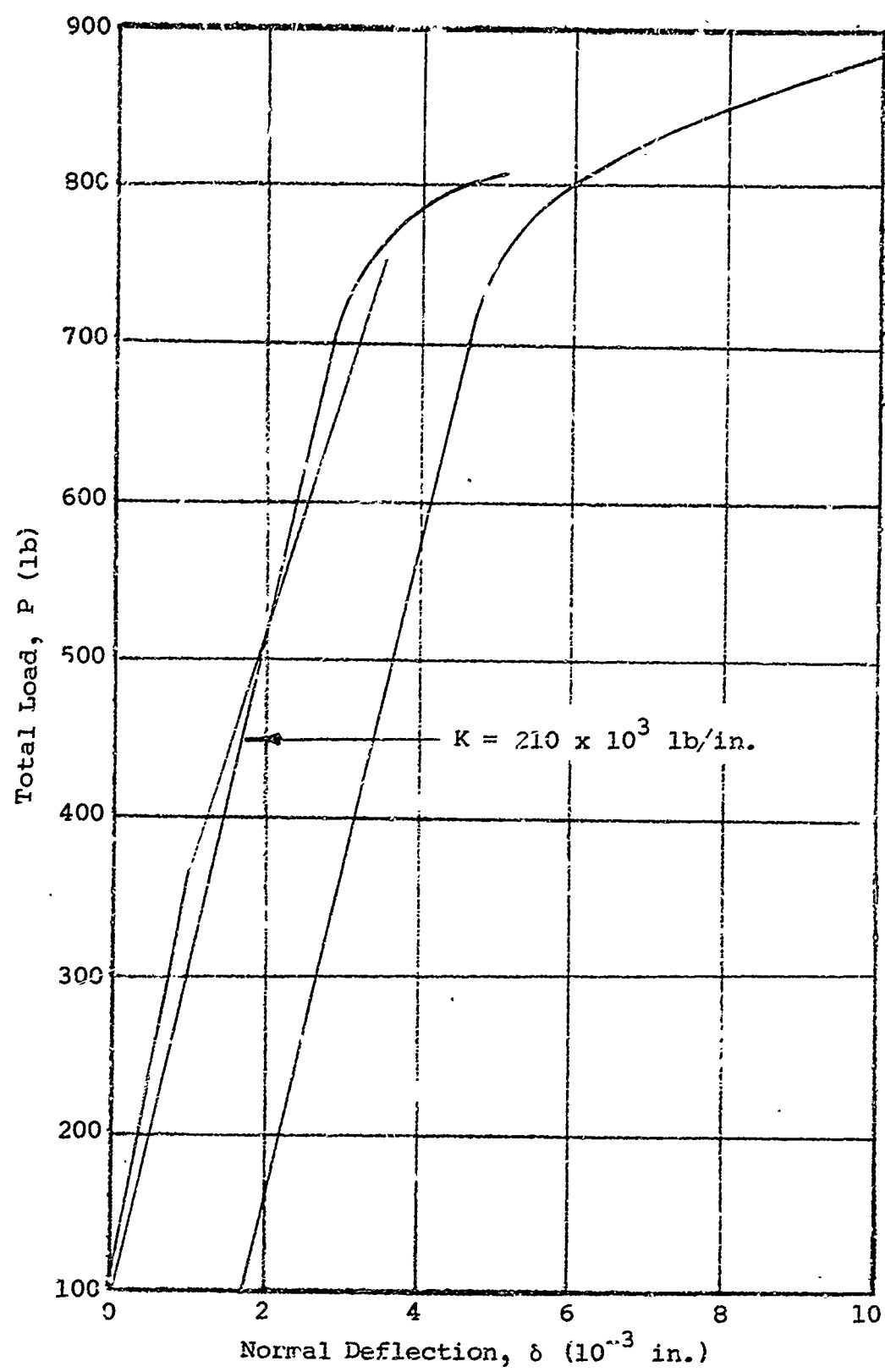
E-1 Seal



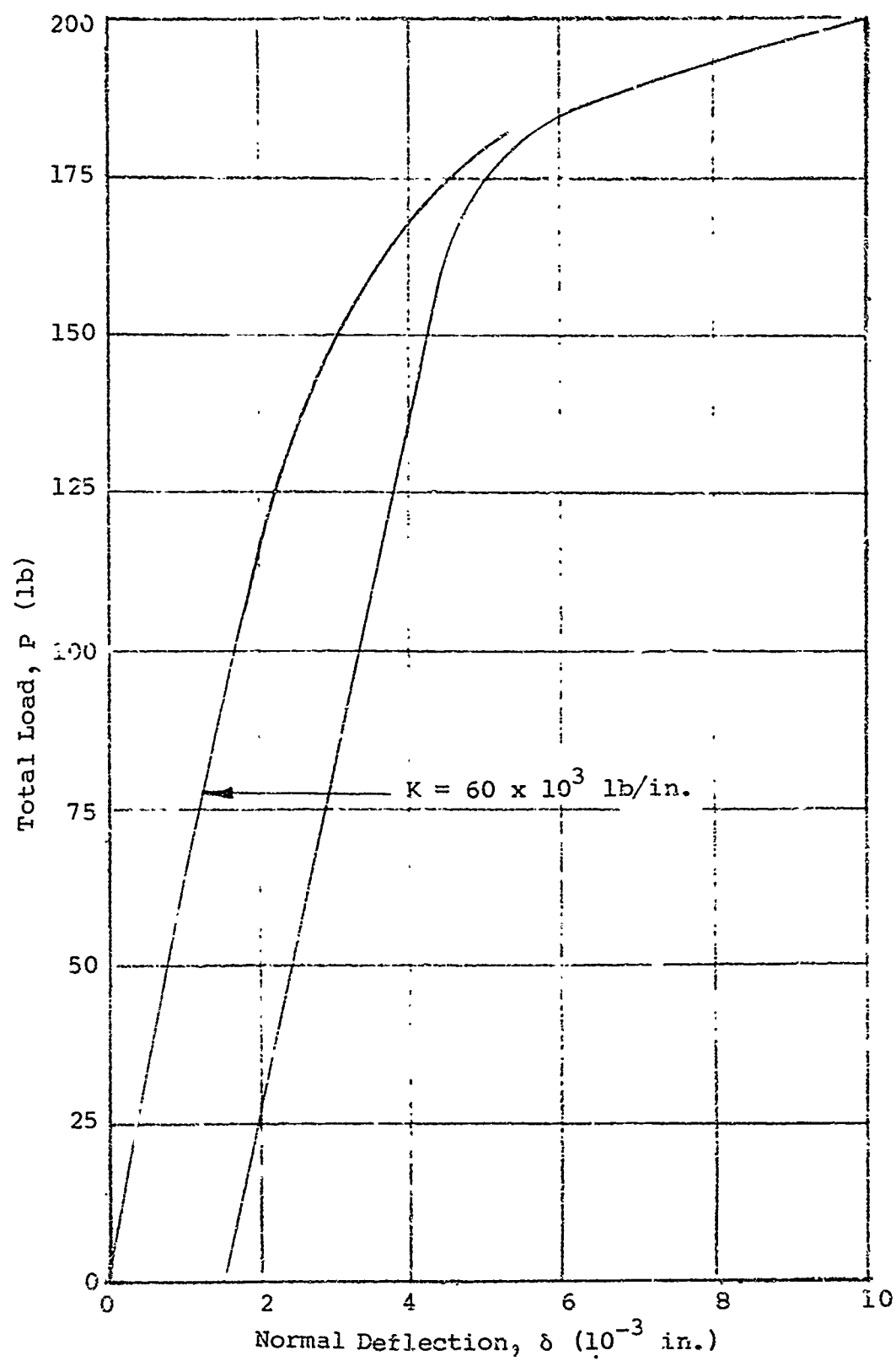


1000 900 800 700 600 500 400 300 200 100 0





C-2 Seal



C-1 Seal

APPENDIX V

CRITERIA FOR COMPONENT COVERS

In view of the large number of cover configurations that the designer can usually choose from to fit a given need, a more systematic and general approach to cover analysis was attempted. Basically, this approach was to separate the cover into two parts, the flange assembly and the cover shell. Unfortunately, the analysis was not carried to completion covering all cases. The approach is worthy of further development and, for this purpose, the following work is presented.

The two major design criteria of component covers are their structural integrity and sealing performance. Adequate stress analyses exist to ensure the structural integrity of a cover, but its leakage characteristics have not been satisfactorily analyzed.

The objective of this task is the development of analytical techniques by which a cover's leakage characteristics can be theoretically computed, resulting ultimately in the provision of quantitative sealing criteria for use by cover designers.

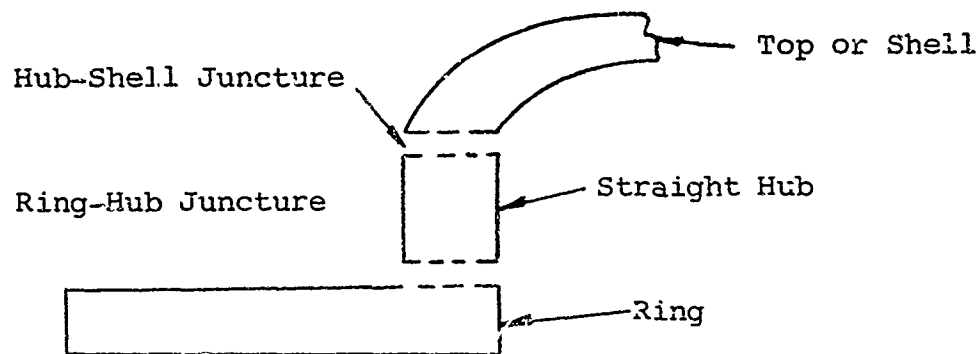
This seals program has firmly established analytical methods for the quantitative determination of leakage past a seal if the seal material, geometry, surface finish and nominal contact stress are known. A seal as part of a component cover is subjected to a variable contact stress dependent on the component pressurization and operating temperature. In particular, the sealing performance depends upon the elastic displacements of the housing in the vicinity of the seal. From the designers viewpoint, the housing must provide tolerable disturbances of the seal under test and operating conditions.

This analysis has established theoretical formulations and the associated computational schemes for the elastic displacements of covers as functions of the component pressurization. The approach is general enough to handle a wide range of cover designs possessing cylindrical symmetry. The analysis is fashioned for application to digital computers resulting ultimately in the preparation of design graphs and tables representing the leakage characteristics of a variety of component cover assemblies.

V-1. Classifications of Covers

The class of covers considered herein must possess cylindrical symmetry, the independent variables being the radial and axial coordinates (quasi-steady state deformations if pressure cycling is present).

The cover is divided into three parts for analysis; the ring, hub (only straight hubs are considered), and top or shell.



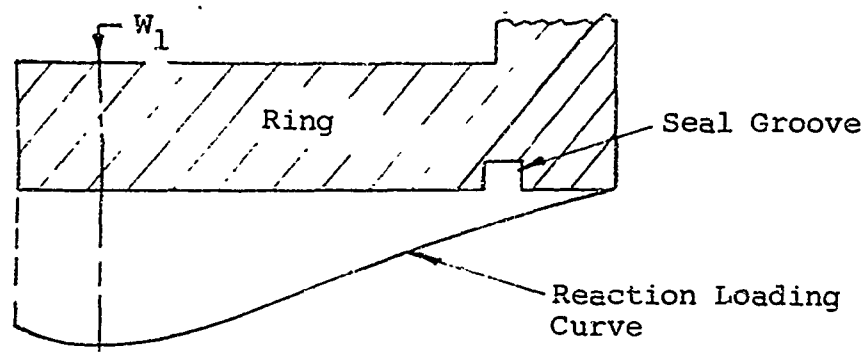
The hub may or may not be present. The identification of these parts depends on the over-all configuration (a possible system of junctures is shown above). The ring (hub) may be integral with or securely attached (e.g., welded) the shell, or it may be loose or screwed to the shell. The integral cover flange is treated in greater detail here, but other types, as suggested, are easily incorporated into the analysis.

It is assumed that the ring is fastened to a flat rigid section by an uniform axial load applied around a circumference (e.g., the bolt load circle).

The reaction loading on the ring is a distribution of forces dependent on the manner of contact with the flat bottom flange and type of sealing. Generally, there may be

- (1) Total contact
- (2) Contact within the Bolt (or other) circle
- (3) Contact outside
- (4) Contact both within and outside but not total

The seal interaction, i.e., its contribution to the reactor load, may be of major importance as with a flat gasket touching the ring everywhere, or insignificant as is the case for a narrow-faced seal in a groove. The initial loading of a ring for the case of complete contact and insignificant seal interaction is illustrated as follows.



It can be assumed that the resultant of the reaction loading curve is collinear with W_1 , thus providing no initial dishing on the ring. For other configurations there may be considerable torque present so that the initial seal deflection is not related directly to the groove depth.

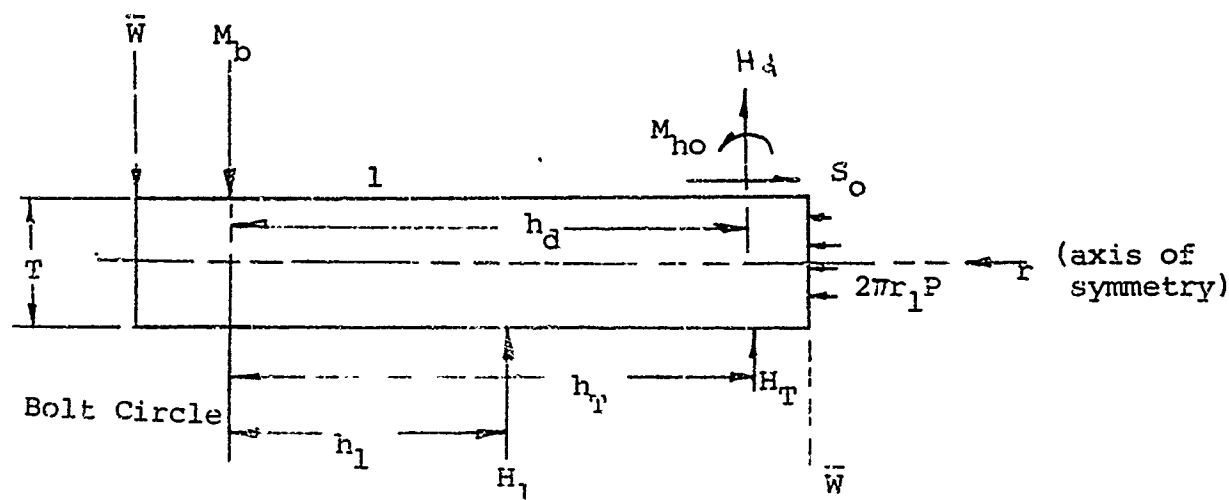
Common shapes of the top or shell are spherical, ellipsoidal, conical, torispherical, toriconical, and the flat plate. Only the spherical and flat plate shells are considered in detail here.

V-2. Theoretical Analysis

Deformation analyses are made of each of the three parts of the cover considered as separate entities. The internal stresses at their junctures are replaced upon separation by undetermined forces and moments treated subsequently as external loads. Articulation of the parts is accomplished by their common boundary conditions of displacement and rotation.

Ring Analysis

A segment of a ring is shown under the applied loads where the hub is replaced by undetermined forces and moments of its juncture



M_b = bolt load (lb)

M_1 = resultant reaction load (lb)

M_t = direct axial pressure load (lb)

M_d = axial pressure load on shell transmitted by hub (lb)

S_o = undetermined radial shear load due to hub (lb/in.)

M_{ho} = undetermined moment due to hub (lb)

For static equilibrium, $M_b = H_1 + M_d + M_t$. It is assumed that the above loading system is equivalent to loading by a couple

$$\bar{W} = M_1 H_1 + M_d h_d + H_t + h_t$$

and the loading then is independent of the actual distributed load. For the case of pure bending by a couple with negligible stretching of the middle surface, the axial deflection $z(r)$ is then given by

$$\frac{d}{dr} \left\{ \left[r \frac{d}{dr} \quad \frac{1}{r} \frac{d}{dr} \quad \left(r \frac{dz}{dr} \right) \right] \right\} = 0 \quad (V-1)$$

Integrating,

$$z = C_1 r^2 \ln r + C_2 r^2 + C_3 \ln r + C_4 \quad (V-2)$$

The rotation, bending moments, and shear are

$$\theta = \frac{dz}{dr} = 2C_1 r \ln r + (C_1 + 2C_2)r + \frac{C_3}{r} \quad (V-3)$$

$$M_r = D \left(\nu \frac{d^2 z}{dr^2} + \frac{1}{r} \frac{dz}{dr} \right) \quad (V-4)$$

$$= D \left\{ \left[2(1+\nu) \ln r + (1+3\nu) \right] C_1 + 2(1+\nu)C_2 + (1-\nu) \frac{C_3}{r^2} \right\}$$

$$M_t = D \left(\frac{d^2 z}{dr^2} + \frac{\nu}{r} \frac{dz}{dr} \right) \quad (V-5)$$

$$= D \left\{ \left[2(1+\nu) \ln r + (3+\nu) \right] C_1 + 2(1+\nu)C_2 - (1-\nu) \frac{C_3}{r^2} \right\}$$

$$Q = - \frac{dM_t}{dr} + \frac{1}{r} (M_r - M_t) = -4D \frac{C_1}{r} \quad (V-6)$$

where

$$D = \frac{ET^3}{12(1-\nu^2)}$$

Equation (V-2) contains four integration constants requiring four boundary conditions. Two of these are immediately known. From the assumed pure couple loading system,

$$Q = - \frac{\bar{W}}{2\pi r} ; \quad C_1 = \frac{\bar{W}}{8\pi D}$$

$$\text{Also, } M_{ti} = M_t (r=r_1) = M_{ho} = 1/2 S_o T$$

Thus, two additional boundary conditions must be specified before an unique solution is attainable.

The radial displacement, or stretching of the middle surface, is given by

$$\frac{d}{dr} \left[\frac{1}{r} \frac{d}{dr} (ry) \right] = 0 \quad (V-7)$$

It should be noted that the cases of pure bending and pure stretching are superposable since this is entirely an elastic analysis. Integrating,

$$y(r) = C_s r + \frac{C_6}{r} \quad (V-8)$$

Also,

$$C_r = \frac{dy}{dr} = \frac{1}{E} (\sigma_r - \nu \sigma_t)$$

$$C_t - \frac{y}{r} = \frac{1}{E} (\sigma_t - \nu \sigma_r)$$

and the radial and hoop stresses are then

$$\sigma_r = E \left(\frac{C_5}{1-\nu} - \frac{C_6}{1+\nu} \frac{1}{r^2} \right) \quad (V-9)$$

$$\sigma_t = E \left(\frac{C_5}{1-\nu} + \frac{C_6}{1+\nu} \frac{1}{r^2} \right) \quad (V-10)$$

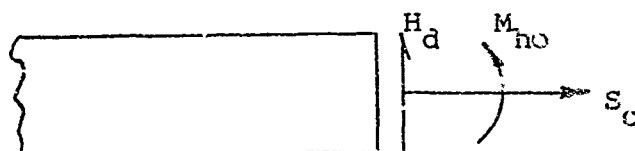
Equation (V-8) contains two integration constants requiring two boundary conditions. One of these is obviously $\sigma_{r2} - \sigma_r (r=r_2)=0$; the other is $\sigma_{r1} = \sigma_r (r=r_1) = -P + S_0/T$, assuming that the shear S_0 is uniform through the ring thickness. (Note: combining the radial and hoop stresses due to the stretching with those from bending or dishing of the ring would provide part of a stress or structural integrity analysis). Thus,

$$C_5 = \frac{1-\nu}{E} \left[\frac{1}{1 - \left(\frac{r_2}{r_1}\right)^2} \right] \left(-P + \frac{S_0}{T} \right)$$

$$C_6 = \frac{1+\nu}{E} \frac{\frac{r_2^2}{1 - \left(\frac{r_2}{r_1}\right)^2}}{\frac{r_2^2}{1 - \left(\frac{r_2}{r_1}\right)^2}} \left(-P + \frac{S_0}{T} \right)$$

and the radial deformation due to radial loading is known from (V-8).

It is often convenient to place the ring-hub (or ring-shell if no hub is present) juncture at a vertical section of the ring as, for example, is done for a flat plate cover.



In this instance, two of the known boundary conditions become

$$M_{t1} = M_{ho} ; \quad \sigma_{r1} = \frac{S_0}{T}$$

In general, changes in cover configuration are effected by means of the boundary conditions.

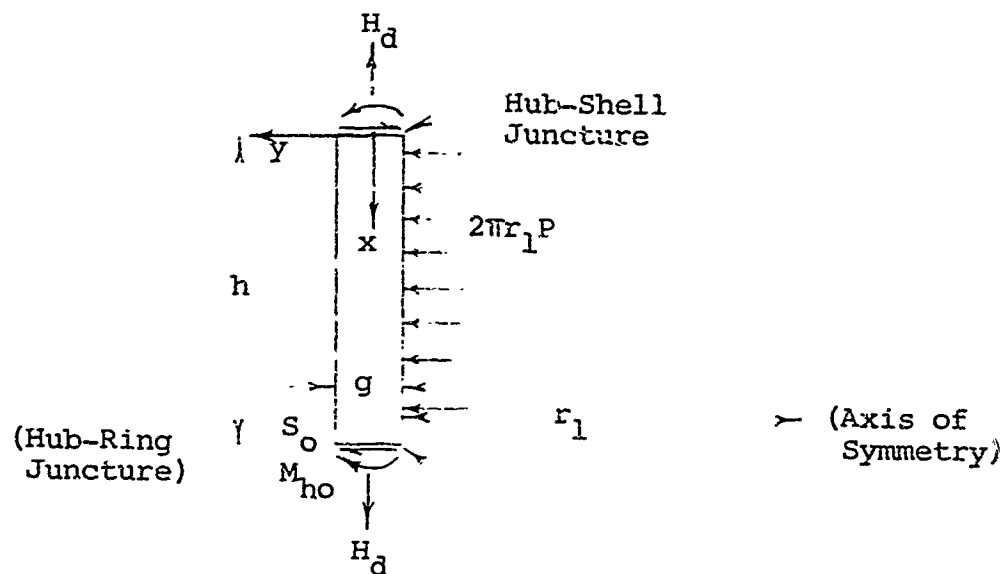
There are yet required two additional boundary conditions for evaluation of all the integration constants appearing in the ring equations. These depend on the cover application. One of these can usually be identified with the ring outside diameter: for example, if the outer edge is free, $M_{t2} = 0$; if it is not free to deflect, $z_2 = 0$; or if it is not free to rotate, $\theta_2 = 0$, the subscript 2 referring to $r = r_2$.

The final boundary condition is taken to be the elastic elongation (or possibly compression) of the bolts (or other securing structure) in this analysis. The ring deformation at the bolt circle must equal the bolt deformation. Since the bolt load depends on the general solution through the reaction load, an iterative procedure must be established. This is discussed in greater detail later.

The undetermined juncture load and moment are, of course, specified by the articulation of the cover components, i.e., two deflection equalities at each juncture.

Hub Analysis

Only the straight (cylindrical) hub is considered.



M_{ho} , S_o , M_{hi} , S_i are the undetermined moments and shears arising from the ring and shell, respectively.

The differential equation for the radial displacement of a straight hub is

$$\frac{d^4 y}{dx^4} + \frac{K}{h^4} y = \frac{K}{h^4} \left(1 - \frac{\nu}{2}\right) \frac{r_1^2 p}{gE} \quad (V-11)$$

$$\text{where } K = \text{hub modulus} = \frac{12(1-\nu^2)r_1^4}{r_1^2 g}$$

The solution is immediately obtainable as

$$y = e^{\beta x} (C_7 \sin \beta x + C_8 \cos \beta x) + e^{-\beta x} (C_9 \sin \beta x + C_{10} \cos \beta x) + \left(1 - \frac{\nu}{2}\right) \frac{r_1^2 p}{gE}$$

$$\text{where } \beta = \frac{1}{h} \sqrt[4]{K/4} \quad (V-12)$$

The rotation, bending moment, and shear are

$$\begin{aligned} \theta_h &= \frac{dy}{dx} \\ M_h &= -\frac{Eg^3}{12(1-\nu^2)} \frac{d^2 y}{dx^2} \\ Q_h &= -\frac{dM_h}{dx} \end{aligned} \quad (V-13)$$

The four integration constants in (V-12) require four boundary conditions:

$$M_h = M_{h1}, Q_h = S_1 \text{ at } x = 0$$

$$M_h = M_{ho}, Q_h = S_o \text{ at } x = h$$

Substituting (V-12) into (V-13) and evaluating for these specified boundary conditions,

$$\bar{M}_{h1} = C_7 - C_9$$

$$\bar{M}_{ho} = e^{\beta h} (C_7 \cos \beta h - C_8 \sin \beta h) + \\ + e^{-\beta h} (-C_9 \cos \beta h + C_{10} \sin \beta h)$$

$$\bar{S}_1 = C_7 - C_8 + C_9 + C_{10}$$

$$\bar{S}_0 = e^{\beta h} \left[C_7 (\cos \beta h - \sin \beta h) - C_8 (\sin \beta h + \cos \beta h) \right] \\ + e^{-\beta h} \left[C_9 (\sin \beta h + \cos \beta h) + C_{10} (\cos \beta h - \sin \beta h) \right]$$

where

$$\bar{M}_h = \frac{12(1-\nu^2)}{2\beta^2 E g^3} M_h; \quad \bar{Q}_h = - \frac{12(1-\nu^2)}{2\beta^3 E g^3} Q_h$$

Solving for C_7, C_8, C_9, C_{10} by Cramer's rule gives

$$C_7 = \frac{1}{2} \bar{M}_{h1} + \frac{1}{2} \bar{S}_1$$

$$C_8 = \frac{1}{2} \frac{\cos^2 \beta h}{\sin^2 \beta h} \bar{M}_{h1} + \frac{e^{-\beta h}}{2} \left(\frac{\cos \beta h - \sin \beta h}{\sin^2 \beta h} \right) \bar{M}_{ho} - \frac{e^{-\beta h}}{2 \sin \beta h} \bar{S}_0 \quad (V-14)$$

$$C_9 = \frac{1}{2} \bar{M}_{h1} + \frac{1}{2} \bar{S}_1$$

$$C_{10} = \frac{1}{2} \frac{\cos^2 \beta h}{\sin^2 \beta h} \bar{M}_{h1} + \frac{e^{\beta h}}{2} \left(\frac{\sin \beta h + \cos \beta h}{\sin^2 \beta h} \right) \bar{M}_{ho} - \frac{e^{\beta h}}{2 \sin \beta h} \bar{S}_0$$

The expressions for the radial displacements and rotations of the hub junctures are obtained from (V-12) and the first of (V-13) by setting $x = 0$ and $x = h$. Doing this and eliminating the integration constants by (V-14) gives

$$\delta_{h1} = y(x=0) = \frac{2\beta^2 r_1^2}{E g} \left\{ \frac{\cos^2 \beta h}{\sin^2 \beta h} M_{h1} + \left[\frac{e^{-\beta h} (\cos \beta h - \sin \beta h) + e^{\beta h} (\sin \beta h + \cos \beta h)}{2 \sin^2 \beta h} \right] M_{ho} \right. \\ \left. + \left(\frac{e^{-\beta h} + e^{\beta h}}{2\beta \sin \beta h} \right) S_0 + \left(1 - \frac{\nu}{2} \right) \frac{P}{2\beta^2} \right\} \quad (V-15)$$

$$\delta_{ho} = y(x=h) = \frac{2\beta^2 r_1^2}{Eg} \left\{ \left[\frac{e^{\beta h}}{2\sin^2 \beta h} (\sin^3 \beta h - \cos^3 \beta h) - \frac{e^{-\beta h}}{2\sin^2 \beta h} (\sin^3 \beta h + \cos^3 \beta h) \right] M_{hl} \right. \\ \left. + \frac{\cos^2 \beta h}{\sin^2 \beta h} M_{ho} - \frac{\sin \beta h}{2\beta} (e^{\beta h} + e^{-\beta h}) S_1 + \left(\frac{\cos \beta h}{\beta \sin \beta h} \right) S_0 \right. \\ \left. + (1 - \frac{\nu}{2}) \frac{P}{2\beta^2} \right\} \quad (V-16)$$

$$\theta_{hl} = \theta_h(x=0) = \frac{2\beta^3 r_1^2}{Eg} \left\{ \left[\frac{e^{-\beta h} (\cos \beta h - \sin \beta h) - e^{\beta h} (\sin \beta h + \cos \beta h)}{2\sin^2 \beta h} \right] M_{ho} \right. \\ \left. - \left(\frac{e^{\beta h} - e^{-\beta h}}{2\beta \sin \beta h} \right) S_0 - \frac{1}{\beta} S_1 \right\} \quad (V-17)$$

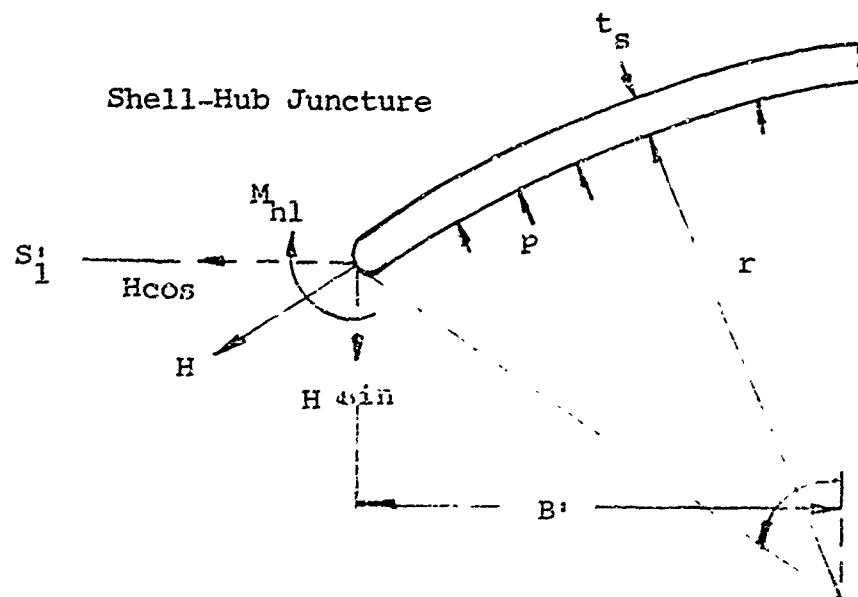
$$\theta_{ho} = \theta_h(x=h) = \frac{2\beta^3 r_1^2}{Eg} \left\{ \left[\frac{e^{\beta h} (\sin \beta h + \frac{2\cos \beta h}{\sin^2 \beta h} - \cos \beta h) - e^{-\beta h} (\sin \beta h - \frac{2\cos \beta h}{\sin^2 \beta h} + \cos \beta h)}{2\sin^2 \beta h} \right] \right. \\ \left. \times M_{hl} - \frac{2\cos \beta h}{\sin \beta h} M_{ho} - \frac{1}{\beta} S_0 \right. \\ \left. - \left[\frac{e^{\beta h} (\sin \beta h + \cos \beta h) + e^{-\beta h} (\cos \beta h - \sin \beta h)}{2\beta} \right] S_1 \right\} \quad (V-18)$$

Articulation of the hub with the ring and shell, i.e., eliminating δ_{hl} , δ_{ho} , θ_{hl} , θ_{ho} via the displacement and rotation equations for the ring and shell, provides the four equations necessary for the evaluation of the undetermined juncture loads M_{ho} , M_{hl} , S_0 , and S_1 .

Top or Shell Analysis

The spherical shell and flat plate are the two classes of tops or shells analyzed. At the hub-shell juncture the internal stresses are replaced by the undetermined edge forces S_1 and H_D and edge moment M_{hl} .

Spherical Shell. The edge loading is replaced by the superposition of a membrane force H (equilibrating the pressure load) and radial force S_1 .



$$H_D = \frac{\pi B'^2 p}{2\pi B'} = \frac{1}{2} B' p = \frac{1}{2} p R \sin \phi = H \sin \phi'$$

$$S_1 = H \cos \phi' = S_1' = H_D \cot \phi' - S_1'$$

The membrane force does not contribute to the rotation. At the edge the rotation is the sum of rotations due to S_1' and M_{hl} .

$$\theta_{sl} = \frac{4\lambda^3}{E t_s K_1} M_{hl} - \frac{2\lambda^2 \sin \phi'}{E t_s K_1} S_1'$$

Similarly, the radial displacement of the edge is the sum of displacements caused by S_1' , M_{ho} , and the radial component of H .

$$\begin{aligned} \delta_{sl} = & \frac{p R^2 (1-\nu) \sin \phi'}{2 E t_s} - \frac{\lambda R \sin^2 \phi'}{E t_s} \left(K_2 + \frac{1}{K_1} \right) S_1' + \\ & + \frac{2\lambda^2 \sin \phi'}{E t_s K_1} M_{hl} \end{aligned}$$

Substituting for $S_1' = H_D \cot \phi' - S_1$,

$$\theta_{sl} = \frac{4\lambda^3}{E t_s K_1} M_{hl} + \frac{2\lambda^2 \sin \phi'}{E t_s K_1} S_1 - \frac{\lambda^2 R \sin \phi' \cos \phi'}{E t_s K_1} p$$

$$\delta_{si} = \frac{2\lambda^2 \sin \phi'}{Et_s K_1} M_{hl} + \frac{\lambda R \sin^2 \phi'}{Et_s} \left(K_2 + \frac{1}{K_1} \right) S_1$$

$$+ \frac{PR^2 \sin \phi'}{2Et_s} (1-\nu) - \lambda \sin \phi' \cos \phi' \left(K_2 + \frac{1}{K_1} \right)$$

where

R = radius of curvature

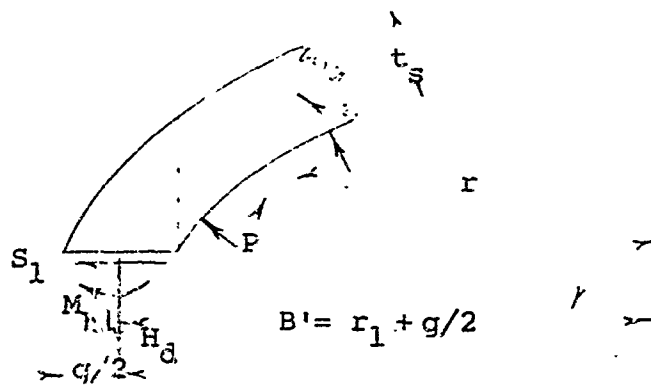
$$\lambda = \sqrt[4]{\frac{3(1-\nu^2)}{\left(\frac{R}{t_s}\right)^2}}$$

$$K_1 = 1 - \frac{1-2\nu}{2\lambda} \cot \phi'$$

$$K_2 = 1 - \frac{1+2\nu}{2\lambda} \cot \phi'$$

and M_{hl} and S_1 are per unit length of circumference.

The effect of the shell's finite thickness should in certain instances be considered although the assumptions of thin shell theory are assumed to always apply. In particular, if the junction is at a plane normal to the axis of symmetry, the edge loads act at a shell location corresponding to the radial center of the hub whereas the pressure acts over a smaller radial section.



Then,

$$\sin \phi' = \frac{r_1}{R} + \frac{q}{2R} = \sin \phi + \frac{q}{2R}$$

$$H_D = \frac{\pi r_1^2 P}{2\pi B'} = \frac{1}{2} \frac{r_1^2}{B'} P$$

Thus,

$$\theta_{s1} = \frac{4\lambda^3}{E t_s K_1} M_{h1} + \frac{2\lambda^2 \sin \phi'}{E t_s K_1} S_1 - \frac{\lambda^2 R \sin \phi' \cos \phi'}{E t_s K_1} \left(\frac{r_1}{B'}\right)^2 P \quad (V-19)$$

$$\begin{aligned} \delta_{s1} = & \frac{2\lambda^2 \sin \phi'}{E t_s K_1} M_{h1} + \frac{\lambda R \sin^2 \phi'}{E t_s} \left(K_2 + \frac{1}{K_1}\right) S_1 \\ & + \frac{P R^2 \sin \phi'}{2 E t_s} (1-\nu) - \lambda \left(\frac{r_1}{B'}\right)^2 \sin \phi' \cos \phi' \left(K_2 + \frac{1}{K_1}\right) \end{aligned} \quad (V-20)$$

If the juncture is parallel to the axis of symmetry (indicated by the dotted line in the above figure), then, of course, $B'=r'$ and $\sin \phi' = \sin \phi$.

Flat Plate. The differential equation for the symmetrical bending of circular plates is

$$\frac{d}{dr} \left(\frac{1}{r} \frac{d}{dr} \left(r \frac{dw}{dr} \right) \right) = \frac{Q}{D} \quad (V-21)$$

where

$$D = \text{flexural rigidity} = \frac{E t_p^3}{12(1-\nu^2)}$$

w = axial deflection at any r

$Q = \frac{Pr}{2}$ for an uniformly (pressure) loaded plate

A general solution to (V-21) is

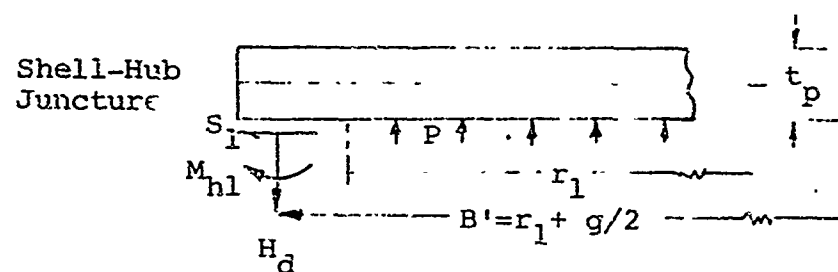
$$w = -\frac{Pr^4}{64D} + \frac{C_1 r^2}{4} + C_2 \ln r + C_3 \quad (V-22)$$

The rotation and moment are given by

$$\theta_p = -\frac{dw}{dr} = \frac{Pr^3}{16D} - \frac{C_1 r}{2} - \frac{C_2}{r} \quad (V-23)$$

$$\begin{aligned} M_r &= -D \left(\frac{d^2 w}{dr^2} + \frac{\nu}{r} \frac{dw}{dr} \right) \\ &= \frac{Pr^2}{16} (3+\nu) - \frac{C_1 D}{2} (1+\nu) + \frac{C_2 D}{r^2} (1-\nu) \end{aligned}$$

The loading system for a juncture normal to the axis of symmetry is shown below



$$H_D = \frac{\pi r_1^2 P}{2\pi B'} = \frac{1}{2} \frac{r_1^2}{B'} P$$

The boundary conditions necessary to evaluate the three integration constants are formed by replacing the shear S_1 with a radial load S_1 acting at the middle-surface and a moment $1/2 t_p S_1$. The plate can be assumed to be simply-supported by loads H_D (any axial deflections of the juncture are due to the ring-hub assembly). Then,

$$w = 0 \quad \text{and} \quad M_r = M_{hl} + \frac{t_p}{2} S_1 \quad \text{at} \quad r = B'$$

$$\theta_p = 0 \quad \text{at} \quad r = 0$$

From (V-22) and (V-23),

$$C_2 = 0$$

$$C_1 = -\frac{2}{D(1+\nu)} \left(M_{hl} + \frac{t_p}{2} S_1 \right) + \frac{PB'^2}{8D} \left(\frac{3+\nu}{1+\nu} \right)$$

$$C_3 = \frac{B'^2}{2D(1+\nu)} \left(M_{hl} + \frac{t_p}{2} S_1 \right) + \frac{PB'^4}{64D} \left[1 - 2 \left(\frac{3+\nu}{1+\nu} \right) \right]$$

Then, from the first of (V-23), the rotation of the plate at its juncture can be found

$$\theta_{pl} = \frac{B'}{D(1+\nu)} (M_{hl} + \frac{t_p}{2} S_1) - \frac{PB'^3}{8D(1+\nu)} \quad (V-24)$$

The radial deflection of the juncture is the superposition of the deflections due to the rotation and the stretching by radial force S_1 in the mid-plane.

$$\delta_{pl} = \frac{(1-\nu)}{E} \frac{S_1}{t_p} B' - \frac{t_p}{2} \theta_{pl} \quad (V-25)$$

where θ_{pl} is given by (V-24) and M_{hl} and S_1 are per unit length of circumference.

If the juncture is parallel to the axis of symmetry, as is the case when the hub is absent, then $B' = r_1$ and the load S_1 contributes no external moment;

$$M_r = M_{hl} \text{ at } r = r_1$$

Equation (V-24) for the edge rotation becomes

$$\theta_{pl} = \frac{r_1}{D(1+\nu)} M_{hl} - \frac{Pr_1^3}{8D(1+\nu)} \quad (V-26)$$

and (V-25) remains unchanged except that (V-26) is used for θ_{pl} .

It bears mentioning that two common requirements for thin plates and shells are that the deflections nowhere exceed half the thickness and that $t/r_1 < 0.1$.

Articulation of the Ring, Hub, and Shell Junctions

The division of the cover structure into a ring, hub, and shell introduced four undetermined juncture loads and moments to compensate for the unknown internal stresses at the junctures. The continuity requirements on the radial deflections and rotations of the junctures provide four equalities which make the problem determinate.

The mathematical task of articulation of the parts is basically algebraic and will not be set down in detail here. However, some general attention will be given to this task below.

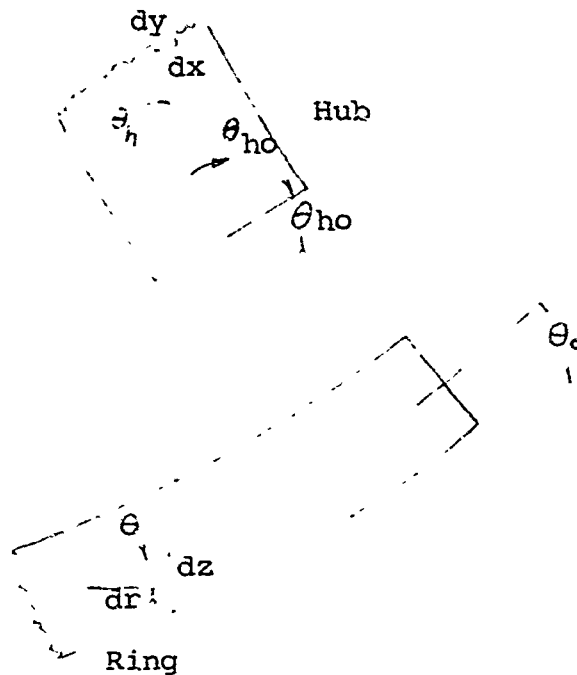
Consider first the junctures' rotations:

$$\theta = \frac{dz}{dr} - \text{ring rotation}$$

$$\theta_h = \frac{dy}{dx} - \text{hub rotation}$$

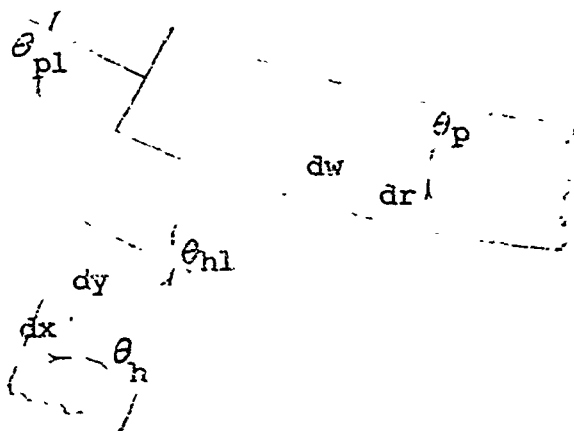
$$\theta_p = -\frac{dw}{dr} \text{ - flat plate rotation}$$

Ring-hub juncture:



$$\theta_{ho} = \theta_o \text{ or } \left(\frac{dy}{dx}\right)_{x=h} = \left(\frac{dz}{dr}\right)_{r=r_1} \quad (V-27)$$

Hub-flat plate juncture:



$$\theta_{hl} = \theta_p \text{ or } \left(\frac{dy}{dx}\right)_{x=0} = \left(\frac{dw}{dr}\right)_{r=B} \quad (V-28)$$

Note: These illustrations are used for matching rotations mathematically and do not indicate any presumed states of deformation.

The radial deflection equalities are given generally by

$$\delta_{ho} = y(r = r_1) - \frac{\pi}{2} \theta_o \quad (V-29)$$

for hub and ring continuity, and

$$\delta_{hl} = \delta_{pl} \quad (V-30)$$

for hub and flat plate continuity. Substitution into (V-27) - (V-30) of the corresponding expressions derived in the Ring Analysis Section through the Top or Shell Analysis Section in terms of S_o , S_1 , M_{ho} , and M_{hl} permit the determination of these hitherto unknown quantities. Note that the equalities given here are algebraically written so that the signs of terms are automatically taken care of.

V-3. Solutions to the Cover Equations

There are yet two unspecified boundary conditions necessary to obtain a solution to the system of cover equations. Mathematically they provide a description of the particular housing design under consideration.

In some instances it may be possible to specify two invariant boundary conditions. For example, if the ring makes no contact outside the bolt circle and the pressure loading is much smaller than the bolt preload, the ring moment M_t at the outer edge is zero, and it may be assumed that the ring deflection at the bolt circle is zero.

To provide a more flexible analysis, it is assumed that one invariant boundary condition is available, the other being imposed by the fastening mechanism for which a load-deflection analysis or curve is assumed to exist. This latter type of boundary condition necessitates an iterative procedure for solution since the loading and deflection of the fastener must be compatible with the loading and deflection of the cover (ring).

The actual process of iteration is accomplished through the reaction loading system which provides a measure of convergence of the solution. In particular, an initial reaction load is chosen; this provides the loading on the fastener, such as bolts arranged along the bolt circle. From the load-deflection characteristic of the fastener, its deflection is determined, which then provides the fourth boundary condition on the ring. All the requirements of the cover equations are then fulfilled, making possible complete cover deformation solution. The reaction load is then adjusted to be compatible with these resulting deformations, and the process repeated until convergence on the reaction load and corresponding deformations is attained.

The next subsection contains a discussion of such a solution for a relatively simple housing configuration. Before pursuing this, it should be emphasized that both the theoretical formulations and method of solution depend upon knowledge of the reaction loading system. Thus, the essence of the problem is one of being able to sufficiently describe the loading of the ring and in such a way as to insure convergence of the solution.

V-4. Sample Cover Problem Solution

The configuration chosen for analysis is a flat plate cover, no hub, whose shell thickness equals the ring thickness and fastened by bolts. The reaction load is provided solely by a narrow-faced seal located entirely within the bolt circle.

There is no radial pressure acting on the ring. The ring-flat plate shell juncture is parallel to the axis, and the juncture conditions are written for a point at their midplane (the ring rotation does not contribute to the ring's radial deflection).

From the ring analysis, (V-3) and (V-8),

$$\theta_o = 2C_1 r_1 \ln r_1 + (C_1 + 2C_2) r_1 + \frac{C_3}{r_1}$$

$$y_1 = C_5 r_1 + \frac{C_6}{r_1}$$

The known ring boundary conditions are

$$Q = -\frac{\bar{W}}{2\pi r}, \quad M_{t1} = M_{ho}, \quad M_{t2} = 0$$

$$\sigma_{r1} = \frac{S_o}{T}, \quad \sigma_{r2} = 0$$

from which

$$C_1 = \frac{\bar{W}}{8\pi D}$$

$$C_2 = \left[\frac{K^2 \ln r_2 - \ln r_1}{1-K^2} - \frac{3+v}{2(1+v)} \right] \frac{\bar{W}}{8\pi D} + \frac{1}{1-K^2} \frac{M_{ho}}{2D(1+v)}$$

$$C_3 = \frac{r_2^2}{1-K^2} \left[2\left(\frac{1+v}{1-v}\right) \ln K \frac{\bar{W}}{8\pi D} + \frac{M_{ho}}{D(1+v)} \right]$$

$$C_5 = \frac{1-\nu}{E} \left(\frac{1}{1-K^2} \right) \frac{S_0}{T}$$

$$C_6 = \frac{1+\nu}{E} \left(\frac{r_2^2}{1-K^2} \right) \frac{S_0}{T}$$

From the flat plate analysis,

$$\theta_{pl} = \frac{r_1}{D(1+\nu)} M_{ho} - \frac{Pr_1^3}{8D(1+\nu)}$$

$$\delta_{pl} = \frac{(1-\nu)}{E} \frac{r_1}{T} S_0 - \frac{T}{2} \theta_{pl}$$

The algebraic juncture equalities are

$$\theta_o = \theta_{pl} \quad \text{and} \quad y_1 = \delta_{pl}$$

Substituting the expressions for the rotations and deflections and eliminating the integration constants yields

$$M_{ho} = \frac{1}{8} r_1^2 (1-\nu) (1-K^2) P - \frac{2(1+\nu) \ln K + (1-\nu)(K-K^2)}{4\pi} \bar{W}$$

$$S_0 = \frac{3}{8} \frac{(1-\nu)(1-K^2)r_1^2}{T} (1-\nu)(1-K^2) - 1 \quad P$$

$$- \frac{3(1-\nu)(1-K^2)}{T} \quad \frac{2(1+\nu) \ln K + (1-\nu)(1-K^2)}{4\pi} \bar{W}$$

for the undetermined juncture moment and shear force.

The fourth boundary condition of axial deflection at the bolt circle is prescribed in terms of the bolt load H_B and preload H_1 as

$$z_B = z(r = r_B) = \frac{H_B - H_1}{n K_B}$$

where n is the number of bolts and $K_B = E_B A_B / l_0$ is the bolt spring constant. To determine K_B the original bolt length, l_0 , must be found. This is done by solving the above system of equations for zero pressure load (the preload state) and using the deflection at the seal, z_G , as the fourth boundary condition (z_G is

determined from the seal load-deflection curve for the preload H_1). This results in the preload deflection at the bolt circle which then permits ℓ_0 to be found. The original bolt length ℓ_0 depends, of course, on the preload.

An iterative procedure for solution can now be established. At a given pressurization a gasket load, i.e., the total reaction load in this case, is chosen. The corresponding bolt load is

$$H_B = H_G + H_D + H_T$$

where H_D and H_T are known in terms of the pressure and H_G is the chosen gasket load. The equivalent moment loading W is

$$\bar{W} = \frac{1}{\ell} (h_G H_G + h_D H_D + h_r H_r)$$

from which M_{ho} , S_0 , and the integration constants C_1 , C_2 , C_3 can be found. The fourth integration constant is then

$$C_4 = \frac{H_B - H_1}{nK_B} - C_1 r_B^2 \ln r_B - C_2 r_B^2 - C_3 \ln r_B$$

where the boundary condition of bolt circle deflection is applied. This permits a complete solution of the cover equations yielding, in particular, the ring deflection at the seal;

$$z_G = C_1 r_g^2 \ln r_g + C_2 r_g^2 + C_3 \ln r_g + C_4$$

The value of z_G then permits a better approximation of the gasket load from the seal's load-deflection curve (not necessarily linear), and the process is repeated until convergent. The final solution is chosen by the criterion that the actual gasket load produce a cover deflection at the seal compatible with the load-deflection characteristic of the seal.

These equations for the flat plate cover were programmed for solution by an IBM 7094 digital computer. The coding was done in Fortran II source language.

The cover dimensions selected are

$$r_1 = 0.5 \text{ in.}$$

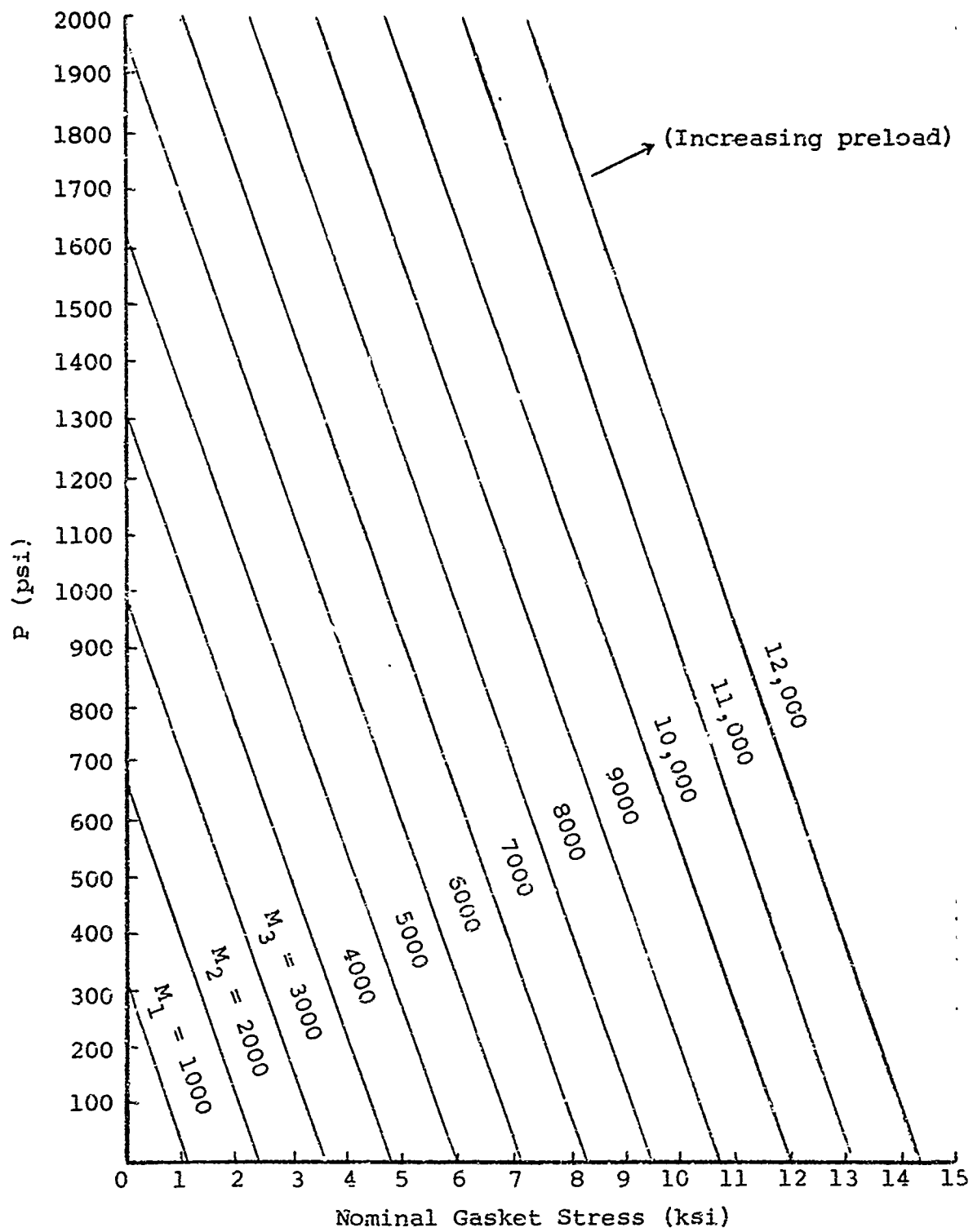
$$r_g = 1.0625 \text{ in.}$$

$$r_B = 2.0 \text{ in.}$$

$$r_2 = 2.5 \text{ in.}$$

$$T = 1.0 \text{ in.}$$

$$A_g \text{ (seal contact area)} = 0.8345 \text{ in}^2$$



Eight steel bolts of cross-sectional area 0.11 sq in. fasten the cover. The seal material chosen was aluminum assumed to have a Young's modulus of 10^7 psi. All seal load-deflection variations were kept in the elastic range. Preloads selected were 1000 lb to 12,000 lb in increments of 1000 lb, and internal pressures ranged from 0 to 2000 psi in 50-psi increments or until the gasket load diminishes to zero.

Curves of nominal contact stress on the seal versus internal pressure are plotted in the accompanying graph where the parameter is the bolt preload. They form a linear family of curves which could easily be described by a single analytical equation. However, the graph illustrates the type of information derivable from the cover theory for more complex cover installations, e.g., seals in the nonlinear ranges of deformations, covers contacting the bottom flange at points other than the seal, etc.

V-5. General Comments and Conclusions

There exist simpler formulations of the cover deflections for cases where the ring behaves approximately as a rigid body.

V-5. Symbols

- A = ring outside diameter
- B = ring inside diameter, also head diameter
- D = flexural modulus of head or ring = $E/12(1-\nu^2)$ (t^3 or T^3)
- d = one-half of central angle of head
- E = Young's modulus
- H_D = axial pressure force on head = $\pi B^4/4 P$
- H_T = equivalent axial pressure force acting directly on ring due to fluid pressure between ring inside diameter and seal
- h_D = lever arm equal to the radial distance between point of application of H_D and bolt circle
- h_T = lever arm equal to the radial distance between point of application of H_T and bolt circle
- l = radial breadth of ring
- M_h = ring-moment of hub at any point
- M_{hi} = ring-moment between hub and ring
- M_{ho} = ring-moment between head and hub
- M_r = moment loading of ring at any radius
- P = internal pressure
- Q = axial shear force of ring at any radius
- R = mean radius of head
- S_h = radial shear load of hub at any point
- S_i = radial load between hub and ring
- S_o = radial load between head and hub
- T = ring thickness
- t = head thickness
- \bar{W} = equivalent bolt load, or total force applied at the ring outside diameter and (oppositely) at the inside diameter such that \bar{W}_1 equals the total moment loading on the ring
- W_1 = initial bolt load under no internal pressure
- W_2 = bolt head under internal pressure
- y = radial displacement of hub at any point
- Z = axial displacement of ring at any radius
- θ = angle of rotation of ring at any radius
- θ_h = angle of rotation of spherical head at its juncture with hub
- θ_p = angle of rotation of flat head at its juncture with hub
- ν = Poisson's ratio (0.3)
- σ_h = radial displacement of spherical head at its juncture with hub
- σ_{ir} = radial displacement of ring at its juncture with hub
- σ_p = radial displacement of flat head at its juncture with hub

APPENDIX VI
STRUCTURAL ANALYSIS OF SEALS
AND DERIVATION OF FACTOR K

Six structural seal configurations--X, K, E, W, O and C cross-sectional shapes--are analyzed and discussed in this appendix. The seals, although commercially available items, were chosen solely on the basis of their structural complexity and general representation of most metallic seals, rather than their ability to seal or provide other benefits. Simple beam theory is employed and the basic assumptions set forth. Seal deflection by external forces is presented along with correlation experimental data. The designer should be able to choose the most applicable analysis and either use it directly or incorporate similar assumptions to suit his needs.

The seal shapes studied ranged from 3/8- to 3-5/8-in. out side diameter and were fabricated from stainless steel, aluminum, and Inconel X. Figures 10-14 through 10-19 show cross sections of the seal, materials of construction, and dimensions.

To facilitate correlation of the theoretical analysis with experimental results, accurate dimensional data of the seal shape are necessary. In many cases, only an average dimension could be obtained because the surfaces to be measured were inaccessible. Closer measurement would have caused destruction of the seal. To illustrate the need for accurate measurement, the leg of a V-shaped seal deflects approximately with the cube of the leg thickness. If the leg thickness is between 0.010 and 0.012 in., a variation of 50 per cent between the two values is predicted. This point is not particularly pertinent to the present analysis but it does emphasize the need for rigid and accurate quality control procedures during seal fabrication.

Dimensions vary not only from point to point along the same circumference and at different cross sections of the same seal, but also from seal to seal of the same commercial model. In the theoretical analyses that follow, dimensions are of extreme importance. Certain dimensions are considered critical. The reason for this is that, although the size variation may be only 0.001 - 0.003 in., most of the critical dimensions lie in the size range from 0.010 - 0.100 in.

The structural analysis performed on the seal configurations in this section is based mainly on simple beam theory and follows procedures outlined in AFRPL-TDR-65-61, Section 5. The same basic assumptions apply here and can be stated as:

- (1) Bulk behavior of seals is elastic over a significant range of their commonly encountered deformations (largely linear load-deflection curves that were experimentally verified).

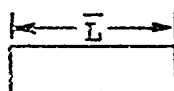
(2) Load-deflection behavior of seals can be determined for all practical purposes by two-dimensional analysis of their cross sections.

(3) The cross-sectional shapes are idealized to the extent that machining effects and irregularities are ignored, e.g., actual fillet corners are idealized as sharp corners.

(4) Where necessary, characteristic lengths are used in calculations, further idealizing certain asymmetric shapes as symmetric working models. For instance, the bar shape



is idealized as



where the characteristic length is $\bar{L} = 1/2 (l_1 + l_2)$. The effects of axial loading on the seal leg can be neglected with an error in bearing moment of less than 5 per cent if the axial load

$$W_A \leq 0.125 \frac{EI}{l^2}$$

where I = leg moment of inertia (in.⁴)

l = seal leg length (in.)

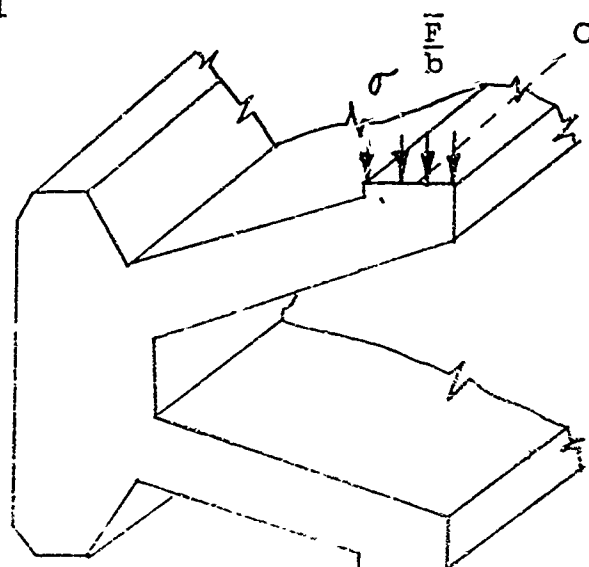
The simple beam approach was used in the analysis of these seals for two basic reasons:

(1) The complex shape of some of the seals makes the homologous approach inapplicable.

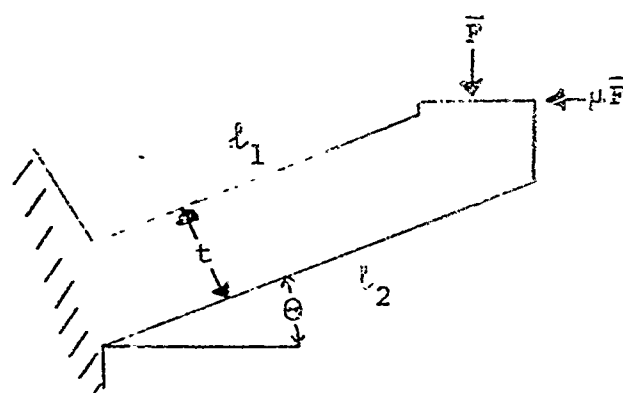
(2) The use of the basic simple beam approach will provide the designer with an illustration of another design tool available for use in seal design.

The six seal configurations (X, K, W, E, O and C) analyzed in detail are representative of many metallic seals. Although the analyses are not intended to cover all seal configurations, they illustrate the applicability of this method to practical seal design.

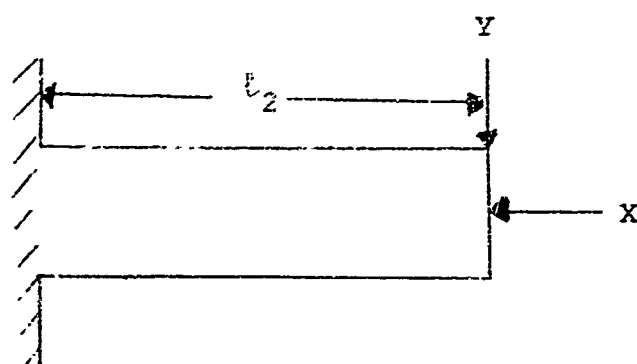
K-Shaped Seal



Seal legs:



Idealized Cantilever Beam:



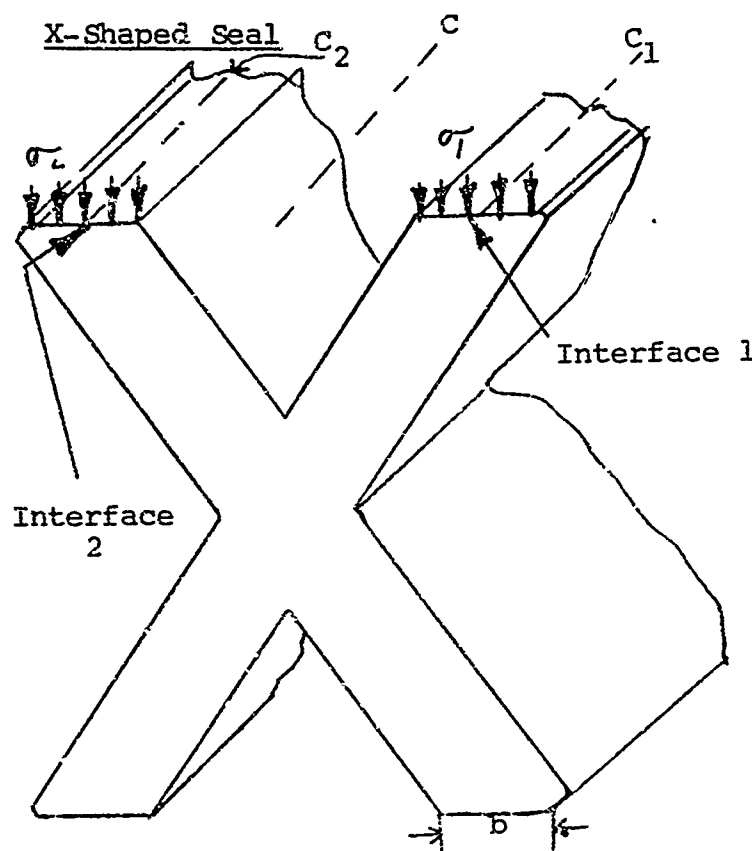
$$X = F (\sin\theta + \mu\cos\theta)$$

$$Y = F (\cos\theta - \mu\sin\theta)$$

The characteristic length is assumed to be l_2 .

Neglecting the axial compressive load Y ,

$$Y_f = \frac{Y(l_2)^3}{3EI}$$



Where:;

σ = contact stress (psi)

C_1 = circumference of area 1 (in.)

C_2 = circumference of area 2 (in.)

C = mean circumference (in.)

F = contact force (lb)

A_1 = contact area 1 (in.²)

A_2 = contact area 2 (in.²)

$A_c = A_1 + A_2$

\bar{F} = force per unit circumference (lb/in.)

y = deflection (in.)

Assume

$$\sigma = \sigma_1 = \sigma_2$$

$$\sigma_1 = \frac{F_1}{A_1}, \quad \sigma_2 = \frac{F_2}{A_2}$$

$$A_1 = bC_1, \quad A_2 = bC_2$$

$$\therefore \sigma_1 = \frac{F_1}{bC_1}, \quad \sigma_2 = \frac{F_2}{bC_2}$$

$$F = F_1 + F_2$$

$$\sigma = \frac{F}{A_c}$$

$$\therefore \sigma = \frac{F_1}{A_c} + \frac{F_2}{A_c}$$

$$\sigma = \frac{F_1}{A_1} \frac{A_1}{A_c} + \frac{F_2}{A_2} \frac{A_2}{A_c}$$

$$\bar{F}_1 \equiv \frac{F_1}{C_1}, \quad \bar{F}_2 \equiv \frac{F_2}{C_2}, \quad A_1 \approx bC_1, \quad A_2 \approx bC_2$$

$$\therefore \sigma = \frac{\bar{F}_1}{b} \frac{A_1}{A_c} + \frac{\bar{F}_2}{b} \frac{A_2}{A_c}$$

But $\sigma_1 = \sigma_2$ by assumption; $\bar{F}_1 = \bar{F}_2 \equiv \bar{F}_{12}$

Hence,

$$\sigma = \frac{\bar{F}_{12}}{b} \left(\frac{A_1}{A_c} + \frac{A_2}{A_c} \right) = \frac{\bar{F}_{12}}{b}$$

Define $\bar{F} \equiv \frac{F}{C}$

$$\therefore \bar{F} = \frac{\sigma A_c}{C} = \frac{\bar{F}_{12} A_c}{bC}$$

$$A_c = bC_1 + bC_2$$

$$\therefore \bar{F} = \bar{F}_{12} \left(\frac{C_1 + C_2}{C} \right)$$

$$C_1 = \pi D_1 = \pi (ID + b); \quad C_2 = \pi D_2 = \pi (OD - b)$$

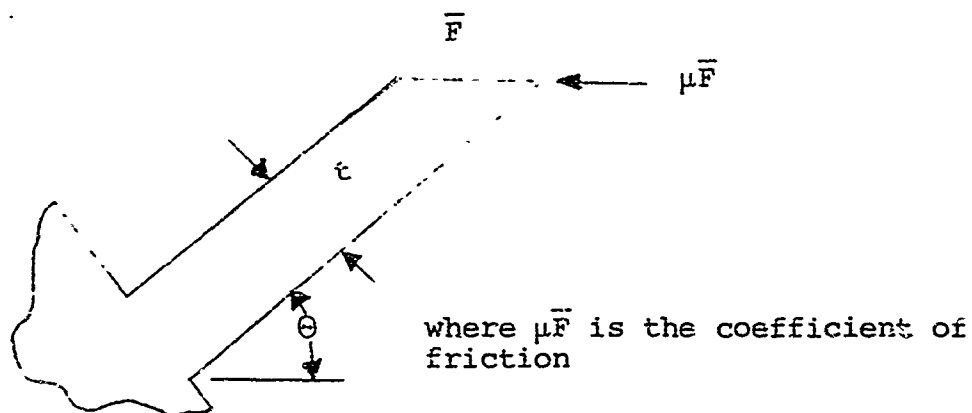
$$C = \pi D = \pi \left(\frac{OD + ID}{2} \right)$$

$$\bar{F} = \bar{F}_{12} \left(\frac{ID + b + OD - b}{\frac{1}{2} (OD + ID)} \right)$$

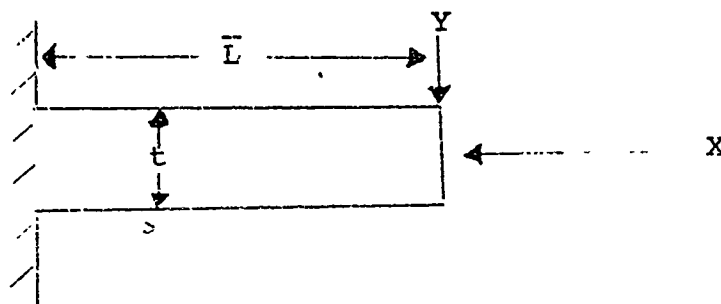
Hence, $\bar{F} = 2\bar{F}_{12}$

Thus, by assuming that the contact stress is distributed equally and symmetrically over the entire contact area, it is shown that the total force per unit length of mean circumference equals twice the force per unit length of circumference of either the inside or outside leg. This assumption allows the derivation of a simpler load-deflection relationship based on the analysis of only one leg.

Seal Leg:



Idealized Cantilever Beam:



$$X = \bar{F}(\sin\theta + \mu\cos\theta)$$

$$Y = \bar{F}(\cos\theta - \mu\sin\theta)$$

Neglecting the axial compressive load, X

$$\delta f = \frac{Y(\bar{L})^3}{3EI}$$

$$\delta f = F(\cos\theta - \mu\sin\theta) \frac{4}{E} \left(\frac{\bar{L}}{t}\right)^3$$

where $I = 1/12 t^3$ per unit length of circumference.

Let $E = 30 \times 10^6$ psi

$\mu = 0.2$ (coefficient of static friction)

$$Y_f = \left(\frac{4}{30} \times 10^{-6}\right) (\cos\theta - 0.2 \sin\theta) \left(\frac{\bar{L}}{t}\right)^3 F_{12}$$

But $\bar{F}_{12} = 1/2 \bar{F}$ and $y_t = 2y_f$ since both upper and lower legs contribute to the total deflection. The deflection of the legs downward is the component $y = \cos\theta y_t$. Hence

$$F = Y$$

where $K = (7.5 \times 10^6) (\cos\theta - 0.2 \sin\theta)^{-1} \left(\frac{t}{\bar{L}}\right)^3 \cos\theta$.

Results:

Seal	θ	$\cos\theta - 0.2 \sin\theta$	t	\bar{L}	$\left(\frac{t}{\bar{L}}\right)^3$	K	K_{ex}^*
X-1	46°1'	0.551	0.017	0.092	6.31×10^{-3}	60×10^3	87×10^3
X-2	47°	0.536	0.026	0.118	10.70×10^{-3}	102×10^3	159×10^3
X-3	39°4'	0.650	0.020	0.102	7.54×10^{-3}	27×10^3	97×10^3

* K_{ex} = experimentally obtained value of K

Consideration of the effects of the end compressive load:
This load can be neglected if

$$X < 0.125 \frac{EI}{l^2}$$

For seal X-2,

$$E = 30 \times 10^6$$

$$I = 1/12 t^3$$

$$t = 0.026$$

$$l = 0.118$$

$$0.125 \frac{EI}{l^2} = 394.5$$

$$X = \bar{F}_{12} (\sin\theta + \mu\cos\theta)$$

$$= \frac{1}{2} (\sin\theta + \mu\cos\theta) \bar{F}$$

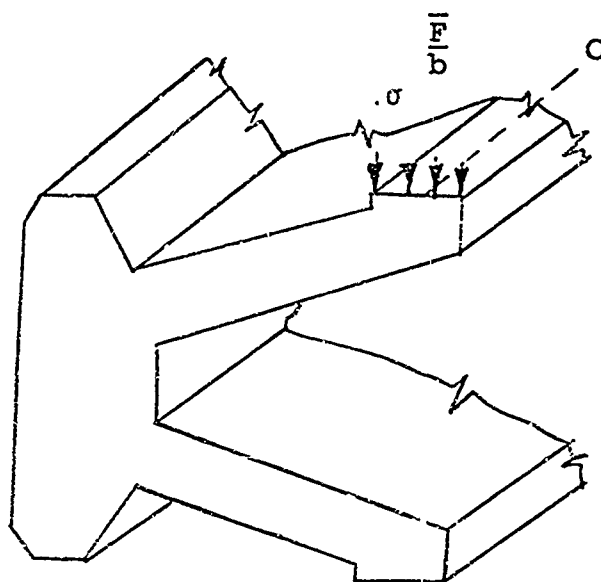
$$\mu = 0.20 = 47^\circ$$

$$\therefore X = 0.434 \bar{F}$$

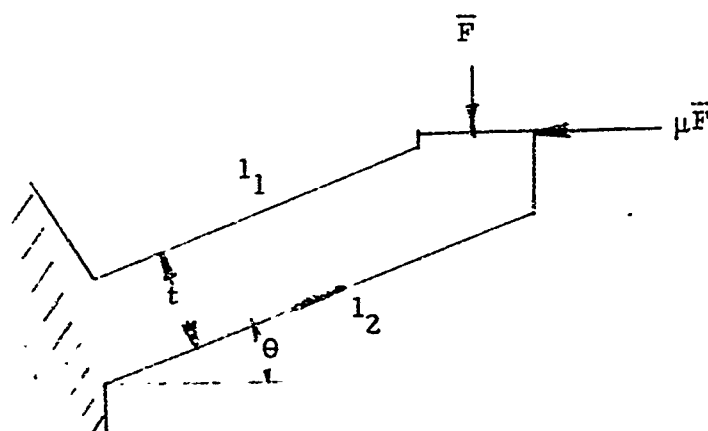
$$F = 909 \text{ lb/in.}$$

The criterion obviously depends on y . When $\bar{F} = (159 \times 10^3)y$, \bar{F} is less than 909 for y up to 0.0057 in. Other seals can be treated in a similar manner.

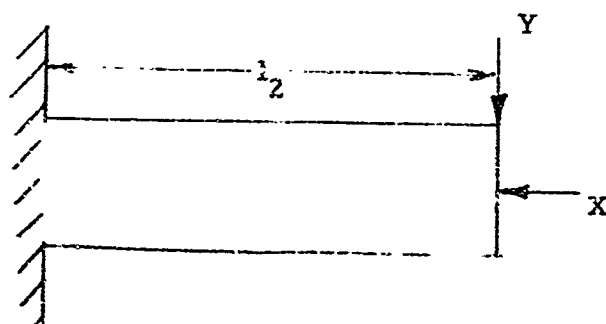
K-Shaped Seal



Seal legs:



Idealized Cantilever Beam:



$$X = \bar{F} (\sin\theta + \mu\cos\theta)$$

$$Y = \bar{F} (\cos\theta + \mu\sin\theta)$$

The characteristic length is assumed to be l_2 .

Neglecting the axial compressive load Y ,

$$y_f = \frac{y(l_2)^3}{3EI}$$

$$y = 2y_f (\cos\theta)$$

Let:

$$E = 30 \times 10^6 \text{ psi}$$

$$I = 1/12t^3 \text{ per unit length of circumference}$$

$$\mu = 0.2 \text{ (coefficient of static friction)}$$

Hence,

$$\bar{F} = Ky$$

where

$$K = (3.75 \times 10^6) (\cos\theta - 0.2 \sin\theta)^{-1} \left(\frac{t}{l_2}\right)^3 \cos\theta$$

Results:

Seal	θ	$\cos\theta - 0.2\sin\theta$	t	l_2	$\left(\frac{t}{l_2}\right)^3$	K	K(exp)
K-1	20° 6'	0.8688	0.012	0.069	5.26×10^{-3}	21.3×10^3	30.4×10^3
K-2	17° 6'	0.8970	0.0135	0.068	7.82×10^{-3}	31.3×10^3	19.5×10^3

Illustration of the effects of the critical dimensions:

Consider the K-1 seal.

$$\text{Let } t = 0.013 \text{ and } l_2 = 0.068$$

$$\left(\frac{t}{l_2}\right)^3 = 6.99 \times 10^{-3}$$

$$K = 30.2 \times 10^3$$

$$\text{Let } t = 0.012 \text{ and } l_2 = l_1 = 0.065$$

$$\left(\frac{t}{l_2}\right)^3 = 6.29 \times 10^{-3}$$

$$K = 27.1 \times 10^3$$

Consideration of the effects of the end compression load:

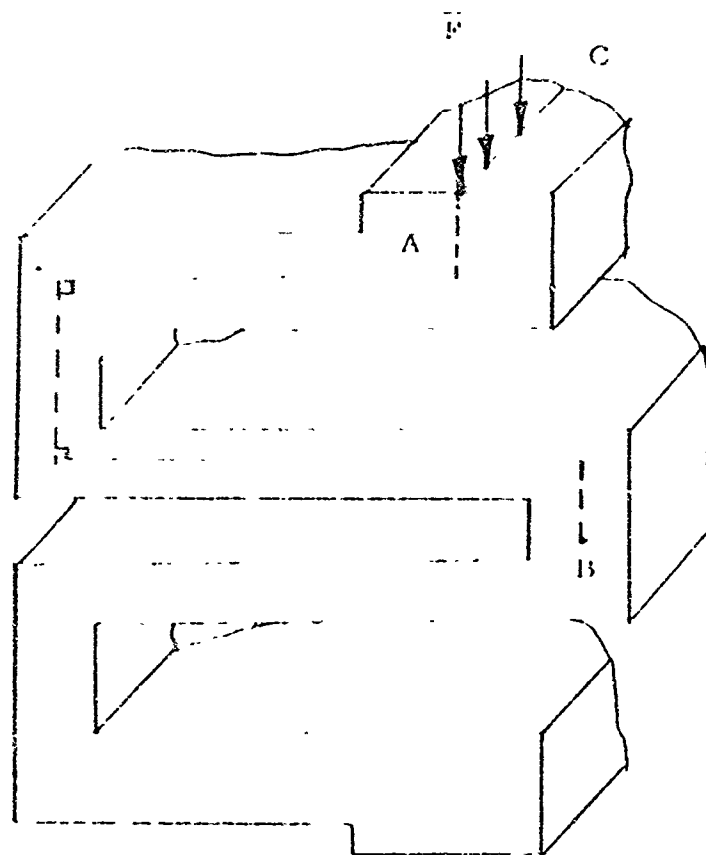
This load can be neglected if, $X < 0.125 \frac{EI}{l^2}$.

For seal K-2,

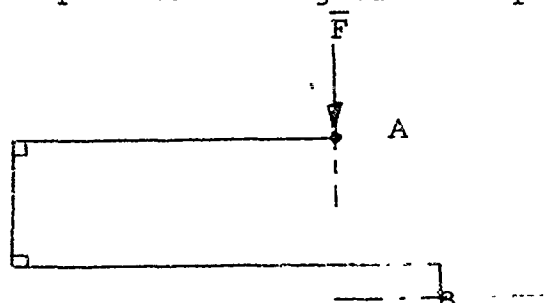
$$\bar{F} = 0.125 (\sin\theta + \mu\cos\theta)^{-1} (2.5 \times 10^6) \frac{t^3}{l^2}$$

$$\bar{F} < 345$$

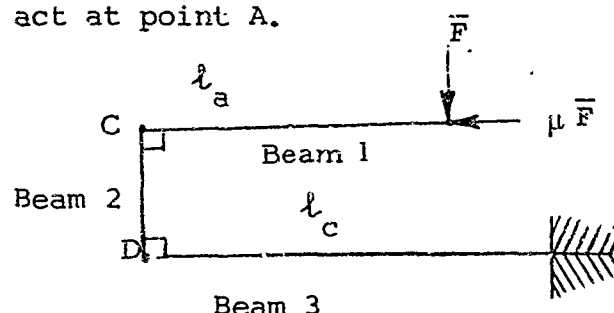
Using $\bar{F} = (19.5 \times 10^3) y$, this criterion is valid for $y < 0.016$ in.



Consider the multiple-beam configuration represented by the dashed lines.



Point A moves along the vertical and Point B along the horizontal. It will be assumed that point B is fixed and that friction forces act at point A.



Two fundamental assumptions are:

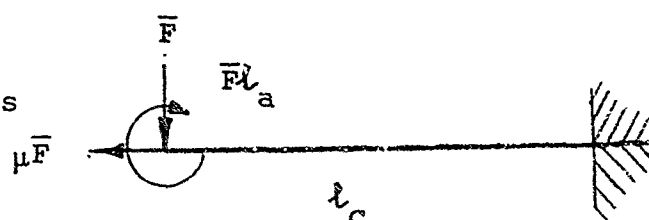
- (1) Right angles remain right angles during deformations.
- (2) Axial loads are negligible in deflections normal to the axis.

Consider beam 3. The loading of beam 3 due to the force \bar{F} applied to the end of beam 1 is approximated by replacing the load \bar{F} with its equivalent load and moment. By the principle of superposition, the deflection at the end of beam 3 is the sum of the deflection caused by load \bar{F} and moment $\bar{F}l_a$

$$y_c = y_1(\bar{F}) + y_2(\bar{F}l_a)$$

The same principle applies to the angle θ

$$\theta_c = \theta_{1c}(\bar{F}) + \theta_{2c}(\bar{F}l_a)$$



The deflection and angle are expressed in terms of the loads and moments as follows

$$y_{1c}(F) = \frac{1}{3} \frac{F(l_c)^3}{EI_c}$$

$$y_{1c}(\bar{F}) = \frac{1}{2} \frac{F(l_c)^2}{EI_c}$$

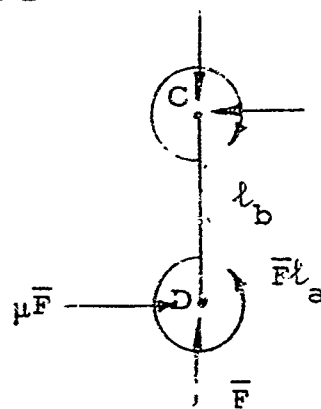
$$y_{2c}(\bar{F}l_a) = -\frac{\bar{F}}{2} \frac{l_2(l_c)^2}{EI_c}$$

$$y_{2c}(\bar{F}l_a) = -\frac{\bar{F}l_a l_c}{EI_c}$$

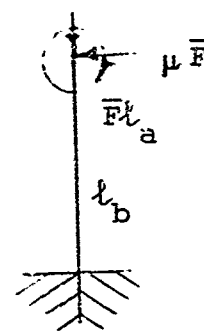
$$y_c = \frac{\bar{F}(l_c)^2}{EI_c} \left[\frac{l_c}{3} - \frac{l_a}{2} \right]$$

$$\theta_c = \frac{\bar{F}l_c}{EI_c} \left[\frac{l_c}{2} - l_a \right]$$

Consider beam 2:



Since end D is fixed to beam 3 and it was assumed that D remains a right angle, beam 2 can be treated as a cantilever beam, with the loading approximated as shown.



The deflection angle of beam 2 can be determined by the principle of superposition

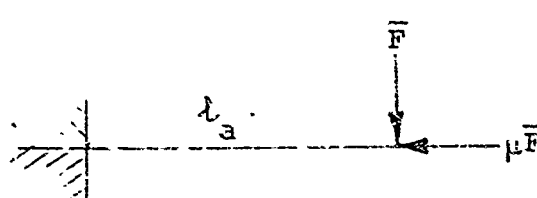
$$\theta_b = \theta_{1b}(\mu\bar{F}) + \theta_{2b}(\bar{F}l_a)$$

$$\theta_{1b} = -\frac{\mu\bar{F}(l_b)^2}{2EI_b}$$

$$\theta_{2b} = \frac{\bar{F}l_a l_b}{EI_b}$$

$$\theta_b = \frac{\bar{F}l_b}{EI_b} \left[l_a - \frac{\mu l_b}{2} \right]$$

Consider beam 1:



$$y_a = \frac{1}{3} \frac{\bar{F} l_a^3}{EI_a}$$

Consider the multiple-beam configuration, $y_T = y_c - l_a \theta_c + l_a \theta_b + y_a$

$$y_T = \frac{12\bar{F}}{E} \left[\frac{1}{3} \left(\frac{l_c}{t_c} \right)^3 - \frac{l_a (l_c)^2}{(t_c)^3} + \frac{(l_a)^2 (l_c)}{(t_c)^3} + \frac{(l_a)^2 l_b}{(y_b)^2} - \frac{l_a (l_b)^2}{2(t_b)^3} + \frac{1}{3} \left(\frac{l_a}{t_a} \right)^3 \right]$$

Hence, the load-deflection equation is

$$\bar{F} = \frac{E}{24} \left[\frac{1}{3} \left(\frac{l_c}{t_c} \right)^3 - \frac{l_a (l_c)^2}{(t_c)^3} + \frac{l_c (l_c)^2}{(t_c)^3} + \frac{l_b (l_b)^2}{(t_b)^3} - \frac{l_b (l_b)^2}{2(t_b)^3} + \frac{1}{3} \left(\frac{l_a}{t_a} \right)^3 \right]^{-1} y$$

where $y = 2y_T$ and

$$E = 30 \times 10^6$$

$$l_a = l_1 - \frac{b}{2} + \frac{t_3}{2}$$

$$l_b = g - \frac{t_1}{2} - \frac{t_2}{2}$$

$$l_c = l_2 - \frac{t_3}{2} + \frac{t_4}{t}$$

$$l_e = t_1$$

$$t_b = t_3$$

$$t_c = t_2$$

$$\mu (\text{coefficient of static friction}) = 0.2$$

Results:

Using the dimensions of the W-1 seal gives:

$$K = 18.8 \times 10^3$$

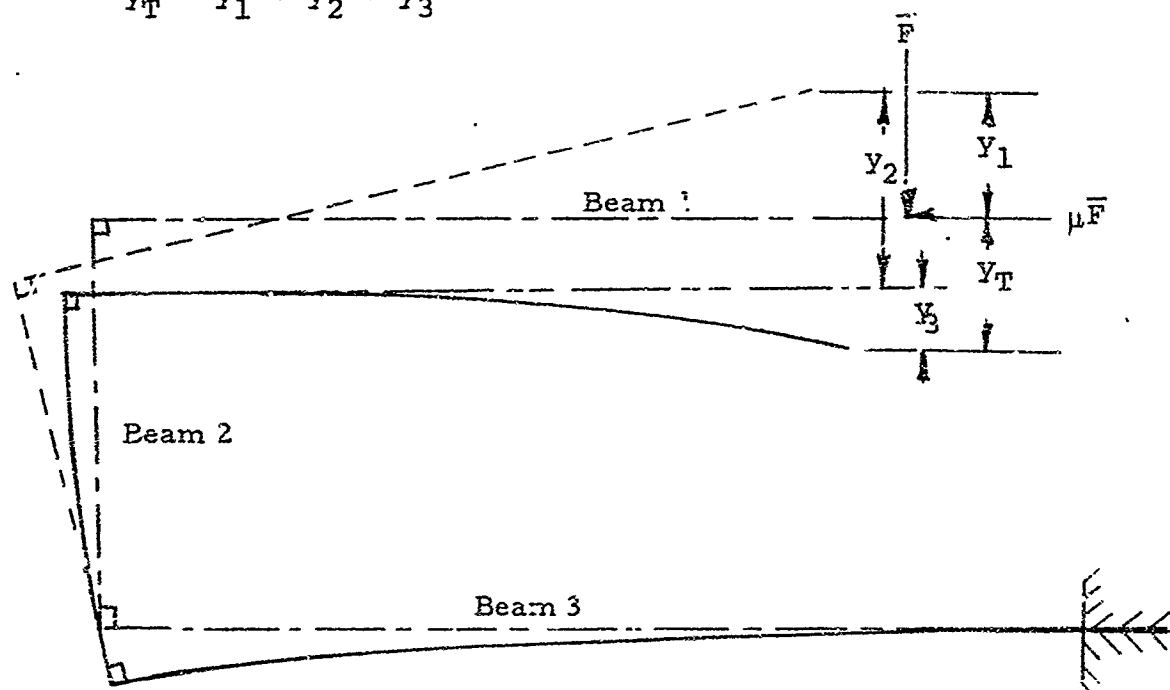
where $K = y\bar{F}$.

Because of difficulties in measuring dimensions of these seals and obtaining accurate average values, the two W-2 seals were not completely dimensioned. However, the cross sections of all these seals are supposed to be identical, therefore, their values of K should be approximately equal.

<u>Seal</u>	<u>K_{ex}</u>
W-1	31.8×10^3
W-2	26.4×10^3
W-3	30.3×10^3

Possible states of deformation:

$$Y_T = Y_1 + Y_2 + Y_3$$



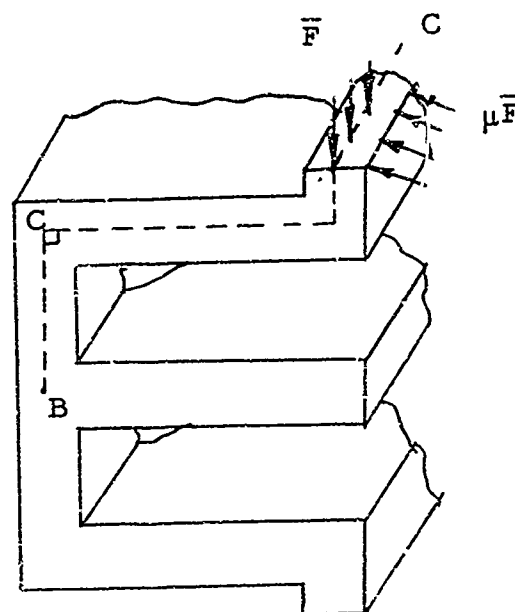
- Initial state
- State after bending of beam 3
- State after bending of beam 2
- State after bending of beam 1
- Final state

$$y_1 = \frac{12\bar{F}}{E} \left[\frac{1}{3} \frac{l_c^3}{(t_c)^3} - \frac{l_a(l_a)^2}{(t_c)^3} + \frac{l_c(l_a)^2}{(t_c)^3} \right]$$

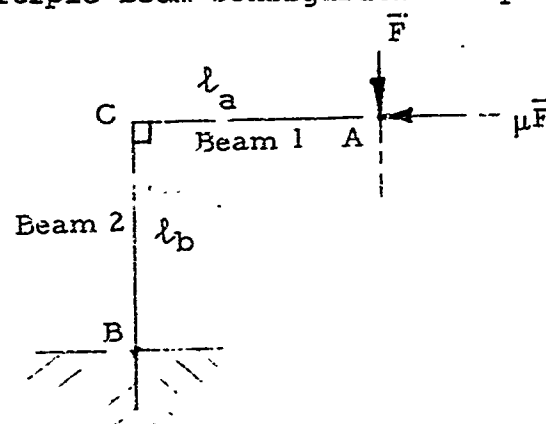
$$y_2 = \frac{12\bar{F}}{E} \left[\frac{l_b(l_a)^2}{(t_b)^2} - \frac{\mu l_a(t_b)^2}{2(t_b)^3} \right]$$

$$y_3 = \frac{12\bar{F}}{3E} \frac{l_a^3}{(t_a)^3}$$

E-Shaped Seal



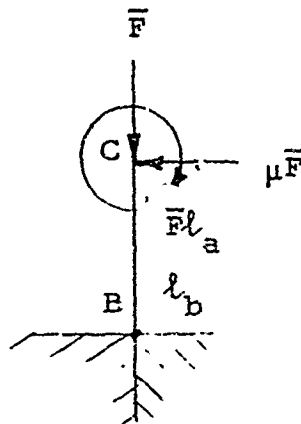
Consider the multiple-beam configuration represented by the dashed lines.



Point A moves along the vertical and point B is assumed fixed in the horizontal direction and able to support movements due to the rigidity of the relatively large, continuous center section, and is fixed in the vertical direction as a result of symmetrical loading. Thus, horizontal friction forces will be assumed to act as point A. The two fundamental assumptions underlying this analysis are:

- (1) Right angles remain right angles during deformations.
- (2) Axial loads are negligible in deflections normal to the axis.

Consider beam 2:



Using the principle of superposition

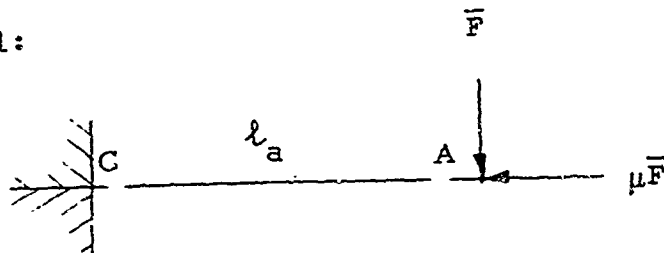
$$\theta_b = \theta_{1b}(\mu, \bar{F}) + \theta_{2b}(\bar{F}, l_a)$$

$$\theta_{1b} = -\frac{\mu \bar{F} (l_b)^2}{2EI_b}$$

$$\theta_{2b} = \frac{\bar{F} l_a l_b}{EI_b}$$

$$\theta_b = \frac{\bar{F} l_b}{EI_b} \left[l_a - \frac{\mu}{2} l_b \right]$$

Consider beam 1:



Since end point C is fixed to the free end of beam 2, its position in space is determined; since the angle between the two beams is assumed fixed, the slope at that point must be zero. Thus, beam 1 can be treated as a cantilever beam as shown.

$$y_a = \frac{1}{3} \frac{\bar{F} (l_a)^3}{EI_a}$$

Consider the multiple-beam configuration:

$$y_T = y_a + l_a \theta_b$$

$$y_T = \frac{12\bar{F}}{E} \frac{1}{3} \left(\frac{l_a}{t_a} \right)^3 + \frac{l_a (l_a)^2}{(t_b)^3} - \frac{\mu}{2} \frac{l_a (l_b)^2}{(t_b)^3}$$

Hence, the load-deflection equation is:

$$\bar{F} = Ky$$

where

$$K = \frac{E}{24} \frac{1}{3} \left(\frac{l_a}{t_a} \right)^3 + \frac{l_b (l_a)^2}{(t_b)^3} - \frac{\mu}{2} \frac{l_a (l_b)^2}{(t_b)^3}^{-1}$$

and

$$y = 2y_T$$

$$E = 30 \times 10^6 \text{ (steel)}$$

$$E = 12 \times 10^6 \text{ (aluminum)}$$

$$l_a = l - \frac{b}{2} + \frac{t_2}{2}$$

$$l_b = \frac{hw}{2} - \frac{t_1}{2}$$

$$t_a = t_1$$

$$t_b = t_2$$

$$\mu = 0.2 \text{ (coefficient of static friction)}$$

Results:

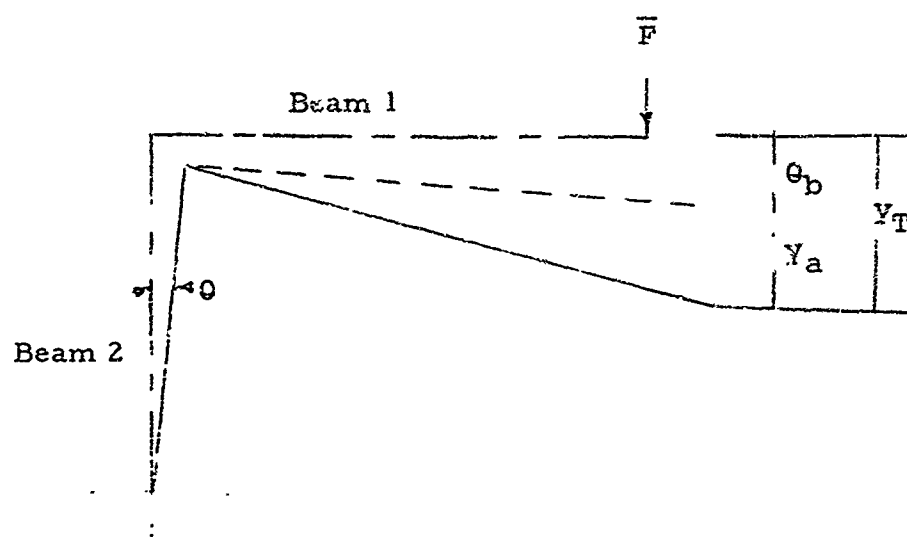
Seal	l_a	l_b	t_a	t_b	K	K_{ex}
E-1	0.052	0.037	0.020	0.0235	96.0×10^3	46.9×10^3
E-2	0.053	0.037	0.020	0.0215	78.5×10^3	42.0×10^3
E-3	0.055	0.037	0.020	0.0185	21.4×10^3	21.9×10^3

The most difficult dimension to measure is the thickness $t_a = t_1$. These calculations are based on $t_a = 0.020$ in. as measured in the gage laboratory. However, microphotographs of the E-1 seal, ground and polished, indicate that this critical dimension might be closer to 0.013 in. Based on this value for the E-2 seal,

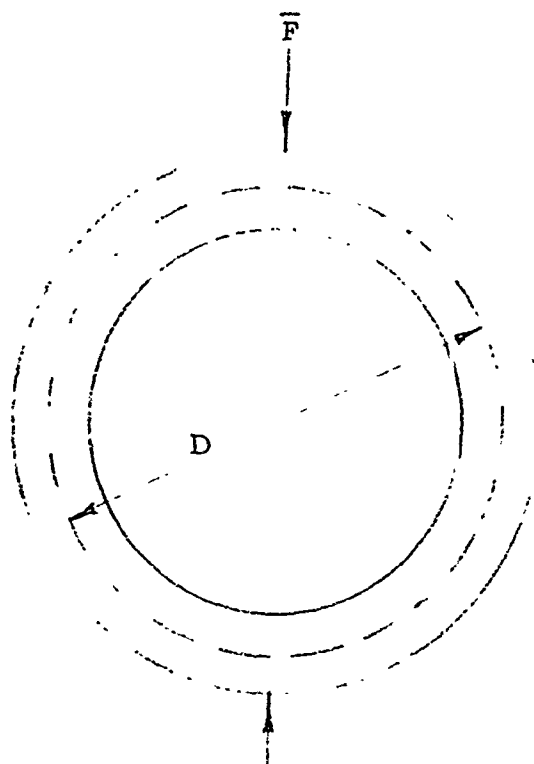
$$K = 43.4 \times 10^3,$$

in closer agreement with the experimental K . Since both this seal and the E-2 seal should have the same cross sections, a similar result could be expected for the latter.

Possible state of deformation:



O-Ring Seal



$$y = 0.149 \frac{\bar{F} R^3}{EI}$$

where

$$R = \frac{D}{2}$$

$$I = \frac{1}{12} t^3 \text{ per unit of contact circumference}$$

$$y = 0.2235 \frac{\bar{F} D^3}{Et^3}$$

For $E = 30 \times 10^6$,

$$\bar{F} = (134.2282 \times 10^6) \left(\frac{t}{D}\right)^3 y$$

or

$$\bar{F} = Ky$$

where

$$K = (134.2282 \times 10^6) \left(\frac{t}{D}\right)^3.$$

Results:

Seal	h	D	t	$(\frac{t}{D})^3$	K	K _{ex}
O-1	0.122	0.112	0.010	0.7118×10^{-3}	95.5×10^3	17.7×10^3
O-2	0.126	0.106	0.020	6.7169×10^{-3}	901.6×10^3	131.2×10^3
O-3	0.063	0.051	0.012	13.0267×10^{-3}	1749×10^3	146.2×10^3

These values of K do not agree well with K_{ex}.

Assume:

$$y = \frac{\bar{F} R^3}{EI}$$

$$\bar{F} = (20 \times 10^6) (\frac{t}{D})^3 y$$

or

$$\bar{F} = K_a \delta,$$

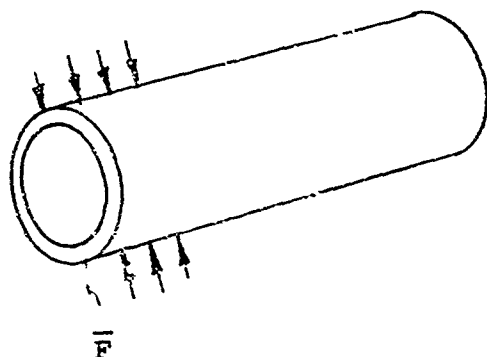
where

$$K_a = (20 \times 10^6) (\frac{t}{D})^3$$

Semiempirical Results:

Seal	K _a	K _{ex}
O-1	14.2×10^3	17.7×10^3
O-2	134×10^3	131.2×10^3
O-3	261×10^3	146.2×10^3

Load - Deflection experiment of a hollow circular cylinder:

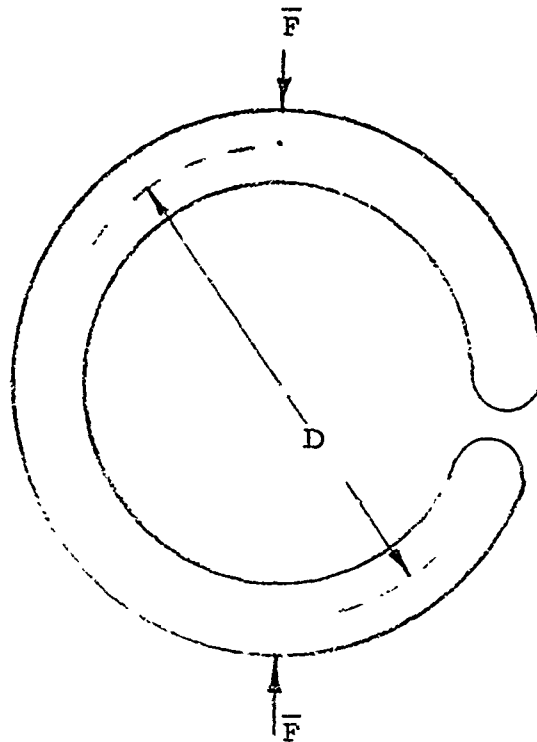


Results:

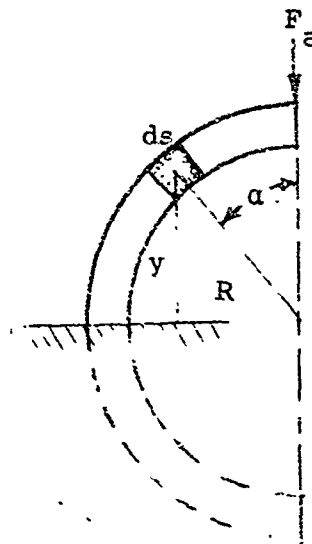
<u>Description</u>	<u>l</u>	<u>t</u>	<u>D</u>	<u>$(\frac{t}{D})^3$</u>	<u>K</u>	<u>K_a</u>	<u>K_{ex}</u>
Hollow circular cylinder	2.56	0.020	0.105	6.91×10^{-3}	928×10^3	138×10^3	141×10^3

Thus, not only for O-rings, but for two-dimensional deformation of a hollow circular cylinder, the equation $y = FR^3/EI$ appears to be the more accurate load-deflection equation.

C-Ring Seal



The C-Ring can be analyzed as a quarter ring by the reflection method.



$$M_a = F_a / R \sin \alpha$$

$$ds = R d \alpha$$

The energy method, by applying a dummy load in the direction of loading, gives

$$y_A = \frac{\pi \bar{F} R^3}{4EI}, \quad F_a = \bar{F}$$

for the quarter ring. The total deflection is $y = 2y_A$.

$$E = 30 \times 10^6 \text{ psi}$$

$$I = \frac{1}{12} t^3 \text{ per unit length of circumference}$$

$$R = D/2$$

Hence,

$$\bar{F} = Ky$$

where

$$K = (12.7324 \times 10^6) \left(\frac{t}{D}\right)^3$$

Results:

Seal	D	t	$\left(\frac{t}{D}\right)^3$	K	K_{ex}
C-1	0.0846	0.010	1.6515×10^{-3}	21.0×10^3	70.9×10^3
C-2	0.0717	0.015	9.1562×10^{-3}	116.7×10^3	74.0×10^3

It is expected that the experimental values of K are not very accurate since the relative magnitudes of $(t/D)^3$ clearly indicate that comparable values for K_{ex} should not be obtained for the two seals.

Note: This quarter ring analysis can be used for the O-Ring configuration with the following two modifications:

$$(1) F_a = 1/2 \bar{F}$$

(2) By symmetry, the slope at the point of loading must be zero. Therefore, a second moment M_D will be applied there, necessitating the following changes:

$$M = M_a = M_D = F_a R \sin \alpha - \frac{2}{\pi} F_a R$$

$$y_A = \frac{\pi F_a R^3}{4EI} - \frac{2}{\pi} \frac{F_a R^3}{EI}$$

Thus, $y = 2y_A$.

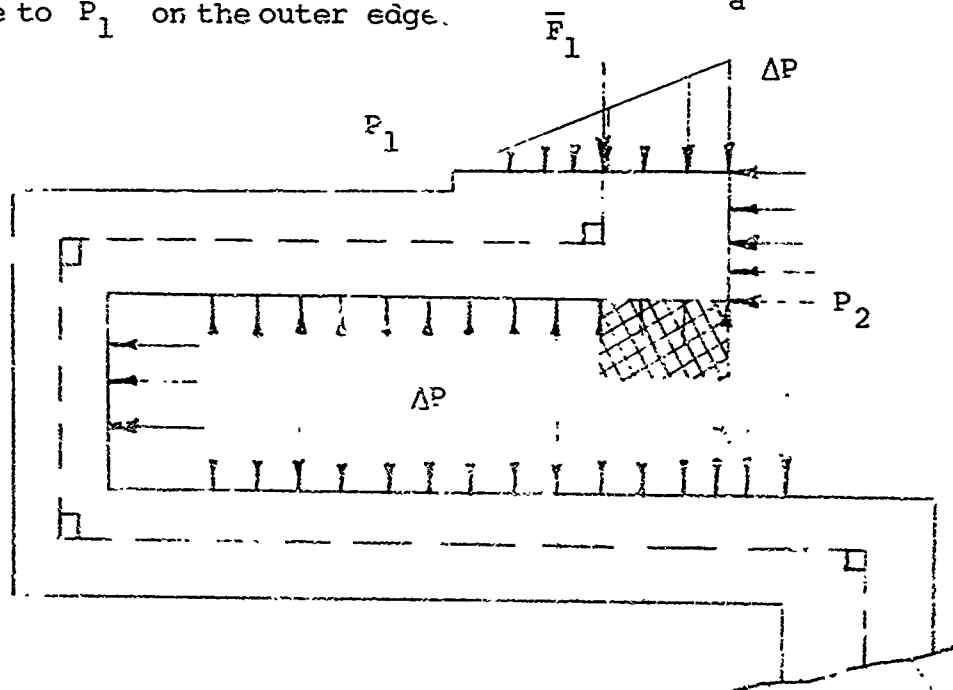
Derivation of the Pressure Energization Factor C_p

To obtain a solution, the shapes of typical seal configurations are simplified considerably in the analysis. Also, a linear pressure gradient is assumed at the seal interface. This assumption is valid for the majority of seals where the pressure-energization stress contribution at the interface is large compared with the opposing effects of the pressure gradient.

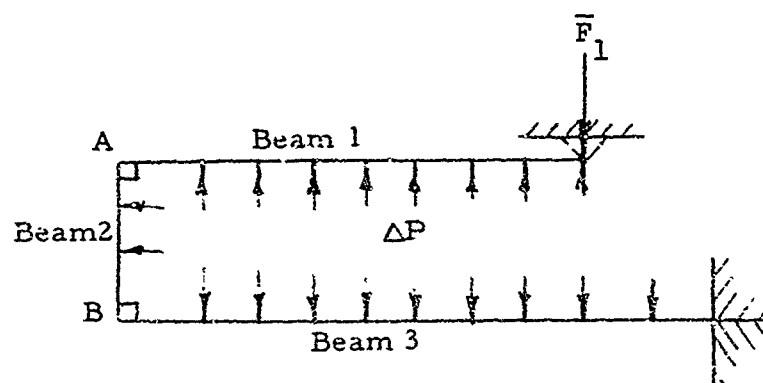
X-Seal Configuration. Pressure forces increase the contact stresses of the inner legs while decreasing that of the outer legs. Thus, a rather complicated analysis is required to derive pressure compensation factors to which leakage may be related. Since experimental leakage--pressure curves were not established for these seals because of their low magnitude of leakages, no pressure compensation considerations are extended.

K-Seal Configuration. For analysis, the general pressure conditions was resolved into two parts: (1) the pressures that are resisted by the flanges, and (2) the pressure gradient across the interface that is resisted by the seal itself. Since the flanges are assumed fixed an increase of pressure on the leg area causes an increase in the contact stress. The pressure gradient causes a decrease in the contact stress. The entire derivation for the pressure energization factor C_p is contained in AFRPL-TDR-65-61, Section 5.

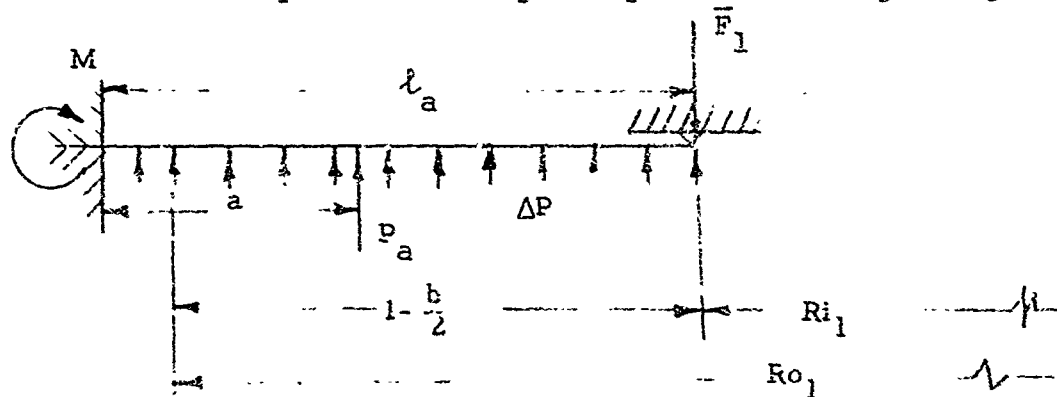
W-Seal Configuration. As before, the internal and external pressures will be combined to yield a pressure gradient over the interfaces that linearly decrease from P_a on the inner edge to P_1 on the outer edge.



Paralleling the theoretical load-deflection analysis of this configuration, the multibeam model indicated by the dashed lines will be considered. The crosshatched internal pressure region will be omitted in the following analysis; it is assumed that its effects cancel the effects of the pressure gradient because, approximately, ΔP acting over $b/2$ is the same as $\Delta P/2$ acting over b . Neglecting horizontal loads,



It is assumed that the effects of beams 2 and 3 can be neglected, i.e., point A and the slope of beam 2 at A are relatively undisturbed. Thus, only beam 1 need be considered; and its end at A can be considered built-in because of this assumption and the assumption that right angles remain right angles.



ΔP acts over $l - \frac{b}{2}$

Paralleling the K-configuration analysis, the following results are obtained:

$$A = \pi (R_{o1}^2 - R_{i1}^2)$$

$$F_a = \pi (R_{o1}^2 - R_{i1}^2) \Delta P$$

$$R_m = \sqrt{\frac{Ri_1^2 - Ro_1^2}{2}}$$

$$p_a = \frac{F_a}{2\pi R_m} = \frac{1}{2} \left(\frac{Ro_1^2 - Ri_1^2}{R_m} \right) \Delta P$$

$$\bar{F}_1 = \frac{1}{2} p_a \left(\frac{3a^2 \ell_a - a^3}{\ell_a^3} \right)$$

or

$$\bar{F}_1 = \frac{1}{4} \left(\frac{Ro_1^2 - Ri_1^2}{R_m} \right) \left(\frac{3a^2 \ell_a - a^3}{\ell_a^3} \right) \Delta P$$

$$a = Ri_1 - R_m + \ell_a$$

$$\sigma_i = \frac{\bar{F}_1}{b}$$

$$\sigma = \sigma_o + \sigma_1 = \sigma_o + C \Delta P$$

Thus

$$C = \left(\frac{Ro_1^2 - Ri_1^2}{4 R_m} \right) \left(\frac{3a^2 \ell_a - a^3}{b \ell_a^3} \right)$$

where

$$R_m = \sqrt{\frac{Ri_1^2 + Ro_1^2}{2}}, \quad a = Ri_1 - R_m + \ell_a$$

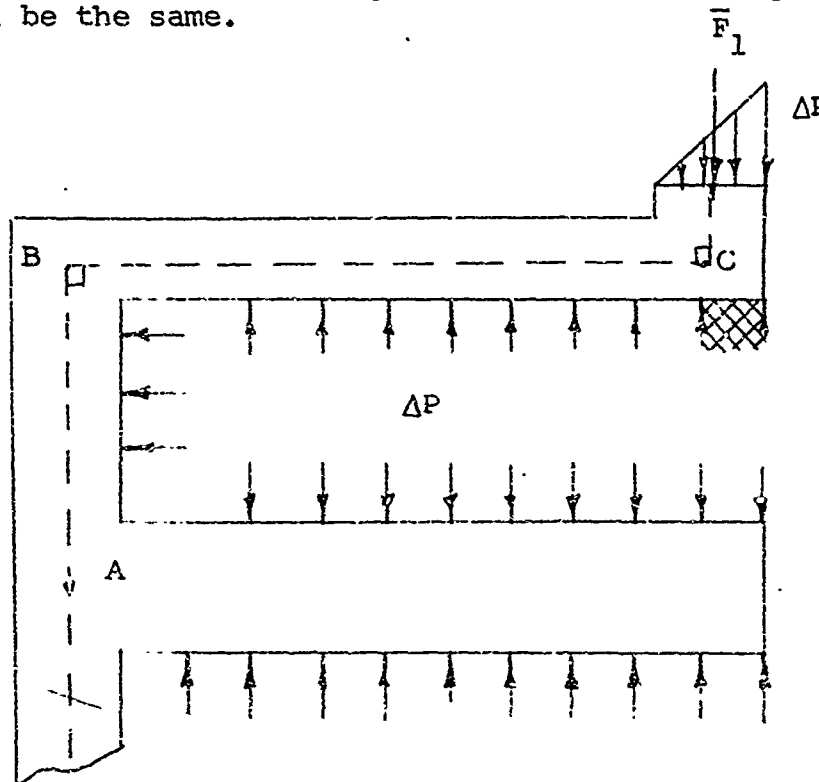
$$\ell_a = \ell_1 - \frac{b}{2} + \frac{t_3}{2}$$

$$Ri_1 = \frac{ID}{2} + \frac{b}{2}$$

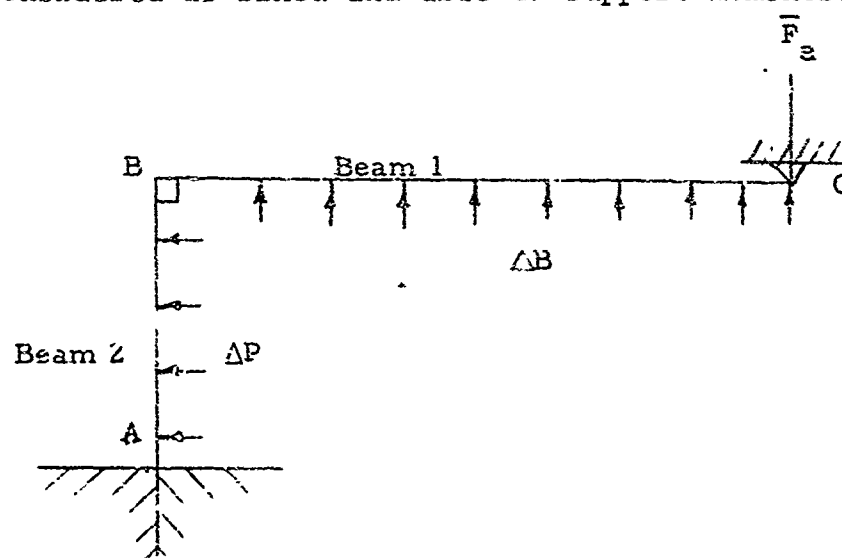
and

$$Ro_1 = \frac{ID}{2} + \ell_1$$

E-Seal Configuration. This configuration will be treated similarly to the W-seal configuration. The handling of pressures will be the same.



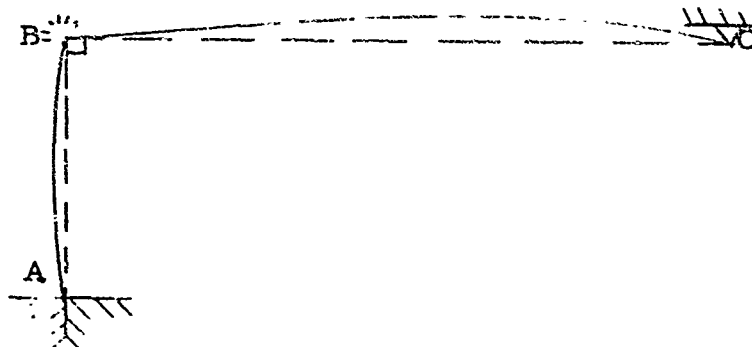
It can be assumed that the crosshatched internal pressure region, which will be neglected in the ensuing analysis, cancels the effects of the pressure gradient. The multibeam model indicated by the dashed lines will now be considered. Point A can be considered as fixed and able to support moments.



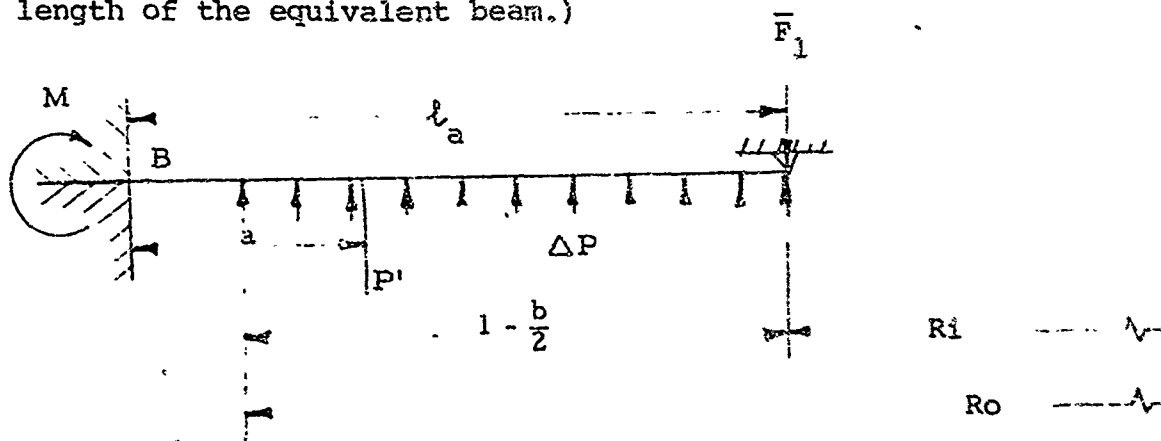
This is a statically indeterminate problem that is difficult to analyze. The following three assumptions permit further idealizations.

- (1) Lateral pressure forces are not great enough to overcome the static friction forces at the interfaces.
- (2) Axial deformations of the beams are negligible.
- (3) Right angles remain right angles.

Thus, it follows that point B is fixed and able to support moments. A possible state of pressure-caused deformation is:



Beam 1 can now be analyzed. It is treated as a beam built-in at one end and simply supported at the other. To account for the O-ring shape, i.e., pressure force per unit length of radial distance being proportional to the radius, the distributed pressure loading will be replaced by a point loading condition. (Note that the pressure does not act over the entire length of the equivalent beam.)



From the preceding analysis, the following results are obtained:

$$A = \pi(R_o^2 - R_i^2)$$

$$F_a = \pi(R_o^2 - R_i^2) \Delta P$$

$$R_m = \sqrt{\frac{R_i^2 + R_o^2}{2}}$$

$$P_a + \frac{F_a}{2 R_m} = \frac{1}{2} \frac{R_o^2 - R_i^2}{R_m} \Delta P$$

$$\bar{F}_1 = \frac{1}{2} P_a \left(\frac{3a^2 l_a - a^3}{l_a^3} \right)$$

$$\bar{F}_1 = \frac{1}{4} \frac{R_o^2 - R_i^2}{R_m} \left(\frac{3a^2 l_a - a^3}{l_a^3} \right) \Delta P$$

$$\sigma_1 = \frac{\bar{F}_1}{b}$$

$$\sigma = \sigma_o + \sigma_1 = \sigma_o + C \Delta P$$

Hence,

$$C = \frac{R_o^2 - R_i^2}{4 R_m} \left(\frac{3a^2 l_a - a^3}{b l_a^3} \right)$$

where

$$R_m = \sqrt{\frac{R_o^2 + R_i^2}{2}}$$

$$a = R_i + l_a - R_m$$

$$l_a = 1 - \frac{b}{2} + \frac{t_2}{2}$$

$$R_i = \frac{DI}{2} + \frac{b}{2}$$

$$R_o = \frac{DI}{2} + 1$$

Table VI-1

CALCULATED RESULTS OF PRESSURE-ENERGIZATION FACTOR C

Scale	Pressure Compensation Factor C, Equation	C
K-1	$\frac{R_i + R_o}{4 R_m} \left[\frac{3a^2 \bar{L} - a^3}{b(\bar{L})^2} \right] \cos \alpha - \frac{1}{3} \frac{R_i + b}{2 R_i + b}$	0.633
K-2	where $R_m = \sqrt{\frac{R_i^2 + R_o^2}{2}} ; a = \frac{R_o - R_m}{R_o - R_i} \bar{L}$	0.557
W-1	$\frac{R_{o1}^2 - R_{i1}^2}{4 R_m} \left[\frac{3a^2 l_a - a^3}{b l_a^3} \right] ,$	0.597
W-2	where $R_m = \sqrt{\frac{R_{i1}^2 + R_{o1}^2}{2}} ; a = R_{i1} - R_m + l_a$	0.592
E-1	$\frac{R_o^2 - R_i^2}{4 R_m} \left[\frac{3a^2 l_a - a^3}{b l_a^3} \right]$	1.876
E-2	where	1.888
E-3	$R_m = \sqrt{\frac{R_o^2 + R_i^2}{2}} ; a = R_i + l_a - R_m$	2.659

BIBLIOGRAPHY

Bauer, Glickman and Iwatsuki, Analytical Techniques for the Design of Seals for Use in Rocket Propulsion Systems Volume I and II AFRPL-TDR-65-61, IIT Research Institute, Chicago May 1965.

Roark, Formulas for Stress and Strain, 3rd ed., McGraw-Hill, 1954.

Shanley, Strength of Materials, pp. 267-269, 467-470, McGraw-Hill, 1957.

Timoshenko and Goodier, Theory of Elasticity, 2nd ed., McGraw-Hill, 1951.

Timoshenko and MacCullough, Elements of Strength of Materials, 3rd Ed., D. Van Nostrand Co., Inc., 1949.

APPENDIX VII

DESCRIPTION OF STATIC AND SLIDING SEALS EXPERIMENTAL APPARATUS

VII-1 Static Seal Apparatus

The static seal apparatus was composed of three parts, as shown on figure VII-1. A base into which fluid and thermocouple connections were incorporated was fabricated from AM355. The upper surface of the base was lap-finished to 7 μ in. PTV and served as a mating interface surface. The seal cavity cover was also fabricated from AM355. The interface surface on the cover was identical to the base. An outer cover or leakage collector served a dual purpose. First, it provided a means of collecting leakage past the seal. The interior of the cover was capable of being evacuated when connected to a helium mass spectrometer. Secondly, the cover provided an element of safety in the event a seal or housing cover occurred. An over-all view of the apparatus is shown on figure VII-2. A top view of the base and internal view of the collector cover is shown on figure VII-3.

Accessory equipment for the apparatus consisted of a heating coil, as shown on figure VII-4. The external surface of the base was heated by passing the products of combustion from oxy-acetylene flame through the tube. Other equipment included thermocouples, helium gas supply, and a CEC helium leak detector. A schematic diagram of the over-all facility is shown on figure VII-5.

VII-2 Sliding Seal Apparatus

The sliding seal apparatus was composed of two, opposed cavities into which an experimental seal was mounted. Individual sliding shafts were connected together to form a common shaft. The shaft assembly was driven by a yoke connected to two driving cylinders. These cylinders were hydraulically actuated by an external power source. At the connection between the experimental shaft and yoke, strain gage load cells were installed to facilitate the measurement of friction loads. Figure VII-6 shows a schematic view of the apparatus while an over-all view is shown on figure VII-7. The apparatus was capable of accepting seals up to 4 in. in diameter.

Leakage measurements were accomplished by measuring leakage flow into the sealed cavities. For correlation of results, leakage could also be measured on the low pressure side of the seal. This measurement was not reliable because a secondary seal on the shaft permitted breakage to by-pass the measuring instrument.

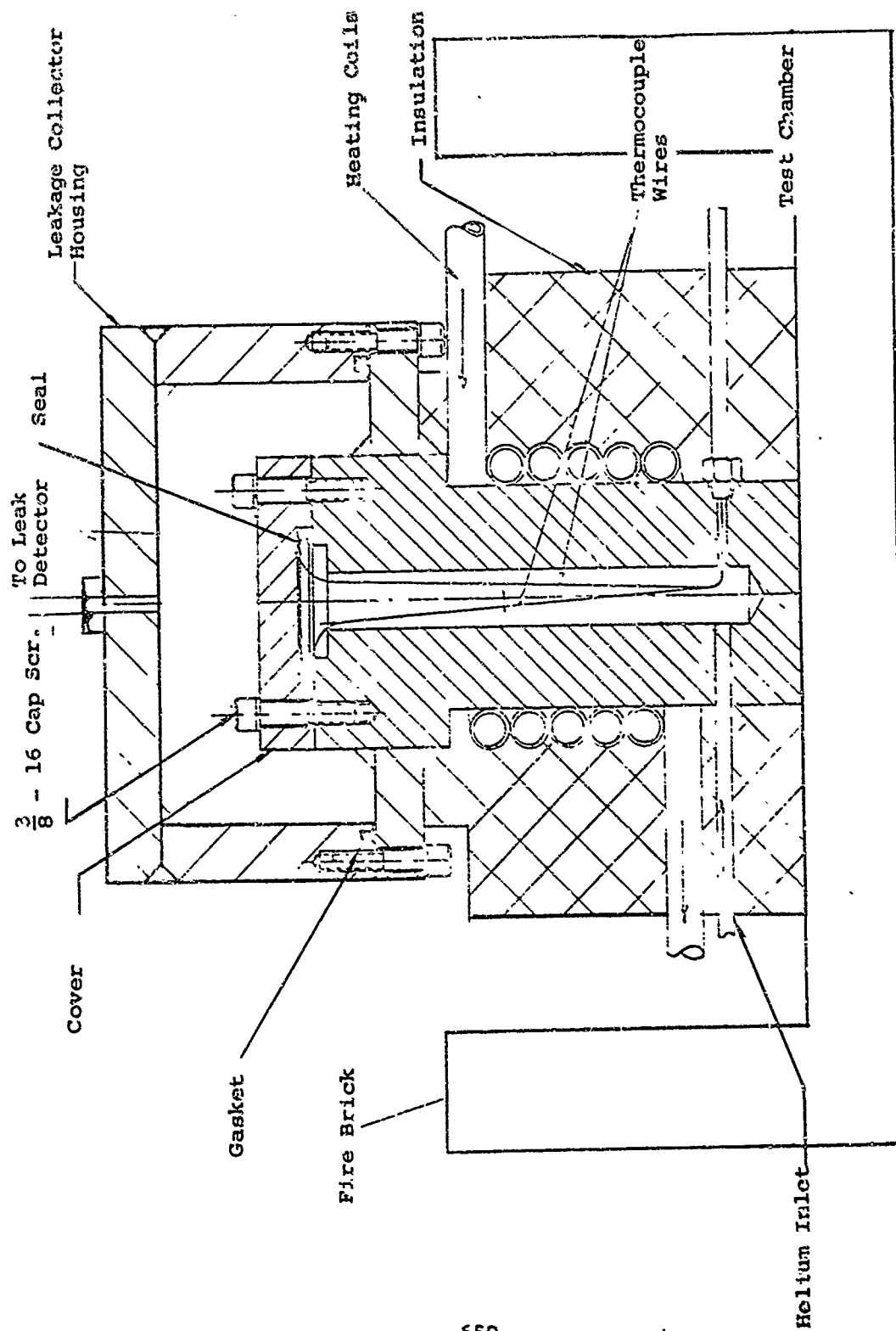


Figure VII-1 Seal test apparatus

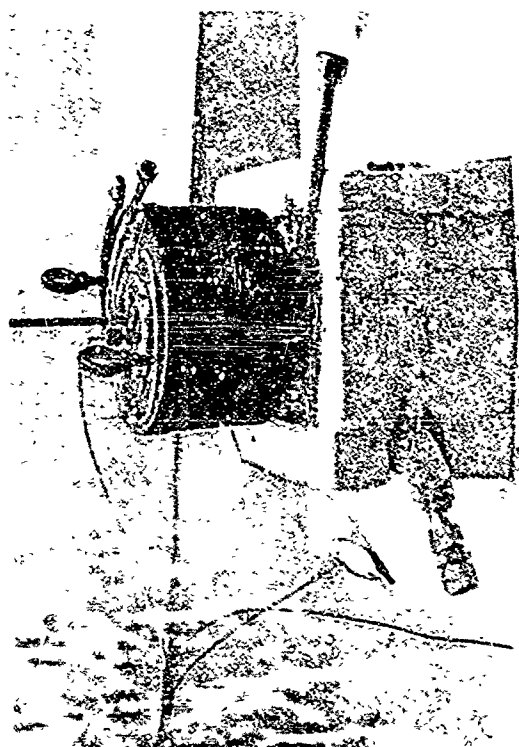


Figure VII-2 Over-all view of the assembled static seal apparatus

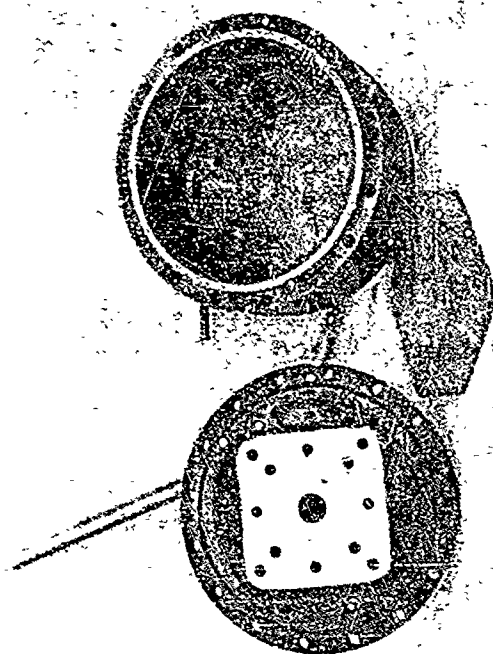


Figure VII-3 Lower base and cover assembly

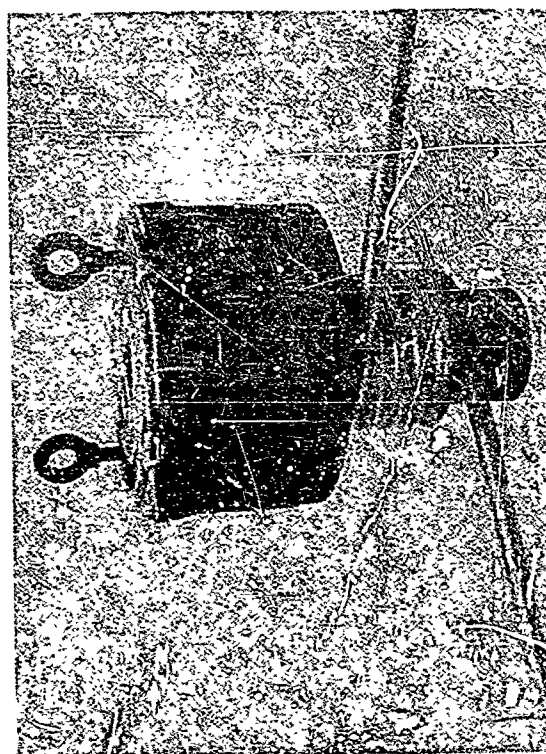


Figure VII-4 View of the heating coil

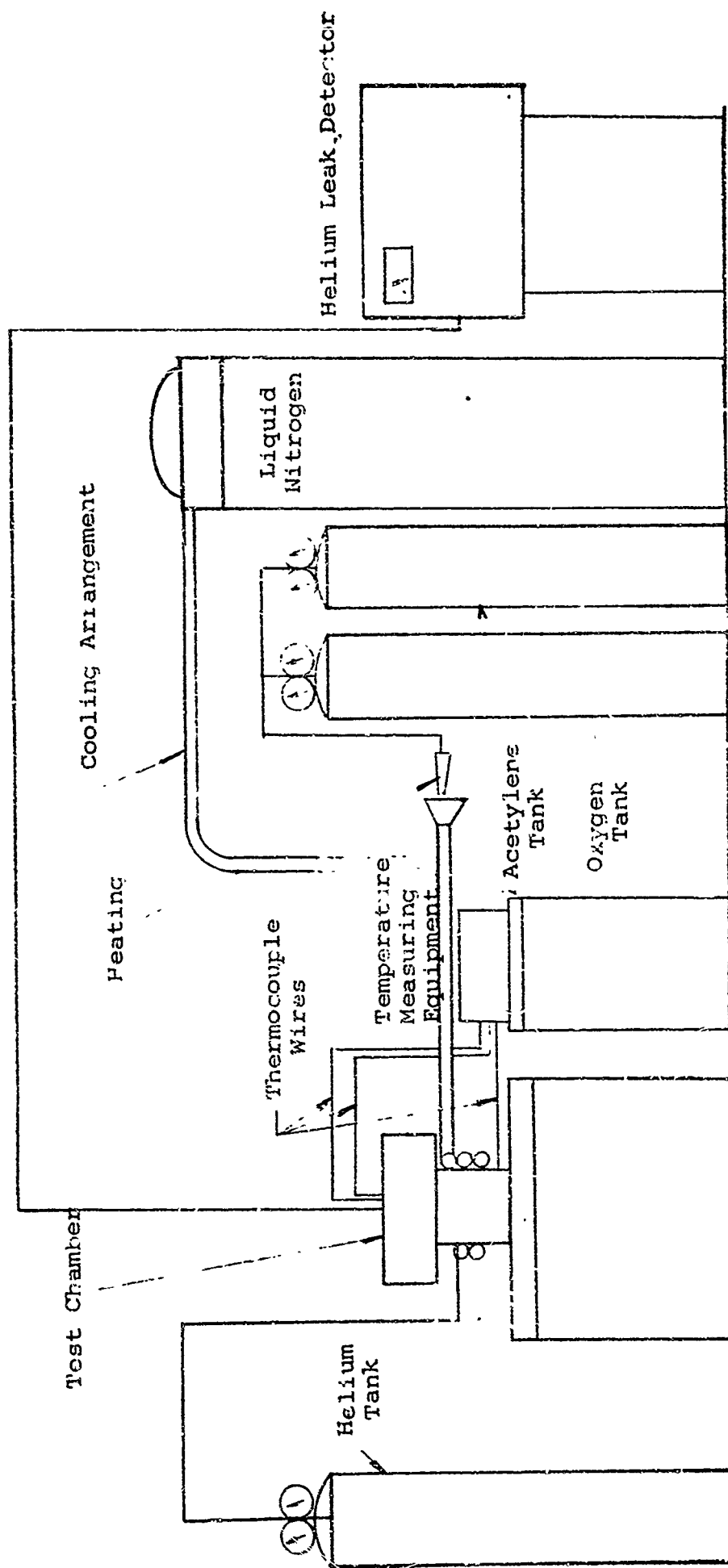


Figure VII-5 Schematic of static seal evaluator facility

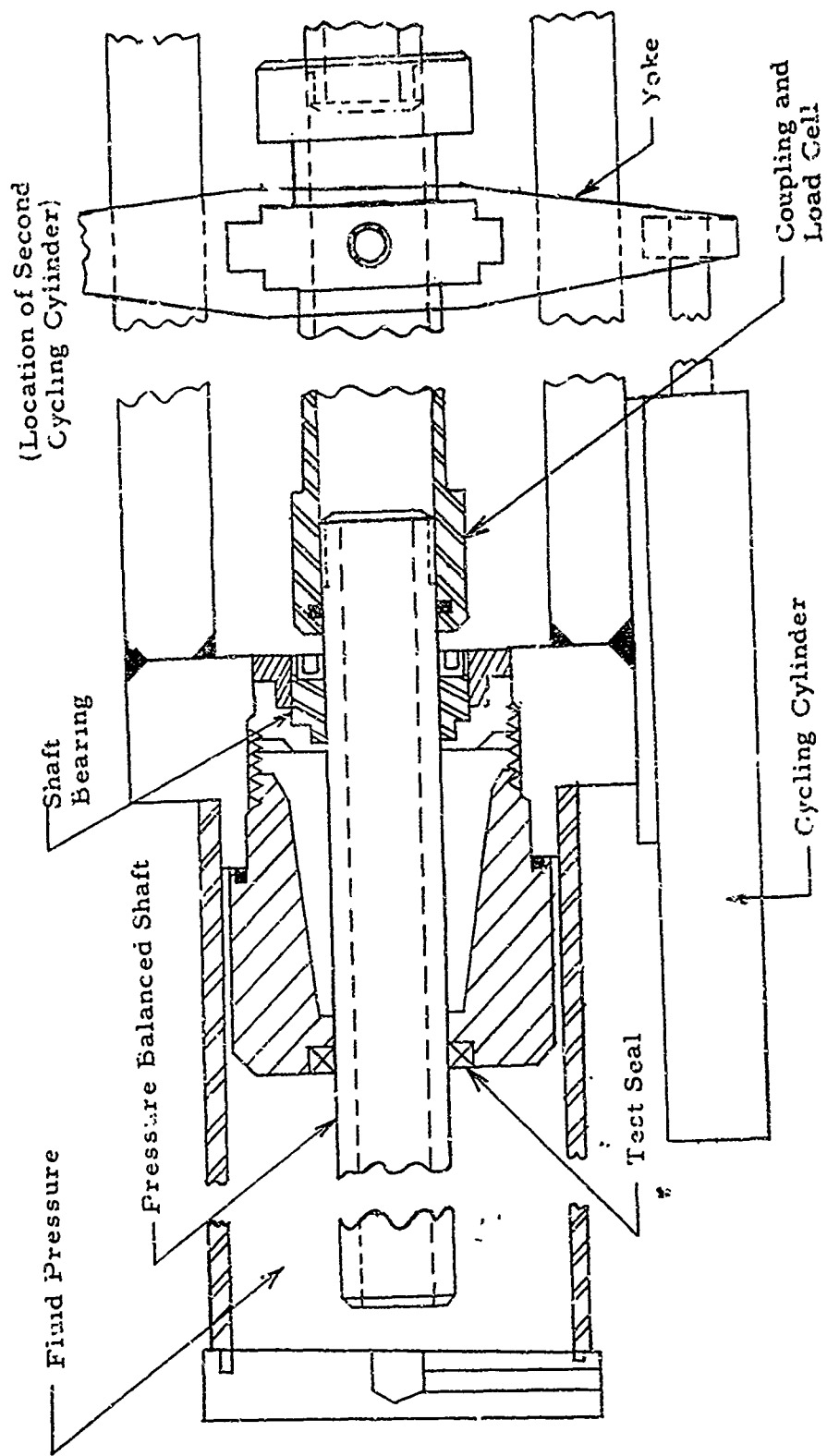


Figure VII-6 Sliding seal experimental fixture

APPENDIX VIII

DEVELOPMENT OF A COMPUTER CODE FOR ESTABLISHING EMPIRICAL CORRELATION FROM EXPERIMENTAL DATA

This discussion is presented for two reasons. First, it describes the procedures used in correlating the rubber interface parameters from experimental data. Secondly, it is a recommended approach for the further reduction of metallic and plastic data presented in Appendix I and discussed in Section 2.

The objective in developing a data reduction process was to obtain an improved correlation of experimental data, thus yielding empirical data. Specifically, the method was to form a systematic and rational mathematical technique and computer code to aid in the graphical and analytical interpretations of experimental results in raw form as a collection of n data points (x_i, y_i) , $i = 1$, to $i = n$.

Mathematical techniques were developed for 1) finding smooth curves that best fit the collection of given data points according to well-defined mathematical criteria, and 2) for finding analytical functions that approximately describe the functional behavior of the system over ranges of its operation.

These formulations have been coded into a Fortran II computer program for high-speed solution on an IBM 7094 digital computer.

The computer output for any given set of input data does not represent purely objective experimental results. The investigator must make certain a-priori decisions concerning the analysis of the data; however, the computerized mathematical techniques permit and actually force him to state his feelings objectively rather than his argument that "this curve just looks best." Furthermore, this program permits the systematic analysis of many sets of similar experimental data and yields results independent of the investigator or all accept common decisions as to the procedure.

The problem simply stated is: given a set of n points, (x_i, y_i) , $i = 1, n$, what smooth curve do they best define and what functional relationship adequately describes their dependence, $y = F(x)$?

If the given set of points is relatively well-ordered with a limited range of scatter, "eye-balling" a smooth curve through them usually provides acceptable accuracy and confidence.

Another approach to establishing the best smooth curve through the set of points is predicated upon a priori knowledge of the functional relationship assumed to exist. For example, it being assumed that elastic displacements are proportional to the

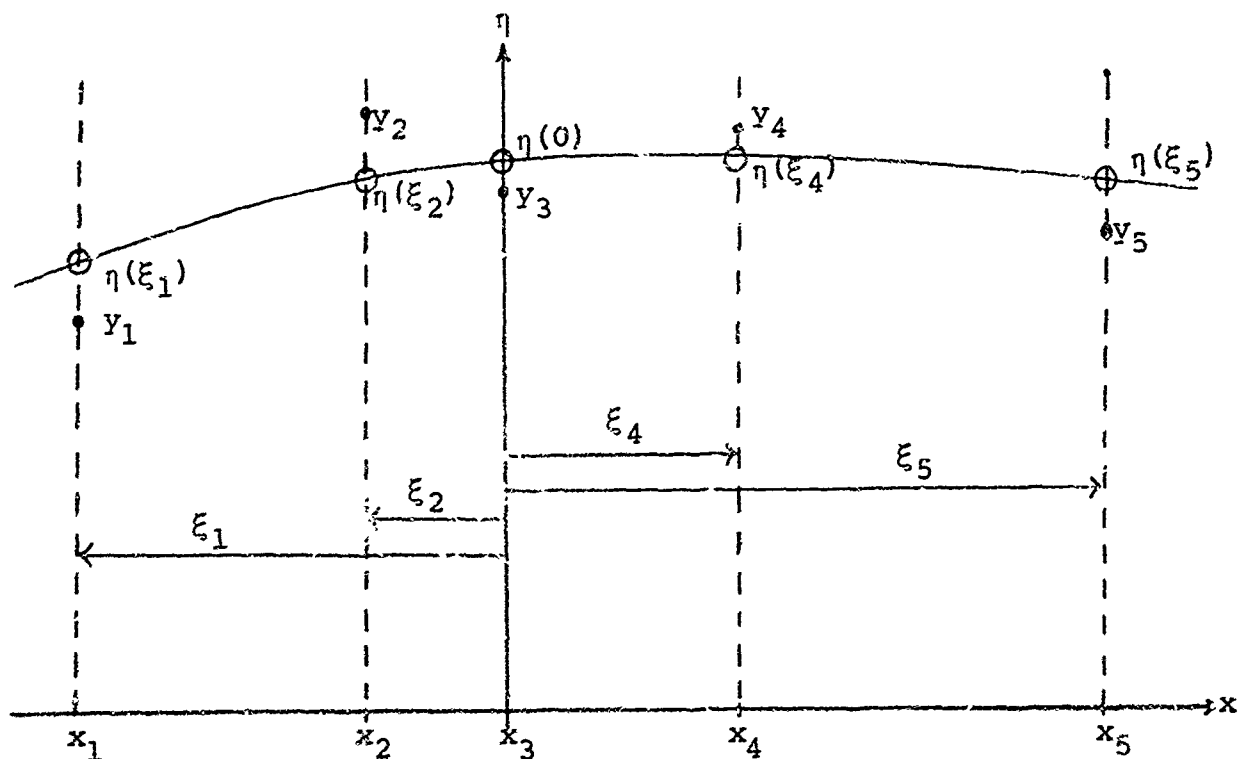
force, it is then a simple step to finding the best straight line through the scatter of points. There exist a number of computer programs for finding the best polynomial of order n through a given set of points. Still another approach would be a rigorous statistical analysis of the data.

None of these approaches is applicable in the present case. The given set of points can have practically any range of scatter, both parameters can vary over many orders of magnitude, no a-priori functional relationship is assumed to exist (e.g., leakage as a function of contact stress), and not enough information is known for a rigorous statistical analysis.

VIII-1 Mathematical Curve-Smoothing Technique

Certain mathematical formulations will be presented leading to a complete description of the smoothing technique programmed for the computer.

Consider any five points, (x_i, y_i) , $i = 1, 5$, of a set of n points. It is assumed that the x 's are fixed and the y 's are to be smoothed. A local coordinate system (ξ, η) is established at the center point:



(Note that the spacings $x_i - x_{i-1}$ need not be equal.)

A second-order (parabolic) equation is to be fitted to the points (x_i, y_i) . In the local coordinate system,

$$\eta(\xi) = A_1 + A_2\xi + A_3\xi^2 \quad (\text{VIII-1})$$

The residuals are defined to be the difference between the original ordinate y_i and the corresponding "smoothed" ordinate $\eta(\xi_i)$ squared. The quantity

$$F \equiv \sum_{i=1}^5 [\eta(\xi_i) - y_i]^2 \quad (\text{VIII-2})$$

is a measure of the fit of (VIII-1) to the original points. The best fit is established by the criterion that F is a minimum for that choice of parameters A_1, A_2, A_3 . Mathematically,

$$\frac{\partial F}{\partial A_i} = 0, \quad i = 1, 2, 3 \quad (\text{VIII-3})$$

From equations (VIII-1) and (VIII-2),

$$F = \sum_{i=1}^5 [A_1 + A_2\xi_i + A_3\xi_i^2 - y_i]^2 \quad (\text{VIII-4})$$

From equations (VIII-3) and (VIII-4),

$$\begin{aligned} 0 &= \sum_{i=1}^5 [A_1 + A_2\xi_i + A_3\xi_i^2 - y_i] \\ 0 &= \sum_{i=1}^5 \xi_i [A_1 + A_2\xi_i + A_3\xi_i^2 - y_i] \\ 0 &= \sum_{i=1}^5 \xi_i^2 [A_1 + A_2\xi_i + A_3\xi_i^2 - y_i] \end{aligned} \quad (\text{VIII-5})$$

Performing the summations yields

$$\begin{aligned} 5A_1 + a_1A_2 + a_2A_3 &= b_1 \\ a_1A_1 + a_2A_2 + a_3A_3 &= b_2 \\ a_2A_1 + a_3A_2 + a_4A_3 &= b_3 \end{aligned} \quad (\text{VIII-6})$$

where
where

$$a_n = \sum_{i=1}^5 (\xi_i)^n, \quad n = 1, 4$$

$$a_n = \sum_{i=1}^5 (\xi_i)^n, \quad n = 1, 4$$

$$b_n = \sum_{i=1}^5 (\xi_i)^{n-1} y_i, \quad n = 1, 3$$

$$b_n = \sum_{i=1}^5 (\xi_i)^{n-1} y_i, \quad n = 1, 3$$

Solving equation (VIII-6) by Cramer's Rule gives the values of the parameters A_i of the best second-order fit to the points (x_i, y_i) , $i = 1, 5$.

$$A_n = \frac{R_n}{D}, \quad n = 1, 3 \quad (\text{VIII-7})$$

$$A_n = \frac{R_n}{D}, \quad n = 1, 3 \quad (\text{VIII-7})$$

where
where

$$R_1 = b_1 [a_2 a_4 - a_3^2] + b_2 [a_2 a_3 - a_1 a_4] + b_3 [a_1 a_3 - a_2^2]$$

$$R_1 = b_1 [a_2 a_4 - a_3^2] + b_2 [a_2 a_3 - a_1 a_4] + b_3 [a_1 a_3 - a_2^2]$$

$$R_2 = b_1 [a_2 a_3 - a_1 a_4] + b_2 [5a_4 - a_2^2] + b_3 [a_1 a_2 - 5a_3]$$

$$R_2 = b_1 [a_2 a_3 - a_1 a_4] + b_2 [5a_4 - a_2^2] + b_3 [a_1 a_2 - 5a_3]$$

$$R_3 = b_1 [a_1 a_3 - a_2^2] + b_2 [a_1 a_2 - 5a_3] + b_3 [5a_2 - a_1^2]$$

$$R_3 = b_1 [a_1 a_3 - a_2^2] + b_2 [a_1 a_2 - 5a_3] + b_3 [5a_2 - a_1^2]$$

$$D_4 = 5a_2 a_4 + 2a_1 a_2 a_3 - a_2^3 - a_1^2 a_4 - 5a_3^2$$

$$D_4 = 5a_2 a_4 + 2a_1 a_2 a_3 - a_2^3 - a_1^2 a_4 - 5a_3^2$$

The equation of the parabola relative to the natural coordinate system (x, y) is found by a simple translation of axes. The equation of the parabola relative to the natural coordinate system (x, y) is found by a simple translation of axes.

$$y(x) = A + Bx + Cx^2 \quad (\text{VIII-8})$$

$$y(x) = A + Bx + Cx^2 \quad (\text{VIII-8})$$

where
where

$$A = A_1 - A_2 x_3 + A_3 x_3^2$$

$$A = A_1 - A_2 x_3 + A_3 x_3^2$$

$$B = A_2 - 2A_3 x_3$$

$$B = A_2 - 2A_3 x_3$$

$$C = A_3$$

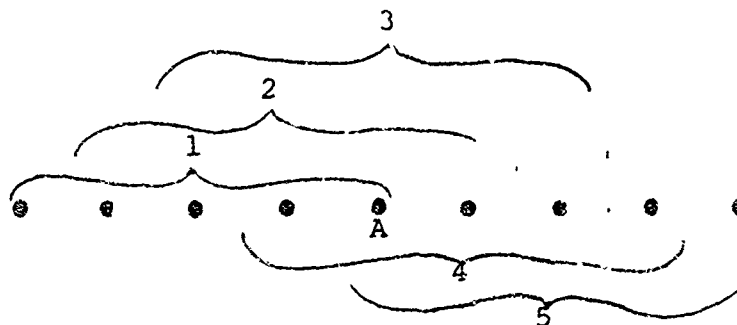
$$C = A_3$$

If the center ordinate y_3 is now replaced by $y(x_3)$ or $\eta(0)$, then the points (x_i, y_i) are replaced by $(x_i, y(x_i))$ or $(x_i, \eta(x_i))$, then that point is said to be smoothed.

Repeating the above process for the set of $n-4$ points (excluding the two points at each end of the set), establishing the new coordinate system at each of these points, gives a set of smoothed points that have less scatter than the original ones.

The smoothed ordinates at the four end points are obtained from the parabolas fitted to the first group of five points and the last group.

A modification of the above procedure that has been used successfully in the past is as follows: Each point belongs to five groups of five adjacent points, as defined above, except for certain end points that belong to fewer groups.



Thus, there are five parabolas through A whose coefficients depend in part upon the coordinates of A. In the former procedure only group 3 above (containing A as the center point) is used to determine the smoothed value of A. The present modification consists of averaging the possible values at A obtainable from each of those five parabolas and defining this average to be the smoothed value of A. At the appropriate end points the average is computed from fewer parabolas.

In this way the smoothed values reflect the influence of a greater range of points, and it therefore may be expected that the curve through these smoothed points will be smoother and more representative of the data. The present computer code incorporates this technique. Although it has worked very well for well-ordered data points over roughly 1 or 2 orders of magnitude, it has not yet been determined if it is as satisfactory for widely-scattered points over many orders of magnitude.

It might also be noted that this modification is extremely useful in computing ordinates at special locations along the x-axis (e.g., at equal spacings) from a given set of arbitrary data points.

Figure VIII-1 is a log-log plot of data points taken from leakage measurements at various rubber gasket contact stresses. Figure VIII-2 shows the smoothed points obtained by applying the above technique to the leakage ordinates. The curve drawn through the smoothed points seems to fit the original data well. The standard error is about 350×10^{-6} .

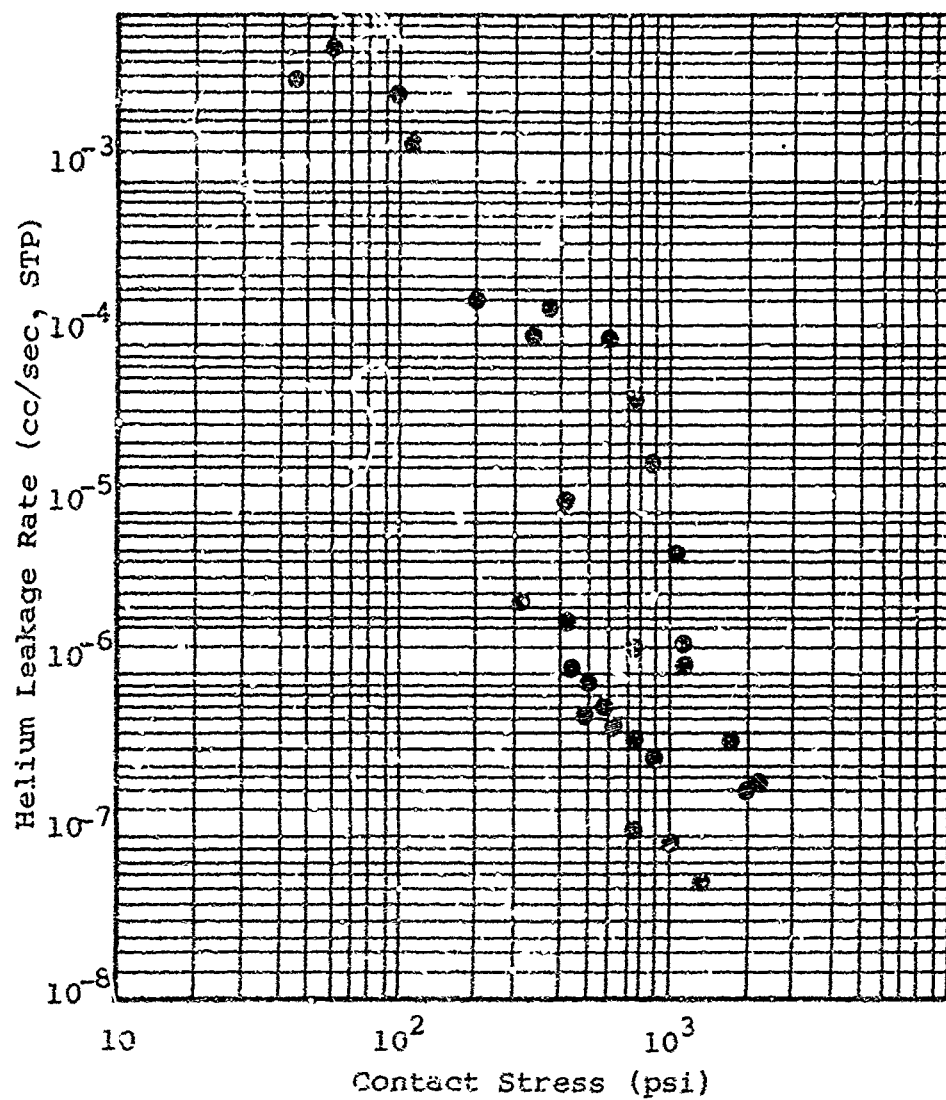


Figure VIII-1 Experimental data scatter

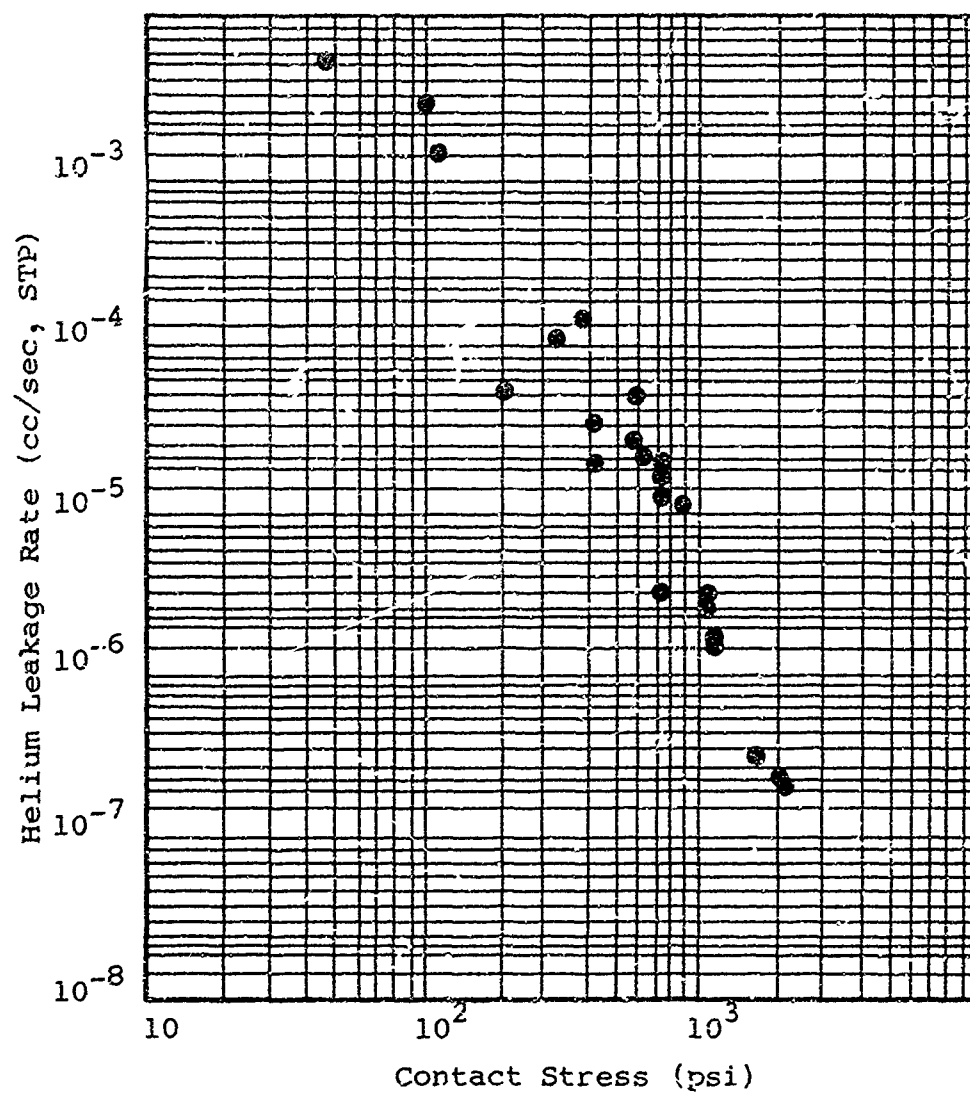
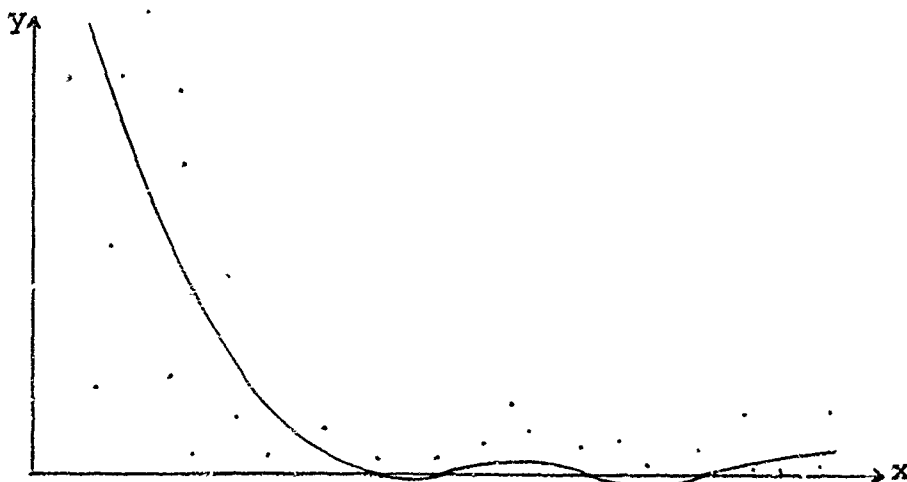


Figure VIII-2 1st smoothing at Y's

Some of the original points do not have corresponding positive smoothed values. This can most easily be understood by visualizing the points on a regular x-y coordinate system. The leakage ordinates vary over 6 orders of magnitude, from 0(1000) to 0(.01) when multiplied by a scale factor of 10^6 . Thus, it is to be expected that a smooth curve based on points of such wide scatter and range, will drop toward the x-axis and oscillate about it. These lone data points on the graph have smoothed values representing such oscillations.



This completes the basic development of a mathematical smoothing technique. The primary result is that it yields a new set of smoothed points of less scatter through which it is easier to draw a curve that fits the original data with a high degree of confidence.

VIII-2 Iterative Smoothing Process

A further technique has been tried, and written into the computer program, for the purpose of obtaining additional accuracy and confidence with the smoothing technique already presented. In particular, the objective is to eliminate such behavior as those oscillations just discussed and further define a smooth curve through the data. This technique is that of successive smoothings.

Successive smoothing of points is accomplished by replacing the points smoothed from by the advanced set of smoothed points and repeating the basic smoothing process on these. The process is basically an iterative one in which only the identities of the advanced values are retained.

If the assumed dependent variable is successively smoothed, the smoothed points ultimately converge to some final curve. However, this curve may or may not represent a best curve through the original points since each successive smoothing reflects the

original points to a less degree. For example, the oscillations about the x-axis described above may grow rather than disappear.

It has been found, however, that by successively smoothing both the y's and x's alternately, convergence is still attained, and the final curve appears consistent with the original data.

The process for doing this is as follows: First, the dependent variable is smoothed holding the x's fixed. Then the x's are treated as the dependent variable to be smoothed and the advanced set of smoothed y's are held fixed. Then the y's are smoothed again holding the new set of x's fixed, and so on.

Figure VIII-3 is the curve defined after two iterations. To obtain this the smoothed y's of figure VIII-2 were held fixed and the x's were smoothed. Thus, the points on this graph are the smoothed y's of figure VIII-2 along with their corresponding smoothed x's.

Figure VIII-4 shows the curve obtained after fifteen iterations of this process. The original data is that given in figure VIII-1. No oscillations about the x-axis were found after the third iteration.

Figure VIII-5 is a plot of the relative standard errors for these iterations, i.e., the standard error of the smoothed points of the i-th iteration relative to those of the i-th-2 iteration (the other coordinate was smoothed during the i-th-1 iteration). The two broken lines represent the smoothings on the y's and x's separately. Clearly, the successively smoothed points converge to some final curve (which may oscillate slightly).

Unfortunately, no measurement can be easily made of the degree of fit of this final curve, or the one shown in figure VIII-4, to the original points. In other words, there is no numerical assurance that the curve defined after say thirty iterations closely approximates a best curve through the data. This difficulty arises since the points migrate unpredictably, i.e., both the y's and x's change during the successive smoothings.

However, other indications will arise later which seem to indicate that confidence can be placed in these iterated curves.

VIII-3 Curve Fitting of an Analytic Function Having Undetermined Parameters

Before a technique can be developed for computing the values of a function's parameters so it best fits a given set of points smoothly, the type of function to be fitted must be established. The class of polynomial functions is often used to fit a set of points and is reasonably straightforward to manipulate. It is, however, quite restricted in its application to a smooth curve

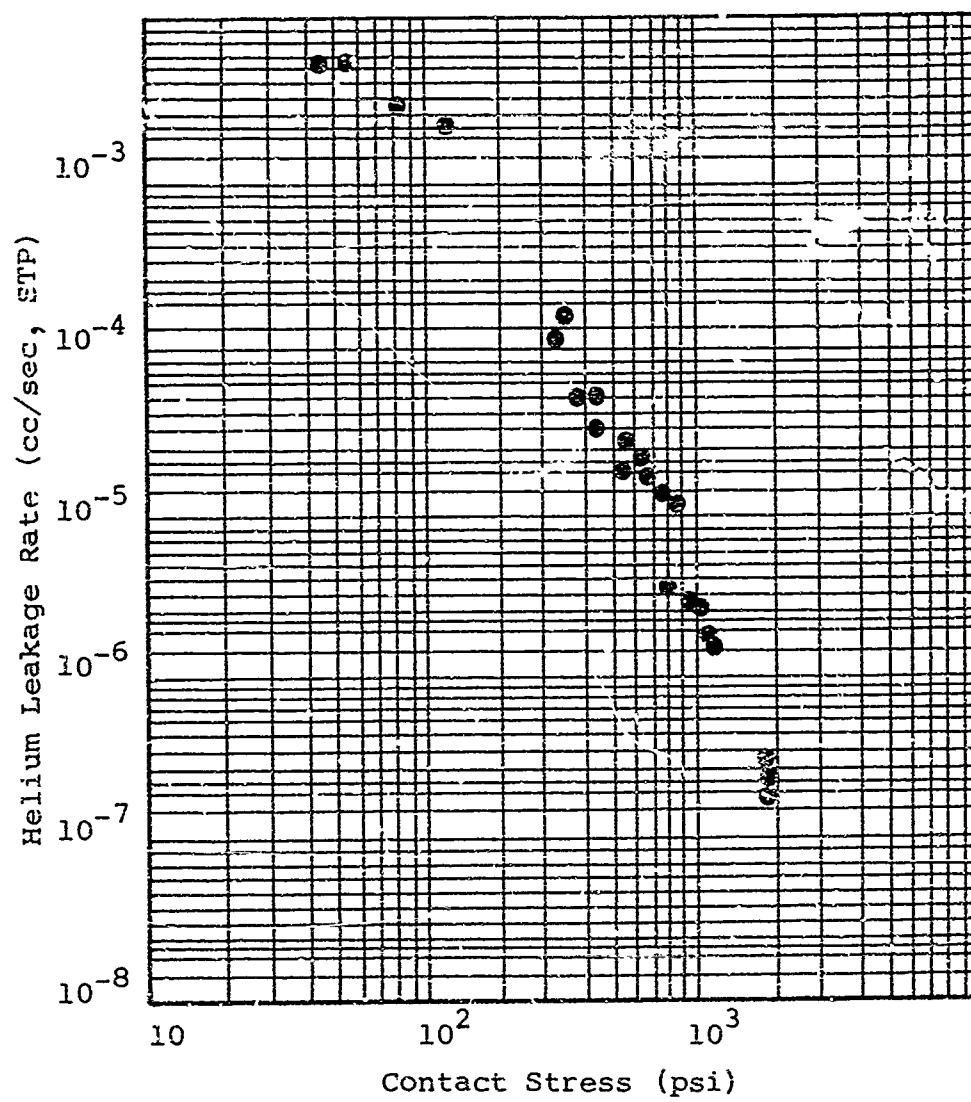


Figure VIII-3 Y's then X's

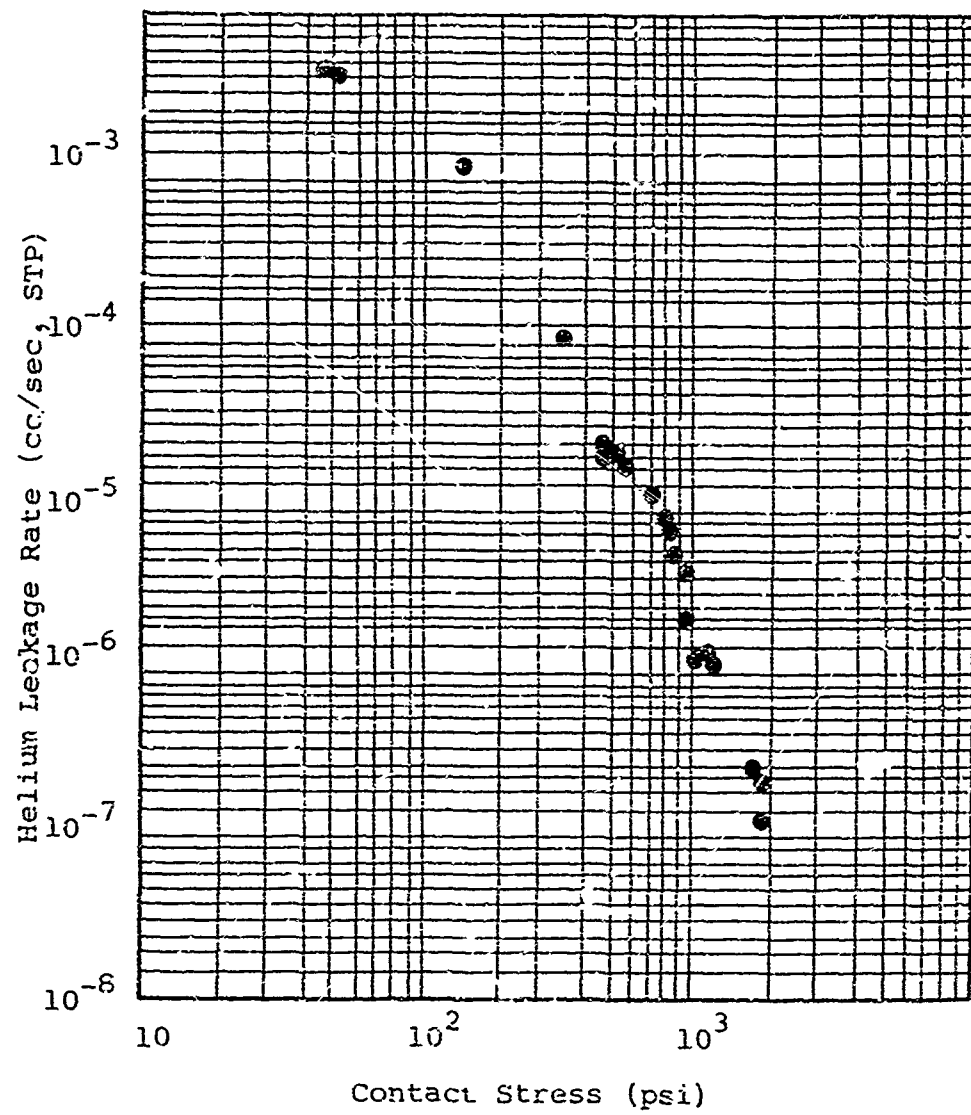


Figure VIII-4 15th Iteration

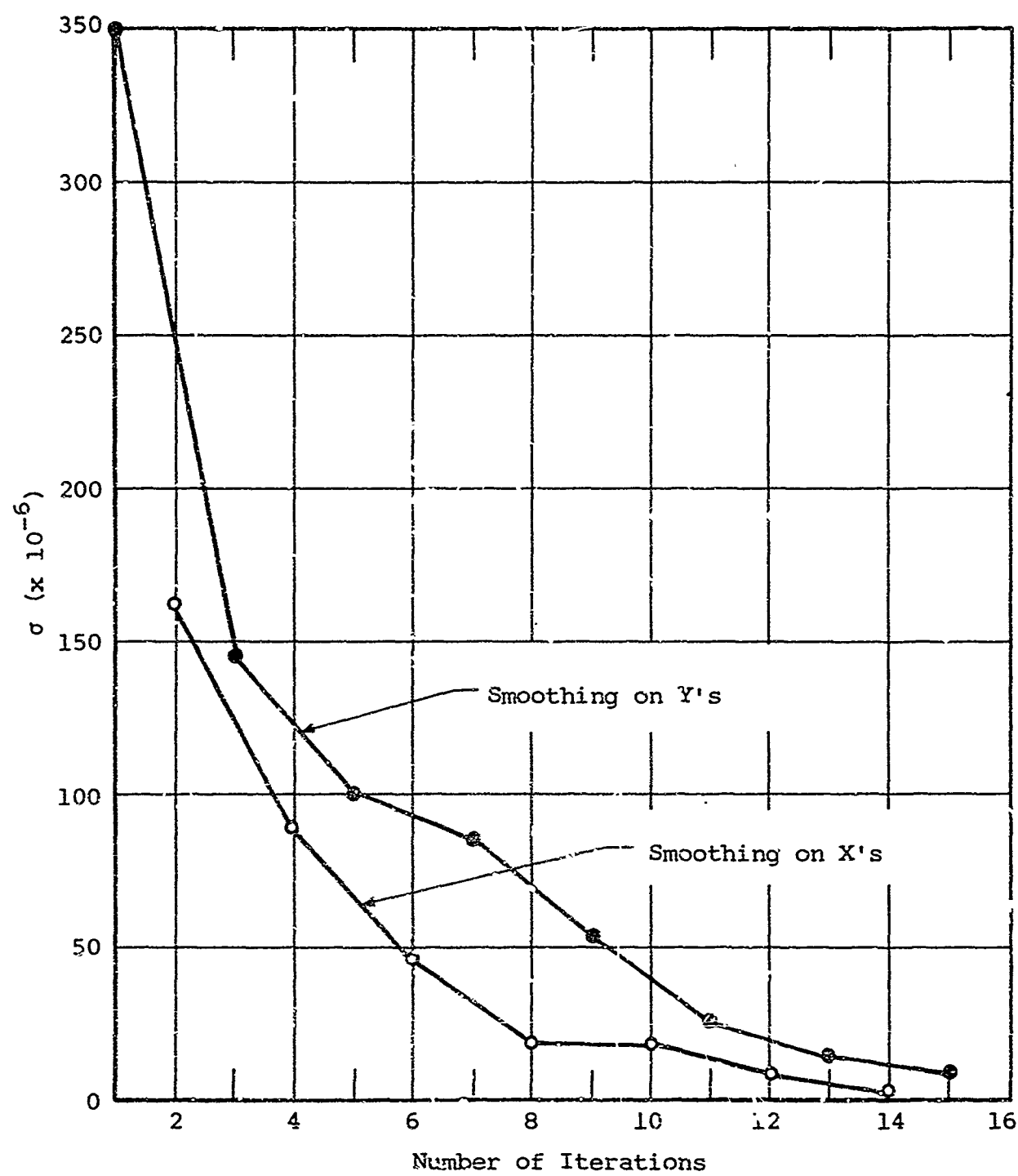


Figure VIII-5 Relative standard error

fitting problem, specifically, to data suspected of exhibiting polynomial behavior.

A more general class of functions, applicable to fitting a set of points smoothly, can be derived from the polynomial class by the introduction of a parameter n in addition to the polynomial coefficients.

$$F(x) \equiv x^{-n} G(x) \quad (\text{VIII-9})$$

where

$G(x)$ is a polynomial,

$$G(x) = \sum_{i=1}^L A_i x^{i-1} \quad (\text{VIII-10})$$

In the present study, $G(x)$ is restricted to a second-order polynomial,

$$G(x) = A_1 + A_2 x + A_3 x^2 \quad (\text{VIII-11})$$

The problem can now be stated as: Given a set of n points, (x_i, y_i) , $i = 1, n$, what is the function $F(x)$ that best fits them? The criterion establishing this is that the standard error of that function be a minimum of its class. Because of the choice of the class of functions to be treated, (VIII-9), the computational procedure retains the basic simplicity of polynomial fitting techniques. This procedure is as follows: From the given set of points a new set can be defined that depends on the value of n .

$$G_i = x_i^n y_i \quad (\text{VIII-12})$$

Once n is chosen, a parabola is fitted to the points obtained from equation (VIII-12). The coefficients A_1, A_2, A_3 of the best parabola through these points, (x_i, G_i) , $i = 1, L$ instead of $i = 1, 5$ (five points). Then, from equations (VIII-9) and (VIII-11), $F(x)$ can be found for that choice of n and the best fitting parabola in the G -plane.

$$F(x) = A_1 x^{-n} + A_2 x^{1-n} + A_3 x^{2-n} \quad (\text{VIII-13})$$

In particular, the values $F(x_i)$ are computed, and the standard error relative to the original ordinates y_i is found.

$$\sigma_n = \sqrt{\frac{1}{L} \sum_{i=1}^L F(x_i) - y_i^2} \quad (\text{VIII-14})$$

These steps are now repeated for a different choice of n resulting in another $\sigma_{(n)}$ from equation (VIII-14). If the original points are scattered roughly about some function of the class defined by equations (VIII-9) and (VIII-11), then eventually an n will be found for which $\sigma_{(n)}$ is a minimum. Then, finally, the best smooth curve through the data is known analytically from equation (VIII-13).

The range of n that describes a large class of functions and which has been used is

$$0 \leq n \leq 2 \quad (\text{VIII-15})$$

For $n = 0$, $F(x)$ is a second-order polynomial.

$$\text{For } n = 1, F(x) = \frac{A_1}{x} + A_2 + A_3x$$

For $n = 2$ and $A_1 = 0$, $F(x) = A_3 + \frac{A_2}{x}$
which is a hyperbola.

For certain types of data often one analytical function is insufficient to fit all the points. For this reason the above procedure was programmed so that any range of data points could be fitted by equation (VIII-13) exclusively of the others.

Figure VIII-6 contains plots of the following analytical functions based upon the original points having no smoothing performed:

$$\begin{aligned} \text{(a)} \quad F(x) &= 1.410 x^{-1.40} - (2.430 \times 10^{-3}) x^{-.4} + (8.987 \times 10^{-7}) x^{.6} \\ n &= 1.40 \quad c = 736 \times 10^{-6} \end{aligned}$$

$$\begin{aligned} \text{(b)} \quad F(x) &= (6.122 \times 10^{-2}) x^{-.55} - (2.471 \times 10^{-4}) x^{.45} + (2.362 \times 10^{-7}) x^{1.45} \\ n &= .55 \quad c = 742 \times 10^{-6} \end{aligned}$$

$$\begin{aligned} \text{(c)} \quad F(x) &= (2.971 \times 10^{-5}) - (3.119 \times 10^{-8}) x + (8 \times 10^{-12}) x^2 \\ n &= 0 \quad c = 14.2 \times 10^{-6} \end{aligned}$$

The first equation was computed using the entire set of points. The second equation was computed using only the first seventeen points, and the last using the final fifteen points. (There are thirty points in all so the ranges of curves b and c overlap slightly.)

The problem of oscillation about the x -axis arises in all cases thus permitting only segments of these functions to be plotted as shown. The dotted line connecting curves b and c permits a continuous curve to be drawn through the data points.

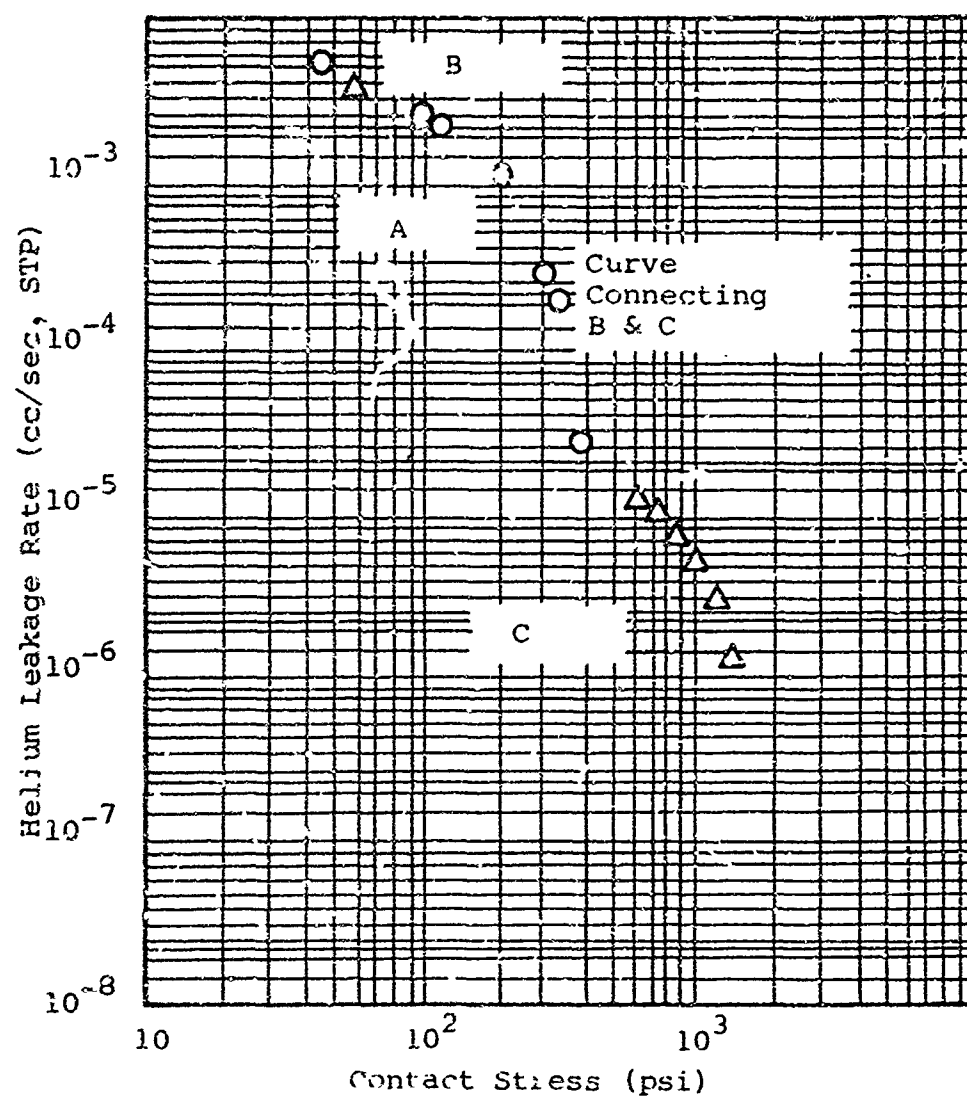


Figure VIII-6 Analytic functions at original points

Figure VIII-7 contains plots of the following analytical functions based upon the leakage ordinates after fifteen iterations of the alternating successive smoothing technique (see figure VIII-4):

$$(d) \quad F(x) = (7.265 \times 10^{-1})x^{-1.25} - (1.346 \times 10^{-3})x^{-.25} + (5.433 \times 10^{-7})x^{.75}$$

$$n = -1.25 \quad \sigma = 746 \times 10^{-6}$$

$$(e) \quad F(x) = (4.287 \times 10^{-2})x^{-.5} - (1.442 \times 10^{-4})x^{.5} + (1.166 \times 10^{-7})x^{1.5}$$

$$n = -.5 \quad \sigma = 795 \times 10^{-6}$$

$$(f) \quad F(x) = (2.639 \times 10^{-1})x^{-1.3} - (3.553 \times 10^{-4})x^{-.3} + (1.169 \times 10^{-7})x^{.7}$$

$$n = -1.3 \quad \sigma = 14.2 \times 10^{-6}$$

Again, the first equation used all the points; the second used the first eighteen points, and the third used the final fourteen points.

Considering the significant variations in the coefficients and exponents of the above six equations, it appears conclusive that the curve fitting technique for the analytic function defined by equations (VIII-9) and (VIII-11) cannot be counted upon to yield a single, or even two or three equations which would describe the functional behavior of the underlying physical phenomena. At best it seems that this computational technique is simply a more sophisticated smoothing process than the five point average parabolic fit method and could be developed along similar lines.

It is significant, however, that the standard errors of equations (a) and (d) are approximately equal. Both equations are based on all thirty points; (a) on the original points, and (d) on the points iteratively smoothed fifteen times. Furthermore, the standard error after the first smoothing is 350×10^{-6} , about one-half of the others. All errors are based upon the original points. Thus, it seems that the smoothing process not only converges in itself but defines a smooth curve representative of the data.

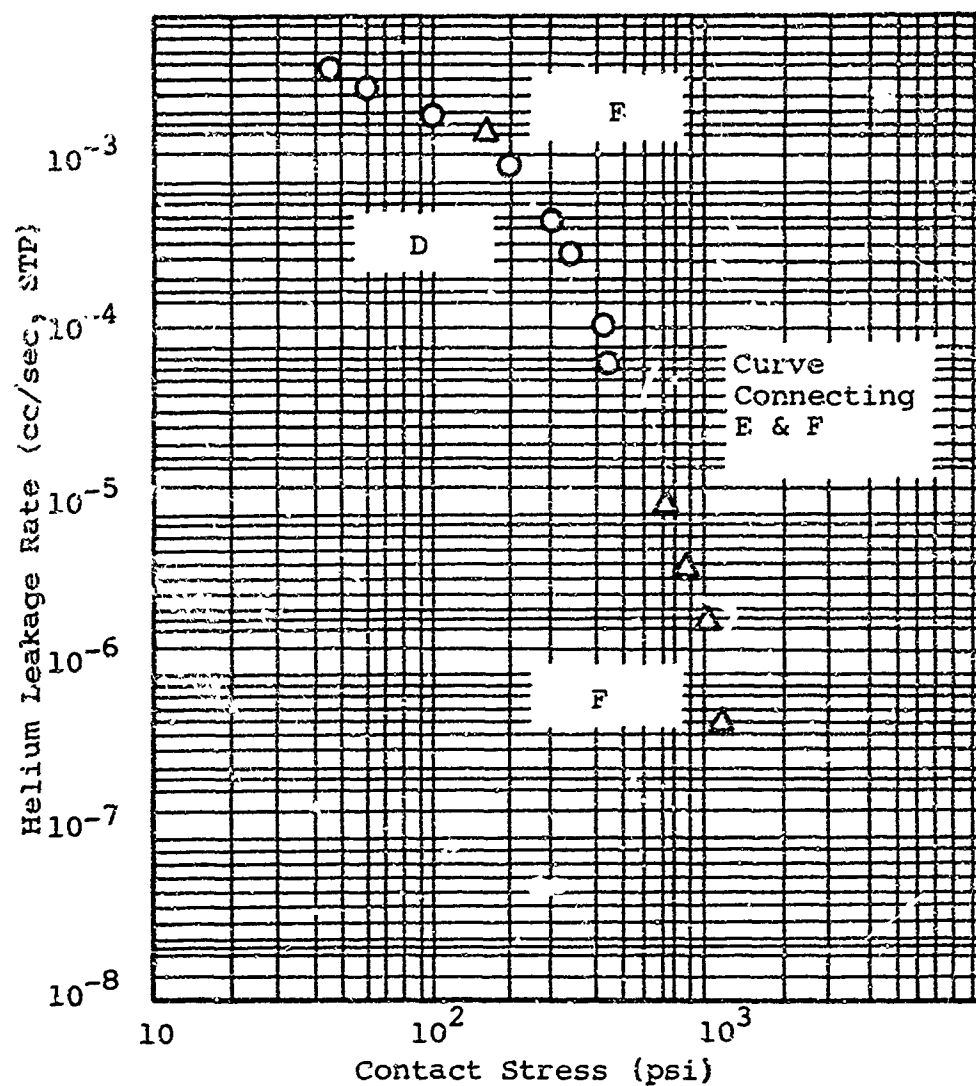


Figure VIII-7 Analytic functions based on smooth points iterated 15 times

UNCLASSIFIED

Security Classification

DOCUMENT CONTROL DATA - R&D		
<i>(Security classification of title, body of abstract and indexing an. This must be entered when the overall report is classified)</i>		
1. ORIGINATING ACTIVITY (Corporate author)		2a. REPORT SECURITY CLASSIFICATION
IIT Research Institute Chicago, Illinois		Unclassified
		2b. GROUP
3. REPORT TITLE		
INVESTIGATION OF LEAKAGE AND SEALING PARAMETERS		
4. DESCRIPTIVE NOTES (Type of report and inclusive dates)		
Final Report		
5. AUTHOR(S) (Last name, first name, initial)		
BAUER, Paul A.		
6. REPORT DATE	7a. TOTAL NO OF PAGES	7b. NO OF REFS
August 1965	678	140
8a. CONTRACT OR GRANT NO	9a. ORIGINATOR'S REPORT NUMBER(S)	
AF04(611)-4704	AFRPL-TR-65-153	
b. PROJECT NO	9b. OTHER REPORT NO(S) (Any other numbers that may be assigned this report)	
6753	K6062-FR	
10. AVAILABILITY LIMITATION NOTICES		
"Qualified requesters may obtain copies of this report from DDC."		
11. SUPPLEMENTARY NOTES		12. SPONSORING MILITARY ACTIVITY
		Air Force Propulsion Laboratory
<p>13. ABSTRACT: This report documents investigations conducted to expand and refine analytical techniques for static and dynamic seals. A systematic investigation was made on those aspects of a seal pertaining to the sealing interface, structure, cavity, and related parts. Since the sealing interface was the problem area most lacking in reliable and concise information, major effort was directed toward its study. The problem was approached both analytically and experimentally by independently studying sealing interfaces with and without gross relative motion. The parameters influencing static interfaces were identified as surface finish, applied load, contact area and material hardness. These parameters were correlated to form design criteria suitable for use by systems designers to predict seal leakage performance. Additionally, these parameters were studied for rubbing contact interfaces with wear added as the most significant parameter. The importance of wear on seal leakage was identified not as surface damage but as the effect of wear debris fragments and frictional heating. To the extent of experimentally supported information, all parameters were correlated in the form of design criteria. The output from these and other investigations produced applicable criteria and provided an insight into the relationship between parameters that can be used to optimize sealing and serve as guidelines for attaining minimum leakage. Commercial and other seals were utilized to show, by example, the design and analysis techniques leading to leakage performance predictions. The degree of success achieved was established by demonstration of experimental performance.</p>		

DD FORM 1473

UNCLASSIFIED

Security Classification

UNCLASSIFIED

Security Classification

KEY WORDS	LINK A		LINK B		LINK C	
	ROLE	WT	ROLE	WT	ROLE	WT
Seals						
Sealing Mechanism						
Seal Application						
Seal Analysis						
Environmental Effects on Seal						
Materials						
Seal Surface Finish						
Leakage Phenomena						
Fabrication Techniques						
Inspection Techniques						
Wear						

INSTRUCTIONS

1. **ORIGINATING ACTIVITY:** Enter the name and address of the contractor, subcontractor, grantee, Department of Defense activity or other organization (corporate author) issuing the report.

2a. **REPORT SECURITY CLASSIFICATION:** Enter the overall security classification of the report. Indicate whether "Restricted Data" is included. Marking is to be in accordance with appropriate security regulations.

2b. **GROUP:** Automatic downgrading is specified in DoD Directive 5200.10 and Armed Forces Industrial Manual. Enter the group number. Also, when applicable, show that optional markings have been used for Group 3 and Group 4 as authorized.

3. **REPORT TITLE:** Enter the complete report title in all capital letters. Titles in all cases should be unclassified. If a meaningful title cannot be selected without classification, show title classification in all capitals in parentheses immediately following the title.

4. **DESCRIPTIVE NOTES:** If appropriate, enter the type of report, e.g., interim, progress, summary, annual, or final. Give the inclusive dates when a specific reporting period is covered.

5. **AUTHOR(S):** Enter the name(s) of author(s) as shown on the report. Enter last name, first name, middle initial. If military, show rank and branch of service. The name of the principal author is an absolute minimum requirement.

6. **REPORT DATE:** Enter the date of the report in day, month, year, or month, year. If more than one date appears on the report, use date of publication.

7a. **TOTAL NUMBER OF PAGES:** The total page count shall follow normal pagination procedures, i.e., enter the number of pages containing information.

7b. **NUMBER OF REFERENCES:** Enter the total number of references cited in the report.

8a. **CONTRACT OR GRANT NUMBER:** If appropriate, enter the applicable number of the contract or grant under which the report was written.

8b. **PROJECT NUMBER:** Enter the project number, contract number, or other identifying number, such as project number, subproject number, system number, or task number, etc.

9a. **ORIGINATOR'S REPORT NUMBER(S):** Enter the official report number(s) which the document will be identified and controlled by the originating activity. This number must be included in this report.

9b. **OTHER REPORT NUMBER(S):** If the report has been assigned any other report number (other than the originator or the sponsor's), enter this number(s).

10. **AVAILABILITY LIMITATION NOTICES:** Enter any limitations on further dissemination of the report, other than those

imposed by security classification, using standard statements such as:

- (1) "Qualified requesters may obtain copies of this report from DDC."
- (2) "Foreign announcement and dissemination of this report by DDC is not authorized."
- (3) "U. S. Government agencies may obtain copies of this report directly from DDC. Other qualified DDC users shall request through _____."
- (4) "U. S. military agencies may obtain copies of this report directly from DDC. Other qualified users shall request through _____."
- (5) "All distribution of this report is controlled. Qualified DDC users shall request through _____."

If the report has been furnished to the Office of Technical Services, Department of Commerce, for sale to the public, indicate this fact and enter the price, if known.

11. **SUPPLEMENTARY NOTES:** Use for additional explanatory notes.

12. **SPONSORING MILITARY ACTIVITY:** Enter the name of the departmental project office or laboratory sponsoring (paying for) the research and development. Include address.

13. **ABSTRACT:** Enter an abstract giving a brief and factual summary of the document indicative of the report, even though it may also appear elsewhere in the body of the technical report. If additional space is required, a continuation sheet shall be attached.

It is highly desirable that the abstract of classified reports be unclassified. Each paragraph of the abstract shall end with an indication of the military security classification of the information in the paragraph, represented as (TS), (S), (C), or (U).

There is no limitation on the length of the abstract. However, the suggested length is from 150 to 225 words.

14. **KEY WORDS:** Key words are technically meaningful terms or short phrases that characterize a report and may be used as index entries for cataloging the report. Key words must be selected so that no security classification is required. Identifiers, such as equipment model designation, trade name, military project code name, geographic location, may be used as key words but will be followed by an indication of technical context. The assignment of links, rules, and weights is optional.

Best Available Copy
UNCLASSIFIED